Coarse-grained molecular simulations of interfaces between fluid formulations and soft biomimetic surfaces

A thesis submitted by

Erik Weiand

to

Imperial College London

for the degree of

Doctor of Philosophy (Ph.D.)

London, March 2024

Tribology Group

Department of Mechanical Engineering

Imperial College London

Abstract

A paradigm shift in the development of new hair and personal care products is required to keep up with increasing demands for more sustainable and biocompatible formulations while further pushing the boundaries of the product performance. Molecular modelling approaches are deemed a strong candidate for accelerating the early stage development of such new formulations.

This work introduces a new coarse-grained molecular dynamics framework for enabling the virtual screening of nanoscale hair friction and more generally soft surface friction for the first time. A new molecular model of the F-layer of human hair is presented and validated against new and existing structural and wetting experiments. Non-equilibrium molecular dynamics simulations are then coupled to preliminary squeeze-out simulations for an accurate load-dependent contact composition to screen the tribological performance of hair surfaces under varying degrees of chemical damage. Bare surfaces and surfaces with adsorbed small ionic compounds and polyelectrolytes commonly used in hair care products are considered. These simulations aim at uncovering new boundary lubrication mechanisms of cationic surfactants and oppositely charged polyelectrolyte-surfactant aggregates on healthy and damaged biomimetic hair surfaces which is beneficial for tuning the deposition behaviour of new formulations.

Finally, the developed methodology is implemented and expanded in an automation tool for high-throughput virtual screening of the nanoscale friction of soft surfaces such as cotton cellulose.

Acknowlegdements

I would like to thank my supervisors, Dr. James Ewen, Dr. Stefano Angioletti-Uberti and Prof. Daniele Dini at Imperial College for their invaluable support throughout the project and for introducing me to the world of molecular simulations. This work would not have been possible without them.

I am also grateful to Dr. Francisco Rodriguez-Ropero, Dr. Yuri Roiter, Dr. Peter König and Dr. Steven Page at Procter & Gamble (P&G) for many valuable and exciting scientific discussions and for introducing me to the world of personal care sciences. I would like to thank Dr. Yuri Roiter in particular for supporting this work with many new experiments. I would like to thank Dr. Carlos Amador and Dr. Husamettin Deniz Özeren at the P&G Newcastle Innovation Center for hosting me during a two-month work placement at P&G and for their collaboration on the automation of textile friction screening.

I also thank my colleagues in the Tribology group at Imperial College. It was a pleasure to meet and work with a team of so many friendly and open-minded people. I will also certainly remember many of the social activities and events hosted by the group. My sincere thanks also go to my friends Dr. Andrea Giusti and his group in Thermofluids at Imperial College for continuing our collaboration on computational fluid dynamics of nanofuels.

I thank the Engineering and Physical Sciences Research Council (EPSRC) and P&G for the financial support of my iCASE studentship as well as the Jost Foundation for funding my visit to the STLE Annual Meeting 2022. I am grateful for computational resources provided by the Imperial College London Research Computing Service (DOI: 10.14469/hpc/2232) and by the UK Materials and Molecular Modelling Hub, which is partially funded by the EPSRC (EP/T022213/1, EP/W032260/1 and EP/P020194/1). This work used the ARCHER2 UK National Supercomputing Service (https://www.archer2.ac.uk).

Most importantly, I thank my family and friends for always supporting me at all times during this journey.

Erik Weiand,
March 2024

Statement of originality

I hereby declare that the work carried out in this document is my own, except where acknowledged. All new model development and simulations shown in this work were carried out by the author in the Department of Mechanical Engineering, Imperial College London and at the P&G Newcastle Innovation Center.

No natural language processing or generative models were used for the production and proofing of this work.

Erik Weiand,
March 2024

Copyright statement

The copyright of this thesis rests with the author. Unless otherwise indicated, its contents are licensed under a Creative Commons Attribution-Non Commercial 4.0 International Licence (CC BY-NC).

Under this licence, you may copy and redistribute the material in any medium or format. You may also create and distribute modified versions of the work. This is on the condition that: you credit the author and do not use it, or any derivative works, for a commercial purpose.

When reusing or sharing this work, ensure you make the licence terms clear to others by naming the licence and linking to the licence text. Where a work has been adapted, you should indicate that the work has been changed and describe those changes.

Please seek permission from the copyright holder for uses of this work that are not included in this licence or permitted under UK Copyright Law.

Many of the surface models and input scripts for the molecular dynamics simulations described in this work can be found as repositories on my public Github profile:



Table of Contents

List of Figures 15

List of Tables 23

Nomenclature 25

1 Introduction 29

2 Understanding and controlling friction and adhesion between human hairs 33
2.1 Introduction 33
2.1.1 Structure of human hair 35
2.1.2 Wear and damage modes on hair 37
2.1.3 Hair care formulations 40
2.2 Experimental techniques 41
2.2.1 Macroscopic hair friction experiments 42
2.2.2 Nanoscale hair tribology experiments 50
2.2.3 Adhesion measurements 54
2.2.4 Wetting experiments 57
2.3 Computational techniques 61
2.3.1 Models of the human hair surface 61
2.3.2 Hair friction modelling 64
2.4 Hair friction mechanisms 65
2.4.1 Humidity & wetting effects 65
2.4.2 Hair damage 67
2.4.3 Scale-dependence of hair friction measurements 69
2.4.4 Influence of contact load & sliding velocity 72
2.4.5 Hair care formulations 73
2.5 Conclusions 78

3 Coarse-grained molecular models of human hair surfaces 81
3.1 Introduction 81
3.2 Methodology 82
3.2.1 Coarse-grained hair model 82
3.2.2 Coarse-grained liquid-phase models 84
3.2.3 MD simulation details 86
3.3 Experimental setup 88
3.3.1 Hair contact angle 88
3.3.2 Biomimetic surface contact angle 90

3.4 Results and discussion 90
3.4.1 Monolayer properties 90
3.4.2 Liquid droplet wetting 94
3.5 Conclusions 100

4 Nanoscale friction of biomimetic hair surfaces 103
4.1 Introduction 103
4.2 Methodology 104
4.2.1 MD System Setup 104
4.2.2 MD Simulation Details 106
4.2.3 Water Model Viscosity 107
4.2.4 Experimental Details 108
4.2.5 Contact pressure estimates 110
4.3 Results and discussion 113
4.3.1 Dry Contacts 113
4.3.2 Wet Contacts 118
4.4 Conclusion 129

5 Effects of surfactant adsorption on the wettability & friction of biomimetic surfaces 131
5.1 Introduction 131
5.2 Methodology 132
5.2.1 Surfactant bulk solutions 132
5.2.2 Surface properties 134
5.2.3 Surfactant adsorption 136
5.2.4 Friction 137
5.2.5 Contact angle 138
5.3 Results and discussion 138
5.3.1 Surfactant bulk self-assembly 138
5.3.2 Surfactant adsorption onto hair surfaces 140
5.3.3 Friction with adsorbed cationic surfactants 148
5.3.4 Wettability with adsorbed cationic surfactants 157
5.4 Conclusions 158

6 Boundary lubrication performance of PE-S complexes on biomimetic surfaces 161
6.1 Introduction 161
6.2 Methodology 162
6.2.1 Polyelectrolyte model 162
6.2.2 Atomistic MD simulations 164
6.2.3 Coarse-grained MD simulations 164
6.3 Results and discussion 170
6.3.1 CGG-SDS adsorption 170
6.3.2 Friction of hair with pure CGG 172

6.3.3 Friction of hair with CGG-SDS complexes 174
6.4 Conclusions 181

7 PE architecture effects on the lubricity of PE-S layers on biomimetic hair surfaces 185
7.1 Introduction 185
7.2 Methodology 186
7.2.1 Cationic guar gum model 186
7.2.2 Simulation protocol 188
7.3 Results and discussion 190
7.3.1 Effect of the polymer charge density 190
7.3.2 Effect of the polymer adsorption density 192
7.3.3 Towards friction screening with realistic CGG chains 195
7.4 Conclusions 202

8 Towards high-throughput friction screening in soft biomimetic contacts 203
8.1 Introduction 203
8.2 Surface model overview & validation 205
8.3 Workflow automation overview 208
8.3.1 Workflow description 208
8.3.2 Numerical details 211
8.4 Case study: model & fabric softener surfactants in cotton cellulose contacts 212
8.4.1 Overview 212
8.4.2 Squeeze-out & NEMD 214
8.5 Conclusions 225

9 Conclusions & outlook 227
9.1 Conclusions 227
9.2 Perspectives for hair and soft surface (nano)-tribology 229
9.3 Practical challenges 231

Bibliography 233

Appendix 271
A.1 Supplementary information for chapter 3 271
A.2 Supplementary information for chapter 4 276
A.3 Supplementary information for chapter 5 281
A.4 Supplementary information for chapter 6 284
A.5 Supplementary information for chapter 7 290
A.6 Supplementary information for chapter 8 291
A.7 Third-party permissions 296

List of Figures

2.1 Schematic representations of the hierachic structure of human hair and the cuticle substructures . . . 35
2.2 Structure of weakly damaged hair from scanning electron microscopy imaging . . . 36
2.3 F-layer damage mode due to hair bleaching . . . 38
2.4 Microscale surface charge and topography maps from scanning ion conductance microscopy and AFM respectively for untreated, bleached and conditioned hair . . . 39
2.5 Schematic overview of macroscopic experimental setups for hair friction 43
2.6 Schematic overview of experimental setups to investigate micro/-nanoscale hair friction: Sharp tip AFM, crossed hair AFM and chemical colloidal probe AFM . . . 50
2.7 Differential friction effect (DFE) on human hair arising from the anisotropic cuticle growth. α denotes the cuticle lift angle. . . . 51
2.8 Sharp-tip AFM friction measurements on virgin, damaged and conditioner-treated hair and for hair from different ethnic origins . . . 52
2.9 Lateral force signals from crossed hair-on-hair AFM friction measured in and against the direction of cuticle growth for the crossed hair-on-hair setup and for parallel fibres . . . 53
2.10 Coarse-grained non-equilibrium molecular dynamics simulations of F-layer contacts containing aqueous solutions with quaternized 3-deoxy-6-deoxy cellulose copolymers, CAPB, SLES and excess sodium chloride 64
2.11 Overview of relevant mechanisms influencing hair friction and therefore the tactile perception of hair. . . . 65
2.12 Relative kinetic coefficients of friction from experiments and simulations between untreated (virgin) and chemically damaged hair in ambient/dry conditions . . . 68
2.13 Relative change in friction forces when scanning 'against' the direction of cuticle growth compared to scanning 'along' cuticles from experiments . . . 70
2.14 Effect of 18-MEA removal on hair entanglement, appearance and perception . . . 71

3.1 Schematics of the coarse-grained *MARTINI* model of the hair surface. . 82
3.2 Snapshots of Cys-18-MEA lipid monolayers at different grafting distances 89
3.3 Snapshots of monolayers in vacuum from $\chi_S = 0$ to $\chi_S = 1$ . . . 91

3.4 Surface coverage ratio, χ_S, as a function of the number damage ratio, χ_N, for the CG hair surfaces in vacuum, water, and n-hexadecane 93
3.5 Circular surface fits of a water droplets on the (a) fully-functionalised, $\chi_N = 0$, and partially damaged, (b) $\chi_N = 0.5$, (c) $\chi_N = 0.85$, monolayers from the CG-MD simulations 95
3.6 Circular surface fits of a n-hexadecane droplets on the a) fully-functionalised ($\chi_N = 0$) and partially damaged (b) $\chi_N = 0.85$ and fully damaged c) $\chi_N = 1$) monolayers from the CG-MD simulations 95
3.7 Water droplet contact angle as a function of actual droplet volume and damage ratio χ_N 96
3.8 Change in the water and n-hexadecane contact angles on model hair surfaces with an increasing degree of random damage and snapshots of water and n-hexadecane droplets at low, medium, and high levels of damage 97
3.9 Cosine of the water contact angle from CG-MD at different degrees of damage and from experiments using silica wafer surfaces at various degrees of C_{18}/SO_3^- functionalisation 98

4.1 CG-MD configurations of squeeze-out systems in dry, wet contacts and sliding contacts for dry and wet contacts 104
4.2 Pressure versus load curves for virgin and damaged hair-on-hair contacts obtained from Hertz theory for a range of normal loads from 10 nN to 1 mN 111
4.3 Pressure versus load curves for biomimetic CCP-AFM using Hertz theory, JKR theory and the procedure presented by Perriot-Barthel 112
4.4 Dry contact monolayer mass density and velocity profiles at $v_s = 1$ m s^{-1} and $\sigma = 10$ MPa for different damage ratios, χ_N 114
4.5 Mean-removed shear stress signals, $\tau - \langle\tau\rangle = F_L/A - \langle F_L/A\rangle$, at $v_s = 0.1$ m s^{-1} for dry and wet systems 115
4.6 Dry COF as a function of sliding velocity v_s and monolayer damage at $\sigma = 10$ MPa in double logarithmic plots 116
4.7 Reference coefficient of friction μ_0, velocity v_0 and corresponding barrier distance d_0 and hopping rate constant k_0 from thermal activation model fits as a function of monolayer damage 117
4.8 Change in the number of water molecules per surface area and the contact thickness between the graphene sheets with time during the squeeze-out simulations at a pressure, $\sigma = 10$ MPa for hair surfaces with different χ_N 119
4.9 Mass density and velocity profiles for wet sliding simulations at $v_s = 1$ m s^{-1} and $\sigma = 10$ MPa at different degrees of monolayer damage 121
4.10 Wet COF as a function of sliding velocity, v_s, for the different damage ratios at $\sigma = 10$ MPa in double logarithmic representation 122

4.11 MSD and RDF of the central polarizable water beads at different sliding velocities and for pristine, virgin and medium bleached hair contacts . . 123
4.12 Ratio between wet and dry COF as a function of sliding velocity v_s and monolayer damage χ_N at $\sigma = 10$ MPa. 126
4.13 Shear stress, τ, as a function of normal pressure, σ, from wet NEMD simulations and biomimetic CCP-AFM experiments in water 128

5.1 Overview of free molecules and *MARTINI* bead types considered in this chapter 133
5.2 Snapshots of self-assembled micellar systems at equilibrium: CTAB at a) $c_0 = 120$ mM, b) $c_0 = 497$ mM and SDS at c) $c_0 = 174$ mM, and d) $c_0 = 664$ mM 138
5.3 Temporal evolution of micelle adsorption to hair surfaces for self-assembled and pre-assembled CTAB micelles 140
5.4 Top row: Equilibrium surface coverage Γ_e of CTAB and SDS on virgin and medium bleached hair surfaces as a function of the initial bulk concentration c_0 and the bulk concentration at equilibrium c_e. Bottom row: Equilibrium mass density profiles for systems with CTAB on virgin and d) medium bleached surfaces, and for systems with SDS on virgin and medium bleached surfaces 141
5.5 CTAB adsorption densities for initial counterion distributions either fully in the bulk or fully adsorbed on the surface 143
5.6 Density profiles of CTAB and ions at the medium bleached hair surface for initial counterion distributions on either the surface or in the bulk . . 143
5.7 Top row: CTAB adsorption densities fitted to a two-step Langmuir adsorption model for a) virgin and b) medium bleached model hair surfaces. Bottom row: Examples of instantaneous coverage fractions from selected points in the adsorption isotherms 145
5.8 Top row: SDS adsorption densities for virgin and medium bleached model hair surfaces. Bottom row: Examples of instantaneous coverage fractions from selected points in the adsorption isotherms 147
5.9 CTAB adsorption at different levels of excess salt concentrations ($c_s = c_{Na+} + c_{Cl-}$) for virgin (square-solid) and medium bleached model (circular-dashed) hair surfaces. 148
5.10 Snapshots of NEMD systems considered in this chapter at $\sigma = 10$ MPa . 149
5.11 Shear stress between hair surfaces with water and SDS at 10 MPa on virgin hair and bleached hair 149
5.12 Shear stress as a function of sliding velocity v_s for virgin and medium bleached hair surfaces with pure water and pre-adsorbed CTAB at low and high coverage at a constant normal stress of 10 MPa 151
5.13 Mass density ρ, charge density ρ_q and velocity profiles v_x for Cys-18-MEA and CTAB during sliding at $v_s = 1$ m s^{-1} for virgin hair and medium bleached hair 152

5.14 Mass density profiles for the Q_0 headgroup of cationic surfactants before compression, after compression for 10 ns and 70 ns, and during sliding simulations . . . 153
5.15 Coefficient of friction and the standard deviation of the shear stress signal ($\sigma = 10$ MPa) both at $v_s = 0.1$ m s^{-1} as a function of total surface coverage from the 18-MEA and cationic surfactants for surfaces representative of virgin and medium bleached hair . . . 155
5.16 Water contact angles for untreated and CTAB-treated hair surfaces as a function of CTAB coverage . . . 157

6.1 Chemical structure of guar hydroxypropyltrimonium chloride and corresponding coarse-grained architecture . . . 163
6.2 Polyelectrolyte-surfactant lubrication workflow consisting of sequential adsorption of CGG and then SDS, followed by squeeze-out simulations to determine the contact composition and finally NEMD simulations. . . . 166
6.3 Mass density profiles for virgin and medium bleached hair at the end of the SDS adsorption stage for a given guar adsorption density of $\Gamma = 0.04$ µg cm^{-2} . . . 170
6.4 Snapshots of NEMD simulations of virgin and medium bleached hair surfaces with CGG at $\Gamma = 0.04$ µg m^{-2}, sliding velocity of $v_s = 0.1$ ms^{-1} and a contact pressure of $\sigma = 10$ MPa . . . 173
6.5 Surface topography of pure CGG on virgin hair surfaces in the direction of sliding, x, and fast Fourier transform of the topography signals . . . 174
6.6 Temporal evolution of the root-mean-square displacement of CGG in virgin hair contacts in the direction of sliding at $\sigma = 10$ MPa and $v_s = 0.1$ ms^{-1} . . . 174
6.7 Shear stress as a function of the sliding velocity v_s at $\sigma = 10$ MPa for a) virgin and b) medium bleached hair surfaces with CGG and SDS . . . 176
6.8 Through-film mass density, charge density, and velocity profiles during sliding at $\sigma = 10$ MPa and $v_s = 1$ m s^{-1} for virgin and medium bleached hair . . . 177
6.9 Snapshots of hair contacts with CGG and SDS for virgin and medium bleached hair at normal stresses of $\sigma = 10$ MPa and $\sigma = 50$ MPa at $v_s = 0.1$ m s^{-1} . . . 179
6.10 Shear stress as a function of the normal load at constant sliding velocity of $v_s = 0.1$ ms^{-1} for virgin and medium bleached hair surfaces with CGG and SDS at variable composition and for pure water cases . . . 179
6.11 Through-film mass density profiles from NEMD of different normal stresses $\sigma = 20$-50 MPa on virgin and medium bleached hair at $v_s = 0.1$ m s^{-1} . . . 180

7.1 Snapshots of coarse-grained CGG chains with a fully random charge functionalization and a blocky functionalization from a first-order Markov chain model . . . 188
7.2 Snapshots of CGG at various charge densities, DS = 10%-100%, at the end of the CGG adsorption stage for virgin and medium bleached hair . 189
7.3 Coefficients of friction from NEMD of different charge densities on CGG with SDS on virgin and medium bleached hair at $\sigma = 10$ MPa and $v_s = 0.1$ ms^{-1} . . . 190
7.4 Mass densities profiles from NEMD of different charge densities on CGG with SDS on virgin and medium bleached hair at $\sigma = 10$ MPa and $v_s = 0.1$ m s^{-1} . . . 191
7.5 Snapshots of adsorbed CGG at $\Gamma = 0.12$ µg cm^{-2} and SDS at the hair interface . . . 192
7.6 CGG mass density profile at $\Gamma = 0.12$ µg cm^{-2} on virgin and bleached hair in the presence of SDS as a function of time . . . 193
7.7 Shear stress as a function of the guar adsorption density with SDS for virgin and medium bleached hair at $v_s = 0.1$ ms^{-1} and $\sigma = 10$ MPa. . . . 194
7.8 Through-film mass density, ρ, charge density ρ_q, and velocity, v_x profiles at $v_s = 1$ m s^{-1} for virgin and medium bleached hair at an elevated guar adsorption density . . . 195
7.9 Instantaneous mass density profiles for adsorbed CGG on virgin and bleached hair for various functionalization architectures at a CGG adsorption density of $\Gamma_0 = 0.26$ µg cm^{-2} (case VI) . . . 196
7.10 Evolution of the instantaneous CGG mass density upon addition of SDS for virgin and bleached hair at a CGG adsorption density of $\Gamma_0 = 0.26$ µg cm^{-2} (case VI) . . . 197
7.11 Mass density profiles for adsorbed CGG on virgin and bleached hair at two CGG forced deposition densities $\Gamma = 0.13$ µg cm^{-2} and $\Gamma = 0.26$ µg cm^{-2} . . . 198
7.12 Overview of the shear stress for virgin and bleached hair with sequentially adsorbed CGG-SDS complexes at more realistic CGG architectures and a sliding velocity of $v_s = 0.1$ ms^{-1} . . . 199
7.13 Snapshots of NEMD simulations for virgin and bleached hair with sequentially adsorbed CGG-SDS complexes at a sliding velocity of $v_s = 0.1$ ms^{-1} and a contact pressure of $\sigma = 10$ MPa . . . 200
7.14 Through-film mass density, ρ, charge density ρ_q, and velocity, v_x profiles at $v_s = 0.1$ m s^{-1} for virgin and medium bleached hair with more realistic CGG architectures . . . 200

8.1 Structure of cotton fibres . . . 204
8.2 Overview of the original cellulose I_β monomer and the refined model . 206
8.3 Wetting on smooth cellulose with the original cellulose model and the revised model for water and tetradecane . . . 207

8.4 Fused half-fibril model for nanocrystalline cellulose . . . 208
8.5 Overview of the nanoscale friction screening workflow. . . . 209
8.6 Cationic quat surfactant architectures considered for NEMD sliding simulations with corresponding coarse-graining parametrizations. . . . 212
8.7 Equilibrium molecule density per unit area of surfactants and water after squeeze-out as a function of the contact pressure for CTAB, DEEDMAC, DPEHEMS, and DOE . . . 214
8.8 Shear stress profiles as a function of the contact pressure at various initial compositions N_0 for CTAB, DEEDMAC, DPEHEMS, and DOE at v_s=0.1 ms^{-1} . . . 215
8.9 Friction coefficients μ and Derjaguin offsets τ_0 from fits of the extended Amontons-Coulomb law to the cotton-on-cotton contact shear stress data. . . . 216
8.10 Mass density profiles at different N_0 (cases II-V) for cotton-on-cotton contacts with four different surfactant types at $\sigma = 10$ MPa and $v_s = 0.1$ ms^{-1} . . . 218
8.11 Radial distribution functions at various initial surfactant concentrations in cotton-on-cotton contacts at $\sigma = 10$ MPa and $v_s = 0.1$ ms^{-1} . . . 218
8.12 Distribution of the molecule opening angle in hairpin surfactants during sliding . . . 219
8.13 Snapshots of full contacts and top views of lubricant films in cotton-on-cotton contacts with CTAB at various $N_0 = 100$, 400, 700, and 1000 at $\sigma = 10$ MPa . . . 220
8.14 Snapshots of full contacts and top views of lubricant films in cotton-on-cotton contacts with DEEDMAC at various $N_0 = 100$, 200, 350, and 500 at $\sigma = 10$ MPa . . . 220
8.15 Snapshots of full contacts and top views of lubricant films in cotton-on-cotton contacts with DPEHEMS at various $N_0 = 100$, 200, 350, and 500 at $\sigma = 10$ MPa . . . 221
8.16 Snapshots of full contacts and top views of lubricant films in cotton-on-cotton contacts with DOE at various $N_0 = 100$, 200, 350, and 500 at $\sigma = 10$ MPa . . . 221
8.17 Snapshots of CTAB at N_0=1000 and DEEDMAC at N_0=500 in sliding cotton-on-cotton contacts at $\sigma = 10$ MPa. . . . 222
8.18 Local order parameter for surfactants at different initial concentrations 223
8.19 Stick-slip tendency in contacts by means of the standard deviation of the friction signals around the mean. . . . 224

A.1.1 Water droplet contact angles on hair surfaces of various degrees of damage and C_1 and C_2 monolayer terminal beads with the original polarisable water model . . . 272

A.1.2 Projected lipid coverage on hair model surfaces in vacuum and with water and n-hexadecane as wetting fluids for different degrees of random damage χ_{N} . . . 273
A.1.3 Circular surface fits of a water droplets on monolayers with a grafting distance of $d_{\mathrm{graft}} = 0.49$ nm and $d_{\mathrm{graft}} = 0.65$ nm from the AA-MD simulations . . . 274
A.1.4 Water and n-hexadecane droplet contact angles as a function of number damage ratio χ_{N} compared to dynamic contact angle measurements for virgin hair and medium bleached hair . . . 275
A.2.5 Dynamic viscosity of bulk system of polarizable MARTINI water beads at $p = 1$ atm and $T = 300$ K and three different simulation box sizes and at different pressures with constant box size . . . 276
A.2.6 Average volume per CG bead in the region of interdigitation as a function of damage and barrier distance d_0 . . . 276
A.2.7 Absolute lipid tilt angles and orientational tilt angles relative to the direction of sliding for dry contacts as a function of sliding speed and surface damage. . . . 277
A.2.8 Top view snapshots of water structures confined between fully-functionalised hair surfaces ($\chi_{\mathrm{N}} = 0$) at sliding speeds of a) $v_s = 0.01$ m s^{-1}, b) $v_s = 0.1$ m s^{-1}, and c) $v_s = 1$ m s^{-1}. . . . 277
A.2.9 Top view snapshots of water structures confined between hair surfaces representative of virgin hair ($\chi_{\mathrm{N}} = 0.25$) at sliding speeds of a) $v_s = 0.01$ m s^{-1}, b) $v_s = 0.1$ m s^{-1}, and c) $v_s = 1$ m s^{-1}. . . . 277
A.2.10 Absolute lipid tilt angles and orientational tilt angles relative to the direction of sliding for wet contacts as a function of sliding speed and surface damage. . . . 278
A.2.11 Wet friction fitting parameters . . . 278
A.2.12 Water-lipid interfacial area, approximated as the perimeter of each water droplet penetrating the contact down to the thioester bond of the 18-MEA/cysteic acid residues multiplied by the thickness of such structures . . . 279
A.2.13 Counterion mobility by means of MSD$_y$ and MSD$_z$ and RDF as a function of the sliding velocity . . . 279
A.2.14 CCP AFM friction forces as a function of normal force for biomimetic surfaces in water . . . 280
A.3.15 Mass density profiles for water and for lipids - comprised of both Cys-18-MEA and CTAB during sliding simulations for various v_s, degrees of hair damage χ and CTAB coverage Γ . . . 281
A.3.16 Mobility fraction of cationic sites on CTAB for virgin and medium bleached hair surfaces at various degrees of surfactant coverage during sliding . . . 282

A.3.17 Mean-square-displacement in the y direction (MSD_y) and z direction of cationic sites on CTAB for virgin and medium bleached hair surfaces at various degrees of surfactant coverage during sliding 282
A.3.18 Distance between the charged cysteic acid groups on the two opposing surfaces for virgin and bleached model hair surfaces 283
A.3.19 Nematic order of cationic sites on CTAB for virgin and medium bleached hair surfaces at various degrees of surfactant coverage during sliding 283
A.4.20 Guar gum bond distributions from atomistic and coarse-grained simulations 287
A.4.21 Guar gum angle distributions from atomistic and coarse-grained simulations. 287
A.4.22 Guar gum radius of gyration as a function of molecular weight from CG-MD simulations and from experiments 288
A.4.23 Temporal evolution of the contact thickness during squeeze-out at $\sigma = 10$ MPa with CGG and SDS on virgin and medium bleached hair model hair surfaces 289
A.4.24 Through-film charge density profiles from NEMD of different normal stresses $\sigma = 20 - 50$ MPa on virgin and medium bleached hair at $v_s = 0.1$ m s^{-1} 289
A.5.25 Mass density profiles of the 18-MEA, guar, SDS and water at the end of the a) single-surface adsorption stage, b) squeeze-out stage, and c) NEMD stage on virgin hair. The 18-MEA density profiles are only partially shown for clarity. The dehydration and compression of the guar layer occurs during squeeze-out (from a) to b)). No strong change in the guar hydration and layer thickness is observed during NEMD simulations. 290
A.6.26 Cationic quat surfactant architectures considered with corresponding coarse-graining parametrizations. 291
A.6.27 Distribution of surfactant orientations relative to the surface-normal direction z for CTAB, DEEDMAC, DPEHEMS and DOE at various initial concentrations N_0 295

List of Tables

3.1 Surface tension for water-vapor and water-hexadecane interfaces for different CG water models and reference experimental and simulation values . . . 85
3.2 Contact angle data on fully-functionalised hair from CG-MD and reference AA-MD and experimental advancing and receding contact angle data for virgin hair . . . 97
3.3 Experimental advancing and receding contact angle data for medium bleached hair . . . 97
3.4 Contact angle data from CG-MD for the C_1 type terminal lipid beads at various degrees of random lipid damage . . . 99

4.1 Properties of single coarse-grained molecular and experimental model surfaces. . . . 108
4.2 COF and Derjaguin offset from wet NEMD simulations in pristine, virgin, medium bleached and ultimately bleached hair contacts. . . . 127

5.1 Surface properties of virgin and medium bleached hair models. . . . 135
5.2 Aggregation numbers of surfactant micelles as a function of the bulk concentration in charge-neutral systems without excess salt. . . . 139
5.3 Overview of friction coefficients from linear fits with respect to the normal stress and water contact angle for model surfaces representative of virgin and medium bleached hair . . . 155

6.1 Overview of the contact composition used in the NEMD simulations on virgin and medium bleached hair surfaces . . . 175

7.1 Overview of test cases for the CGG architecture parameter study . . . 187
7.2 Contact composition in NEMD simulations on virgin and medium bleached hair surfaces with larger CGG chains at DS = 30%. . . . 198
7.3 SDS content within the layer of adsorbed CGG on a single hair surface before preliminary squeeze-out. . . . 201

8.1 Contact angles obtained with the original and revised cellulose model compared to all-atom wetting simulations . . . 206
8.2 Overview of discrete pre-equilibrated surface oxidation levels for the rough cellulose surface model . . . 208
8.3 Overview of system parameters for automated cotton-on-cotton friction screening with cationic surfactants relevant in fabric softeners. . . . 212

8.4 Overview of simulation test cases with different initial cationic surfactant content N_0. 212

A.1.1 Fully-functionalised monolayer structure and wetting data for all-atomistic, coarse-grained MD cases and comparison to reference AA-MD data for 18-MEA 274

A.2.2 Number of water molecules ($4 \cdot N_{\mathrm{w,CG}}$) per surface area $N_w A^{-1}$ for different normal loads and levels of hair damage. Units are in nm^{-2}. 280

A.3.3 CG water surface densities in the contact at the end of the squeeze-out simulations with pre-adsorbed CTAB as a function of normal pressure σ, hair damage and CTAB adsorption density Γ 281

A.4.4 MARTINI 2 bead type definitions for CGG. 284

A.4.5 Pol-MARTINI 2 non-bonded Lennard-Jones parameters for CGG. 285

A.4.6 CGG MARTINI 2 bond parameters. 286

A.4.7 CGG MARTINI 2 angle parameters. 286

A.6.8 MARTINI 2 bead types definitions for DEEDMAC. 291

A.6.9 CGG MARTINI 2 bond parameters for DEEDMAC. 291

A.6.10 CGG MARTINI 2 angle parameters for DEEDMAC. 292

A.6.11 MARTINI 2 bead types definitions for DPEHEMS. 292

A.6.12 CGG MARTINI 2 bond parameters for DPEHEMS. 292

A.6.13 CGG MARTINI 2 angle parameters for DPEHEMS. 293

A.6.14 MARTINI 2 bead types definitions for DOE. 293

A.6.15 CGG MARTINI 2 bond parameters for DOE. 293

A.6.16 CGG MARTINI 2 angle parameters for DOE. 294

Nomenclature

Acronyms

Symbol	Description
18-MEA	18-methyleicosanoic acid
AA	All-atom
AFM	Atomic force microscopy
CCP	Chemical colloidal probe
CG	Coarse-grained
CGG	Cationic guar gum
CMC	Critical micelle concentration
COF	Coefficient of friction
CPAB	Cocamidopropyl dimethylamine
CTAB	Cetrimonium bromide
DEEDMAC	Diethyl ester dimethyl ammonium chloride
DOE	Dioleoyl dimethylammonium chloride
DPD	Dissipative particle dynamics
DPEHEMS	Dipalmitoylethyl hydroxyethylmonium methosulfate
DS	Degree of substitution
FFM	Friction force microscopy
GCMD	Grand-canonical molecular dynamics
IBI	Inverse Boltzmann inversion
JKR	Johnson-Kendall-Roberts contact theory
LJ	Lennard-Jones
MD	Molecular dynamics
MSD	Mean square displacement
NEMD	Non-equilibrium molecular dynamics
NPT	Isothermal-isobaric ensemble
NVE	Microcanonical ensemble
NVT	Canonical ensemble
PE	Polyelectrolytes
PPPM	Particle-particle particle-mesh
QCM-D	Dissipative quartz crystal microbalance
RDF	Probability density function
RDF	Radial distribution function

RH	Relative humidity
RMSD	Root mean square displacement
SCFT	Self-consistent field theory
SDS	Sodium dodecyl sulfate
SEM	Scanning electron microscopy
SFA	Surface force apparatus
SLES	Sodium laureth sulfate
SPM	Scanning probe microscopy
TOF-SIMS	Time-of-fight secondary ion mass spectrometry
VMD	Visual Molecular Dynamics (Software)
XPS	X-ray photoelectron spectroscopy

Greek Symbols

Symbol	Description
χ	Damage ratio
ε	LJ well depth
Γ	Adsorption density
γ	Surface tension, surface energy
$\varkappa$	Wavelength
λ	Correlation parameter
ρ	Density
σ	Normal stress, LJ van-der-Waals radius
τ	Shear stress
Θ	Contact angle

Roman Symbols

Symbol	Description
$\mathcal{L}$	Domain side length
A	Surface area
c	Concentration
D	Diffusion coefficient
d	Distance, thickness
e	Elementary charge
F	Force
f	Frequency, target degree of substitution
g	Radial distribution function
k	Bonded potential harmonic constant
L	Fibril width
M	Molecular weight

N	Number of beads, molecules
P	Probability matrix, ordering parameter
p	Pressure, conditional probability
R	(Charge) ratio)
r	Radius
T	Temperature
v	Velocity, molecule vector

1 Introduction

Human hair is a fibrous material which is present in most of our everyday lives. As such, it is subject to natural influences, such as humidity, sunlight and pollution and artificial manipulations. Hair styling is often seen as an expression of individuality. Many therefore subject their scalp hair to artificial treatments that go beyond cutting, such as dyeing, bleaching, waving and perming. Both natural weathering and artificial treatments can induce damage to the the hair fibre. At the same time, a clean appearance and sensory pleasant feeling of softness on hair is seen as desirable. Hair care treatments therefore represent a way of protection or mitigation of common fibre degradation mechanisms. Today, the world market for personal care products has evolved into what was a 430-billion-dollars [a] worth of retail sales in 2022, with further projected growth up to 580 billion dollars until 2027.[1]

Ancient hair and skin treatments made use of naturally-sourced ingredients such as clay[2] or even olive oil.[3] With increasing consumer demands on the functionality of hair care products, the formulation chemistry has considerably grown in complexity compared to ancient natural products. A closer look at the label of modern hair care products such as a popular commercial anti-dandruff shampoo [b] will typically reveal no less than ten different ingredients. Up to 30 ingredients are conceivable in some instances.[4] This is a results of years of formulation development[5] of products which aim to fulfil more than a simple cleansing or conditioning role. Cleansing, i.e., the removal of dirt, excess fats and pollutants as well as conditioning are the two primary roles of typical hair care products. Perfuming and an appropriate texture for good handling are also desirable. Furthermore, foaming agents, viscosity modifiers, pH balancing agents, preservatives, opacifiers and sequestering agents are commonly present in modern hair care products[6,7] to improve their visual appearance, longevity and universal performance under different external conditions and water qualities. Anti-dandruff shampoos furthermore contain active ingredients for effective scalp treatment.[6]

On the other hand, societal and environment-focused transformations demand for greener and more sustainable care products. The need for a reduction of the carbon, wastewater and more generally pollutant footprint requires re-imagining the product lifecycle. This includes replacing components sourced from mineral oil by returning to naturally-sourced alternatives. Furthermore, specific care product components such as phosphates are problematic due to the post-use wastewater contamination[8] and

a US dollars

b Head & Shoulders® (P&G): https://www.headandshoulders.co.uk/en-gb/ingredients/ (accessed 11 January 2024)

should therefore be substituted. The many commercially available shampoos also still contains sulphate-based surfactants as a cleansing base which can be perceived as harsh by consumers with sensitive hair or skin. The substitution by suitable alternatives is therefore also in the consumers' interest. Even silicones and cationic polyelectrolytes which still form the conditioning basis for many hair care formulations have been found to be difficult to remove from wastewater.[9,10] Replacing those potentially environmentally and dermatologically harmful components is an integral task for today's formulations and researchers in personal care. While the transformation towards greener care products has already begun, it has also been recently highlighted that consumers are unlikely to tolerate a degradation in the product performance when replacing these impactful components.[10] This presents a fundamental challenge in formulation design and the underlines need for both fundamental and applied research in bulk product chemistries and hair surface sciences.

The conditioning performance of a product is one handle which will likely determine the success of new formulations among consumers. Trüeb defines hair conditioning as the role of a product to 'maintain the natural condition of newly grown hairs for as long as possible'.[6] This underlines the lack of self-repair mechanisms which are commonly found in other parts of the human body but cannot occur in the dead hair fibre upon its exfoliation from the root. As a consequence of conditioning, hair should appear shiny, should easily detangle and have a pleasant *soft* tactile perception. Hair which easily detangles will have a superior combing performance.[11] Both detanglement and tactile performance are inherently linked to hair friction and adhesion, which fall under the more general field of *hair tribology*. Tribology constitutes the surface sciences related to friction, lubrication and wear.[12] While tribology is often associated with mechanical engineering disciplines such as transportation and power generation, its relevance for soft substrates and smaller scales is of equal importance. Years of work in the field of *biotribology* have led to uncovering a wide range of mechanisms and technological advances in areas such as total joint replacements,[13,14] or skin ageing[15] just to name a few. It is therefore not surprising that fundamental and applied tribology research is also applied in personal care product development.

As will be reviewed thoroughly later in this work, the evaluation of the combing and sensory performance of hair care products has historically relied on macroscopic experimental techniques. In the past 25 years, nanoscale experiments have also more and more contributed to gaining mechanistic insights about the handles which influence the tribology of human hair. However, some fundamental questions remain yet to be answered and represent the the principal *motivations* for the outlined work:

1. **How do changes in the surface roughness and surface chemistry of hair affect friction?** Some studies suggest that the chemistry might indeed play an important role,[16] particularly when considering hair at different degrees of damage. Other studies have also attributed friction increases to changes in the surface

roughness.[17]

2. **What are the relevant handles for tuning hair friction for an optimum sensory perception and superior detangling performance?** The investigation of small scale friction mechanisms on hair is becoming more and more of a focal point in formulation design and is expected to provide valuable design guidelines to future formulators. This knowledge could also be a key factor in benchmarking new biocompatible and more sustainably sourced biomolecules for hair care formulations.
3. **How can complex formulations containing oppositely charged molecules be fine-tuned for a favorable lubrication performance?** One mechanism in many modern shampoos is the dilution deposition of so-called coacervates to the hair surface.[18,19] The lubrication mechanisms of deposited complexes constituting of oppositely charged molecules on hair are however not clearly understood to date.

Computational models lend themselves to being a capable extension or even candidate for replacing some of the laboratory hair tribology evaluation techniques. Molecular simulations in particular allow for resolving nanoscale structures and system dynamics that are impossible to obtain even with the highest resolution of nanoscale probing techniques. Molecular dynamics (MD) simulations allow for capturing both bulk and interfacial phenomena which has led to its widespread popularity in the field of tribology and lubricant design.[20] The use of coarse-graining, i.e., the grouping of several atoms into larger blocks - so-called 'beads' - has enabled access to even larger time and length scales in MD.[21] Thus, they are ideally suited for investigating nanoscale effects of surface chemistry on both equilibrium and non-equilibrium phenomena and can potentially help explaining some of the macroscopic observations at interfaces. Additionally, the development of a robust and efficient computational framework for the screening of nanoscale hair tribology could accelerate the formulation design process. This would also open up the potential to screen a wide range of new, biocompatible formulations with respect to their hair friction performance.

The fundamental *objectives* of this work are therefore defined as follows:

1. **Evaluate the feasibility of coarse-grained molecular simulations for studying hair friction.**
2. **Uncover the fundamental nanoscale mechanisms of hair friction in the presence of care products.**
3. **Enable molecular simulations as a tool for rapid tribological screening of existing and new bio-derived hair care products.**

The methods and workflows presented in this work are also expected to be directly transferable to other soft surfaces such as skin and textiles. This enables opportunities to screen the tribological performance of other consumer and home care products such as fabric softeners which will be considered towards the end of this work.

This manuscript is outlined as follows: This chapter is followed by a thorough review of hair tribology in chapter 2. This will cover the relevant background on the structure of human hair, the functions and deposition of hair care formulations and most importantly the state-of-the-art experimental and computational hair tribology literature. We will also discuss the known handles to influencing hair tribology. Chapter 3 introduces and validates a new coarse-grained molecular model of the outer layer of human hair at various degrees of hair damage. This is followed by four chapters in which the molecular mechanisms of hair friction and product deposition are investigated using both equilibrium and non-equilibrium molecular dynamics (NEMD) simulations. Specifically, chapter 4 considers the friction between two bare hair surfaces under dry and wet conditions at various levels of chemical hair damage. The adsorption of ionic and particularly cationic surfactants for conditioning to hair and their effect on nanoscale hair friction are discussed in chapter 5. The role of more complex formulations on hair friction fulfilling both cleansing and conditioning purposes is investigated for the case of oppositely charged polyelectrolyte-surfactant complexes. Both boundary-lubricated (chapter 6), thicker layers and different polyelectrolyte architectures (chapter 7) are considered. Towards the end of this work, the scope of the coarse-grained MD methodology developed in the first part is expanded to other soft substrates such as cotton cellulose in context of the nanoscale lubricity of fabric softeners. Specifically, an automated high-throughput screening framework for nanoscale friction simulations with small molecules on soft surfaces is presented, validated and applied in chapter 8. Finally, this work's findings and discuss future perspectives in the field of hair tribology and more generally soft surface tribology will be highlighted in chapter 9.

2 Understanding and controlling friction and adhesion between human hairs

The content of this chapter is in preparation for submission as a review article to Advances in Colloid and Interface Science.

2.1 Introduction

Biotribology, the study of friction, wear and lubrication in biological systems,[13] plays a central role in our everyday lives.[22] For example, the feeling when we touch, brush or comb our hair is affected by the friction between the hairs, as well as between hair and the polymers that are commonly used for the brush and comb prongs.[23] The surface of hair is covered by a scaly layer of overlapping cuticle cells, which are approximately 0.5 μm high and 5 μm long.[23] The microscale roughness due to the cuticle edges leads to characteristic stick-slip friction behaviour.[17,24] When healthy hair is brushed or combed conventionally (from root to tip), the cuticles and friction is relatively low.[22] However, when hair is combed in the opposite direction (from tip to root), a ratcheting mechanism from the cuticle edges can lead to much higher friction.[25] This is known as the differential friction effect (DFE), which has also been reported for other keratinous fibres, such as wool.[26] The DFE is more pronounced at high relative humidity,[27] or when the hair is chemically damaged by bleaching,[28] which has been attributed to lifting of the cuticle edges. Bleaching also leads to increased hair friction through other non-topological nanoscale effects. In particular, bleaching damages the protective 18-methyleicosanoic acid (18-MEA) monolayer on the outer surface of the cuticle, which can lead to dramatic increases in friction.[29]

Hair is composed of dead cells that mostly contain α-keratin protein and cannot be repaired through biological means. Therefore, the only way to restore the low-friction properties of damaged hair is to physically repair it by depositing compounds onto the hair surface from conditioners or other care products.[30] In many instances, the reduction of hair friction and adhesion is desirable for styling and combing hair.[31] Low hair friction is particularly beneficial for avoiding hair entanglement[31] and for providing a pleasant sensory perception[32] and high combability.[33] The development of hair care products that maintain low hair friction after rinsing requires insights from the nanoscale to the macroscale of both the hair fibre and the hair care formulations. This is because factors such as surface roughness, surface chemistry, deposition and aggregation are relevant across all these scales. A wide range of experimental techniques has been applied to measuring the friction of hair sliding against various materials. Moreover, experiments have focused on providing structural insights into

the hair surface and its interactions with hair care ingredients. Although hair has been found to deform even metallic materials such as steel,[34] it is still a relatively soft and thin fibrous material, which can make surface characterization experiments difficult.[35] Computational methods, such as molecular dynamics simulations, have become an integral tool for studying the nanoscale structure and friction of human hair[36] and will likely gain even more popularity.

On the other hand, the development of the next generation of hair care products is driven by customer demands for an improved product performance and regulatory and societal requirements for more sustainable, environmentally-friendly formulations.[10] It is becoming increasingly important to improve biocompatibility and biodegradability by replacing common hair care ingredients derived from crude oil, sulfates, and silicones with surrogates produced from natural sources.[10] At the same time, consumers expect the product performance, e.g., the cleansing efficiency, look and feel of hair to not degrade, or to even improve.[10] Achieving such a compromise requires an understanding of all relevant scales of soft surfaces – from the nanoscale (chemistry, structure) to the macroscale (look, feel).

The review presented in this chapter aims at providing a historic perspective of the available tools and learnings in the realm of hair tribology. First, the physio-chemical details, structure of human hair and damage modes are introduced, as they are important to the understanding of hair tribology. Then, an overview of both macroscopic and nanoscale experimental techniques for measuring hair friction and adhesion will be given. Theoretical and numerical models such as molecular dynamics (MD) simulations and continuum approaches will be discussed subsequently, as they have become a cornerstone in hair care development in recent years. This first part of this work will follow a linear, mostly chronological fashion to adequately capture and honor the developments in hair tribology across the years. In the second part of this chapter, the contributions from experimental and numerical studies are put into context to review and discuss of the relevant mechanisms that affect hair tribology and the appropriate handles for tuning it.

It is worth noting that this review will primarily focus on the tribology of hair and how hair care formulations such as shampoos and conditioners can affect it. There are additional important factors in the design of hair care products such as cleansing, perfuming performance and formulation sustainability that are out of scope for this work but are discussed in detail elsewhere, for instance by Luengo and co-authors.[5,10] Luengo et al.[37] also reviewed aqueous lubrication concepts in cosmetics. Bhushan[31] and Luengo et al.[38] also previously highlighted experimental techniques, particularly atomic force microscopy (AFM), to investigate the nanoscale properties of hair and the role of conditioners at this scale. Tokunaga et al.[39] recently reviewed degradation of the hair surface, with focus on the epicuticle and the 18-MEA monolayer. While some of the work

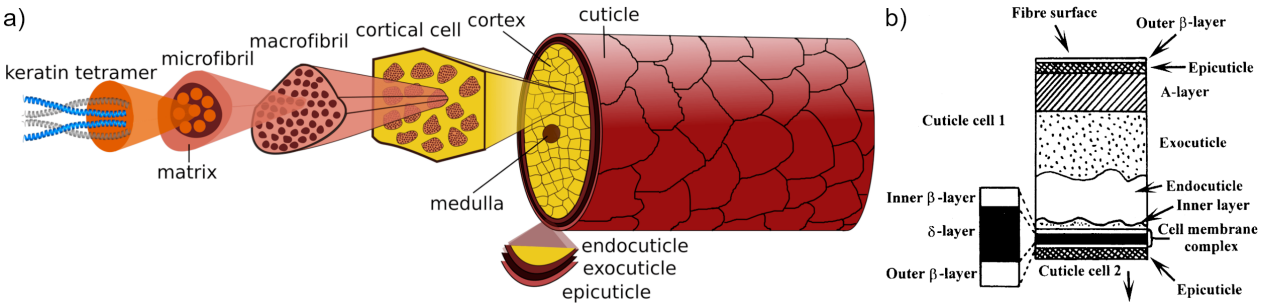


Figure 2.1: Schematic representations of (a) the hierachic structure of human hair and (b) the cuticle substructures. (a) Reprinted from Ref.[40] licensed under a CC-BY 4.0 license. (b) Reprinted from Ref.[41] with permission from Wiley.

in these areas are relevant for tribology and will therefore be covered here as well, this chapter also extends to macroscopic hair tribology experiments, computational models and significant new advances in nanoscale hair tribology in the last 15 years.

2.1.1 Structure of human hair

The human hair is a complex biological and hierarchical structure formed by several characteristic building blocks. The diameter of scalp hair is typically reported in the range of 50-100 µm.[5,42,43] A narrower range of 60-80 µm for scalp hair was also reported.[44] A schematic representation of the hierarchical structure of hair due to Cruz et al.[40] is given in Fig. 2.1(a). The majority of the mass in hair is contained in keratin fibres in the cortex giving rise to its elasto-mechanical properties.[45] Additional hollow cells, the so-called medulla, can be found in the core region of thicker hair.[46,47] The cortex consists of macrofibrils, which themselves contain rod-like microfibrils surrounded by a matrix.[47] The matrix contains amorphous cysteine-rich polymers.[48]

A noteworthy characteristic of hair and other mammalian fibres is their tendency to swell in the presence of water, as first highlighted by Astbury and Woods in 1933 by means of X-ray screening.[49] This observation was further confirmed by Wolfram[44] who observed similar swelling and water absorption for pristine hair and hair damaged by either dying, bleaching or alkaline-relaxation. An increase in humidity resulted in a strong decrease in Young's modulus due to the increased water content in the keratineous matrix.[44,50] Popescu and Höcker[50] highlighted another interesting property of the hair fiber: while being hygroscopic, i.e., sensitive to absorbing water in humid environment, the surface of healthy or *virgin* hair is hydrophobic. This is due to additional protective layers surrounding the cortex which are discussed below. Seshadri and Bhushan[45] investigated the effect of damage and conditioning on stress-strain curves of hair. No significant differences were found among the configurations. These findings supported the hypothesis that deformation and elasticity properties of dry hair are mainly governed by the cortex, which is typically not strongly affected by chemical or mechanical damage.

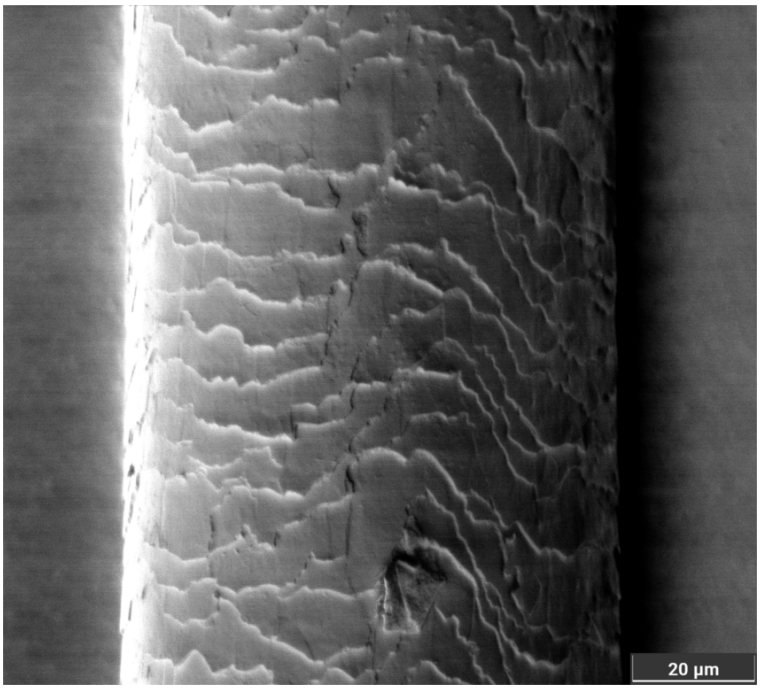


Figure 2.2: Structure of weakly damaged hair from scanning electron microscopy (SEM) imaging obtained at a beam energy of 0.5keV (TESCAM). Courtesy of Marie-Louise Schlichting (Imperial College London).

The cortex of human hair is covered by overlapping cuticle cells,[51] which serve as a protective layer. The anisotropic, scale-like orientation of the cuticles in the root-tip direction is depicted in Fig. 2.2 which results in a directional dependence of hair friction.[52] The cuticle cells themselves consist of several characteristic layers. The original cuticle model due to Swift and Smith[41] is depicted in Fig. 2.1(b). A cell membrane complex (CMC) provides separation and adhesion between overlapping cuticle cells.[44] The outer layers of the cuticle are of particular interest in hair tribology as their chemical composition and structure are responsible for the surface characteristics of hair. The epicuticle and outer β-layer are largely constituent of cysteine residues.[53] The existence of the epicuticle layer has been reported in many studies, e.g., Refs.[41,54,55] but is not universally accepted. Recent evidence from AFM measurements due to Breakspear et al.[56] suggests that the outmost layer of of the cuticle (β-layer in their work) is directly connected to the A-layer and an epicuticle is not required. Some open questions remain on the formation processes of some of the cuticle layers which have been discussed elsewhere[57] but are not expected to be highly relevant to hair tribology.

It is well-accepted that a fatty acid monolayer, consisting of covalently bound 18-MEA molecules, covers the cuticle cells in healthy hair.[29,53,58] This *F-layer*,[59,60] is grafted to the cysteine-rich proteins in the epicuticle via thioester bonds.[61] The existence of the 18-MEA on the hair surface has been highlighted in many studies.[5,39,58,62–64] The first systematic evidence of the F-layer on the surface of mammalian fibres was provided by Evans et al.[62] in 1985 by chemical extraction of the lipids from wool fibers. Jones and Rivett[58] predicted a disordered structure of the fatty acids due to the additional methyl branch of the 18-MEA which differentiates it from its linear sibling, the eicosanoic acid

($C_{20}H_{40}O_2$). This results in additional resistance from environmental influences.[58] The intact 18-MEA monolayer also gives rise to the strong hydrophobicity of virgin hair.[44,58] The exact organization of lipids on the epicuticle has been subject to discussion in the past. Both a closely packed monolayer[29,65] and more disordered structures[66–68] have been considered. Based on nanoscale adhesion experiments,[68] a heterogeneously ordered structure of the 18-MEA with patches of the exposed proteins is presently favored.[5]

Recent experimental investigations using AFM and X-ray photoelectron spectroscopy (XPS)[39] indicate a decrease in 18-MEA content on the hair surface from root to tip. These findings are consistent with earlier hypotheses by Kamath et al.[69] who predicted weathering to lead to a non-uniform chemical composition of the hair from root to tip. McMullen and Kelty[70] highlighted the existence of micropores on hair which would only become visible in AFM imagery when bleaching or solvent-extracting hair. It was assumed that these pores where not a result of the chemical bleaching routine but rather a natural feature of human hair. Furthermore, specific hair manipulations and damage modes can also have an effect on wear and and the hair chemistry and will be discussed next.

2.1.2 Wear and damage modes on hair

Several hair damage modes have been identified in the literature. Damage to the internal hair structure, i.e., to the cortex, can occur from waving[71,72] and UV radiation from the sun.[73,74] The degradation of the F-layer can occur through dying, bleaching, rubbing, combing or UV exposure.[74] Rare conditions such as Maple Syrup Urine Disease (MSUD)[75] or monilethrix may also affect the hair fibre health but are rare in comparison to damage from hair manipulations and weathering.[76,77] The structural damage from weathering of untreated hair was found to be highly heterogeneous due to the non-uniformity of the external effects acting on the cuticles as they move away from the root of the hair over time.[78] Additionally, the overlapping nature of the cuticles leads to a higher exposure to wear near the tip of the cuticles. Increased polarity was found in this region in surface potential measurements[79] hinting at a reduced fatty acid coverage. For long hair, prolonged weathering can also lead to cuticle fracture, lifting or complete cuticle cuticle cell delamination.[77] This shows that the length of hair is typically directly linked with the degree of weathering due to longer exposure to external influences.

Hair which has not been treated artificially is commonly referred to as *virgin* hair in the literature. LaTorre and Bhushan define virgin hair as 'having an intact cuticle and absence of chemical damage'.[17] However, virgin hair may also show a degree of wear or mechanical damage quantifiable in typical experiments.[17] Heavy combing was found to strongly impact the cuticle structure across the scales, including microscopic damage such as holes in the cuticle and exposing parts of the endocuticle.[80] Both the

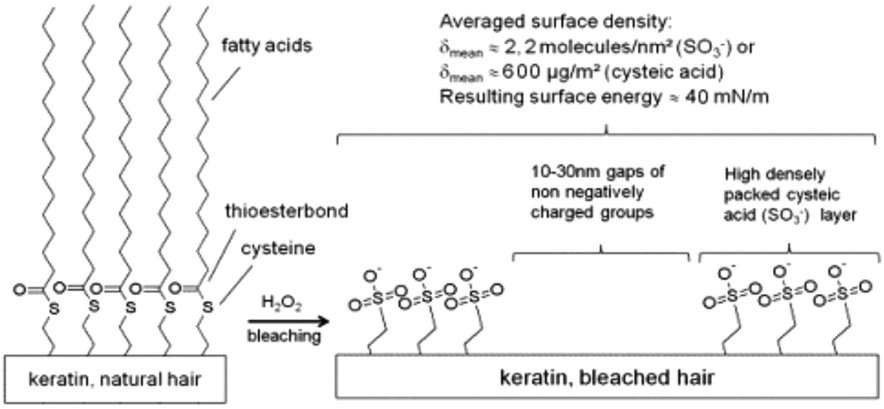


Figure 2.3: F-layer damage mode due to hair bleaching. Reprinted with permission from Ref.[92] © 2014 American Chemical Society.

interactions between hairs and the comb as and hair-hair interactions were found to be relevant mechanisms for hair breakage due to combing.[81] The process of combing hair results in mechanical stress on the hair fibers, which can cause damaged cuticles to flake and strip away.[80] This is known as delamination[25] and can even lead to exposure of fresh cuticles with intact 18-MEA monolayers.[82] Severe bending and exposure to sun can also induce fracture, splitting and cuticle delamination on the hair fibre.[83] The UV irradiation process can also result in the formation of small bumps (up to 5 nm height) on the cuticle surfaces.[84] Air pollution and cigarette smoke further induce measurable chemical damage of hair cuticles affecting both the wetting and combing resistance of hair fibres.[85] Variations in hair breakage and mechanical damage can also be a result of different hair styles and morphological fibre differences among ethnic groups. McMullen et al.[86] reported differences in mechanical properties, lipid content and fracture between hairs of African and Caucasian origin. Under strain, lifting of cuticles was found to be more pronounced in Caucasian than Asian hair, while undamaged African hair was more prone to fracture than Caucasian hair.[87] It is common to classify hair characteristics by the above three ethnic groups: African, Asian and Caucasian.[17,86,87] However, more refined classifications have also been proposed recently to account for more regional diversity.[88–91]

Hair bleaching is particularly impactful with regard to changes in the hair morphology as it induces chemical damage to the outer layers of the epicuticle.[29,93,94] Both mechanical and chemical damage or a combination of both can lead to partial and even complete removal of the 18-MEA monolayer.[63,64,93] Masukawa et al.[93] further reported a strong sensitivity of the 18-MEA content on hair with the number of bleaching treatments which is expected due to the lack of any natural repair mechanism. The depletion of surface lipids results in a more hydrophilic behavior due to the exposure of the polar proteinaceous structure and oxidation to negatively charged sulfonate groups.[5,92] A schematic of the F-layer damage due to bleaching is shown in Fig. 2.3 due to Korte et al.[92] Tokunaga et al.[39] highlighted an important mechanism in hair upon the removal of the 18-MEA from the cuticle: in the wet state water spreads more

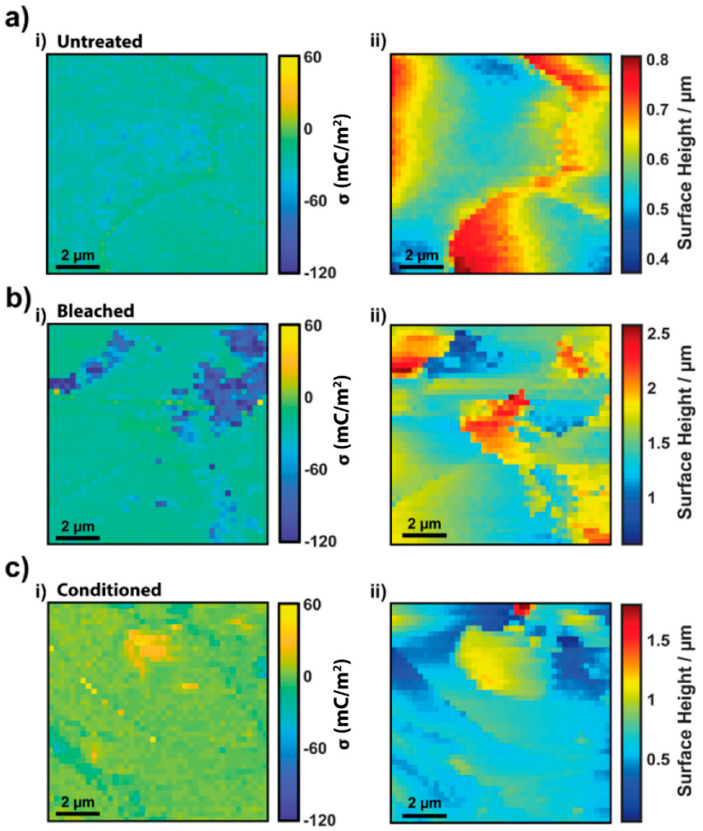


Figure 2.4: Microscale surface charge and topography maps from scanning ion conductance microscopy and AFM respectively for (a) untreated, (b) bleached and (c) conditioned hair. Reprinted with permission from Ref.[99] © 2019 American Chemical Society.

easily between hairs due to the reduced hydrophobicity. This was found to increase entanglement after drying compared to virgin hair.[39] Ageing also affects the composition of the hair surface. Both the external and internal lipid content have been found to decrease in older individuals[95] and in grey hair as a result of ageing, which made hair more permeable.[96] Ethnicity also seem to play a role for the location of damage on hair fibers during ageing: weathering damage on African-American hair was found to occur closer to the root than in Asian and Caucasian hair.[97] Bloch et al. also noticed that curly hair was more prone to chemical damage from thermo-mechanical treatments due to a higher mechanical resistance.[98] This was expected to affect hair of African origin more severely due to a higher occurrence of curliness. Higher combing forces in African hair were also attributed to mesoscale differences in the characteristic lengthscales of curls.[98]

The experimental techniques to quantify the degree of hair damage constitute chemical composition measurements of the hair surface,[39,96] surface energy or contact angle experiments,[100] surface charge,[92,99] or direct imaging and topography methods.[93] Surface charge maps for virgin, bleached and conditioned hair are shown in Fig. 2.4 due to Maddar et al.[99] These approaches also present a valuable references for setting up and validating new numerical models for hair tribology which will be discussed later in this review. Indirect indications of fibre damage can also be obtained from combing

and friction force measurements on single hairs or bundles, which will be reviewed later in this chapter.

2.1.3 Hair care formulations

Hair care formulations play a integral role in the modification of hair tribology. It is therefore important to first discuss the relevant surface deposition mechanisms associated with such formulations before reviewing their tribological implications later. Here, a brief overview of the most important components of shampoos and conditioners with respect to their tribological performance is provided. More detailed reviews of the different components found in these formulations can be found elsewhere.[4,6,101,102] A typical shampoo is composed of 10 to 30 different ingredients.[6] Cleansing and conditioning are among the primary roles of most hair care products.[6] Additionally functionality, such as anti-dandruff treatment by the addition of active ingredients, may further contribute to formulations.[6] Cleansing, i.e., the removal of dirt, excess lipids and sebum is typically achieved through an anionic surfactant base in shampoo formulations.[4,102] Another important role of anionic surfactants is to increase the viscosity of the product,[102] which they achieve through the formation of worm-like micelles.[103] Conditioning is defined as the effort to restore the surface and bulk properties of healthy hair,[6] as the fibres are exposed to prolonged external damage and wear. This is typically associated with an effective detangling performance, facilitated combing,[4] as well as a visually appealing look and sensory pleasant feel.[31] Hair conditioning can be performed either directly by applying standalone conditioners after the wash or by deposition of relevant conditioning molecules from a 'two-in-one' shampoo. Standalone hair conditioners typically contain functional molecules in the form of cationic surfactants, cationic polymers, fatty alcohols and silicones.[31,104] Such conditioners usually exist in single-phase conformations, such as lamellar gel networks.[105–107] The efficacy of conditioning products from aqueous solution is a result of the adsorption of molecules from the formulation during the application. Cationic surfactants and polymers effectively deposit onto hair due to available negative surface charges. On chemically damaged hair, more cationic surfactants adsorb due to an increase in cysteic acid residues as more of the hydrophobic F-layer is oxidized.[108] The adsorption of conditioners onto hair has been studied extensively in the past and can span from single molecules lying flat on hair to the deposition of monolayer, bilayers and compact aggregates.[109,110]

The addition of cationic polymers to a shampoo with an anionic cleansing base might not only be desirable for conditioning purposes but also as viscosity modifiers.[10] A central mechanism in contemporary shampoos is the dilution-induced or 'precipitation-enhanced'[111] deposition of conditioning molecules such as cationic polymers[112–114] and silicones[115,116] to hair. This mechanism founds on a phase transition from a single-phase solution during application into a two-phase region in the phase diagram during rinsing.[111] The baseline shampoo will typically contain

polyelectrolytes and surfactants in concentrations where where the polyelectrolytes are neutralized by micellar pinning, also referred to as 'string of beads'[117] or 'pearl-necklace structures'.[118,119] Additionally, free micelles are prevalent in solution. This is therefore referred to as the 'resolubilized region'[113] in the phase diagram. During rinsing, the surfactant concentration then decreases which leads to the formation of precipitates (dense viscous phase or 'coacervate').[118,120] These precipitates contain high concentrations of polyelectrolyte-surfactant complexes and favorably deposits to the hair surface, thus providing a conditioning effect during the rinse.

On charged surfaces such as hair, the competition between anionic surface sites, polycation charges, anionic surfactants, counterions and possibly excess salt complicates robust predictions of the deposition behaviour.[121] The ratio between the polyelectrolyte and surfactant concentration is one of the main control parameters determining the conformation of complexes and films adsorbed on surfaces. Svensson et al.[122] observed a strong local maximum in the film thickness and adsorption density for cationic polysaccharides with SDS on hydrophilic silica. This maximum was found to occur at similar surfactant concentration as phase separation in bulk solution. It was therefore suggested that bulk turbidity measurements could be a suitable tool to predict adsorption of polyelectrolyte-surfactant complexes onto surfaces.[122] On the other hand, dilution-induced swelling experiments of oppositely charged polyelectrolytes and surfactants via quartz crystal microbalance (QCM) showed strong differences in surface adsorption between petroleum-derived polymers and bio-inspired derivatives despite a similar behaviour in bulk solution.[111,114] Additionally, a wide range of precipitation regimes in solution have been observed in the literature,[122] further underlining the inherent complexity associated with the design of such formulations. Recently, dilution deposition has seen a increase in research interest as more sophisticated but also more sustainable formulation designs are explored.[114,121,123–125] Thermodynamic models to describe such processes in bulk[126,127] and on substrates[128,128–130] have also recently become available. Further in-depth reviews of polyelectrolyte-surfactant complexation and deposition are provided elsewhere.[113,118,119] The known effects of oppositely charged polyelectrolyte-surfactant complexes on hair tribology will be discussed later.

2.2 Experimental techniques

The evolution of hair tribology experiments shows a clear trend from early macroscopic and mesoscale friction devices to nanoscale friction microscopy and colloidal probe techniques. Early hair friction studies stem from methods to assess wool friction in the context of textile industry applications, such as felting. A relevant selection of early wool friction works will therefore also be briefly reviewed. The focus is then shifted towards macroscopic hair tribology studies and the advances in nanoscale hair friction. Adhesion and wetting experiments at all relevant lengthscales will also be reviewed.

2.2.1 Macroscopic hair friction experiments

a) Early friction experiments of mammalian fibres

Historically, physical experiments have been the driving force in determining the tribological properties of hair. Early experiments (1930s and 40s) of the friction of wool fibres,[131–142] which show a close physiological resemblance to human hair fibres,[143] paved way for systematic hair friction studies. Speakman and co-workers[131,132] provided some of the earliest scientific reports on the resistance to extension of wool fibres under load in the context of industrial wool milling processes. Their work already suggested a 'scaly' fibre structure based on macroscopic water-submerged friction experiments. Gralén and Olofsson[136] measured the static and dynamic friction between two dry wool fibres using a crossed fibre friction meter and observed an anisotropic behaviour (differential friction effect - DFE)[26] in the friction coefficient depending on the direction of motion. Mercer and Makinson[134,137] used a modified version of an experimental setup devised by Bowden and Leben[144] to record temporal friction signals on wool. Friction measurements were carried out between a straight hair and sheep horn and confirmed an anisotropic behaviour in dry and wet environment, although stick-slip events were more pronounced in the dry state. A molecular orientation mechanism was proposed as a potential explanation for the anisotropic friction behaviour.[133] However, the observations could be better explained by the overlapping, scale-like nature of wool cuticles, as observed from early electron microscopy imagery.[145] This 'ratchet mechanism' was also supported by directional friction measurements of metal-coated wool fibres[135] and systematic variations in the contact roughness of wool sliding against a flat secondary substrate.[138]

By carrying out macroscopic friction measurements on wool fibres, Frishman et al.[139] also noted that by nature, there is a wide variability in the friction coefficient (COF) of wool. In the same study, the authors observed a consistently higher COF of wet wool fibres compared to the dry state. Frishman et al.[139] conducted further wet hair friction experiments and reported a lower variability in hair friction forces compared to wool which was correlated with a reduced felting efficiency of hair compared to wool. Lindberg and Gralén[140] developed an alternative 'fibre twist' method where two fibres would be wrapped around each other in several turns to increase the area of contact and therefore the robustness of friction measurements. Their results confirmed the directional dependence of wool friction with reduced variability and clear adherence to the extended Amontons-Coulomb law as initially proposed by Derjaguin:[146,147]

$$F = F_0 + \mu \cdot F_L. \tag{2.1}$$

Wool friction was also found to increase after chemically treatment, e.g., with potassium hydroxide in ethanol (KOH)[141] and chlorine.[142] Treatment with soaps containing sodium oleate were found to reduce the friction of the chemically damaged wool fibres.[142] Grosberg[148] devised a new theory that DFE in wool was due to the anisotropic

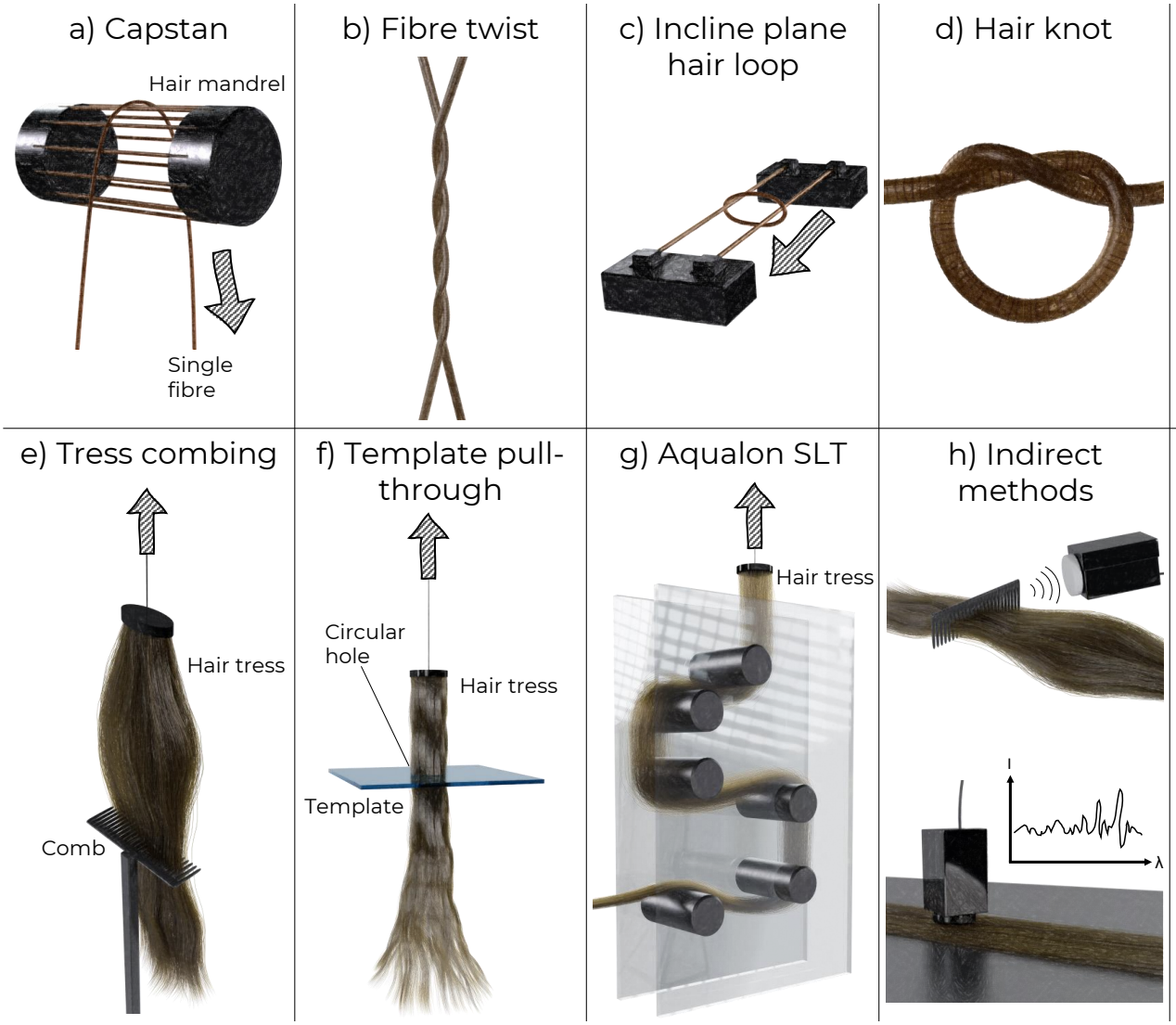


Figure 2.5: Schematic overview of macroscopic experimental setups for hair friction (not to scale). Individual fibre tests (top row): (a) Capstan test,[150,151] (b) Fibre-twist method,[140] Incline plane loop,[152] Hair knot setup[153] Tress test (bottom row): (e) Tress combing,[154] (f) Template pull-through setup,[155] (g) Aqualon SLT,[156] and (h) indirect methods using acousic emissions[157] and Diffuse Reflectance Near-Infrared Spectroscopy (NIR-DR).[158] Inspired by Refs.[140,150–154,156–158]

elastic properties of moist keratin. Later work by Flanagan[149] showed that no DFE was observed for wool if the counter-fibre had a radius greater than about 40 µm.

b) Friction between individual hair fibres

Many of the initially observed tribological characteristics of wool and measurement devices for textile fibres are also transferable to hair tribology. A schematic overview of historically popular macroscopic measurement techniques for hair tribology is presented in Fig. 2.5. The experimental setups involving bundles of hair will be discussed in the next section. Schwartz and Knowles[151] used a friction meter (*capstan* method), originally developed for textile fibres due to Röder,[150] to study the static and dynamic friction of hair-hair contacts and single hair fibres in contact with a wide range of different comb materials. The *capstan* method involves a single hair fibre

wrapped around a cylindrical mandrel of different materials, including an array of hair fibres, as depicted in Fig. 2.5(a). The dynamic hair-on-hair and comb-on-hair friction coefficients obtained from this method were found to be consistently higher in wet than in dry hair. The authors further reported a strong increase in hair-on-hair friction due to bleached and waving, while the application of conditioner formulations led to a restoration low friction on bleached and waved hair.[151] Scott and Robbins[159] applied a modified version of the *capstan* method to perform a comprehensive study of the effect of different ionic surfactants and background electrolytes on hair-comb friction at various degrees bleaching with hydrogen peroxide and ammonia.

Adams et al.[160] used a crossed fibre setup between two hairs to compare hair treated with CTAB versus hair contacts fully wetted by water. Miyamoto et al.[161,162] recently compared how ionic polymer-surfactant hair care formulations could be effective at reducing both the average friction coefficient on hair and stick-slip behaviour characteristic of bleached hair. Remarkably, their mesoscale setup allowed for deriving a relatively detailed model of the expected nanoscale deposition of polymers and oppositely charged polyelectrolytes and surfactants which will be discussed later. Moreover, macroscopic single fibre tests are capable of capturing mesoscale heterogeneities in hair. Typically, hair damage and 18-MEA content in the F-layer is increased at the fibre tip which has been exposed longest to external manipulations and wear.[39] Single hair high-load *capstan* test friction measurements of hair at various positions on the fibre showed an average 23% increase in friction force from root to tip when measured against the direction of the cuticles.[163] When measured in the direction of cuticular growth, no clear trend was observed by the authors.

The 'fibre twist' method due to Lindberg and Gralén[140] as shown in Fig. 2.5(b) was later also applied to measure hair-on-hair friction and the corresponding effects of chlorine treatments.[164] Chlorine treatment of hair was accompanied by not only an increase in both the mean static and kinetic friction coefficient, but moreover by an increase in the stick-slip amplitude in the friction signals. At elevated number of chlorine treatment cycles or high chlorine concentrations, the cuticle structure was visibly damaged as evident from scanning electron microscopy (SEM) measurements.[164] The authors further attributed the increase in friction accompanied by a visibly smoother surface to a softening effect of the cuticle structure. Chevalier[153] recently proposed an easily-repeatable measurement technique building on the previous 'fibre twist' works in Refs.[140,164] In this work, hair friction was evaluated by means of tying a knot in a single hair fibre as shown in Fig. 2.5(d). The technique accurately captured the previously observed trends in the mean and variation of friction coefficient in dry, wet and conditioner-treated hair.[153] Dussaud and Fieschi-Corso[152] introduced an 'incline plane hair loop' friction measurement setup in which a single hair fibre was taught and dragged along two parallel hairs. This setup was then used to measure the lubrication performance of silicones for different hair types and formulations.

c) Hair tress friction & combing work

A wide range of macroscopic hair friction measurement techniques involve the use of hair bundles, or so-called *hair tresses* or *swatches*, as depicted in Fig. 2.5(e-h). Direct measurements of hair tress combing work were first conducted by Newman and colleagues.[154] They measured the resistance of already-detangled hair bundles dragged along a mounted comb. The method was able to pick up the quantitative combing force increase of wet compared to dry bundles and subsequent friction reductions due to conditioning of the wet bundles. High friction in wet hair was attributed to the swelling of the fibres due to water uptake and inter-fibre capillary forces.[154] In a similar tress combing rig designed to purposely eliminate the effect of hair entanglement using a double comb setup, Kamath and Weigmann[33] investigated the direct effects of treatments and different levels of humidity on friction between hair bundles and the comb. They found that moderate levels of humidity led to combing work reductions, possibly due to aqueous lubrication, while artificial wetting resulted in strong interfibre forces, consistent with Ref.[154] The existence of such strong capillary forces were later measured directly on model hair brush experiments.[165]

Jachowicz[166] measured an increase in combing forces of few hundred percent for dry and wet hair treated with oxidative dye compositions. They hypothesised that the most damaging effect of the dye compositions on the properties of hair was the formation of dye deposits on the fiber surface, which they suggested could considerably increase the frictional coefficient and, consequently, combing force.[166] They showed that this problem could be circumvented by the post-dyeing application of suitable conditioners.[166] This observation implies that it was the oxidative properties of the hair dye (similar to bleaching[167]) that led to the increase in combing work, rather than deposition of dye compounds on the hair surface.

Garcia and Diaz[168] developed a similar tress combing measurement device to that of Newman et al. Their setup did not include any preliminary detangling step or pre-combing device to achieve a more realistic comparison with natural hair. Hair tresses were mounted on a tensile tester to measure the average and peak combing work under different treatment conditions. A range of commercial shampoo and conditioning products were ranked with regard to their effect on wet and dry hair tress (peak) combing work compared to either untreated or bleached baseline tresses. The authors highlighted the particular efficiency of quaternary ammonium surfactants in reducing the wet friction on bleached hair.[168] A setup lending from the rig due to Garcia and Diaz was used by Robbins and Crawford[155] to measure the work required to pull a hair tress through a circular holes of various diameters in plastic templates, see Fig. 2.5(f). The authors uncovered a linear relationship between the resisting work and the template diameter which was used to extrapolate to a 'zero work' diameter. This quantity was interpreted as a measure of *hair body*, which Robbins and Crawford defined as the 'apparent thickness or volume of an assembly of hair'.[155] While the

method could not distinguish the effects of different selected shampoo formulations on hair body, an increase in the zero work diameter of tresses was found with increasing curliness (curvature) of hair tresses.[155] Robbins and Reich further used the the method due to Garcia and Diaz to study the combing work of dry and wet hair tresses at different treatment conditions and related the combing work to different properties of the single hair fibre.[169] They reported a strong increase in macroscopic hair friction with increasing hair curvature and noticeable decreases in combing work with increasing fibre stiffness. Changes in fibre diameter were however not regarded to be particularly influential on tress combing work. The work further highlighted the mechanical properties that tend to influence hair friction and combing work at the mesoscale. Additionally, the effect of hair treatment with oily substances was found to contribute to a favorable detanglement of fibres and thus generally lower combing work.[169] An extension to the traditional tensile tester setup was presented by Vaynberg and Nall.[156] In the presented setup, named *Aqualon SLT* and shown in Fig. 2.5(g), a hair tress was pulled through an arrangement of PTFE-coated pins using a tensile tester while recording the resisting work.

Hair tress combing experiments have also been used to systematically investigate the effect of specific components in hair care productions on combing force and hair friction. The effect of conditioning agents such as silicones,[152,170] free fatty acids,[171] cationic surfactants[172] and cationic polymers[112,173] on combing work and hair friction has been studied extensively using the tensile tester setup. Cationic compounds are of particular interest because they favorably adsorb on hair to form a protective layer, which is particularly desirable on chemically damaged hair. Tress combing experiments are also suitable for screening the tribological performance of more complex hair care formulations which aim to fulfill multiple functions such as cleansing and conditioning.[112,173] Hössel et al.[112] used wet combing experiments to benchmark different petroleum-based and bio-sourced cationic polyelectrolytes with anionic surfactants (sodium laureth sulfate, SLES) with regard to their combing force reduction on bleached hair tresses.

An advantage of macroscopic tress friction and combing experiment is that they are suitable to screen hair friction at a high throughput. This is highly beneficial for benchmarking different hair care products by their frictional response. This is also true for other noteworthy alternatives to direct single fibre and tress combing friction measurements such as acoustic emissions from combing[157,174] and tress friction prediction using near-infrared diffuse reflectance[158] shown in Fig. 2.5(h). Waggoner and Scott[157] processed acoustic signals emitted from combing pristine and bleached hair tresses to obtain a qualitative measure of the hair 'raspiness' (or roughness). However, later Garcia and Diaz[168] later commented on the method to complicate the combing work measurement through an intermediate step of sound emissions. More recently, analyses of the acoustic emissions from stroking between dry hairs and skin have been used to

investigate the surface properties of hair.[175] However, details of the underlying tribological mechanisms are typically not directly accessible from macroscopic setups. This is particularly true when hair surface chemistry and small-scale structures play a dominant role on hair friction. It is possible to gain further insights to tribological mechanisms influencing these macroscopic friction experiments by coupling them to complementary surface or bulk formulation characterization experiments. Gao et al.[100] for instance related combing work reductions on conditioner-treated hair to surface energy measurements from dynamic wetting experiments. Benhur et al. furthermore compared the rheology of oppositely charged polymer-surfactant conditioning shampoos to changes in combing force reductions.[176] For direct insights into the small-scale features and associated tribological mechanisms, tools from the realms of nanoscale experiments and simulations are more appropriate. These will be discussed in depth further below.

d) Skin-on-hair friction

While the hair detanglement performance is closely associated with hair-on-hair and comb-on-hair friction, it is also important to consider the skin-on-hair contact in the context of hair tribology. This is because the sensory (or tactile) perception of hair softness is a direct outcome of the skin-on-hair interactions during rubbing and touching of hair with the human finger. Both direct tactile evaluations by sensory panels[23,32,177–179] and friction experiments with either in-vivo skin[32,180] or an artificial skin probe [27,181–184] fall under the category of skin-on-hair friction.

Sensory panel tests allow for a direct evaluation of the tactile perception by either an untrained or trained panel. Panels can provide valuable insights to formulation designers on how a specific care product's performance will be perceived by customers in the absence of external product attributes such as marketing, pricing and packaging. The human finger is capable of perceptually distinguishing surfaces varying in roughness levels down to the nanoscale[185] and even changes in surface chemistry.[186] Pleasant sensory perception has been linked to low friction for a wide range of materials.[186,187] Tanamachi et al. related the sensory perception of moisture evaluated from panel tests to the temperature drop induced by evaporation cooling on hair.[177] They reported a clear effect of the temperature drop on the perception of moisture. This is a somewhat different interpretation to the previously discussed hypothesis of reduced (inter-fibre) friction due to lubricating effects as described by Kamath and Weigmann.[33] Tanamachi et al. also reported a consistent effect of hair surface damage due to alkali treatment on the perceived dryness. This was attributed to a more pronounced macroscopic fibre entanglement caused by the 18-MEA removal.[188] In trained panel tests, Bloch et al. assessed various attributes of virgin and damaged hair tresses.[178] The score for the attribute 'smoothness' which is linked to the friction between skin and hair was found to be higher (smoother) for untreated hair compared to damaged tresses. However, the subjective assessment of combability was found to be little affected by artificial

damage modes and only increased in UV-damaged (weathered) hair.[178]

One of the few in-vivo studies investigating the interactions between skin and hair with respect to tactile friction and sensory properties was carried out by Zeng et al.[32] In this work, participants rubbed their finger against a hair bundle which was fixed on a force and torque transducer. Virgin, bleached and permed hair as well as virgin hair treated with various silicon-based and silicon-free conditioner products were considered. The in-vivo methodology and complementary sensory evaluations could clearly and consistently distinguish between the different hair treatments and hair care formulations applied. Interestingly, a decrease in the friction coefficient by means of the shear force was observed with increasing normal load. This suggests a departure from the extended linear Amontons-Coulomb law which is typically fulfilled in hair-on-hair contacts.[16,17] The authors attributed this behaviour by the strong viscoelasticity of skin resulting in a non-linear dependence of the friction force as a function of the normal load, as reported in previous skin friction work.[189] It was further reported that the wet macroscopic friction coefficient would decrease after hair bleaching, which is not in line with other macroscopic and nanoscale studies which considered various materials of the second substrate (skin, hair, AFM tip etc.).[16,27,183] One reason for this discrepancy may be the lack of exact control over the applied normal loads and sliding velocities which were controlled by rubbing a human finger against the hair. Conversely, the measured friction coefficient in dry contacts moderately increased upon bleaching.[32] Kawasoe et al.[180] introduced an in-vivo setup in which participants rubbed their finger against a macroscopically flat polyimide surface mimicking the roughness features of hair cuticles at different feature heights and wavelengths. Friction tests with an artificial finger probe were also conducted for comparison. It was found that the irregular mesoscale roughness features associated with damaged hair rendered higher measured friction and perception of 'coarseness'.[180] While this is not directly transferable to real hair due to an effectively different surface chemistry, this study highlighted the potential importance of surface roughness features on hair friction. Similarly, Okuyama et al.[190] considered patterned hair mimic surfaces from polyimide resin to evaluate the tactile performance against skin under dry, wet conditions and after treatment with hair conditioning products.

On the other hand, direct friction measurements on hair bundles with synthetic skin probes can provide more detail on macroscopic mechanisms influencing the skin-on-hair tribology. The use of an artificial skin probe also allows for mounting on a tribometer which greatly improves the repeatability and control over the normal load and sliding velocity. (Poly)-Urethane and PDMS substrates are commonly in use as skin mimics.[23,27,180,182,184,191] A polyurethane skin model probe on hair tribometer was used by Bhushan et al.[27] to measure friction on virgin, damaged and conditioner-treated parallel, aligned hair fibres. It was reported that both the applied normal load and the contact area did not influence the macroscopic skin-mimic-on-hair friction

coefficients. Consistently with hair-on-hair contacts, hair damage led to higher friction, which could be mitigated by conditioner treatment. Bhushan et al.[27] also showed that the DFE for polyurethane-hair contacts was insensitive to temperature, but increased with relative humidity. The effect of hair ageing was assessed in a similar setup to that of Bhushan et al.[27], combined with sensory evaluations of hair properties ('fineness, roughness and slipperiness')[181] associated with hair tribology. The sensory evaluation scores of all considered hair properties monotonically decreased with the age of the hair sample donors (higher was better). The three properties were found to be closely correlated to the chosen respective measurement properties of spectral centroid (SC), surface roughness and friction coefficient.[181,192] Thieulin et al. applied finger-mimic tribometer measurements on a single hair fibre, considering either virgin, colored or bleached hair.[183] Consistently with the previous studies, bleaching or coloring increased the mean interfacial friction and vibration levels. As opposed to previous studies opting for a chemical treatment with conditioners, a thermo-mechanical treatment routine was applied on damaged hair. This was found to have a smoothing effect on the damaged fibres, thus reducing the friction coefficient to levels associated with virgin hair. However, the treatment was also found to modify the mesoscale hair structure and brightness levels.

Sensory panel tests of similar perceived hair properties were compared to friction experiments conducted between various types of hair swatches with finger mimic urethane probe.[23] The study showed that both cleansing and conditioning shampoo formulations can effectively reduce friction compared to untreated hair. As expected, higher friction reductions were obtained with the conditioner-based formulation containing silicones and cationic polymers. The sensory panel results further indicated that friction alone does not necessarily correlate with the perception of softness. The authors argued that thinner hair was perceived as rougher due to a change in vibrational modes when in contact with the (inherently rough) skin surface.[23]

Aita et al performed human finger mimic friction experiments on wet hair bundles treated with either silicone oil, oil-water emulsions or water only.[182] A lubricating effect of silicone oil with water was observed which was maintained after drying. It was further reported that reductions in the surface temperature due to water evaporation on hair with either water or oil-water emulsions led to improvements in the perceived moisture of hair during drying, consistent with Ref.[177] Sano et al. used the finger probe on hair bundles setup to study how cationic surfactants influence the friction between hairs and skin.[184] They reported stick-slip-like oscillations between the finger probe and hair in the case of pure water which was attributed to surface roughness features in both hair (cuticle edges) and the probe (artificial finger grooves).

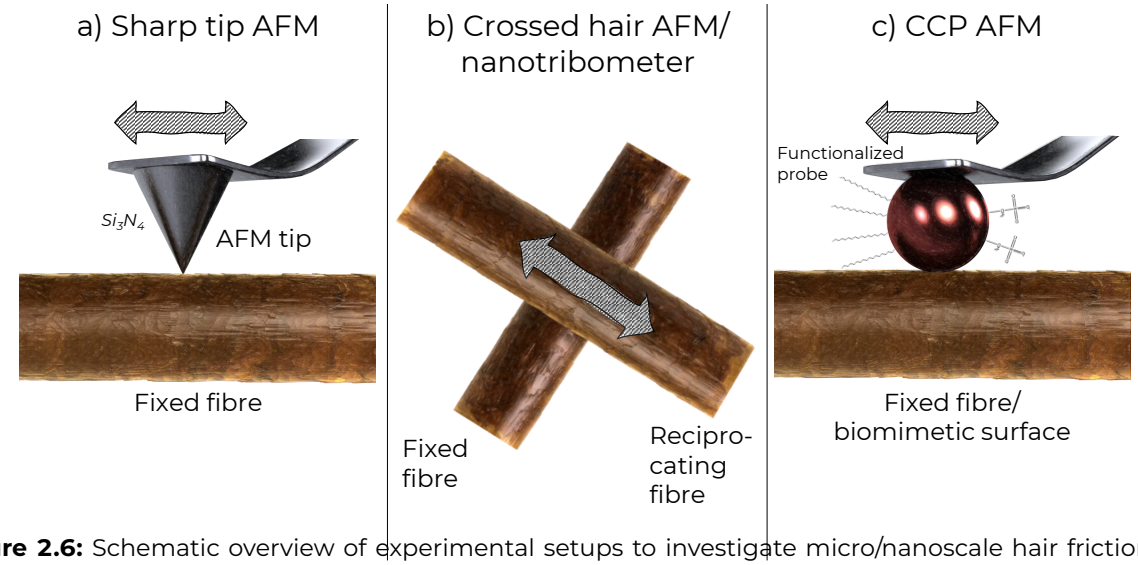


Figure 2.6: Schematic overview of experimental setups to investigate micro/nanoscale hair friction. (a) Sharp tip AFM ($r \approx 10$ nm), (b) crossed hair AFM ($r \approx 10$ µm), and (c) chemical colloidal probe (CCP) AFM ($r \approx 10$ µm). The relative dimensions of the AFM probes and fibres are not to scale.

2.2.2 Nanoscale hair tribology experiments

Small-scale contributions to friction on human hair are best resolved using mechanical force microscopy techniques. An overview of common nanoscale friction measurement setups is shown in Fig. 2.6 Atomic force microscopy (AFM)[193] has proven particularly successful for investigating the hair surface structure and tribology. One of the first AFM studies on the morphology of hair was performed by O'Connor et al.[194] who visualized the overlapping structure of cuticle cells on the hair surface. The authors chose a traditional scanning tip AFM setup, where a sharp tip mounted on a cantilever is used to 'scan' the substrate surface. This approach has since then been used extensively to scan the surface topography of virgin,[45,51,79,87,195–203] mechanically damaged[45,203] and chemically damaged hair.[45,51,79,87,199,202,203] While one could argue that the contact between an AFM probe and the hair is a tribological system by itself, we will only focus on those AFM studies that specifically focus on hair friction or link changes in the surface topography to changes in the frictional behaviour.

A predecessor to small-scale hair friction measurements was devised by Adams et al.[26] who use an intermediate-scale cantilever apparatus to probe the DFE attributed to the cuticle structure of hair fibres. A schematic illustrating the DFE is shown in Fig. 2.7 Smith[195] used lateral force microscopy (LFM),[204] an extension to AFM which takes the torsional deformation of the AFM tip into account. Smith applied LFM to visually identify areas of higher friction between the LFM tip and the hair surface. The highest frictional forces were observed at the cuticle edges which mark the region of most pronounced variability in surface topography. McMullen and Kelty[70] applied AFM and LFM to specifically study hair friction and morphological changes of the fibre surface upon bleaching or solvent-extraction. Both hair manipulations led to a considerable increase in the slope of the reported friction signal as a function of the applied normal load at ambient conditions. Their results showed close adherence to the extended Amontons-

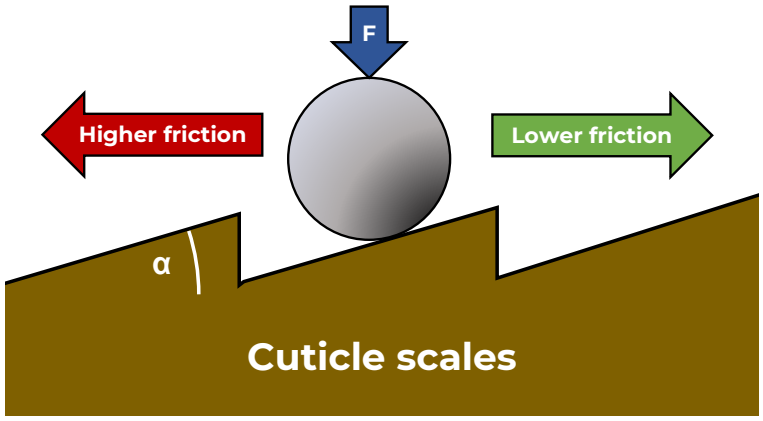


Figure 2.7: Differential friction effect (DFE) on human hair arising from the anisotropic cuticle growth. α denotes the cuticle lift angle.

Coulomb law with non-zero Derjaguin offset. The authors further considered virgin hair treated with a cationic polymer, which produced even higher dry friction forces compared to the chemically damaged cases. These trends were found to be consistent with dry combing force experiments under the same hair treatment conditions.[205]

Breakspear et al.[29] later applied AFM to measure friction and adhesion on natural hair surfaces with a fully intact 18-MEA lipid monolayer and an 18-MEA depleted fibre. The aim of this study was to identify the contribution of the 18-MEA to hair tribology as will be discussed later. They also compared the friction of untreated, bleached and hydroxylamine-treated hair fibres. Bleaching and hydroxylamine treatment led to a moderate increase in the relative friction coefficient. Grey hair was observed to render the highest friction coefficients across all investigated fibres. African hair overall rendered lower friction coefficients from the AFM than Caucasian hair.

At the same time LaTorre and Bhushan[17,42,105,191] published a series of AFM studies characterizing the friction and adhesion of various morphologically different hair surfaces. The authors measured hair friction using a sharp AFM tip setup (referred to as friction force microscopy, FFM, in their work)[206] coupled to experiments using macroscopic skin and hair probes on hair tresses.[17] They studied virgin, chemically-mechanically damaged and conditioner-treated hair of different ethnicity. The AFM results are shown in Fig. 2.8 A consistent increase in nanoscale friction with hair damage was reported, which could however be mitigated by treatment with a commercial hair conditioner. No strong differences among the hairs of different ethnicity (African, Asian, Caucasian) were observed. Treatment of damaged hair with conditioner over different number of cycles was found to monotonically reduce friction forces, while resulting in moderately increased frictional forces on virgin hair.[42] LaTorre and Bhushan further highlighted the anisotropy and scale-dependence of hair friction measurement techniques and provided fundamental hypotheses for why friction is different across the scales.[191] These will be reviewed separately when discussing hair friction mechanisms. The effect of different hair conditioner types including cationic

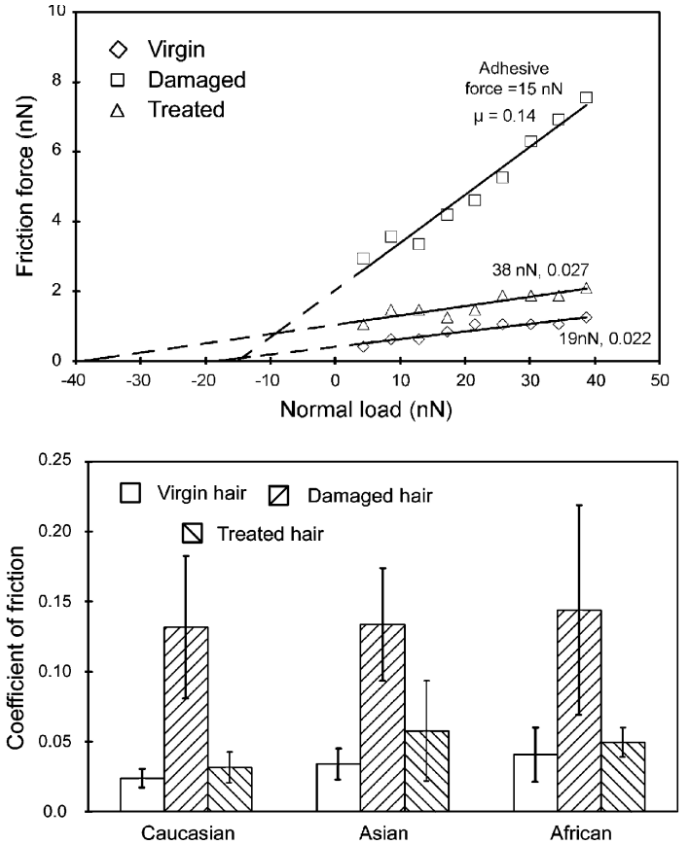


Figure 2.8: Sharp-tip AFM friction measurements on virgin, damaged and conditioner-treated hair and for hair from different ethnic origins. Reprinted from Ref.[17] with permission from Elsevier.

surfactants and silicones was also probed by the authors using the same AFM and complementary macroscopic friction measurement setup as described above.[105] Wei and Bhushan extended LaTorre and Bhushan's previous AFM studies to include nanoscratch indentation tests on hair to consider.[207] They investigated the effect of different normal loads on indentation and cuticle wear at different hair treatments and ethnic origins. The nanoscratch technique was later applied to study the tribological properties of Brazilian hair.[89] Smith et al.[208] performed localized AFM friction and adhesion measurements on the cuticle surface of virgin. Notably, the exposure of new cuticles from partial delamination and wear potentially led to local reductions in friction coefficients.

In perspective of the sensory perception of hair and real-life hair manipulations, gaining insights to hair friction in both ambient *and* wet conditions is desirable. Numerous studies have looked at measuring the nanoscale friction of wet hair[16,39,209] and hair at various levels of relative humidity[42] using the sharp AFM tip setup. Wet hair AFM friction is typically measured using a *liquid cell* setup, in which both the substrate (hair fibre) and measurement device (AFM tip) are fully immersed in water. The liquid cell setup bears the advantage over measurements in humid conditions of removing any contributions from capillary adhesion to friction forces.[16] As with AFM under ambient conditions, the liquid cell setup can be used to study the effect of hair damage and

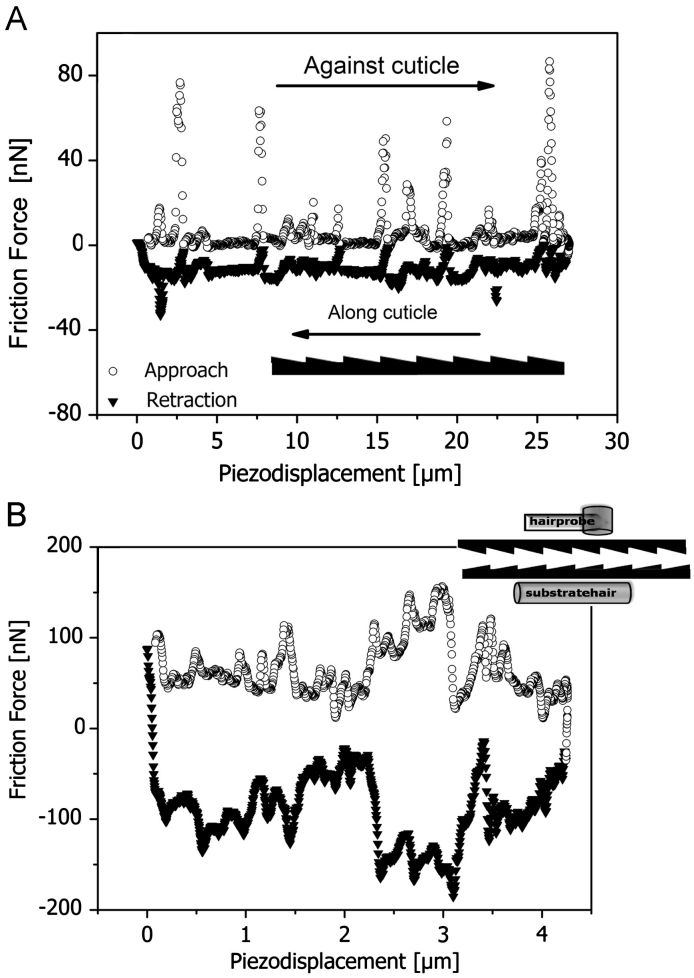


Figure 2.9: Lateral force signals from crossed hair-on-hair AFM friction measured in and against the direction of cuticle growth (a) for the crossed hair-on-hair setup and (b) for parallel fibres. Reprinted from Ref.[210] with permission from Elsevier.

chemical treatments such as conditioners.[16,209]

It is also possible to combine hair AFM or FFM directly with macroscopic measurement techniques to draw a connection between nanoscopic and mesoscale friction mechanisms. Tanamachi et al. specifically focused on the effect of 18-MEA depletion on hair friction via FFM and linked frictional increases to changes in macroscopic wetting behaviour, surface energy and thus a degraded fibre detanglement performance on the mesoscale.[188]

Atomic force microscopy has also been applied to study the hair-hair friction by mounting a small slice of a hair fibre to an AFM cantilever instead of using a sharp tip.[28,210–212] Max et al.[210] first applied this setup to study this setup to study hair-on-hair friction in a *crossed* fibre configuration, which was originally developed to study friction between polyester fibres.[213] A schematic representation of this setup is shown in Fig. 2.6(b). Mizuno et al also developed a similar setup for hair-on-hair nanoscale interfacial force measurements.[211] As with the sharp AFM tip, this setup is suitable to study both

friction and adhesive forces, but is capable of evaluating them directly between two fibres. Thus, the crossed hair AFM setup has been used to study hair friction and adhesion at various hair treatment conditions[210,211] and relative angles between the fibre primary axes.[28] The method is also capable of picking up the differential friction effect induced by the anisotropic orientation of cuticle scales as shown by the spikes in the friction force signals in Fig. 2.9 due to Max et al.[210] Wood et al. compared measurements from the crossed hair AFM setup to macroscopic wet combing tests and a commercial friction measurement device to study hair treated with with shampoos containing various conditioning polymers.[212] Bowen et al. used a nanotribometer to perform crossed-fibre friction tests on virgin and conditioned hair fibres.[214] Their setup also considered the evolution of the frictional response as a function of the operating cycles to include hair wear mechanisms. They showed that hair cleaned with hexane presented 25% higher friction coefficients than those retaining their sebum. When the cleaned hair was conditioned, the friction coefficient returned to a similar value as for the sebum-coated hair. The inherent anisotropic morphology of the hair cuticles also makes it difficult to separate surface roughness from surface chemistry effects on hair friction. In traditional AFM, only the sharp tip setup can somewhat eliminate these effects, as it can be locally restricted to only scan areas of the cuticle far away from the edges. As shown by Mizuno et al.[211], the crossed hair-on-hair AFM setup will typically include spikes in the friction signal when (purposely) scanning areas including cuticle edges.

Chemical colloidal probe (CCP) AFM[215] is an alternative approach to the hair-on-hair AFM setup where biomimetic surfaces are used to represent one or both hair surfaces. More generally, CCP-AFM can be used to study friction between two arbitrary substrates with a given surface functionalization and energy. In CCP-AFM, a (spherical) probe is chemically functionalized with a film which aims to represent a specific surface such as the healthy or damaged F-layer of hair. This setup is depicted schematically in Fig. 2.6(c). The setup is particularly useful for studying chemically and mechanically damaged hair, where surface roughness features might make it difficult to analyze the effect of the surface chemistry on hair friction. Sadaie et al[216] gold-coated silicon-nitride AFM tip functionalized with octadecanethiols as a model probe for the 18-MEA on hair. Coefficients of friction were measured between the functionalized AFM probe and single virgin hair fibres.

2.2.3 Adhesion measurements

Adhesive and cohesive forces can contribute as resistance to both lateral and surface-normal motion. While knowledge about these forces is important for the sensory perception of hair, appropriate adhesion measurement techniques can also provide valuable insights into the nanoscale structure of the hair surface. A common pathway to determining adhesion forces between two contacting substrates is to perform force-distance curve measurements. This involves bringing two surfaces of the same

or different material in (approaching) or out of contact (receding) in a controllable fashion. The AFM, scanning probe microscope (SPM) and the surface force apparatus (SFA)[217] are suitable devices for determining forces as a function of separation distance.[66,211,218] Bhushan et al. used a sharp AFM tip to probe the thickness of hair conditioners on virgin hair by means of force-distance curve modulation through the formation of a fluid meniscus.[199,219] Breakspear et al.[29] collected mean adhesion forces from force-distance curves on hair with and without 18-MEA lipids and found reduced adhesion forces in the 18-MEA-depleted hair. In combination with nanoscale friction tests in the same study, as discussed above, the authors postulated that the 18-MEA would cover the epicuticle as a consistent, ordered monolayer, although some heterogeneity was to be expected. Recently, Labarre et al.[220] used sharp-tip AFM with methyl, carboxylic acid and amine functionalizations to probe hair adhesion forces in different environments (dry/wet) on virgin and platinum-bleached hair. This allowed to identify the magnitude of either hydrophobic or electrostatic force contributions to adhesion[220] and are therefore a suitable tool for investigating the surface chemistry of both untreated and conditioned hair.

The deflection of an SPM was used by Maxwell et al. to record force-distance curves of on hair and other keratin fibres in low relative humidity and in highly humid and wet environments.[66] A consistent decrease in mean adhesion forces from low to high relative humidity (RH) and wet contacts was observed which was attributed to a water-induced change in the surface chemistry of keratin fibres. The authors suggested that lipids and proteins on the epicuticle surface would reorient, effectively turning the surface more hydrophilic. More generally, this study sparked considerations of an alternative epicuticle structure of keratin fibres such as hair of wool compared to that proposed by of an ordered lipid monolayer.[29] The proposed configuration suggests a more disordered intercalation of surface lipids with the underlying protein matrix.[16,66,67] Baghdadli and Luengo[68] performed adhesion force mapping on virgin and bleached hair using a thiol-coated hydrophobic AFM tip. The nanoscale resolution from the AFM suggested that virgin hair is predominantly dominated by hydrophobic regions with local hydrophilic patches which supported a heterogeneous distribution of an 18-MEA monolayer on top of a protein matrix. In the same experiments, the overall hydrophobicity was drastically decreased upon bleaching but could be restored with a polyelectrolyte treatment.[68]

The effect of bleaching and combing on hair topography, elasticity and adhesion was probed using hybrid-mode AFM.[80] The hybrid setup extends the traditional approach and receding setup by inducing an oscillation in the distance between the tip and substrate while monitoring the forces exerted on the AFM tip. This would allow for recording both adhesion, stiffness, elasticity and topography at the same time.[80,221] Both bleaching and combing led to a reduction in the mean of adhesion forces and a narrower force distribution. Thorough combing was even more effective in reducing

adhesion which was also reflected by severe mechanical damage observed in the cuticle topography leaving behind holes and even partial exposure of the endocuticle.

In the previous section, the application of the crossed hair fibre AFM setup for friction measurements was discussed. The setup is equally suitable to investigate adhesive contact properties by means of force-distance curves in both the approaching and receding direction.[210,211] In humid environments hair-on-hair adhesion is almost always influenced by capillary effects from residual water.[210] Previously, capillary adhesion between hair fibres was also identified as a contributing factor to high friction in wet, but not fully immersed hair.[154,160,165] In the liquid cell setup, capillary effects can be eliminated which allows for investigating the effect of hair surface chemistry and adsorption on adhesion and even out-of-contact forces (e.g., van der Waals and Coulombic forces).[211,220] Mizuno et al.[211] reported a faster decay of long-range van der Waals forces between two hairs by treatment with a cationic model surfactant. The study also showed that theoretical models such as DLVO theory can appropriately describe the force-distance curves at various surfactant and salt concentrations. The surface force apparatus (SFA) is another device suitable to conduct adhesion measurements. Cristiani et al.[218] modified the SFA to conduct automated screening of adhesion forces between two virgin hairs in the crossed fibre configuration. The automated setup significantly extended the scanned area and obtainable force statistics compared to previous studies. Adhesion measurements were further compared to predictions from an adhesion model operating on hair topography scans from a laser confocal microscope. The agreement between the model and adhesion scans was linked to the strong influence of surface morphology and roughness on adhesion.

A macroscopic approach to quantifying hair adhesion forces was chosen by Kamath et al.[222] A crossed fibre configuration was adopted to measure adhesion between single hairs as well as between two synthetic fibres. While no adhesion was evident from the virgin hair samples, treatment with cationic polymers (JR-400) reversibly increased the adhesive interactions with a large variability across the hair surface. Several other wetting liquids such as glycerol and commerical hair tonics were found to increase adhesion compared to virgin hair which was attributed to rheological and capillary effects which would heavily depend on the size of the contact area.[222] Treatment with synthetic sebum also increased adhesion between single hair fibres.[222] This may explain the tendency for greasy hair to clump together.[37] In a second step, Kamath et al.[222] conducted dynamic pull-out experiments of hair tresses from an aluminum cylinder. The recorded force from withdrawing the hair tress was attributed to adhesive forces from multiple contacts within the hair tress and the contact with the external cylinder. While the authors reported that the withdrawal force is essentially constant above a certain level of hair tress packing, the chosen setup cannot fully separate adhesive inter-fibre forces from dynamic friction caused by a higher lateral load on the cylinder wall due to changes in packing.

The pull-out setup due to Kamath et al.[222] highlights an important aspect which connects dynamic sliding friction with adhesion: In a sliding contact, adhesive forces are commonly attributed to the so-called Derjaguin offset.[146] The Derjaguin offset appears in the extended Amontons-Coulomb law[147] as a non-zero contribution to friction at zero load. Through NEMD simulations, both the surface chemistry[223] and surface roughness[224] have been found to directly influence the Derjaguin offset in the boundary lubrication regime.

2.2.4 Wetting experiments

While not directly falling under the classical definition of tribology, the surface energy and wetting behaviour of a substrate provide valuable insights which are often transferable to the substrate's expected frictional and adhesive response. Wetting studies, either by means of dynamic[43,63,64,69,188,225–227] or static[227] contact angle measurements are a proven tool to determine the surface energy of pristine, damaged and treated hair. Water contact angles larger than 90 degrees are generally associated with a hydrophobic surface, while those lower than this threshold would be associated with a more hydrophilic surface.

a) Dynamic contact angle experiments

The macroscopic contact angle on hair can be measured using the Wilhelmy force balance method.[228] In a series of publications, Kamath et al.[63,69,225,226] were among the first to explore the dynamic wetting of single human hair fibres using the Wilhelmy force balance. For undamaged hair, a water contact angle larger than 90 degrees was observed in the advancing stage, suggesting an overall hydrophobic surface.[69] The work of adhesion and contact angles however strong varied across different hair fibres. Notably, the authors also found a large difference between the wetting force during advancing of the fibre into the liquid and the stationary wetting. They suggested that this might be due to a reorientation of polar groups on the hair surface during prolonged wetting. Contact angles and the work of adhesion in polar (water) and apolar liquids (diiodomethane) were further reported to be dependent on both the direction of the fibre and the dynamic wetting mode (hair advancing into or receding from the liquid bath). The difference in wetting was most pronounced between two different possible orientations of the hair fibre in relation to the liquid during the receding stage. The authors explained this by the likelihood of uneven damage on the cuticle edge which might render different surface chemistries on the front and dorsal side of the cuticle. Potential meniscus effects during the receding stage were also highlighted.[69]

Dynamic wetting experiments in the presence of adsorbed cationic polymers *or* surfactants suggest that cationic compounds can drastically alter the wetting forces and contact angles on virgin hair.[225] Cationic polymers such as JR-400 were found to

heterogeneously adsorb on virgin hair which was reflected by drastic fluctuations in the recorded wetting forces. The investigated surfactants and polymers were found to partially desorb upon multiple fibre immersions. On chemically damaged hair by oxidation, wetting forces substantially increased effectively rendering the surface hydrophilic. It was inferred from the further increase in wetting forces that subsequent polymer adsorption was greatly increased on oxidized hair. The authors identified the hysteresis ratio of wetting forces between the advancing and receding stage as a qualitative measure of surface coverage of adsorbed molecules and surface heterogeneity.[225] Wettability with polymers or surfactants was also found to be highly sensitive to the temperature during the treatment stage.[63]

Kamath et al.[226] later used similar wetting force experiments to study the effect of additional anionic surfactants in solution on the deposition of cationic polymers to hair. Wetting forces directly allowed for quantifying whether the complexes of polymers and surfactants would be hydrophobic, where polymer cationic sites would be neutralized by surfactants, or hydrophilic, suggesting that polymers were 'overcharged' due to excess surfactants adsorbing. Hydrophilic complexes were found to render a lower adsorption density due to the reduced affinity to the anionic sites on hair. Kamath et al. also highlighted the importance of dilution which could lead to a maximum in the adsorption density of the polymer-surfactant complexes due to an undergoing phase change.[226] The implications of this mechanism, later referred to as 'coacervation' will be discussed below.

Molina et al.[64] confirmed the hydrophobic nature of virgin hair by advancing contact angle measurements at various pH ($\approx 102°$ for pH = 1-13). Treatment with alkaline and alkaline hydrogen peroxide reduced the contact angle to values as low as 53°, associated with hydrophilic surfaces. This reduction in surface hydrophobicity was attributed to the removal of fatty acids on the hair surface. Further evidence of the exposed sub-18-MEA structure was given by performing a variation study of the pH value of the wetting fluid. Higher pH values correlated an increase in the acid-base contribution to the total adhesion work. This was interpreted as proof for the exposed cysteic acid residues (SO_3^-) found in the epicuticle.[64] This is consistent with values of contact angles of untreated and chemically damaged hair due to Lodge and Bhushan[43] who performed additional dynamic contact angle experiments on chemically damaged hair which was subjected to treatment with a gel conditioner containing cationic surfactants. Both initially dry hairs and hairs pre-soaked in water were investigated. It was found that conditioner treatment could increase contact angles compared to the chemically damaged hair but could not restore the full hydrophobicity of untreated virgin hair. On the other hand, application of conditioner on the healthy hair would result in a decrease in contact angles compared to the untreated case. This was interpreted be a result of 'overconditioning' due to excess cationic surfactants hydrophobically adsorbing on hair and exposing their cationic headgroup to the liquid phase, thus

reducing the overall surface hydrophobicity.[43] Moderate overconditioning on virgin hair was consistently made in later experimental dynamic and pseudo-static contact angle measurements after treatment proteolipids.[227] However, excess surfactants do not notably change the lubrication performance of virgin hair which Lodge and Bhushan attributed to capillary forces remaining relatively unchanged during sliding. Excess surfactants might also be easily depleted from the sliding contact due to the external shear, which is consistent with reports of carboxylic acid surfactants on mica.[229] Another important finding due to Lodge and Bhushan was the distribution of conditioner formulations on the hair surface. Based on hysteresis of the contact angle in untreated and conditioner-treated hair, the authors concluded that conditioner is mainly deposited at the base of the overlapping cuticle scales, leaving their edges exposed to external influences.[43,219] Subsequent treatment of bleached hair with cationic surfactants and amino acids was found to partially restore the hydrophobicity of pristine hair. The treatment with alanine was particularly effective with regard to mitigating chemical damaged from bleaching.[230] Similar improvements hair wetting as well as improvements in tensile properties and water uptake were observed when treating bleached or permed hair with keratin peptides or keratin proteins.[231]

Dynamic contact angle experiments on hair due to Tanamachi et al.[188] confirmed the previous reports of changes in the wetting behaviour during the receding mode when probing single hair fibres with or against the direction of the growth of the cuticle cells.[64,69] The depletion of the 18-MEA across hair was also directly linked to a reduction in both advancing and receding contact angle, where the reduction in contact angle in the latter was most pronounced.

Gao et al. evaluated the surface energy on virgin, damaged and treated hair by measuring dynamic advancing contact angles using a fully apolar wetting liquid (diiodomethane) and a polar liquid (benzyl alcohol).[100] The application of the Owens-Wendt theory[232] allowed for directly determining the polar and dispersive contribution of the surface energy from measuring the wetting with these two types of liquids. The dispersive component of the surface energy was found to increase between virgin and bleached hair while the polar component was reported to remain approximately constant. This is somewhat surprising since bleaching would be expected to remove the 18-MEA lipids from the surface, thus leaving behind a more polar and hydrophilic surface. This may be due to the choice of using benzyl alcohol as a second wetting liquid which produced similar contact angles between virgin and bleached hair. It is also possible that the bleaching routine could be different from other studies which reported much more pronounced decreases in advancing contact angles with another polar wetting liquid (water).[64,188] The effect of the exposure time, temperature and chemistry of the bleaching solvent on wetting had indeed been shown to have a severe effect on the advancing contact angle of water on bleached hair.[64]

The microscale distribution of hydrophobic group on untreated hair was further investigated by Wortmann et al.[78] who provided evidence of periodic patterns in the surface chemistry on the hair surface obtained from the Wilhelmy force balance. The observed patterns were attributed to weathering of the natural hair and shows that an idealized homogeneous fatty acid monolayer might be insufficient to describe the interactions of the hair surface with wetting fluids. The existence of damage patterns has been further studied by Korte et al.[92] who performed nanoscale adhesion force measurements on bleached hair. Korte and co-authors were able to visualize micro- and nanoscale damage patterns for simplex bleaching with hydrogen peroxide. This confirmed the observations observed in Ref.[78]

b) Pseudo-static wetting experiments

Static wetting experiments on the other hand allow for eliminating some anisotropic effects such as capillary formation on cuticle edges during dynamic wetting. A potential downside of static contact angles is that droplets are microscopic compared to a liquid bath which can lead to other dynamic perturbations such as, for instance in the case of pure water, rapid evaporation or absorption into the hair fibre.[200,227] We therefore refer to the following experiments more generally as pseudo-static[227] although some wetting liquids have been suggested to be more suitable in avoiding the above transient effects. Dupres et al.[79,200] linked the static wetting behaviour of various wetting liquids on hair to AFM topography images and surface potential maps in both virgin and lipid-extracted fibres. Squalane was found to be a suitable alternative to water due to its much slower evaporation. The AFM results showed no particular hints of strong inhomogenities on both virgin and delipidated hair surfaces. However, the authors still suspected the existence of such patterns on 18-MEA-extracted fibres due to the observed wetting behavior of small droplets which adhered to the damaged surface even far from the cuticle edges. For virgin hair, squalane was only found near the cuticle edges which was attributed to the strong hydrophobicity of the center of the cuticle surface. Liquid would thus quickly de-wet from this area and only wet the region around the cuticle edge which was found to be more polar.[79]

Dynamic and pseudo-static wetting experiments were carried out on virgin hairs, artificially weathered hair and hairs subjected to various degrees of bleaching before and after treatment with cationic proteolipids.[227] Reductions in the dynamic advancing contact angle were more pronounced for strongly bleached than for weathered hair. Pseudo-static contact angles of water droplets on medium bleached hair confirmed that treatment with proteolipids could restore the hydrophobicity of virgin hair.

2.3 Computational techniques

2.3.1 Models of the human hair surface

Numerical models of human hair have been developed with the incentive to serve as a complimentary tool to experiments. At the largest relevant scales, efficient hair entanglement simulations could be a welcome extension to combing experiments with the key advantage of being able to resolve individual fibre dynamics. However, these macroscopic hair models are still relatively rare in the literature. Lee et al. presented a continuum model to study fibre entanglement in carding machines.[233] Plumb-Reyes et al.[234] recently presented a numerical thin filament model based on Kirchhoff-Cosseral theory to model human hair detanglement. However, no friction forces were included in the model so investigations of different surface chemistries are not yet accessible. The model due to Plumb-Reyes et al. was further used by Hughes et al.[235] to compare to automated combing experiments. Further multi-fibre hair models are available in the field of computer graphics.[236–238] These models are mostly aimed at producing a realistic or stylized appearance of hair styles. However, some of these models may also be leveraged for conducting physics-based simulations. One such example is the work due to Daviet et al.[238] where Coulomb friction was incorporated into a simulation framework for hair dynamics.[238]

On smaller scales, molecular models of hair have become more common in recent years. These models allow for capturing nanoscale interactions and surface chemistry effects which can be difficult to impossible to capture by experiments. Atomistic structures can provide further insights into the surface properties of hair and its interactions with hair care products under various damage modes. With the increase of computational power and robust biomolecular force fields for atomistic[239] and coarse-grained[240] molecular dynamics simulations, this pathway has recently become more popular and has opened up new opportunities for the virtual screening[241,242] of formulated hair care products.[243]

Some focus has been placed on modeling the hair cortex to investigate mechanical properties of the hair fibre and the affinity of the core towards external molecules. Akkermans and Warren[244] developed a multiscale model of hair to study its mechanics. They used molecular dynamics (MD) of hair keratins and an analytic two-stage model to study the yield stress of hair. They further derived a particle model of filament proteins embedded in a matrix to obtain mesoscale stress-strain curves. Antunes et al.[245] presented a coarse-grained representation of the protofibrils constituting the macrofibrils in hair cortex cells. They coupled this model with fluorescence microscopy experiments in order to study the affinity of peptides and solvents towards hair keratins. Their model indicated a destabilizing effect of benzyl alcohol towards the keratineous fibrils and a subsequent increase in absorption of peptides in agreement with their microscopy experiments.

For tribological purposes, models of the surface of human hair are of particular interest, as friction, lubrication and wear mechanism are localized in this part of the hair. Two approaches have been commonly chosen to study nanoscale hair surface interactions, namely mean-field theory approaches and the molecular dynamics route. Mean-field approaches allow for insights into the thermodynamics and structure of formulations near interfaces and in bulk, while neglecting short-distance density fluctuations.[246] Banerjee et al. used self-consistent field theory (SCFT) to study the interaction of oppositely charged polyelectrolytes and surfactants in bulk[247] and subsequently near biomimetic surfaces representative of healthy and bleached hair.[128] Guzmán et al.[130] extended this to studying different polyelectrolyte-surfactant architectures and formulations in their adsorption behaviour. Leermakers et al.[129] further applied SCFT to tune the wettability of hydrophilic surfaces, comparable to virgin hair, to allow for the deposition and spreading of hair care formulations. While SCFT are certainly suitable to study adsorption and aggregation of complex solutions to hair, they are not directly applicable to studying non-equilibrium phenomena which are intrinsically associated with tribology. It was also noted that non-equilibrium processes might exist during adsorption of polyelectrolyte-surfactant complexes in reality,[130,248] which can also not be captured by equilibrium theories such as SCFT.

Molecular dynamics and dissipative particle dynamics (DPD) on the other hand consider explicit atoms (all-atom MD) or groups of atoms (united-atom, coarse-grained MD, DPD) as discrete beads and can accurately capture three-dimensional structures and dynamics on the nanoscale. MD simulations typically consider van-der-Waals (*vdW*), electrostatic and intramolecular interactions such as bonds, angles and dihedrals to obtain a force balance on each bead which is then integrated in time to obtain a physical trajectory of the simulated system. The first known MD representation of the human hair surface was developed in the early 2000s by Beard and Hare[249], who modeled the cuticle as a sheet of polypeptide chains to study the adsorption of quaternary amine surfactants. Practical applications for molecular hair models go beyond the use for the hair care industry. Efremenko et al.[250] studied the adsorption of explosive molecules by the hair surface. They conducted density functional theory (DFT) and MD simulations to study how explosives adsorb on 18-MEA molecules and on hair proteins. McMullen and Kelty[251] presented an united atoms model in the GROMOS96 force field[252] of both eicosanoic acid (EA) and the 18-methyleicosanoic acid (18-MEA) fatty acid monolayers, the latter of which is the predominant constituent on the F-layer on hair. An extended all-atom MD model of the 18-MEA monolayer on ultra-high sulphur protein beta-sheets of the virgin hair endocuticle was developed by Natarajan and Robbins.[253] They considered the experimentally-observed[254] thioester linkage between the 18-MEA and the cuticular protein matrix below. They used the antifreeze protein from snow fleas as a simplified protein model.[253] This model was later validated through a combination of Raman, infrared, and vibrational circular

dichroism experiments.[255] The grafting density chosen by Natarajan and Robbins.[253] resulted in a disordered 18-MEA monolayer, which was in agreement with previous X-ray photoelectron spectroscopy (XPS) thickness measurements of the F-layer.[256]

An extension to the comparison between EA and 18-MEA was presented by Cheong et al.[65] using the OPLS-AA forcefield for carbohydrates.[257,258] The authors considered various lipid grafting densities for both EA and 18-MEA to obtain structural insights of the thioester-grafted monolayers in vacuum and in the presence of water. They were able to predict an optimum lipid separation distance (0.49-0.65 nm) for the 18-MEA from a thermodynamic free energy minimum with respect to the packing distance and by quantitatively comparing the thickness of the observed monolayers with transmission electron microscopy (TEM) measurements on hair.[259] Cheong et al. also commented on the observation of a higher monolayer thickness in their MD study (2.0-2.6 nm) compared to previous XPS measurements on hair (0.9 nm).[260,261] They propose multiple solutions to this discrepancy: the potential removal of free and covalently bound fatty acids in the experiments, the variability of hair across different people and the possibility of perturbations due to vacuum conditions in the XPS experiments.[65] Another noteworthy characteristic of their model is the simplification of the protein matrix below the F-layer. They used a stack of graphene sheets as surrogate, which was also useful for systematically varying the grafting density of the 18-MEA and has since been used in recent coarse-grained models of the F-layer.[36] Recently, Sanders et al.[262] used the all-atom OPLS4 forcefield[263] to model the 18-MEA with explicit covalent bonds to ultra-high sulphur proteins to study the wetting and adsorption of free lipids on virgin hair. Their model differed from the previous model by Natarajan and Robbins not only by the different choice of force field but also in a more accurate protein representation and packing density of the 18-MEA in the F-layer (1.26-1.41 molecules/nm^2).

Larger length and timescales compared to all-atom MD can be captured by using so-called coarse-grained molecular models. These models typically compromise resolution for performance by grouping several atoms into larger beads. Šindelka et al.[110] used DPD to model the pristine F-layer of hair in the presence of lamellar-phase hair care products containing cationic surfactants and fatty alcohols. Adsorption and desorption mechanisms of various product compositions were studied in equilibrium conditions and under an external shear flow. The coarse-grained MARTINI 2 forcefield[264,265] has also been used for modeling hair surface interactions with external molecules at larger system dimensions compared to what is feasible with atomistic MD. Coscia et al.[36] presented a modified-MARTINI coarse-grained model of the F-layer with larger cylindrical damage patches to study the tribological interactions with thick films containing polyelectrolytes and ionic surfactants. Further details of this model will be discussed in the next section on hair friction modeling.

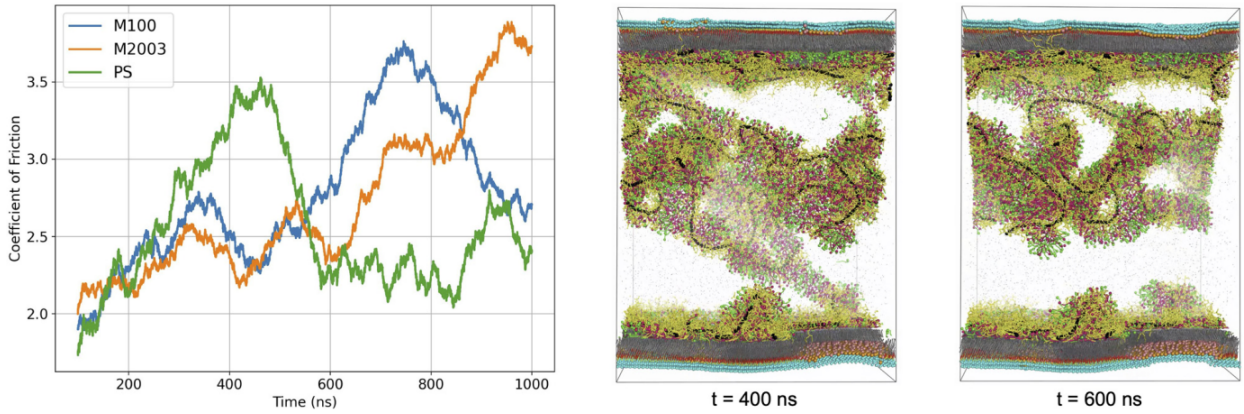


Figure 2.10: Coarse-grained non-equilibrium molecular dynamics simulations of F-layer contacts containing aqueous solutions with quaternized 3-deoxy-6-deoxy cellulose copolymers, CAPB, SLES and excess sodium chloride. Reprinted from Ref.[36] by Coscia et al. licensed under a CC-BY-NC 4.0 license.

2.3.2 Hair friction modelling

Models for investigating the tribology of hair have become more accessible in recent years. Special interest has been expressed in studying the behaviour of hair under the influence of shear. Most friction-related models focus on the nanoscale of hair, as this directly allows insights into the chemistry and molecular kinematics at length and time scales which cannot be resolved accurately in experiments. Non-equilibrium molecular dynamics[20] allow for measuring shear stresses for two contacting surfaces under normal load and for single surfaces with an applied external shear. This is particularly useful for applying the aforementioned molecular models to obtain a direct estimate of friction. Morozova et al.[266] conducted adsorption and shear simulations of polymers on biomimetic hair surfaces. A planar coarse-grained model of the human hair surface was established by a Fourier transform approach that allows for creating randomly patchy hydrophobic-hydrophilic surfaces representing the 18-MEA and oxidized regions on hair. They considered In an extension to this work, polymer architectures found in biodegradable polysaccharides were benchmarked against a more traditional rigid polyelectrolyte architecture from petrol with respect to the adsorption and desorption behaviour under equilibrium conditions and in the presence of a linear shear flow.[267]

Coscia et al.[36] modelled contacts between two hair surfaces containing cationic polyelectrolytes and ionic surfactants in the hydrodynamic lubrication regime. Their fully-deformable F-layer model discussed in section 2.3.1 was used as a representation of the hair surface. Figure 2.10 shows a the coefficients of friction evolution in time and snapshot of their NEMD simulation trajectories containing either petrol-based polymers (M100, M2003) or a cationic polysaccharide (PS) and ionic surfactants typically used in hair care formulations. Specifically, they considered the anionic surfactant sodium laureth sulfate (SLES) and the zwitterionic surfactant cocamidopropyl betaine (CAPB). Additionally, excess salt was added to their formulation, which can be beneficial for tuning the formulation viscosity in the presence of the chosen surfactant types.[176,268] Their model successfully demonstrated the capability to simulate the

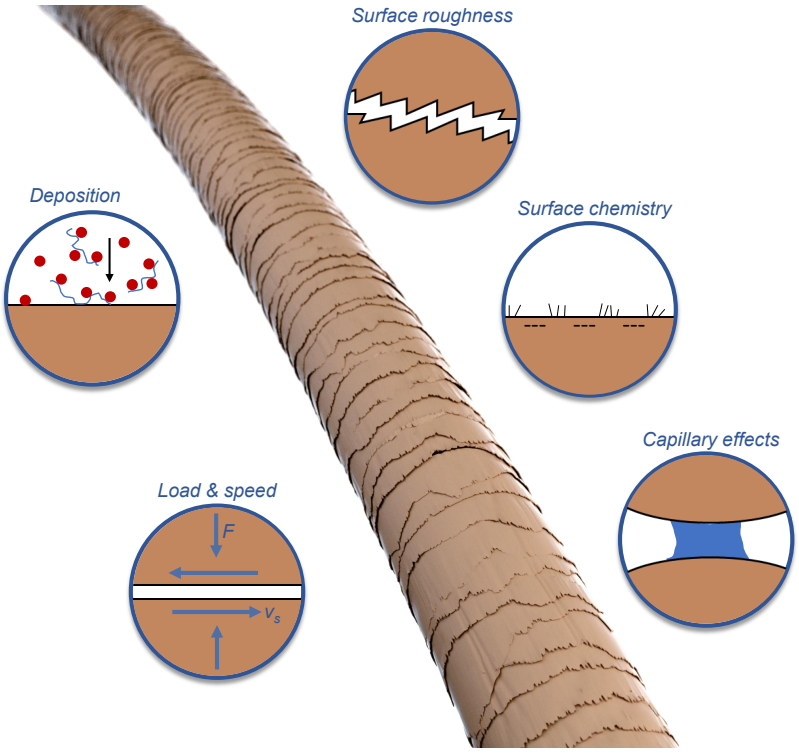


Figure 2.11: Overview of relevant mechanisms influencing hair friction and therefore the tactile perception of hair.

tribological response of nanoscale hair-on-hair contacts containing large aggregates of polyelectrolytes close to realistic molecular weights and oppositely-charged surfactants.

2.4 Hair friction mechanisms

The previous sections provided an overview of historic and state-of-the-art experimental and numerical techniques to study hair tribology. Now, we will provide a review of the relevant mechanisms for that affect hair friction in particular. We will further discuss the appropriate handles for tuning hair friction and sensory perception which is particularly important in the context of formulating hair care products. An overview of the identified handles relevant for hair friction is shown in Fig. 2.11 It is worth noting that many of the highlighted mechanisms are expected to be closely coupled, which is why, as will be shown, small-scale experiments tend to be more successful at isolating specific mechanisms.

2.4.1 Humidity & wetting effects

The wetting state of hair strongly affects its frictional response. In humid environments, residual water is present on the hair surface and also within the cell membrane complex between cuticle cells.[231,269] Fully dry hair is therefore expected to be encountered rather rarely in most ambient environments but will also be discussed to some extent

below. Conversely, fully wet conditions are encountered during and after washing and rinsing. Wet hair has also been studied extensively in laboratory conditions using the liquid cell setup as discussed earlier in perspective of nanoscale friction and adhesion measurements.[16,210,211]

Differences in nanoscale hair friction between fully dry and water-immersed setups for virgin and bleached hair were reported by Nikogeorgos et al.[16] For both virgin and chemically damaged hair, the friction coefficient increases in the wet case.[16,151] Over the years, two mechanisms have been brought forward that aim at explaining this observation:

1. Water is absorbed by hair leading to a swelling which in turn increases the softness and contact area during sliding.[16,105,194] On damaged hair the swelling is further amplified due a higher internal water uptake as the hydrophobic protection from the F-layer is removed.[231]

2. 'Proteolipid reorientation' as a surface chemistry-induced mechanism for increased friction in (fully) wet hair was first proposed by Maxwell et al.[66] and later considered in AFM friction experiments on hair.[16,208] It was proposed that the F-layer lipids on hair or wool would reorient away from the solution, with the hydrophilic protein matrix of the epicuticle being exposed.

There is clear evidence of swelling of the hair surface and cuticle softening in aqueous environment.[194,207,270,271] This discovery was soon followed by a search for an accurate description of the organization of the covalently bound 18-MEA lipids on the epicuticle. Some studies proposed a densely packed monolayer structure of lipids.[29] A heterogeneous distribution of covalently bound lipids is generally more accepted now due to evidence of hydrophilic patches on virgin hair from nanoscale adhesion measurements.[56,68] Nikogeorgos et al.[16] proposed that the reorientation of 18-MEA lipids might only be possible if sufficient lipids had already been removed in the first place due to chemical treatment. This was explained by the observation that the friction increases between dry and fully wet states was more pronounced in KOH-treated hair than on virgin hair. On virgin hair, reorientation would be substantially limited as a result of the dense 18-MEA packing.[16]

The key morphological difference of hair in humid environments compared to either fully dry or immersed conditions lies in the existence of capillary effects due to a triple phase boundary between the substrate, the wetting liquids and the ambient vapor phase. Capillary forces further increase wet hair friction and therefore combing forces.[160,226] However, it is difficult to separate these forces directly from the friction increases due to the hair swelling and softening mechanism, which will naturally also occur to some extent in humid environments. In contrast to the observations due to Nikogeorgos et al.,[16] a moderate decrease in friction on virgin hair was observed by LaTorre and Bhushan[105] for soaked hair. The authors attributed this to the lower

degree of water update in virgin hair due to its hydrophobic protection. However, it is also worth noting that the soaked hair friction was measured at relative humidity of 50%, so capillary effects might still play a role. Avoiding capillary effects is also beneficial for reducing the scatter of nanoscale friction experiments under laboratory conditions. Lee et al.[209] reported that friction measurements in a liquid cell drastically reduced the statistical scatter observed in ambient conditions when studying the effect of polyelectrolytes on the surface.

The sensory perception of wet hair is not only influenced by friction forces but can also be tuned by means of a surface temperature drop from evaporation cooling.[182] This underlines that hydrating hair conditioning products are indeed beneficial for providing a feeling of 'moisture' for some time after application (1-2 hours) according to Ref.[182].

2.4.2 Hair damage

Clear evidence has been provided that artificial mechanical[17,80] and chemical treatments[16,17] as well as weathering and aging[181,272,273] induce an increase in hair friction. Chemical treatments such as bleaching, coloring and perming strongly alter the surface properties of hair and therefore represent a particular area of research. Hair care formulations may also be tailored to particularly focus on repairing chemically damaged hair. Fig. 2.12 shows an overview of the relative increase in the friction coefficient induced by chemically damaging hair from macroscopic,[42,183,191] microscopic[191] and nanoscale experiments.[16,17,70] The relative friction coefficients are defined as the ratio between the friction coefficients of chemically treated and virgin hair.

A relatively strong scatter in the magnitude of the relative friction increases is evident. Relative friction coefficients from nanoscale experiments and simulations are significantly increased compared to either microscale AFM or macroscopic experiments (combing and model skin-on-hair). The probe material might be one factor leading to the difference in relative friction increase. However, the micronscale AFM results with a silicon oxide spherical probe[191] also show similarly low friction increases, which might suggest that lengthscale effects might also play a major role. This hypothesis will be discussed further in the next section. Surprisingly, the largest difference in friction increases is observed between the two nanoscale AFM studies due to Breakspear et al.[29] and LaTorre and Bhushan.[17] Breakspear et al. also considered hydroxylamine-treated hair which was expected to have all 18-MEA removed, but reported comparable friction increases (+30%) as observed with bleaching. While both studies used a similar AFM setup, Breakspear et al. considered lower normal loads during friction measurements between 0.5-4 nN while LaTorre and Bhushan considered normal forces in the range of 5-45 nN. However, for adherence to the extended Amontons-Coulomb law a difference in normal load would be expected to render such differences in the friction coefficient increase as long as both results are extracted from the slope of the linear

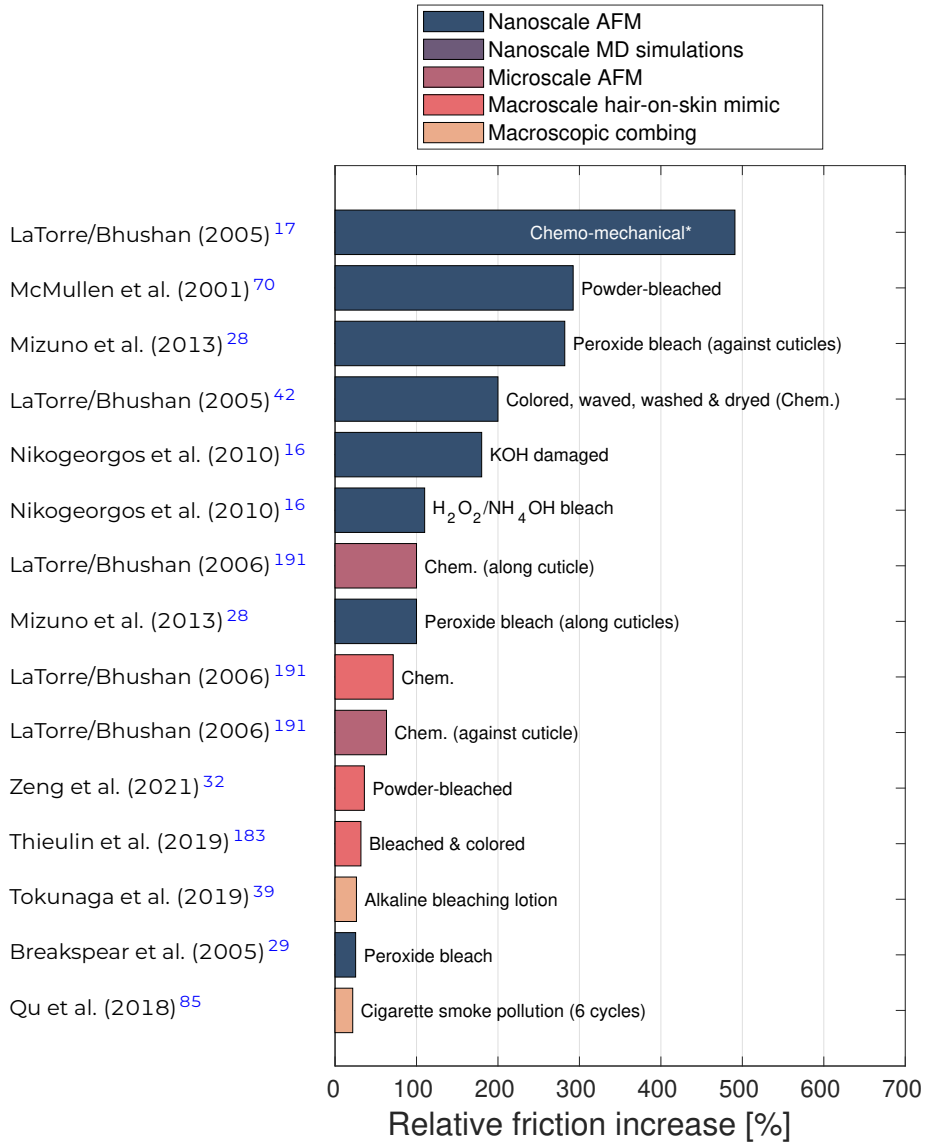


Figure 2.12: Relative kinetic coefficients of friction from experiments and simulations between untreated (virgin) and chemically damaged hair in ambient/dry conditions. The values from Ref.[32] measuring friction in and against the direction of cuticle growth were averaged. *Chemo-mechanical treatment in Ref.[17] constitutes coloring, waving, washing, drying and combing.

fit to the friction force data versus normal load. LaTorre and Bhushan also considered mechanical damage due to combing on top of the chemical treatment, which might also explain why their nanoscale AFM results showed the highest friction increases across all considered studies.

Two tribological mechanisms for the friction increases due to chemical damage have been proposed:

1. Increasing surface roughness increases the number of asperities in contact and therefore friction by means of a 'nanoscale ratchet mechanism'.[17,31]

2. Surface chemistry changes modify the interaction forces between the contacting substrates.

Increases in the surface roughness were observed on multiple accounts across the relevant lengthscales for both chemical damaging[17,181] and mechanical damage due to combing.[80] However, it was also reported that both bleaching and treatment with methanolic potassium hydroxide (KOH) did not notably increase the surface roughness, as determined by AFM scans.[16] While changes in the mesoscopic surface roughness will most probably also affect the friction coefficient on hair,[180] hair treatments of chemical nature do not always necessarily induce this morphological change. Homogeneous or nanoscopically heterogeneous modifications to the surface chemistry due to treatment could be sufficient to explain certain increases in hair friction. In reality, both modes might contribute to changes in hair tribology, especially when hair subjected to a combination of chemical damage, mechanical stress and weathering. This has directly been observed in hair subjected to air pollution which resulted in observable cuticle degradation and loss of the 18-MEA.[85] Theoretical and computational models coupling both the nanoscale insights and surface roughness features across the lengthscales might be helpful in predicting the frictional response and expected sensory perception.

Hair ageing represents a much more long-term degradation mode. It has been found that hair aging increases in both the perception of slipperiness and the measured hair friction[181] which is probably due to the depletion of hair lipids with ageing.[274] Meanwhile, the hair surface roughness also increased with age.[181] Weathering of hair also induces a reduction of F-layer lipids from the root to the tip of hair.[39] This is reflected in higher friction coefficients at the tip as observed in single fibre friction tests.[163]

2.4.3 Scale-dependence of hair friction measurements

In the previous section, it was shown that the relative increase in the friction coefficient from macroscopic friction experiments was lower compared to nanoscale AFM measurements on chemically damaged hair. There is a variety of morphological influences which could contribute to such a scale-dependent frictional response of hair. Naturally occurring roughness features such as the overlapping cuticle scale arrangement,[26] the existence of striations on the sub-cuticle scale of virgin hair[25,78,80,216,276] and weathering effects[39,163] have all been found to render anisotropic and non-uniform friction force profiles. The screening of roughness features with an AFM tip contributes to the high variability of the friction force when measured at different positions on the hair surface.[208,209] LaTorre and Bhushan consistently suggested that the tribological mechanisms observed at the nanoscale and at the macroscale might be fundamentally different.[191] They highlighted potential contributions at the macroscale such as capillary effects, surface roughness and (morphological) cuticle edge effects[17,42,105,191] which are expected to be less pronounced or non-existent at smaller scales.

At the cuticle scales, we previously highlighted the influence of the differential friction effect (DFE). The relative change in friction force when measuring friction against

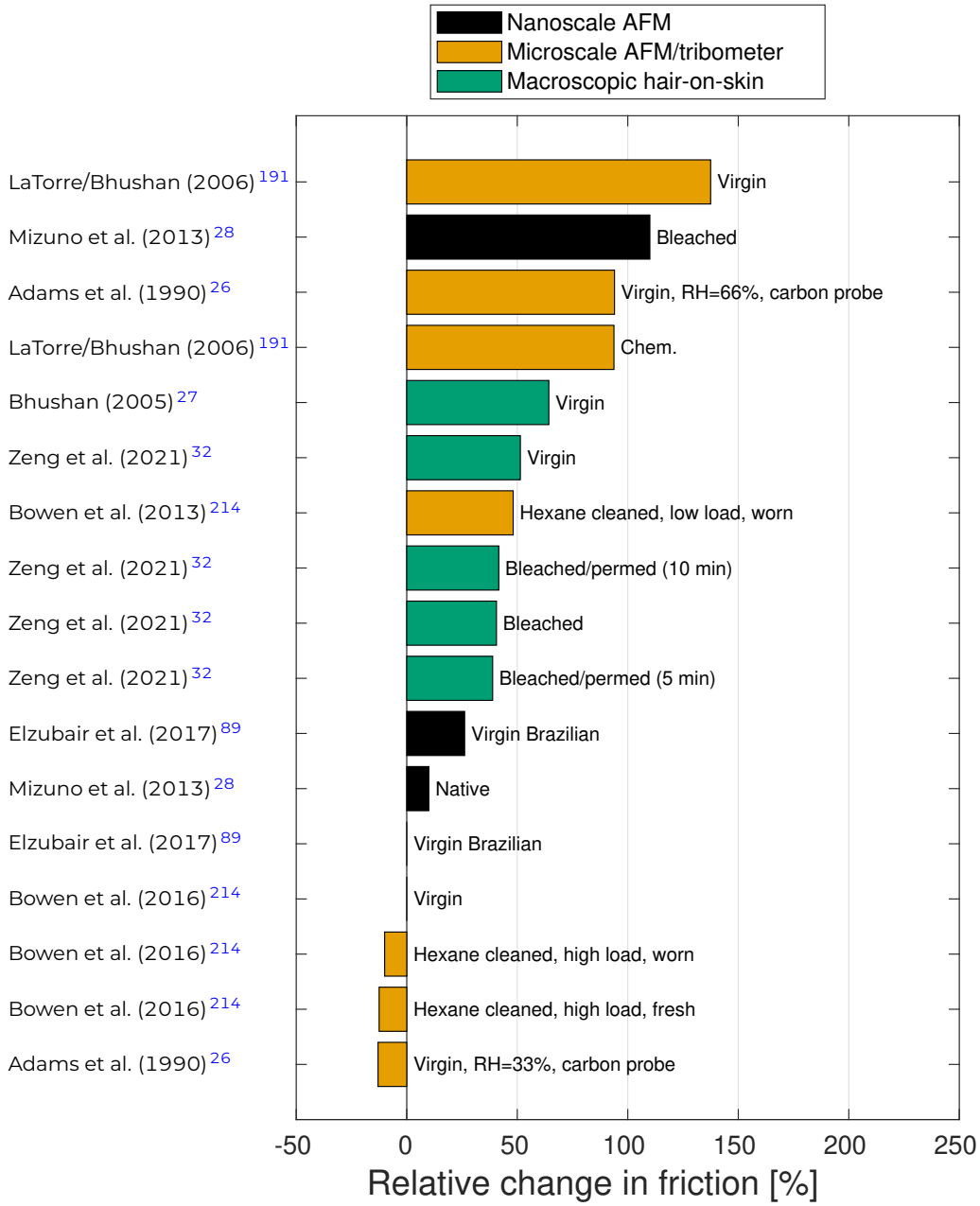


Figure 2.13: Relative change in friction forces when scanning 'against' the direction of cuticle growth compared to scanning 'along' cuticles from experiments. For the experiments by Bowen et al.[275], 'low' and 'high' loads indicate $F_N = 10$ mN and $F_N = 100$ mN respectively, while 'fresh' and 'worn' indicate data after 30-100 and 100-10^4 scratch cycles.

or along the direction of hair growth from several experiments across the scales is summarized in Fig. 2.13 Scale-dependent effects are less evident here than with damage-induced changes in the frictional response discussed in the previous section. Moreover, we observe no clear trend with respect to the treatment type. However, the majority of experiments confirm the trend of higher friction forces when measuring against the cuticle growth direction as opposed to measuring along the growth direction.

When taking into account hair bundles, additional complexity arises due to multiple

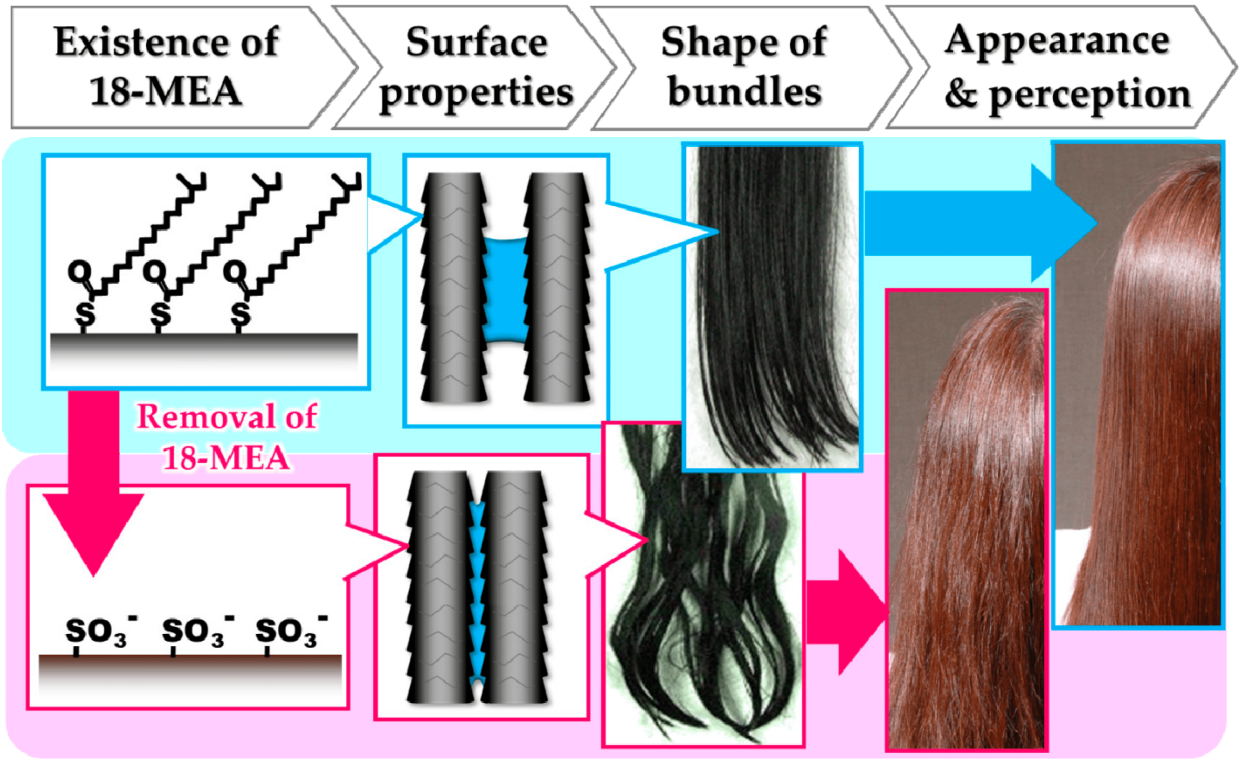


Figure 2.14: Effect of 18-MEA removal on hair entanglement, appearance and perception. Reprinted from Ref. [188] licensed under a CC-BY 4.0 license.

points of fibre-fibre interaction and interactions with the external manipulator such as a comb or finger. Here, hair entanglement also plays a major role. Tokunaga, Tanamachi et al.[39,188] proposed that changes in the nanoscale chemistry of hair directly influence the interplay of hair wetting and entanglement and therefore macroscopic hair friction. The authors suggested that the increase in hair hydrophobicity due to the depletion of the F-layer lipids would facilitate water distribution and therefore entanglement during drying. Their hypothesis was corroborated by wetting experiments as well as nanoscale, macroscale friction tests and macroscopic evaluation of hair bundle structure between different levels of hair damage and conditioner treatments. A schematic overview of the effects of removing the 18-MEA from hair due to Tokunaga et al.[39] is shown in Fig. 2.14 This further supports the idea that the nanoscale surface chemistry is driving the macroscopic hair structure and manipulations.

With plenty of evidence that nanoscale experiments and simulations can provide insights to the fundamental tribological mechanisms, it is worth asking whether investing resources in macroscale investigations are even required. There are clear arguments that justify further continuing the macroscopic tribological research on hair: High-throughput screening of formulation effects on the sensory perception is one advantage of macroscopic setups, which is only starting to become practical in nanoscale simulations but is still limited to few examples in nanoscale experiments, e.g. Ref.[218] Furthermore, previous sensory perception studies have found that the feel of hair might also be influenced by inherent macroscopic properties of the hair

such as the diameter.[23] This underlines the need for integrating knowledge from all accessible lengthscales into the development of hair care products if both the direct effect and underlying mechanisms of a specific hair treatment are of interest. This is in fact not unique to hair but a challenge common to many other soft tribological contacts.[277] Multiscale hair friction studies are rare in experiments to date (e.g., Ref.[42]) but could become more accessible due to computational models, especially when an educated high-throughput screening approach is desired. Reproducing and thus understanding trends from sensory perception in repeatable laboratory experiments is also essential to enabling fine-tuning of hair care formulations to consumer needs. Some work has already been done in this area, including wetting, combing and friction experiments.[23,32,278] Nonetheless, these macroscopic approaches should be complemented by mechanistic insights from smaller scales which will be explored as part of this work.

2.4.4 Influence of contact load & sliding velocity

It is essential to consider the difference in the normal load that is subjected to hair contacts in different laboratory setups and real environments. Most experimental studies reported the friction coefficient as a linear fit to lateral forces versus normal load according to the extended Amontons-Coulomb law.[17,70] The linear increase of friction forces opposing the direction of sliding as a function of the normal load is usually attributed to an increase in contact area.[17] However, irreversible processes at the nanoscale are equally relevant,[147] as has been confirmed in numerous NEMD studies where the macroscopic contact area was kept constant for varying normal loads.[147,223,279] The nanoscale heterogeneity, surface potential and local amount and distribution of lubricants within the contact all contribute to friction, although might be masked by surface roughness effects in macroscopic measurements. The contact composition as a function of the normal load has been identified to strongly influence the shear stress when varying the contact pressure in NEMD simulations, which is why preliminary squeeze-out simulations can be helpful when considering different normal loads.[279] An exception to an ideally linear behaviour has been observed on damaged and subsequently conditioned hair in AFM friction measurements, where a step-wise linear behaviour was reported.[16] This was attributed to the depletion of cationic surfactants at higher loads under shear.

AFM experiments allow for accessing the nanoscale tribology of hair but are inherently limited to sliding velocities in or below the range of μm s^{-1} to avoid hydrodynamic perturbations.[211] This is much lower than what would be considered physiologically relevant (on the order of tens of centimeters per second) assuming manipulation scenarios such as combing and rubbing against skin.[11,154] NEMD simulations on the other hand are still limited to higher sliding velocities than the AFM but can well reach physiologically relevant sliding speeds of a couple of centimeters per second. In general, trends from nanoscale experiments and simulations cannot always be extrapolated to physi-

ologically relevant operation conditions. In some instances, sufficient amounts of data might allow for fitting to either the extended Amontons-Coulomb law, or even more general frameworks such as stress-augmented thermal activation models.[229,280,281]

2.4.5 Hair care formulations

By definition, conditioning formulations are intended to repair damaged hair and provide a smooth appearance, a pleasant, soft sensory perception and good hair detanglement performance.[31] Shampoos should typically also serve a cleansing role,[101] removing excess oils and detrius. Secondary roles such as perfuming, hair root and scalp treatments are not discussed here, as the involved compounds in the formulations are not expected to be highly relevant to hair tribology at typical concentrations. Rather than discussing shampoos and conditioners separately, we will differentiate by the capability of a formulation to undergo a macroscopic phase transition upon dilution. Finally, we will also review in this section how, and if at all, the bulk properties of a hair care formulation can be linked to the friction response of treated hair.

a) Single-phase conditioning formulations

It has been long-known that cationic surfactant conditioners reduce hair friction.[151,159] Scott and Robbins measured the friction coefficient as a function of the cationic surfactant concentration and observed a minimum friction value on several comb materials at relatively low surfactant concentrations (0.005% for CTAB in a pH-buffered solution).[159] A contribution from the formation of micellar aggregates on elevated friction was ruled out by additional experiments with different surfactants or salt addition to control the onset of the critical micelle formation (cmc) concentration, which produced similar coefficients of friction. The frictional response as a function of the surfactant concentration in Ref.[159] showed a clear resemblance with a typical Stribeck curve. However, the authors argued that hydrodynamic lubrication due to an increase of surfactants in the contact was likely not responsible for the non-monotonic nature of friction with CTAB. They rather suggested that this behaviour might be due to a change in the electrostatic nature of the contact, where negatively charged sites on bleached hair are neutralized at intermediate surfactant concentrations but excess surfactants lead to a net-positive surface charge. Scott and Robbins also observed that such excess cationic surfactants could be easily rinsed off the hair surface.[159] Crossed fibre tribometer friction consistently tests also yielded lower friction for hair treated with low concentrations of CTAB compared to contacts fully wetted with water only.[160] LaTorre and Bhushan observed further that commercial hair conditioners containing cationic surfactants could effectively restore the friction coefficient of virgin hair on chemically damaged fibres.[17] The adsorption of cationic surfactants from aqueous solution onto hair can also effectively eliminate high-frequency stick-slip phenomena between hair bundles and human skin.[184]

More complex aggregate structures of adsorbed surfactants on hair are also conceivable and could have interesting implications for hair lubrication. Nagahara et al.[172] reported that a model shampoo containing cationic surfactant vesicles provided combing force reductions on color-damaged hair below the value of the untreated virgin hair. However, the exact structure of the deposited aggregates is not known as only the structure in solution was analyed. It is therefore unclear whether the lubrication effect was due to the vesicles breaking up into thinner layers or if *intact vesicle deposition*[282,283] was achieved. It has been shown for phospholipids (DSPC) on mica surfaces that intact vesicles could provide substantially lower coefficients of friction than lipid bilayers.[284] Softening mechanisms on textile surfaces have also been attributed to the deposition of cationic surfactant vesicles.[285]

Free fatty acids have also been found to be a suitable additive for restoring a hydrophobic character and low friction properties on chemically damaged hair.[171] The addition of silicones to shampoos and conditioning products[121,176] containing cationic conditioners has also been found to provide a superior lubrication performance. This was attributed to binding of silicones to polymer backbones on the surface. Additionally, fatty alcohols and silicones are commonly used in combination with cationic compounds to form the class of lamellar gel conditioners.[105–107] LaTorre et al.[105] investigated the hair friction in the presence of conditioners containing cationic surfactants, fatty alcohols and silicones. They reported a highly heterogeneous distribution of conditioners on the cuticle of damaged hair which was attributed to the intrinsic hair heterogeneity and distribution of anionic sites. The addition of PDMS improved the lubrication efficiency of the conditioners during sliding conditions.[105] Amino silicones were found to be similarly effective at reducing combing work even for virgin hair.[170] It was also found that the size and chemistry of the counterions for cationic surfactants in lamellar phase conditioners directly influenced the wet friction of hair tresses. A less swollen, more densely packed surfactant layer was found on hairs treated with behenyl trimethyl ammonium methyl sulfate (BTAMS) compared to behenyl trimethyl ammonium chloride (BTAC), which resulted in substantially reduced wet friction and a higher acceptance rate in sensory panel tests.[106]

The deposition efficiency and structure of larger molecules such as polymers and cationic polyelectrolytes on hair will strongly depend on the architecture, polyelectrolyte charge density and salt concentration. Pfau et al. reported a decrease in the deposition of cationic polymers by mass with increasing molecule charge density on hair, which was attributed to a more efficient neutralization of surface charges at higher polymer charge density.[286] It was also shown that a higher molecular weight of polymers reduced adsorption which was attributed to steric hinderance.[286] Hössel et al.[112] compared different quaternary polymer architectures with respect to their hair conditioning performance. While all four considered polymers yielded substantial combing force reductions, a branched polyelectrolyte (Polyquaternium 44) was

found to out-perform the other compounds with 40-50% force reductions at low bulk concentrations (0.1-0.5 wt-%). This was attributed to a more pronounced coiling of P44 compared to the other polymers arising from its branched vinylpyrrolidone group which would allow fast deposition on the surface and avoidance of surface 'overcharging'. P44 was also found to desorb more easily compared to the other polymer-surfactant formulations. Wet combing force reductions due to cationic quat-based polymers were attributed to the arrangement of polymers in brush-like layers on the hair surface, where uncharged parts of the polymers would protrude in the bulk in the form of loops and tails.[112] Friction reductions were also observed on bleached hair treated with PLL-*g*-PEG polymers which are known to form brush-like conformations on negatively charged surfaces.[209] Lubrication by polymer brushes is common in other biological systems such as articular cartilage, where ultralow friction is essential to the longevity and wear resistance of joints.[287]

Treatment with conditioners can also increase hair-hair adhesion forces[152] and adhesion between a single hair and an AFM tip[105,220] due to the formation of a meniscus between the two contacting surfaces. It was also found that surface-normal adhesion forces increased with the molecular weight of a conditioning silicone polymers.[152] Adhesion forces are further increased by an 'overconditioning' effect, i.e. the deposition of excess conditioner than required for optimum lubrication. This was found to increase capillary forces and lead to the formation of a thick, viscous film on hair.[70,205] The hydration of the adsorbed layers on hair also affects the lubrication performance. Polymers can render high friction forces on dry hair by means of a soft, thick viscous film but still be effective at reducing wet combing forces as capillary effects are suppressed.[70,205] By measuring hair adhesion using functionalized AFM tips, Labarre et al. reported strong differences in the structure of deposited conditioners between virgin and platinum-bleached hair.[220]

b) Oppositely charged polyelectrolyte-surfactant formulations

The importance of oppositely charged polyelectrolyte-surfactant formulations for the deposition of personal care products has been highlighted in the introduction of this work and elsewhere numerous times.[5,119,288] However, the hair friction mechanisms related to the presence of adsorbed oppositely charged polyelectrolyte-surfactant complexes are not fully understood to date. One working theory on the effectiveness of polyelectrolyte-surfactant as a lubricant is that complexes adsorb on hair as a highly swollen film which through exposure of hydrophobic polymer tails provides beneficial lubrication similar to that observed in polymer brushes or hydrogels.[289]

Early experiments on hair with adsorbed synthetic cationic polyelectrolytes and anionic detergents at high charge densities reported no significant effect on the tactile perception and combing work.[173] This was explained by the desorption of neutralized complexes forming between the oppositely charged compounds. The des-

orption process was also further corroborated by streaming potential measurements during the titration of anionic surfactants on hair fibres with pre-adsorbed cationic polyelectrolytes.[173] Treatment of virgin hair with polymer-surfactant formulations containing the cationic polymer Merquat, anionic (SLES) and zwitterionic surfactants (CPAB) rendered significant combing work reductions.[176] Changes in the polymer concentration and therefore the solution viscosity did not have any quantifiable impact on the combing force without excess salt. Upon addition of excess salt, the solution viscosity profoundly decreased along with combing force reductions which was attributed to a decreased spreading efficiency on the surfaces.[176] The deposition of complexes from shampoos containing micrometer-sized coacervates reduced both the friction and surface roughness off perm-damaged hair, as measured by lateral force microscopy.[290] Miyamoto et al.[161] proposed an alternative explanation to friction reductions observed from the deposition of polyelectrolyte-surfactant formulations which also contained non-ionic polymers. Their results were explained by a model in which free non-ionic polymers would deposit to the hair surface, while charge-neutralization between the remaining polycations and anionic surfactants occurred in the bulk. The polyelectrolyte-surfactant complexes would then adsorb on top of the non-ionic polymers to from a multilayer structure.[161] This suggests that kinetic processes also play a role, as previously highlighted by Nylander.[118]

Thin-film coating experiments were used to evaluate both pure cationic polymer formulations and polymer-surfactant formulations with SDS with respect to gloss, opacity and film-on-film friction.[291] It was observed that strong friction reductions were observed with SDS for polyquaternium polymers in particular. For cationic guar, friction was relatively constant between purely polymeric and polymer-SDS formulations, with little dependence on the molecular weight of guar.[291] This once more suggests that the frictional response of such polymer-surfactant layers might be highly sensitive to the polymer architecture. It has indeed been shown in self-consistent field theory calculations that the structure of polymer-surfactant layers on biomimetic hair surfaces strongly depends on the polymer architecture.[129,247]

Interfacial friction NEMD simulations of hydrodynamic hair-hair contacts containing self-assembled oppositely charged polyelectrolyte-surfactant complexes[36] suggest that shear-induced polymer stretching and detachment might contribute to strong temporal fluctuations in friction forces. These simulations were performed under hydrodynamic lubrication conditions, which will only occur at low normal loads in aqueous films[292] or for highly viscous lubricants. Lubrication mechanisms in more confined systems and in the boundary lubrication regime remain yet to be investigated and will be discussed later in this work. On another note, there are also indications of kinetically trapped states of adsorbed polymer-surfactant complexes,[118,123,248,288] which are deemed difficult to be accurately captured in either equilibrium SCFT or molecular dynamics. Advanced sampling techniques[293,294] might be suitable accel-

erators for molecular simulations allowing to screen a higher fraction of the extremely intricate energy landscape of large polyelectrolyte-surfactant complexes on interfaces.

c) Relationship between bulk properties and hair friction

The capability of linking bulk properties to the expected behaviour on surfaces is an intricate idea for simplifying the formulation development in many biochemical systems. Some studies have tried to draw a direct link between the rheology of hair care formulations and their lubrication or tactile performance.[107,112,176,295–297] Ozkan et al.[295] coupled non-linear rheological measurements with expert sensory perception panel test on hair to demonstrate that 'rheological fingerprinting' would be suitable to predict the tactile performance of cosmetic products. A high viscosity is generally beneficial to forming a consistent film on the substrate,[107,176] as capillary droplet formation is suppressed. This aligns with the classical Stribeck curve perspective of a shift towards higher Hersey numbers ($He = \mu \cdot v_s / \sigma$) with higher viscosities and therefore towards the hydrodynamic lubrication regime where surfaces are fully separated by lubricants.[176] Davies et al. consistently reported that a higher viscosity in lamellar gel conditioners containing cationic surfactants and fatty alcohols resulted in a more even distribution of a conditioning film on hair and as a result yielded lower combing work.[107] On the other hand, it was highlighted by Iwata et al. that friction reductions observed on hair treated with lamellar gel conditioners were not due to an increased deposition efficiency of a formulation with a higher storage modulus but rather due to superior structural properties after adsorption, thus a higher resistance against breaking.[106] A direct causality of rheology of polymeric solutions on hair friction is in fact not always apparent. For soft matter systems, the traditional Stribeck curve behaviour is in fact not universally applicable, as noted by Selway et al.[298] Other works also found no direct correlation between combing work and the formulation viscosity.[296,297]

This suggests that predictions of the tribological response on hair by treatment with hair care formulations based on the rheology are not always adequate. One factor is probably the sheer number of morphological transitions that aggregates can be subjected to during adsorption and rinsing (dilution). The link between viscosity and lubrication might indeed be highly non-linear beyond what is predicted by a typical Stribeck curve and subject to a vast number of variables (water hardness, dilution factor) which are hard to control in real application. Surface overconditioning might also affect the tactile perception of overly viscous conditioners, while sufficient spreadability might not be obtained at low formulation viscosities. To date, no openly available theoretical or computational models have been applied to investigate the link between formulation viscosity and hair tribology to the authors' knowledge. Also in the case of shampoos, water is almost always either an integral part of the applied formulation or indirectly present on the hair surface due to a humid environment or explicit wetting. This complicates drawing conclusion from the bulk, as additional mechanisms such as phase separation and dilution-deposition occur, often by design, as discussed above.

2.5 Conclusions

The understanding of hair tribology is essential controlling the tactile perception and detanglement performance and therefore the success of hair care products. In this chapter, we discussed the different approaches to quantifying hair tribology with a main focus on friction and adhesion. A wide range of scales has been covered in hair tribology studies ranging from nanoscale experiments and simulations to macroscopic high-level studies on hair bundles.

Macroscopic hair friction studies are primarily suitable for high-throughput screening of many different care formulations. It is expected that formulators will continue to rely on macroscopic evaluation techniques despite their more qualitative nature. The majority of tribological mechanisms on hair are best resolved by resorting to micro- and nanoscale screening techniques such as AFM and more recently computational models. Molecular models provide a suitable basis for preliminary screening of optimum hair care formulations with respect to hair tribology and other relevant handles in an integrated approach. They are in fact a candidate for accelerating the exploration of greener, as well as previously untested chemistries that are otherwise difficult to synthesize in the laboratory. The use of multiscale approaches by means of coupling molecular simulations to larger-scale continuum models may ultimately resolve the limit of being able to fully capture macroscopic phenomena with molecular simulations.[20]

Formulators are presented with a number of function optimization parameters for hair care products going beyond the reduction of hair friction, for instance product degradation performance, handling (rheology) and perfuming performance. This suggests the use of an integrated design approach not only tuning one of such formulation properties at a time. It might for instance be practical to link some tribological properties of hair care formulations to formulation bulk properties. However, as discussed in this chapter, there is no clear evidence that such predictions can be made universally and that surface sciences are expected to to remain essential to the formulation process. There may also be situations in which low friction or adhesion, generally perceived as a handle for hair sliperiness and softness, might be counterproductive. It might for instance be sensible to avoid ultra-low friction of shampoos on skin for the sake of practicality as consumers might otherwise spill the product during the washing process before it can even be transferred to hair. Bhushan[31,104] also highlighted that some hair styles for curly hair might actually benefit from a certain degree of hair adhesion. This highlights another challenge that formulators are faced with: one the one hand, the universality of a care product will likely drive its success. On the other hand, more specialized products might be required, also due to regional differences in hair styling preferences and variations in damage mechanism among different ethnic groups.[86] Some research has already focused on highlighting more refined regional and ethnic differences in the hair structure and surface chemistry, including Brazilian[89]

and Mongolian hair.[90]

With regards to experimental hair tribology, biomimetic surfaces lend themselves as a suitable alternative to direct tribological measurements on hair, skin or other soft substrates. Coated AFM tips[216] as well as monolayer-functionalized mica surfaces and colloidal probes (this work) have already been used to mimic the surface chemistry of hair at various degrees of chemical damage. Macroscopic hair mimic surfaces imitating the cuticle scale structure for tactile evaluations against skin were also applied in the past to study hair tribology.[180,190] PDMS and polyurethane are suitable skin mimics for measuring skin-on-hair friction at macroscopic scales.[23,27,180,182,184,191] One advantage of using biomimetic surfaces over real hair is the increased control over repeatability and surface roughness. Colloidal probe AFM either with or without chemical functionalization further allows for capturing the soft nature of the hair substrate, as opposed to sharp AFM tips. Further advances in the manufacturing process of such probes is expected to allow for more controllable bulk probe properties and surface roughness features.[277]

With regards to the structure and morphology of human hair, relatively few questions remain open.[56,57] However, hair tribology, particularly at the nanoscale, is not fully understood to date. This constitutes the relative importance of surface roughness and surface chemistry as well as the lubrication mechanism of polymer-surfactant complexes on hair. Recent nanoscale experiments suggest that surface chemistry could account for the majority of the increase in hair friction when chemically damaging the hair. This will be explored in the following chapters by using molecular modeling on new biomimetic hair surface models at interfaces. The nanoscale mechanisms of lubrication and organization of conditioning agents in such hair care products are also not fully understood and will therefore also be part of the following work. In the last chapter, we will also return to link some of the concepts and methods discussed in this chapter with future perspectives in hair tribology and the following simulations.

3 Coarse-grained molecular models of human hair surfaces

The content of this chapter was published as a journal article in Soft Matter.[299] *The novel wetting experiments shown in this chapter were fully conducted by Dr. Yuri Roiter (Procter & Gamble).*

3.1 Introduction

As outlined in the previous chapter, a detailed understanding of the chemical composition and structure of the surface of human hair is important for the development of more effective and sustainable hair care products.[5] In the previous chapter, a range of molecular modelling techniques was reviewed for studying the tribological properties of hair. This included both continuum approaches such as SCFT,[128,129,300] atomistic[65,262] and coarse-grained MD.[36,110,301] However, none of these models considered chemical hair surface damage which is integral to studying all pristine, treated and weathered hairs.[a] Direct compatibility for further NEMD simulations would also be desirable. Therefore, a new molecular model of the F-layer of human hair is introduced in this chapter. A coarse-grained molecular dynamics approach for modeling the F-layer in the fully-functionalised state and at various degrees of damage is pursued. In particular, the coarse-grained *MARTINI* force field[264,265] is used throughout. The level of coarse-graining provided by *MARTINI* allows for significant system upscaling compared to AA force fields.[65] Local three-dimensional structural details, thermodynamic properties, and certain phase transitions can still be resolved,[265,302] all of which is particularly relevant for the hair surfaces studied here. This is a distinct advantage over mean field approximations, such as SCFT, which has been used to study surfactant and polymer adsorption on model hair surfaces.[128,129] For fully-functionalised hair, a three-dimensional surface model of fatty acids is constructed and grafted to a graphene substrate in a hexagonal arrangement. This model is validated against the previous AA-MD model due to Cheong et al.[65] To represent damaged hair, we randomly replace an increasing proportion (0-100 %) of the neutral fatty acid molecules with anionic sulfonate groups. We study how the surface structure changes with increased damage in vacuum, aqueous, and n-hexadecane environments. Using contact angle measurements, we confirm that the *MARTINI* model can capture the wetting behaviour of fully-functionalised and damaged hair in both polar (water) and non-polar (n-hexadecane) solvents.

It is anticipated that the proposed models will facilitate MD simulations of the adsorp-

a Most of the otherhair MD models[36,110,262] have only been published after the release of the model presented in this work.

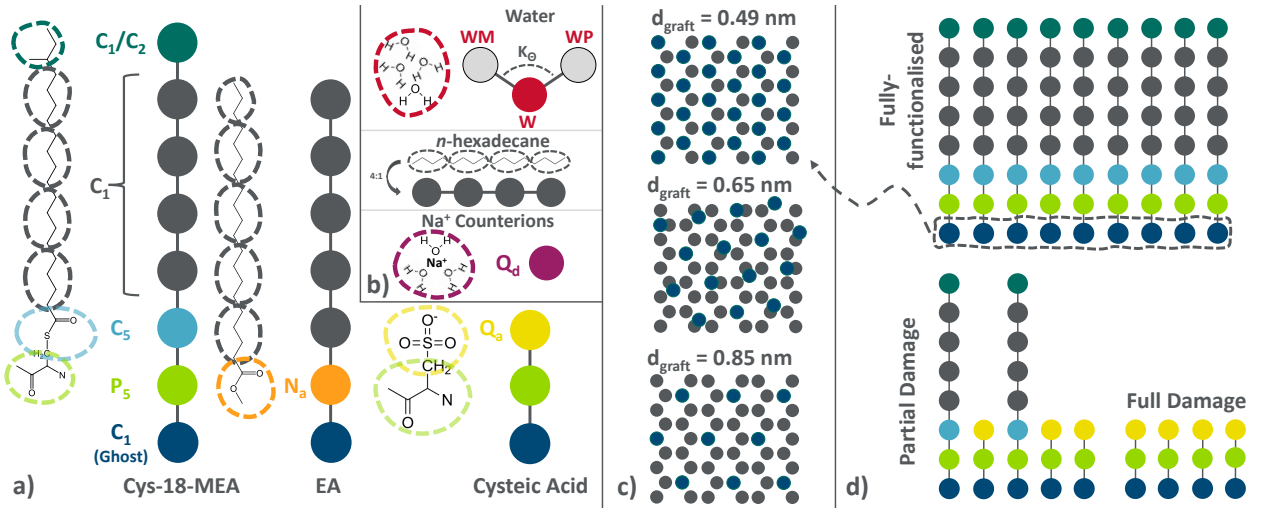


Figure 3.1: Schematics of the coarse-grained *MARTINI* model[264,265] of the hair surface. a) Coarse-grained mapping of the Cys-18-MEA, EA and cysteic acid molecules. The fully-functionalised 18-MEA molecules are represented by P_5, C_5, C_1, and C_2 beads.[303] The EA molecule is represented by C_1 and N_a beads.[304] The sulfonate groups are represented by negatively charged Q_a beads.[305] b) Coarse-grained 4:1 mapping of the polarizable water beads[306], n-hexadecane (C_1) and sodium cations with first hydration shell (Q_d).[265] c) Nominal grafting distances relative to CG graphene. The graphene layer, as employed in previous atomistic MD studies of the hair surface,[65] is represented by a 4:1 mapping to C_1 beads.[307–309] Ghost bead positions overlap with graphene beads on the graphene lattice where positions coincide. d) Different degrees of damage (0-100 % fatty acids removed) are considered.

tion of surfactants and polymers found in hair care formulations onto the surface of hair. The reduction in computational cost compared to AA force fields will enable the simulation of large macromolecules that are used to improve the feel and appearance of hair.[5] The coarse-grained models proposed here will also enable non-equilibrium MD simulations of hair friction in dry and aqueous environments - to be discussed in the following chapters.

3.2 Methodology

3.2.1 Coarse-grained hair model

Coarse-grained MD simulations are used to study both fully-functionalised and damaged hair surfaces. The *MARTINI 2* force field [264,265] is selected for this purpose. The *MARTINI* model typically coarse-grains four heavy atoms into one coarse-grained bead.[310,311] One particular use-case of MARTINI has been modelling of lipid molecules in liquid water atmosphere.[265,310] Its successful use in coarse-grained simulations of supported lipid monolayers[312] and bilayers[304,310,313] makes this forcefield particularly suitable for this work.

Schematics of the model structures for fully-functionalised and damaged hair are depicted in Fig. 3.1. The fully-functionalised hair surface model includes a complete monolayer of 18-MEA groups, which are covalently bound to cysteine amino acids that are grafted to a rigid graphene substrate. This approach is similar to that used in the

AA-MD study by Cheong et al.[65] The 18-MEA molecules consist of C_{20} chains with a methyl branch on the eighteenth C atom and are modeled here as a chain of five C_1 (alkyl) beads. In preliminary MD simulations, a chain of four C_1 beads and a terminal C_2 bead was also tested, which increases the alkyl-water LJ interaction strength.[314] This could be sensible for 18-MEA (compared to EA) due to the conformational disorder[315] caused by the methyl branch-containing alkyl group.[316]

The C_1 beads are connected to a C_5 and P_5 bead, which are representative of the thioester and amine/carboxyl groups in cysteine, respectively. This structure is an extension of the palmitoyl cysteine (C_{16} chain) *MARTINI* parametrisation suggested by Atsmon-Raz and Tieleman[303] by one additional C_1/C_2 bead. The P_5 beads, which represent the outer protein layer of the epicuticle, are grafted to the graphene layer below using a bonded potential. The graphene sheets are represented by a 4:1 coarse-grained mapping[307–309] Unlike 3:1[317] and 2:1[318] mapping, this retains a hexagonal lattice of atomistic graphene. This graphene layer prevents solvent molecules from escaping through the monolayer surface and can also be used to control pressure and sliding in future non-equilibrium MD simulations. The hexagonal structure of the graphene sheet is somewhat different from the proteinaceous structure below the 18-MEA on real hair.[253] However, it effectively represents an atomically-smooth, impermeable surface to support the lipid monolayer.[65] We expect the effect of this simplification on the monolayer structure and wettability to be small. The graphene beads only directly interact with the other beads through Lennard-Jones (LJ) interactions, which are relatively short ranged. The additional P_5 beads (which have stronger LJ interactions) provide sufficient separation from the graphene beads to ensure that direct interactions with the lipid and solvent beads are negligible.

The lipids are positioned in a hexagonal arrangement on top of the graphene layer, which is supported by experimental observations.[53,319] The grafting positions are independent from the graphene bead positions to allow for intermediate grafting distances, similar to those used in the AA-MD simulations by Cheong et al.[65]. These intermediate values would otherwise not be possible using the 4:1 mapping for the graphene. Therefore, ghost beads were introduced in the plane of the graphene sheet and solely interact with the P_5 bead of the lipid chain through a bonded potential. For the comparisons with the AA-MD simulations by Cheong et al.[65], lipid grafting distances of 0.49, 0.65, and 0.85 nm were considered, which correspond to surface coverages of 4.2, 2.4, and 1.4 molecules nm^{-2}, respectively. From these comparisons, the intermediate grafting distance of 0.65 nm was selected for the MD simulations to calculate the contact angle.

In the case of damaged hair, the 18-MEA molecules are randomly removed by breaking the thioester bond (C_1 to C_5) and replacing the neutral P_5 bead with an anionic Q_a bead to represent a sulfonate group.[305] This is representative of the oxidation of Cys-18-MEA

to cysteic acid, which has been observed in several experimental studies of bleached hair.[29,92,320] Charge neutrality is maintained by adding the appropriate number of non-polarizable sodium cation (Na^+) beads Q_d,[264] which also represent the first hydration shell in the *MARTINI* model.[265] Since they are expected to be easily removed through washing, free fatty acid molecules are not considered in the current MD simulations. We randomly remove chains at a number corresponding to the desired damage ratio defined as:

$$\chi_N = N_{rem}/N_{FF}, \tag{3.1}$$

where N_{rem} is the number of fatty acid chains to be removed and N_{FF} is the number of grafted chains in the fully-functionalised system. Discrete damage ratios of $\chi_N = 0$ (fully-functionalised), $\chi_N = 0.25, 0.5, 0.75, 0.85, 0.92$ (partially damaged) and $\chi_N = 1$ (fully damaged) are considered here. Previous experiments have suggested that the surface of bleached hair mostly consists of negatively charged sulfonate groups, with a mean surface coverage of approximately 2.2 molecules nm^{-2} (2.8 molecules nm^{-2} in the damaged regions).[92] For the chosen grafting distance (0.65 nm), this coverage of sulfonate groups is approximately reproduced by using $\chi_N = 0.85$.

The projected surface area ratio between lipid coverage and exposed charged groups:

$$\chi_S = (S_{total} - S_{MEA})/S_{total} \tag{3.2}$$

is used as an additional measure for quantifying monolayer damage. Macroscopic wetting theories such as the Cassie-Baxter model[321] rely on the exposed surface area. Here, S_{MEA} and S_{total} are the projected area occupied by the Cys-18-MEA chains and the total projected surface area respectively. The Cys-18-MEA surface area S_{MEA} is obtained from projecting all remaining Cys-18-MEA beads with an assumed radius of $r_b = 0.235$ nm onto the xy-plane of the periodic simulation box. This approach accounts for the effects of collapsing Cys-18-MEA chains onto the charged layers below.

3.2.2 Coarse-grained liquid-phase models

The original *MARTINI* water model is single-site and non-polarizable.[264] A single CG water bead represents four water molecules. Previous CG-MD simulations of supported lipid bilayers have suggested that the polarizable *MARTINI* water model gives more accurate results with respect to aggregation.[313] Several coarse-grained polarizable water models are available in the literature and were assessed with respect to their surface tension at the water-vapor and water-hexadecane interface: The Original polarizable water model (POL),[306] *refPol*,[322], BMW-MARTINI,[323] and refined BMW-MARTINI.[324] The *refPol* model provided improvements over the original polarizable model, such as better agreement of mass density and dielectric constant with respect to experimental values.[322] The *BMW-MARTINI* model was originally optimised to reproduce a range of properties, including the water-vapor surface tension.[325] A slab configuration ($\mathcal{L}_x = 5.57$ nm, $\mathcal{L}_y = 5.57$ nm, $\mathcal{L}_z = 33.1$ nm) with a central water layer of initial thickness

Table 3.1: Surface tension for water-vapor and water-hexadecane interfaces for different CG water models and reference experimental and simulation values

		Exp.	Orig. POL[306]	*refPol*[322]	BMW-MARTINI[323]	Ref. BMW-MARTINI[324]
$\gamma_{Wat\text{-}Vap}$	[mN/m]	n/a	31	17	78	77
$\gamma_{Wat\text{-}Vap}$ (Ref)	[mN/m]	72[327]	31[306]	n/a	79[324]	79[324]
$\gamma_{Wat\text{-}Hex}$	[mN/m]	n/a	40	34	96	65
$\gamma_{Wat\text{-}Hex}$ (Ref)	[mN/m]	54[328]	43[329]	n/a	93[324]	69[324]

$d_z = 14.3$ nm was used for simulating the interfacial tension. This was found to be sufficiently large in the x and y directions to prevent finite-size effects.[326] Treatment of long-range electrostatics was considered in the same manner as described in section 3.2.3.

The surface tension results are shown in Table 3.1 with reference values from the original papers where available. The surface tension at the hexadecane-vapour interface (24 mN/m) is the same for all of the *MARTINI*-based water models and is in good agreement with experiment (27 mN/m).[324] Surface tension values reported in the reference publications differ slightly from our results in several instances. This is expected to be a result of differences in integration timesteps and the choice of cut-off length and/or long range solver used for the LJ potential and electrostatic interactions. Preliminary simulations showed a high sensitivity to the LJ cut-off length in particular. The best agreement with the reference studies was obtained for a cut-off radius of $r_c = 1.4$ nm.

The underestimation of the water-vapour surface tension is a well known limitation of *MARTINI* water models.[265] While the *refPol* model improves a range of bulk properties, the water-vapor surface tension was not evaluated in the original publication and turns out to provide poor agreement compared to all the other models and the experimental reference. We further observed significantly a lower water-hexadecane surface tension for the *refPol* model compared to both the original polarizable model and experiments. It was therefore discarded after preliminary analysis. Both BMW-MARTINI models[323,324] suffered from freezing artefacts when departing from the bulk configuration towards a nanoscale droplet configuration on the substrate. Moreover, previous studies[314,324] found that the water-alkane surface tension was significantly over-estimated with the original *BMW-MARTINI* model. This is an unfavourable side-effect of the stronger LJ interactions used to increase the surface tension of water. The *BMW-MARTINI* model was therefore also deemed unsuitable for the current study because the systems contain both water and alkane components. We eventually selected the original polarizable *MARTINI* water model due to Yesylevskyy et al.[306] for the remainder of the CG-MD simulations. Although the water-vapor surface tension is underestimated by more than 50% with this model[306] (similar to the non-polarizable *MARTINI* model[264]), the n-hexadecane-water and n-hexadecane-water surface tensions are within 15% and 30% of the experimental values, respectively.[324,329]

It is to be stressed that the choice of integration timestep in LAMMPS is of utmost importance for producing valid results with the polarizable water models. For example, energy conservation in the NVE ensemble was not achieved for trial runs with the *BMW-MARTINI* model at timesteps of 10 and 20 fs. The timestep is therefore limited to 5 fs in LAMMPS, contrary to common simulation procedures for other codes such as Gromacs[330] as described in previous publications.[323] The vast majority of available bottom-up CG water models were also designed to reproduce a set of specific validation parameters, but tend to lack generality which can ultimately limit their application to specific purposes deviating from design configurations. Droplet wetting has not been considered in the parametrisation of any of the water models above. Future CG water modeling efforts in the *MARTINI* framework should focus on an integrated approach, considering several optimization parameters including the surface tension and wetting behavior of nanoscale systems. The recently published *MARTINI 3* force field[331] provides promising improvements to *MARTINI 2* but still lacks the integration of a suitable polarizable water model to date. This is also a chance to incorporate additional validation quantities into the parametrization of such a model.

3.2.3 MD simulation details

The MD simulations are performed in LAMMPS[332] using the velocity-Verlet[333] integration scheme with a timestep of 5 fs.[264] Non-bonded interactions between beads are represented by the LJ potential for the uncharged beads and the LJ and Coulomb potentials for the charged beads. LJ interactions between beads are shifted to zero between the cut-off radius $r_{LJ,cut} = 0.9$ and $r_{LJ,shift} = 1.2$ nm.[264] Bonds and angles are treated using weak harmonic potentials as in the original *MARTINI* framework.[264] The bond lengths in the water units are constrained using the SHAKE[334] algorithm. The full set of force field parameters used in this study can be found in the appendix, section A.1. Long-range electrostatic interactions are treated using a slab implementation[335] of the particle-particle particle-mesh (PPPM) method[336] with a Fourier grid spacing of at least $\Delta x = 0.2$ nm, a Coulombic switching radius of $r_{C,cut} = 0.12$ nm, and a relative energy tolerance of 10^{-5}.

All systems were constructed using the Moltemplate software.[337] The systems are periodic in the lateral (x and y) directions. A reflective boundary condition is imposed at the top of the simulation cell in the z direction to prevent water molecules from escaping the simulation cell. Interactions of the vapor phase water beads with these boundaries are rare due to sufficient separation distance of surfaces and droplets from the surface. A nominal box size for the water droplet wetting systems of $\mathcal{L}_x = 35.7$ nm, $\mathcal{L}_y = 30.9$ nm and $\mathcal{L}_z = 25$ nm was found to be sufficient to prevent interactions between the droplets and their periodic images. For n-hexadecane, which has lower contact angles at moderate damage levels, the system size in x and y was increased to $\mathcal{L}_x = 71.5$ nm, $\mathcal{L}_y = 61.9$ nm, respectively.

The thickness of a human hair is typically 50-100 μm and each cuticle cell is approximately 5-10 µm long.[31] This is much larger than can be directly simulated in the *MARTINI* framework. The surfaces used in the current CG-MD simulations are therefore representative of a small region of the epicuticle surface. For the damaged surfaces, the outer F-layer is partially removed, which occurs during a single bleach treatment.[320] More severe damage, such as that caused by repeated bleaching,[338] can lead to cuticle removal. This can change the microscale topography[80] and porosity[339] of the hair surface, which cannot be accounted for in the current CG-MD simulation framework.

The initial conditions for the monolayer-vacuum configurations consist of fully extended lipid chains normal to the graphene sheet and Q_d counter-ions placed at random positions above the monolayer ($\Delta z = 0.4$ nm) for the damaged hair surfaces. Other initial configurations for the counter-ions were also tested but led to similar distributions after equilibration. Energy minimization is performed for the monolayer surfaces in vacuum. The model surfaces are then equilibrated for 10 ns in the canonical (NVT) ensemble using a Nosé-Hoover thermostat[340,341] set at $T = 298$ K. A production run was then performed for a further 10 ns. The graphene layer and corresponding ghost beads are excluded from the thermostatting. Convergence to equilibrium values was monitored by means of the global kinetic and potential energies, monolayer thickness and tilt angles as well as first and second moments of the monolayer bead positions.

Coarse-grained droplet wetting MD simulations were run in the NVT ensemble for at least 20 ns. The data shown below were extracted over the final 10 ns of these simulations. The initial hemispherical droplet configuration is obtained from bulk simulations in the isoenthalpic-isobaric (NPT) ensemble at atmospheric pressure and $T = 298$ K.[342] The total number of polarizable water units in the base configuration is $N = 18{,}121$, leading to an initial droplet radius, $r \approx 10$ nm. For n-hexadecane, $N = 4{,}036$ molecules are used for the initial droplets, which resulted in a similar initial droplet radius. The hemispherical droplets are placed at the centre of the equilibrated monolayer surfaces and simulated in the NVT ensemble along with the lipid molecules.

Equilibrium contact angles for water and n-hexadecane are obtained based on the procedure described by de Ruijter et al.[343] and Werder et al.[344] and successfully applied to *MARTINI* water droplets on graphene surfaces by Sergi et al.[310]. Discretization sizes of $\Delta z = 0.05$ nm and $\Delta z = 0.025$ nm in the surface-normal direction are used for high contact angle droplets ($\chi_N \leq 0.75$) and low contact angles ($\chi_N > 0.75$) respectively. Circular fits are obtained from averaging over five individual snapshots within a bin of $\Delta t_{bin} = 0.25$ ns each. One LJ cut-off length normal to the hair surface is excluded at both the base and top of the droplet. As noted in de Ruijter et al.[343], the droplet base is prone to deviations from the spherical shape as non-bonded interactions with the

surface are strongest in that region. This is expected particularly for the heterogeneous damaged surfaces. We also exclude the top of the droplet due to the high angular offset with respect to the droplet surface, which leads to poor fitting results for the density profiles in the Cartesian coordinates. The vertical position of measurement for the contact angle is determined as the surface-normal position z corresponding to a threshold of 99 % of the cumulative monolayer mass distribution function:

$$M(z) = \int_0^z m(\hat{z})d\hat{z} \,/\, \int_0^\infty m(\hat{z})d\hat{z}. \tag{3.3}$$

The heterogeneous nature of the damaged surfaces and nanoscale droplet sizes mean that pinning is possible in the wetting simulations.[345] To account for this variability, two different initial water droplet positions shifted diagonally across the periodic box ($\Delta x = \pm 14$ nm, $\Delta y = \pm 9$ nm) and two different random monolayer damage seeds with a water droplet at the centre position are considered. This leads to five trials per damage level, which are used to obtain the equilibrium contact angles shown below. Similar position and random seed investigations were omitted for n-hexadecane because these results show less variability.

Further MD simulations with AA force fields were also conducted to validate the structure of the fully-functionalised CG hair model. For this purpose, we used the optimised potentials for liquid simulations (OPLS)[257,258] force field for the 18-MEA monolayers and the extended simple point charge (SPC/E)[346] force field for water. Two lipid grafting distances were considered ($d_{graft} = 0.49$ nm, 0.65 nm). The simulation protocol of fully-functionalised monolayers in vacuum follows the approach by Cheong et al.[65] All bonds containing H atoms were constrained using the SHAKE algorithm.[334] A water droplet consisting of 14,642 molecules (droplet radius ~ 5 nm) was introduced on the equilibrated surface and contact angles were obtained following the same procedure as for the CG model.[347] The surface tension of the water-vapour and n-decane-vapour interfaces was recently evaluated for several force fields, including SPC/E and OPLS.[348] The authors found good agreement with experimental data for both the water-vapour (underestimated by 15 %) and n-decane-vapour (underestimated by 5%) interfaces,[348] which underlines the suitability of the AA-MD as reference cases for comparison with the corresponding CG-MD configurations.

3.3 Experimental setup

3.3.1 Hair contact angle

Dynamic contact angle measurements on hair surfaces were conducted using the Wilhelmy force balance method.[228] We chose the dynamic approach over pseudo-static contact angle measurements on single hair fibres for practical reasons. Nanoscale water droplets have been found to be quickly evaporate from or penetrate into the hair surface.[200] While nanoscale droplets of non-polar solvents (e.g. squalane) are

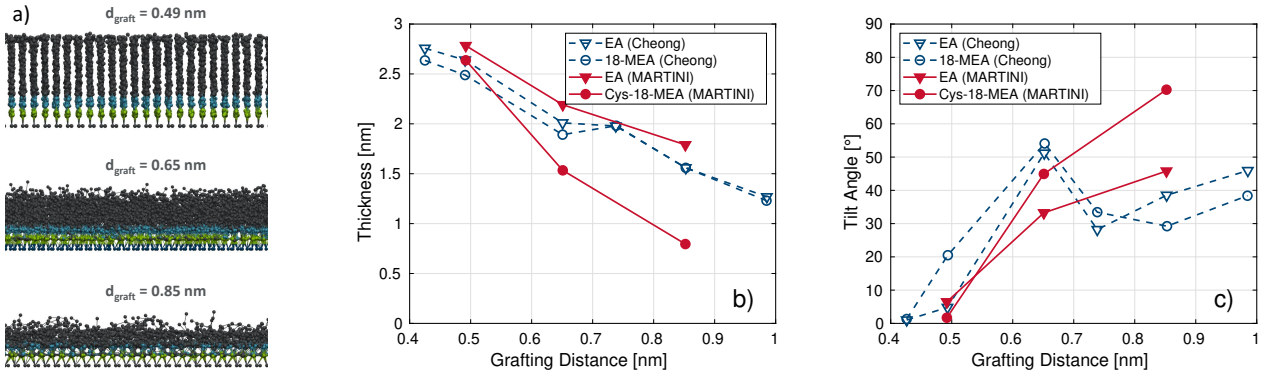


Figure 3.2: Snapshots of Cys-18-MEA lipid monolayers at different grafting distances rendered using VMD[349] a). C_1 beads are shown in black, C_5 in blue, and P_5 in green. EA and Cys-18-MEA monolayer b) film thickness and c) tilt angles compared to AA-MD reference data for EA and 18-MEA from Cheong et al.[65]. Lines are guides for the eye. The thickness and tilt angles are measured from the centre of mass of the N_a bead to the terminal C_1 bead for EA and the P_5 bead to the terminal C_1/C_2 bead for Cys-18-MEA.

more stable,[79,200] they tend to be perturbed by both the hair curvature and the overlapping cuticle edges. Pseudo-static contact angle measurements of water have been successfully measured using larger droplets on multiple aligned hairs, and these were found to be in good agreement with the advancing contact angle from dynamic measurements with single hairs.[227]

Our experimental procedure closely follows the approach described in the literature for dynamic contact angle measurements of single hairs.[43,69] A ∼2 cm segment of single fibre hair is mounted on a Kruss mount with double sided sticky tape tabs. A straight 1.5 cm segment is extended from the mount parallel to the axis of the mount to ensure perpendicular hair contact with the solvent. The diameter of the hair was measured optically. A bath of 99+% n-hexadecane or distilled water is raised at 6 mm min^{-1} until the lower end of the fibre is wetted. The segment is then immersed 0.2 mm to avoid the cut tip. The hair is further immersed at 3 mm min^{-1}, stopping every 0.2 mm for one second to measure the wetting force on the hair. This is continued until 6 mm length of hair is measured.

To validate the coarse-grained hair models at different levels of damage, we investigate two types of hair samples experimentally: virgin (pristine) and medium bleached (single bleach treatment) hair. During the bleach treatment, the hair swatches were soaked for 35 minutes in 6 % hydrogen peroxide solution (also containing 2 % ammonium hydroxide, 0.5 % acetic acid, and 0.2 % EDTA). The hairs were then washed for 20 minutes using tap water, with excess water being removed by squeezing with a towel before dying with a commercial blow drier and comb for 3 minutes. Five hairs from 120 virgin and 80 medium bleached hair swatches were analysed at the tip, middle and root positions. The results given below correspond to the mean, minimum, and maximum of these experimentally measured values.

3.3.2 Biomimetic surface contact angle

Biomimetic hair surfaces were produced by functionalising atomically-smooth silicon wafers with eicosanoic acid (C_{18}) and/or sulfonate (SO_3^-) groups. Virgin hair was represented by a pristine C_{18}-terminated monolayer, while complete damage was represented by a SO_3^--terminated monolayers. Intermediate levels of damage (e.g. medium bleached and heavily bleached) are represented by co-functionalised surfaces. The use of biomimetic surfaces eliminates any damage-induced change in microscale surface topography[80] or porosity,[339] from the experimental contact angle measurements. They therefore facilitate a more direct comparison to our CG-MD simulation results.

The ASTM D7490-13 Standard[350] test method for measurement of the surface tension of solid coating, substrates and pigments using contact angle measurements which utilizes a traditional sessile drop approach.[351–353] Both temperature (23.1 ± 0.3 °C) and humidity (50 ± 1%) were controlled. Approximately 3 µL DI water droplets were deposited on horizontally positioned silica wafers by dangling a drop about 200 µm from the surface and slowly growing the drop at 0.5 µL s^{-1} until it detached from the needle. Profiles of the droplets wetting and equilibrating on the surface were captured at 50 frames per second for 10 s. The First Ten Angstroms software [b] was used to extract contact angles from the resultant movie. Equilibrium contact angles were determined and measurements were repeated five times for each sample.

3.4 Results and discussion

3.4.1 Monolayer properties

Figure 3.2 depicts the variation in film thickness and tilt angle of the equilibrated fully-functionalised lipid monolayers at increasing nominal grafting distance. Comparisons to the AA-MD reference data by Cheong et al.[65] are also shown. A simplified CG model equivalent to their AA model of EA has been included to facilitate more direct comparison to our CG-MD results. This simplified CG EA model only differs from our final model (Cys-18-MEA) by means of the P_5 bead being omitted and a change in bead type from C_5 (thioester) to N_a (ester) for the first bead in the lipid chain. The monolayer thickness is evaluated as the mean of the distance in the surface-normal direction z between the P_5 bead (N_a for EA) and the bead with the highest position in z. The length of a fully extended EA and Cys-18-MEA chain in the *MARTINI* framework is ∼3 nm. Note that the definition for the tilt angle used by Cheong et al.[65] is based on the difference in centre of mass between the top and bottom C atoms in the lipid chain within a finite set of regions. Such a definition effectively captures regional anisotropic lipid tilt, which is not relevant for our CG-MD simulations. Instead, the tilt angle in our CG-MD simulations is computed as an average over all individual lipid chain tilt angles

b Portsmouth, U.S.A., Version 2.1, Build 381

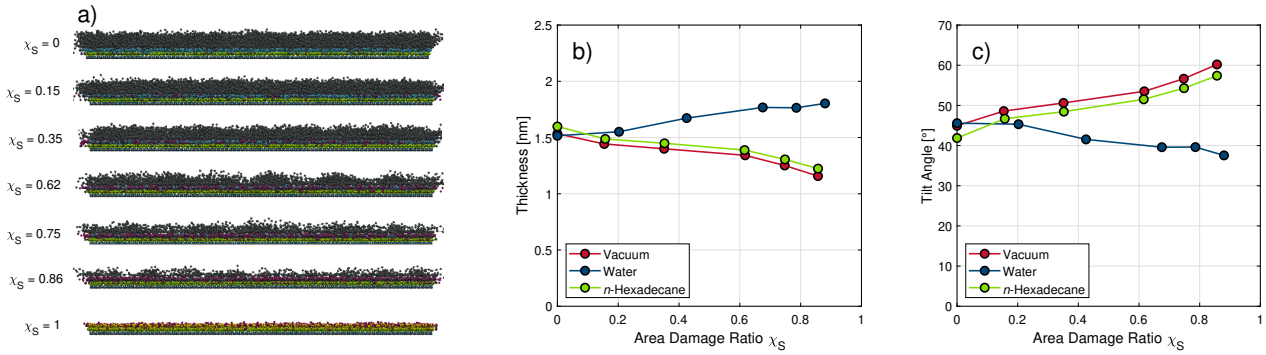


Figure 3.3: Snapshots of monolayers in vacuum from $\chi_S = 0$ (top) to $\chi_S = 1$ (bottom) rendered using VMD.[349] a). Monolayer thickness b) and tilt angle c) at a nominal grafting distance of $d_{graft} = 0.65$ nm and various degrees of random damage in vacuum environment and with water and n-hexadecane. Lines are guides for the eye.

between the P_5 (N_a for EA) and the terminal C_1 beads.

All of the molecules and models in Figure 3.2 show a general collapse of fatty acids with increasing grafting distance, as indicated by the decreasing monolayer thickness and increasing tilt angles. As the grafting distance increases, the molecules move from being aligned mostly perpendicular to the surface (tilt angle $\approx 0°$) to aligning more parallel to the surface ($\approx 90°$). This is due to a reduction in inter-chain van der Waals interactions as the distance between them increases and a concurrent increase in van der Waals interactions between the chains and the graphene layer as more of the surface is exposed.[354] There is excellent agreement between the AA-MD[65] and CG-MD results for the thickness and tilt angle of the EA monolayer at the three chosen grafting distances. In general, the CG monolayers are thicker than the AA ones, although the difference is always less than the van der Waals radius of a single CG bead (~0.5 nm). The thickness of the Cys-18-MEA decreases faster than EA due to the presence of the P_5 bead, which enables the chains to align more parallel with the surface to maximise the van der Waals interactions with the graphene surface.

The estimate of the optimum separation distance of the 18-MEA molecules of $d_{graft} = 0.49$ nm to $d_{graft} = 0.65$ nm presented by Cheong et al.[65] from their AA-MD simulations is supported by our CG-MD results. This grafting distance yields a thickness that is consistent with previous TEM experiments of virgin hair.[259] Moreover, the cysteic acid molecular density presented by Korte et al.[92] for bleached hair closely agrees with a grafting distance of 0.65 nm. In the remainder of this study, we only consider a nominal $d_{graft} = 0.65$ nm for both fully-functionalised and damaged hair.

We also investigated the effects of random damage to the lipid monolayer. Several methods for quantifying the degree of damage on the hair surface can be applied within our CG-MD simulation framework. The simplest approach is to directly use the damage ratios by means of the number of randomly removed fatty acids, χ_N, and surface coverage, χ_S, introduced in Eq. 3.1 and Eq. 3.2 respectively. The area damage

ratio, χ_S, is selected as the damage quantification parameter in the remainder of this study, since it is most representative of the degree of damage that can be measured experimentally (e.g. from AFM scans[92,266]). The relationship between the various damage ratios, both in vacuum and in the presence of wetting fluids, is shown in Fig. 3.4. The morphology of the damaged hair surfaces will depend on the external influences causing such damage. Random removal of lipid chains is likely from chemical treatments such as bleaching. Other authors have observed roughly circular[266] and striped[92] damage patterns on hair surfaces. However, the size of these regions is comparable to the size of the surfaces employed in our CG-MD simulations.

Fig. 3.3 shows the variation in the film thickness and tilt angle of the monolayers at a nominal grafting distance of 0.65 nm with an increasing degree of damage (χ_S) in vacuum and in the presence of water and n-hexadecane. In vacuum, a collapse of the lipid chains is observed with an increasing degree of damage, similar to that observed with increasing grafting distance. Introducing wetting fluids to the surface leads to intermolecular interactions with the solvent beads as well as between the chains and the surface. The addition of n-hexadecane molecules on top of the monolayer surfaces does not have any significant effect on the thickness and tilt angles compared to those obtained in vacuum. This is because the van der Waals interactions between the n-hexadecane molecules and the grafted chains are similar in strength to those between proximal grafted chains. On the other hand, swelling is observed for the damaged surfaces as water penetrates into the monolayer. In polymer brushes, such swelling behavior is observed when the interactions between solvent molecules (i.e. water hydrogen bonding) are strong compared to the interactions between solvent and polymer (i.e. van der Waals).[355] This leads to a slight increase of the monolayer thickness with higher degrees of damage in water. The degree of swelling increases with increasing damage because a reduced number of lipid chains result in weaker inter-chain interactions and allow increased water penetration into the monolayer. This is consistent with experimental measurements that have shown an increase in swelling in less densely packed monolayers.[356] The maximum degree of swelling relative to the vacuum case ($\sim$0.5 nm) is also in good agreement with previous experimental measurements of ionic surfactant monolayers adsorbed on mica surfaces from water.[356] Swelling is further confirmed by increased area damage ratios with water as opposed to the vacuum cases (see Fig. 3.4).

Figure 3.4 shows the evolution of the surface coverage of the hair monolayer (χ_S) for different degrees of damage (χ_N) in vacuum, water, and n-hexadecane environments. For all of the partially damaged systems, χ_S is lower than χ_N. This is because the flexible lipid molecules rearrange to cover the surface, increase the surface-molecule van der Waals interactions, and reduce the surface energy. The reduction in χ_S compared to χ_N is less for water than for the vacuum and n-hexadecane environments. This is due to the swelling behaviour observed in Fig. 3.3 for water. Water penetrates into the

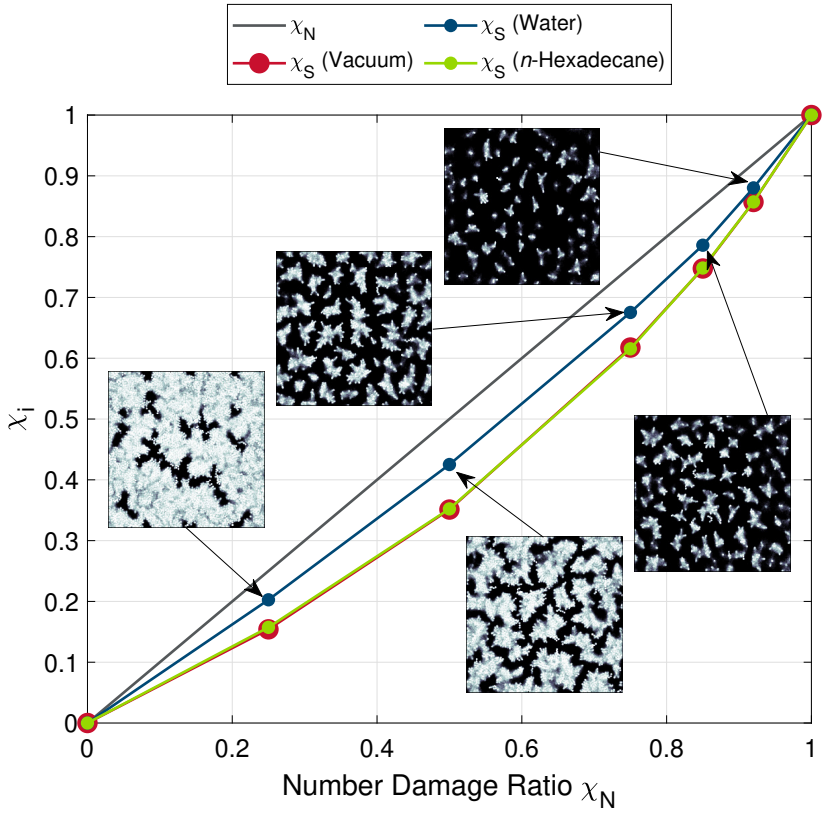


Figure 3.4: Surface coverage ratio, χ_S, as a function of the number damage ratio, χ_N, for the CG hair surfaces in vacuum, water, and n-hexadecane. Snapshots show the projected lipid coverage for the partially damaged surfaces in vacuum.

lipid layer and reduces agglomeration of the lipid chains, which means that less of the surface is covered.

Projected surface coverage maps are shown for water in Fig. 3.4 (vacuum and n-hexadecane cases shown in Fig. A.1.2 in the appendix, section A.1). The coverage maps were obtained by projecting individual beads using their van der Waals radius onto a continuous planar surface. For the vacuum case at $\chi_N = 0.25$, negatively-charged islands are observed within an otherwise dense monolayer surface. When $\chi_N = 0.50$, the size of the damaged islands increases and they begin to merge. As a result of lipid reorganisation to maximise the chain-surface van der Waals interactions, less than half of the underlying charged surface is exposed. The surfaces at higher damage ratios then show a transition from charged damaged islands to isolated lipid islands. These islands of agglomerated lipid chains shrink in size as the damage ratio is increased further. At $\chi_N = 0.92$, some islands constituent of single lipids are observed due to the mean distance to neighboring lipids being too large to be bridged, even when fully collapsed onto the charged surface below. The shape of the damage patterns is qualitatively similar to that observed in previous AFM experiments at lower resolutions.[92,99,266]

For water, more of the charged surface sites are exposed at each damage ratio due to swelling of the monolayer as evident from Fig. 3.3. For n-hexadecane, the surface

coverage is essentially identical to the vacuum case (see Fig. A.1.2 in the appendix, section A.1)). This is because of the similar interaction strength between the grafted chains and the solvent in this case, which means that swelling is negligible (Fig. 3.3). As a result of these similar interactions, there is some coarsening of the coverage pattern underneath the n-hexadecane droplet, but this does not affect χ_S (Fig. 3.4).

3.4.2 Liquid droplet wetting

The CG hair surface models are further evaluated by evaluating the equilibrium contact angle of nanoscopic water and n-hexadecane droplets placed on top of the surfaces. Examples of the fits to the density profiles of from the CG-MD simulations are shown for the fully-functionalised and partially damaged surfaces for water in Fig. 3.5 and for n-hexadecane in Fig. 3.6. Contact angle fits for AA-MD water are also provided (Fig. A.1.3 in the appendix). For the fully-functionalised system shown in Fig. 3.5 a), there is negligible penetration of water into the closely-packed lipid layer and the lipid-water interface is easily defined. The water penetration distance into the fully-functionalised monolayer is consistent between the AA-MD (1.29 nm) and CG-MD (0.85 nm) simulations (see Table A.1.1 in the appendix). For the damaged systems shown in Fig. 3.5 b) and c), water molecules penetrate into the lipid monolayer and form layers in the z-direction. The penetration distance and solvent layering increase with increasing damage level for water. For n-hexadecane, the opposite trend is observed; the solvent molecules penetrate into the lipid monolayer for the fully-functionalised system but the solvent and monolayer form separate layers for the damaged systems. These observations are consistent with previous experiments.[357] The penetration of both fluids into the monolayers layering justifies the exclusion of the region close to the interface from the density fitting for the contact angle determination. There was also good agreement between the mass density profiles from the AA-MD and CG-MD simulations for the fully-functionalised surfaces (not shown here).

The effect of the water droplet size on the equilibrium contact angle was investigated by testing droplets with approximately half (N = 8,994), two times (N = 36,464), and four times (N = 73,268) the number of beads in the initial hemisphere at t_0.[310] All damage ratios where $\chi_N < 1$ were considered for this comparison. A significant increase in contact angle with droplet size is observed between N = 8,994 and N = 18,121, indicating that the former droplet size is too small to be representative of macroscale contact angles.[347] The contact angle is more sensitive to droplet size on surfaces with a larger damage ratio. This is likely due to the size of characteristic damage features in the model. Above the baseline droplet size ($N \geq 18{,}121$), the contact angle increase is sufficiently small (within the statistical uncertainty intervals) to be considered representative of experimental measurements.[310] A modified Cassie-Baxter relationship for *fuzzy interfaces*[358] is used to perform a volume-based fit to the contact angle simula-

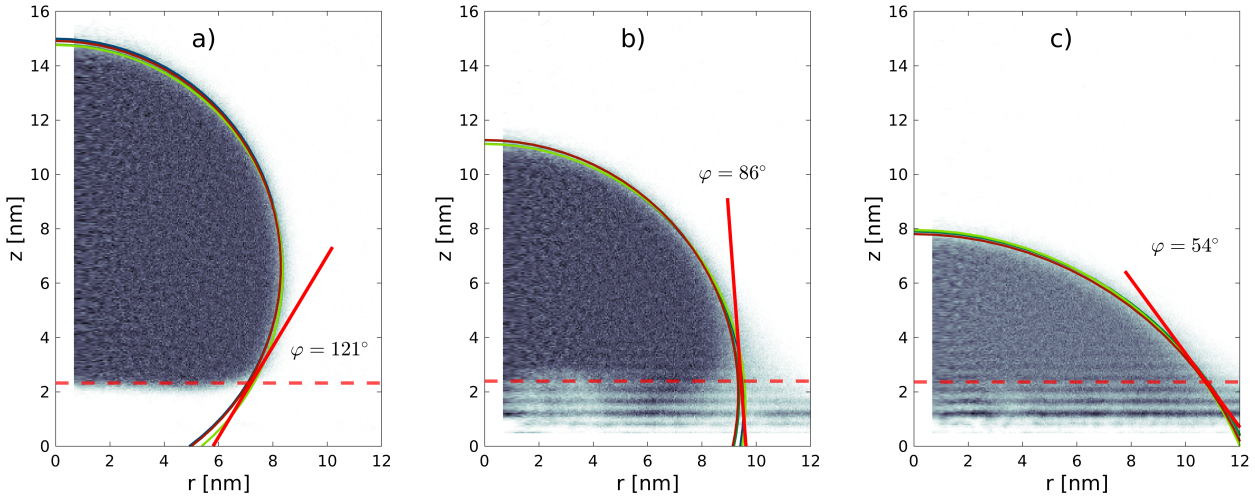


Figure 3.5: Circular surface fits of a water droplets on the (a) fully-functionalised, $\chi_N = 0$, and partially damaged, (b) $\chi_N = 0.5$, (c) $\chi_N = 0.85$, monolayers from the CG-MD simulations. Four temporal bin fits for the droplet surface (solid circles) are shown. Averaged contact angles (solely from the shown four temporal bins) are indicated by bold red lines. The surface-normal position for the contact angle measurement is shown (dashed red line). Individual surface density fits in the radial direction are omitted for the sake of clarity. Note that the CG-MD simulation domain is larger than the radial section shown here.

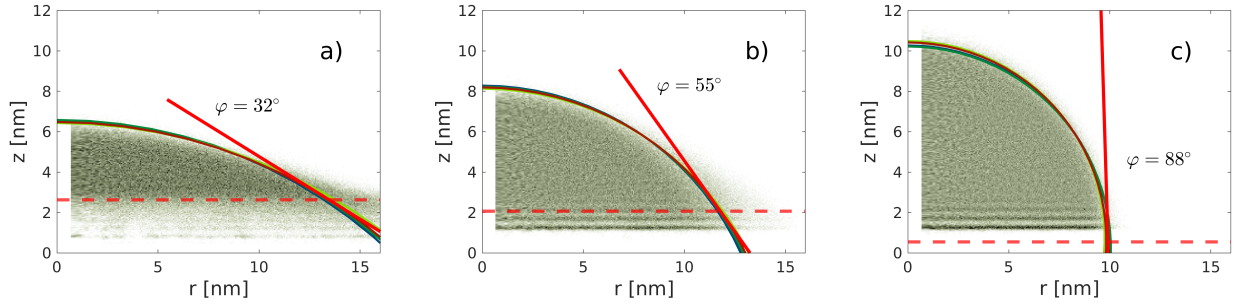


Figure 3.6: Circular surface fits of a n-hexadecane droplets on the a) fully-functionalised ($\chi_N = 0$) and partially damaged (b) $\chi_N = 0.85$ and fully damaged c) $\chi_N = 1$) monolayers from the CG-MD simulations. Four temporal bin fits for the droplet surface (solid circles) are shown. Averaged contact angles are indicated by bold red lines. The surface-normal position for the contact angle measurement is shown (dashed red line). Individual surface density fits in the radial direction are omitted for the sake of clarity.

tion data:

$$\cos\theta = \chi_S \cos\theta_{i,ref} \left(\frac{V}{V_{ref}}\right)^{m_i^{SL}-\frac{2}{3}} + (1-\chi_S)\cos\theta_{j,ref}\left(\frac{V}{V_{ref}}\right)^{m_j^{SL}-\frac{2}{3}} \tag{3.4}$$

The fitting coefficients are m_i^{SL} and m_{jSL} for a specified reference volume V_{ref} (droplet volume with N = 18,121 water molecules) and reference contact angles (fully-functionalized and fully damaged).

The nominal contact angle data from the CG-MD model, AA-MD, and experimental data of dynamic contact angle measurements for water and n-hexadecane on virgin hair are given in Table 3.2. Experimental values for advancing and receding contact angles for medium bleached hair are given in Table 3.3. Water shows much larger hysteresis between the advancing and receding contact angles, which is partially due to the swelling effects described above.[359] The advancing contact angles are used

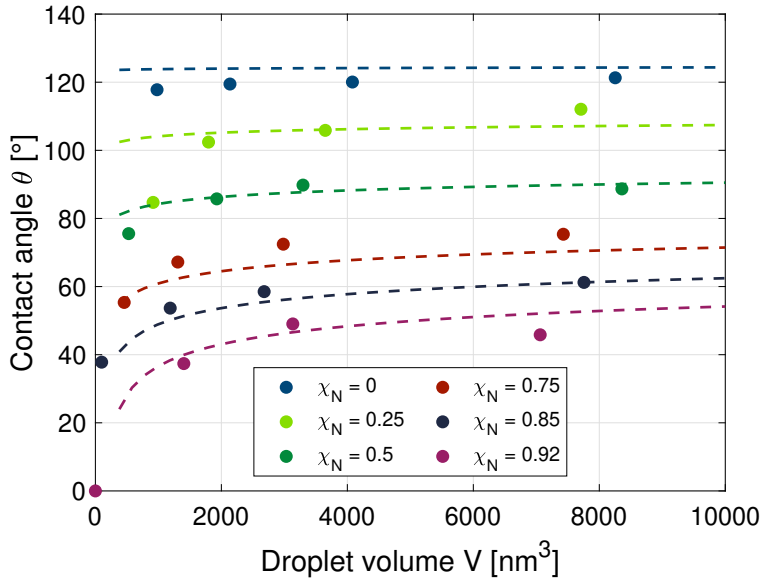


Figure 3.7: Water droplet contact angle as a function of actual droplet volume and damage ratio χ_N. Contact angle fits using a modified Cassie-Baxter relationship for *fuzzy interfaces*[358] ($m_i^{SL} = 0.5427$, $m_j^{SL} = 0.6725$) are shown by solid lines.

for comparison with the MD simulations because the receding contact angles are particularly sensitive to microscale roughness effects (e.g. cuticle edge trapping[43]), which cannot be captured in the current simulations. The preferential use of the advancing contact angle from dynamic measurements is common practice.[359] Moreover, previous experiments have suggested that the pseudo-static water contact angle (as quantified in the MD simulations) is similar to the advancing contact angle on both virgin hair (both 103°) and medium bleached hair (86° vs. 79°).[227] Good agreement is obtained between the contact angles obtained from the AA-MD and CG-MD simulations of the fully-functionalised hair surface. In both the experiments and CG-MD simulations, the fully-functionalised/virgin hair surfaces are hydrophobic (water contact angle $> 90°$) and oleophilic (n-hexadecane contact angle $< 90°$). The experimental advancing contact angles for virgin hair are slightly overestimated by both of the molecular modeling approaches. One potential cause of the differences between the experiments (106°) and the CG-MD simulations (120°) for the water contact angle is the underestimated water-vapor surface tension (~50 %) with the polarizable *MARTINI* water model.[264,306] However, the AA-MD simulations (116°), which use an atomistic water model (SPC/E[346]) that has a water-vapour surface tension much closer to the experimental value,[348] overestimates the water contact angle by 15% compared to virgin hair experiments. This suggests that the virgin hair surfaces in the experiments are not completely covered by a lipid surface and are, in fact, partially damaged.

The effect of terminal bead type (C_1 or C_2) on water and n-hexadecane contact angle for the different damage levels was investigated in further CG-MD simulations (see Fig. A.1.1 in the appendix). As expected, the use of the C_2 bead, which has stronger LJ interactions, resulted in a lower contact angle for both water and n-hexadecane on the fully-functionalised surface.[314] Use of the terminal C_2 bead improves the agreement

Table 3.2: Contact angle data (in degrees) on fully-functionalised hair from CG-MD (*MARTINI 2*) and reference AA-MD (OPLS-AA + SPC/E) and experimental advancing and receding contact angle data for virgin hair. Ranges shown are maximum and minimum values measured.

	Water	n-hexadecane
CG-MD (C_1)	120 − 10 + 3	28 − 10 + 7
CG-MD (C_2)	112 −3 +2	26 −14 +9
AA-MD	116 − 2 + 3	n/a
Experiments (Advancing)	106 − 2 + 4	36 −7 +7
Experiments (Receding)	44 −12 +11	22 −9 +9

Table 3.3: Experimental advancing and receding contact angle data (in degrees) for medium bleached hair. Ranges shown are maximum and minimum values measured.

	Water	n-hexadecane
Exp. (Advancing)	72 − 14 + 8	72 − 8 + 7
Exp. (Receding)	17 − 6 + 14	70 − 6 + 6

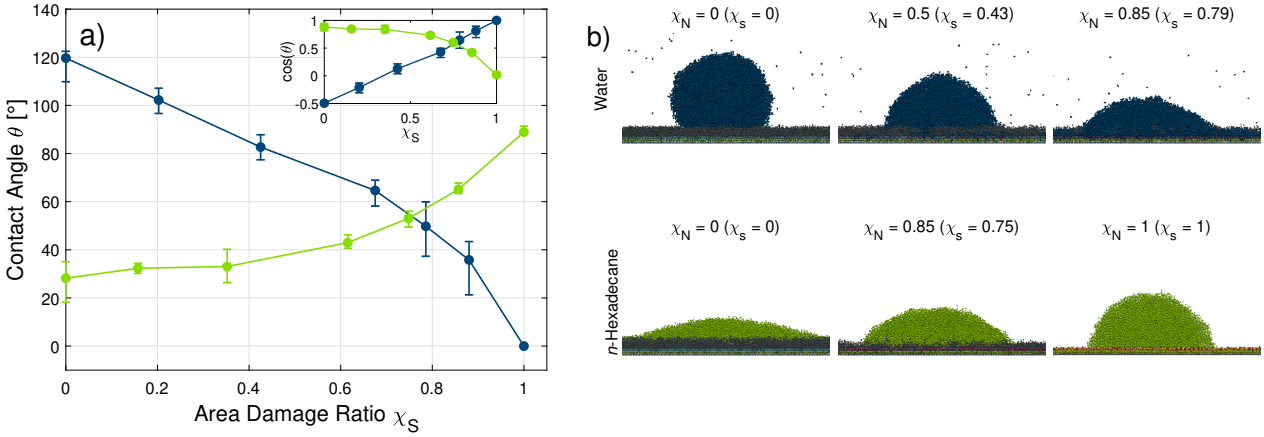


Figure 3.8: (a) Change in the water and n-hexadecane contact angles on model hair surfaces with an increasing degree of random damage. Points show mean values from three different initial droplet positions and three different initial random damage seeds. Vertical bars show the minimum and maximum values observed across the temporal binning of the different position and seed trials. Solid lines are guides for the eye. (b) Snapshots of water (blue) and n-hexadecane (green) droplets at low, medium, and high levels of damage rendered using VMD.[349] The inset shows the change in the cosine of the angle, rather than the angle.

with experimental results for the water contact angle on virgin hair compared to C_1, but leads to poorer agreement for n-hexadecane (Table 3.2). Therefore, for the remainder of this study, we employ a C_1 terminal bead.

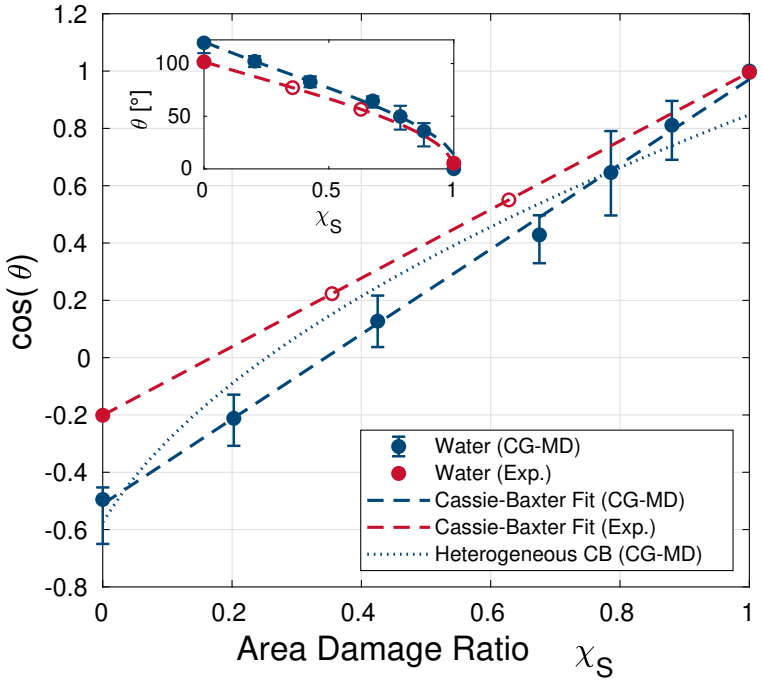


Figure 3.9: Cosine of the water contact angle from CG-MD at different degrees of damage and from experiments using silica wafer surfaces at various degrees of C_{18}/SO_3^- functionalisation. Dashed lines are Cassie-Baxter[321] fits ($\cos(\vartheta) = \chi_S \cos(\vartheta_d)$ + $(1\text{-}\chi_S) \cos(\vartheta_{ff})$) and predict contact angles for fully-functionalised and fully damaged monolayers of $\vartheta_{CG,ff} = 121°$ ($\vartheta_{exp,ff} = 102°$) and $\vartheta_{CG,d} = 14°$ ($\vartheta_{exp,d} = 5°$) respectively. The blue dotted line indicates the Cassie-Baxter fit for chemically heterogeneous surfaces.[360] Open symbols represent points where the surface coverage has been obtained from the Cassie-Baxter relation based on experimental contact angles. The inset shows the data in raw contact angle format.

Fig. 3.8 and Table 3.4 show the change in the contact angles of the water and n-hexadecane droplets on the hair surfaces as the level of damage is increased. Uncertainties are obtained from temporal binning of contact angles obtained from five individual snapshots within bins of $\Delta t_{bin} = 0.25$ ns. Fluctuations of the droplet surface are also considered. Further uncertainties from the fluctuation of the droplet base were found to be negligible. The data for each degree of damage (apart from the fully-functionalised and fully damaged cases) is obtained from different initial droplet position and random damage seed trials, leading to a total number of five trials per configuration. The nominal contact angle for each damage ratio is ensemble averaged over all five individual binned temporal datasets. The minimum and maximum limits are obtained by means of the extreme values observed among all data points from binning with additional consideration of uncertainties of the individual binned droplet surface circle fits. These two extreme values resemble the error bars shown for the data points in Fig. 3.8. The one-sided 95% confidence intervals for both the droplet radius and centre position along the surface-normal direction are evaluated to obtain the two extreme slopes of the circle fits in Figs. 3.5, 3.6 at the intersection with the monolayer surface.

The fully-functionalised hair surface is characterised by large water droplet contact angles, which is indicative of a hydrophobic surface. The droplet shape in this case is well defined because the hair surface is homogeneous and there is clear separation

Table 3.4: Contact angle data from CG-MD for the C_1 type terminal lipid beads at various degrees of random lipid damage.

	Water		n-hexadecane	
χ_N	χ_S	ϑ[°]	χ_S	ϑ[°]
0.00	0.00	120	0.00	28
0.25	0.20	102	0.16	32
0.50	0.43	83	0.35	33
0.75	0.68	65	0.62	43
0.85	0.79	50	0.75	53
0.92	0.88	36	0.86	65
1.00	1.00	0	1.00	89

between the water and lipid monolayer layers. This is reflected in relatively small uncertainties in the water contact angle at low damage ratios. Increasing the damage ratio leads to the formation of chemically heterogeneous surfaces.[360,361] Islands of charged SO_3^- groups become exposed, which reduces the water contact angles, indicating that the hair surfaces become more hydrophilic. These observations are consistent with previous experiments of bleached hair.[43,64,227] For moderate damage ($\chi_S < 0.7$), an approximately linear reduction of the water contact angle with increasing damage ratio is observed. Complete wetting by water occurs when the lipid F-layer is completely removed and replaced by anionic cysteic acid groups. Previous experiments have measured contact angles as low as 48° for heavily bleached hair,[227] which suggests that around 85% of the lipid molecules have been removed (see also Fig. A.1.4 in the appendix). An increase in the uncertainty in the contact angle is observed at higher damage ratios due to both the larger droplet radius and the increasing heterogeneity of the surface. The transition from strongly hydrophobic to increasingly hydrophilic surfaces agrees with the experimental contact angle measurements of water on virgin and bleached hair, as shown in Table 3.2 and Table 3.3, respectively. To match the experimental advancing contact angle of virgin hair (106±3°), a lipid surface coverage ratio, $\chi_S \approx 0.2$ is required in the CG-MD simulations ($\chi_N = 0.25$, Fig. A.1.4 in the appendix). A damage ratio larger than zero seems reasonable for virgin hair, since they will have been subjected to weathering effects and are therefore unlikely to be completely covered by a pristine 18-MEA monolayer.[320] The experimental advancing contact angle of medium bleached hair (72±11°) is approximately reproduced at $\chi_S \approx 0.8$ ($\chi_N = 0.85$, Fig. A.1.4 in the appendix).

For n-hexadecane, consistently low contact angles (< 50°) are sustained over a wide range of area damage ratios ($\chi_S < 0.7$). Unlike water, electrostatic interactions between the wetting fluid and the surface are not relevant due to the uncharged, non-polar nature of the coarse-grained n-hexadecane molecules. The hair surface becomes less oleophilic as the damage ratio increases above $\chi_S > 0.7$, as indicated by an increase in n-hexadecane contact angles. This transition is consistent with the experimental measurements of the advancing contact angle of n-hexadecane on virgin (36±7°) and medium bleached (72±8°) hair. These experimental contact angles can also be approximately matched in the CG-MD simulations by using $\chi_S \approx 0.2$ ($\chi_N = 0.25$, Fig. A.1.4

in the appendix) for virgin hair and $\chi_S \approx 0.8$ ($\chi_N = 0.85$, Fig. A.1.4 in the appendix) for medium bleached hair. Reassuringly, these values are the same as those required to match the experimental water contact angles (Fig. A.1.4 in the appendix). The contact angles at intermediate damage are in good agreement with static nanoscale droplet experiments on hair samples with non-covalently bound lipids removed using another non-polar wetting fluid, squalane (45°),[79] which has a comparable surface tension to n-hexadecane. The observed χ_N values or both water and n-hexadecane are also consistent with chromatography measurements of the content of the 18-MEA on virgin hair (25 % reduced compared to the root content) and single-bleached hair (80% content removed compared to the root).[320]

The dynamic contact angle experiments are further complemented by static contact angle measurements on biomimetic silica wafer surfaces with different degrees of functionalisation with eicosanoic acid (C_{18}) and sulfonate (SO_3^-) groups. The experiments on these model surfaces are not perturbed by hysteresis, curvature effects, or microscale cuticle effects. The Cassie-Baxter[321] model is applied to the experimental contact angle data to estimate the surface area coverage of C_{18} and SO_3^- groups respectively. Fig. 3.9 compares the cosines of contact angles of water from the CG-MD simulations with the corresponding experimental values. A good agreement in the slope of the contact angle as a function of damage is found between the experimental and numerical values for water at moderate damage ($\chi_S < 0.7$). The offset in absolute water contact angle values is a result of the underestimated water-vapor surface tension of the polarizable *MARTINI* water model[264,306] (and consequent overestimation of the contact angle[310]). Lines of best fit corresponding to the linear Cassie-Baxter[321] model have been included for the experimental and simulation data. The Cassie-Baxter line of best fit for the simulations lies within the uncertainty bounds for all of the data points. The CG-MD data can also be fit using the extension of this equation proposed by Israelachvili and Gee for chemically heterogeneous surfaces,[360] although the agreement with the data is poorer than the standard Cassie-Baxter[321] model. Reasonable agreement between the slopes of the experimental and simulation data fits is obtained suggesting that the Cassie-Baxter model (or its extensions[358,360]) can serve as a simple approach to describe the hydrophobic-hydrophilic transition of the idealised surface of the epicuticle of virgin and bleached hair.

3.5 Conclusions

In this chapter a coarse-grained molecular model of the F-layer that protects the surface of the hair epicuticle was developed using the *MARTINI* 2 forcefield. The 3D models presented accurately reproduce the experimental surface properties of virgin and medium bleached human hair in MD simulations. The surface coverage of lipids grafted to the underlying protein (graphene) layer is determined from comparisons to atomistic MD simulations and previous TEM experiments. We replicate the effects of

bleaching by randomly removing different fractions of fatty acid molecules from the surface and replacing them with anionic sulfonate groups. This leads to nanoscale heterogeneities due to the clustering of the remaining lipid chains to form damaged islands. The size of these islands increases with an increasing degree of damage.

The wetting characteristics of the models show good agreement with the trends observed in experiments and atomistic MD simulations. The highly hydrophobic surface in the fully-functionalised state becomes increasingly hydrophilic as the degree of damage increases, up to complete wetting when all of the fatty acids are removed. Conversely, the surfaces become less oleophilic as the level of damage increases. Accounting for the uncertainties from the two methods, we can define number damage ratios (fatty acid/sulfonate) in the MD simulations that replicate the experimental contact angles for water and n-hexadecane on both virgin hair ($\chi_N = 0.25$) and medium bleached hair ($\chi_N = 0.85$). The cosine of the water contact angle increases linearly with the area damage ratio, as predicted by the Cassie-Baxter equation. The slope of this increase is similar to that obtained with biomimetic hair surfaces functionalised with different fatty acid/sulfonate ratios.

These results pave way for equilibrium MD simulations of adsorption on the hair surface and more importantly for non-equilibrium MD simulations of the tribological behavior of hair and which will be explored in the following chapters. This is expected to facilitate the virtual screening of surfactants and polymers for the development of improved and more sustainable hair care formulations. Additionally, the new F-layer model may contribute to the development of new bioinspired surfaces with tunable oleophilicity and hydrophilicity. Such chemically heterogeneous surfaces are commonplace in nature and could be of interest in many other areas of research, for example skin and textiles.[104]

4 Nanoscale friction of biomimetic hair surfaces

The content of this chapter was published as a journal article in Nanoscale.[362] *The chemical colloidal probe AFM experiments presented in this chapter were fully conducted by Dr. Yuri Roiter (Procter & Gamble).*

4.1 Introduction

As with most natural materials, the structure and friction of hair shows considerable variability between individuals and populations.[17] The application of synthetic biomimetic surfaces with reproducible properties would therefore be useful for the screening of the tribological performance of different hair care formulations.[5] Artificial hair mimics have been constructed to reproduce the microscale roughness features of overlapping cuticles[180] and the F-layer has been represented by a gold AFM tip coated with a thiol monolayer.[216] However, the friction of biomimetic surfaces for chemically damaged hair had not yet been investigated prior to this project. The use of atomically-smooth, biomimetic surfaces in nanotribology tests allows for reduced variability compared to real hair and for the detailed investigation of the effects of surface chemistry and treatments, while eliminating the influence of microscale roughness, which otherwise leads to friction anisotropy.[26]

Confined nonequilibrium molecular dynamics (NEMD) simulations have been used to study the friction behaviour of a wide range of systems.[20] Surfactant monolayers adsorbed on solid surfaces are one of the of the most widely studied systems with NEMD simulations due to their importance in engineering and biological systems. These studies have investigated a wide range of applications from organic friction modifier (OFM) lubricant additives[280,354] to synovial joints.[363,364] While most of these studies have employed all-atom force fields,[20] the large, heterogenous surfaces and macromolecules commonly encountered in biological systems are more suited to the use of coarse-grained representations.[21] Coarse-grained force fields have already been used to study, for example, the intermonolayer friction of lipid bilayer membranes[365,366] the friction of protein translocation through nanopores,[367] and the adsorption and desorption of polymers on heterogeneous substrates that are representative of the surface of the hair under shear flow.[266,267]

In this chapter, NEMD simulations and chemical colloidal probe (CCP) AFM are used to study the kinetic friction between model hair surfaces. In the AFM experiments, the frictional response of water-lubricated biomimetic surfaces that are representative of virgin and ultimately bleached hair is studied. In the NEMD simulations, the *MARTINI* F-

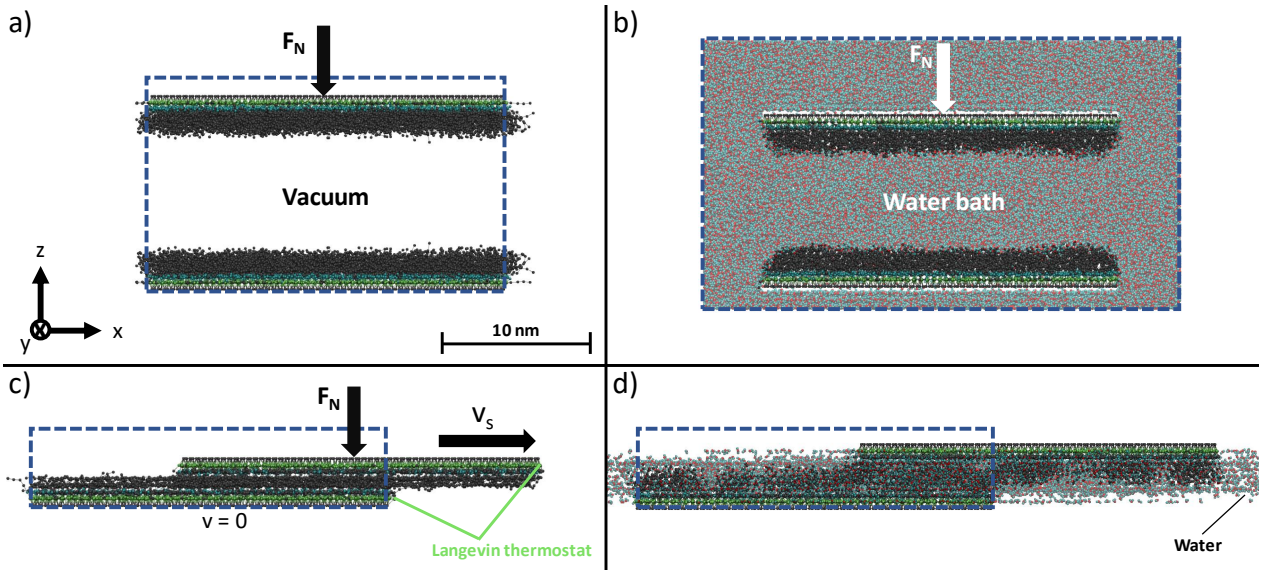


Figure 4.1: CG-MD configurations of squeeze-out systems in (a) dry, (b) wet contacts and sliding contacts for (c) dry and (d) wet contacts. Sliding contacts are shown in the unwrapped state as opposed to the periodic, wrapped bead coordinates to indicate the relative motion. Beads are coloured by type: C_1 (gray), C_5 (cyan), P_5 (lime) and water (central red, satellite cyan opaque). Rendered with VMD.[349]

layer model developed and validated in the previous chapter is employed for virgin and bleached hair surfaces. Both dry and wet contacts are considered under a wide range of sliding velocities. Both the experimental and simulation frameworks will serve as a useful benchmark for the high-throughput screening of the tribological performance of potential hair care formulations.[5,36] The methodology presented in this chapter is also expected to be applicable to investigate the nanotribology of other heterogeneous biological surfaces such as natural textiles and skin[27] which will be explored at the end of this work.

4.2 Methodology

4.2.1 MD System Setup

The coarse-grained molecular model of the hair surface at different degrees of damage, as introduced in chapter 3 is used to describe the contact interface. The *MARTINI 2* force field[264,265] is used in conjunction with the polarizable water model.[306] The description of the coarse-grained bead types of the pristine and damaged F-layer is provided in full in chapter 3. The systems were constructed using the Moltemplate[368] and packmol[369] software. All numerical settings related to LJ cutoffs, electrostatics and bond constraints are set as explained in chapter 3 with exception of the below. For NEMD simulations in semi-periodic systems (x and y), long-range electrostatic interactions are considered using the Yeh-Berkowitz slab implementation[335] of the particle-particle particle-mesh (PPPM) method.[336]

Fig. 4.1 shows a representative example of a dry and wet system (pristine hair) during compression and sliding. A graphene sheet is used as an impenetrable substrate for

grafting the lipid monolayer at a separation distance $d_{graft} = 0.65$ nm. This separation distance reproduces the experimentally-measured thickness of the F-layer.[259,299] Harmonic bonds are added between the coarse-grained carbon chain beads (C_1).[264] Deformation of the graphene beads in the z (surface-normal) direction is possible, but they are constrained in the x and y directions. The lipid grafting positions are independent from the graphene beads at a nominal grafting distance of $d_{graft} = 0.65$ nm in a hexagonal lattice (surface coverage = 2.7 molecules nm^{-2}), which is achieved using ghost beads in the same plane as the hexagonal sheet, see chapter 3. The ghost beads are coupled to the motion of the graphene sheet during compression and shearing. The hexagonal arrangement of the molecules is motivated by experimental observations.[319]

The surface dimensions are $\mathcal{L}_x = 23.8$ nm and $\mathcal{L}_y = 20.6$ nm. Given that the thickness of a human hair is typically 50-100 µm and each cuticle cell is approximately 5-10 µm long,[31] this represents a small patch of a single cuticle. We tested the effect of surface size on the convergence of the thermodynamic and friction properties of interest in preliminary simulations. No statistically significant differences were found between the selected surface size and simulations with an increase in box length of 50% in x and y. We advise against using smaller surfaces to ensure that characteristic damage patterns are properly resolved, particularly at low degrees of hair damage, where only a few damage islands exist on the surface.

An idealized contact between the cuticle F-layers of two hair fibers is considered. The contact is treated as macroscopically flat, which is an adequate simplification at the length scales of the simulation box compared to the diameter of a hair (curvature $= 0.02°$ at $\mathcal{O}(\mathcal{L}_x) = 10$ nm for $d_{hair} = 50$ µm). The surface damage is once again quantified by the number damage ratio χ_N, i.e., the ratio of the number of eicosane chains randomly replaced by sulfonate groups to the number of eicosane chains in a pristine monolayer, as defined in the previous chapter. We consider pristine hair monolayers ($\chi_N = 0$), as well as those we showed previously to be representative of the surface of virgin hair ($\chi_N = 0.25$) and medium bleached hair ($\chi_N = 0.85$), as well as ultimately bleached ($\chi_N = 1.0$) and other intermediate degrees of damage. For the damaged surfaces, sodium counterions (Na^+) are added to the systems to maintain charge neutrality, which is a requirement for stable simulations of partially periodic systems when considering long-range electrostatic forces.[335] The Na^+ cations and hydration shells (three water molecules) are represented by the Q_d beads with a charge of +1.[265] The contacts studied in the NEMD simulations consist of two surfaces with an equal degree of damage. Excluding the screening effect of the counterions, the damaged surfaces carry a surface charge density reaching from $\rho_q = -11.0$ µC cm^{-2} to $\rho_q = -37.2$ µC cm^{-2} for virgin and medium bleached hair, respectively. These values are somewhat larger than those from previous experimental measurements of the surface charge of virgin (-1.5µC cm^{-2}) and bleached (-8.0 to -10.0 µC cm^{-2}) hair.[99] This

discrepancy is probably due to partial screening of the negative hair surface charges by the K^+ counterions present in the experimental solutions. This effect is not considered in the simulations surface charge values in Table 4.1. The surface coverage of SO_3^- groups in the medium bleached hair case ($\chi_N = 0.85$) of 2.3 nm^{-2}, is very close to the value estimated from experiments (2.2 nm^{-2}).[92]

4.2.2 MD Simulation Details

Classical MD simulations are performed using the LAMMPS software.[332] The velocity-Verlet[333] integration scheme is used with a timestep of 5 fs. First, the systems are energy minimized using the conjugate gradient algorithm, before being equilibrated at $T = 298$ K with a global Nosé-Hoover thermostat.[340,341] During this phase, the position of the graphene sheets is fixed in the z-direction. Next, a constant normal force ($F_N = 4.9$ nN) equivalent to a pressure of 10 MPa is added to all of the beads in the top graphene sheet (A = 490 nm^2), while the beads in the bottom graphene sheet remain fixed. The chosen pressure is based on an estimate of the Hertz pressure in previous AFM experiments of friction in hair-hair contacts.[28,211] Here, the applied load, $F_N \approx 0.1$ mN, and the Young' modulus of virgin and chemically damaged hair were taken as $E = 0.9$ GPa or $E = 0.5$ GPa, which is representative of virgin and chemically damaged soaked hair, respectively.[45] Further details on the corresponding contact pressure estimates are discussed below in section 4.2.5.

In the dry systems, the force is maintained until the average pressure reaches the target value. The dry systems are periodic in the x and y directions and finite in the z direction. In the wet systems, the normal force is maintained until the number of water molecules remaining in the contact and corresponding contact thickness reach a steady state value, to simulate the squeeze-out process at the target pressure.[354] For these squeeze-out simulations, a fully periodic system is used, as shown in Fig. 4.1(b). Water beads are initially distributed randomly in the contact using PACKMOL[369] with additional reservoir space added around the contact. The number of water units in the system is fixed throughout the squeeze-out simulations. The initial surface-normal separation distance between the two graphene layers of the surfaces is set at $d = 11.5$ nm. Before the compression phase, the system is equilibrated at 300 K and atmospheric pressure (1 atm) is followed using a Parrinello-Rahman barostat acting in the z direction.[370] Once the system volume reached a steady state value, the dimensions were fixed again for the compression phase. For the sliding phase of the wet contacts, new systems are constructing containing the steady state number of water beads from the squeeze-out simulations and the additional space in the x direction is removed. The simulation boxes for the dry and wet NEMD simulations are periodic in the x and y directions and finite in the z direction. These systems are energy minimised, equilibrated at 300 K, and then compressed to 10 MPa prior to the sliding phase.

For the sliding phase, at sustained normal force, the upper graphene surface is moved in the x direction at a constant sliding velocity, v_s, while the bottom slab remains stationary. The motion of individual graphene beads in the other directions (y and z) is rigidly constrained. Sliding velocities between 10^{-2} and 10^{0} m s^{-1} are considered, which are several orders of magnitude higher than typical velocities in AFM experiments using hair that typically operate in the 10^{-6} to 10^{-3} m s^{-1} range.[207,211,216] The v_s values considered in the NEMD simulations are, in fact, closer to realistic scenarios of hair manipulations such as brushing and combing ($v_s \approx 10^{-1}$ m s^{-1})[11,154] or rubbing with a finger.[371] The requirement to sample a sufficient fraction of each surface in contact at reasonable computation times imposes a lower limit on the sliding velocity.

During the sliding phase, thermostatting is applied only to the P_5 beads of the hair surfaces in the direction lateral (y) to compression and sliding[372] to act as a heat sink for thermal dissipation from frictional heating close to the sliding graphene sheets. This is a more physically realistic thermostatting strategy compared to thermostatting the entire system, which prevents thermal gradients from developing.[373] For this purpose, a Langevin thermostat[374] is applied to the P_5 beads at $T = 298$ K and a time relaxation constant $\tau_t = 0.1$ ps. Production sliding simulations are run for at least 200 ns. At the lowest sliding velocities considered here ($v_s = 0.01$ m s^{-1}), simulations are run up to 500 ns to sample at least 5 nm of surface displacement.

4.2.3 Water Model Viscosity

Since the viscosity of fluids is important to their tribological behaviour of soft contacts,[375] we validated the pressure-viscosity response of the polarizable *MARTINI* water model against experimental data. Viscosity calculations with the *MARTINI* force field have been performed in few instances,[365,366,376–378] but the viscosity of the polarizable *MARTINI* water models have not been previously reported. Here, we employ the Green-Kubo method[379,380] to determine the dynamic viscosity $\eta$of polarizable *MARTINI* bulk water[306] at ambient conditions ($T = 298$ K, $p = 1$ atm) in the NVT ensemble after equilibration using a Nosé-Hoover thermostat.[340,341] A value of $\eta = 54.8 \pm 1.5$ mPas is found, which underestimates the experimental value[381] by ~39 %. The magnitude of this deviation is comparable to that of other atomistic water models[382], such as SPC/E[346] or TIP5P[383]. The size of the simulation cell did not significantly affect the viscosity for the three tested box lengths ($\mathcal{L} = 6$, 8, 12 nm) shown in Fig. A.2.5(a) in the appendix. Furthermore, we evaluated the dynamic viscosity at system pressures of $p = 0.1, 100, 200, 300$ MPa using a Nosé-Hoover thermostat and barostat.[340,341] The corresponding viscosity-pressure plots are shown in Fig A.2.5(b) in the appendix. Unlike for experimental water, the viscosity of the polarizable *MARTINI* model strongly increases with pressure. At high pressure, the model overestimates viscosity compared to experimental values. This is believed to result from the well-known attribute of *MARTINI* water to be prone to strong reordering[265], thus transitioning to a solid-like behaviour at significantly lower bulk pressures than real water. We also observe this

behaviour at elevated temperatures (T = 323 K), although shifted towards slightly higher bulk pressures. Thus, we conclude that the range of system pressures should be limited to p < 100 MPa to remain in a realistic viscosity regime. Such pressures are generally sufficient to match those observed experimentally inside the soft contacts found in biological systems.[384]

4.2.4 Experimental Details

We performed CCP-AFM[215] experiments in a liquid cell to study the friction of atomically-smooth hair mimic surfaces in a water-lubricated environment. Biomimetic hair surfaces were produced by silanizing silicon wafers and 5 µm silica colloidal AFM probes with either octadecyl (C_{18}) or sulfonate (SO_3^-) groups. The silicon wafers (Silicon Valley Microelectronics, Inc., California) had dimensions of 12 × 12 mm^2 with a 1.2 nm thick native oxide layer and 0.2 nm root-mean-square (RMS) roughness. We used custom-ordered 5 µm radius colloidal silica NovaScan (Boone, Iowa) AFM probes attached to Si_3N_4 cantilevers with a nominal spring constant of 0.35 N m^{-1}. The radius (5.0±0.1 µm) and smoothness (0.2 nm RMS roughness) of the CCP probes were confirmed using scanning electron microscopy (SEM). The extremely small roughness of both experimental substrates enables the use of atomically-smooth surfaces in the simulations. Considering the large radius of the probe and accounting for its deformation during contact results in negligible curvature (< 1°) on the scale of the NEMD simulation box, which justifies the use of flat surfaces. Tipless reference cantilevers were used to calibrate the normal spring constant and microscopic geometrical calculations were used to calculate the torsional spring constants.[385]

The pristine hair mimic was represented by silica surfaces functionalised with octadecyltrimethoxysilane (OTMS), while ultimately bleached hair was represented by silica surfaces functionalised with a p-sulfonated phenylalkylsilane. These functionalized substrates are similar to those applied in the previous chapter for studying the wettability of biomimetic hair surfaces. Proprietary methods were used to produce the functionalised surfaces, but similar methods have been described previously for alkylsilanes[386] and p-sulfonated phenylalkylsilanes.[387] Piranha solutions were used to prepare the silica surfaces prior to functionalisation. The same functionalisation methods were used for the silicon wafer and the silica colloidal probe. Time-of-flight secondary ion mass spectrometry (ToF-SIMS) measurements (TOF.SIMS 4, IONTOF,

Table 4.1: Properties of single coarse-grained molecular and experimental model surfaces.

		Simulations		Experiments	
Property	Unit	Pristine	Ult. bleached	C_{18}-funct.	SO_3^--funct.
Monolayer thickness	nm	1.96±0.01	0.47±0.08	2.12±0.09	0.52±0.08
Grafting density	nm^{-2}	2.73	2.73	3.95*	1.65*
Surface energy	mJ m^{-2}	21.4	31.1	26.4	76.7

*inferred from the difference between the measured thickness and that expected for a close-packed monolayer.

Germany) were applied to investigate the chemical composition of the monolayers. They confirmed that the expected species were present on the surfaces. For the SO_3^- systems, TOF-SIMS was used to confirm almost complete (91%) conversion of chlorosulfonyl precursor groups into SO_3H groups. Sulfonic acid is a very strong acid, so the SO_3H groups will be mostly deprotonated in water at neutral pH. Despite the use of deionised water in the friction experiments, it is reasonable to assume the presence of sodium counterions to ensure local electroneutrality (as in the NEMD simulations) from external contamination, for example the glassware[388] used during the functionalisation process.[387]

Comparisons of the surface properties from the experiments and simulations are shown in Table 4.1. Uniform monolayer formation was confirmed using spectroscopic ellipsometry (M-2000DI/EC-400, J. A. Woollam Co., Inc., Nebraska), which was used to measure the film thickness across nine different locations on each surface. These measurements spanned a 18 mm^2 area of the substrate. Table 4.1 shows that the monolayer thickness values for both surfaces are in excellent agreement between the experiments and simulations. The thickness measured for pristine hair is also consistent with previous experimental measurements of the F-layer on real hair.[259] The experimental grafting densities were estimated by comparing the film thicknesses measured using ellipsometry to the expected thicknesses for upright molecules in close-packed monolayers.[389] The expected thickness is 2.7 nm for OTMS[390] and 0.8 nm for the p-sulfonated phenylalkylsilane.[387] Based on the difference in thickness, the calculated packing efficiency for OTMS was 79% of the theoretical maximum, while for the p-sulfonated phenylalkylsilane it was 65%. The theoretical maximum coverage was estimated from the cross-sectional area of the molecules: for OTMS, this was taken as 0.2 nm^2,[391] while for the larger p-sulfonated phenylalkylsilane a value of 0.4 nm^2 was used.[392] This rough calculation resulted in the experimental grafting densities shown in Table 4.1. Due to the nature of the way that the damaged surfaces for the NEMD surfaces were prepared (random replacement of C_{18} groups with SO_3^- groups) to match experimental wetting data, both groups have an equal grafting density. From the ellipsometry measurements, it seems that the packing density of the C_{18} groups is somewhat higher in the experiments than the simulations, while the packing density of the SO_3^- groups is higher in the simulations than the experiments. Thus the selected packing density for the simulations represents a reasonable compromise between the two experimental systems. The SO_3^- group coverage for ultimately bleached hair in the experiments and simulations is in reasonable agreement with previous experimental estimates for bleached hair (2.2 nm^{-2}).[92]. The differences in packing density between the experiments and simulations may have a minor effect on friction. Previous experiments[389] and NEMD simulations[354] using different surfaces and surfactants containing C_{18} groups have shown that higher surface coverages generally lead to lower friction. Therefore, it might be expected that friction in the C_{18} system will be somewhat overestimated in the NEMD simulations compared to

the experiments. For the SO_3^--functionalised surfaces, the main effect of the higher surface coverage in the simulations than the experiments will be an increased charge density, which may also affect friction. Given the major differences in surface chemistry and thus friction mechanisms between the C_{18} and SO_3^- systems, the differences in packing density between the simulations and experiments are expected to have only a small effect on friction.

The surface energies (polar + nonpolar) shown in Table 4.1 were calculated using the Owens-Wendt method.[232] The underlying contact angle measurements of polar (water) and nonpolar (n-hexadecane or diiodomethane) liquids are obtained from the previous chapter. Both the simulations and experiments show a higher surface energy for the SO_3^- system than the C_{18} system. This is in agreement with previous wetting experiments, which showed that the surface energy is higher for bleached hair (29.8 mJ m^{-2}) than virgin hair (18.9 mJ m^{-2}).[100] AFM experiments also suggested higher surface energies for bleached hair (44 mJ m^{-2}) than virgin hair (24 mJ m^{-2}) from adhesion measurements.[92] The surface energy of both surfaces is higher in the current experiments than the simulations. This can mainly be attributed to the lower surface tension values in the simulations due to the systematically lower water-vapor surface tension of the polarizable *MARTINI* water model.[299,306]

The CCP-AFM experiments were performed using a Bruker (Billerica, Massachusetts) MultiMode 8 scanning probe microscope in contact mode. The contact was immersed in deionised water medium. A scan angle of 90° was used with respect to the cantilever long axis. The typical scan length during the lateral (friction) force measurements was 30-100 nm at a scanning frequency of 1 Hz. The friction forces were measured at applied normal loads between 1-3000 nN. The lateral deflection signal (cantilever twist) was converted to a friction force from the cantilever geometry and torsional spring constant.[385] The use of smooth biomimetic surfaces eliminates any damage-induced change in microscale surface topography[80] or porosity[339] from the friction measurements, which is not the case with real hairs.[17,211] Separate CCP-AFM measurements were made without sliding to quantify the repulsion in the SO_3^- system (-20 nN) and adhesion in the C_{18} system (+450 nN). This is consistent with previous AFM measurements that have shown reduced hair-hair adhesion following chemical damage[17] or bleaching.[211] The larger adhesion for the C_{18} system in water is due to hydrophobic interactions.[393]

4.2.5 Contact pressure estimates

Given the difference in the contact area between the experiments and simulations, our aim was to match the contact pressure rather than the load. The graphene sheet used for functionalisation in the CG-MD simulations is fully periodic in the x and y directions and is therefore considered macroscopically inelastic. Elastic deformation in the sim-

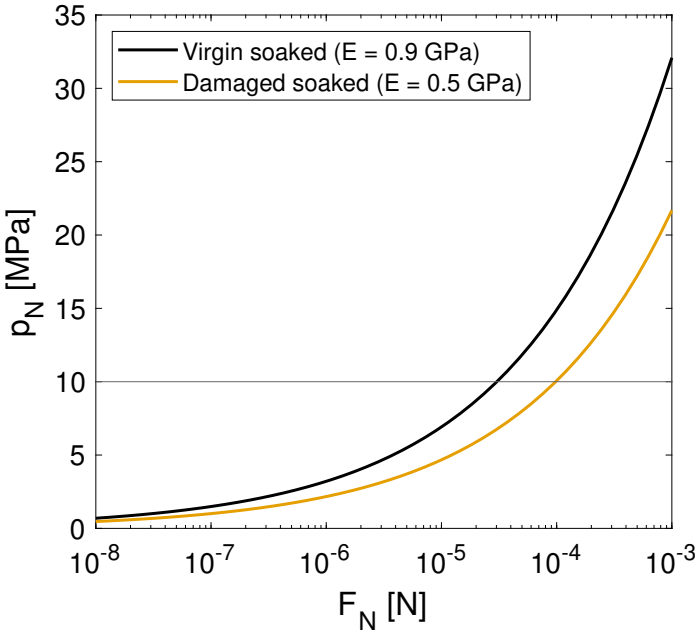


Figure 4.2: Pressure versus load curves for virgin and damaged hair-on-hair contacts obtained from Hertz theory for a range of normal loads from 10 nN to 1 mN. Horizontal line represents the pressure chosen for the NEMD simulations ($\sigma = 10$ MPa).

ulations is thus limited to the functionalised molecules. The pressure can be calculated simply by dividing the force applied in the z direction by the area of the surfaces. Conversely, in the experiments, the elasticity of the substrate and the functionalised molecules both need to be considered.

a) Crossed hair-on-hair contacts

A crossed-cylinder contact is assumed for a contact between two hair fibres which is a common experimental setup to measure hair-on-hair friction and adhesion.[28,210,211] The contact radius from Hertzian theory in this case is given by:

$$a^3 = \frac{3RF_N}{4E},$$

where R is the fibre radius, F_N is the applied normal load and E is the Young's modulus of a fibre. Here, a Young's modulus of $E = 0.9$ GPa or $E = 0.5$ GPa is used, which is in accordance with deformation experiments of soaked, virgin and chemically damaged hair, respectively.[45] With an estimate of the hair diameter $d = 2R = 75$ µm, the remaining variable is the normal load. Using a baseline value of $F_N = 0.1$ mN, which is slightly higher than in previous AFM experiments of hair-hair friction,[28,211] we obtain a contact pressure estimate in the range of $p_N = 10$ MPa, as shown in Fig. 4.2. This is still a relatively low load compared to hair manipulation scenarios such as rubbing with a finger ($F_N \approx 50$-100 mN),[27] but is deemed suitable as a baseline to describe friction between two individual hair fibres in AFM experiments.

It is worth noting though that for previous AFM experiments using hair-hair contacts,

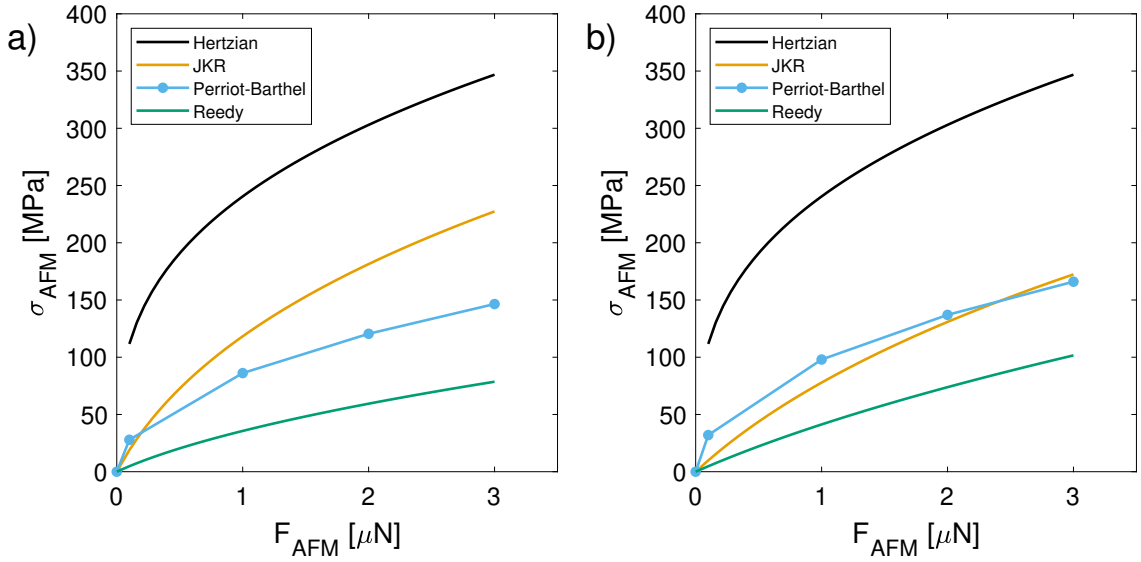


Figure 4.3: Pressure versus load curves for biomimetic CCP-AFM using Hertz theory, JKR theory[394] and the procedure presented by Perriot-Barthel.[395] for a) C_{18}-C_{18} surfaces and a) SO_3^--SO_3^- surfaces. Adhesion forces between the monolayers are used for the JKR estimate. Coating deformation properties of the monolayers are applied for the Perriot-Barthel estimate. Adhesion and monolayer deformation are both considered in the Reedy method.

the load had no effect on the coefficient of friction over a range of 10 to 1000 nN.[210] High-load nanotribometer experiments of hair-hair contacts showed that the COF decreased from 10 to 100 mN, at which point wear began to occur.[214] Thus, we consider our chosen baseline pressure in the NEMD simulations (10 MPa) to be representative of the current CCP-AFM experiments using biomimetic surfaces and previous AFM experiments of nanoscale hair friction where no wear occurred. We also performed a subset of squeeze-out and NEMD simulations over a wider range of pressures (5-50 MPa) to enable more direct comparison with the CCP-AFM experiments. The variable-pressure NEMD simulations were all performed a sliding velocity of $v_s = 0.1$ m s^{-1}.

b) Chemical colloidal probe AFM experiments

A range of different theoretical contact mechanics models was considered for the CCP-AFM experiments which were bound to an available load range of 1-3000 nN. We first estimated the Hertzian pressure in the chemical colloidal probe (CCP) AFM experiments using the C_{18}-functionalised biomimetic surfaces. A Young's modulus of $E = 73$ GPa and Poisson ratio of $= 0.25$ were used for both the silica probe and oxidised silicon substrate,[396] obtaining pressures of $p_H <$ 347 MPa over the applied load range ($F_N < 3$ µN), as shown in Fig. 4.3(a).

In addition to Hertz theory, we compared three other methods to estimate the contact pressure in the CCP-AFM experiments using the biomimetic surfaces that account for adhesion and/or deformation of the monolayer coatings. Johnson-Kendall-Roberts theory (JKR)[394] was used to account for adhesion between the monolayers ($w_0 = 26.4$ mJ m^{-2}). This is similar to the surface free energy measured for 1-hexadecanethiol mono-

layers on silicon wafers in water.[397] Using the same mechanical properties for the silica surfaces as above, the pressures decrease to $p_{JKR} <$ 200 MPa. This pressure range is comparable to previous JKR estimates from CCP-AFM experiments between a non-functionalised silica glass sphere and flat silica surface.[398]

To account for the deformation of the compliant monolayer, we also developed a Newton solver with respect to the contact radius to optimize the constitutive Equation (A15) due to Perriot and Barthel.[395] The contact is idealized as a single coating indented by a rigid spherical probe, therefore neglecting adhesion. A Poisson ratio coating $= 0.4$ and Young's modulus $E_{coating} = 0.2$ GPa were used for the coating. This is similar to the Young's modulus measured using AFM for stearic acid monolayers prepared using the Langmuir-Blodgett method on silicon wafers.[399] The resulting pressure range is $p_{PB} < 146$ MPa for the octadecyltrimethoxysilane functionalized surfaces.

Finally, we used the method proposed by Reedy to account for both deformation of the monolayer and adhesion.[400] Using the same parameters as above, we obtain pressures of $p_R < 79$ MPa. An overview of the contact pressure as a function of the normal load obtained by Hertzian theory, JKR, Perriot-Barthel, and Reedy methods is shown in Fig 4.3(a). The same formalism was repeated for the sulfonic acid-functionalised biomimetic surfaces, as evident in Fig. 4.3b). Hertzian pressures do not change compared to the C_{18}-C_{18} contacts as the underlying substrate is the same. Using the Johnson-Kendall-Roberts (JKR)[394] contact theory modified by Reedy[400] for thin coatings with experimentally measured adhesion and elastic properties of the silica (substrate)[396] and surfactant monolayers (coating),[399] we estimate that the contact pressure in the experiments varies between 5-79 MPa over the chosen load range (1-3000 nN).

4.3 Results and discussion

4.3.1 Dry Contacts

To investigate the molecular-scale origins of the friction behaviour, we first study the structure of the hair surfaces during compression and sliding at different degrees of damage. Fig. 4.4 shows the surface-normal (z) mass density and through-film velocity profiles (v_x) for dry contacts from the NEMD simulations. At low damage levels, the thickness of the F-layer on each surface is approximately 2 nm, which is consistent with previous experimental measurements.[259] It is also similar to the thickness measured by ellipsometry for the pristine hair biomimetic surface (Table 4.1). At all damage levels, there is clear layering, which is strongest close to the sliding surfaces, but extends into the centre of the contact ($z = 0$ nm). The mass density profiles are insensitive to the sliding velocity, which is consistent with previous atomistic NEMD simulations of stearic acid monolayers adsorbed on iron oxide surfaces.[280] The monolayers on the opposing surfaces are interdigitated with each other, as shown by the overlap in mass density

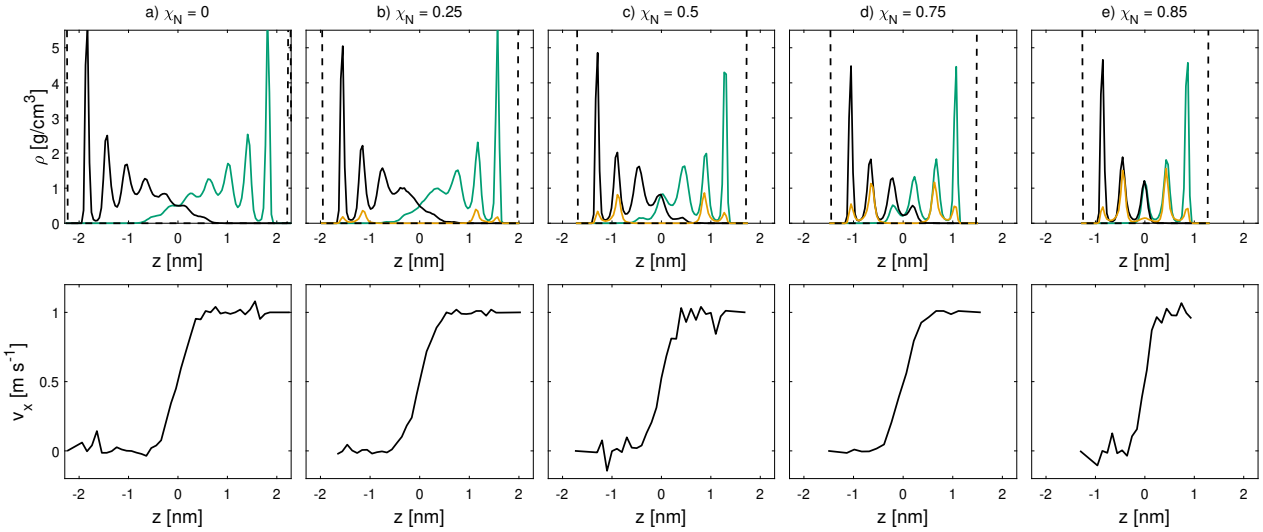


Figure 4.4: Dry contact monolayer mass density (top) and velocity (bottom) profiles at $v_s = 1$ m s^{-1} and $\sigma = 10$ MPa for different damage ratios, χ_N. The damage ratio increases from left to right. The densities of the lower surface (solid black), upper surface (solid green), sodium counterions (orange) and graphene sheets (black dashed) are shown.

profiles. There is a general increase in the amount of interdigitation with increasing damage ratio. The outer layers of the lipids move at the same velocity as the graphene surfaces to which they are grafted and the velocity changes linearly between the two extremes in the interdigitated region. This observation is also consistent with previous atomistic NEMD simulations of surfactant monolayers adsorbed on iron oxide surfaces.[354] There do not appear to be any velocity slip planes between the layers shown in the mass density profiles, which would appear as discontinuous changes in the velocity profiles.

An overview of the discrete shear stress signals obtained from dry and wet NEMD simulations as a function of the surface damage is shown in Fig. 4.5 The COF (μ) in the single-pressure NEMD simulations is obtained using the Amontons friction law by dividing the lateral force (F_L) by the normal force (F_N) acting on the outer layer of beads.[147] Previous nanoscale AFM hair friction experiments have shown a linear relationship between F_L and F_N, with a negligible intercept.[17,211] The mean COF between dry surfaces from the NEMD simulations is shown in Fig. 4.6 as a function of sliding velocity for the various levels of damage considered. At the lowest sliding velocity considered ($v_s = 0.01$ m s^{-1}), the COF increases monotonically with damage ratio, which is consistent with previous experimental measurements of virgin, chemically damaged and bleached hair.[16,17,70] At low sliding velocity, the NEMD simulations show a difference in COF of almost two orders of magnitude between the virgin ($\chi_N = 0.25$) and medium bleached hair ($\chi_N = 0.85$). Experiments in a dry nitrogen atmosphere (RH ≈ 4%) showed that compared to virgin hair, the COF was approximately three times higher for chemically damaged (KOH-treated) hair and twice as high for bleached hair.[16] There are several differences between these previous experiments

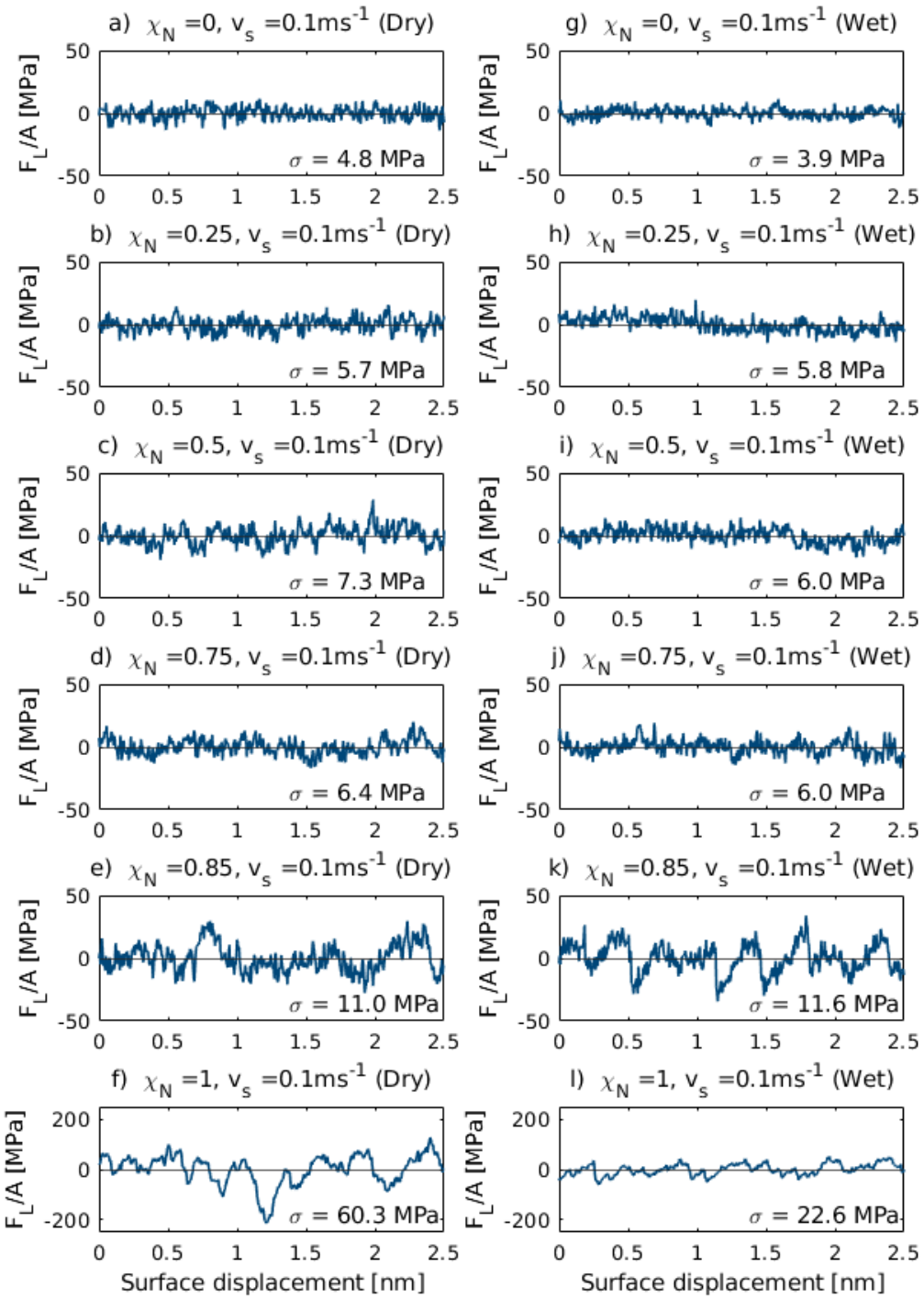


Figure 4.5: Mean-removed shear stress signals, $\tau - \langle\tau\rangle = F_L/A - \langle F_L/A\rangle$, at $v_s = 0.1$ m s^{-1} for dry (left column) and wet (right column) systems. Note that the fully damaged friction signals in f) and l) have increased y axis limits. The standard deviation, σ, is given for each signal.

and the current simulations that may explain the larger difference between virgin and damaged hair in the simulations compared to the experiments. Firstly, due the hair samples in the AFM experiments would have still contained some residual water molecules, despite the low relative humidity. Secondly, the experiments used silicon nitride tip-hair contacts, rather than hair-hair contacts. Finally, the sliding velocity used in the experiments (4×10^{-6} m s^{-1}) is well below those that can be directly simulated

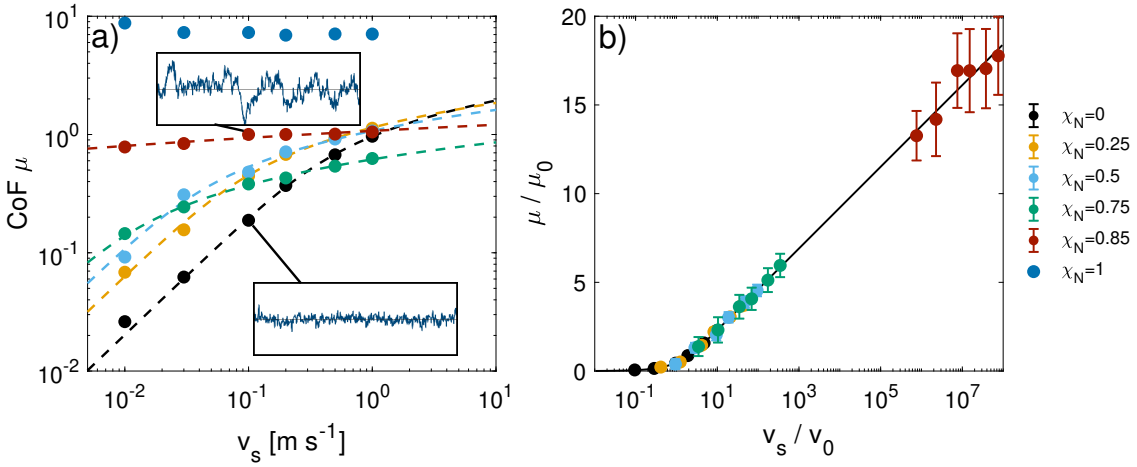


Figure 4.6: Dry COF as a function of sliding velocity v_s and monolayer damage at $\sigma = 10$ MPa in double logarithmic plots. Eq. 4.1 (dashed lines) is fitted to the data for all damage ratios except $\chi_N = 1$.[280] Uncertainty bars are omitted in (a) to improve clarity. (b) Shows the same data as a nondimensional representation, collapsed by the fitting parameters v_0 and μ_0. Vertical bars show one standard deviation. Insets in (a) show raw friction vs. time signals at the same x and y axis scale.

using the current CG-MD framework (1×10^{-2} m s^{-1}).

For low and moderately damaged hair ($\chi_N < 0.85$), the COF increases rapidly with sliding velocity, as expected for liquid-like systems.[401] For higher damage levels, the friction dynamics are more solid-like, showing only moderate increases in friction force with sliding velocity, as well as stick-slip behaviour.[402] The transition from liquid-like, smooth friction towards a more solid-like, stick-slip regime (insets in Fig. 4.6a and Fig. S4) can be observed by an increase in the standard deviation of the COF around the mean (shown in Fig. 4.6(b). This is attributed to the reduction in the number of flexible lipids on each surface and increase in the number of inflexible charged groups, which leads to increasingly stiff and heterogeneous surfaces. At high sliding velocity, a crossover is observed where the COF at moderate damage exceeds that at higher damage. The ultimately bleached ($\chi_N = 1.0$) surfaces have a higher COF by one order of magnitude compared to the medium bleached ($\chi_N = 0.85$) case. At this degree of damage, COF is completely insensitive to sliding velocity, as expected for solid-solid friction.[402] The much higher friction for the damaged surfaces is mainly due to the strong electrostatic interactions between the negatively charged sliding surfaces and the positively charged confined counterions. Similarly high COFs have also been observed for negatively charged surfaces with strongly confined ionic liquid cations.[403]

For all systems with $\chi_N \leq 0.85$, the COF increases logarithmically with sliding velocity, v_s. This behaviour is indicative of a stress-augmented thermal activated (SATA) process,[281] similar to the Eyring model for liquid viscosity.[404] Such behaviour has been observed in many boundary-lubricated contacts protected by adsorbed or grafted monolayers in both experiments[229,401,405] and NEMD simulations.[280,354,406,407] The logarithmic dependency of the COF on v_s predicted by SATA models generally only holds for intermediate v_s. At very low sliding velocities, a linear relationship is more common, because

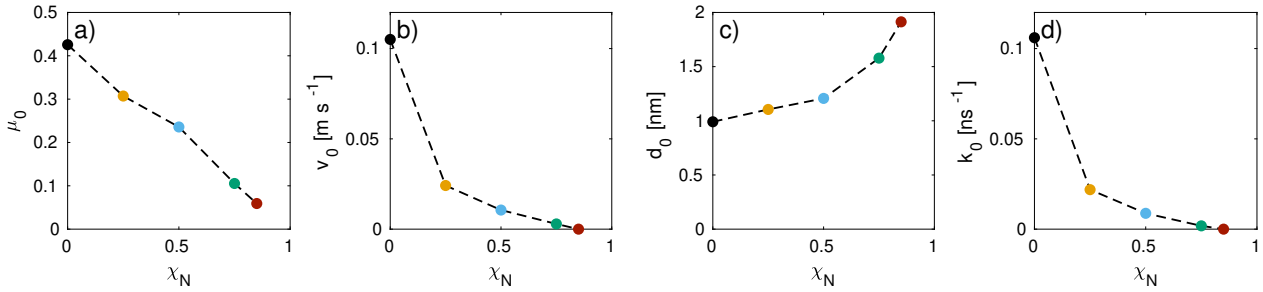


Figure 4.7: Reference (a) coefficient of friction μ_0, (b) velocity v_0 and corresponding (c) barrier distance d_0 and (d) hopping rate constant k_0 from thermal activation model fits [280] as a function of monolayer damage.

thermal fluctuations dominate the activation process, as opposed to the external shear stress.[401,402,405] An extended SATA model describing both the $v \propto \ln(v_s)$ behaviour at high v_s and the $v \propto v_s$ at low has been applied to COF data from NEMD simulations using both all-atom [280] and CG [407] force fields:

$$\mu = \mu_0 \cdot \ln\left(\frac{v_s}{2v_0} + \sqrt{\left(\frac{v_s}{2v_0}\right)^2 + 1}\right) \tag{4.1}$$

where the reference coefficient of friction, μ_0, and reference sliding velocity, v_0, are fitting parameters. The applicability of this model to our data is confirmed for dry hair contacts by means of the dimensionless representation in Fig. 4.6(b). The fitting parameters are shown in Fig. 4.7(a) and (b) as a function of surface damage. The ultimately bleached case ($\chi_N = 1.0$) has been excluded from this fitting since the COF is insensitive to sliding velocity for this system. The fitting parameters $\mu_0 = k_B\,T\,/\,(p_N\,{d_0}^3)$ and $v_0 = k_0 \cdot d_0$ from the SATA model can be related to physical quantities. Specifically, d_0 represents the distance between the molecular-scale energy barriers, while k_0 is the hopping rate constant. In these systems, the barriers are likely related to the molecular-scale roughness due to the lipid islands that form on the damaged surfaces. The reference COF and reference velocity both decrease with increasing damage ratio. Fig. 4.7(c)-(d) shows that there is an increase in the distance between barriers, d_0, and a decrease in the hopping rate constant, k_0, with increasing damage. These changes in d_0 and k_0 indicate that energy hopping events occur more infrequently and with a larger energy barrier distance as the damage ratio increases. This is because, as the damage level increases, the number of lipid islands decreases, while their physical separation increases, as shown in the previous chapter. The transition towards smaller, more widely spaced lipid islands is consistent with the appearance of stick-slip friction at high damage levels (inset in Fig. 4.6a and Fig. S4).

The molecular-scale roughness from the lipid islands imposes a physical barrier to overcome during sliding. The d_0 value correlates with the interdigitation between the lipid monolayers on the opposing sliding surfaces evident from Fig. 4.4. We quantify the degree of interdigitation by means of the average volume available per bead in the region of direct interdigitation between the two contacts. We find the available volume

per bead to increase monotonically from $\langle V_i \rangle \approx 0.1$ nm^3 for pristine hair monolayers to $\langle V_i \rangle \approx 0.14$ nm^3 for $\chi_N = 0.85$ (Fig. A.2.6(a) in the appendix). Therefore, more space per CG bead is available at higher damage. This is in contrast to the interdigitation distance, which reaches its peak at intermediate degrees of damage, consistent with a maximum in the expected degree of heterogeneity (see chapter 3). We observe that the volume per bead (rather than the interdigitation distance) is highly correlated with the barrier distance d_0 from the fits to Eq. 4.1 (Fig. A.2.6(b) in the appendix).

The orientation of the lipid molecules may also affect the friction behaviour. Absolute tilt angles of the vector from the lipid root bead (P_5) to the terminal bead (C_1) relative to the xy-plane are shown in Fig. A.2.7 in the appendix. For the dry contacts, the absolute tilt angle decreases from $\approx 50°$ for pristine hair surfaces, to $\approx 25°$ for medium bleached hair. This suggests that the lipids go from a mostly upright conformation to lying more parallel to the surface as the damage level increases. There is a slight decrease in the absolute tilt angle with increasing sliding velocity. We also quantified the orientational tilt angle, which is measured between the projection of the P_5-C_1 vector in the xz-plane and the x unit vector, as shown in Fig. A.2.7 in the appendix. The lipids move from being aligned parallel to the z direction (perpendicular to the hair surface and sliding direction) at low sliding velocity, to being almost completely aligned with the sliding direction at high sliding velocity. Friction is often reported to increase as a function of monolayer alignment in the direction of sliding, which is generally attributed to higher commensurability between the interacting monolayers.[408,409] In the current study, however, the monolayers are relatively loosely packed (maximum lipid coverage = 2.7 nm^{-2})[223,354] and the interface does not form a crystalline, commensurate interface, even when the molecules are aligned with the sliding direction. Indeed, at low damage levels, where high commensurability is most likely due to the highest lipid coverage, there is no stick-slip behaviour evident in the friction versus sliding distance signals in Fig. 4.5. Molecular alignment does not seem to have a significant effect on the friction behaviour.

The absence of water in biological systems is rare, even in dry environments. The presence of residual water in the cuticle,[269] absorbed water from ambient humidity,[231] and the frequent contact of hair with water during washing[27] mean that the addition of water molecules at the interface is an essential component of realistic NEMD simulations which will be considered in the next section.

4.3.2 Wet Contacts

a) Squeeze-out Simulations

Squeeze-out simulations are performed at various degrees of chemical hair damage to establish an equilibrium film thickness at the target pressure (10 MPa) for subsequent sliding NEMD simulations.[354] The equilibrium number of water units

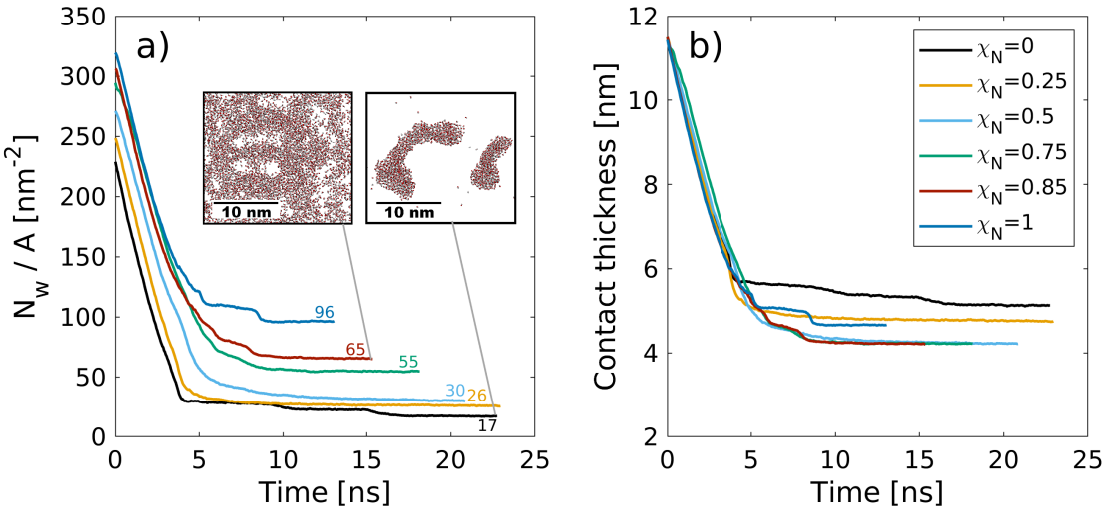


Figure 4.8: Change in the number of water molecules ($4 \cdot N_{w,CG}$) per surface area N_w A^{-1} (a) and the contact thickness between the graphene sheets (b) with time during the squeeze-out simulations at a pressure, $\sigma = 10$ MPa for hair surfaces with different degrees of χ_N. The molecule number densities per unit area at equilibrium are shown as text labels in (a). Insets in (a) show snapshots of the confined water beads at the end of the squeeze-out simulations rendered with VMD.[349] The contact thickness in (b) includes the monolayer thickness.

and examples of temporal evolution of the number of polarizable water units (N_W) and contact thickness at p = 10 MPa are shown in Fig. 4.8. A steady-state thickness between 4-6 nm is reached after 13-20 ns, depending on the degree of damage. A decrease in the equilibrium thickness and increase in the number of water units is observed with increasing damage. As the damage level increase, the number of hydrophobic lipids decreases and hydrophilic sulfonate groups become more prevalent on the surface. Stronger intermolecular interactions between the sulfonate groups and the water beads keep more water trapped inside the contact.[393] The steady state contact thickness decreases until reaching a constant value ($d = 4.2$ nm) at $\chi_N > 0.5$ due to the combined effects of a reduced number of lipids and an increase in water content. The equilibrium contact thickness is largest at low damage levels due to the increased physical separation caused by the higher density lipid monolayers.

Recent small-angle neutron scattering (SANS) experiments suggest that the cell membrane complex of the hair cuticles in healthy hair contains water clusters with a size of 40 Å (correlation length, estimated from a Debye-Bueche model).[269] For formic acid treatment, which removes internal lipids from the hair, the number of such clusters was reduced.[269] While this transition takes place below the exposed F-layer, the proposed mechanism is comparable to the contacts modeled in this work. In the cell membrane complex, the contact between the 18-MEA monolayers on two neighbouring cuticles is essentially the same as between the outer cuticles of two virgin hairs. In our NEMD simulations, we observe the formation of water clusters of similar size as those observed experimentally[269] for the pristine hair systems ($\chi_N = 0$). Droplets are energetically favored over thin film formation due to the hydrophobic nature of the two monolayer surfaces. The formation of droplets between hydrophobic monolayers was also observed in pre-

vious NEMD simulations.[410] At higher damage levels, water progressively attaches to regions where the lipids have been removed, which is consistent with the CG-MD simulations in the previous chapter and AFM experiments.[200] For the ultimately bleached hair surfaces ($\chi_N = 1.0$), an equivalent atomistic water number density per unit area of $N_W\ A^{-1} = 96\ nm^{-2}$ is obtained, which is distributed within six hydration layers normal to the two surfaces. This value is in good agreement with the largest value used in atomistic NEMD simulations that studied the friction of water confined between hydrophilic alkylsilane monolayers ($N_W\ A^{-1} = 85\ nm^{-2}$).[411] For the fully-funtionalised surfaces ($\chi_N = 0.0$), the final water coverage ($N_W\ A^{-1} = 17\ nm^{-2}$) is in good agreement with the plateau value ($N_W\ A^{-1} = 20\ nm^{-2}$) obtained from previous atomistic Monte Carlo simulations of water adsorption between hydrophobic graphene surfaces separated by 1.6 nm.[412]

b) NEMD Simulations

We used systems containing the equilibrium number of water molecules from the squeeze-out simulations to investigate the friction between the wet hair surfaces with different damage levels. We first looked at the structure of the water-containing systems. Mass density profiles at $v_s = 1\ m\ s^{-1}$ and $\sigma = 10$ MPa are shown in Fig. 4.9 for all damage levels where $\chi_N \leq 0.85$. As for the dry systems, the density profiles are insensitive to the sliding velocity. Strong layering is observed at the solid-liquid interface for both the grafted monolayers and water molecules. Strong layering has also been noted in several previous molecular simulation studies of water confined between hydrophobic and hydrophilic surfaces.[412,413] Ordered water layers have also been observed experimentally between adsorbed cetyltrimethyl-ammonium bromide (CTAB) surfactant monolayers and have been shown to facilitate low friction.[414]

The hydrophobic nature of the pristine hair surfaces ($\chi_N = 0.0$) favors the formation of water droplets over thin films. The droplets are stretched in the direction of sliding, as is evident from the inset in Fig. 4.9(a). Additional snapshots at different sliding velocities are shown in Fig. A.2.8 and Fig. A.2.9 in the appendix. For these undamaged systems, the water droplets penetrate around 2 nm into the lipid monolayers and adhere to the hydrophilic P_5 beads at their base. At higher damage levels, thin water films form that are interspersed with lipid islands, as shown by the top view snapshots in Fig. 4.9. Even at $\chi_N = 0.85$, we observe interdigitation between the lipid monolayers on the two opposing surfaces. This is due to swelling of the monolayers, which results in mostly upright conformations, even at high damage levels. At $\chi_N = 1$ (not shown), there are no lipids remaining on the surface and thus no interdigitation. In this case, there is a complete thin (4 nm) water film between the sulfonate-covered surfaces. Fig. 4.10 shows the velocity profiles of the lipids among both surfaces and water at the interface. In the pristine hair case, there is a slip plane between the lipid monolayers on the opposing surfaces, while the water beads are sheared to the depth that they penetrate the lipid monolayer. This is attributed to the pinning of the water droplets to the lower

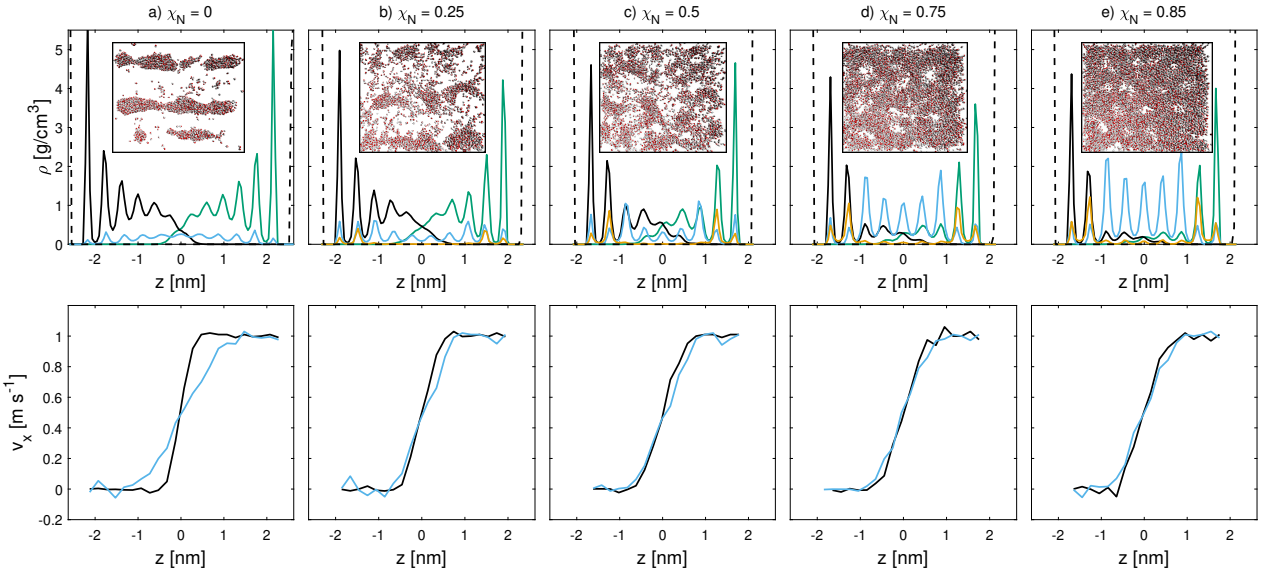


Figure 4.9: Mass density (top) and velocity (bottom) profiles for wet sliding simulations at $v_s = 1$ m s^{-1} and $\sigma = 10$ MPa at different degrees of monolayer damage. Water (blue), lower hair (black), upper hair surface (green), Na^+ counterions (orange) and base graphene sheets (dashed black) density profiles are shown. Velocity profiles of lipids (black) and water (blue) are shown. Insets show top view snapshots ($\mathcal{L}_x \times \mathcal{L}_y \approx 2.4 \times 2.1$ nm) of water inside the contacts. Rendered with VMD.[349]

regions of the displaced monolayers. In all other cases, the water beads move at the same velocity as the neighbouring lipid beads.

For the wet contacts, the absolute tilt angle (Fig. S9(a)) tends to be invariant to damage at a value of $\approx 50°$. This confirms that swelling of the monolayer occurs in water under confinement, with the lipids retaining an upright conformation even at high damage levels. This observation is consistent with our previous single-surface CG-MD simulations in chapter 3. As for the dry contacts, there is a slight decrease in the absolute tilt angle at higher sliding velocities. At low sliding velocity, the orientational tilt angle decreases more in the dry systems (Fig. S6(b)) than the wet systems (Fig. S9(b)). This suggests that the lipids align with the sliding direction more readily in the dry systems than the wet ones. As with the dry systems, molecular alignment seems to have a negligible effect on the friction behaviour in wet contacts.

Fig. 4.10(a) shows the COF in the wet contacts as a function of sliding velocity for the different damage levels at 10 MPa. At $\chi_N = 0.75$ and below, smooth, liquid-like friction signals are observed. Despite the presence of water in the contact, stick-slip friction is observed at $\chi_N = 0.85$ and above, as evident from the inset in Fig. 4.10(a) for $\chi_N = 1.0$. The water film thickness is insufficient to provide complete surface separation, even at the relatively low pressure simulated. Interdigitation is confirmed by the overlapping lipid density profiles in Fig. 4.9(e). In contrast, the ultimately bleached systems ($\chi_N = 1.0$) are fully separated by a water film with a thickness of ≈2.6 nm, distributed among six hydration layers. Nonetheless, stick-slip is observed in this system, as indicated by the standard deviation of the friction force signal of 37% around

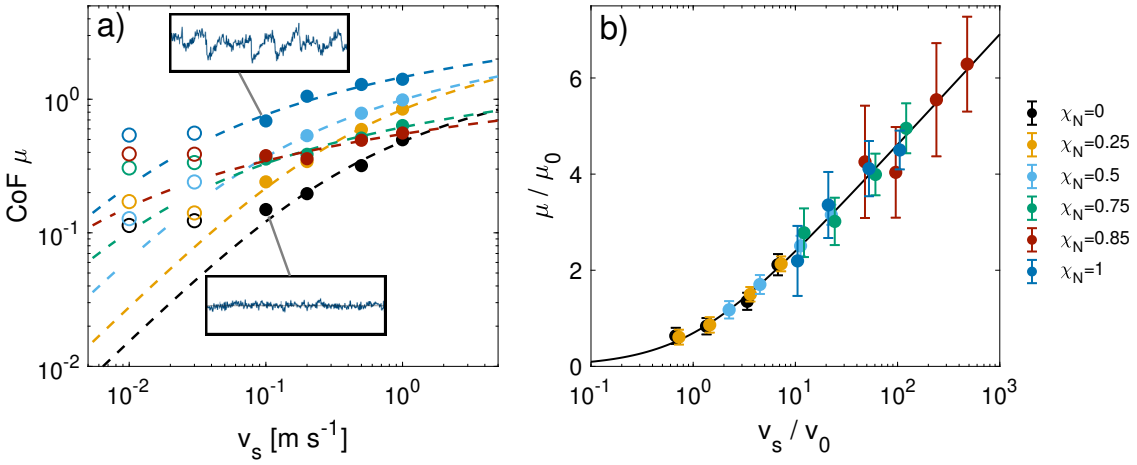


Figure 4.10: Wet COF as a function of sliding velocity, v_s, for the different damage ratios at $\sigma = 10$ MPa in double logarithmic representation. Dashed lines indicate fits Eq. 4.1.[280] Open symbols represent data not included in the fits. (b) Friction-velocity data normalized by the fitting parameters.

the mean COF. Stick-slip friction was also observed in previous experiments using wet bleached hair-hair contacts.[161] The highest COFs in Fig. 4.10(a) are obtained for the ultimately bleached system across all sliding velocities. In this case, stick-slip is promoted by interlayer sliding of commensurate surface-bound hydration layers on the highly hydrophilic surfaces. High stick-slip friction was also observed in previous atomistic NEMD simulations of water confined between hydrophilic surfaces.[415]

At low sliding velocity, the COF increases monotonically with damage ratio. Here, the COF for bleached hair ($\chi_N = 0.85$) is much higher than for virgin hair ($\chi_N = 0.25$), which is consistent with previous AFM experiments using real hair.[17] At high velocities, a crossover is observed where the COF for virgin hair exceeds that for medium bleached hair. For $v_s > 0.1$ m s^{-1}, the COF data is fitted to Eq. 4.1.[280] Figure 4.10(b) shows the non-dimensional representation of the COF included in the fits normalized by the fitting constants $\mu_0 = k_B\,T\,/\,(p_N \cdot d^3)$ and $v_0 = k_0\,d$.[280] For completeness, the changes in fitting constants as a function of surface damage are also shown in Fig. A.2.11 in the appendix. At high v_s, the model accurately describes the observed friction behaviour. At $v_0 < 0.1$ m s^{-1}, the COFs strongly deviate from the fits on the high sliding velocity data. The COFs become almost independent of sliding velocity below $v_s = 0.1$ m s^{-1} for all degrees of damage and clearly no longer follow the typical SATA behaviour. The corresponding data points are therefore omitted from the fitting, as indicated by open symbols in Fig. 4.10(a).

One mechanism by which the COF could exceed that expected from Eq. 4.1 at low sliding velocities is capillary condensation. Previous AFM experiments using nanoscale silica-silica contacts at moderate relative humidity showed that friction decreased logarithmically with increasing sliding velocity before levelling off.[416] Although there are no water-vapour interfaces in our NEMD simulations, these are water-lipid interfaces. Increased adhesion forces have been reported previously due to capillary

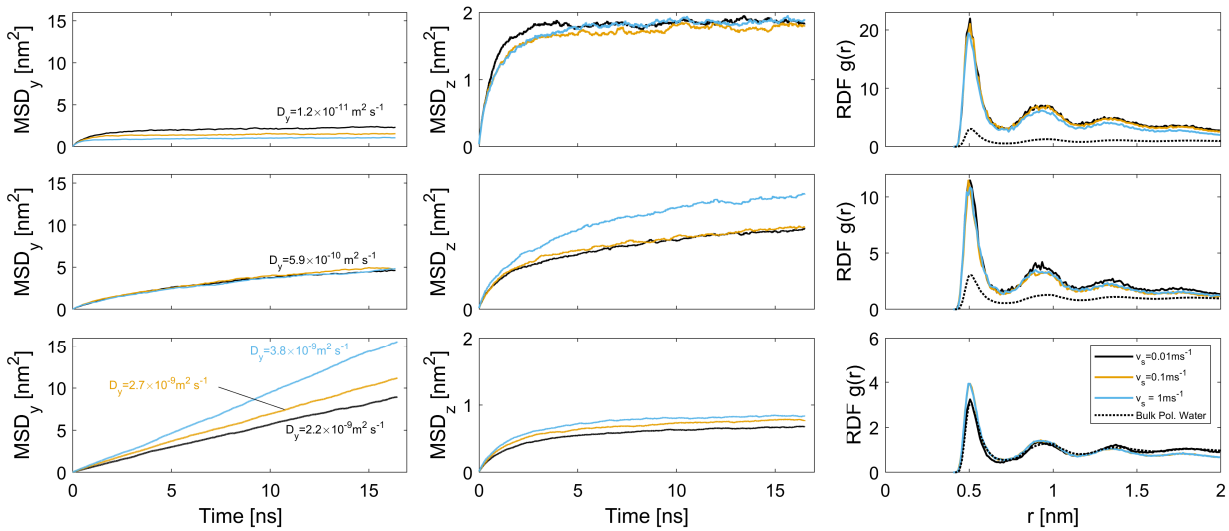


Figure 4.11: Mean-square displacement (MSD) of the central polarizable water beads perpendicular to the direction of sliding (y: left; z: middle) at different sliding velocities and for pristine (top row), virgin (middle row) and medium bleached hair surfaces (bottom row). $t = 0$ ns indicates a time at which the contact has long reached dynamic equilibrium. Approximate diffusion coefficients for subdiffusive configurations are obtained from linear fits for $t > 10$ ns. Right side: Radial distribution function (RDF) of central water beads compared to the RDF in bulk.[310].

forces at water-oil interfaces.[417] In the low-velocity regime, nanoscale water droplets (low damage) could give rise to additional cohesive forces through the presence of well-defined phase boundaries. Indeed, previous AFM experiments have shown that water nanodroplets in n-hexadecane can increase friction.[418] Snapshots of these water structures in the pristine hair contacts are shown at different sliding velocities in Fig. A.2.8 in the appendix. At full surface damage, no such phase boundary is present in the lateral direction because a thin water film forms.

We quantified the area of the contact-bridging water-lipid interface by tracing the perimeter of the water droplet (low damage) or lipid islands (high damage) and multiplying by the average thickness of those structures in the surface-normal direction, shown in Fig. A.2.12 in the appendix. There is a clear transition between intermediate ($\chi_N = 0.5$) and high ($\chi_N = 0.75$) damage where there is a large increase in the interfacial area. However, the interfacial area weakly increases with sliding velocity and thus cannot be linked to increased capillary adhesion at low velocities, where a higher interfacial area would be expected.[417] Moreover, capillary condensation would be expected to increase friction on hydrophilic surfaces more than hydrophobic ones,[419] which is the opposite to the trend we observe in our NEMD simulations.

Related to capillary effects, freezing of the confined water bridges is another possible explanation for elevated friction at low sliding velocities. Indeed, previous AFM experiments of the phenomenon have observed higher than expected friction at low sliding velocities,[420] as shown in Fig. 4.10(a). To investigate this effect, the diffusion and structure of the confined water molecules were studied at different sliding velocities

and damage levels. The mean-square displacement (MSD) and radial distribution function (RDF) of the central water beads were analysed, as shown in Fig. 4.11. While the lateral MSD increases linearly with time for highly damaged systems, it approaches a plateau at low degrees of damage, which is indicative of subdiffusion. The more pronounced subdiffusive behaviour at low degrees of damage is partially due to a decrease in confinement lengthscale (Fig. 4.9). The majority of the surfaces are covered by lipids and water resides within small droplet-like regions. This is in agreement with previous studies of water confined by soft materials,[421] where the lengthscale of confined water was found to play a role in the tendency of water to show subdiffusion.

The diffusion coefficients D in Fig. 4.11 are generally larger in the lateral direction (y) than the direction perpendicular to the surfaces (z). This suggests that the water molecules move more freely along the surface plane than between the confined water layers shown in Fig. 4.9. An increase of the lateral diffusion coefficient, D_y, is observed with increasing damage ratio. For the medium bleached model hair surfaces ($\chi_N = 0.85$), water diffusion coefficients perpendicular to the direction of sliding increase at higher sliding velocity, from $D_y = 2.2 \times 10^{-9}$ to 3.8×10^{-9} m^2 s^{-1}). These values are similar to those obtained previously for bulk polarizable *MARTINI* water ($D = 2.5 \times 10^{-9}$ m^2 s^{-1})[306] and liquid water from experiments ($D = 2.3 \times 10^{-9}$ m^2 s^{-1}).[422] For the virgin model hair surfaces ($\chi_N = 0.25$), long-time lateral diffusion is much slower than for bulk water ($D_y = 5.9 \times 10^{-10} m^2$ s^{-1}). This reduction is similar to that observed in previous atomistic MD simulations of water inside lipid bilayers.[423] For pristine hair ($\chi_N = 0.0$), the lateral diffusion coefficient is more than two orders of magnitude lower ($D_y = 1.2 \times 10^{-11} m^2$ s^{-1}) than in the bulk. This reduction in lateral diffusion is similar to that observed previously for confined bilayer ice by atomistic MD simulations ($D_y \approx 10^{-12}$ m^2 s^{-1}).[424] This implies that the confined water dynamics are solid-like in the pristine hair systems. It has also been suggested that surface hydrophobicity might be crucial to confinement-induced liquid-solid water phase transitions[425] since freezing has not been observed for hydrophilic surfaces in either experiments[426] or simulations.[427,428] Indeed, we note that the lateral diffusion coefficient increases as the damage level (and thus surface hydrophilicity) is increased. In our NEMD simulations, the water mobility is more sensitive to damage than sliding velocity and, at low damage, the lateral diffusion coefficients suggest that the water remains in the same state at both low and high sliding velocity.

Structural ordering of the confined water molecules as shown in the RDFs in Fig. 4.11 is consistent with bulk ordering of polarizable *MARTINI* water as shown by Sergi et al.[310]. Although the peak intensities increase somewhat at lower sliding velocity, there are only small shifts in the peak positions for a given degree of surface damage. Additional peaks do not appear at larger distances, which would be indicative of long-range order. This suggests that the reduction in water diffusion at low damage levels is due to a confinement-induced liquid-amorphous transition, rather than crystallisation.

This is consistent with previous atomistic MD simulations of water confined between hydrophobic surfaces.[427]

We also investigated the structure and mobility of the hydrated sodium counterions (Na^+) that are adsorbed near the damaged regions of the surfaces of virgin ($\chi_N = 0.25$) and medium bleached ($\chi_N = 0.85$) hair. These results are shown in Fig. A.2.13 in the appendix. For both surfaces, the counterion RDF is similar to the bulk RDF for cations[306] and is independent of the sliding velocity. We observe similar changes in counterion diffusion with surface damage and sliding velocity as seen for water. The mobility of the counterion beads is generally lower than the water beads due to the stronger electrostatic interactions with the SO_3^- surface groups. Immobilisation of counterions on charged substrates has also been observed in previous simulations.[429] The higher friction in damaged hair could therefore arise from overcoming attractive electrostatic interactions between the negatively-charged sulfonate groups on the surfaces and the strongly adsorbed sodium cations confined between them during sliding. Kagata et al.[430] made a similar hypothesis to explain the high friction of like-charged gels in the presence of counterions. The proposed electrofriction mechanism could be investigated further by changing the size and charge of the counterions.

The COF in wet systems are now compared to the dry counterparts discussed in the previous section. The ratio between the wet and dry contact COF as a function of sliding velocity at equal pressure is shown in Fig. 4.12. At sliding velocities of $v_s = 0.1$ m s^{-1} and above, wet contacts render a friction reduction for all of the systems. The largest reduction at all sliding velocities is for the ultimately bleached ($\chi_N = 1.0$) system. At low sliding velocities, wet friction forces exceed dry friction forces for the systems with low damage levels ($\chi_N < 0.85$). This is attributed to increased adhesive contributions of solid-like interfacial water droplets confined between the surface-bound lipids. Conversely, large friction reductions are found for the ultimately bleached surfaces at all sliding velocities because the thin water film provides sufficient separation to lubricate the contact interface.

Previous experiments have also shown higher friction for wet hair than dry hair.[151] Previously, this has been attributed to microscale effects, specifically the swelling of the cuticles leading to increased contact area and rougher surfaces.[27] Such mechanisms are not captured by our CG-MD model, apart from swelling within the lipid monolayer, see chapter 3. Our NEMD simulations suggest that solidification of confined water droplets[420] is an additional nanoscale mechanism that could lead to increased adhesion and friction between wet hairs.

c) Comparison between NEMD Simulations and AFM Experiments

As a final step, the friction behaviour from the NEMD simulations of the wet systems is compared to previous AFM experiments on real hair in humid air[17] and new CCP-AFM

experiments with the biomimetic surfaces in water. The shear and normal forces for virgin and damaged hair obtained in the previous AFM experiments[17] were converted to stresses τ_0 using JKR theory[394] with previously measured surface energies for virgin and bleached hair.[100] The CCP-AFM shear stress and normal stress values are converted from the measured forces using the extension to JKR theory[394] for thin coatings due to Reedy.[400] The experimentally-measured normal and friction forces from the CCP-AFM experiments, prior to conversion to stresses, are shown in Fig. A.2.14 in the appendix.

In the NEMD simulations (Fig. 4.10), a monotonic increase of the COF with the damage ratio is observed at the lowest sliding velocity ($v_s = 1 \times 10^{-2}$ m s^{-1}). For the pristine hair surfaces ($\chi_N = 0.0$) at 10 MPa, we obtain a COF (τ/σ, i.e. ratio of shear stress to normal stress) of $\mu = 0.11 \pm 0.04$, which increases to a maximum of $\mu = 0.54 \pm 0.21$ in the case of ultimately bleached surfaces ($\chi_N = 1.0$). The biomimetic surfaces using CCP-AFM functionalised with C_{18} (pristine hair) and SO_3^- (ultimately bleached) yield COFs of $\mu = 0.023 \pm 0.002$ and $\mu = 0.67 \pm 0.03$, respectively. This means that the COF of the ultimately bleached contact is ~29 times greater than the pristine hair contact. Therefore for surfaces representative of ultimately bleached hair, the agreement in the COF from the experiments and NEMD simulations at a single pressure is excellent (-19 %). For the pristine hair surfaces, the COF is around five times larger higher in the simulations than the experiments. One source of this difference could be the higher C_{18} surface coverage in the experiments than the NEMD simulations (Table 4.1), which has been shown previously to lead to higher friction.[354,389] In the C_{18} systems, the CCP-AFM experiments show a non-negligible load-independent adhesive contribution

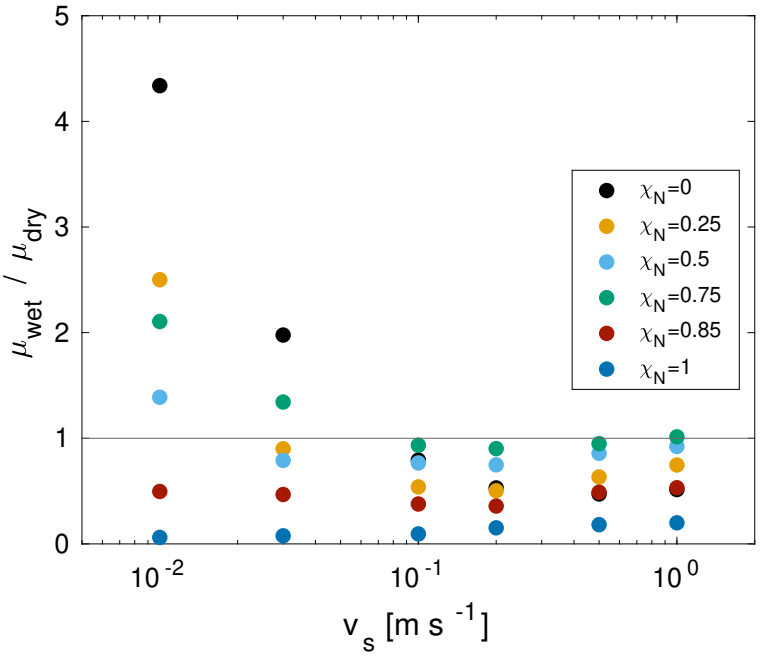


Figure 4.12: Ratio between wet and dry COF as a function of sliding velocity v_s and monolayer damage χ_N at $\sigma = 10$ MPa.

to the friction force, known as the Derjaguin offset.[147,223] To quantify this contribution in the simulations, we performed additional squeeze-out and NEMD simulations at a wider range of pressures ($\sigma = 5$-50 MPa). A summary of the amount of water after squeeze-out for all configurations is given in Table A.2.2 in the appendix. In all of the the variable-pressure NEMD simulations, a sliding velocity of $v_s = 0.1$ m s^{-1} was applied. While this is much larger than in the CCP-AFM experiments (v_s = 10^{-7} m s^{-1}), it is within the regime of approximately constant $\mu \neq \mu(v_s)$ behaviour (Fig. 4.10) in the simulations. Thus, only relatively small reductions in the COF would be expected were the COF-velocity results to be extrapolated to experimental velocity. Since additional datapoints in the low-velocity regime would be required to enable accurate extrapolation, we directly compare the COFs obtained for the virgin and damaged hair from the experiments and simulations conducted at higher sliding velocities. It is worth noting that similarly high sliding velocities to those applied in the NEMD simulations are encountered physiologically during hair brushing and combing ($v_s \approx 0.1$ m s^{-1}).[11,154]

Fig. 4.13 shows the shear stress, τ, as as a function of normal stress, σ, for (a) the NEMD simulations and (b) CCP-AFM experiments. In both the experiments and NEMD simulations, there is a linear increase in $\tau$with σ, as expected from the Amontons friction law.[147] However, in some cases, there is a non-negligible intercept, which is indicative of an adhesive contribution that can be quantified though the Derjaguin offset.[147,223] The COFs (gradient) and Derjaguin offsets (intercept) shown in Table 4.2 are extracted from the linear fits shown in Fig. 4.13 to the equation: $\tau = (\sigma \cdot \mu) + \tau_0$, where τ_0 is the Derjaguin offset.[147,223]

In the CCP-AFM experiments, the Derjaguin offset is small and negative for the ultimately bleached system, suggesting negligible adhesion. For the pristine hair system, the Derjaguin offset is small and positive ($\tau_0 = 0.52 \pm 0.1$ MPa), suggesting some adhesion. Some adhesion for the pristine hair and moderately damaged systems is expected in water due to hydrophobic interactions between the lipid monolayers.[393] The NEMD simulations also give a non-negligible Derjaguin offset for the equivalent systems, but the high uncertainties do not allow for a quantitative distinction between the damage levels. The Derjaguin offsets seen in the previous AFM experiments with real hair[17] were much larger than those found in both our NEMD simulations and

Table 4.2: COF, μ, and Derjaguin offset, τ_0, from wet NEMD simulations ($\sigma = 5$-50 MPa) in pristine ($\chi_N = 0.0$), virgin ($\chi_N = 0.25$), medium bleached ($\chi_N = 0.85$) and ultimately bleached hair ($\chi_N = 1.0$) contacts. Experimental results from CCP-AFM using C_{18} (pristine hair) or SO_3^- (ultimately bleached) contacts ($\sigma = 1$-60 MPa) and previous AFM results for silicon nitride tips on virgin and damaged hairs ($\sigma = 6$-47 MPa) in humid air (RH $\approx$ 50%).[17] Experiments (v_s = 10^{-6}–10^{-7} m s^{-1}) were conducted at lower sliding velocities than the simulations (v_s = 10^{-1} m s^{-1}).

	Exp. μ	Sim. μ	Exp. τ_0 [MPa]	Sim. τ_0 [MPa]
Pristine hair mimic (Wet)	0.023±0.002	0.028±0.018	0.52±0.1	1.5±0.5
Ult. bleached hair mimic (Wet)	0.67±0.03	0.227±0.223	-0.5±1.8	1.1±6.5
Virgin hair (Air)[17]	0.03±0.01	0.054±0.010	2.3	1.7±0.3
Damaged hair (Air)[17]	0.13±0.05	0.20±0.08	5.7	1.3±2.4

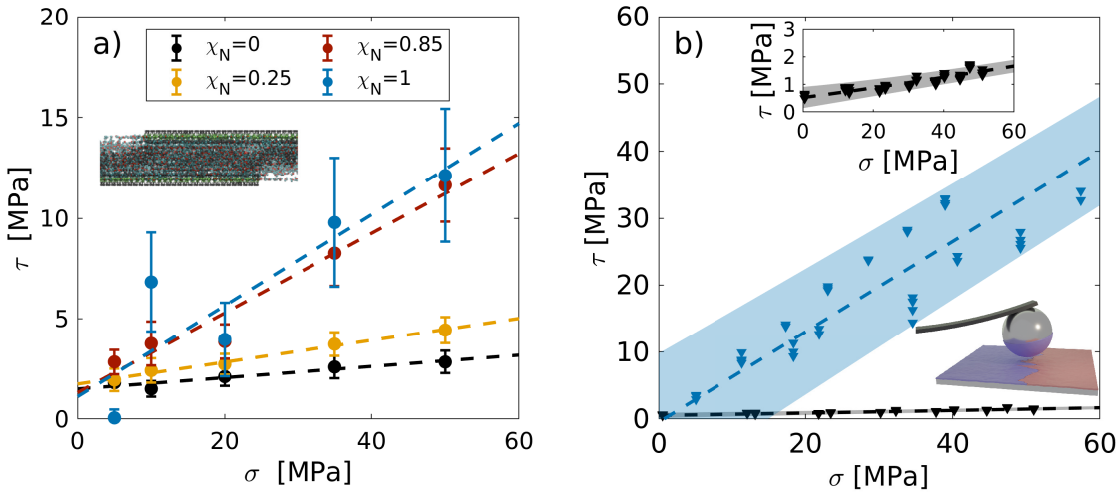


Figure 4.13: Shear stress, τ, as a function of normal pressure, σ, from (a) wet NEMD simulations and (b) biomimetic CCP-AFM experiments in water. Experiments for C_{18} ($\chi_N = 0$) and SO_3^- ($\chi_N = 1$) functionalised surfaces. Experiments (v_s = 10^{-7} m s^{-1}) were conducted at lower sliding velocities than the simulations (v_s = 10^{-1} m s^{-1}). Vertical bars for the NEMD data represent the standard deviation of the friction signals. The inset in (b) shows the magnified C_{18} friction data. Linear fits for NEMD and experimental data are shown as dashed lines. Corresponding prediction intervals on the experimental data with 95% confidence are shown as shaded areas. Experimental pressures are obtained from the extension to JKR theory[394] for thin coatings due to Reedy.[400]

CCP-AFM experiments. Moreover, the Derjaguin offset was observed to be larger for damaged hair than virgin hair,[17] which is the opposite trend to that observed in the CCP-AFM experiments. This suggests that there are other contributions to ahdesion in real hairs than are captured by the biomimetic surfaces, which is likely related to the microscale roughness of the cuticles.[218]

The trends between the COF values for the different damage levels from the NEMD simulations are in qualitative agreement with the CCP-AFM experiments, as shown in Fig. 4.13. For the pristine hair surfaces, the COF is slightly overestimated (+22 %) by the simulations compared to the experiments, while for the ultimately bleached surfaces, the COF is underestimated (-66 %). The differences for pristine hair likely originate from lower surface coverage of the C_{18} groups in the simulations,[354,389] while the difference for ultimately bleached hair could be due to differences in the counterions,[430] the exact nature of which are not known in the experiments. Previous simulations with *MARTINI*, the intermonolayer friction of lipid bilayers was underestimated by around an order of magnitude compared to experiment.[366] Thus, the level of agreement with experimental friction results achieved here with a CG force field can be considered acceptable.

The COF of the pristine hair mimic surfaces in CCP-AFM ($\mu = 0.023 \pm 0.002$) is in excellent agreement with that obtained with a silicon nitride AFM tip on hair ($\mu = 0.03 \pm 0.01$).[17] However, the COF for the ultimately bleached hair mimic ($\mu = 0.67 \pm 0.03$) was much higher than that between a silicon nitride AFM tip and damaged hair ($\mu = 0.13 \pm 0.05$).[17] This is probably due to the fact that only the substrate was charged in the previous AFM experiments, rather than both contacting

surfaces, as in the current CCP-AFM experiments, leading to weaker counterion trapping and thus lower friction.[430]

For the single-pressure NEMD simulations of the intermediate systems, which are representative of virgin ($\chi_N = 0.25$) and medium bleached ($\chi_N = 0.85$) hair contacts (Fig. 4.10), COFs of $\mu = 0.14 \pm 0.05$ and $\mu = 0.39 \pm 0.12$ were respectively obtained at 10 MPa and the lowest sliding velocity ($v_s = 1 \times 10^{-2}$ m s^{-1}). Thus, the COF for medium bleached hair is more than twice that of virgin hair. For the variable-pressure (5-50 MPa) NEMD simulations (Fig. 4.13), the COFs were $\mu = 0.054 \pm 0.010$ for virgin hair and $\mu = 0.20 \pm 0.08$ for medium bleached hair. Thus, the COFs for both systems are somewhat overestimated in the NEMD simulations compared to the previous AFM experiments.[17] However, the trends between the different damage levels are in excellent agreement with the experiments,[17] where the COF of damaged hair was approximately four times higher than virgin hair (Table 4.2). The fourfold increase in COF compared to virgin hair is also consistent with several other previous AFM experiments in humid air and water environments for both medium bleached and KOH-damaged hair.[16,70]

Overall, there is good agreement between the friction results from the nanoscale AFM on hair,[17] the CCP-AFM experiments with biomimetic surfaces, and the NEMD simulations (Table 4.2). The COF is generally higher in the simulations than the experiments (other than the ultimately bleached system). This is probably due to the higher sliding velocity necessary in the NEMD simulations ($v_s = 1 \times 10^{-2}$ m s^{-1}) than the CCP-AFM ($v_s = 2 \times 10^{-7}$ m s^{-1}) and hair-tip AFM ($v_s = 2 \times 10^{-6}$ m s^{-1}) experiments.[17] The agreement of the NEMD data with experiments suggests that nanoscale friction increases associated with hair damage are primarily induced by the changes in surface chemistry rather than changes in microscale surface roughness, as suggested from previous experimental results.[17] In support of this hypothesis, it has recently been shown using an AFM relocation method that the nanoscale roughness of hair does indeed not change significantly for a single 10-minute bleaching treatment.[202] The NEMD simulations suggest that confinement-induced solidification of water[420] and counterion trapping[430] respectively lead to elevated nanoscale friction in virgin hair and bleached hair.

4.4 Conclusion

In this chapter, the nanoscale friction between biomimetic hair surfaces at different degrees of damage was investigated using coarse-grained NEMD simulations and CCP-AFM experiments. In the experiments, the silica surfaces were functionalised with either octadecyl groups, to represent the outer 18-MEA monolayer on pristine hair, or sulfonate groups, to represent the oxidised cysteic acid groups that form on the

surface of ultimately bleached hair. In the CCP-AFM experiments, much higher COFs were observed for the ultimately bleached hair model surfaces than the pristine hair model surfaces. This observation is in agreement with previous AFM experiments of silicon nitride tips sliding on virgin and damaged hair.

In the NEMD simulations, we measured the friction between surfaces representative of pristine, virgin, medium bleached, and ultimately bleached hair, as well as intermediate degrees of damage. Both dry and wet contacts were considered over a wide range of sliding velocities. For dry and wet contacts at high sliding velocities, we find a near-logarithmic dependency of friction on sliding velocity, which is indicative of a SATA process. We successfully applied an Eyring-like extended SATA model to our NEMD simulation data. For wet contacts, we observe a departure from the SATA behaviour at low sliding velocities as the COF levels off and approaches a constant value. A reduction in COF due to the presence of water in the contact is observed at all sliding velocities for hydrophilic bleached hair, but only at high sliding velocity for hydrophobic pristine and virgin hair. For pristine and virgin hair, the confined water molecules become more solid-like at low sliding velocities, which explains the increase in friction compared to the dry systems.

In the NEMD simulations, we observed a monotonic increase of friction forces with increasing chemical damage at low sliding velocities. This is in good agreement with previous AFM experiments on real hair surfaces and the new CCP-AFM measurements with biomimetic surfaces. We also performed additional NEMD simulations at varied pressure to quantify the adhesive contribution to the shear stress, known as the Derjaguin offset. In both the NEMD simulations and CCP-AFM experiments, a non-negligible Derjaguin offset was observed for pristine and virgin hair, which is due to hydrophobic interactions. This adhesive contribution was underestimated in both the CCP-AFM experiments and NEMD simulations compared to previous AFM experiments with real hair, which is due to the absence of microscale roughness from the overlapping cuticles. A fourfold increase in COF was observed in the variable-pressure NEMD simulations moving from the virgin to medium bleached hair models, which is in excellent agreement with previous AFM experiments with real hair. We identify the role of counterion trapping on charged surfaces as a potential nanoscale mechanism for the elevated COF on chemically damaged hair. These observations demonstrate that friction increases of bleached or chemically damaged hair at the nanoscale are controlled by the modified surface chemistry, rather than solely due to roughness changes or subsurface damage. In the next step, the NEMD framework established in this chapter will be coupled to equilibrium adsorption simulations to study the effect of small ionic molecules relevant to hair care products on hair-on-hair friction.

5 Effects of surfactant adsorption on the wettability and friction of biomimetic surfaces

The content of this chapter was published as a journal article in Physical Chemistry Chemical Physics (PCCP).[431]

5.1 Introduction

The adsorption of surfactants on heterogeneous solid surfaces is important for the performance of a wide range of industrial and domestic formulations, from fluids for oil extraction[432] and lubricants[433] to laundry detergents[434] and cosmetics.[5] Despite this, the vast majority of experimental and computational studies of surfactant adsorption are conducted using flat homogeneous substrates.[435] It has been shown that nanoscale surface roughness and chemical heterogeneity can strongly impact surfactant performance, so it is important to include these substrate effects in the surfactant design and formulation process.[435] Human hair is one such heterogeneous surface where surfactant adsorption plays an important role in modifying interfacial behaviour.

As previously discussed, hair has no natural self-repair mechanism for the 18-MEA layer apart from the exposure of fresh cuticles through delamination,[53,197] which only occurs following strong chemical hair treatments[436] or extended weathering.[53] Therefore, one of the main functions of hair care formulations[111] is to repair the damaged 18-MEA monolayer.[5] Hair care products, such as shampoos and conditioners, contain a wide range of anionic, cationic, zwitterionic, and non-ionic surfactants to aid the maintenance and grooming processes.[101] The main function of shampoos is to clean the hair,[101] while conditioners repair hair damage to make it easier to comb and improve its feel, shine, and softness.[31] Shampoos contain mostly anionic surfactants due to their superior cleaning performance,[4,101] they have been shown to successfully remove dirt and sebum from the hair surface.[4] Conditioners typically contain cationic surfactants or polymers due to their ability to form strong ionic bonds with negatively-charged regions on the hair surface to act as a repairing agent and remain bound after rinsing and drying.[31] Many experimental studies have investigated the adsorption of anionic surfactants,[437,438] cationic surfactants[109,437,439,440] and cationic polymers[122,173,441–443] on hair.

It has been shown that the friction between a single bleached hair and hard rubber can be decreased by increasing the concentration of cetyltrimethylammonium bromide (CTAB).[159] Friction reductions in single hair-hair contacts were also observed using

AFM as the concentration of tetradecyltrimethylammonium bromide (TTAB) was increased.[211] CTAB was also found to reduce friction at larger scales in rubbing experiments with a model finger on hair bundles.[184] In addition to friction reduction, cationic surfactants and polymers can also be added to formulations to make hydrophilic bleached hair more hydrophobic.[43,63,74,171,172,211,227,230] Dynamic and static wetting experiments on bleached hair showed that the water contact angle increased through the deposition of cationic surfactants.[39,100,227]

Theoretical and numerical models can help in providing insights to surfactant interactions with hair and other biological substrates that are otherwise inaccessible through experiments. In chapter 2, both mean-field theory approaches, such as self-consistent field theory (SCFT)[128,130,300,444] and molecular dynamics simulations were highlighted in the context of hair tribology modeling. The adsorption of non-ionic surfactants on chemically heterogeneous surfaces, comparable to those found on damaged hair, has been studied with DPD.[445] Recently, the adsorption and desorption under shear of cetrimonium chloride (CTAC) and fatty alcohols on 18-MEA monolayers grafted to a planar surface as a model for virgin hair were investigated using DPD.[110] MD simulations with atomisitic resolution have also been used to study the adsorption of fatty acids onto the 18-MEA-covered ultrahigh sulfur proteins.[262]

In this chapter, the adsorption of cationic and anionic surfactants onto virgin and bleached hair surfaces are studied using coarse-grained MD simulations. We simulate surfactant adsorption isotherms with bulk systems at concentrations above the critical micelle concentration (cmc). Subsequently, we investigate the friction of hair surfaces with adsorbed ionic surfactants using squeeze-out and NEMD simulations at a wide range of contact pressures and sliding velocities. Our NEMD simulation results are compared to previous hair friction experiments, in particular those with various cationic surfactants. Finally, nanodroplet wetting simulations are carried out to compare the contact angle on surfaces with adsorbed cationic surfactants to previous results on bare model hair surfaces. The methodology introduced in this chapter is expected to be applicable to screening of a wide range of different ionic surfactants with regards to their surface affinity, aggregation at heterogeneous surfaces, wetting and ultimately their effect on friction between hairs and other soft matter interfaces.

5.2 Methodology

5.2.1 Surfactant bulk solutions

Self-assembly MD simulations of the ionic surfactants in aqueous solution to establish equilibrated bulk systems for subsequent surface adsorption simulations are carried out. CTAB is used as a model cationic surfactant and sodium dodecyl sulfate (SDS) as a model anionic surfactant. We also consider systems with excess salt (NaCl) to study the effect on self-assembly and adsorption. An overview of all free molecules considered

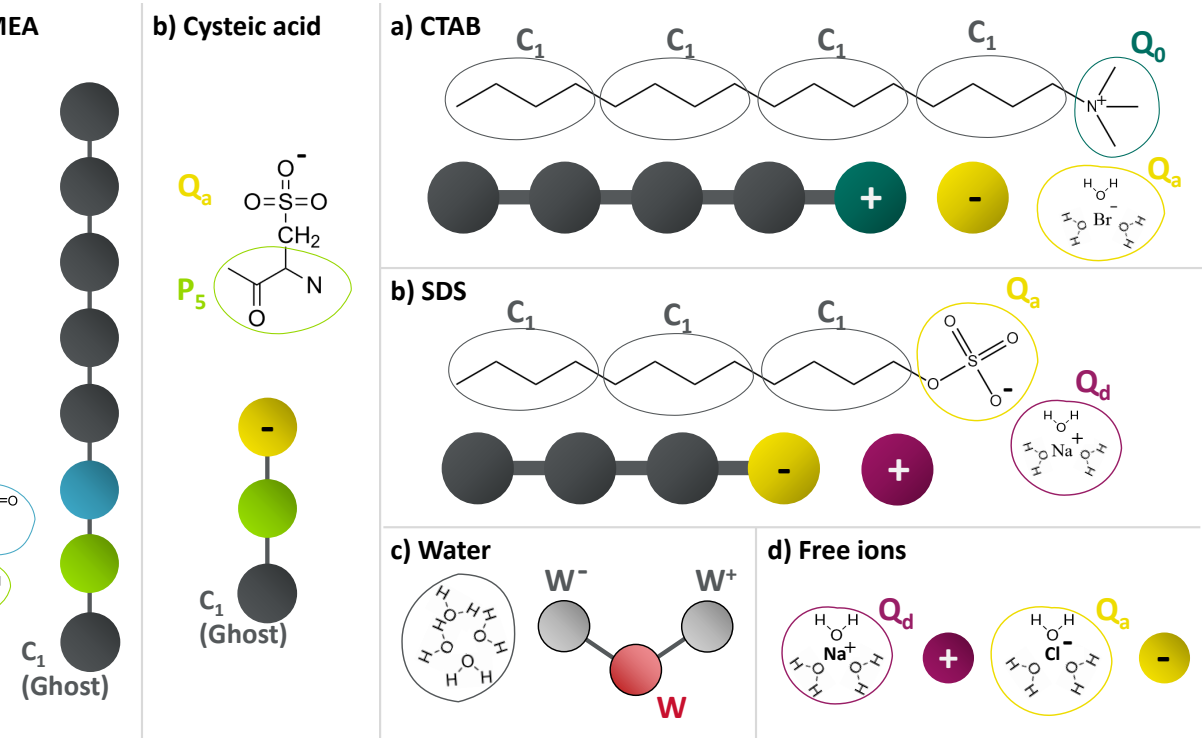


Figure 5.1: Overview of molecules and *MARTINI* bead types considered in this chapter: a) CTAB, b) SDS, c) polarizable water, and d) (excess) ions with their first hydration shell.

and their coarse-grained bead types is shown in Fig. 5.1. We employ the *MARTINI 2* model[264,265] in conjunction with the polarizable *MARTINI* water model introduced by Yesylevskyy et al.[306] throughout. This combination has been validated in the last chapter for the structure, wettability, and frition of virgin and bleached hair surfaces.

CTAB is described as a linear chain of four apolar C_1 beads with a terminal positively-charged Q_0 bead and negativly-charged Q_a bead representative of the bromide counterions.[446–448] For CTAB, we consider bulk concentrations in the range of $c_0 = 120$-973 mM, where c_0 is the concentration prior to any adsorption. The equilibrium bulk concentration, c_e, can potentially differ from the initial concentration due to surfactant adsorption and therefore depletion from the finite-size bulk.[449] SDS is modelled as three apolar C_1 and a terminal negatively-charged Q_a bead with a positively-charged sodium counterion (Q_d).[446,450,451] Initial SDS concentrations in the range of $c_0 = 173$-701 mM are considered.

All simulations were performed in the open-source code LAMMPS.[332] We use the velocity-Verlet[333] integration scheme with a timestep of 5 fs.[264] The fully periodic bulk systems are equilibrated to atmospheric pressure ($p = 1$ atm) for 0.1 ns in the isothermal-isobaric (NPT) ensemble and are then run in the canonical ensemble (NVT) at $T = 300$ K for at least 100 ns. We used a global Nosé-Hoover thermostat[340,341] and barostat[452] with a damping coefficient of 1 ps for the temperature and 3 ps for the pressure. All MD and forcefield-related numerical settings are consistent to what was outlined in chapter 3 for the hair surface model unless specified otherwise below. As

before, long-range electrostatic interactions are calculated using the particle-particle particle-mesh (PPPM) method at a relative energy tolerance of 10^{-5}.[336] The importance of accurate long-range electrostatics to correctly capture the self-assembly and adsorption problems of ionic surfactant solutions was highlighted in previous surfactant studies using the *MARTINI* force field.[446,449]

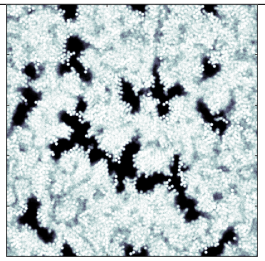
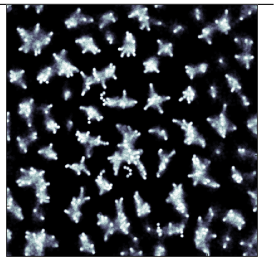
We performed additional simulations with pre-assembled micelles to assess how a variation in micelle aggregation number would affect the micelle stability and adsorption to the hair surface. Aggregation numbers of $N_{ag} = 82$ for CTAB and $N_{ag} = 45$ for SDS were chosen in accordance with experiments and previous coarse-grained simulations with standard *MARTINI* water.[446,453–456] The pre-assembled micelles were generated using PACKMOL.[369] For the pre-assembled micelles, we consider low and intermediate concentrations for both CTAB ($c_0 = 120$ mM and $c_0 = 509$ mM) and SDS ($c_0 = 170$ mM and $c_0 = 584$ mM) used in the self-assembled systems. Micelle stability simulations were run in a fully periodic system for at least 100 ns. Afterwards, we transferred the bulk systems to the hair surfaces and conducted adsorption simulations, as described below.

5.2.2 Surface properties

The same coarse-grained *MARTINI* models introduced in chapter 3 are used to describe the surface of virgin and bleached hair. In this chapter, we consider two surfaces with different degrees of alkyl and sulfonate groups with a combined packing density of 2.73 nm^{-2}. For virgin hair, we use a random arrangement of 75% alkyl groups and 25% sulfonate groups. For medium bleached hair, we use a random arrangement of 15% alkyl groups and 85% sulfonate groups. These groups are grafted to a flat graphene sheet made up of *MARTINI* C_1 beads.[307] The graphene sheet serves as a simple representation of the protein layers below and conveniently serves as a slider to apply normal forces and constant shear rates to the contact. A detailed model description of the *MARTINI* parameters and their validation for hair surface wettability can be found in chapter 3. The x $\times$ y dimensions of both periodic surfaces are 24 × 21 nm for the adsorption simulations. The surface properties of the two hair models are given in Table 5.1.

The surface energies (polar + non-polar) were calculated using the Owens-Wendt[232] method from previously reported contact angle measurements from coarse-grained MD simulations using the same hair surfaces with water (polar) and n-hexadecane (non-polar). The surface energy is larger for bleached hair than virgin hair, mainly due to the increase in polar contribution. The surface energies in Table 5.1 are in good agreement with those obtained from wetting experiments on real virgin hair (18.9 mJ m^{-2}) and bleached hair (29.8 mJ m^{-2}).[100] The virgin hair surface energy is somewhat overestimated in the simulations compared to the experiments, while the bleached hair surface energy is underestimated. The underestimation of the surface energy of the medium bleached hair surface is probably due to the systematically

Table 5.1: Surface properties of virgin and medium bleached hair models.

Property	Symbol	Virgin hair	Med. bleached hair
Surface snapshots			
18-MEA grafting density	ρ_{MEA}	2.05 nm^{-2}	0.41 nm^{-2}
SO_3^- grafting density	ρ_{SO3-}	0.68 nm^{-2}	2.32 nm^{-2}
Surface charge density	ρ_c	-11.0 μC cm^{-2}	-37.2 μC cm^{-2}
Surface energy	γ	20.4 mJ m^{-2}	23.5 mJ m^{-2}
RMS Roughness	σ	1.77 nm	0.94 nm
Fractal dimension	$D_f = 3 - H$	2.59	2.78

lower water-vapour surface tension of the polarizable *MARTINI* water model.[306] On the other hand, the n-hexadecane-vapour surface tension with the *MARTINI* force field is close to experiments.[299,329]

The surface charge densities from the simulations are somewhat larger than those from previous experimental measurements of the surface charge density of virgin (-1.5 μC cm^{-2}) and bleached (-10.0 μC cm^{-2}) hair.[99] However, the density of cysteic acid groups on bleached hair is in good agreement with estimates (ρ_{SO3-} = 2.2 nm^{-2}) from another experimental study.[92] This suggests that the surface charge measured in the experiments[99] is lower than the simulations due to partial screening of the negative charges by the K^+ counterions present in solution. The screening effect by Na^+ counterions is not considered in the simulations surface charge density values reported in Table 5.1. The charge density for the medium bleached hair surface is very similar to that measured for an SDS monolayer at the hexadecane-water interface (-37.9 μC cm^{-2}).[457]

We also determined the root-mean-square (RMS) roughness of our model surfaces by obtaining a discrete time-averaged topography map of the surface. The surface was discretized by treating the coarse-grained beads as hemispheres with a radius equivalent to half the Lennard-Jones potential energy minimum $\sigma/2$ and using a grid spacing of $\Delta x = 0.071$ nm^{-1}. The RMS roughness of our model surfaces (24 nm × 21 nm) is somewhat larger for virgin hair than medium bleached hair. On the other hand, experimental AFM measurements with a 200 × 200 nm scan area suggested that the RMS roughness of hair increased slightly from 1.48 nm for a region where the 18-MEA layer was intact (virgin hair) to 1.74 nm in a region where the 18-MEA layer had been removed by bleaching.[80] This discrepancy between the experiments and simulations is likely a result of the simplified atomically-smooth surfaces used in the simulations. In reality, the underlying disordered protein layer[262] is likely to be rougher than the graphene layer used to represent it in the simulations. Despite this

opposite trend, the RMS roughnesses for both model surfaces are quite close to the experimental values using a small scanning area.[80] AFM experiments with larger scan areas (10 µm × 10 µm) showed higher RMS roughness values, which also increased from 10 nm for virgin hair and hair bleached for 10 minutes to 13 nm for hair bleached for 20 minutes (mean of three locations).[202] These larger area scans also included features such as cuticle edges, which are not considered in the current simulations.

The fractal dimension of the hair surfaces was estimated using a surface roughness spectral approach as described by Persson.[458] Approximate experimental fractal dimension of D_f = 2.20 for virgin hair (2 × 2 µm scan area),[80] and D_f = 2.71 for bleached hair (7 × 7 µm)[266] were estimated from AFM images available in the literature. The increase in fractal dimension for the bleached hair model compared to virgin hair is in good agreement with these experimental estimates. This observation suggests that the bleached hair surfaces are more irregular than virgin ones,[459] which is due to the formation of lipid islands as an increasing proportion of alkyl groups are replaced by sulfonate groups, see chapter 3. Previous MD simulations of hydrophobic surfaces have shown that wettability is sensitive to the nanoscale RMS roughness, but not the fractal dimension.[460] However, for the current biomimetic surfaces, where hydrophobic groups in virgin hair are replaced by hydrophilic groups in bleached hair, the wettability is expected to be affected by both of these parameters.

5.2.3 Surfactant adsorption

A single hair surface is brought into contact with the equilibrated bulk solution, similar to a previous coarse-grained MD[449,461] and DPD[110,301,445] adsorption studies on different surfaces. The bulk is placed approximately 3 Å above the surface to avoid initial overlap of the beads. Excess counterions in the bulk corresponding to the number of hair surface charges were randomly removed for systems with CTAB and added for systems with SDS to maintain an overall charge-neutral system. We also investigated the effect of counterion condensation by considering an initially charge-neutral surface (counterions adsorbed). The configurational differences arising from the initial distribution of counterions are discussed below in section 5.3.2.

The transfer to the surface breaks the periodicity of the bulk in the direction normal to the hair surface (z), so care was taken to ensure that surfactant micelles in the bulk were not sliced. For large surfactant concentrations ($c > 300$ mM), no separating plane could be found that would not divide at least one micelle. Adsorption simulations were run in the canonical ensemble (NVT) at a temperature of $T = 300$ K. Periodic boundary conditions were applied in the x and y directions, while the systems were finite the the z direction. A repulsive 12-6 Lennard-Jones wall potential was added at the top of the simulation cell in the z-direction. Long-range electrostatic interactions were evaluated using a slab implementation[335] of the PPPM method.[336] All other simulation parameters follow those presented for the bulk systems.

5.2.4 Friction

We further investigate the effect of cationic surfactants on friction between two hair surfaces using NEMD simulations.[20] The methodology for the NEMD simulations is similar to that described for water-lubricated hair surfaces in the previous chapter. First, squeeze-out simulations between two hair surfaces are performed in a water bath to establish equilibrium contact thickness and composition for a given contact pressure, σ. The cationic surfactant is pre-adsorbed on the surfaces in the configurations obtained from the adsorption simulations. We select two surface adsorption densities Γ based on our adsorption study for the virgin and medium bleached hair surface models. The surfaces were duplicated and reflected at an initial distance of 10 nm between the surfaces. This is sufficiently large to accommodate the adsorption structures from both surfaces.

A normal stress of $\sigma = 5$-50 MPa was applied between two hair surfaces of equal surface damage. This range is consistent with the estimate of physiologically relevant contact pressures between two hairs in the previous chapter. No excess surfactants are present in the bath since we do not expect the surface coverage of surfactants to increase during squeeze-out due to micelle entrapment or further physical adsorption. Very few CTAB molecules were squeezed out from the contact due to the strong affinity to the surfaces. Therefore, only the number of water molecules in the contact was considered a free variable with respect to the normal load applied during squeeze-out.

NEMD simulations were then performed to investigate the friction between two hair surfaces based on the composition and thickness obtained from the surfactant-containing squeeze-out simulations. Two hair surfaces with equal surface damage are slid against each other in the x direction at a constant sliding velocity v_s. We consider sliding velocities of 0.01-1 m s^{-1}, which are deemed realistic for typical hair manipulations (brushing and combing).[11,154] During squeeze-out and sliding a constant contact pressure (5-50 MPa) is maintained by applying an average normal force to the coarse-grained beads of the upper graphene sheet, while keeping the lower graphene sheet fixed. Using a global Nosé-Hoover thermostat[340,341] in the NEMD simulations could artificially influence the behaviour of the confined fluid molecules.[20] Therefore, temperature is controlled by applying a one-dimensional Langevin thermostat[374] to the grafted P_5 beads in the direction perpendicular to compression and sliding (y) set at $T = 300$ K with a time relaxation constant of 0.1 ps. This leads to a negligible temperature rise (< 1 K) within the contact for the sliding velocities applied. Production sliding simulations are run for at least 200 ns. For the lowest sliding velocities considered, simulations are run up to 500 ns to sample at least 5 nm of surface displacement. For NEMD simulations, the slab implementation[335] of the PPPM method is used.[336]

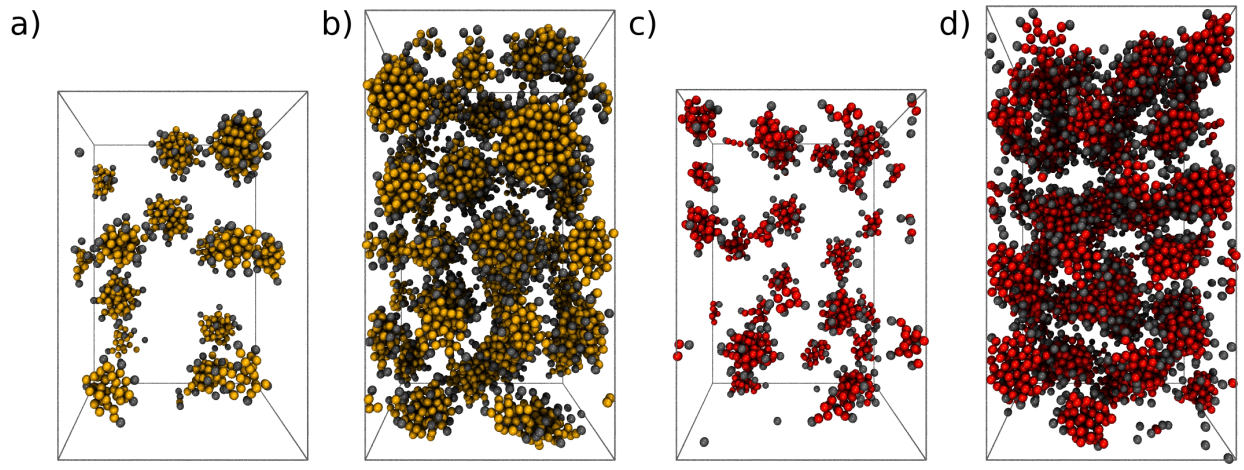


Figure 5.2: Snapshots of self-assembled micellar systems at equilibrium: CTAB at a) $c_0 = 120$ mM, b) $c_0 = 497$ mM and SDS at c) $c_0 = 174$ mM, and d) $c_0 = 664$ mM. Ionic headgroups are coloured in gray. Counterions are not shown here for clarity. Rendered with VMD.[349]

5.2.5 Contact angle

The wettability of the CTAB-treated hair surfaces is investigated by the deposition of water nanodroplets. CTAB molecules are not present in the water droplet and negligible desorption occurs during the wetting simulations. Thus, we consider the effect of the surfactant on the solid-liquid and solid-vapour surface tensions, but not the liquid-vapour surface tension.[462] This is equivalent to measuring the contact angle of pure water on hair previously treated with cationic surfactant.[227]

The methodology for the wetting simulations is the same as described in chapter 3 for base virgin and bleached hair surfaces. This was based on a previous study of the wetting of graphene by water and various surfactants using the *MARTINI* model.[310]. The diameter of the initially hemispherical droplet is d = 20 nm, containing 18,121 polarizable water molecules. In chapter 3, this droplet size was found to be sufficiently large to be representative of the contact angle of macroscale droplets. The side lengths of the hair surface models for the wetting simulations are consistent with those used in chapter 3. The model surfaces were equilibrated for 10 ns in the canonical (NVT) ensemble, followed by a production run with the droplet added for a further 10 ns. We apply a global Nosé-Hoover thermostat[340,341] with a damping coefficient of 1 ps. We measure the water nanodroplet contact angle at the interface using 10 block averages of 1 ns.

5.3 Results and discussion

5.3.1 Surfactant bulk self-assembly

The formation of micelles is expected for both cationic (CTAB) and anionic surfactants (SDS) in water in the range of concentrations used in the current study.[446] Examples of the bulk systems containing CTAB and SDS are shown in Fig. 5.2. Spherical micelles are observed in all of our systems, apart from the system with the highest

CTAB concentration (c = 963 mM), where the onset of a transition from spherical micelles to hexagonally-ordered structures is observed. The formation of non-spherical micelles at high CTAB concentrations is in agreement with the phase diagrams from experiments[463,464] and MD simulations with the *MARTINI* force field.[446] For SDS, the concentrations considered here are below the phase boundary limit of the hexagonal (H_α) phase at ambient conditions.[446,463]

Table 5.2: Aggregation numbers of surfactant micelles as a function of the bulk concentration in charge-neutral systems without excess salt.

a) CTAB		b) SDS	
c [mM]	$\overline{N}_{agg}$ [-]	c [mM]	$\overline{N}_{agg}$ [-]
139	7.1	174	8.1
278	11.6	312	12.5
368	20.0	447	15.9
484	23.9	563	22.1
579	28.9	664	21.5

We investigated the implications of using the polarizable *MARTINI* water model[306] on the aggregation behaviour of the surfactants. Aggregation numbers as a function of the bulk concentration are provided in Table 5.2. The size of surfactant micelles with the polarizable water model is underpredicted in comparison to both experiments and the standard non-polarizable *MARTINI 2* water model.[447] For CTAB at c = 90 mM, aggregation numbers around $N_{agg} = 70$ were reported with the standard *MARTINI* water model[447], compared to experimental aggregation number measurements up to $N_{agg} \approx 150$ above the second cmc (m = 0.24 mol kg^{-1}) obtained using nuclear magnetic resonance (NMR) spectroscopy.[465] Finite-size effects[466] were briefly checked by comparing self-assembly simulations for systems with box lengths of 11.9×10.3 nm^2 and 23.8×20.6 nm^2. No significant differences in micelle aggregation numbers between these systems were observed. It has been recently observed that the polarizable *MARTINI* force field tends to underpredict the micelle aggregation numbers of other surfactants, such as zwitterionic dodecylphosphocholine (DPC) compared to both experiments and the standard *MARTINI* water model.[466] At the same time, the use of the polarizable force field was found to be detrimental to producing micelles of zwitterionic surfactants that are in structural accordance with experiments.[467] It is also worth noting that a systematic underestimation of the aggregation numbers of CTAB and SDS compared to experiments was reported for the standard water model on multiple occasions.[446,447,466] This is in contrast to larger-than-experimental aggregation numbers numbers of SDS above c = 100 mM found during self-assembly simulations with standard *MARTINI* water and a modified Lennard-Jones potential of the SDS hydrocarbon tails.[377] We conclude that capturing the experimental aggregation numbers of specific surfactant types likely requires fine-tuning of the force field parameters when using either polarizable or non-polarizable water models. This is beyond the scope of the current study, where we are more interested in the adsorption

of surfactants on solid surfaces.

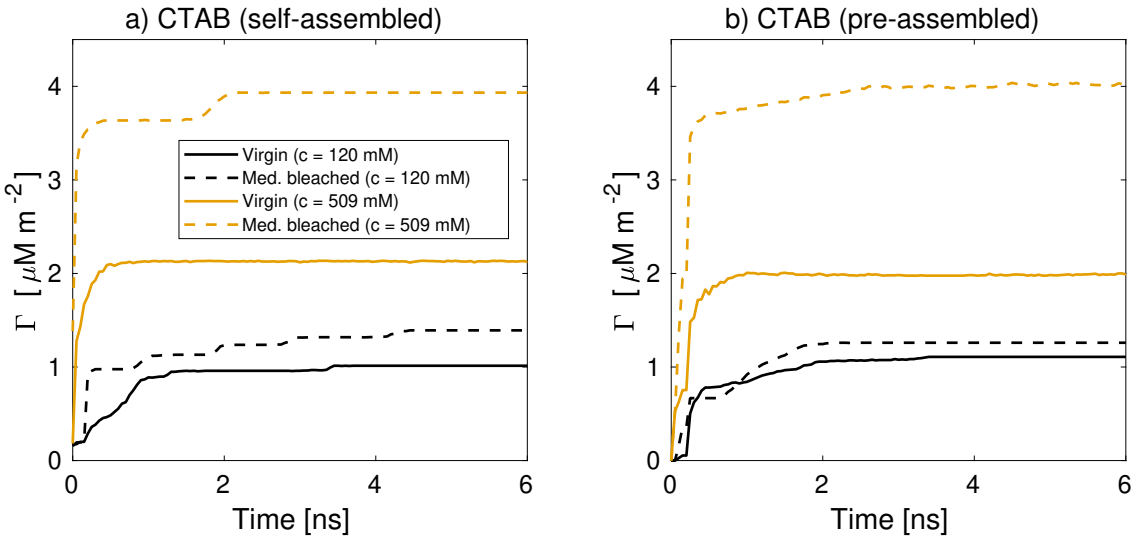


Figure 5.3: Temporal evolution of micelle adsorption to hair surfaces for a) self-assembled ($\overline{N}_{agg} = 7.1$-28.9) and b) pre-assembled CTAB micelles ($\overline{N}_{ag} = 82$). The agreement in adsorption kinetics and equilibrium adsorption densities suggests that adsorption is not sensitive to the size nor stability of the micellar aggregates in bulk - likely because complete micelle break-up occurs near the surface due to electrostatic interactions with the anionic surface sites.

We conducted short bulk and adsorption simulations of larger pre-assembled CTAB ($N_{agg} = 82$) and SDS ($N_{agg} = 45$) micelles to investigate if the reduced micelle size due to the force field parameters would have a significant effect on surface adsorption. These micelle sizes were selected based on previous experiments[453–456] and molecular simulations with standard *MARTINI* water.[446] The pre-assembled micelles were stable in bulk simulations over more than 100 ns. The adsorption densities and kinetics from pre-assembled and self-assembled micelles were very similar across a wide range of surfactant concentrations, as shown for CTAB in Fig. 5.3. This indicates that the aggregation number does not seem to be an important consideration for the adsorption of surfactants since micelles tend to break up in the proximity of the surface. We therefore only discuss the results using bulk systems with self-assembled micelles in the remainder of this study.

5.3.2 Surfactant adsorption onto hair surfaces

a) Cationic surfactants

Simulated adsorption isotherms of the cationic and anionic surfactants are shown in Fig. 5.4a)-b). Examples of the temporal evolution of the surface coverage are given in Fig. 5.3. The initial concentration of surfactants in the bulk c_0 serves as reference to estimate the effective change in bulk concentration upon reaching equilibrium. The equilibrium concentration is computed as $c_0 = c_0 - \Gamma \cdot A$, where A is the substrate surface area. This approach has been utilized in a previous coarse-grained MD simulation study of SDS adsorption.[449] Examples of the mass density profiles of the

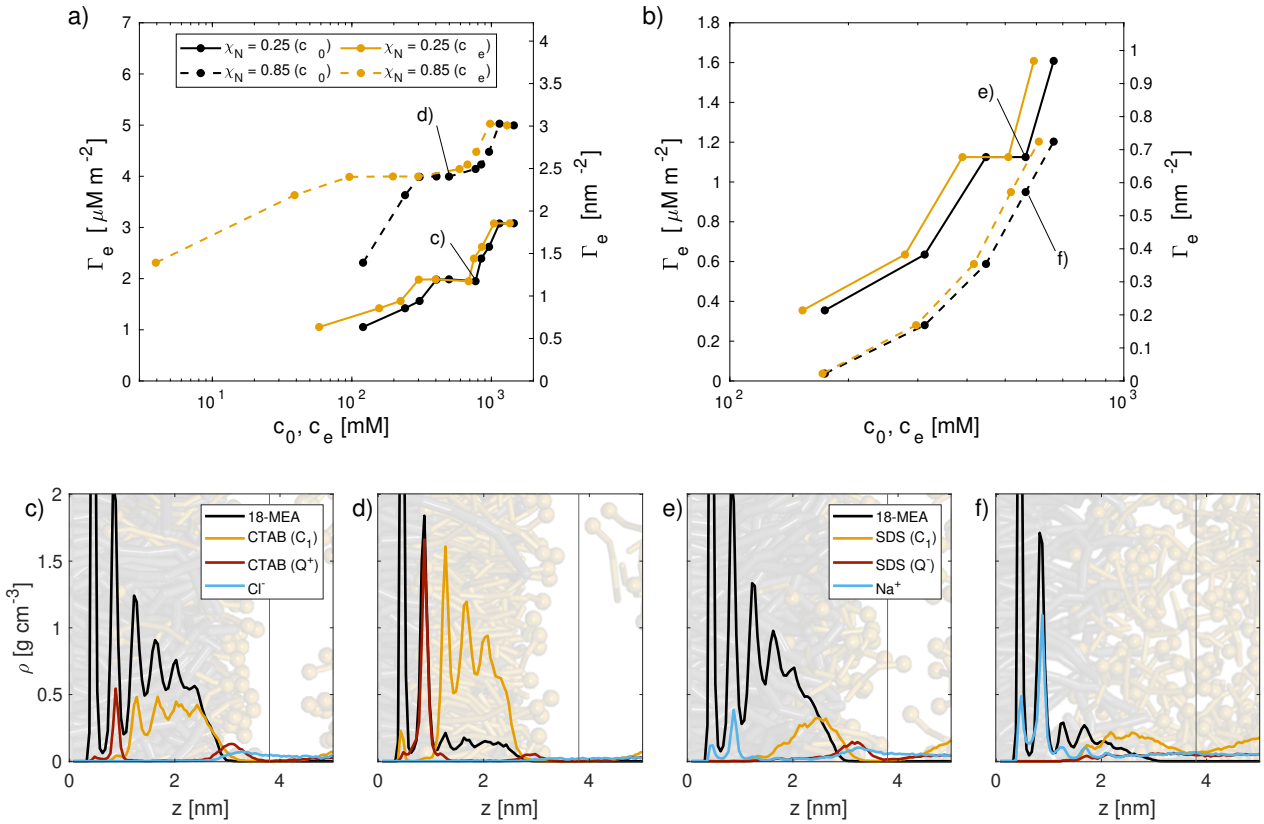


Figure 5.4: Top row: Equilibrium surface coverage Γ_e of a) CTAB and b) SDS on virgin (solid lines) and medium bleached (dashed lines) hair surfaces as a function of the initial bulk concentration c_0 and the bulk concentration at equilibrium c_e. Lines only serve as a guide to the eye. Bottom row: Equilibrium mass density profiles for systems with CTAB on c) virgin ($c_e = 687$ mM) and d) medium bleached surfaces ($c_e = 300$ mM), and for systems with SDS on e) virgin ($c_e = 509$ mM) and f) medium bleached surfaces (c_e=516 mM). Vertical lines indicate the cutoff for contributions to the surface coverage ($z = 3.8$ nm).

CTAB/SDS, 18-MEA and counterions are shown for a single concentration in Fig. 5.4c)-f).

The adsorption isotherms of CTAB can be divided into three characteristic regions. (i) At low concentrations, a sharp increase in surface coverage is observed, which is due to electrostatic adsorption of the cationic surfactants to the negatively charged sulfonate sites. (ii) A region of saturation is found at intermediate concentrations (virgin: c_e=300-690 mM, medium bleached: $c_e = 95$-300 mM) where all anionic surface charges are saturated by adsorbed cationic surfactant molecules. Here, surfactants are predominantly arranged in a combined monolayer with the grafted 18-MEA lipids. The positively charged terminal bead are oriented towards the surface, as evident from the mass density profiles in Fig. 5.4c)-d). For virgin hair, the region of saturation is shifted towards higher concentrations. A secondary peak for the charged CTAB beads in Fig. 5.4c) suggests an onset of hydrophobic-driven adsorption at the end of the saturation plateau. (iii) When further increasing the surfactant bulk concentration, a sharp increase in the adsorption densities is observed on both virgin and medium bleached hair surfaces. Here, hydrophobic-driven adsorption leads to the formation of a secondary surfactant layer on top of the existing mixed monolayer of CTAB and covalently-bound 18-MEA.

Overall, the adsorption densities on virgin hair are reduced compared to medium bleached hair surfaces, as fewer negatively charged damage sites are available on the virgin hair surface. Previous experiments of hair fibres treated with hair conditioners also found higher levels of cationic surfactants on bleached than on virgin hair fibres.[108,220,439] It is also worth noting that the initial distribution of counterions on either the surface or in the bulk can affect the structure and to some extent the adsorption density of the cationic surfactants. When all counterions are initially adsorbed on the surface, the adsorbed structure might appear more disordered and micelle-like as opposed to the layered structures discussed here. Further details are discussed below in section 5.3.2.

The multi-stage adsorption behaviour observed here is in qualitative agreement with experimental investigations of cationic surfactant adsorption on hair. Ran et al.[109] previously reported a multi-stage behavior of the cationic surfactant dimethylpabamidopropyl laurdimonium tosylate (DDABDT) on virgin hair samples. Two plateaus regions were identified and attributed to monolayer and bilayer configurations of the surfactants on the surface.[109] Tyrode et al.[468] also reported multi-stage adsorption isotherms for CTAB on hydrophilic silicon surfaces. They also identified two plateau regions, the first at a CTAB coverage of around 1 nm^{-2} and the second at around 3 nm^{-2}, which the same range seen in Fig. 5.4 for our model hair surfaces. These works considered surfactant concentrations below and slightly above the cmc, whereas in our simulations the concentrations are all above the cmc due to the significant computational cost of these large-scale explicit solvent simulations.[446] Nonetheless, the plateau adsorption densities reported in this work are similar to those observed experimentally for comparable cationic surfactants on virgin hair[109] and CTAB on other hydrophilic surfaces.[468] We therefore expect that, despite the higher surfactant concentrations and finite-size limitations of the MD adsorption simulations, they provide a useful pathway for obtaining similar equilibrium adsorption configurations as seen experimentally for subsequent MD simulations of friction and wetting.

b) Initial counterion distribution

Previous all-atom simulations of CTAB adsorption on mica surfaces suggest a strong dependency of the presence of a potassium (K^+) layer on the substrate.[469] Upon removal of this ionic layer, the conformation of adsorbed CTAB at equilibrium changed from a micellar structure towards a bilayer conformation. We conducted additional simulations to compare the configurations with all counterions initially distributed in the liquid phase to configurations where counterions were initially adsorbed to the negative surface charges on the hair surface (locally charge neutral). Fig. 5.5a)-b) shows the adsorption densities Γ and snapshots of adsorbed surfactant structures on surfaces representative of virgin and medium-bleached hair. For virgin hair, the adsorption density and corresponding ordered structure of CTAB on the surface do

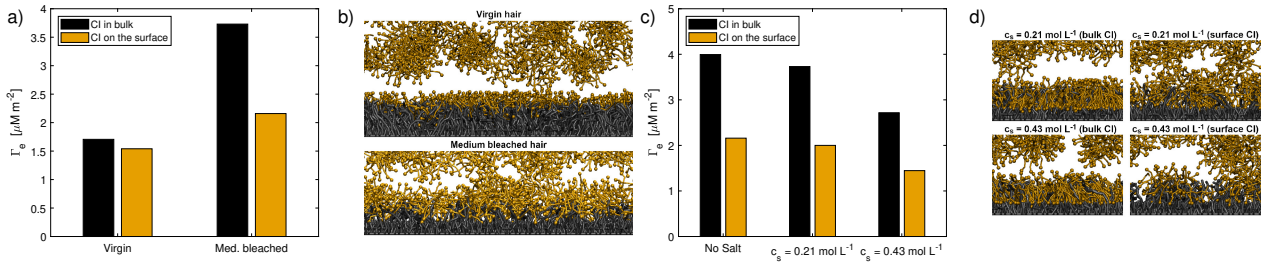


Figure 5.5: CTAB adsorption densities for initial counterion distributions either fully in the bulk or fully adsorbed on the surface. a) Difference between different degrees of surface damage with b) snapshots of the interface for virgin (top) and medium bleached (bottom) model hair surfaces when all counterions are initially located on the surface. c) Adsorption densities on medium bleached hair surfaces for different levels of background salt with d) corresponding snapshots of the interface. The CTAB concentration is $c_0 \approx 500$ mM for all shown cases. Salt ions are not shown for clarity.

not change significantly between the two counterion configurations. For the strongly negatively charged surfaces representative of moderately bleached hair, we find that an initial distribution of neutralizing counterions on the surface leads to a decreased adsorption density of CTAB on the surface. The structure of adsorbed CTAB also becomes significantly more disordered as the surfactants appear to adsorb as micelles, which is consistent with Ref.[469] The corresponding equilibrium density profiles for the two extreme initial counterion configurations on bleached hair are shown in Fig. 5.6. In agreement with the snapshots in Fig. 5.5b), we find that the configuration of counterions (Cl) initially on the surface indeed leads to a more disordered distribution of CTAB,

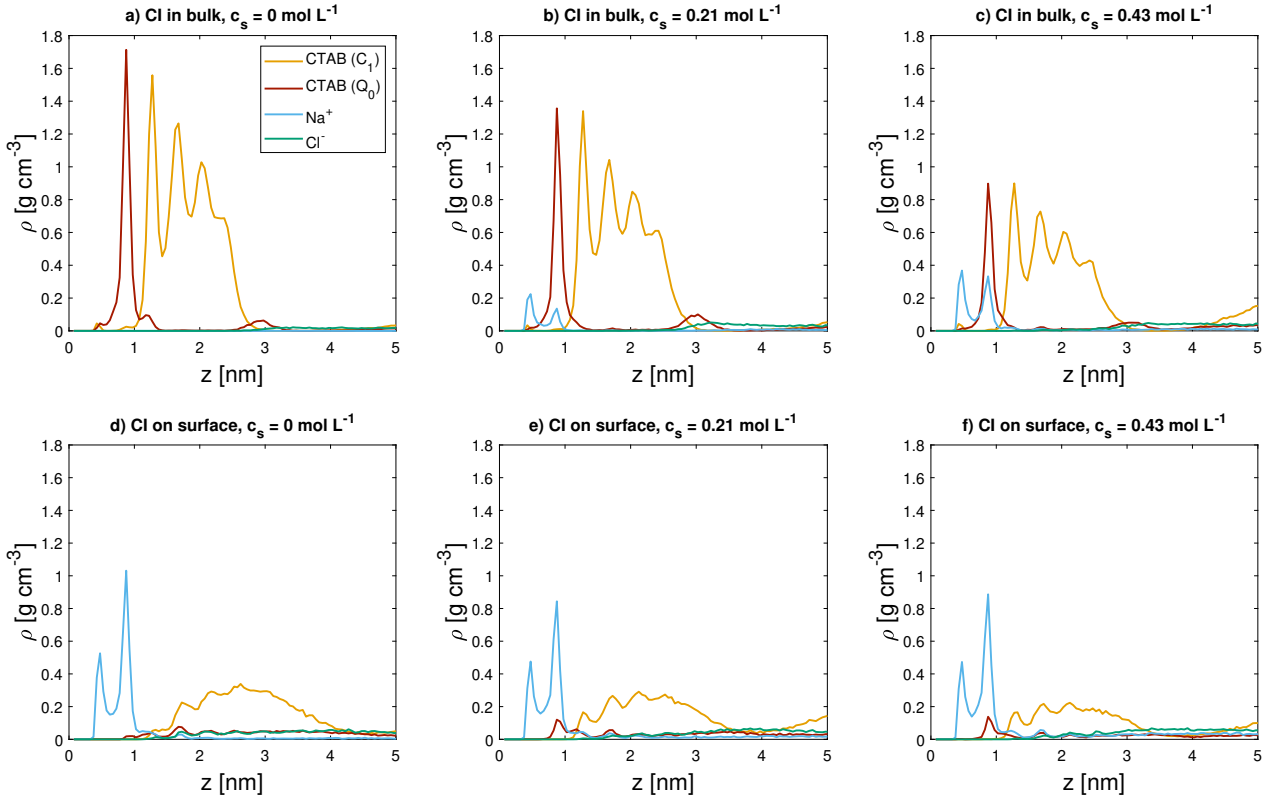


Figure 5.6: Density profiles of CTAB and ions at the medium bleached hair surface for initial counterion (Cl) distributions on either the surface or in the bulk. Three levels of excess salt concentrations are considered.

as indicated by the density profiles of the cationic headgroup (Q_0). The counterions remain in their initial surface-adsorbed state during the adsorption simulations, thus reducing the absolute electrostatic surface potential. The electrostatic attraction thus becomes insufficient to break up the cationic surfactant micelles in the bulk, which explains the reduced adsorption density and more disordered nature of the adsorbed surfactant layer.

The coexistence of two adsorption states from different initial ion distributions indicates that at least one of these states should be metastable. In the case where all counterions are initially adsorbed, a transition to the first state could only be obtained by releasing counterions from the negatively charged surface sites. This mechanism is not observed at the timescales accessible in our simulations but might only be observed at significantly larger timescales. We conducted additional simulations for the two initial counterion distributions with an increased background ionic strength. Fig. 5.5c)-d) show the adsorption density and surface structure on bleached hair at long runtimes. The corresponding density profiles near the surface are shown in Fig. 5.6.

c) Anionic surfactants

For SDS, we observe a monotonic increase of the surface coverage with the logarithm of the concentration on both virgin and bleached surfaces, as shown in Fig. 5.4b). Adsorption of SDS is much weaker than for CTAB, as the former is primarily driven by hydrophobic attraction (physical adsorption), due to the repulsive nature between the anionic headgroup and the anionic sulfonate surface sites. This is in agreement with previous experimental comparisons of cationic and anionic surfactants on virgin and bleached hair.[437] At all concentrations, the adsorption densities on virgin hair are higher than on medium bleached surfaces, due to the higher availability of hydrophobic sites from the increased proportion of 18-MEA lipids and reduced like-charge repulsion from the lower proportion of anionic cysteic acid groups. This observation is in contrast to previous experiments, which showed similar SDS adsorption on bleached and virgin hair at low concentrations, but higher surface coverages of SDS on bleached hair than virgin hair at high conctrations.[437] This is likely because concentrated SDS solutions can cause significant damage to the hair cuticle,[201,470] which will inevitably change its surface properties. Such damage is likely to be more severe on bleached hair, where the protective 18-MEA layer has already been partially removed.

For virgin hair, SDS primarily adsorbs as a monolayer with the anionic group extending into the bulk, while the hydrophobic tail adsorbs to the 18-MEA lipids on the surface, as shown in Fig. 5.4e). For medium bleached hair, the mass density profiles and corresponding snapshot in Fig. 5.4f) suggest a more disordered behavior, where surfactants adsorb to the few remaining 18-MEA lipids in a hemimicellar configuration. No preferential orientation of the anionic headgroups is evident from the snapshots. The interface between adsorbed surfactants and bulk SDS is also considerably less

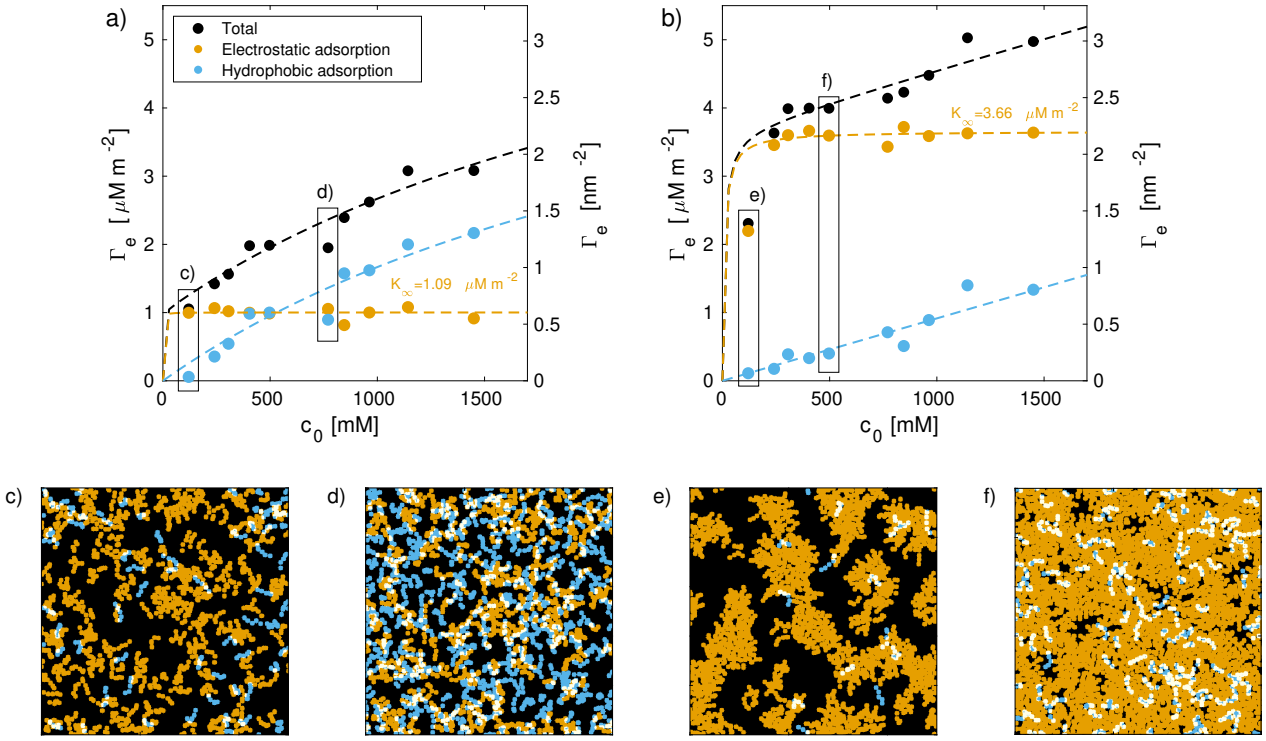


Figure 5.7: Top row (a-b): CTAB adsorption densities fitted to a two-step Langmuir adsorption model for a) virgin and b) medium bleached model hair surfaces. The fraction of surfactants in monolayer and bilayer configuration from simulations is shown for comparison with the individual components from the theoretical model. Bottom row (c-f): Examples of instantaneous coverage fractions from selected points in the adsorption isotherms in a) and b). Coarse-grained beads are modelled as planar disks with $r = \sigma_{LJ}/2$. Overlapping regions are colored in beige. 18-MEA lipids are not shown for clarity.

well-resolved on medium bleached hair than on virgin hair.

The shape of the adsorption isotherms for SDS are in qualitative agreement with previous MD simulations of SDS adsorption at the water-air interface.[471] No plateau region is identified in the accessible concentration range due to the low affinity of SDS to the anionic surfaces. At higher bulk concentrations, further increases in the SDS surface coverage would be expected for both virgin and medium bleached hair, eventually reaching a plateau region.[471] However, at such high bulk concentrations, effects such as liquid-liquid phase transitions from spherical micelles to hexagonally-ordered structures would need to be considered,[446] which are beyond the scope of the present study.

d) Surfactant orientation

The characteristic regions in the adsorption isotherm of CTAB in Fig. 5.4a) raise questions regarding the transitions in adsorption mechanism as the concentration is increased. Previous analytic models for ionic surfactant adsorption on solid surfaces considered both electrostatic-driven and hydrophobic-driven adsorption at the interface.[109,472,473] The density profiles shown in Fig. 5.4c)-d) suggest the arrangement of CTAB molecules into distinct layers on the surface. To give additional insights, we calculated the orientation of surfactants adsorbed on the surface from the MD simula-

tions. This enables us to quantify the fraction of surfactants residing in a monolayer or a bilayer. We use this information to apply a general two-step Langmuir model to the systems with cationic surfactants:

$$\Gamma_t = \frac{K_{\mathrm{el}} b_{\mathrm{el}} c_e}{1 + b_{\mathrm{el}} c_e} + \frac{K_{\mathrm{hyd}} b_{\mathrm{hyd}} c_e}{1 + b_{\mathrm{hyd}} c_e}, \tag{5.1}$$

where electrostatic (monolayer) and hydrophobic-driven (bilayer) adsorption mechanisms are considered by linear superposition. The adsorption isotherm Γ_{t} of CTAB, consisting of primary electrostatic adsorption and secondary hydrophobic-driven adsorption, Γ_{el} and Γ_{hyd} respectively, is fitted to the individual adsorption densities from our MD simulations. Fig. 5.7a)-b) shows the theoretical fits to the isotherms for virgin and medium bleached hair and individual contributions calculated from the orientation of surfactant molecules. Instantaneous snapshots of the surfactant distribution and orientation on the surface by treating the surfactants as simplified two-dimensional disks are shown in Fig. 5.7c)-f). The coverage snapshots reveal the formation of heterogeneous adsorption patches at relatively low concentrations. These observations agree with previous experimental QCM-D adsorption measurements of CTAB on rough surfaces by Wu et al.[325], which showed a reduction of the adsorption density above the cmc compared to the adsorption of a monolayer. In our simulations, the surface roughness changes are accompanied by a change in surface chemistry, which is expected to be the driving mechanism for the observed increases in adsorption density between virgin and bleached hair rather than roughness effects.

For virgin hair surfaces, a cross-over in the orientation of CTAB is observed. At low concentrations, electrostatic adsorption dominates as the a few negatively charged sites on the surface are quickly saturated by the cationic surfactants. Above $c_0 \approx 500$ mM, hydrophobic processes dominate the equilibrium surface coverage and the majority of free surfactants adsorb with their hydrophilic headgroup exposed towards the bulk.

For medium bleached model hair surfaces, the surfactants predominantly adsorb as a monolayer with the cationic group facing towards the negatively charged sites on the hair surface. With increasing surfactant concentration, the contributions from a secondary layer on top of both adsorbed CTAB and few remaining 18-MEA lipids start to become significant. A fraction of 22% of the hydrophobic-driven bilayer component is found at the highest concentration considered here ($c_e = 1.3$ M). The increase in hydrophobic-driven surface coverage is approximately linear with c_0 for both degrees of hair damage across all concentrations considered. Hydrophobic or physical adsorption thus becomes the rate-determining process at high concentrations, where electrostatic adsorption has saturated. This is in line with our initial hypothesis explaining the three observed regions in the total adsorption isotherm: (i) At low concentrations, increases in Γ are mostly caused by the electrostatic component. (ii) At intermediate concentration, this components saturates and (iii) the hydrophobic-driven contribution

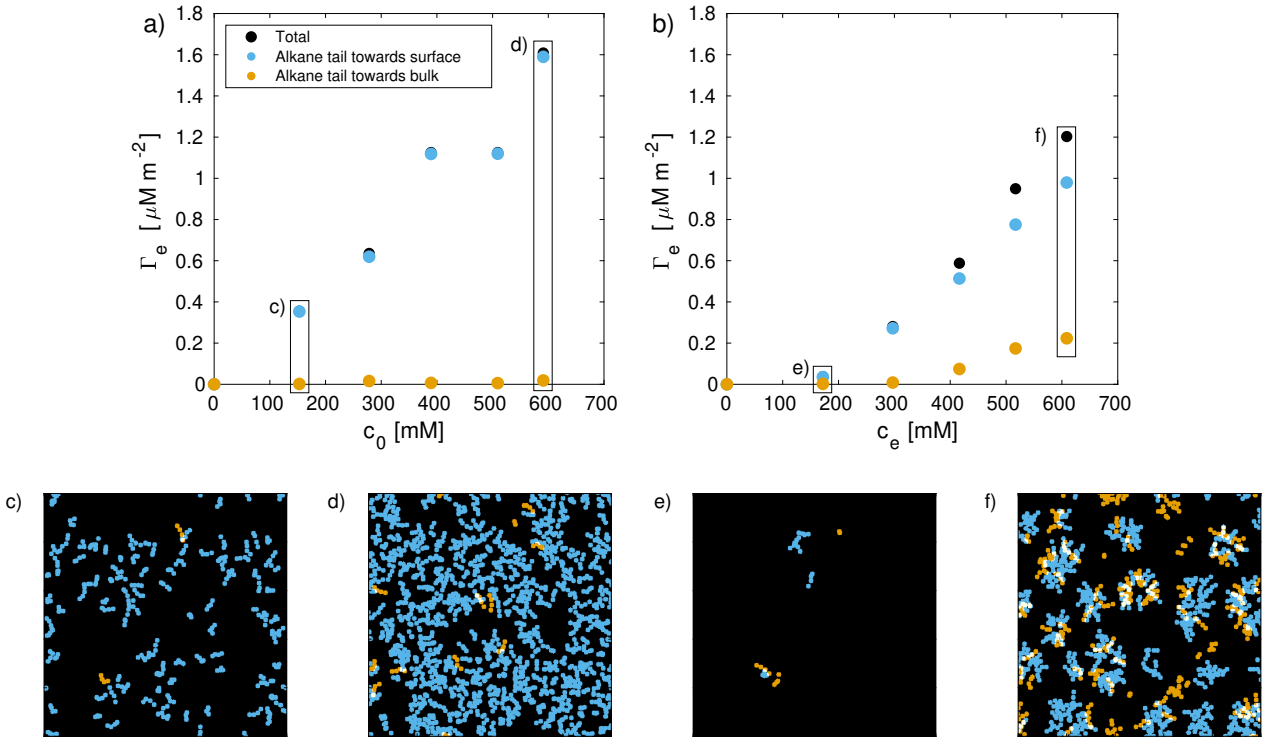


Figure 5.8: Top row: SDS adsorption densities for a) virgin and b) medium bleached model hair surfaces. The fraction of surfactants that adsorb with the alkane tail towards the surface (hydrophobic adsorption) and facing towards the bulk is shown for reference. Bottom row: Examples of instantaneous coverage fractions from selected points in the adsorption isotherms. Regions of overlap are colored in beige. 18-MEA lipids are not shown for clarity. No fitting to a Langmuir model was attempted for SDS, as saturation is not observed on either of the two components nor on the total adsorption isotherm.

becomes significant. This adsorption behaviour is accurately described using the general two-step Langmuir model.[474]

We also calculated the orientation and distribution of SDS adsorbed on the hair surfaces, as shown in Fig. 5.8. SDS molecules are primarily oriented with the hydrophobic tail facing towards the surfaces on virgin hair at all concentrations studied. Adsorption of SDS is localised in the regions of high 18-MEA coverage with damaged regions of anionic cysteic acid groups remaining uncovered. On medium bleached hair, SDS molecules agglomerate in a hemi-micellar configuration around the few remaining patches of 18-MEA on the surface. This is demonstrated by the increase in the fraction of SDS molecules favoring a preferential orientation of their anionic site towards the surface.

e) Effects of ionic background strength

Hair care formulations usually contain around 0.5-2 wt.% salt.[121] The addition of a background electrolyte to the bulk could affect the adsorption of ionic surfactants on the hair surface. To study this effect, we repeated a subset of the CTAB adsorption simulations with coarse-grained sodium Na^+ and chloride Cl^- ions (with their first hydration shell)[265] into the bulk solutions at $c_{Na+} = c_{Cl-} = 0.11$-0.22 mol L^{-1} in addition to the surfactant counterions. The equilibrium CTAB adsorption densities for the three

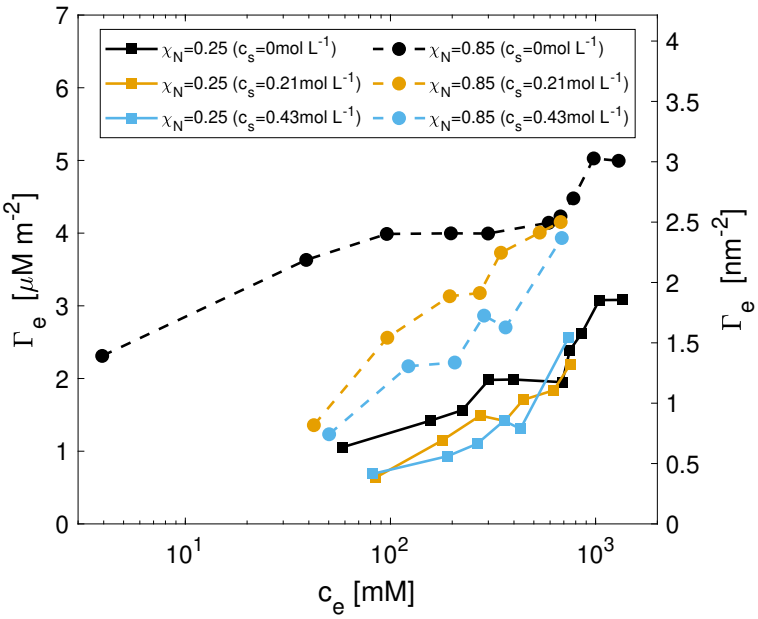


Figure 5.9: CTAB adsorption at different levels of excess salt concentrations ($c_s = c_{Na^+} + c_{Cl^-}$) for virgin (square-solid) and medium bleached model (circular-dashed) hair surfaces.

levels of background ionic strength are shown in Fig. 5.9. For medium bleached hair, a clear decrease in CTAB adsorption is visible at low and moderate CTAB concentrations as the concentration of excess salt is increased. Previous experiments also showed a decrease of cationic polymer adsorption on hair when excess salt was added.[173,475] The reduction in adsorption is mainly due to the screening of negative surface charges by the chloride ions in the bulk. At high concentrations, no clear trend can be identified with regard to background salt concentration effects on CTAB adsorption. This is likely because, for the high CTAB concentrations studied, the number of surfactant molecules is considerably higher than that of the number of excess sodium ions.

CTAB adsorption densities were much less sensitive to background salt concentration on virgin hair. This supports our previous suggestion that CTAB adsorption on virgin hair is primarily driven by hydrophobic interactions, where charge screening will not play a significant role. The type of counterions may also affect the structure and kinetics of ionic surfactant adsorption and aggregation on solid substrates.[476,477] Therefore, it may be interesting to study different monovalent and divalent ions and their interactions with the surface charges and surfactants in future studies. However, atomistic force fields are likely to be required for that purpose as the *MARTINI 2* force field cannot differentiate between hydrated monovalent ions.

5.3.3 Friction with adsorbed cationic surfactants

a) Shear stress dependence on sliding velocity

We conduct NEMD simulations to quantify the friction between hair surfaces in the presence of adsorbed CTAB molecules. Friction with adsorbed SDS molecules are

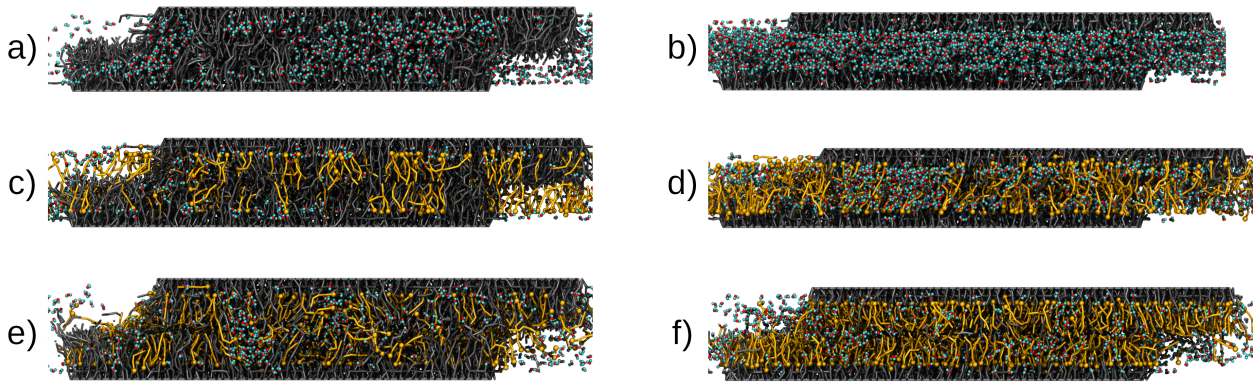


Figure 5.10: Snapshots of NEMD systems considered in this chapter at $\sigma = 10$ MPa: a) virgin hair, $\Gamma = 0$ µM m^{-2}, b) medium bleached hair, $\Gamma = 0$ µM m^{-2}, c) virgin hair, $\Gamma = 1.1$ µM m^{-2}, d) medium bleached hair, $\Gamma = 2.3$ µM m^{-2}, e) virgin hair, $\Gamma = 2.0$ µM m^{-2} and f) medium bleached hair, $\Gamma = 4.0$ µM m^{-2}. 18-MEA (grey), CTAB (orange) and water (cyan/red) molecules are shown. The structure and contact thickness in a) and f) underline that cationic surfactants can efficiently repair the surface of bleached hair.

only briefly considerd, due to the much lower adsorption densities of SDS on the hair surfaces and its potential to quickly desorb during compression, sliding and rinsing.[63,478] A set of friction results from NEMD simulations at intermediate SDS adsorption densities ($\rho_{SDS} = 0.98$ nm^{-2} after squeeze-out) is shown in Fig. 5.11. Adsorbed SDS molecules do provide considerable friction reductions compared to the water case, which is primarily due to enhanced electrostatic repulsion between the sliding surfaces. However, concentrated SDS solutions can cause damage to the hair cuticle surfaces,[201,470] which is not accounted for in our current simulations framework. This is likely to increase the surface roughness and remove some of the protective 18-MEA layer, which could perhaps play a more significant role than the enhanced electrostatic repulsion effect simulated here.

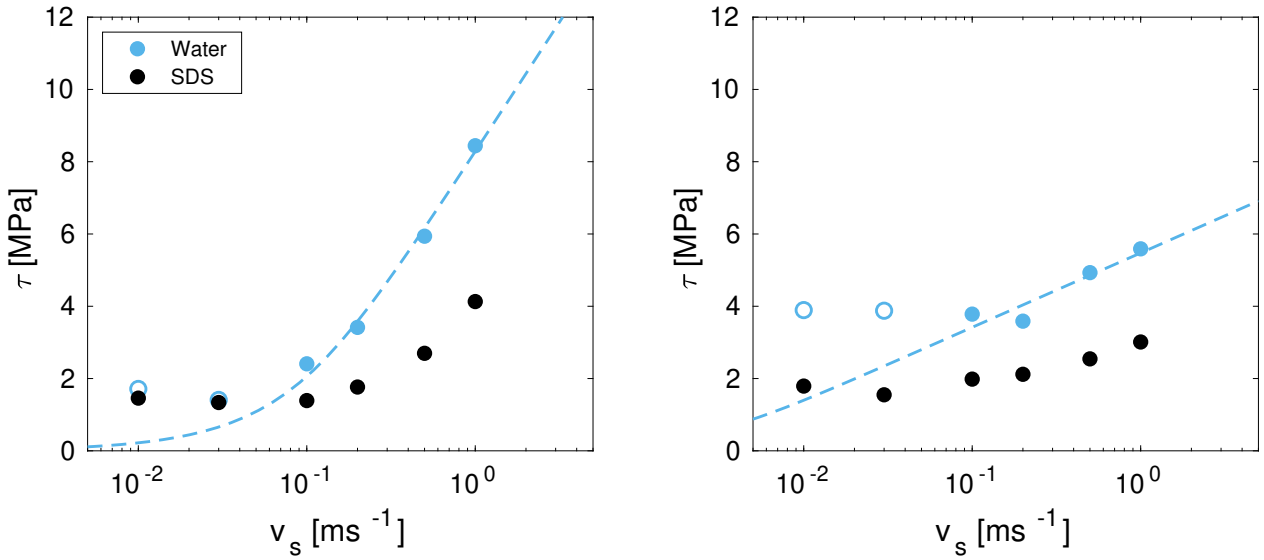


Figure 5.11: Shear stress between hair surfaces with water and SDS at 10 MPa on a) virgin hair ($\rho_{SDS} = 0.28$ nm^{-2} after squeeze-out) and b) bleached hair ($\rho_{SDS} = 0.98$ nm^{-2} after squeeze-out). A comparison to pure water contacts is provided with corresponding SATA fits according to Ref.[362].

On the other hand, CTAB is not expected to damage the hair surface, so its effects on friction can be fully captured by the current simulation framework. We selected two points from each CTAB adsorption isotherm, corresponding to points c)-f) in Fig. 5.7 to be representative of the adsorption structures low ($c_0 = 120$ mM) and high ($c_0 = 770$ mM) CTAB concentrations. This translates to adsorption densities of $\Gamma = 1.1$ µMm^{-2} and $\Gamma = 2.0$ µMm^{-2} on virgin as well as $\Gamma = 2.3$ µMm^{-2} and $\Gamma = 4.0$ µMm^{-2} on medium bleached model hair surfaces. The surfaces with adsorbed surfactants were duplicated and reflected before squeeze-out simulations were applied to determine the number of water molecules remaining in the contact for a given normal load, as shown in Table A.3.3 in the appendix. The number of water molecules in the contact is below the amount observed for pristine 18-MEA monolayers in water, and does not show a strong dependence with respect to the contact pressure, σ.

Representative snapshots of the systems studied in the NEMD simulations are shown in Fig. 5.10. We first investigated the friction behavior as a function of sliding velocity v_s at a constant pressure of $\sigma = 10$ MPa. Fig. 5.12a) and b) show the shear stress, τ, as a function of sliding velocity for virgin and medium bleached hair with CTAB adsorbed on both surfaces. Friction results for the same surfaces lubricated by water without adsorbed CTAB molecules from chapter 4 are also shown for reference. We applied an extended stress-augmented thermal activation (SATA) model[280] to the shear stress versus sliding velocity data for $v_s \geq 0.1$ m s^{-1}. This model was extended from the earlier SATA model for monolayer friction due to Briscoe and Evans,[229] as discussed in the previous chapter. Data points at low velocities, $v_s < 0.1$ m s^{-1}, are excluded from the fits due to the shear stress plateau.

The addition of CTAB generally leads to reduction in the shear stress of hair-hair contacts compared to pure water across all considered sliding velocities. This observation is in agreement with previous experiments with CTAB on bleached hair.[159] An exception to this behaviour is observed at $v_s = 1$ m s^{-1} for medium bleached hair, where the shear stress for surfaces with intermediate CTAB coverage is higher than in contacts with pure water. On virgin hair, intermediate degrees of CTAB coverage provide the lowest shear stress, $\tau(\Gamma = 1.1\mu Mm^{-2}) < \tau(\Gamma = 2.0\mu Mm^{-2}) < \tau(\Gamma = 0\mu Mm^{-2})$. A cross-over in the shear stress between moderate and high surfactant coverage is observed around $v_s = 0.1$ m s^{-1}. Above this threshold, the shear stress at moderate coverage approaches the levels observed in pure water contacts. On medium bleached hair, the shear stress is generally reduced monotonically with increasing CTAB coverage, i.e., $\tau(\Gamma = 4.0\mu Mm^{-2}) < \tau(\Gamma = 2.3\mu Mm^{-2}) < \tau(\Gamma = \mu Mm^{-2})$. These results suggest that, at physiologically relevant sliding velocities,[11,154] moderate coverages of CTAB adsorption tend to be more effective for providing friction reductions on virgin hair, while a larger coverage is favorable on bleached hair. This is due to the reduction of 18-MEA on bleached surfaces, which can be balanced by increased adsorption densities of the cationic surfactant on the hair surface. The combined surface coverage of the 18-MEA

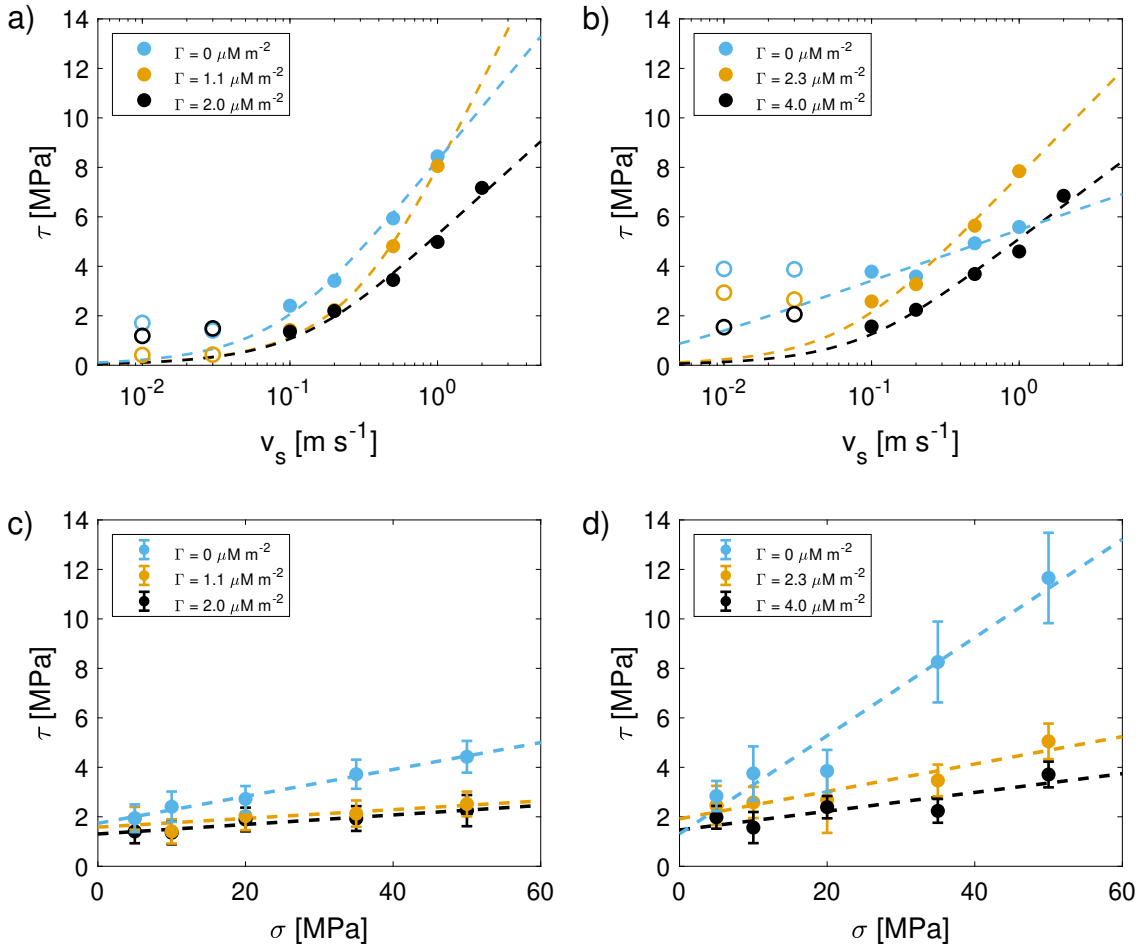


Figure 5.12: Shear stress as a function of sliding velocity v_s for a) virgin and b) medium bleached hair surfaces with pure water (from Ref.[362] and chapter 4) and pre-adsorbed CTAB at low and high coverage at a constant normal stress of 10 MPa. The high-velocity data ($v_s \geq 0.1$ m s^{-1}) is fit to an extended SATA model.[280] Open symbols represent data points excluded from fitting. Normal-load variation for c) virgin and d) medium bleached hair surfaces at a constant sliding velocity $v_s = 0.1$ m s^{-1}.

lipids and adsorbed CTAB ρ_t are 2.82 nm^{-2} and 3.26 nm^{-2} for virgin hair at low and high CTAB coverage respectively. On moderately bleached hair, the total surface coverage amounted to respective 1.60 nm^{-2} and 2.77 nm^{-2} for low and high surfactant coverage. We previously estimated the grafting density of a fully-functionalised layer of the 18-MEA on hair at 2.73 nm^{-2},[299] which is in close agreement with the reported densities for virgin hair surfaces with low CTAB coverage, as well as for medium bleached hair with high CTAB coverage. The total adsorption densities are summarized in Table 5.3.

We analysed the structure of the contact during sliding to investigate the molecular-scale mechanisms linked to friction reduction with CTAB. Mass density, charge density and velocity profiles of the contact at $v_s = 1$ m s^{-1} are shown in Fig. 5.13. We also report additional combined mass density profiles for the 18-MEA and CTAB at different sliding velocities in Fig. A.3.15 in the appendix. Mass density profiles and interdigitation are insensitive to the sliding velocity, which is consistent with previous NEMD simulations of other surfactants.[280,354] For virgin hair, there is some interdigitation between the 18-MEA lipid monolayers grafted to the sliding surfaces. Interdigitation

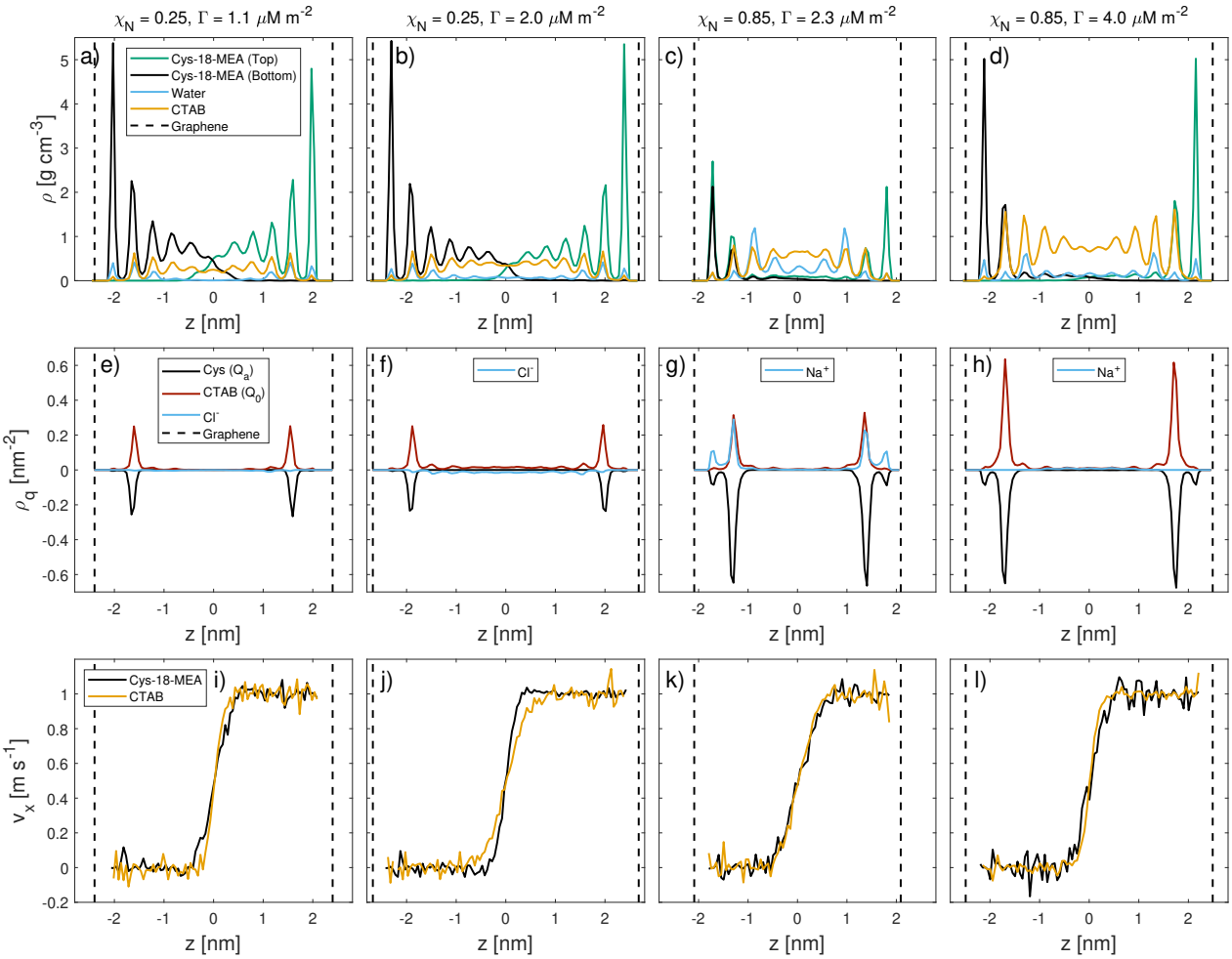


Figure 5.13: Mass density ρ (top), charge density ρ_q (middle) and velocity profiles v_x for Cys-18-MEA and CTAB (bottom) during sliding at $v_s = 1$ m s^{-1} for virgin hair at a) $\Gamma_e = 1.1$ μM m^{-2} and b) $\Gamma_e = 2.0$ μM m^{-2} and for medium bleached hair at c) $\Gamma_e = 2.3$ μM m^{-2} and d) $\Gamma_e = 4.0$ μM m^{-2}.

of the 18-MEA layers is less pronounced at higher CTAB coverages, suggesting that it is more effective in separating the two surfaces compared to sodium counterions. For medium bleached hair, there is much less interdigitation of the 18-MEA monolayers than virgin hair. Nonetheless, there is reduced interdigitation of the remaining 18-MEA on the surface by high coverage CTAB films. The interface mostly consists of the hydrophobic tails of the cationic surfactant containing small amounts of residual water ($\rho_w \approx 5.4$-8.1 nm^{-2}).

During sliding, the structure of confined CTAB molecules differs considerably from that on single hair surfaces (Fig. 5.4). For the single surfaces, we observed CTAB bilayer on the virgin hair surface at high coverages, where a significant amount of surfactant molecules were oriented with their cationic group facing towards the bulk. Conversely, once a dynamic equilibrium is reached during sliding simulations, most CTAB molecules are oriented with the hydrophobic tail facing the centre of the contact, as shown in Fig. 5.13. We analyzed the mass density profiles at the beginning and at equilibrium of both compression and sliding simulations, as shown in Fig. 5.14. The bilayer is observed after compression of the two surfaces for up to 10 ns. For

prolonged compression in the absence of shear for up to 70 ns, surfactant diffusion leads to a distribution of the bilayer in the contact, as previously observed in diffusion experiments of ionic surfactants confined between mica surfaces.[479] Once the constant shear is applied, any remaining bilayer contributions are redistributed within the first 5-10 ns of sliding, independent of the sliding velocity. Previous experiments with carboxylic acid surfactants on mica surfaces have also shown that multilayers are easily removed and show similar friction behaviour to monolayers.[229] Surface force balance experiments with CTAC on mica surfaces showed a transition from adsorbed micelles to bilayers under compression and shear.[480] The tendency for surfactants to desorb from the hair surface under shear has also been reported both experimentally[16] and in DPD simulations.[110] At dynamic equilibrium during sliding, friction is invariant to the pathway leading to such equilibrium, from either shear-driven or diffusion-driven redistribution.

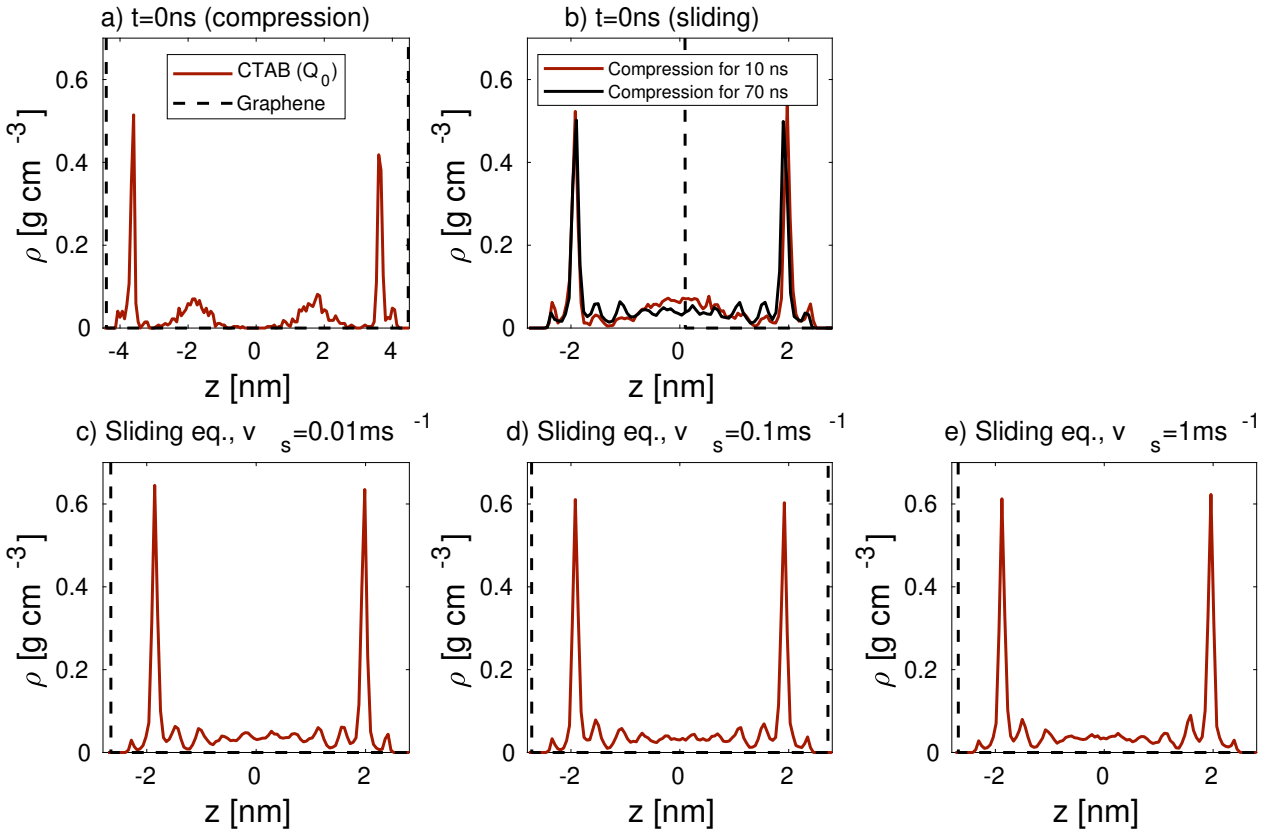


Figure 5.14: Mass density profiles for the Q_0 headgroup of cationic surfactants (CTAB) a) before compression, b) after compression for 10 ns and 70 ns, and c)-e) during sliding simulations (at dynamic equilibrium) for various v_s on virgin hair at $\Gamma_{CTAB} = 2.0$ μMm^{-2}, where the bilayer contribution is most prominent at the end of the adsorption simulations.

The charge density profiles in Fig. 5.13 highlight the dominant electrostatic interactions inside the contact during sliding. Surface charges are locally neutralized by free cationic surfactants and counterions, where relevant. For virgin hair, CTAB fully adsorbs to the charged sites on the surface for both degrees of coverage. On medium bleached surfaces with low CTAB coverage, the number of cationic surfactants is insufficient to

fully neutralize the surface charges. In this case, positively charged counterions (Na^+ with its first hydration shell) equally contribute to local charge neutralisation near the surfaces. At high CTAB coverage, CTAB again predominantly occupies the negatively charged sites on the surface. The centre of the contact is generally sparse in charged beads. When CTAB molecules are present at the interface, the surface charges on the opposing surfaces are separated by a larger distance, as shown Fig. A.3.18 in the appendix. This makes trapping of the cations between the sliding anionic surfaces[430] less likely for CTAB than when the charges are neutralised by sodium counterions.

Fig. 5.13 also shows the velocity profiles for CTAB and the 18-MEA molecules during sliding. The velocity profiles of CTAB and the 18-MEA overlap for all contacts, with minor deviations for virgin hair at high CTAB coverage ($\Gamma = 2.0$ µM m^{-2}). This overlap suggests that there is no significant slip of the CTAB monolayer relative to the grafted 18-MEA lipids. Shear is confined to a small region ($d \approx 1$ nm) near the contact centre for all degrees of damage and CTAB coverages. On virgin hair at $\Gamma = 2.0$ µM m^{-2}, a slightly wider CTAB region is sheared compared to that for 18-MEA. No slip of cationic surfactants is observed near the cysteic acid groups on the surfaces, which suggests that the attractive forces between electrostatically-adsorbed surfactants and the anionic sulfonate groups on the surface are strong enough to counteract any shear-driven desorption. The charge density and velocity profiles for virgin hair at high surfactant coverage suggest that there is a non-negligible fraction of CTAB molecules from the bilayer component that are not adsorbed to either of the sliding surfaces. Here, the combined CTAB and lipid surface coverage is above the value of a pristine 18-MEA monolayer, suggesting that the surface is somewhat over-saturated. We briefly investigated the mobility fraction[481] of cationic surfactants at the interface shown in Fig. A.3.16 in the appendix. During sliding, there is a much higher mobility fraction of the CTAB surfactants on virgin hair surfaces at $\Gamma = 2.0 \mu M m^{-2}$ than the other surface-coverage combinations, which confirms our hypothesis of an over-saturation. The mobility fraction is not sensitive to the sliding velocity for any of the surfaces or CTAB coverages. The mean-square-displacement (MSD) of cationic beads (Q_0) on CTAB in the directions normal to the sliding direction (y and z) also confirmed an increased mobility of surfactants for virgin hair at high CTAB concentrations, as shown in Fig. A.3.17 in the appendix. These investigations show that excess surfactants from the secondary hydrophobically-adsorbed layer can desorb in the presence of a wide range of shear rates.

We also investigated the order within the adsorbed CTAB films. Figure A.3.19 in the appendix shows the change in nematic order of CTAB molecules with sliding velocity for the various surfaces and coverages. The CTAB chains form fluid-like rather than solid-like monolayers, with a maximum nematic order parameter of approximately 0.6 for the high coverage bleached hair system.[481] The nematic order only weakly increases with the sliding velocity.

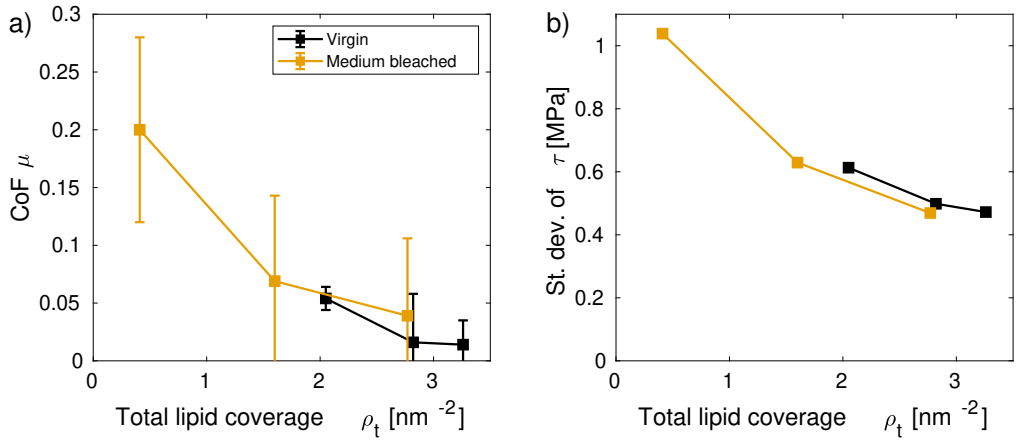


Figure 5.15: a) Coefficient of friction (COF) and b) the standard deviation of the shear stress signal ($\sigma = 10$ MPa) both at $v_s = 0.1$ m s^{-1} as a function of total surface coverage from the 18-MEA and cationic surfactants for surfaces representative of virgin and medium bleached hair.

b) Shear stress dependence on normal stress

We also consider the effect of different contact pressures on the shear stress. For this purpose, the sliding velocity is kept constant at $v_s = 0.1$ m s^{-1}, while varying the normal stress, $\sigma = 5$-50 MPa. Fig. 5.12c) and d) show the shear stress, τ, as a response to the normal stress, σ, for the three degrees of CTAB coverage. We calculate the friction coefficient, μ, from the slope of the linear fits shown in Fig. 5.12c) and d), $\tau = \mu \cdot \sigma + \tau_0$, where τ_0 is the load-independent Derjaguin offset due to adhesion. Table 5.3 summarizes the friction coefficient values calculated from Fig. 5.12c) and d).

For virgin hair, the addition of CTAB to the contact leads to significant reductions in the COF compared to water for both surfactant coverages. The Derjaguin offset, τ_0, is comparable for pure water and the CTAB-containing solutions. Nikogeorgos et al.[16] used AFM to study the friction of the cuticle surface of virgin and damaged hair at $v_s = 4$ μm s^{-1}. Under wet conditions, they reported a small increase in the coefficient of friction (+10%) of virgin hair treated with a conditioner containing cationic surfactants and silicone polymers compared to the untreated fibre.[16] Conversely, AFM experiments of virgin hair-hair contacts[211] conducted at $v_s = 4$-20 μm s^{-1} showed a consistent de-

Table 5.3: Overview of friction coefficients from linear fits with respect to the normal stress σ (at $v_s = 0.1$ m s^{-1}) and water contact angle from CG-MD for model surfaces representative of virgin and medium bleached hair. Friction coefficient uncertainties resemble the 90% confidence interval of linear fits to the mean data points in Fig. 5.12c)-d).

Virgin hair		CTAB coverage, $\Gamma =$	0 nm^{-2}	0.77 nm^{-2}	1.21 nm^{-2}
CTAB + lipid coverage	ρ_t		2.05 nm^{-2}	2.82 nm^{-2}	3.26 nm^{-2}
Friction coefficient	μ		0.054±0.010	0.018±0.023	0.019±0.012
Contact angle	ϑ		102.2±0.9°	106.1±0.6°	79.6±0.6°

Medium bleached hair		CTAB coverage, $\Gamma =$	0 nm^{-2}	1.19 nm^{-2}	2.36 nm^{-2}
CTAB + lipid coverage	ρ_t		0.41 nm^{-2}	1.60 nm^{-2}	2.77 nm^{-2}
Friction coefficient	μ		0.20±0.08	0.055±0.034	0.038±0.040
Contact angle	ϑ		49.8±0.9°	71.6±2.7°	106.5±0.8°

crease in friction as the concentration of cationic surfactant TTAB was increased. From pure water to a TTAB concentration of 0.2 cmc, the COF was reduced by approximately 50%. Between 0.2 and 1 cmc, the COF increased slightly, while at concentrations above the cmc, the COF remained relatively constant.[211] This is consistent with our NEMD results at physiologically relevant sliding velocities ($v_s = 0.1$ m s^{-1}), where the magnitudes of the shear stress for both CTAB coverages are comparable. The COF values for virgin hair (∼0.6) and treated virgin hair (∼0.3) reported by Mizuno et al.[211] are considerably higher than the values reported in this study. This is likely due to the crossed fibre experimental setup, where interactions between topographical features of the hair such as cuticle edges are also measured. Dhopatkar et al.[414] also observed reductions in the COF for CTAB solutions with increased concentrations lubricating hydrophobic polymer surfaces. They reported a large reduction in COF from 0.1 cmc (∼1.5) to 1 cmc (∼0.5) and further friction reductions up 1o 10 cmc (∼0.2). Generally, the surfactant structure on the surface rather than the bulk concentration is dominating the friction since none of the micelles remained intact on the surfaces in our adsorption simulations. Friction reductions due to conditioners on undamaged hair have also been observed in macroscopic tress combing experiments at elevated sliding velocities ($v_s = 0.1$-20 mm s^{-1})[296]. Overall, friction of treated virgin hair observed in experiments is in good agreement with our simulations.

On the medium bleached hair surfaces, we observe more pronounced reductions in the COF due to CTAB adsorption. The highest reduction in the COF (∼80%) is observed for high degrees of CTAB coverage, $\Gamma = 4.0$ μMm^{-2}. No clear differences in adhesive contributions to friction by means of the Derjaguin offset, τ_0, are identified from the simulations. Our simulations are in excellent agreement with the trend observed in friction experiments on chemically damaged and bleached hair surfaces. Scott and Robbins observed a large decrease in the COF in a rubber-on-bleached-hair contact moving from pure water ($\mu = 0.54$) to a 0.5 wt.% CTAB solution ($\mu = 0.25$).[159] The treatment of KOH-damaged hair with a cationic surfactant and silicone polymer formulation decreased the COF by up to 65%, as reported from AFM measurements under wet conditions at low normal loads ($F_N < 5$ nN).[16] At higher normal loads, the COF was similar to untreated KOH-damaged hair, suggesting that the formulation was removed from the hair surface. This mechanism would not be captured in our simulations due to the periodic surfaces. Moreover, the estimated contact pressure in the hair-AFM tip contact experiments ($\sigma \approx 120$ MPa) is substantially higher than in our simulations and in real hair-hair contacts. The COF from the NEMD simulations of bleached hair treated with CTAB ($\mu = 0.041$) is comparable to that for virgin hair with pure water ($\mu = 0.054$). This observation is in good agreement with the findings by Nikogeorgos et al.,[16] who also found very similar friction for KOH-treated bleached hair to virgin hair. The COF values are somewhat higher than those observed for CTAC bilayers on atomically-smooth mica surfaces ($\mu \approx 0.001$).[480] We observe a large decrease in the standard deviation of the friction signal for hair with cationic surfactants (error bars

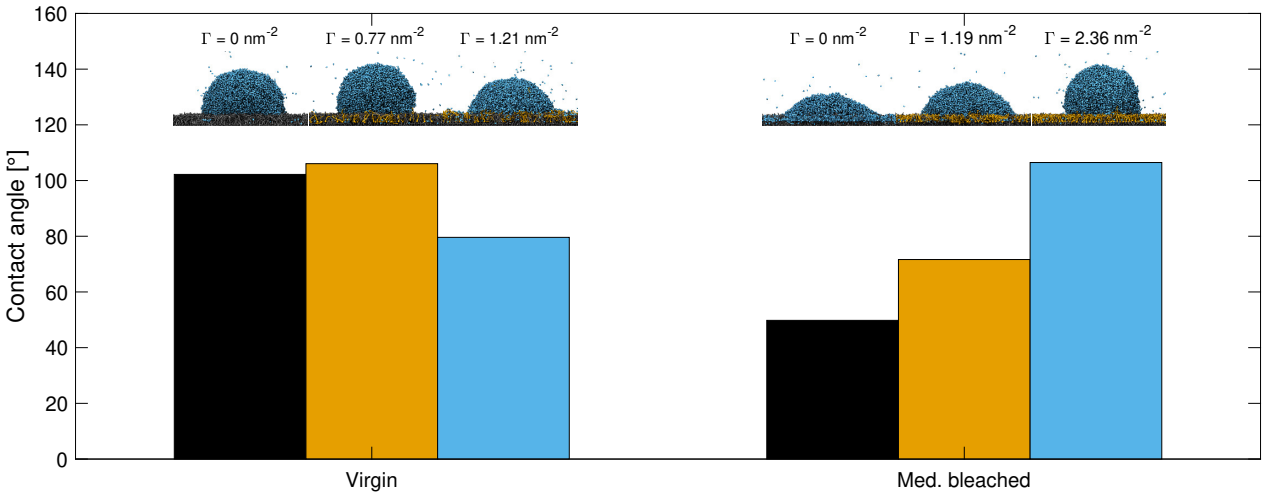


Figure 5.16: Water contact angles for untreated (from Ref.[299] and chapter 3) and CTAB-treated hair surfaces as a function of CTAB coverage. Snapshots show the equilibrium nanodroplets on bare and surfactant-coated surfaces.

in Fig. 5.12c-d), which suggests that stick-slip phenomena are partially eliminated. This is consistent with observations from AFM experiments, where the signal error was found to be largest for KOH-damaged hair, followed by conditioned KOH-damaged and untreated virgin hair.[16]

We also related the total surface coverage ρ_t from surfactants and 18-MEA, as summarized in Table 5.3, to the COF at $v_s = 0.1$ m s^{-1}. Fig. 5.15 shows a consistent decrease in friction as well as in the amplitude of the shear stress oscillation (prevalence of stick-slip events) with increasing lipid coverage for both virgin and medium bleached hair surfaces. The overlap between the two profiles at different degrees of damage clearly motivates that the presence of the hydrophobic tails (from either the 18-MEA or CTAB) exposed on each surface dominates the friction reductions, as the surface heterogeneity is reduced and damaged surface patches are repaired.

5.3.4 Wettability with adsorbed cationic surfactants

Finally, wetting simulations at the two surface coverages of CTAB are performed for the model surfaces representative of virgin and medium bleached hair. Nanodroplets of pure water are placed on the surfaces with pre-adsorbed surfactants, following the methodology described in chapter 3. The equilibrium contact angles obtained from the wetting of these droplets gives an indication on how efficiently the hydrophobicity of virgin hair can be restored by treatment with cationic surfactants. Fig. 5.16 depicts the contact angles for the four configurations considered here. Contact angles from hair surfaces without surfactants from chapter 3 are also included for comparison. Table 5.3 further shows a summary of contact angles at the various degrees of CTAB coverage.

On virgin hair, moderate CTAB adsorption ($\Gamma = 1.1$ µM m^{-2}) leads to a moderate increase

of the contact angle to $\vartheta = 106.1°$ compared to the bare surfaces, $\vartheta = 102.2°$. The majority of free surfactant molecules adsorbs to the few damaged patches on the surface, therefore increasing the contact angle to nearly the value reported for a pristine monolayer ($\vartheta = 120°$). At elevated surfactant concentrations on virgin hair, the contact angle decreases to $\vartheta = 79.6°$. This decrease in ϑ is attributed to the adsorbed CTAB bilayer. In this bilayer configuration, a significant fraction of CTAB molecules is oriented with their hydrophilic cationic sites exposed towards the bulk, thus increasing the affinity of water to the surface. The decrease in contact angle on virgin hair is in good agreement with experimental wetting measurements of virgin hair with adsorbed proteolipids.[227] The agreement with these wetting experiments also suggest that the observed bilayer might be resistant to being rinsed off when being locally wetted at macroscopic timescales and in the absence of strong shear stresses.

Unconditioned bleached model hair surfaces show an increase in wettability, as highlighted in chapter 3 and previous experimental studies on hair wetting.[100,231] This is typically attributed to the surface oxidation and subsequent increase in the polar component of the surface energy.[100,231] The presence of cationic surfactants on the surface restores the hydrophobicity of the medium bleached surface, as indicated by the increase in contact angles to $\vartheta = 71.6°$ and $\vartheta = 106.5°$ for low and high CTAB coverage respectively. On surfaces representative of bleached hair, nearly all cationic surfactants adsorb through electrostatic interactions with their cationic site facing towards the cysteic acid groups on the surface and exposing their hydrophobic tail to the bulk. At high concentrations, the observed contact angle exceeds that observed on bare virgin hair surfaces. This increase in contact angle in further quantitative agreement with the experimental results on conditioned bleached hair reported by Schulze Zur Wiesche et al.[227]. Treatment of bleached and permed hair with K-peptide and K-protein also led to moderate increases in advancing contact angle from dynamic wetting force measurements.[231] In contrast, virgin hair wetting was largely unaffected by treatment of these molecules.[231] The observed increase in water contact angle and decrease in the COF on bleach damaged hair surfaces treated with CTAB demonstrate that cationic surfactants can restore the hydrophobicity and low friction properties of the virgin hair surface.

5.4 Conclusions

In this chapter, the adsorption, friction and wettability of ionic surfactants on virgin and chemically bleached model hair surfaces were investigated using coarse-grained MD simulations. For virgin hair, adsorption of cationic surfactants occurs through both electrostatic and hydrophobic-driven adsorption. At low concentrations, CTAB forms a complete monolayer where the hydrophobic tailgroups point away from the surface due to electrostatic attraction between the cationic headgroup and the anionic sulfonate groups. At higher concentrations, CTAB forms a bilayer due to hydrophobic interactions between the hydrophobic tailgroups of the adsorbed CTAB molecules.

On medium bleached hair, CTAB adsorption is dominated by electrostatic attraction between the anionic sulfonate groups and the cationic headgroup of the cationic surfactant. At low concentrations, CTAB forms a partial monolayer, while a complete monolayer is formed at higher concentrations. We also highlighted that the the background salt concentration significantly reduces CTAB adsorption to the surface at lower CTAB concentrations. The shape and plateau surface concentrations in our multi-stage adsorption isotherms are in qualitative agreement with experimental studies of cationic surfactant adsorption on hair, despite the increased bulk concentrations required in our simulations. Adsorption of the anionic surfactant SDS is solely driven by hydrophobic interactions with the grafted alkyl layer due to the like-charged nature of surfactants and surface charges. Adsorption densities were found to be significantly lower compared to cationic surfactants.

Subsequently, the tribological response of adsorbed cationic surfactants on virgin and bleached model hair surfaces was investigated using NEMD simulations. Cationic surfactants reduce friction on both virgin and bleached hair to below the value of the untreated virgin hair surface. On virgin hair, an intermediate CTAB coverage was found to be most effective at lowering friction at low sliding velocities. At physiologically relevant sliding velocities, no strong difference in friction was observed for the two degrees of surfactant coverage considered. Excess cationic surfactants residing in a secondary layer on virgin hair surfaces were found to desorb during sliding. On bleached hair, increased adsorption densities are necessary to achieve low friction comparable to untreated virgin hair, due to increased surface heterogeneity caused by the lower coverage of alkyl groups and a higher coverage of sulfonate groups on the surface. Friction reductions of up to 80% were observed on bleached hair at high surfactant coverage.

Water nanodroplet wetting simulations confirmed that cationic surfactants effectively restore the hydrophobic character of untreated hair after bleaching. On virgin hair, moderate levels of CTAB adsorption further increased the hydrophobicity of the surface due to electrostatic adsorption of surfactants to the few available damaged sites on the surface. Excessive CTAB adsorption on virgin hair led to a decrease in contact angle induced by the formation of a bilayer. On medium bleached hair, the contact angle monotonically increased with higher adsorption densities due to the formation of a CTAB monolayer with increasing surface coverage. The results are in excellent agreement with experimental friction and wetting measurements on hair and show why hair conditioners based on cationic surfactants are effective at repairing chemically damaged hair fibres.

The simulations in this chapter also highlight that the structure of surfactants during sliding of two hair surfaces in contact is perturbed in comparison to the structure on

a single hair surface. Moreover, the molecular modeling techniques presented in this chapter are applicable to screening more complex and multi-component hair care formulations. This includes the interactions of charged polymers and polymer-surfactant complexes with hair which are subject of the following two chapters.

6 Boundary lubrication performance of polyelectrolyte-surfactant complexes on biomimetic surfaces

The content of this chapter was published as a journal article in Langmuir (accepted manuscript).[482]

6.1 Introduction

Shampoos contain a wide range of surfactants and polymers to facilitate the cleansing and conditioning of hair.[4,5] A conditioning effect can be achieved by using cationic surfactants or polyelectrolytes, which strongly adsorb onto the damaged regions on the hair surface.[442,483] On the other hand, the primary role of anionic surfactants in hair care formulations is to remove dirt particles and sebum from the hair surface.[101] They do this by forming micelles at relatively low concentrations, which can trap oily substances in their core.[101] Since anionic surfactants only weakly adsorb on the negatively-charged hair surface through hydrophobic interactions, as shown in the previous chapter, they can readily desorb from the hair surface to remove the trapped substances. Thus, most shampoos now contain both cationic polyelectrolytes (PE) for conditioning and anionic surfactants for cleansing.[101] Additionally, polymeric compounds may be used as viscosity modifiers for better handling and spreading performance.

As briefly discussed in chapter 2, adding ionic surfactants to aqueous solutions of polyelectrolytes with the opposite charge can cause the spontaneous formation of supramolecular complexes.[484] These polyelectrolyte-surfactant complexes are important to the function of many formulated consumer products such as cosmetics, pharmaceuticals, and foods.[113] Depending on the surfactant concentration, the complexes can either remain soluble in water or undergo liquid-liquid (coacervation) or liquid-solid (precipitation) phase separation, which can be utilised to deposit complexes onto solid surfaces by dilution.[113] In hair care products, this behaviour is used to promote the deposition of insoluble cationic polymers onto the hair surface during rinsing.[120] This process can also be used to aid the deposition of other beneficiary agents onto hair, most commonly silicones, which are used for their conditioning properties.[102] The formation of polyelectrolyte-surfactant complexes can be beneficial to the bulk properties of the hair care product such as enhancements of viscosity, foaming or gelling performance.[117] Once deposited on the hair surface, polyelectrolyte-surfactant complexes can significantly reduce friction and stick-slip between hairs.[121,161,176,291] Several factors, such as the surfactant and salt concentration, as well as the polyelectrolyte charge density and molecular weight, can affect the amount of polyelectrolyte

deposited and its conformation on the hair surfaces.[19,111,118] This has direct consequences for the lubrication performance for polyelectrolyte-surfactant complexes.[485] Despite its importance to a wide range of products, the boundary lubrication mechanisms of polyelectrolyte-surfactant complexes remain mostly unknown.[486]

More environmentally-friendly alternatives to petroleum-based feedstocks are urgently being sought by hair care formulators. These alternatives can be derived from natural sources, but should provide an equal or superior performance.[10] One promising class of sustainable polymers are polysaccharides,[5] such as guar gum, which can be extracted from the seeds of the guar plant.[297] Guar gum is used extensively in food products as a texture and rheology modifier and its derivatives, such as cationic guar gum (CGG), have become increasingly important in several industries, such as oil and gas extraction as well as textile and paper processing.[487] CGG is known to be effective in reducing the friction between hairs and the addition of anionic surfactants, such as sodium dodecyl sulfonate (SDS), can further improve its lubrication performance.[291]

In this chapter, the NEMD simulation routine introduced in the previous chapters is extended to investigate the friction of biomimetic hair surfaces lubricated by complexes formed from CGG and SDS. As with the previous MD simulations of hair wettability and friction, the coarse-grained *MARTINI 2* force field is employed.[264,265] First, new parameters for CGG are developed using a bottom-up approach from atomistic MD simulations. We then perform sequential adsorption simulations of CGG and then SDS on biomimetic surfaces representative of virgin and chemically damaged hair. Squeeze-out simulations are run to determine the composition within the contact at physiologically-relevant pressures. Finally, NEMD simulations are performed to probe the friction between two hairs with adsorbed polyelectrolyte-surfactant complexes at various physiologically-relevant sliding speeds and pressures. By changing the surface model, the methodology can be readily extended to investigate other formulated products that contain polymer-surfactant complexes, such as in fabric softeners[488] or for drug delivery.[489]

6.2 Methodology

6.2.1 Polyelectrolyte model

For the polyelectrolyte, we selected CGG, or more specifically guar hydroxypropyltrimonium chloride, which is a quaternary ammonium-functionalized polysaccharide with high-molecular weight ($M_W = 1{,}000{,}000$-$3{,}000{,}000$ g mol^{-1})[122,297,491] and promising friction properties on hair.[291] Fig. 6.1a) shows the structural formula of the guar hydroxypropyltrimonium chloride monomer. The backbone consists of two β-D-mannopyranose units and a α-D-galactose branch functionalized with a quaternary ammonium group.[297]

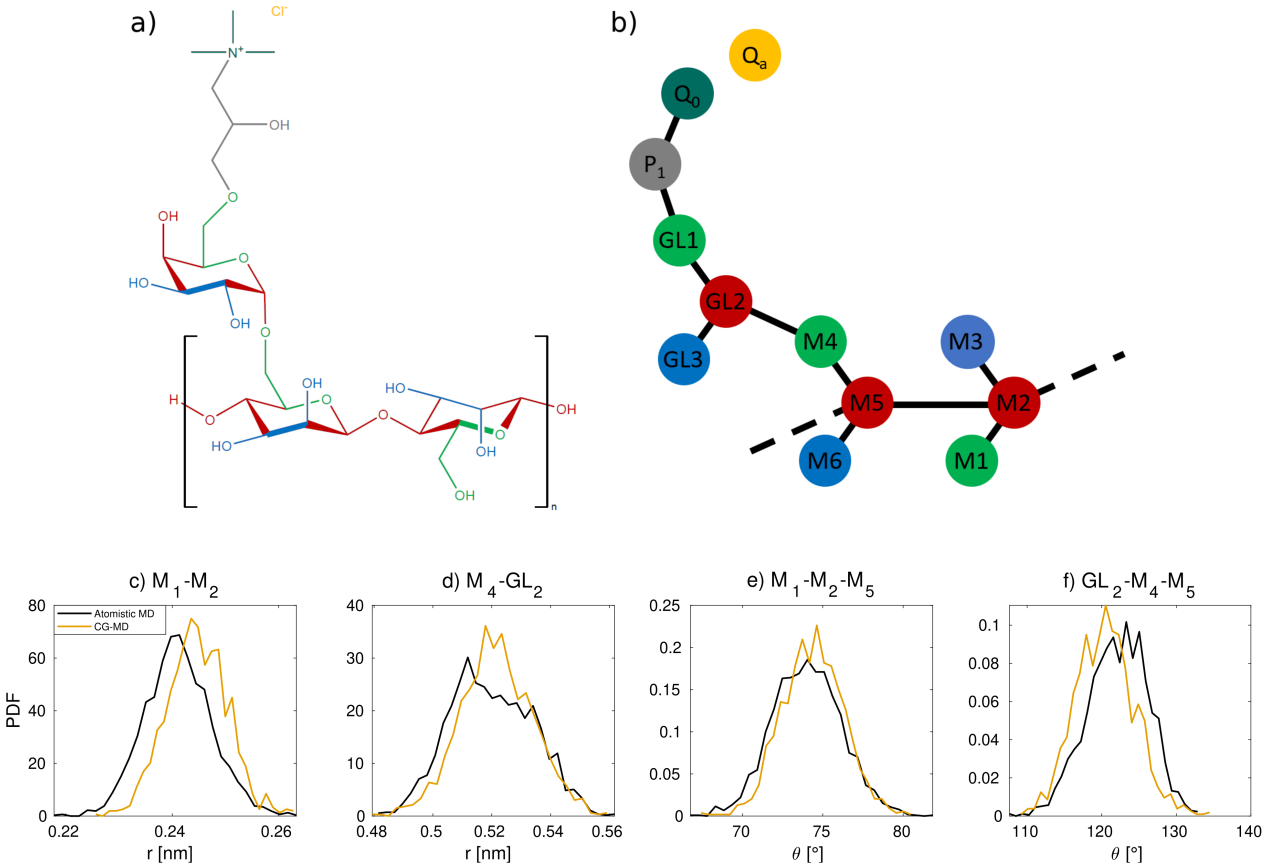


Figure 6.1: a) chemical structure of guar hydroxypropyltrimonium chloride and b) the corresponding coarse-grained architecture. The coarse-grained color coding for carbohydrate groups is in accordance with Ref.[490] Examples of the mapping of bond and angle potential between atomistic and coarse-grained simulations for non-ionic guar gum are shown in c)-f).

The *MARTINI* force field[264,265] has been used to study a wide range of oppositely charged polyelectrolytes and surfactants in bulk[90,492–494] and in the presence of surfaces.[36] MARTINI typically uses a 4:1 mapping of heavy atoms to coarse-grained beads.[264,265] The first *MARTINI 2* parameterization for saccharides was developed by López et al.,[495] who established a set of building blocks required for parametrizing a wide range of polysaccharides. Shivgan et al.[490] proposed a significantly different mapping to that proposed by López et al.,[495] which overcame the overestimated aggregation propensity of polysaccharides using this model.[496] Xu et al.[492] presented a coarse-grained model of the polysaccharide chitosan using the polarizable *MARTINI* water model due to Yesylevskyy et al.,[306] which was recently used by Gotla et al.[493] to study chitosan interactions with SDS. Tsanai et al.[494] and Liu et al.[90] used *MARTINI 3*[331] to investigate the salt-dependant coacervation of oppositely charged polyeletrolyes. MARTINI 2 with the polarizable *MARTINI* water model has also been used to study polelectrolyte complexes, such as those formed between poly(styrene sulfonate) and poly(diallyldimethylammonium).[305] A more heavily coarse-grained force field for guar was proposed by Liang et al.[497] in which one bead was used for each monosaccharide (∼10 heavy atoms), resulting in 3 beads per repeat unit, as opposed to the 9 used in *MARTINI*. However, to our knowledge, no parametrization for guar or its cationic

derivatives is currently available in the *MARTINI* framework. Therefore, we first generate new *MARTINI 2*[264,265] parameters for guar and guar hydroxypropyltrimonium chloride. We chose *MARTINI 2*[264] over *MARTINI 3*[331] due to the significant amount of previous validation work that was performed for hair surfaces using *MARTINI 2* and the availability of a polarizable water model.[306] The parameters are determined using a bottom-up approach from atomistic MD simulations.

6.2.2 Atomistic MD simulations

All of the atomistic and coarse-grained MD simulations in this work were conducted using the open-source Large-scale Atomic/Molecular Massively Parallel Simulator (LAMMPS) software.[332] Atomistic MD simulations of solvated guar and cationic-modified guar monomers and short oligomers were conducted using the OPLA-AA force field,[257] which has been extensively validated for polysaccharides.[498,499] Initial atomistic topologies for non-ionic and cationic guar were obtained from LigParGen.[500–502] The monomers and short oligomers were solvated in 4180 SPC/E water molecules[346] in a fully periodic simulation box. The Lennard-Jones (LJ) interactions were cut off at a distance of 1.2 nm. Long-range Coulombic interactions are calculated using the particle-particle, particle-mesh (PPPM) method[336] with a relative energy tolerance of 10^{-5}. The system was energy minimized and subsequently thermostatted at a temperature of 300K and barostatted at a pressure of 1 atm in the isothermal-isobaric (NPT) ensemble using a Nosé-Hoover thermostat[340,341] and barostat[452] with damping constants of 0.1 ps for temperature and 1 ps for pressure. An integration time step of 2 fs was applied while constraining all hydrogen bonds using the SHAKE algorithm.[334] The equations of motion were integrated using the velocity-Verlet algorithm.[333] After energy minimization and an equilibration run of 1 ns, monomer trajectories were recorded every 2 ps for a duration of 4 ns.

6.2.3 Coarse-grained MD simulations

Guar and CGG *MARTINI* parametrization

The coarse-grained mapping of guar hydroxypropyltrimonium monomers is shown in Fig. 6.1a)-b). A modified Boltzmann inversion technique is used via the open-source Py-CGTOOL software[503] to obtain bonded interaction parameters for the coarse-grained molecule based on the trajectories from the atomistic MD simulations. Entire trajectories are used to obtain the *MARTINI* bond and angle parameters from the atomistic MD simulations.[503] The GROMACS files are then converted to LAMMPS files using GRO2LAM.[504] We developed parameters for both non-functionalized guar monomers and cationic-functionalized guar monomers to enable a varying degree of substitution (DS) and thus polyelectrolyte charge density. The guar mapping is identical to that in Fig. 6.1b), but without the hydroxypropyltrimonium group. The non-bonded LJ interactions for the mannose and galactose building blocks in guar are obtained from previous *MARTINI 2* parametrizations of polysaccharides by Shivgan et al.[490]. Unlike

Shivgan et al.,[490] we do not downscale the LJ interactions to maintain consistency with our validated unscaled *MARTINI* LJ parameters for hair surfaces. The non-bonded LJ interactions for the trimethylammonium ion (Q_0 bead, which carries a permanent charge of +1e) and chloride counterion (Q_a bead, which carries a permanent charge of -1e), as commonly employed for cationic surfactants.[447] For the hydroxypropyl group, we use a P_1 bead, which is the standard alcohol group in *MARTINI 2*.[264] The non-bonded LJ interactions from the polarizable water model due to Yesylevskyy et al.[306] were used without modification. Therefore, we developed new parameters for the bonds and angles between the beads. Dihedral interactions were omitted after initial tests showed reduced numerical stability during the MD simulations, as is commonly observed when using the *MARTINI* model[265] and other coarse-grained force fields.[497] The full list of *MARTINI 2* parameters for both guar and guar hydroxypropyltrimonium chloride is provided in section A.4 in the appendix. Figure 6.1c)-f) shows four examples of the mapped harmonic bond and angle potentials from atomistic and coarse-grained bulk simulations of cationic guar in aqueous environment. Comparisons of the other bonds and angles parameterised here are shown in section A.4 in the appendix.

A comparison of the increase in the radius of gyration, R_g, of neutral guar with molecular weight, M_w, between *MARTINI* and experiments is shown in Fig. A.4.22 in the appendix. At a given M_w, our *MARTINI* parameters consistently underestimate the absolute values of R_g compared to previous scattering experiments.[505] This discrepancy could be attributed to the high polydispersity of the experimental samples, since higher M_w species are emphasized in scattering experiments.[497] The R_g follows the power-law scaling law $\propto M_w^{0.62}$, which is in good agreement with previous experiments ($\propto M_w^{0.62}$)[505] and coarse-grained MD simulations ($\propto M_w^{0.60}$).[497]

The linear CGG polymer chains were constructed according to a self-avoiding random walk using the *genpoly* extension available in Moltemplate.[368] The degree of substitution, DS, which represents the fraction of monomers functionalized with a cationic group, can vary between around 4-30% for guar hydroxypropyltrimonium chloride.[491,506] In this work, we consider cationic guar gum at maximum charge density (DS = 100%). Higher charge densities are potentially interesting for industrial formulations due to their stronger affinity towards negatively charged surfactant molecules and hair substrates.[121] A molecular weight of $M_w = 36{,}900$ g mol^{-1} was chosen for our monodisperse CGG, which corresponds to 50 repeat units. This is much shorter (1-4%) than the reported values for industrial cationic guar derivatives ($M_w = 1{,}000{,}000$-$3{,}000{,}000$ g mol^{-1}),[491] but allows for system dimensions which are computationally accessible.[36] The application of shear is expected to lead to stretching and preferential orientation of the polymers in the direction of sliding, as shown in previous coarse-grained NEMD simulations of polymers on biomimetic hair surfaces.[266]. Such extended polymers with an end-to-end distance larger than the dimensions of the simulation box could cause unphysical self-interactions across

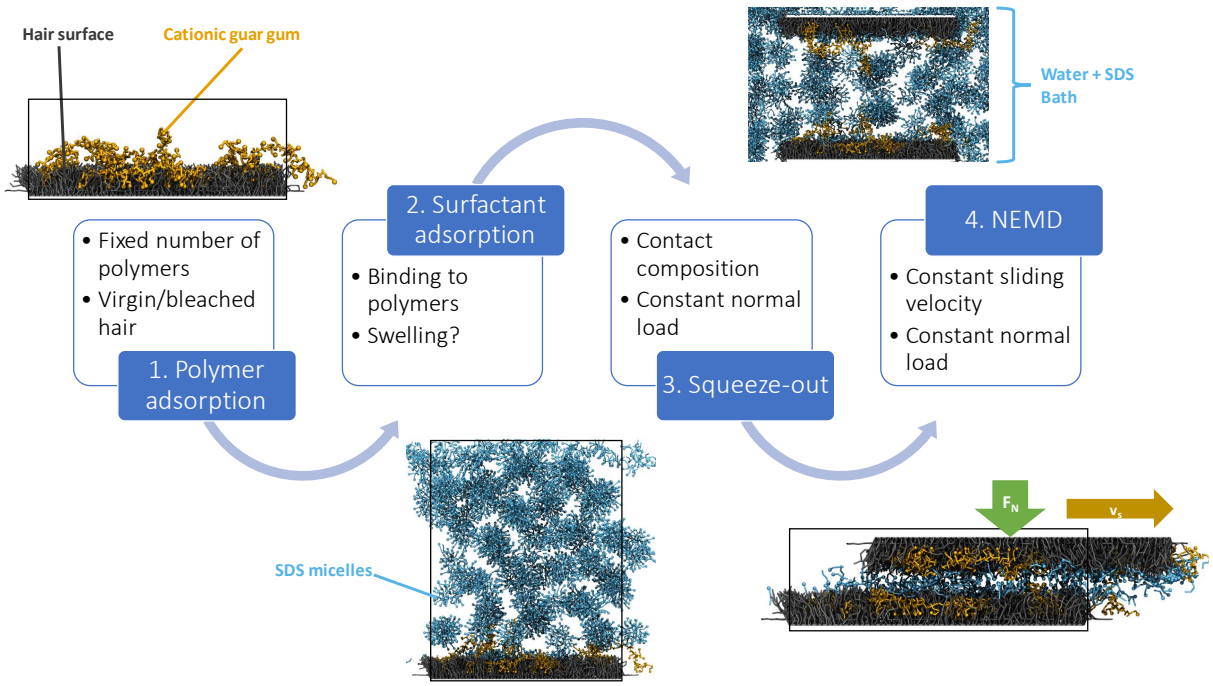


Figure 6.2: Polyelectrolyte-surfactant lubrication workflow consisting of sequential adsorption of CGG and then SDS, followed by squeeze-out simulations to determine the contact composition and finally NEMD simulations.

periodic images during sliding. Thus, the relatively short polymer size is necessary to facilitate a computationally tractable system size. The systems used for the NEMD simulations in this work contain approximately 75,000 coarse-grained beads, while some squeeze-out simulations contain more than 500,000 beads.

Adsorption of CGG & SDS

To study friction of polymers and surfactants at hair surfaces, we apply a workflow consisting of sequential adsorption, squeeze-out and NEMD simulations, as summarized in Fig. 6.2. Adsorption of cationic guar gum and anionic surfactants to biomimetic hair surfaces is studied using the existing model of the outer layer of virgin and medium bleached hair introduced in chapter 3. In this chapter, we establish the polymers and surfactants on the surface by means of sequential adsorption, where cationic polyelectrolytes are adsorbed first, followed by adsorption simulations of anionic surfactants from a micellar bulk. The adsorption of self-assembled polymer-surfactant complexes, as recently studied by Coscia et al.[36] is also of interest but requires fundamental changes of our proposed routine to establish the amount of water, salt and anionic surfactants at the interface (squeeze-out simulations). We justify the sequential adsorption procedure pursued in this work by three possible scenarios on real hair surfaces:

1. Fast adsorption of cationic polymers from the bulk compared to surfactants due to the long-range electrostatic interactions ($\propto r^{-2}$) with the oppositely charged surface charges.[507] Previous SCFT calculations[128,247] reported a similar layered ad-

sorption structure for branched cationic polyelectrolytes with anoinic surfactants on biomimetic hair surfaces.

2. In some situations, cationic polymers are already present on the hair surface before treatment with other products containing anionic surfactants, for example conditioned hair that is washed with a shampoo.[508]

3. Even in experiments, adsorbed polyelectrolyte-surfactant complexes can be trapped in quasi-equilibrium states[509] and the true equilibrium may only be reached after time scales inaccessible to our simulations (days).[510]

The sequential adsorption simulation protocol proposed here also allows for a direct observation of potential SDS-induced swelling effects of the cationic polymer on the surface, as observed in previous ellipsometry measurements on hydrophilic silica.[511] The approach was also previously used in adsorption studies of cationic polysaccharides on silica which where then gradually exposed to increasing SDS concentrations.[512,513] It is worth noting that the polyelectrolyte-surfactant structures obtained through sequential adsorption might be fundamentally different to those obtained from adsorption of pre-formed complexes due to kinetic entrapment.[118]

We use the polarizable *MARTINI* water model,[306] which consists of a central LJ bead and two oppositely-charged satellite beads. Compared to the non-polarizable *MARTINI* water model,[264] the polarizable model is less prone to freezing under confinement. All other numerical settings for the coarse-grained deposition, squeeze-out and NEMD simulations are consistent with the previous chapters.

Using Moltemplate,[368] we first create bulk systems, containing 4 or 12 CGG polymers, 200 or 600 hydrated chloride counter-ions, and 34,299 or 64,310 water beads for low and high guar concentrations, respectively. The total number of coarse-grained beads in the bulk systems is 105,297 for the low CGG concentrations and 200,130 for the high concentration. The guar bulk system is energy minimized using the conjugate gradient method and subsequently undergoes thermal relaxation at $T = 600$ K and $p = 1$ atm in the NPT ensemble. We use the Nosé-Hoover thermostat[340,341] and barostat[452] with damping constants of 1 ps for temperature and 3 ps for pressure. Then, the entire bulk system containing the final number of polymers is further thermally relaxed in aqueous solution at $T = 600$ K for 30 ns, before equilibrating for another 5 ns at a target temperature of $T = 300$ K. This equilibrated bulk system is then transferred to above the hair surface for subsequent adsorption simulations. We selected an initial number of CGG polymers on each of the surfaces, $N_{CGG} = 4$, which assuming full adsorption, corresponds to an equilibrium adsorption density of $\Gamma = 0.04$ µg cm^{-2}. The chosen adsorption density, Γ, is motivated by ellipsometry measurements of the adsorption density of CGG on hydrophobic (virgin hair model), where $\Gamma = 0.04$-0.05 µg cm^{-2}) and hydrophilic silica (bleached hair model), where $\Gamma = 0.06$ µg cm^{-2} after an adsorption time of 5000 seconds.[122] Such timescales are beyond the limits of our coarse-grained

MD simulations, so polymers are placed close to the surface to ensure full adsorption at a given coverage. This approach was also used in previous atomistic MD simulations of surfactants adsorbed on iron oxide surfaces.[354] Dissipative quartz crystal microbalance (QCM-D) adsorption measurements of another cationic polysaccharide, JR400, to uncharged thiol surfaces (virgin hair model) conducted by Guzmán et al.[507] also indicated similar surface coverages ($\Gamma = 0.05$ µg cm^{-2}). Higher surface coverages of JR400, $\Gamma \approx 0.12$ µg cm^{-2}, have been observed by QCM-D measurements of JR400 on negatively charged thiol monolayers (bleached hair model).[507] We will return to these higher adsorption densities in the next chapter. The use of biomimetic surfaces, rather than real hair for these experimental measurements, eliminates the need to convert adsorption densities that are typically given as a fraction of the weight of the measured hair sample, thus requiring an accurate measurement of the surface area per unit weight.[514] The effect of an increasing adsorption density is expected to be particularly relevant for bleached hair, where a comparable increase in the charge density is expected.

An equilibrated system containing anionic surfactants, specifically SDS molecules $N_{SDS} = 4{,}328$, are then introduced on top of the existing surfaces with adsorbed CGG at an initial concentration of $c_{SDS} = 664$ mM and finite system height of $\Delta z = 21$ nm. Standard *MARTINI 2* parameters for SDS are employed, with three C_1 beads attached to one Q_a (-1e) bead, with a Q_d (+1e) bead for the hydrated sodium counter-ion.[449] In commercial shampoos, the anionic surfactant SLES is generally present at concentrations of between 50-150 mM.[101] Similar SDS and SLES concentrations were also used in previous friction experiments of complexes formed with cationic guar.[291,508] The selected concentration is well above the critical micelle concentration (CMC) of SDS $c_{cmc} = 82$ mM,[515] so the molecules are predominantly present as cylindrical micelles.[449] The high SDS concentration was chosen to obtain a strong local excess of anionic sites (22:1), which was required to obtain binding of micellar SDS to guar within reasonable computational times. We use the *MARTINI* parametrization of SDS due to Wang and Larsson,[449] which consists of three apolar C_1 beads and a negatively charged Q_a bead. Either coarse-grained sodium (Na^+) or chloride (Cl^-) counterions with their first hydration shell[265] are added to the CGG and SDS bulk systems to ensure charge neutrality during adsorption. No excess salt was considered in these simulations. It was shown in the previous chapter that excess salt reduced the propensity for adsorption of cationic surfactants on models for virgin and bleached hair.

The x $\times$ y dimensions of the virgin and bleached hair surfaces are 24×21 nm$_2$ for the adsorption simulations. The adsorption simulations are conducted with periodic boundary conditions applied in the x and y directions. These systems are finite in the z direction and a repulsive boundary is added at the top of the simulation cell.[445] Simulations are run at a temperature of $T = 300$ K for a maximum duration of 50 ns. The temperature is controlled with a Nosé-Hoover thermostat[340,341] with a damping constant of 1 ps.

Squeeze-out and NEMD

Squeeze-out MD simulations are conducted between two hair surfaces following the protocols that were developed in previous chapters for water between biomimetic hair and n-hexadecane between iron oxide substrates.[354] Contacts are created by replicating and reflecting the surfaces containing CGG and SDS from the adsorption simulations with an initial separation distance of 24 nm. The contact is immersed in an equilibrated micellar SDS solution ($c_{SDS} = 664$ mM), as shown in Fig. 6.2. The $x \times y \times z$ dimensions of the systems are $40 \times 21 \times 32$ nm_3 for the squeeze-out simulations, with periodic boundary conditions applied in all directions. The contact length in the y direction is equal to the box length in y and is therefore periodic in this direction. During compression, water and SDS molecules are squeezed out into the reservoir space. Compression between the two hair surfaces was achieved by applying a constant normal load ($\sigma = 5$-50 MPa) between the graphene sheets of the opposing hair surfaces. The contact thickness was recorded as a function of time and simulations were run until equilibrium contact conditions were established, which was typically within 50-100 ns, as shown in Fig. A.4.23 in the appendix. At $\sigma = 10$ MPa, the equilibrium contact thickness was approximately 6 nm for both virgin and medium bleached hair, which is somewhat thicker than for pure water (4-5 nm). The CGG polymers remain adsorbed and are not squeezed out due to the multiple cationic groups that form strong ionic bonds with the sulfonate groups on the hair surfaces. Previous experiments have shown that cationic polymers are resistant to squeeze out up to high loads on anionic-modified surfaces.[516] Similar observations were made for cationic surfactants in the previous chapter, which were also resistant to squeeze out.

Constant shear-rate NEMD simulations[20] are then conducted between the two compressed hair surfaces with a contact composition established by the squeeze-out simulations. For the sliding simulations, the external reservoir is removed and the $x \times y$ dimensions of the system are reduced such that they are the same as the hair surfaces (24×21 nm). Physiologically relevant constant sliding velocities of $v_s = 0.03$-1 ms^{-1} are applied to the anchoring substrate of the upper surface, while maintaining the constant normal load from the squeeze-out simulations. This range of velocities is relevant to hair manipulations such as touching, brushing, and combing. The system temperature is controlled using a Langevin thermostat[374] applied only in the y direction and to the base bead of the surface-grafted molecules (18-MEA and cysteic acid). Further information on the NEMD protocol applied are provided in chapters 4 and 5.

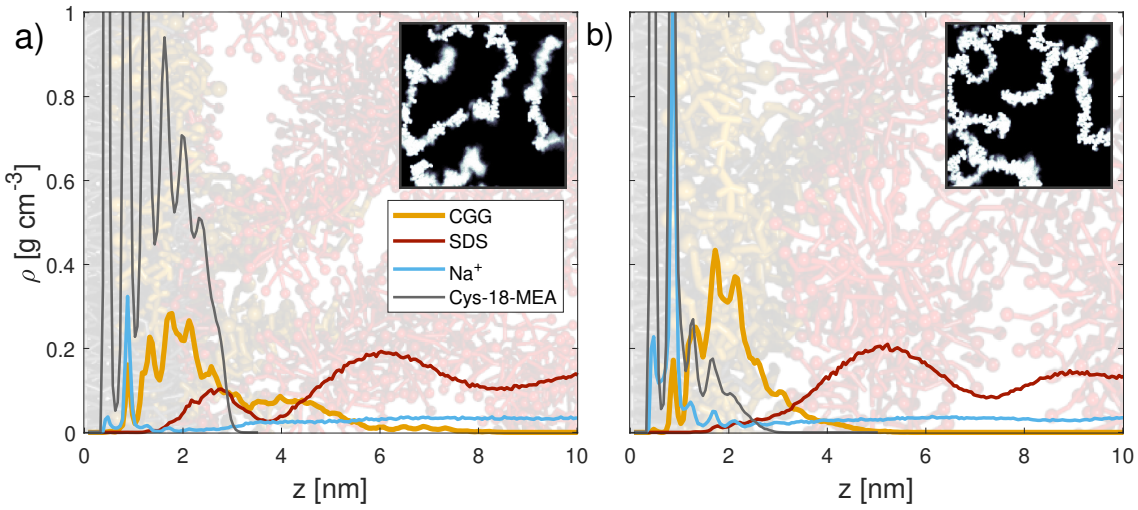


Figure 6.3: Mass density profiles for a) virgin and b) medium bleached hair at the end of the SDS adsorption stage for a given guar adsorption density of $\Gamma = 0.04$ µg cm^{-2}. Water densities are not shown for clarity. Snapshots show the corresponding systems with CGG beads shown in orange, SDS in red, Na^+ in blue, and 18-MEA in gray. Insets show the top-view distribution of cationic guar on the surfaces.

6.3 Results and discussion

6.3.1 CGG-SDS adsorption

Sequential adsorption

We first perform adsorption simulations of CGG at a degree of substitution, DS = 100% onto biomimetic virgin and medium bleached hair surfaces. There is a strong electrostatic affinity between the cationic groups on CGG and the negatively charged sites on the hair surfaces. This means that the CCG polymers lie mostly flat on the surface, which is consistent with previous experiments for high-charge density polyelectrolytes.[517] We define the thickness of the CGG film as the distance in the surface-normal direction containing 98% of the CGG mass (between 1 and 99% of the time-averaged cumulative mass density distribution). For the pure CGG systems (Fig. S6), we measure film thicknesses of 4.4 nm for virgin and 2.9 nm for bleached hair surfaces. In previous experiments, the thickness of CGG layers on hydrophilic silica was reported as around 19 nm.[122] This discrepancy is probably due to i) the much larger CGG M_W in the experiments (around 2,000,000 g mol^{-1}) than the simulations (36,900 g mol^{-1}) and ii) the high charge density used in the simulations. Previous studies have shown that increasing the charge density of CGG resulted in a more compact layer.[506] The mass fraction of water in the CGG film is 65% for virgin hair and 72% for bleached hair. The observed hydration levels are slightly lower than that observed in combined QCM-D and ellipsometry measurements of another cationic polysaccharide (JR400) adsorbed onto surfaces functionalised with anionic groups (75%).[507] It should be noted that JR400 has a different polysaccharide backbone and lower charge density (DS = 27%) compared to the CGG simulated here (DS = 100%). Previous experimental studies have suggested that more highly charged polyelectrolytes result in less hydrated layers than those obtained from low charged polyelectrolytes.[518] Thus, the small deviation in

polyelectrolyte hydration between the experiments[507] and current simulations can be attributed to the differences in charge density.

Adsorption of micellar SDS is then studied in a second step. Fig. 6.3 shows two simulation snapshots overlaid with equilibrium mass density profiles of the CGG and SDS adsorption structures on the virgin and medium bleached hair surfaces. SDS predominantly adsorbs as intact micelles that bind to the cationic sites on the CGG chains that are not adsorbed on the surface. On the virgin hair surface, some SDS molecules also bind through hydrophobic adsorption to the tail beads in the 18-MEA layer on the surface. Hydrophobic adsorption was also observed in coarse-grained MD adsorption simulations of SDS on untreated virgin hair surfaces in chapter 5.

When SDS is added, the CGG film thickness on virgin hair increases to $d = 6.3$ nm, which is due to swelling. Compared to the pure CGG systems discussed in the previous section, more of the polymers are in loop or tail conformations, but the majority remain in flat train conformations.[266] Tails and loops have previously been postulated to be important for the lubrication performance of CGG.[508] Previous experiments observed swelling of the CGG layers up to 100 nm at high concentrations on functionalized anionic silica.[122] The reduced swelling in our simulations can again probably be related to the relatively short polymers. Another factor is that in the experiments, the surface charge is usually overcompensated by the oppositely-charged adsorbed polyelectrolyte.[516] In the systems studied in our simulations, the surface charge is not overcompensated, as shown in Table 6.1 (surface:CGG charge ratio < 1 for overcompensation). The remaining fraction of anionic sites on the surface is locally neutralized by sodium counterions. Therefore, there are fewer free cationic groups available to adsorb the SDS micelles and cause swelling. Higher CGG surface coverages would lead to overcompensation of the surface charge, which may lead to increased swelling and improved lubrication.[508]

When SDS is added to the system with CGG adsorbed on medium bleached hair, most of the polymers remain in a train conformation on the surface.[266] There is some swelling upon addition of SDS, with the CGG layer extending to 3.8 nm. Swelling is less pronounced on bleached hair than virgin hair, due to the higher negative surface charge density. The mass fraction of water in the CGG films is 64% for virgin and 65% for medium bleached hair. Thus, the CGG films remain highly hydrated upon adsorption of SDS, which may be important for effective lubrication.[121] The similarity in the degree of hydration for the CGG on virgin and medium bleached surfaces, despite the higher CGG film thickness on virgin hair, can be explained by the volume exclusion due to the higher 18-MEA coverage on virgin hair. The insets in Fig. 6.3 show that CGG polymers are distributed heterogeneously on the surfaces in stretched conformations, which are similar to those observed experimentally for polyelectrolytes adsorbed on oppositely-charged surfaces.[519] This means that a large fraction of the water content will be located within

the voids between the polyelectrolyte chains. Recent experiments have also been used to estimate the water content of polyelectrolyte-surfactant complexes,[18,19] but none of the combinations are similar enough to directly compare to our simulation results.

6.3.2 Friction of hair with pure CGG

Prior to introducing anionic SDS surfactants into the contact, the conditioning performance of pure CGG with high charge density (DS = 100%) was investigated in NEMD simulations at a normal load of $\sigma = 10$ MPa and sliding velocity of $v_s = 0.1$ ms^{-1}. None of the CGG molecules were removed from the contact during the squeeze-out stage in a pure water bath due to the formation of strong ionic bonds with the surfaces. The water trapped within the contact at $\sigma = 10$ MPa increases by around 60% from a surface coverage of $\rho_w = 6.5$ nm^{-2} for untreated virgin hair, to $\rho_w = 10.4$ nm^{-2} for virgin hair with adsorbed CGG. On the bleached hair surfaces, the water coverage increases by approximately 10% from $\rho_w = 16.3$ nm^{-2} for untreated hair, to $\rho_w = 18.1$ nm^{-2} with CGG adsorbed. The observed increase in water beads trapped in the contact can be explained by the relatively high charge density of the CGG, which means that not all of the cationic sites bind to the surface, exposing an increased number of hydrophilic sites to the aqueous bulk.

Fig. 6.4a)-b) shows snapshots of the sliding contact and corresponding shear stress signals for virgin and medium bleached hair in the presence of adsorbed CGG at $v_s = 0.1$ ms^{-1}. The shear stress with CGG on virgin hair, $\tau = 3.9 \pm 1.7$ MPa is significantly increased in comparison to values previously reported on untreated virgin hair surfaces, $\tau = 2.4$ MPa at 10 MPa. For virgin hair, strong periodic oscillations are observed at a characteristic frequency of $f \approx 0.015$ ns^{-1}. Previous investigations of stick-slip of polymers at interfaces revealed a strong correlation of the friction signal amplitude with local displacement of polymers.[520] We checked the root-mean square displacement (RMSD) of the polymers and found no periodic fluctuations of the displacements as shown in Fig. 6.6, which suggests that polymer dynamics are not directly linked to the oscillations. However, around $t = 50$ ns, a single guar molecule detaches from the bottom hair surface and is dragged in the direction of sliding ($v/v_s \approx 0.5$), which increases the RMSD and might contribute to higher CoFs. However, this does not seem to contribute further to the observed oscillatory behaviour. The time-averaged mass density profiles shown in Fig. 6.4e)-f) indicate that the interdigitation between opposite surfaces is more pronounced for virgin than for bleached hair. This might explain parts of the higher observed CoF. An increase in stick-slip is however deemed unlikely to be solely caused by interdigitation of the 18-MEA, due to the high coverage of lipids. A fast Fourier transform (FFT) of the topography signal of guar on the respective surfaces revealed a characteristic wavelength of $\varkappa = 0.016$ nm^{-1}, which is directly connected to the previously observed stick-slip frequency via the transport velocity $v_s = f / \varkappa$. The surface topography distributions and corresponding FFT spectra are shown in Fig. 6.5 The agreement of the oscillation frequency with the characteristic wavelength suggests

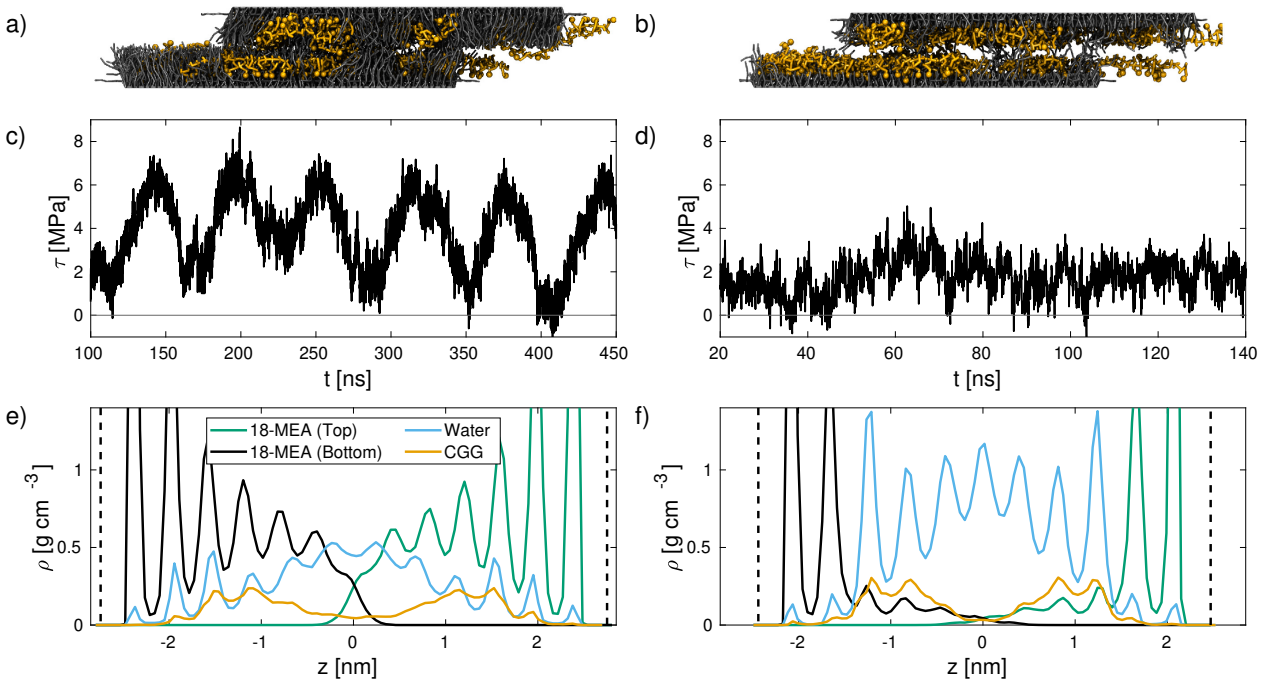


Figure 6.4: Snapshots of NEMD simulations of a) virgin and b) medium bleached hair surfaces with CGG at $\Gamma = 0.04$ µg m^{-2}, sliding velocity of $v_s = 0.1$ ms^{-1} and a contact pressure of $\sigma = 10$ MPa. Respective shear stress profiles as a function of time are shown in c)-d). Signals are only shown from the point when a dynamic equilibrium has been reached. Time-averaged mass density profiles for e) virgin and f) medium bleached hair are shown for for surface lipids (only up to ± 1 nm from the contact center for clarity), guar and water within the contact.

that the observed oscillations are promoted by the local heterogeneous distribution of guar in the direction of sliding x on each surface. The high charge density on the studied CGG molecules might further contribute to rigid, heterogeneous distribution of polymers on the respective surface which is resistant to sliding.

Our analysis reveals that the studied levels of CGG adsorption do not contribute to favorable friction reductions on virgin hair at relatively low sliding velocities. Our previous NEMD simulations with cationic surfactants suggest that friction forces are significantly reduced ($\mu = 0.14$) compared to both CGG-treated and untreated virgin hair surfaces at the same load and sliding conditions. Miyamoto et al.[161] also reported high stick-slip amplitudes for damaged hair treated with certain shampoo formulations but attributed this to entire layers of adsorbed coacervates being sheared off the surface during sliding. An increase in CGG adsorption density further might be beneficial for effectively reducing friction.

Interestingly, no significant periodic fluctuations in the friction signal are observed for pure guar on medium bleached hair. On bleached hair, guar provides considerable reductions in friction ($\tau = 1.7 \pm 0.9$ MPa) compared to the bare wet bleached contact ($\tau = 3.8$ MPa). The corresponding mass density profiles reveal little surface interdigitation between the remaining 18-MEA lipids. The considerable friction reductions might be a result of the guar being able to distribute more evenly on the lipid-depleted

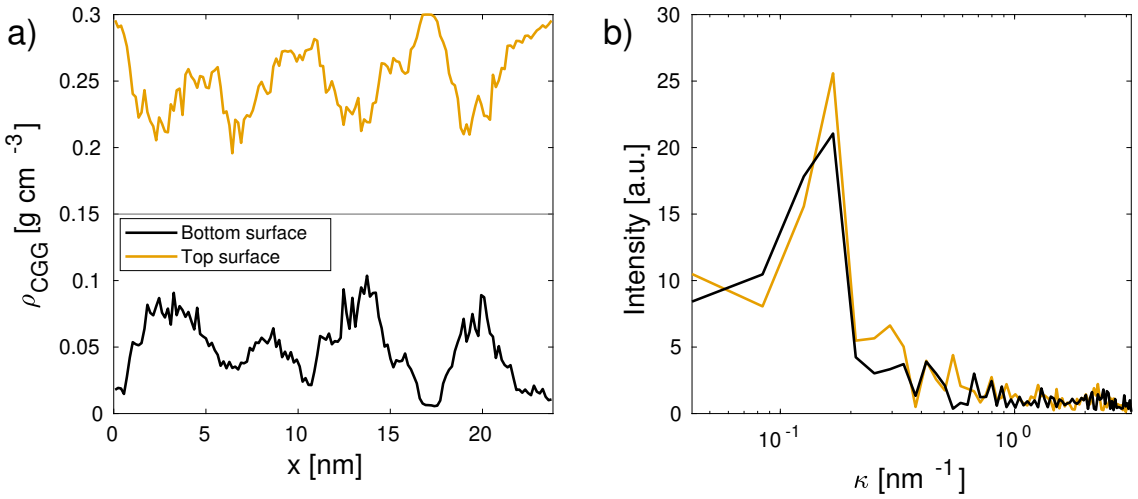


Figure 6.5: a) surface topography of pure CGG on virgin hair surfaces in the direction of sliding, x. The averaged mass density signal for the upper surface is flipped and shifted by $\Delta\rho = 0.3$ g cm^{-3} for clarity. The characteristic wavelength of the lateral guar distribution, f' = 0.016 nm^{-1} is revealed from b) a fast Fourier transform (FFT) of the topography signals.

bleached model surfaces. On bleached surfaces with adsorbed guar, the coarse-grained water film shows moderate ordering in the surface-normal direction. This is consistent with our previous NEMD simulations on unconditioned bleached model hair surfaces.

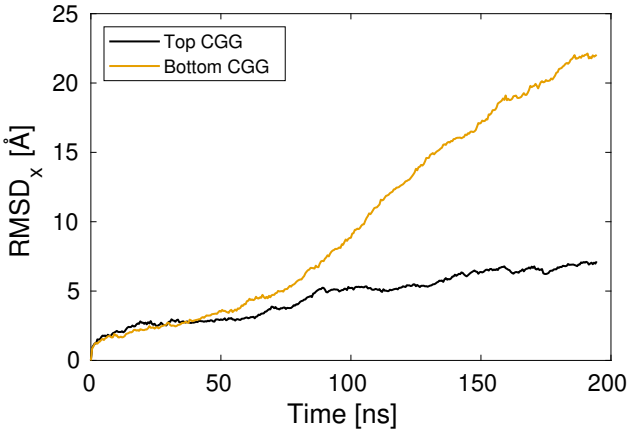


Figure 6.6: Temporal evolution of the root-mean-square displacement (RMSD) of CGG in virgin hair contacts in the direction of sliding at $\sigma = 10$ MPa and $v_s = 0.1$ ms^{-1}. Different curves show the polymer displacement relative to the respective surface they are initially adsorbed to.

6.3.3 Friction of hair with CGG-SDS complexes

The final systems from the sequential adsorption simulations are replicated and flipped and a water/SDS bath is added in the x direction for the squeeze-out simulations. For the squeeze-out simulations at 10 MPa, the final contact thickness is approximately 6 nm for the CGG-SDS complex between both virgin and bleached hair surfaces, as shown in Fig. A.4.23 in the appendix. The effect of CGG-SDS complexes on friction is investigated with NEMD simulations using the configurations obtained from the squeeze-out simulations with the water/SDS bath removed and periodic surfaces

Table 6.1: Overview of the contact composition used in the NEMD simulations on virgin and medium bleached hair surfaces at contact pressures of $\sigma = 5$-50 MPa. The initial surface area density of CGG chains, $\rho_{CGG} = 0.016$ nm^{-2}, remained unchanged during squeeze-out. The baseline case at $\sigma = 10$ MPa is shown in bold.

Virgin hair	$\sigma =$	5 MPa	**10 MPa**	15 MPa	20 MPa	35 MPa	50 MPa
Coarse-grained water	ρ_W	23.1 nm^{-2}	**16.9 nm^{-2}**	11.1 nm^{-2}	10.1 nm^{-2}	8.8 nm^{-2}	7.7 nm^{-2}
SDS	ρ_{SDS}	1.52 nm^{-2}	**1.11 nm^{-2}**	1.15 nm^{-2}	0.96 nm^{-2}	0.73 nm^{-2}	0.66 nm^{-2}
SDS:CGG charge ratio	R_{SDS}	1.88	**1.37**	1.41	1.18	0.90	0.81
Hair:CGG charge ratio	$\lvert R_{surf} \rvert$	1.68					

Med. bleached hair	$\sigma =$	5 MPa	**10 MPa**	15 MPa	20 MPa	35 MPa	50 MPa
Coarse-grained water	ρ_W	28.1 nm^{-2}	**20.9 nm^{-2}**	18.2 nm^{-2}	16.8 nm^{-2}	13.4 nm^{-2}	12.9 nm^{-2}
SDS	ρ_{SDS}	1.04 nm^{-2}	**0.87 nm^{-2}**	0.80 nm^{-2}	0.69 nm^{-2}	0.57 nm^{-2}	0.54 nm^{-2}
SDS:CGG charge ratio	R_{SDS}	1.28	**1.07**	0.98	0.85	0.70	0.66
Hair:CGG charge ratio	$\lvert R_{surf} \rvert$	5.62					

restored in x. The water and SDS surface coverages used in the NEMD simulations are summarized in Table 6.1. On virgin hair at $\sigma = 10$ MPa, the surface coverages inside the contact equate to $\rho_W = 16.9$ nm^{-2} for water and $\rho_{SDS} = 1.11$ nm^{-2} for SDS. The SDS coverage is somewhat higher than that adsorbed on virgin hair (1.0 nm^{-2}) at the same concentration ($c_{SDS} = 664$ mM) prior to squeeze out. This is due to the electrostatic attraction between the anionic SDS headgroup beads and non-surface bound CGG cationic beads, which are stronger than the hydrophobic interactions between the SDS tailgroup beads and the surface-grafted 18-MEA tailgroup beads. The presence of the anionic surfactant is responsible for an increase in water content compared to both untreated ($\rho_W = 6.5$ nm^{-2}) and CGG-treated virgin hair ($\rho_W = 10.4$ nm^{-2}). The ratio between anionic sites from SDS and cationic sites on CGG is approximately 1.37 on virgin hair at $\sigma = 10$ MPa, which is comparable to experiments.[122] The excess of SDS molecules results from the adsorption of intact micelles docking during the adsorption stage and this is retained during squeeze-out at $\sigma = 10$ MPa. On medium bleached hair surfaces, the adsorption densities of CGG are the same as for virgin hair. Squeeze-out simulations at $\sigma = 10$ MPa on medium bleached hair lead to a surface coverage of $\rho_W = 20.9$ nm^{-2} for water, which moderately increased compared to bleached hair without CGG treatment ($\rho_W =$ 16.3 nm^{-2}). For SDS, a surface coverage of $\rho_{SDS} = 0.87$ nm^{-2} is observed, which corresponds to a moderate excess (ratio of 1.07) of anionic charges compared to cationic sites from CGG. The SDS coverage is higher than that adsorbed on medium bleached hair (0.7 nm^{-2}) at the same concentration ($c_{SDS} = 664$ mM) prior to squeeze out. Thus, CGG locks SDS molecules inside the contact at high pressure through electrostatic interactions.

First, NEMD simulations of the compressed contact at a normal load of $\sigma = 10$ MPa were conducted at a range of sliding velocities v_s. Fig. 6.7 shows the shear stress as a function of the sliding velocity in a double-logarithmic representation. As is commonly noted for boundary-lubricated systems,[401] the shear stress increases with sliding velocity for all of the systems. At sufficiently high sliding velocities, the logarithm of the shear stress obeys a power-law scaling. This behaviour has previously been observed for self-mated polymer and hydrogel friction in both experiments and simulations.[521]

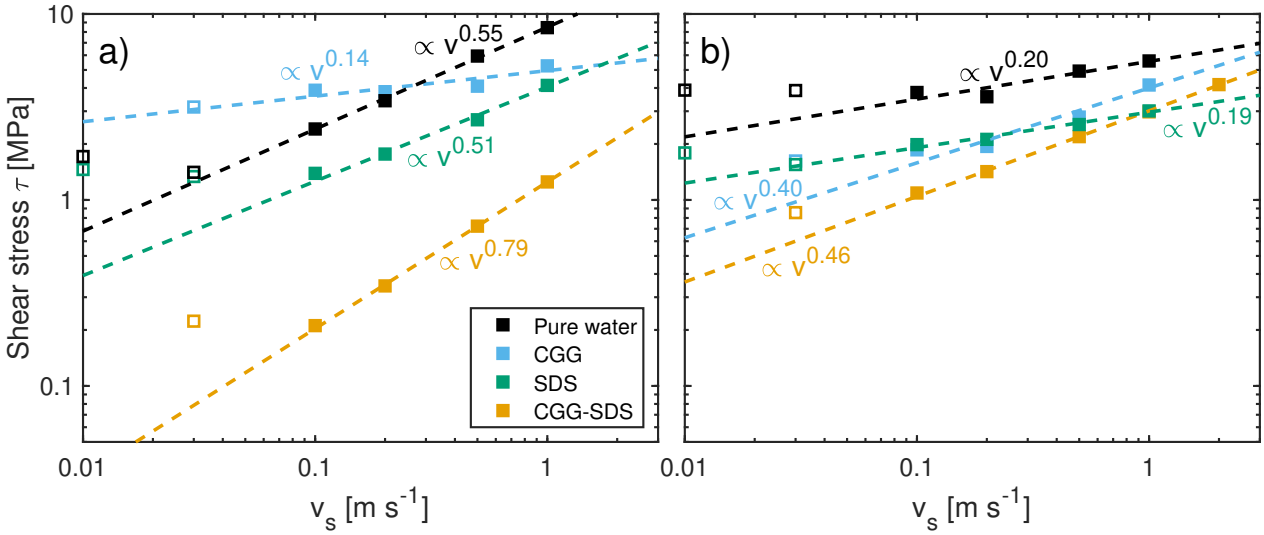


Figure 6.7: Shear stress as a function of the sliding velocity v_s at $\sigma = 10$ MPa for a) virgin and b) medium bleached hair surfaces with CGG and SDS. The shear stress profiles for CGG-only, SDS-only and pure water contacts are shown for comparison. Dashed lines are power-law fits to the data.[521]

For CGG-SDS adsorbed on virgin hair, we find a dependency of $\propto v_s^{0.79}$, and $\propto v_s^{0.46}$ for medium bleached hair. These values for polyelectrolyte-surfactant complexes are higher than for contacts with pure water, which show a weaker velocity dependence. For the pure water systems, we previously attributed this power-law scaling to a shear-augmented thermal activation behaviour in the contacts for virgin and bleached hair. The CGG-SDS complex shear stress is also lower than that observed for pure SDS and pure CGG. Thus, there is synergism between the CGG and SDS in terms of their lubrication performance.[522]

On virgin hair, the CGG systems increase the shear stress at low sliding velocity compared to pure water, but decrease it at high sliding velocity. On bleached hair, CGG reduces the shear stress at all studied sliding velocities. Overall, CGG-SDS systems render a lower shear stress than systems with the respective single component, CGG or SDS, which suggests that synergistic effects are relevant.[522]

The CGG-SDS complexes deposited on the surfaces provide low shear stress on both virgin ($\tau =$ 0.2-1.2 MPa) and medium bleached hair surfaces ($\tau =$ 1.1-2.9 MPa) at all considered sliding velocities. The shear stress is consistently lower than in the pure water contacts as well as values reported for cationic surfactants on virgin ($\tau =$ 0.4-8.0 MPa) and medium bleached ($\tau =$ 1.6-7.8 MPa) hair surfaces under identical conditions, $v_s =$ 0.03-1 ms^{-1} and $\sigma = 10$ MPa. Thus, friction is lower than both the pure CGG and pure SDS cases, suggesting that the combination of cationic polymers and anionic surfactants provides synergistic friction behaviour.[522] The presence of surfactants is crucial to obtaining low friction, which is consistent with previous experiments of other polyelectrolyte-SDS complexes.[523]

Fig. 6.8 shows the mass density, charge density and velocity profiles for the various

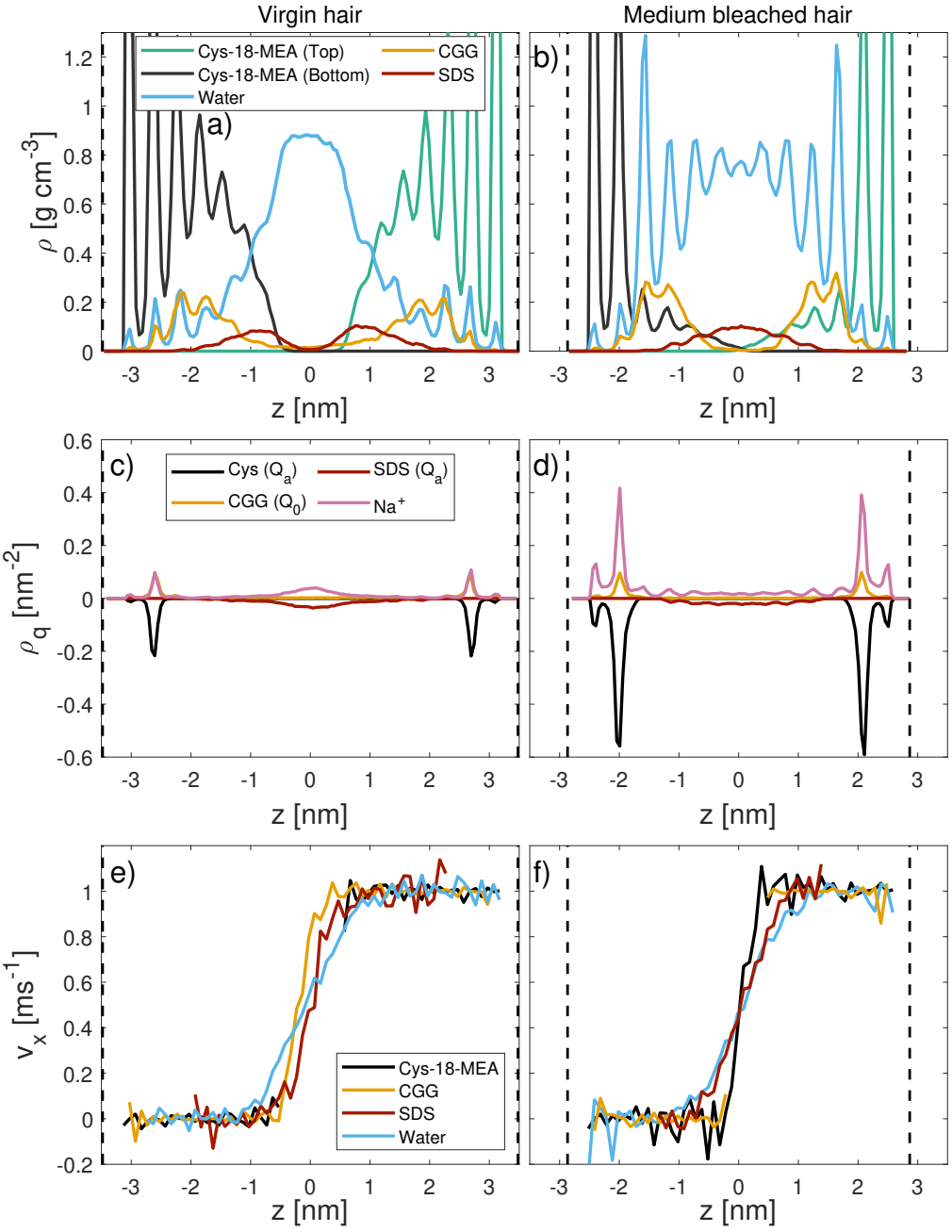


Figure 6.8: Through-film mass density, ρ(a,b), charge density, ρ_q (c,d), and velocity, v_x (e,f) profiles during sliding at $\sigma = 10$ MPa and $v_s = 1$ m s^{-1} for virgin (a, c, e) and medium bleached (b, d, f) hair.

components at the contact, including the covalently bound 18-MEA layers at $v_s = 1$ ms^{-1}. As reported in the previous chapters, we find the mass and charge density profiles are insensitive to the sliding speed. For virgin hair, a clear separation between the 18-MEA monolayers on the opposing surfaces is apparent at $\sigma = 10$ MPa and there is also a gap between the adsorbed CGG layers on each surface. The adsorbed SDS micelles break up during the squeeze-out stage and re-orient to form a reverse-bilayer structure,[524] which is evident from the distribution of the polar headgroup in the charge density profile in Fig. 6.8c). A transition from micelles to partially flipped bilayers under high loads has also been observed in previous experiments of cationic surfactants between mica surfaces.[480] The charge density profile for virgin hair reveals

that the anionic groups on SDS are predominantly oriented towards the center of the bilayer. Such a configuration is only stable due to charge neutralisation by the sodium counterions, which are localised at the middle of the contact. The formation of the reverse-bilayer structure can be explained by hydrophobic adsorption of the SDS tailgroups onto the 18-MEA monolayer. The water beads are concentrated mostly in the centre of the contact and retain a disordered structure. The increased water uptake in CGG-SDS treated systems compared to bare virgin hair is expected to be closely coupled to the reverse-bilayer of SDS which renders the surfaces more hydrophilic. The velocity profiles for virgin hair suggest that only the central $\sim$1 nm of the film is sheared, which contains almost exclusively water and SDS. The reduction in interdigitation, due to increased levels of retained water and SDS compared to untreated hair surfaces, is expected to contribute to the lower friction.

On medium bleached hair at $\sigma = 10$ MPa (Fig. 6.8b), the 18-MEA monolayers on the two opposing surfaces are slightly interdigitated. There is also some overlap of the strongly adsorbed CGG layers on the opposing surfaces. SDS is concentrated at the contact center in a single layer and the charge density profile (Fig. 6.8d) reveals a more disordered structure of SDS compared to the virgin hair case. A strongly layered water film ($d \approx 4$ nm) provides further surface separation. In chapter 4 we observed water layering in NEMD simulations of bare damaged hair surface mimics which was attributed to the anionic surface charges. Similar ordering has been observed in previous experiments of water under nanoscale confinement between cationic surfactant monolayers.[414] The relatively low degree of CGG adsorption in this work does not completely suppress this layering, despite introducing additional disorder to the system. The presence of somewhat less ordered water at the contact centre is expected to be beneficial for lubrication rather than increasing friction, as observed in pure water contacts on bleached hair in chapter 4. We expect that the presence of SDS at the bleached hair interface also leads to further friction reductions due to its repulsive effect and increase in physical separation, which seems to outweigh any dissipative contributions at the present conditions. Friction is further reduced by 18% at $v_s = 0.1$ ms^{-1} compared to the previous pure CGG simulations. Wu et al.[291] observed similar experimental friction reductions of CGG mixed with SDS compared to the pure CGG case. Hössel et al.[508] also reported wet combing work reductions between 10 and 50% for SLES shampoo formulations containing low CGG concentrations.

Overall, our results suggest that CGG promotes increased electrostatic SDS adsorption on the surfaces. This leads to increased surface separation at a given pressure. Therefore, friction observed in the CGG-SDS systems primarily arises from viscous dissipation in the fluid SDS/water layer at the sheared interface, rather than interdigitation between the rigid adsorbed CGG or grafted 18-MEA layers.

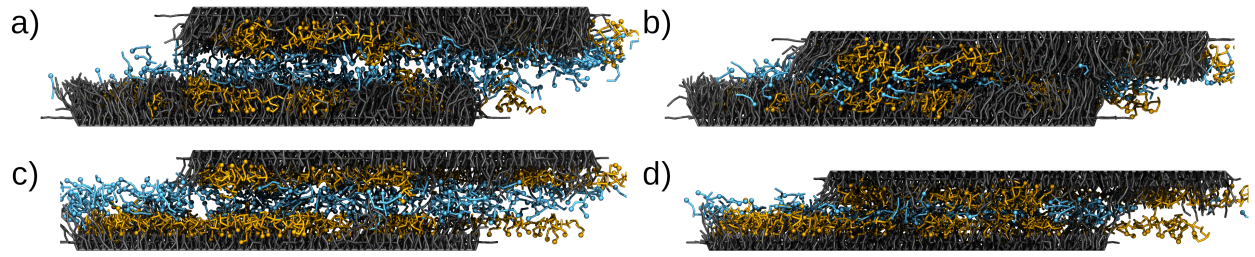


Figure 6.9: Snapshots of hair contacts with CGG (orange) and SDS (cyan) for virgin (a-b) and medium bleached hair (c-d) at normal stresses of $\sigma = 10$ MPa (left) and $\sigma = 50$ MPa (right) at $v_s = 0.1$ m s^{-1}. Water and counterions are not shown for clarity.

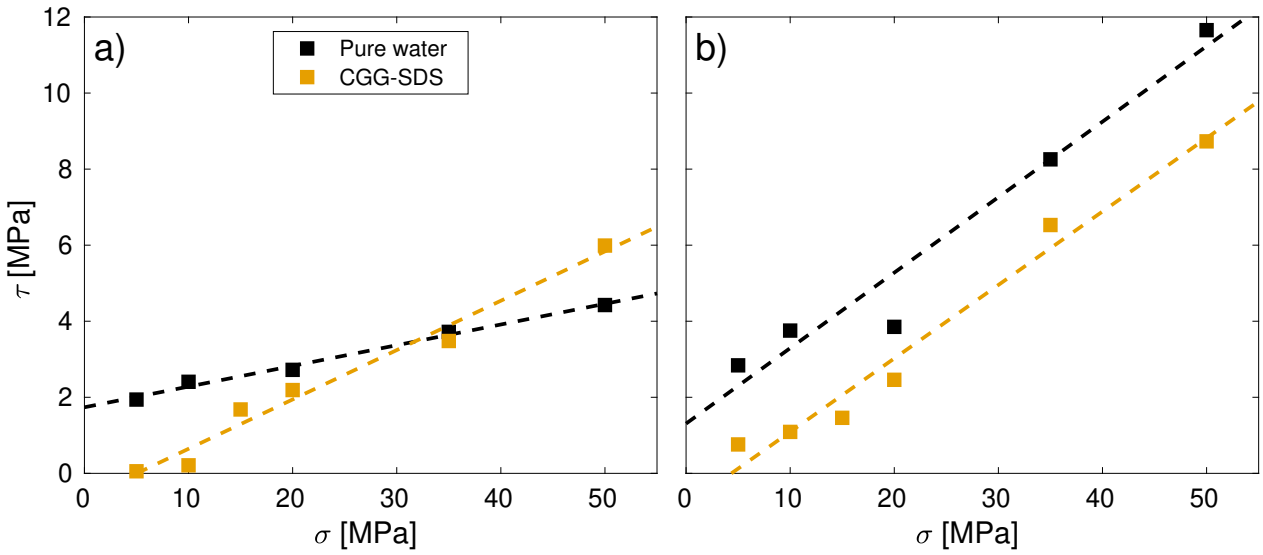


Figure 6.10: Shear stress as a function of the normal load at constant sliding velocity of $v_s = 0.1$ ms^{-1} for a) virgin and b) medium bleached hair surfaces with CGG (DS = 100%) and SDS at variable composition and for pure water cases. For comparison, the shear stress for pure water contacts is shown for comparison. Dashed lines are linear fits to the extended Amontons-Coulomb equation.

Effect of varying pressure

The change in the shear stress with normal stress is shown in Fig. 6.10 for a constant sliding velocity of v_s =0.1 ms^{-1}. Snapshots of virgin and bleached hair contacts at the baseline normal stress of 10 MPa and the maximum normal stress of 50 MPa are shown in Fig. 6.9. On both virgin and bleached hair, the shear stress for the CGG-SDS lubricated systems is very low ($\tau < 1$ MPa) at low normal stress ($\sigma < 10$ MPa), before increasing linearly with normal stress. This step-wise increase in shear stress with normal stress is consistent with previous experiments using a different polyelectrolyte-SDS complex to lubricate mica surfaces.[523] This means that the highest lubrication performance of the CGG-SDS is at low normal stresses (< 10 MPa). This regime is probably the most relevant to hair manipulation during touching, brushing, and combing.

The extended Amontons friction law (see Eq. 2.1) was applied to the data. The mass density profiles of the contact are shown in Fig. 6.11 for $\sigma = 20$-50 MPa ($\sigma = 15$ MPa omitted due to a lack of space) and in Fig. 6.8a)-b) for the baseline case at $\sigma = 10$ MPa. The corresponding charge density profiles are shown in Fig. A.4.24 in the appendix.

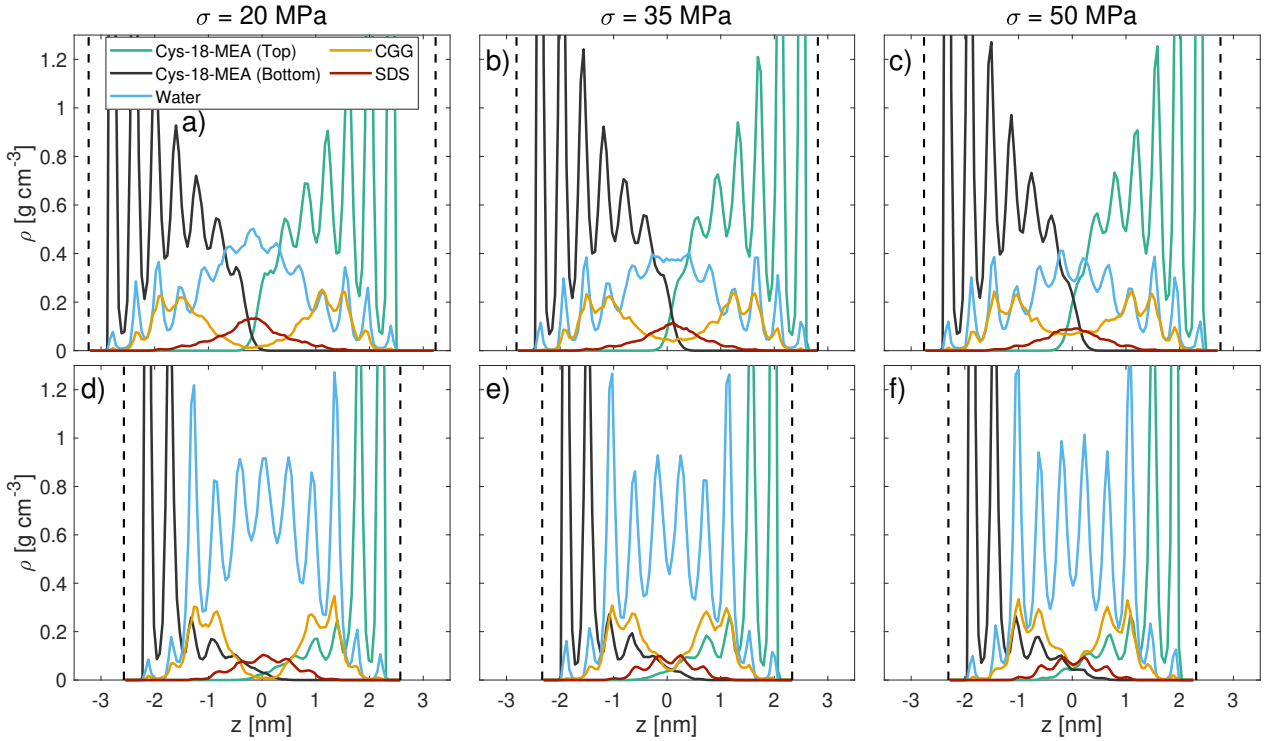


Figure 6.11: Through-film mass density profiles from NEMD of different normal stresses $\sigma = 20$-50 MPa on virgin (a-c) and medium bleached hair (d-f) at $v_s = 0.1$ m s^{-1}.

For all systems and conditions shown in Fig. 6.8, the shear stress is higher on medium bleached hair than virgin hair. However, the shear stress is more similar for the bleached and virgin hair when they are lubricated by CGG-SDS complex rather than water. On virgin hair, the shear stress, τ, of the CGG-SDS complex strongly increases with the normal stress, σ. At low normal stress ($\sigma < 35$ MPa), the CGG-SDS-lubricated contact shows lower shear stress than pure water; however, the trend reverses at higher normal stress. Thus, the CGG-SDS complex reduces the Derjaguin offset, but increases the friction coefficient compared to pure water. On bleached hair, the CGG-SDS complex reduces the shear stress by a similar amount at all normal stress values simulated. This means that CGG-SDS decreases the Derjaguin offset and maintains a similar friction coefficient to when the contact is lubricated by pure water. Thus, the main benefit of the CGG-SDS complex is a reduction in the Derjaguin offset, i.e. the shear stress at low normal stress, which is mainly due to adhesion. Indeed, previous experimental studies have shown that complexes formed from cationic polyelectrolytes and anionic surfactants can significantly reduce adhesion between negatively-charged silica surfaces.[517]

The mass density profiles in Fig. 6.11 suggest that the 18-MEA of the opposite hair surfaces become more interdigitated at higher normal loads. This is particularly evident on virgin hair model surfaces. This mechanical effect due to stronger compression is accompanied by a decrease of SDS and water at the interface from squeeze-out. On virgin hair, the SDS bilayer structure observed at $\sigma = 10$ MPa also vanishes at higher loads leading to a more disordered distribution of individual SDS molecules at the

interface. The removal of the fluid SDS and water layers and increase in CGG and 18-MEA interdigitation at higher normal stress lead to strongly increasing shear stress and thus relatively high friction coefficients. Higher CGG surface coverages might lead to increased SDS trapping and thus lower friction. Moreover, higher CGG surface coverages and lower CGG charge densities may enable more tails and loops to form, which could be important to lubrication.[508] These factors will be investigated in a future study.

Future extensions of this work could also investigate the adsorption, squeeze-out and friction of phase-separated polyelectrolyte-surfactant networks, or coacervates,[90,494] to hair surfaces, as has been studied experimentally.[161,291] However, additional method development is required to consider microscale aggregate sizes since the current squeeze-out setup is limited to systems in which all polyelectrolytes strongly adsorb to the surfaces so they remain within the contact. Moreover, the framework presented in this chapter could be applied to virtually screen the lubrication performance of a wide range of hair care formulations on biomimetic surfaces. By changing the surface model, the methodology can be readily extended to investigate other formulated products that contain polymer-surfactant complexes, such as in fabric softeners[488] or for drug delivery.[489]

6.4 Conclusions

In this chapter, we investigated the lubrication performance of adsorbed complexes formed from cationic polyelectrolytes and anionic surfactants between two hair surfaces using coarse-grained NEMD simulations. New *MARTINI 2* parameters of guar hydroxypropyltrimonium chloride were developed by employing existing mappings and bead types for saccharides and fine-tuning the bond and angle interactions using Boltzmann inversion from atomistic simulations with the OPLS force field. The new *MARTINI 2* parameters are able to reproduce the probability distribution functions for the relevant bonds and angles from the atomistic simulations. The power-law scaling of the guar radius of gyration with molecular weight seen experimentally is also reproduced with the new *MARTINI 2* parameters.

In the MD simulations, short CGG polymers were first deposited onto biomimetic surfaces representing virgin and medium bleached hair at an adsorption density similar to that measured experimentally for another cationic polysaccharide. Due to computational constraints, we limit ourselves to the study of relatively short CGG polymers with a high charge density. The cationic groups on CGG strongly adsorbed to the anionic groups on the hair surfaces, leading to a mostly flat train conformations. This observation is in agreement with experiments for high charge density cationic polyelectrolytes on anionic-functionalized surfaces. Next, we introduced the anionic surfactant SDS to the hair surfaces containing adsorbed CGG. SDS predominantly adsorbed as intact cylindrical micelles, binding to the cationic sites on CGG that were

not attached to the anionic groups on the hair surfaces. We observe some swelling of the CGG layers upon addition of SDS, but far less than is seen experimentally. This discrepancy might be due to the relatively high charge density and small degree of polymerization of the polyelectrolytes used in our simulations. Another factor is the relatively low polyelectrolyte surface coverage studied, which means that the negative surface charge is not overcompensated by CGG.

We then performed squeeze-out and NEMD simulations between two hair surfaces containing adsorbed CGG and SDS. Pure CGG was found to reduce shear stress at high sliding velocity compared to pure water, but increased shear stress and stick-slip amplitudes at low sliding velocity. This was likely caused by the heterogeneous distribution of strongly adsorbed CGG and the resulting oscillatory interactions of hydrophilic CGG sites sliding relative to each other across the otherwise hydrophobic 18-MEA monolayers. On bleached hair, pure CGG reduced friction considerably compared to untreated contacts at all sliding velocities.

The CGG-SDS complexes significantly reduced the shear stress on both virgin and medium bleached hair compared to water, pure CGG, and pure SDS across all the sliding velocities considered. Thus, there is synergistic lubrication performance for the CGG-SDS complex compared to CGG and SDS. CGG strongly adsorbs to the hair surface, neutralising the surface anionic groups and providing cationic sites for the adsorption of SDS micelles. The adsorbed SDS micelles provide a direct lubrication effect, while also leading to a hydrophilic-induced increase of water trapped within the contact. At low normal stress, friction is dominated by viscous dissipation in the fluid SDS and water interfacial layer. With increasing normal stress during squeeze-out, an larger fraction of SDS and water are depleted from the contact. This means that the highest lubrication performance of the CGG-SDS is at low normal stresses (< 10 MPa). This regime is probably the most relevant to hair manipulation during touching, brushing, and combing. On virgin hair, the shear stress of the CGG-SDS complex eventually exceeds that of pure water at high (> 30 MPa) normal stress. Thus, CGG-SDS leads to a decrease in Derjaguin offset, but an increase in friction coefficient on virgin hair. On bleached hair, the shear stress with CGG-SDS remains lower than for water under all studied normal stresses. In this case, CGG-SDS leads to a reduction in Derjaguin offset and a similar friction coefficient as for water. The friction coefficient becomes less sensitive to hair damage for CGG-SDS lubricated contacts.

The computational framework presented in this chapter is expected to be useful for benchmarking a wider range of polymers and surfactants for their relative lubrication performance on hair surfaces. It can also be readily extended to screen the performance of other formulations where polyelectrolyte-surfactant complexes play and important role. In the following chapter, we will discuss effect of various system and polyelectrolyte properties of CGG including the adsorption density, chain length, charge density and

charge functionalization on nanoscale hair friction with SDS.

7 Polyelectrolyte architecture effects on the lubricity of polyelectrolyte-surfactant layers on biomimetic hair surfaces

7.1 Introduction

In the previous chapter, the boundary lubrication performance between two biomimetic hair surfaces in the presence of thin layers of oppositely charged polyelectrolyte-surfactant complexes was assessed. This feasibility study provided fundamental insights on how short cationic polymers at low adsorption densities decorated with anionic surfactants can drastically reduce friction. Typically, hair care formulations such as shampoos deposit conditioning agents with lower charge density and higher molecular weight to the hair surface. Previous experiments of the adsorption from oppositely charged polyelectrolyte-surfactant formulations reported conditioner film thicknesses up to several microns on hair[123,297] which is much larger than those investigated in the last chapter. This suggests that thin-film adsorption is not always possible in real world applications. One reason for this observation is the prevalence of dilution deposition of formulations containing oppositely charged polyelectrolytes and surfactants as a central mechanism for hair conditioning from shampoos as highlighted in chapter 2 and elsewhere.[18,19] Capturing such scales and complexes in MD-only simulations is currently deemed infeasible, at least at the level of coarse-graining used by the MARTINI forcefield. However, somewhat larger aggregates are expected to be feasible, as has been demonstrated recently elsewhere.[36] Recently, coacervation[494,525,526] and surface interactions[36] of smaller aggregates have been captured successfully using MARTINI. However, interfacial simulations with macromolecules on solid or soft substrates are likely to require simplifications such as a reduced size of the involved molecules.

In this chapter, different polyelectrolyte properties will be varied systematically. We first investigate the effect of the polyelectrolyte adsorption density on adsorption, complexation and hair lubrication using the short, highly charged CGG chains used in the previous chapter. Then, lower, more realistic charge densities will be considered. Finally, the lubrication efficiency of longer CGG chains with a realistic charge density is probed which is also expected to lead to a variation in the CGG composition during the squeeze-out stage. This systematic parameter variation is expected to allow for further fine-tuning of the polysaccharide synthesis process for hair care products with a low-friction performance. It might also serve as guidance for choosing polymers other than guar or related surfactants such as glucolipids for further screening with respect to their conditioning performance.

7.2 Methodology

All simulation parameters in this chapter are consistent with those discussed in the previous chapter unless specified otherwise. CGG and SDS as pre-assembled micelles are used in solution together with the polarizable *MARTINI* water model.

7.2.1 Cationic guar gum model

a) CGG parameter variation study

An overview of the systems considered for adsorption, squeeze-out and NEMD simulations is shown in Table 7.1. Previously, we considered a CGG degree of substitution (DS) of 100%, meaning a quaternary ammonium functionalization on every galactose side branch. In the next step, additional DS of 10 and 50% are considered (cases I-II). This is closer to CGG degrees of substitution in the range of 4 to 30% as reported in the literature.[491,506] Next, a higher CGG adsorption density, $\Gamma = 0.04$ µg cm^{-2}, is considered (case IV), as thicker polyelectrolyte layers have also been observed upon dilution.[19] Similar adsorption densities were previously reported for CGG on charged hair mimic surfaces using QCM-D and ellipsometry measurements.[507] Finally, we consider two CGG configurations with an increased chain length of N = 100, DS = 30% and higher adsorption densities. A baseline adsorption density of $\Gamma = 0.13$ µg cm^{-2} was considered (case V), which about three times higher than the value considered in the previous chapter ($\Gamma = 0.04$ µg cm^{-2}). An even higher forced deposition adsorption density of $\Gamma = 0.26$ µg cm^{-2} is also considered (case VI) which is expected to form multilayers of CGG on both virgin and bleached hair.

For this last set of test cases case V and VI, it is worth noting that another modification was implemented in the CGG model: Recently, other studies reported improvement in the aggregation behaviour of coarse-grained polysaccharides[490,497] by reducing the self-interaction LJ energy ε. Consequently, the Lennard-Jones (LJ) self-interaction energy for CGG chains in cases V and VI was scaled down by 10% compared to the polarizable MARTINI force field parameters presented in the previous chapter and used in cases I through IV. It is worth noting that this is not expected to fundamentally affect the results shown in the previous chapter as those were conducted with a higher CGG charge density, which would lead an adsorption behaviour dictated by the anionic surface sites. For the more weakly charged polysaccarides considered in this chapter, this is however expected to lead to a more realistic formation of tails and loops on the surface. The radius of gyration of non-ionic guar gum is as a function of the polyelectrolyte molecular weight M_w is shown in Fig. A.4.22 in the appendix for both the unscaled and scaled chains and for previous experiments with non-ionic guar gum due to Liang et al.[497] The radius of gyration increased by an average 37% in the range of $M_w = 24{,}000$-97,000 g mol^{-1} compared to chains with a nominal LJ self-interaction strength. However, R_g is still somewhat underestimated compared to the experiments. The LJ self-interaction strength scaling is not expected to have considerable effects on the NEMD

Table 7.1: Overview of test cases for the CGG architecture parameter study. The baseline case (III) as presented in chapter 6 is denoted in bold.

Test case	N_{mon}	DS	Charge distribution	$\Gamma_{0,CGG}$
I	50	10%	Regular	0.04 µg cm^{-2}
II	50	50%	Regular	0.04 µg cm^{-2}
III	**50**	**100%**	**Regular**	**0.04 µg cm^{-2}**
IV	50	50%	Regular	0.12 µg cm^{-2}
V	100	30%	Regular/Random/Markov	0.13 µg cm^{-2}
VI	100	30%	Regular/Random/Markov	0.26 µg cm^{-2}

simulations of shorter, strongly adsorbed chains in the previous chapter, longer chains with a reduced charge density might be more prone to the formation of loop structures upon adsorption to hair.

b) Charge distribution models

In reality, the cationic functionalization process of native guar gum to CGG is expected to influence the charge distribution of the latter. The most common synthesis approach is an etherification reaction of 2,3-epoxypropyltri-methylammonium chloride with hydrochloric acid and subsequent attachment to native guar.[527,528] However, some uncertainty remains regarding the attachment position and the distribution of quaternary ammonium groups on CGG. Concentration gradients in the solvent could lead to a more blocky functionalization as opposed to a fully random polymer charge distribution. Three different polymer architectures were therefore considered for the final two test cases (V/VI) with longer, moderately charged CGG chains:

1. Fully random charge distribution,
2. A Markov chain model approach, and
3. A regular charge functionalization pattern.

1) and 2) were run with a charge density equivalent to DS=30%. The regular distribution represents a quaternary amine functionalization on every third monomer (DS=33%) For 2), a first-order Markov chain polymerization model was used for constructing polymer chains. The conditional probability matrix for the next monomer in the chain is defined as:[126]

$$P = \begin{bmatrix} p_{++} & p_{+0} \\ p_{0+} & p_{00} \end{bmatrix} = \begin{bmatrix} 1-(1-\lambda)(1-f) & f(1-\lambda) \\ (1-\lambda)(1-f) & 1-f(1-\lambda) \end{bmatrix} \tag{7.1}$$

where p_{ij} denotes the conditional probability that a monomer of type j is followed by a monomer of type i.[126] Here, we consider either charge-neutral (0) or cationic, quat-functionalized monomers (+). The individual probabilities arise as a function of the target DS, f, and the correlation parameter, $\lambda \in [0,1]$, where a higher λcorresponds to a more blocky behaviour. The DS and correlation parameter are linked to polymerization process properties such as the monomer feed ratio and reactivity ratios.[126] It is worth noting that this model is only valid for copolymerization in theory which is not the synthesis approach for CGG. However, this pragmatic approach still allowed

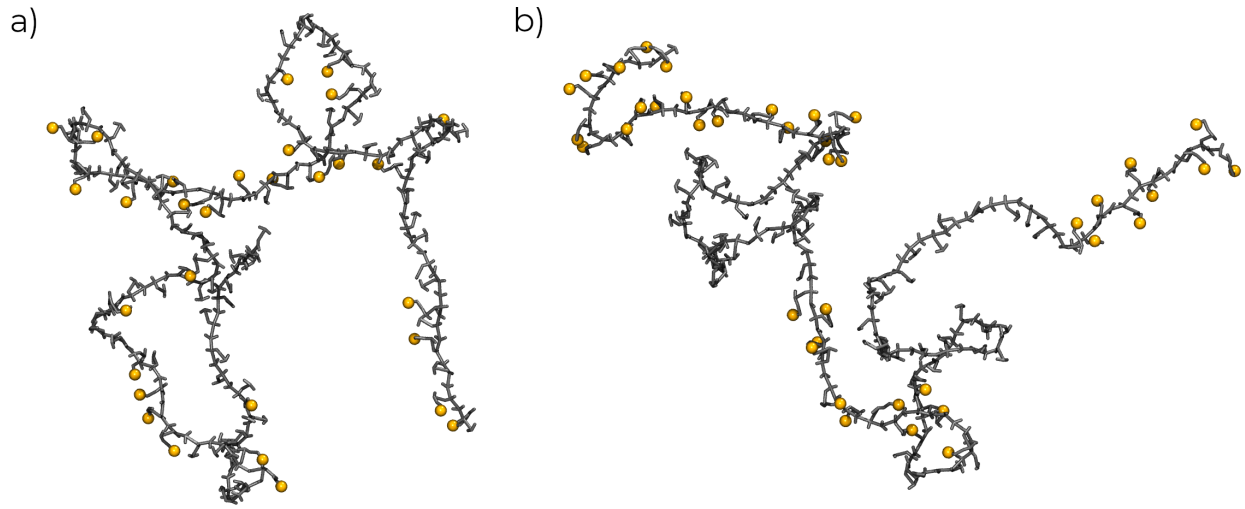


Figure 7.1: Snapshots of coarse-grained CGG chains with a fully random charge functionalization and a blocky functionalization from a first-order Markov chain model.

us to qualitatively mimic a stochastically blocky CGG architecture without resorting to more realistic, but also computationally more costly approaches such as kinetic Monte Carlo.[529] With a target DS of $f = 0.3$, we found a correlation parameter value of $\lambda = 0.9$ to yield a reasonably blocky structure as shown in Fig. 7.1

Initial conformers were generated using a self-avoiding random walk routine. For each system, all polymers were functionalized individually in the case of randomly distributed charges and Markov chains. The cationic functionalization is restricted to only the hydroxymethyl group of the galactose sidechains for all polymers. The effect of varying the functionalization position on adsorption and nanoscale tribological properties could be a valuable addition for future works.

7.2.2 Simulation protocol

The simulation protocol introduced in chapter 6 is adopted in this chapter. Polyelectrolytes and SDS are again sequentially deposited to virgin and bleached model hair surfaces. Additionally, a forced deposition approach was employed for the initial CGG adsorption step in order to reach the surface adsorption of all polyelectrolytes in the bulk. This is different to other computational studies, e.g., Ref.[267] where excess polymers were removed from the bulk upon reaching equilibrium. A weak spring force ($k = 2$ kcal mol^{-1} Å^{-2}) is applied to the polymers in the surface-normal direction with a tethering point on the hair surface. Once all guar chains are fully adsorbed, the system is relaxed for another 2.5 ns by switching off the spring force. SDS was subsequently added in bulk at the previously used concentration of $c = 664$ mM.

SDS adsorption simulations were run for 50 ns. The increase of both the CGG chain length and the target adsorption densities led to a substantially larger simulation box size in the z direction during adsorption (up to $\mathcal{L}_z = 38$ nm) and squeeze-out simula-

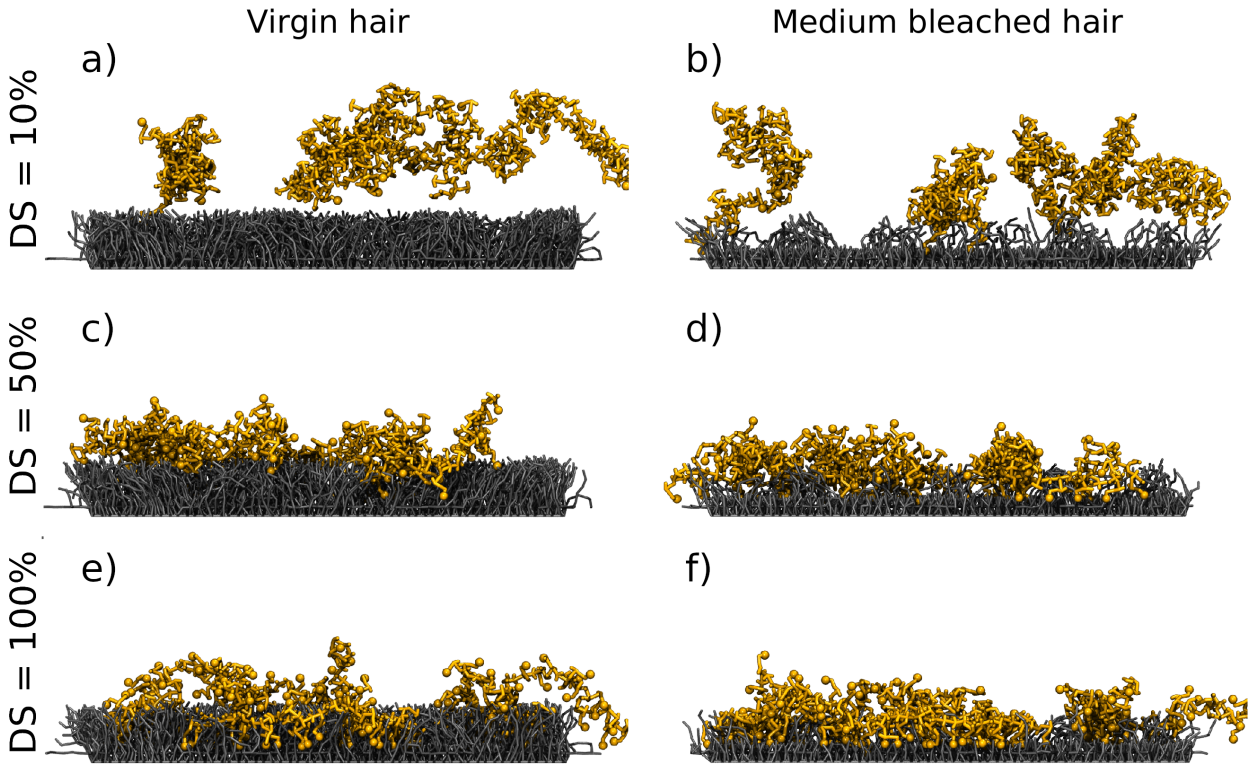


Figure 7.2: Snapshots of CGG at various charge densities, DS = 10%-100%, at the end of the CGG adsorption stage for virgin (left) and medium bleached hair (right).

tions. The substrate surface area is consistent with the previous chapters. During the squeeze-out stage, no constraints were applied to either CGG nor SDS, thus allowing for depletion from the contact. Upon equilibrium, the contact composition and thickness were extracted. Partial squeeze-out of CGG is expected for cases with low polymer charge density (I, V, VI) as opposed to the observations in the previous chapter. The number of CGG chains for the NEMD simulations was rounded to the nearest even number obtained from squeeze-out to obtain the same number of polymers on each surface for symmetry. For NEMD simulations, excess CGG chains were removed based on their distance from the substrate. CGG deletion was performed on the output of the CGG adsorption stage which retains the system periodicity in x and y. SDS and water were then introduced in a slab at the center of the contact with the updated composition from squeeze-out. Semi-periodic NEMD simulations were run at a fixed sliding velocity of $v_s = 0.1$ ms^{-1} and a contact pressure of $\sigma = 10$ MPa. For the cases with increased chain length and realistic CGG charge density, were also consider higher normal loads up to $\sigma = 50$ MPa. All remaining force field cutoffs, electrostatics and numerical integration settings in LAMMPS were adopted from the previous chapters.

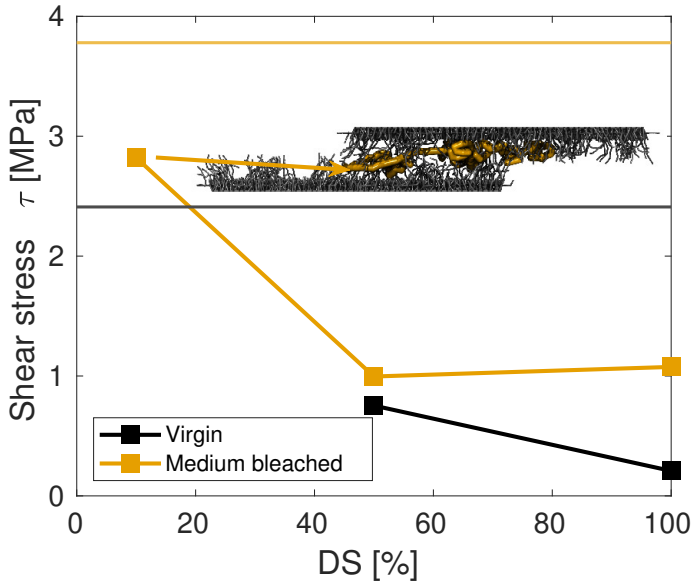


Figure 7.3: Coefficients of friction from NEMD of different charge densities on CGG with SDS on virgin and medium bleached hair at $\sigma = 10$ MPa and $v_s = 0.1$ ms^{-1}. For reference, horizontal lines indicate the shear stress obtained on bare hair surfaces with water.

7.3 Results and discussion

7.3.1 Effect of the polymer charge density

The effect of the polyelectrolyte charge density is expected to influence both surface deposition[122] and friction.[36] We therefore performed additional adsorption, squeeze-out and friction simulations with CGG at reduced charge densities corresponding to a degree of substitution (DS) of 10% and 50% (cases I and II). Snapshots of of CGG at different charge densities on virgin and bleached hair model surfaces at the end of the CGG adsorption stage are provided in Fig. 7.2. CGG strongly adsorbs for DS = 50% and 100% (case II/III). The CGG film thickness strongly decreases with increasing DS. This is consistent with previous studies showing that increasing the charge density of CGG resulted in a more compact layer.[506] For DS = 10%, CGG only weakly adsorbs on bleached hair but does not adsorb to virgin hair surfaces. This leads to all CGG chains being depleted from the contact during squeeze-out on virgin hair. For medium bleached hair, a partial squeeze-out was observed. The guar depletion on virgin hair indicates that CGG chains with DS = 10% are not ideal for providing a conditioning effect on virgin hair when deposited by itself, or sequentially with SDS. Due to the relatively low initial number of guar molecules present in this system, we cannot fully rule out the possibility that guar molecules could be trapped at adsorption densities density below that of a single chain confined between two of our finite model surfaces. Further evaluations would require much larger surfaces which is out of the scope of the present work.

NEMD simulations were run at a baseline pressure of $\sigma = 10$ MPa and a sliding velocity of $v_s = 0.1$ ms^{-1}. Figure 7.3 shows the coefficient of friction for the three degrees of the CGG charge density on virgin and medium bleached hair surfaces. No data is reported

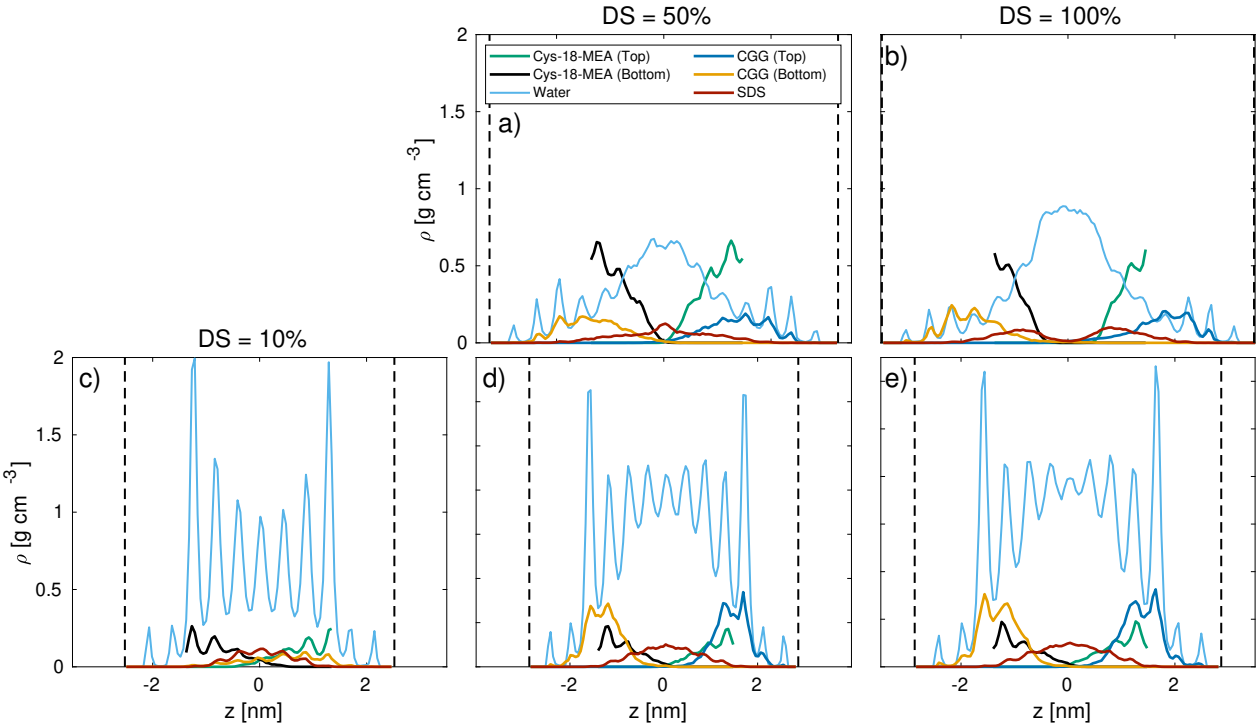


Figure 7.4: Mass densities profiles from NEMD of different charge densities on CGG with SDS on virgin (top row, a-b) and medium bleached hair (bottom row, c-e) at $\sigma = 10$ MPa and $v_s = 0.1$ m s^{-1}.

for the low-charge density guar on virgin hair as all CGG was removed from the contact during squeeze-out. On virgin hair, friction reductions are observed from DS = 50% to DS = 100%. The corresponding mass density profiles for virgin and bleached hair are shown in Fig. 7.4. The lower charge density on guar leads to moderate reductions in SDS ($\rho = 0.97$ nm^{-2}) and water content ($\rho = 13.5$ nm^{-2}) in the virgin hair contact. As a result, the separation between opposite 18-MEA monolayers is considerably reduced. The characteristic bilayer configuration on SDS also disappears at the lower DS. A single peak in the SDS distribution suggests that SDS is more disordered, which might limit the previously discussed charge repulsion effects together with the overall reduced number of SDS molecules in the contact. Little interdigitation is observed between the guar molecules from the opposing surfaces, which is in agreement with the high-charge density results.

On medium bleached hair, the low-charge density guar also adsorbs via few charged sites on the surfaces as evident from Fig. 7.2. This leads to a partial squeeze-out and a guar adsorption density of $\Gamma \approx 0.02$ µg cm^{-2} which corresponds to two whole polysaccharides per surface. Surface area densities of $\rho_{SDS} = 0.74$ nm^{-2} and $\rho_W = 19.0$ nm^{-2} are found for SDS and water at DS = 10%. At a DS of 50%, all guar molecules remained inside the contact during squeeze-out. The corresponding SDS and water area densities within the contact equal $\rho_{SDS} = 0.86$ nm^{-2} and $\rho_W = 21.5$ nm^{-2} respectively, which is nearly identical to the values for the fully substituted guar polymers reported in the previous chapter. Strong friction reductions on bleached hair are observed between DS = 10-50%, while friction is nearly constant in the range of DS = 50-100%. The

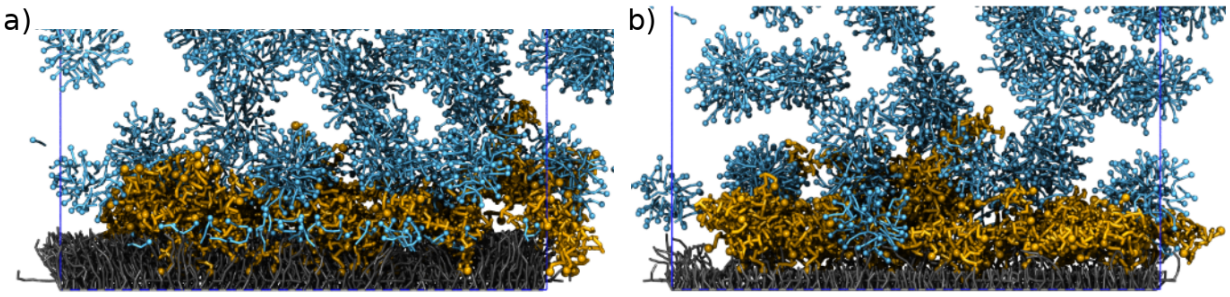


Figure 7.5: Snapshots of adsorbed CGG at $\Gamma = 0.12$ µg cm^{-2} and SDS at the hair interface for a) virgin and b) bleached hair surfaces.

initial friction reductions can be explained by an increase of the guar and SDS mass inside the contact and by the asymmetric slip of the remaining guar molecules in the low-charge density contact, as evident from the snapshot in Fig. 7.3. Due to the low surface separation, guar can temporarily adsorb on both surfaces simultaneously. During sliding, the molecule is then stretched in the direction of sliding and eventually desorbs on one side of the contact, which is expected to create strong dissipative contributions as a secondary slip plane is introduced. Nonetheless, the observed friction coefficient at low guar charge density is somewhat decreased compared to the untreated model hair surface (-24%). This shows that the low guar adsorption densities (DS = 10%) coupled with a weak binding of SDS is still moderately effective at reducing hair friction, although this cannot fully recover the lubrication performance of virgin hair in chemically damaged hair contacts.

Between 50% and 100% of degree of substitution, the structure of the bleached hair contacts does not change considerably, with similar degrees of water and SDS content confined within the contact during sliding. This is in good agreement with the observed coefficients of friction. Compared to the untreated bleached hair contacts, friction is reduced by 73% at DS = 50%. These results indicate that a DS of 50% is indeed sufficient to obtain considerable improvements in the lubrication performance on bleached hair at the given adsorption densities.

7.3.2 Effect of the polymer adsorption density

We will now investigate the effect of the CGG adsorption density on SDS deposition, squeeze-out and hair friction. In the baseline simulations presented in the previous chapter, the majority of negative surface charges was balanced by adsorbed counterions rather than by cationic polysaccharides. This is a result of complete adsorption of the few polymers available in the finite-size simulation bulk. Experimental QCM-D adsorption studies of similar cationic polysaccharides (JR400) on biomimetic charge-functionalized thiol layers conducted by Guzmán et al.[507] suggest a threefold increase in adsorption densities compared to the value on uncharged thiols. A strong increase in adsorption density of cationic surfactants on bleached hair compared to virgin hair was also observed in chapter 5. It is therefore reasonable to assume, that chemical

damage to the hair surface will increase the affinity and equilibrium adsorption density of larger cationic polysaccharides such as guar.

We therefore conducted simulations with increased guar adsorption densities of $\Gamma = 0.12$ µg cm^{-2} on bleached hair surfaces. This is similar to the adsorption densities reported for JR400 on functionalized thiols due to Guzmán et al.[507] Virgin hair surfaces are also considered at this adsorption density for completeness but may be of less relevance, as the adsorption is expected to be closer to the value discussed above. Snapshots of the adsorbed structures are shown in Fig. 7.5. Upon addition of an SDS bulk, SDS micelles migrate to the surface and electrostatically adsorb to the cationic sites on the polysaccharide layer. In the presence of SDS, the CGG layer thickness on virgin and bleached hair surfaces is 6.5 nm and 2.5 nm respectively. Previous experiments of oppositely charged polymer-surfactant structures on hydrophilic surfaces[530] also reported swelling of the adsorbed networks which could provide brush-like conformations with favorable lubrication properties. The degree of swelling of CGG when exposed to the SDS bulk is shown in Fig. 7.6. Negligible changes in the surface-normal mass density profiles are observed even at long times ($t > 70$ ns) in the present configurations. This might be due to the relatively high charge density of the polysaccharides (DS = 50%) resulting in a high number of electrostatically adsorbed quaternary amonium group and strong attractive forces to the substrate. Longer polymers, increased adsorption densities or reduced CGG charge densities might be required to observe this effect. Such systems will be considered in the next section. It is also worth noting that no direct entropy-driven counterion release was observed here from either CGG or SDS micelles. This mechanism has been observed during coacervation in both experiments[118] and coarse-grained bulk simulations[494] but may require much longer simulation times to take effect.

The shear stress for virgin and bleached hair as a function of the guar adsorption den-

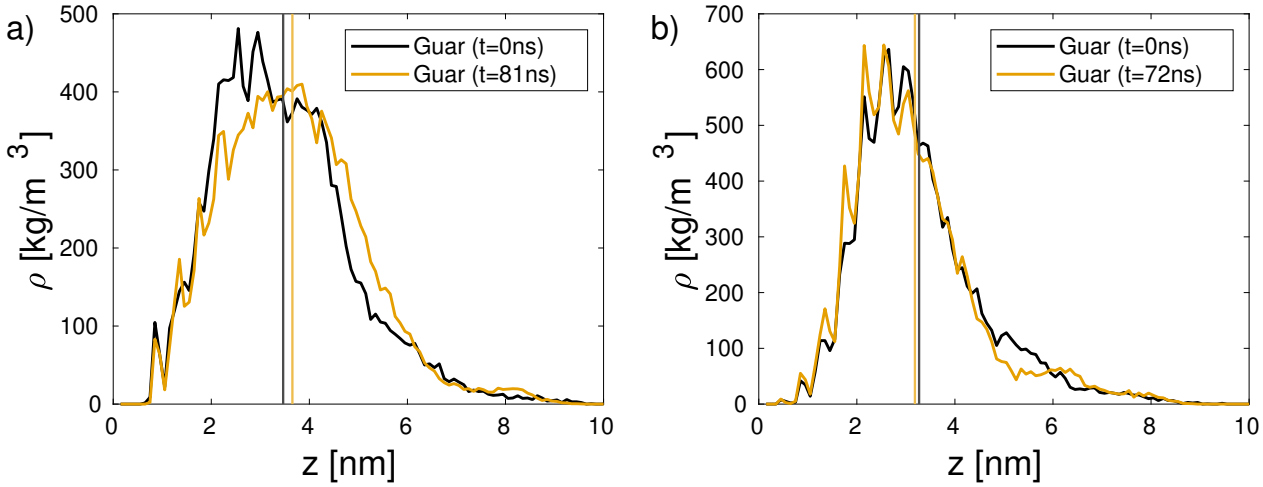


Figure 7.6: CGG mass density profile at $\Gamma = 0.12$ µg cm^{-2} on a) virgin and b) bleached hair in the presence of SDS as a function of time. Vertical lines indicate the guar center of mass at the respective time.

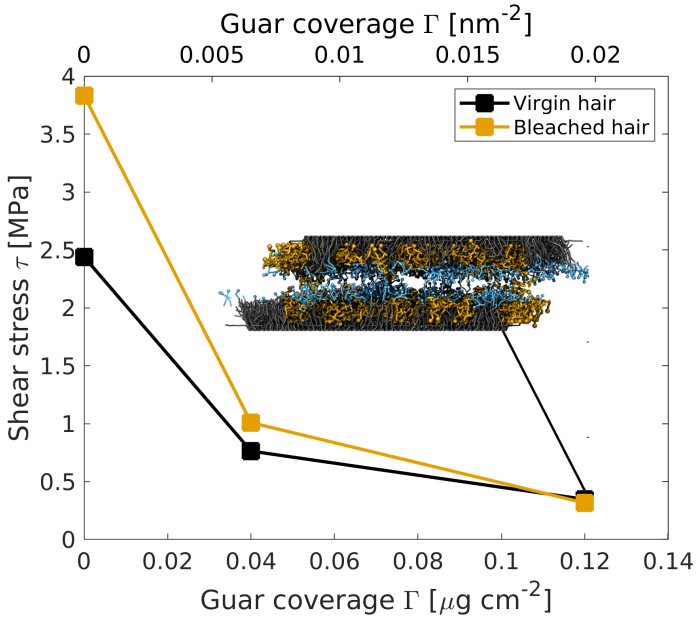


Figure 7.7: Shear stress as a function of the guar adsorption density with SDS for virgin and medium bleached hair at $v_s = 0.1$ ms^{-1} and $\sigma = 10$ MPa.

sity ($\Gamma = 0$-0.12 µg cm^{-2}) with SDS are shown in Fig. 7.7. We find further friction reductions at the highest guar coverage considered here ($\mu = 0.031$-0.034). The absolute shear stress also becomes less sensitive to the degree of hair damage. Fig. 7.8 provides insights into the structure of the contacts with elevated guar adsorption densities. The mass density profiles suggest full surface separation for both virgin and medium bleached hair by means of a thick water layer. As with the previous simulations, SDS is hydrophobically adsorbed on top of the guar and 18-MEA on virgin hair, allowing for higher water uptake during squeeze-out. On virgin hair under compression, the majority of guar is confined between the covalently bound 18-MEA. The water content in this region is considerably reduced compared to the contact centre which is probably a result of the applied compression. This is similar to what is commonly observed in hydrogels, which release water under applied normal or shear stress. To quantify, whether the applied shear or normal stress is responsible for this conformational change compared to the single surfaces, we compared the mass density profiles of the contact before squeeze-out, before the beginning of the NEMD and at dynamic equilibrium in the NEMD simulations. The respective mass density profiles on virgin hair are provided in Fig. A.5.25 in the appendix and suggest that the conformational change occurs during compression of the two surfaces in the squeeze-out simulations. For medium bleached hair, the water depletion from the guar-dense region is less pronounced. This is because of the compression-induced intercalation of guar with the dense 18-MEA monolayer on virgin hair, which is mostly removed on bleached hair. Overall, a further increase in the guar adsorption density does lead to further friction reductions at physiologically relevant normal loads and sliding velocity.

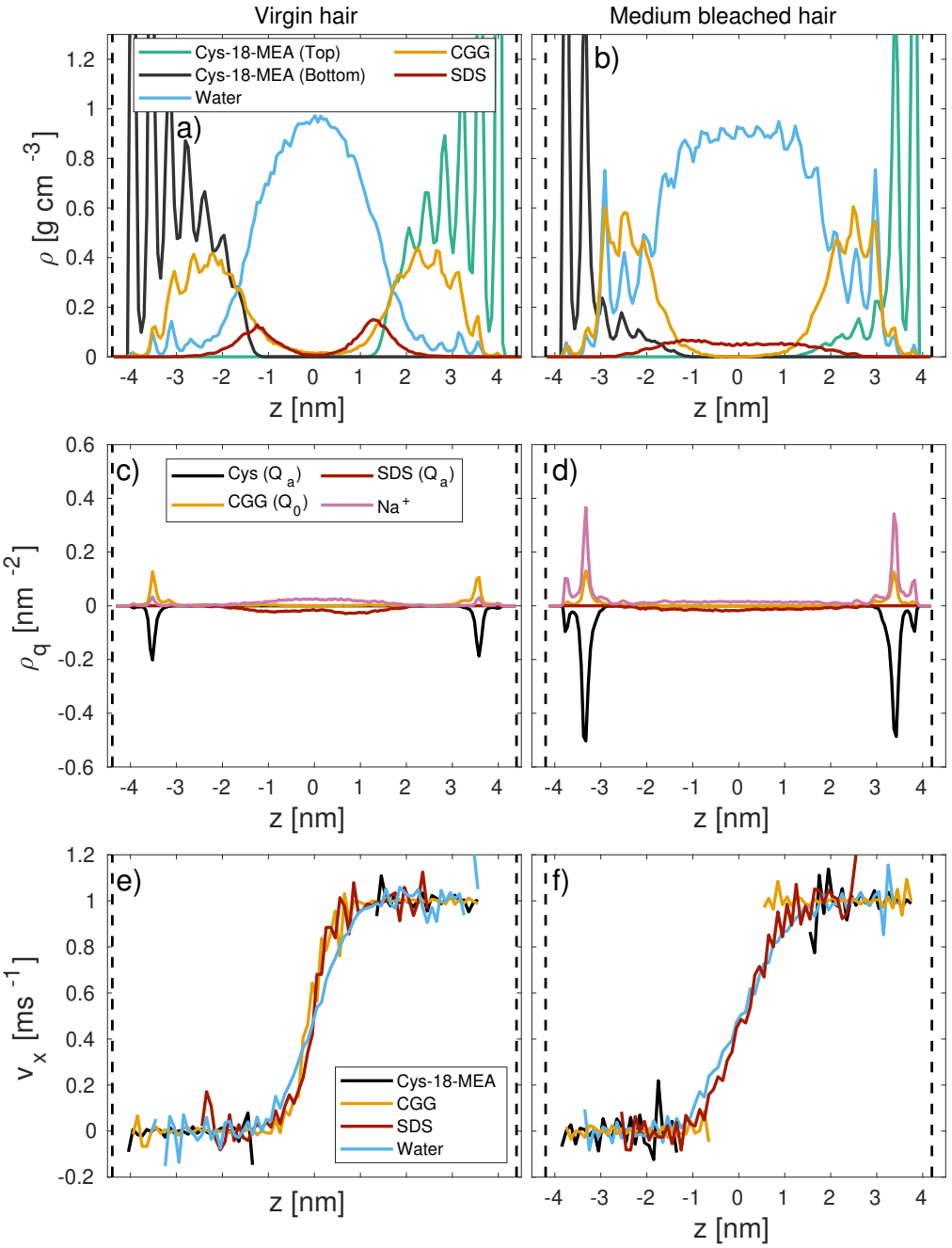


Figure 7.8: Through-film mass density, ρ (a, b), charge density ρ_q (c, d), and velocity, v_x (e, f) profiles at $v_s = 1$ m s^{-1} for virgin (a, c, e) and medium bleached hair (b, d, f) at an elevated guar adsorption density $\Gamma = 0.12$ µg cm^{-2}.

7.3.3 Towards friction screening with realistic CGG chains

In this section, CGG with a DS of approximately 30% and a chain length of 100 are considered for deposition and NEMD simulations. First, the effect of different CGG charge functionalizations and surface area densities a will be discussed in the context of forced deposition before performing NEMD simulations on a select case.

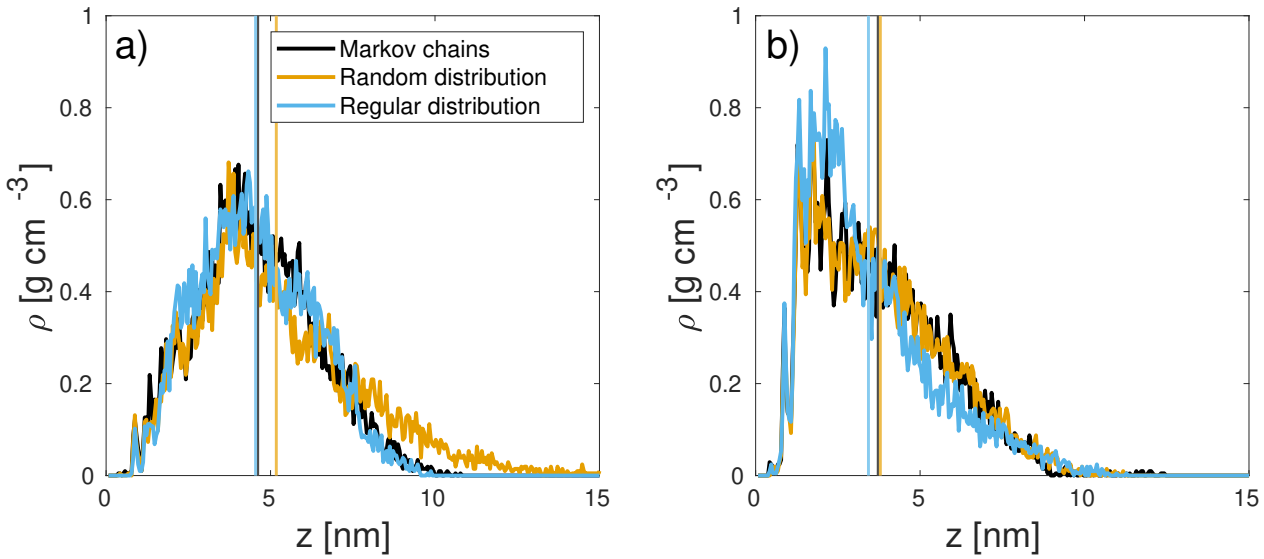


Figure 7.9: Instantaneous mass density profiles for adsorbed CGG on (a) virgin and (b) bleached hair for various functionalization architectures at a CGG adsorption density of $\Gamma_0 = 0.26$ µg cm^{-2} (case VI). Vertical lines indicate the center of mass of the adsorbed layers in z.

a) CGG charge distribution effects

We first investigate the effect of the polyelectrolyte functionalization architecture on CGG adsorption. The mass density profiles for random, regular and blocky charge functionalizations are shown in Fig. 7.9. Only profiles for the high adsorption density case are shown since this is the case where the difference in functionalization would be expected to be most pronounced. Interestingly, no strong differences in the mass density profiles are observed across the three different CGG architectures on both virgin and medium bleached model hair surfaces. On virgin hair, the random conformation protrudes slightly further into solution which is considered to be within the range of uncertainty of temporal averaging. Therefore, the blocky (Markov chain) and regular architectures were discarded after the CGG adsorption stage and only random chains were considered for the next steps. It is worth noting that other variations in the polymer architecture such as the backbone flexibility, the degree of branching and the backbone hydrophobicity might also fundamentally change the adsorption behaviour as reported in recent CG-MD adsorption simulations[266,267] could be interesting topics for future work.

Once SDS is introduced, surfactant micelles bind to the exposed anionic sites. The reduced CGG charge density and increased adsorption densities make the polyelectrolyte layer more prone to SDS-induced swelling, as shown for mass density profiles at the beginning and end of the SDS adsorption stage in Fig. 7.10 A shift in the CGG center of mass is observed on both virgin ($\Delta z = 1.7$ nm) and bleached hair ($\Delta z = 0.7$ nm) after 50 ns of simulation time. The swelling is more pronounced on virgin hair as CGG is less strongly adsorbed as a result of the reduced number of available anionic sites on the surface. Overall, the swelling is still moderate compared to experimental studies, where the film thickness was found to increase by multiples of the initial value.[19,122]

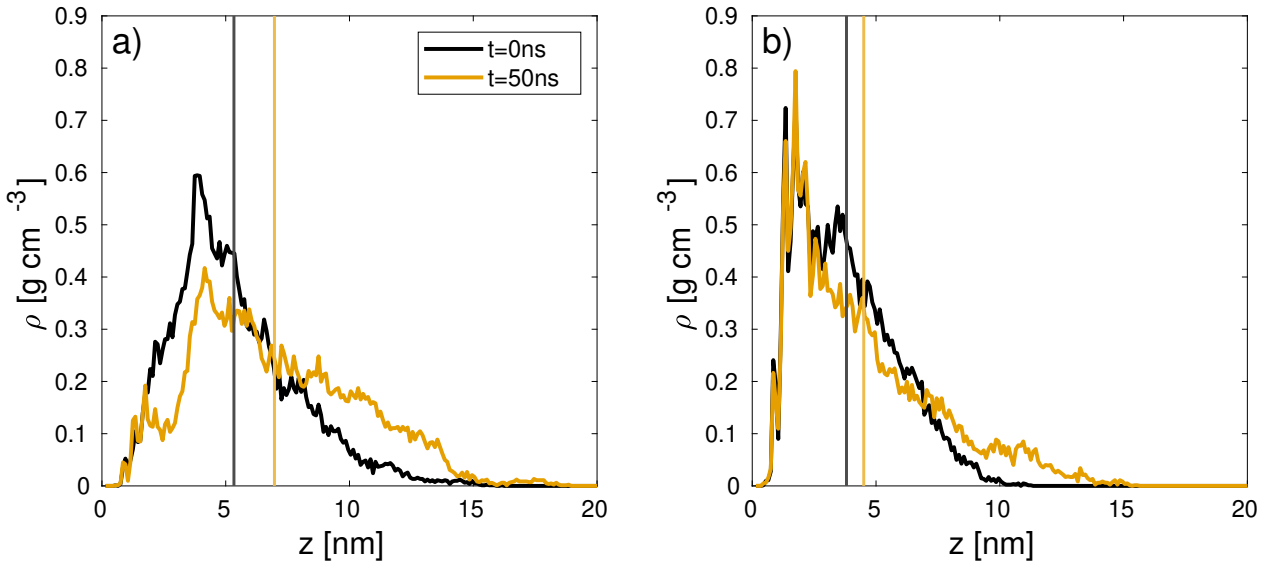


Figure 7.10: Evolution of the instantaneous CGG mass density upon addition of SDS for (a) virgin and (b) bleached hair at a CGG adsorption density of $\Gamma_0 = 0.26$ µg cm^{-2} (case VI).

b) CGG adsorption density variation

Time-averaged mass density profiles of CGG after the initial adsorption stage are shown in Fig. 7.11. The overall mass density profiles were subdivided into trains lying flat on the surface, loops and tails. This classification has proven successful in other CG-MD studies of polymer adsorption to biomimetic hair surfaces[118,266,267] The automated classification was performed by a recursive walk across polymers where loops are classified as parts of the polymers between two adsorbed backbone beads. Tails are either blocks of polymers only bound by one adsorbed site (literal tails), or, by definition, entire polymers residing on top of other polymers (multilayers).

Loops and trains are observed across all four systems. The highest contribution to flat trains on the surface is observed on bleached hair and high CGG deposition as a result of the high number of anionic sites and number of cationic charged on the polyelectrolytes. By mass, tails account for the majority of adsorbed CGG in all systems. This shows that a large number of polyelectrolyte material is adsorbed on top of other CGG, forming multilayers. This is most pronounced for the high CGG adsorption density cases. The upper layers in these aggregates are only weakly bound by hydrophobic interactions with other polymers. It was found that these multilayers were squeezed out in preliminary test simulations. We therefore only focus on the low adsorption density systems (case V) for the following NEMD simulations.

c) Lubrication with CGG & SDS

The system composition after squeeze-out is summarized in Table 7.2. Equilibrium in the contact thickness and composition is reached around 30-50 ns. In contrast to the PE cases at DS = and above, a partial squeeze-out of CGG is observed. The transition point at which all polymers are retained in the present system is therefore located

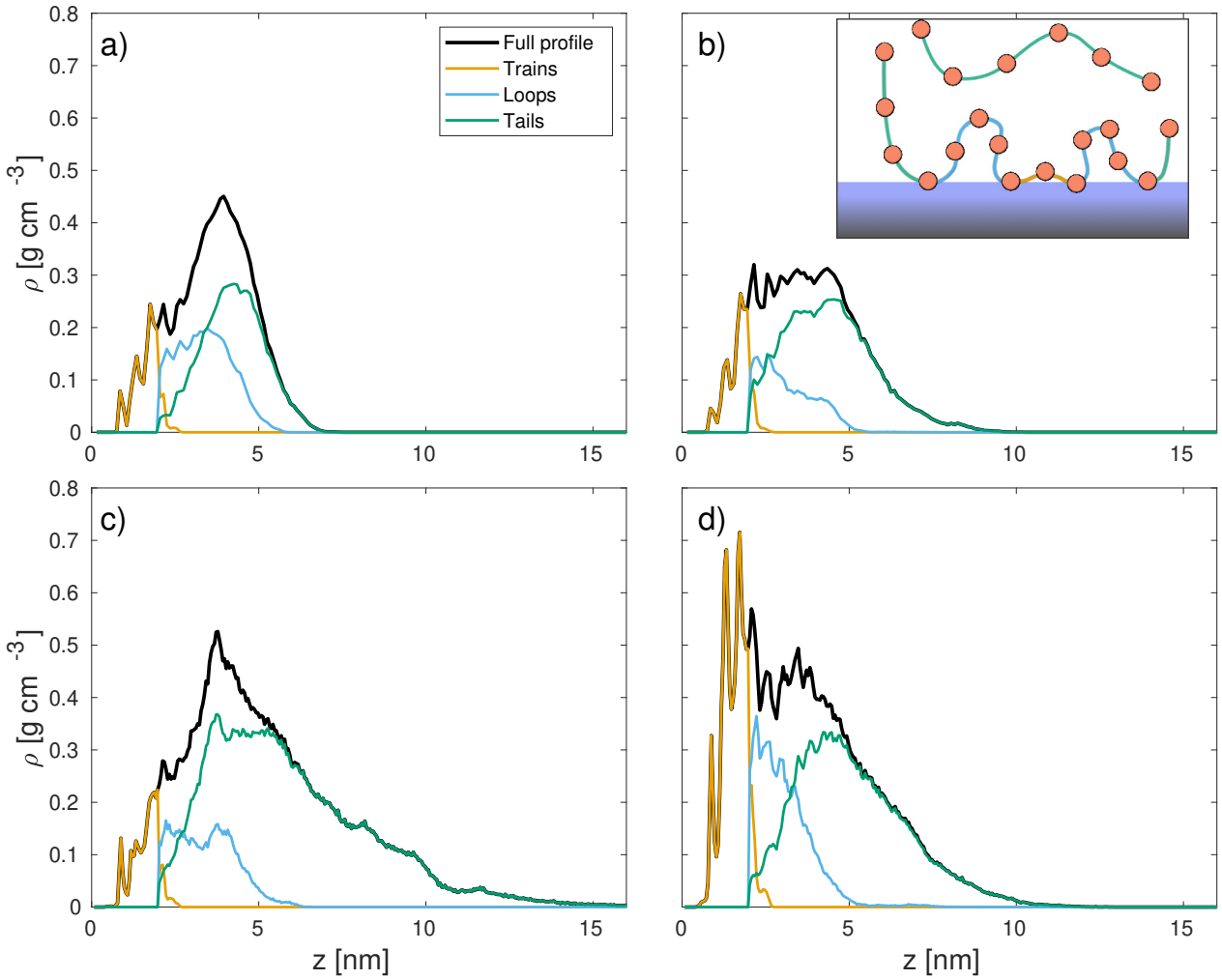


Figure 7.11: Mass density profiles for adsorbed CGG on virgin (left) and bleached hair (right) at two CGG forced deposition densities (a-b) $\Gamma = 0.13$ µg cm^{-2} and (c-d) $\Gamma = 0.26$ µg cm^{-2}. The density profiles are divided into parts of CGG chains residing in trains, loops or tails.

Table 7.2: Contact composition in NEMD simulations on virgin and medium bleached hair surfaces with larger CGG chains at DS = 30%.

Virgin hair		σ=	10 MPa	20 MPa	35 MPa	50 MPa
Coarse-grained water	ρ_W		21.4 nm^{-2}	13.8 nm^{-2}	10.8 nm^{-2}	9.5 nm^{-2}
SDS	ρ_{SDS}		0.90 nm^{-2}	0.66 nm^{-2}	0.45 nm^{-2}	0.33 nm^{-2}
SDS:CGG charge ratio	$\lvert R_{SDS} \rvert$		4.95	3.57	2.45	1.80
Surface:CGG charge ratio	$\lvert R_{surf} \rvert$		2.78			

Med. bleached hair		σ =	10 MPa	20 MPa	35 MPa	50 MPa
Coarse-grained water	ρ_W		25.3 nm^{-2}	19.8 nm^{-2}	16.5 nm^{-2}	15.5 nm^{-2}
SDS	ρ_{SDS}		0.23 nm^{-2}	0.17 nm^{-2}	0.13 nm^{-2}	0.13 nm^{-2}
SDS:CGG charge ratio	$\lvert R_{SDS} \rvert$		0.96	0.71	0.53	0.53
Surface:CGG charge ratio	$\lvert R_{surf} \rvert$		9.52			

in the range of DS = 30-50%. As mentioned in the methods section, the number of polymers for NEMD simulations was rounded to the nearest even integer to ensure each surface contained the same number of chains. This leads to three CGG chains per surface and four chains per surface on virgin and medium bleached model hair surfaces respectively. The amount of squeezed out polymers did not vary significantly

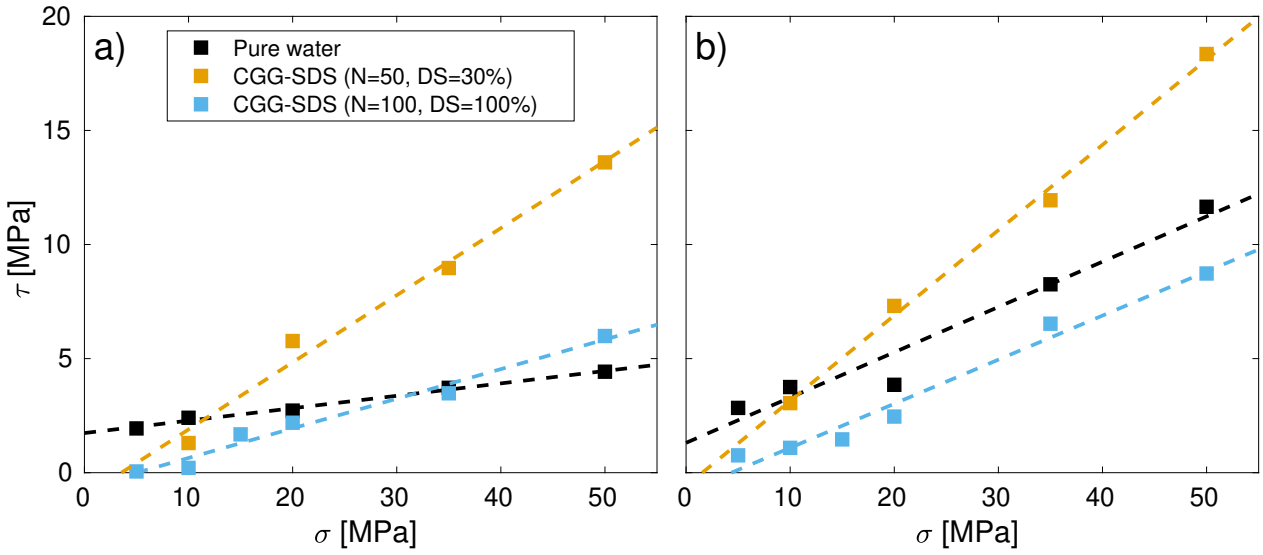


Figure 7.12: Overview of the shear stress for (a) virgin and (b) bleached hair with sequentially adsorbed CGG-SDS complexes at more realistic CGG architectures and a sliding velocity of $v_s = 0.1$ ms^{-1}.

within the range of applied normal loads (constant $|R_{surf}|$ in Table 7.2). On the other hand, the water and SDS content monotonically decreases with the contact pressure. The number of SDS molecules in all systems considered here is substantially lower than with highly charged chains (DS=100%).

The shear stress as a function of the contact pressure $\sigma$for NEMD simulations at a sliding velocity of $v_s = 0.1$ ms^{-1} is shown in Fig. 7.12. For comparison, the results from the baseline simulations in chapter 6 are shown as well. Insets show shear stress signals for $\sigma = 10$ MPa. Longer NEMD simulations were required for sufficient sampling which is expected to be due to the increased CGG chain length and corresponding increase in the polymer relaxation time. This trend is also consistent with NEMD simulations of even larger polymers and small surfactants in hair contacts in the hydrodynamic lubrication regime.[36] The simulations at lower DS and increased chain length render COFs of $\mu = 0.29$ for virgin and $\mu = 0.37$ for medium bleached hair which is higher compared to both bare surfaces with water and for short, highly charged CGG chains with SDS (case III).

Snapshots of the NEMD simulations at $\sigma = 10$ MPa are shown in Fig. 7.13. The corresponding mass and charge density profiles in the surface-normal direction are shown in Fig. 7.14. The brushy nature of the adsorbed polysaccharides is lost under load and confinement. Strong interdigitation between the CGG chains adsorbed on opposite surfaces is evident from the snapshots and mass density profiles. The associated viscous dissipation at the contact interface could explain the COF increase which is consistent for virgin and bleached model hair contacts. The interdigitation is promoted by the higher degree of SDS squeeze-out compared to the baseline case (III). Interestingly, the amount of water in the new NEMD simulations reported in Table 7.2 is similar or even higher than for the baseline system in the previous chapter. The water film thick-

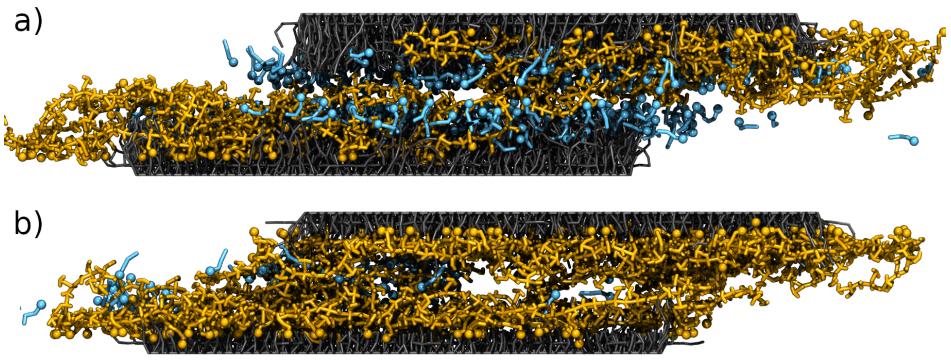


Figure 7.13: Snapshots of NEMD simulations for (a) virgin and (b) bleached hair with sequentially adsorbed CGG-SDS complexes at a sliding velocity of $v_s = 0.1$ ms^{-1} and a contact pressure of $\sigma = 10$ MPa.

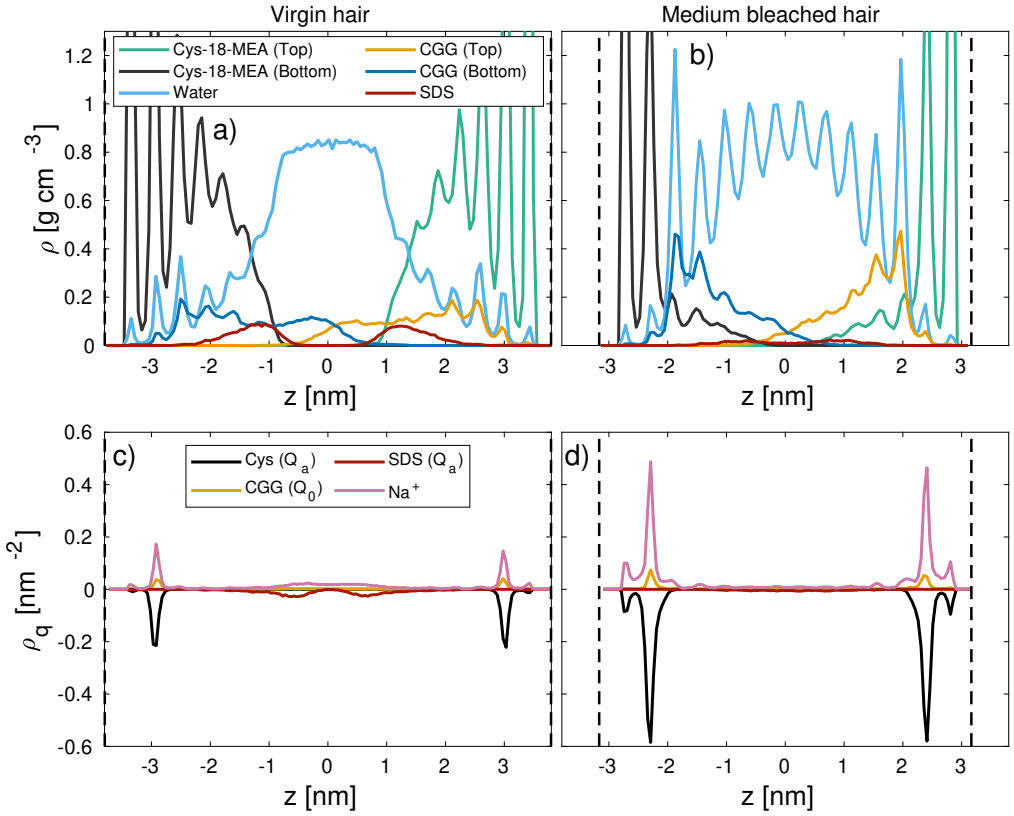


Figure 7.14: Through-film mass density, ρ (a, b), charge density ρ_q (c, d), and velocity, v_x (e, f) profiles at $v_s = 0.1$ m s^{-1} for virgin (a, c, e) and medium bleached hair (b, d, f) with more realistic CGG architectures.

ness is comparable to the configuration with highly charged CGG and elevated CGG adsorption density (case IV) as evident from the respective snapshots and mass density profiles in Fig. 7.8(a,b) and Fig. 7.14(a,b). However, the CGG-water-CGG interface is considerably more heterogeneous in the new simulations with weaker CGG charge density.

The reduced SDS coverage at the end of the squeeze-out stage was investigated in more detail. Two modes of SDS depletion are conceivable during squeeze-out: 1) Independent of CGG squeeze-out, and 2) 'cooperative' squeeze-out in which CGG-attached SDS is depleted along polyelectrolyte chains. In the previous chapter, the former mode was dominant since CGG chains were strongly adsorbed to the surfaces and did not

Table 7.3: SDS content within the layer of adsorbed CGG on a single hair surface before preliminary squeeze-out.

Virgin hair		DS =	30%	100%
Hair + CGG layer thickness	Δz		12.1 nm	8.5 nm
SDS surface density	ρ_{SDS}		2.22 nm^{-2}	1.57 nm^{-2}
SDS volume density	ρ_{SDS}		0.18 nm^{-3}	0.18 nm^{-3}
SDS:CGG charge ratio	$\lvert R_{SDS} \rvert$		6.19	3.86

Med. bleached hair		DS =	30%	100%
Hair + CGG layer thickness	Δz		12.1 nm	5.5 nm
SDS surface density	ρ_{SDS}		2.11 nm^{-2}	1.60 nm^{-2}
SDS volume density	ρ_{SDS}		0.17 nm^{-3}	0.29 nm^{-3}
SDS:CGG charge ratio	$\lvert R_{SDS} \rvert$		5.88	3.94

detach. Here, chains are more weakly charged and, as previously mentioned, undergo partial squeeze-out for all considered normal loads. To illustrate this, Table 7.3 shows the SDS content within the pre-adsorbed CGG films on a single hair surface prior to squeeze-out. By mass density per unit volume, the amount of SDS within the CGG layers is similar for the two degrees of CGG substitution on virgin hair. In fact, the weakly charged chains are more 'overcharged' by SDS due to micellar attachment. During squeeze-out, a lower DS leads to more SDS being depleted per initial volume of CGG; likely due to cooperative squeeze-out with CGG chains. It is also worth noting that no significant alignment of CGG in the direction of sliding is observed at the present loads and sliding velocity. This is, as mentioned earlier, a prerequisite for the NEMD simulations to avoid self-interactions of polymer chains across the periodic system boundaries.

Overall, the new simulations underline that SDS significantly promotes lubrication in sequentially adsorbed CGG-SDS layers on hair. There seems to be a transition between DS = 30% and 50% which leads to an increased amount of entrapped SDS with higher polyelectrolyte charge density. At the same time, while longer CGG chains were thought to be more effective at forming brush-like loop and tail conformations during adsorption, they break down in the present range of contact pressures. This indicates that the load-bearing capability of CGG at the present adsorption densities and normal loads is not sufficient to enhance lubricity despite an increase in the polymer chain length. Consistently, combing experiments comparing several types of CGG found that combing reductions were more sensitive to the charge density rather than the molecular weight in polyelectrolyte-surfactant complexes on hair.[297]

These results suggest that chemical properties of the aggregates seem to be more important for lubrication than the capability of the polymers to form brushes and loops. These insights could be beneficial for evaluating the longevity of the conditioning performance of oppositely-charged CGG-SDS complexes. During shearing against an open environment, SDS might be depleted from hair-on-hair contacts which could lead to a relatively fast loss of conditioning performance. It will be interesting to further evaluate this 'wear' mechanism in finite system simulations and experiments. On the other hand, polymers with a more rigid backbone or more brush-like conformations might

further shift the benefit of (cationic) polymers to reduce the lubricant heterogeneity. Inspiration could be drawn from previous studies on polymer brushes such as that by Lee et al.[209] who reported to provide low friction on hair due to PLL-*g*-PEG.

7.4 Conclusions

In this chapter, different properties of cationic guar gum (CGG) were explored with respect to their effect on hair lubrication in the presence of oppositely charged surfactants (SDS). In a first instance, lower CGG charge densities compared to the previous chapter were tested. At DS = 10%, CGG was found to be prone to squeeze-out under physiologically relevant normal loads. This is due to a lack of or weak adsorption to anionic sites, especially on virgin hair. Strong friction reductions at low normal loads were observed for DS = 50% and above for both virgin and bleached hair. The effective onset for friction reductions might in fact happen in the range of $10\% < \mathrm{DS} < 50\%$; this range could be worth resolving in future simulations. On the other hand, no further friction reductions were obtained from doubling the CGG charge density from DS = 50% to 100% on bleached model hair surfaces.

The CGG adsorption density was then increased to values representative of polysaccharides on bleached hair. This resulted in further friction reductions compared to the baseline CGG case which suggests that thicker layers consisting of short, strongly charged CGG chains are effective at trapping SDS and water for a well-defined lubricating layer. At the considered adsorption density, friction is also independent of the degree of damage on our model hair surfaces.

Finally, a set of longer CGG chains with a charge density corresponding to DS = 30% was selected for deposition and NEMD simulations. As a result of the weaker polymer charge, the clear formation of loops and tails was observed on both virgin and bleached hair. At the same time, these chains were found to be more prone to being squeezed out under load compared to the baseline case in chapter 6. This squeeze-out in combination with the reduced CGG charge led to weaker entrapment of SDS and water within the contact which results in a reduced lubrication efficiency. The COF increased to levels above those observed in the NEMD simulations with pure water in chapter 4 for both virgin and bleached hair. This is due to stronger polymer entanglement and subsequent viscous losses.

This chapter also highlighted some of the constraints associated with MD of macromolecules at interfaces. The need for updating the composition with respect to the normal load requires preliminary squeeze-out simulations. These become more challenging as polymer chain lengths and charge densities approach realistic values. Potential pathways to resolving this challenge will be discussed in the conclusions, chapter 9.

8 Towards high-throughput friction screening in soft biomimetic contacts

Some of the work presented in this chapter was carried out during a two-month placement (Oct.-Dec. 2023) with Procter & Gamble at the Newcastle Innovation Center (NIC).

8.1 Introduction

The methodology and workflows introduced for wet hair contact friction using coarse-grained molecular dynamics is directly transferable to other soft substrates of interest for the scientific community and the personal care industry. Particular substrates of interest are textiles (cotton, polyesters, wool) and human skin. The tribological interaction between textile fibres as well as the interactions between textiles and human skin are directly responsible for the perceived softness of textiles.[285,488,531] Similarly to hair surfaces, both large scale surface roughness and the nanoscale chemistry are expected to play a role on lubrication and tactile perception.

Cotton is the most common naturally sourced material used in clothing and homecare textiles. Native cotton has a fibrous structure which, similar to hair, consists of several characteristic layers as shown in Fig. 8.1 due to Easson et al.[532] Cellulose makes up for the vast majority of the mass within cotton fibres (>88%).[533,534] A lipid-rich cuticle protects the inner layers of native cotton. The primary wall consists of a hierarchic fibril structure where larger macrofibrils contain several so-called micro or nanofibrils of crystalline cellulose chains. The secondary wall can be separated into three individual layers which are wound against each other in a spiralling manner. The core of cotton fibres contains the so-called lumen which can also contain some proteinaceous and saline compounds.[533]

Native cotton is moderately hydrophilic. A contact angle of $\vartheta = 40\text{-}69°$ was reported in wetting experiments on unbleached cotton fibres using the Wilhelmy force balance.[535] This behaviour also translated to woven cotton fabrics,[535] suggesting little influence of the wetting state (Cassie-Baxter/Wentzel). During processing, cotton is typically subjected to scouring and bleaching. This removes the waxes and lipids of the cuticle[533] and only leaves the primary wall behind which then determines interfacial fibre properties such as wetting and friction. When subjected to scouring and bleaching, contact angles decrease, indicating that the surfaces become more hydrophilic.[533,536] Atomistic MD simulations of crystalline I_β cellulose indicate a high sensitivity of the static contact angle of water nanodroplets on the orientation of the exposed crystal.[537]

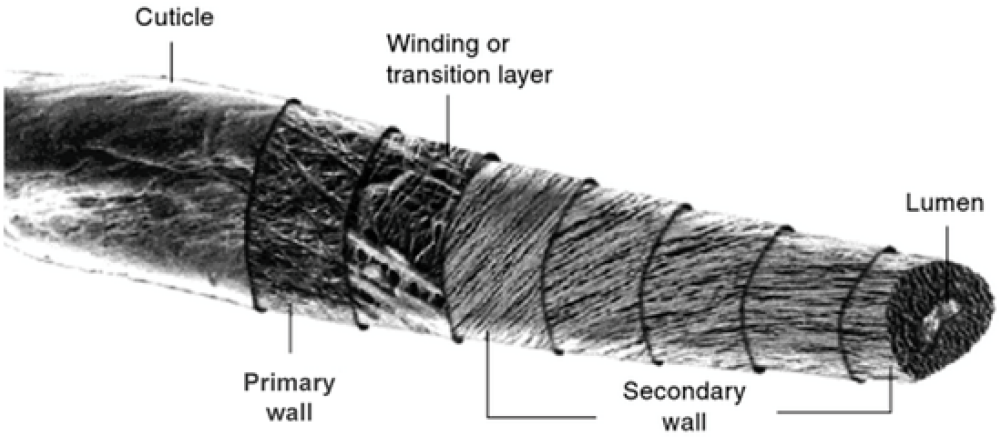


Figure 8.1: Structure of cotton fibres. Reprinted from Easson et al.[532] licensed under a CC BY 4.0 license.

Nanocrystalline cellulose water contact angles from simulations of $\vartheta = 23°$ were reported. Full wetting was observed for apolar solvents such as tetradecane.[537]

The frictional properties of cotton and more generally cellulose substrates have been investigated across many lengthscales.[538–546] Friction coefficients between bleached cotton fibres of 0.6 and 0.5 have been reported from crossed fibre experiments in wet and dry environment respectively.[539] Stiernstedt et al. reported even higher values ($\mu = 1.02$) for rough cellulose fibres using colloidal probe AFM friction experiments in a liquid cell with background salt.[541,542] On the other hand, Hosseinali et al.[546] reported COF values of 0.066-0.08 in macroscopic friction tester experiments of cotton fibres against flat metal surfaces. The nature of the countersurface and experiment scales by means of contact area, load and sliding speeds are therefore equally sensitive parameters to cotton friction as observed in hair (see chapter 2).

Fabric softeners modify the surface chemistry of textiles by deposition of lubricant additives. These are often cationic compounds which have a high affinity towards the anionic, polar sites of bleached cotton. The friction reduction between woven fibres and between textiles and skin due to the formation of a lubricating layer is one key mechanism for an increase in the perceived softness of textiles.[285,547] Igarashi et al.[285] also proposed depositing fabric softeners may inhibit hydrogen bonds between fibres caused by ordered water, thus increasing cotton fabric softness. Adsorption isotherms of linear cationic quaternary ammonium surfactants (quats) have also been measured in neutron reflectivity experiments.[548] Ester-based quats with C_{16} or C_{18} alkyl chains are most commonly used in modern fabric softener products.[549,550] Such molecules often adapt a hairpin conformation and form larger aggregates such as vesicles which can be leveraged for depositing perfuming agents to the surface.[488] It has been found that entire vesicles formed of DEEDMAC can adsorb to cotton surfaces.[283] The deposition of cationic polysaccharides leads to significant friction reductions on bleached cotton with increasing polymer concentration in solution.[539] Friction reductions have also been observed with commercial fabric conditioners using

the friction force microscope (FFM).[543]

The elementary lubrication mechanisms related to the inter-fabric friction (cotton-on-cotton) are not fully understood to date. Molecular models could provide nanoscale insights into the structure of lubricants during sliding motion while also capturing shear forces as shown for hair-on-hair contacts in the previous chapters. Many molecular models of cellulosic materials have been used by the scientific community with both atomistic[537,551–554] and coarse-grained forcefields.[555–557] To date, these models have been applied to study crystal structure,[556,558] mechanical properties of cellulose nanofibrils,[554,556] adsorption,[552] wetting[537,559] and solvent interactions.[556] Non-equilibrium properties have also been investigated in cellulose MD models in few instances.[551,553] Wu et al.[551] performed atomistic NEMD friction simulations between dry I_β cellulose sheets at various rotation angles. Zhang et al.[553] carried out NEMD simulations between hydrophobic and hydrophilic cellulose surfaces in the presence of interfacial water.

In this chapter, a new nanoscale cellulose model representing the surface of cotton fibres is developed and validated. This model is integrated into a new high-throughput automation workflow for investigating the friction on biomimetic model surfaces for soft surfaces in the presence of small molecules such as lipids and surfactants. The new workflow is then applied to study the nanoscale lubrication of linear and 'hairpin' cationic surfactants in aqueous cotton-on-cotton. This case study aims at demonstrating the suitability for virtual high-throughput tribological screening which is expected to accelerate the development of new, biocompatible personal and home care formulations.

8.2 Surface model overview & validation

López et al.[556] developed coarse-grained MARTINI 2 models for I_β and III_I cellulose nanofibrils. Cellulose I_β is the predominant cellulose type in the primary wall of cotton[534] which makes this model suitable for biomimetic simulations of the surface of bleached and scoured cotton. The model was primarily developed for reproducing the correct crystal parameters and structural nanofibril properties in standard MARTINI water. We consider infinitely extending cellulose chains through bonds across the periodic system boundary along the primary chain direction. This is a reasonable approximation given that the degree of polymerization in the primary wall is typically in the range of DP = 500-8,000[560,561] which means that chains are much longer than the average cross-section of cotton cellulose nanofibrils (3.6-4.7 nm).[534]

Here, the model due to López et al. is extended for studying interfacial properties such as wetting and friction. Preliminary nanodroplet contact angle simulations with the baseline model[556] on ideally flat I_β crystals indicated that the surface was too hy-

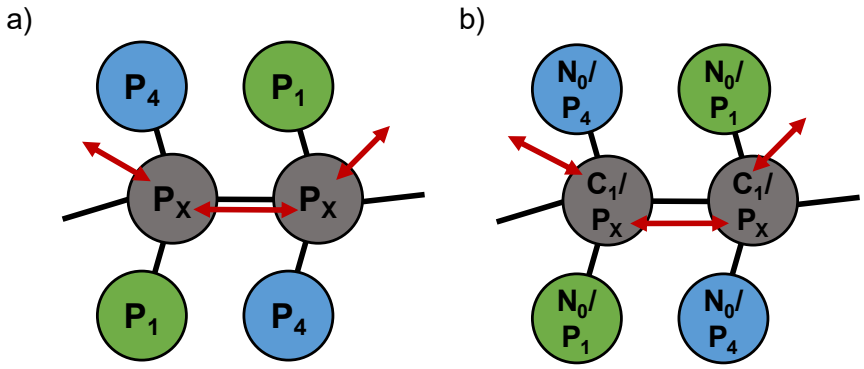


Figure 8.2: Overview of (a) the original cellulose I_β model due to López et al.[556] and (b) the refined model with modified interactions with external CG beads and unchanged inter-crystal interactions.

drophilic compared to previous all-atom MD simulations.[537,559] This is not surprising, given that the CG original model used three polar beads, P_1, P_4, and a central P_5 bead with a reduced LJ self-interaction strength termed P_X.[556]

Fig. 8.2 shows the original model[556] and the refined version considered in this work. The polarity of the side chain beads was reduced by replacement to non-polar N_0 beads. Arguably, changing the side chain beads to P-type beads with lower polarity (P_1) would be more appropriate when solely following the standard *MARTINI 2* coarse-graining philosophy[264]. However, the N_0 bead yields a better match with wetting AA-MD and was therefore selected for the final model. The LJ interactions of the backbone bead with external molecules were changed to the apolar C_1 bead type. This is similar to a recent cellulose model in the MARTINI 3 model with reduced polarity.[557] All inter-crystal LJ interactions remained unchanged compared to the original model to retain the crystal captured in Ref.[556] Figure 8.3 and Table 8.1 show the changes in the static contact angles for the polarizable water model and tetradecane ($C_{14}H_{30}$) between the original and refined CG cellulose model. The wetting behaviour of the refined model is in excellent agreement with the AA-MD simulations of TIP4P/2005 water and tetradecane on I_β cellulose due to Malaspina et al.[537]

After fine-tuning on ideally flat surfaces, a molecular model for the surface of rough nanocrystalline cellulose was devised as shown in Fig. 8.4. A model of two fused, periodic half-nanofibrils was created using Moltemplate[337] and LAMMPS.[332] A packing density of 54 cellulose chain per full fibril was adopted. The packing density in cotton cellulose nanofibrils has been subject to discussions[534,562–564] with some studies reporting values as low as 18 chains per fibril[562–564]. The present value was taken from

Table 8.1: Contact angles obtained with the original and revised cellulose model compared to all-atom wetting simulations from Ref.[537].

Wetting fluid		Original model[556]	Revised model	AA-MD[537]
Water	$\vartheta_w =$	0°	24.5°	23°
Tetradecane	$\vartheta_t =$	53.9°	0°	0°

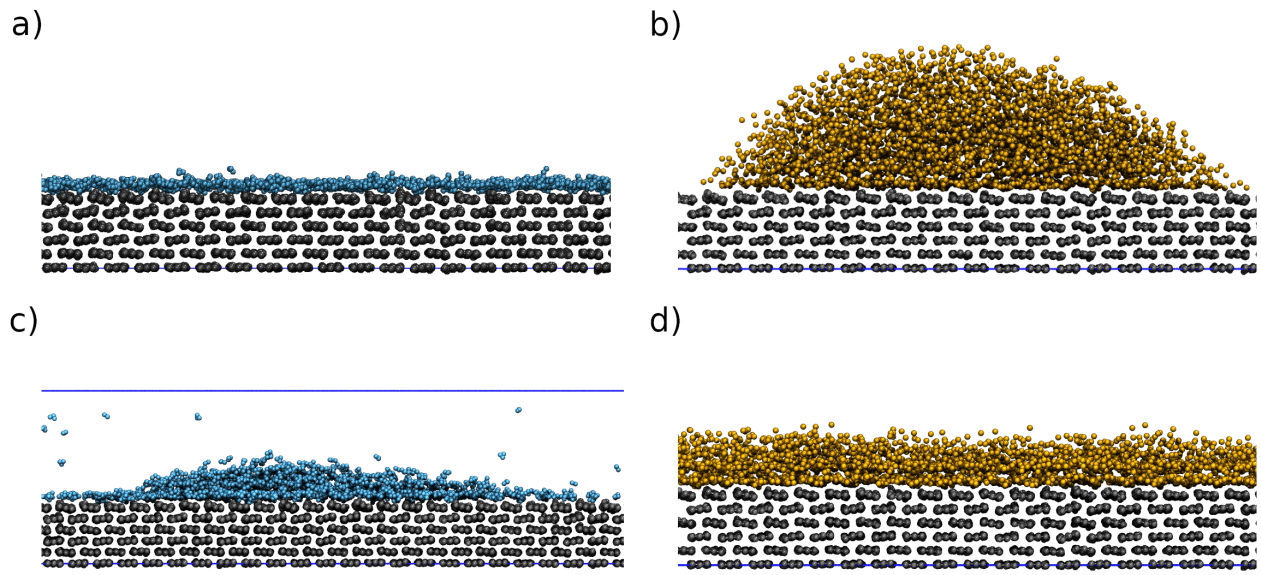


Figure 8.3: Wetting of on smooth cellulose with the original cellulose model (a,b) and the revised model (c,d) for water (a,c, cyan) and tetradecane (b,d, orange). Rendered using VMD.[349]

small angle scattering experiments on *Gossypium arboreum* cotton.[534] With this fibril packing density, a root-mean-square (RMS) surface roughness of 3.6 nm is obtained in our model. This is comparable to the lowest roughness values reported in friction measurements on cellulose (RMS = 2.1 nm) due to Stiernstedt et al.[541] The bottom two cellulose sheets are immobilized and act as a slider in squeeze-out and NEMD simulations. The third cellulose sheet is thermostatted using a directional Langevin thermostat perpendicular to the direction of loading and sliding. For tribological screening, two rough model surfaces are brought into contact at a relative rotation angle of 90 degrees along the z direction to ensure incommensurability.

Surface oxidation is considered in rough cellulose model to mimic the effect of bleaching which is typically performed for cotton in textiles.[543,565] This leads to a slightly negative surface charge, with reported values around -0.012 C m^{-2}.[566] Surface bleaching is implemented by replacing a given fraction of surface-exposed N_0/P_4 side chain beads by negatively charged Q_a beads ($+1e^-$) representing carboxylate groups. We only oxidize beads beads which are directly exposed on the surface, assuming that the bleaching solution does not penetrate into the substrate. This is in line with previous all-atom simulations of TEMPO-bleached cellulose nanofibrils due to Paajanen et al.[552] A fraction between 0 and 30% of exposed P_2 beads accurately captures the above range of reported charge densities. At higher oxidation levels, charge-induced crystal amorphization was observed. Table 8.2 provides an overview of the discrete surface charge density levels available in the new automation tool. For the below case study, an oxidation fraction of 20% (ρ_q = -0.0597 C m^{-2}) is selected. Future adsorption and NEMD simulations might also consider variations in the surface charge. This is fully supported by the new workflow at the discrete charge density levels in Table 8.2.

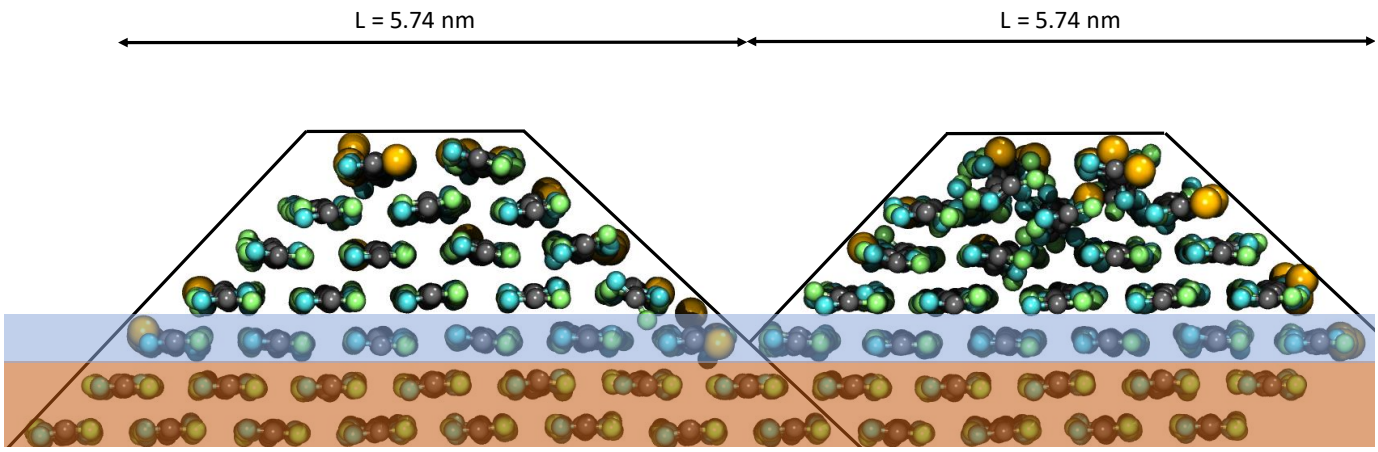


Figure 8.4: Fused half-fibril model for nanocrystalline cellulose. Orange beads represent carboxyl oxidation sites modeled by negatively charged Q_a beads. Some fibril amorphization is observed in the present snapshot which was produced with the substrate immersed in water (not shown). The rigid and thermostated layers are shown by red and blue overlays respectively. Rendered using VMD.[349]

8.3 Workflow automation overview

8.3.1 Workflow description

An overview of the implemented workflow for automating the nanoscale friction screening with small molecules is shown in Fig. 8.5 The specific user inputs will be discussed in the next section. The automation workflow developed in this chapter draws from the knowledge and simulation steps developed for hair-on-hair contacts in the previous chapters. Furthermore, a range of open-source tools and molecular simulation codes are leveraged including LAMMPS, version 28 Mar 2023 - Development,[332] Gromacs, version 5.1.4,[567] Moltemplate,[337] packmol,[369] cg_param,[568] acpype,[569] PyCGTool,[503] intermol,[570] and rdkit.[571]

All available lubricant molecules and substrate models are stored in a central database. This database contains molecule names and coordinate files (.xyz), Moltemplate template files (.lt), SMILES strings and LAMMPS data files for pre-equilibrated substrates. For user-specified molecules that are not contained in the database, the CG parametrization subroutine launches automatically. This routine couples a sub-set of the above open-source coarse-graining tools with all-atom simulations using the GAFF forcefield[572] in Gromacs 5.1.4[567] The SMILES string of the input molecule is passed to the *cg_param.py* tool due to Potter et al.[568] which automatically generates a coarse-grained MARTINI 2 mapping. The reader is referred to the original publication, Ref.[568],

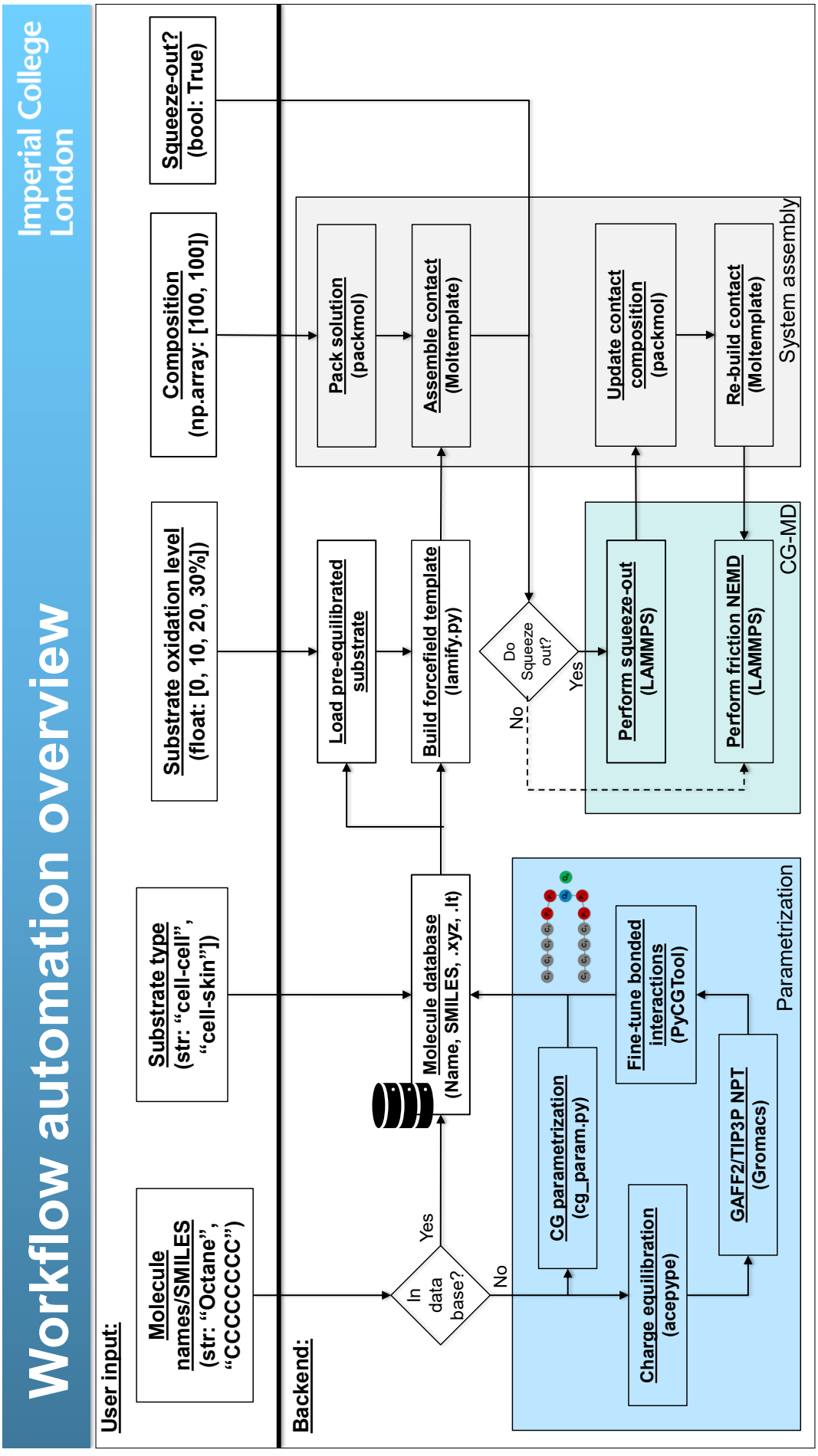


Figure 8.5: Overview of the nanoscale friction screening workflow.

for background information on the mapping routine. The *cg_param.py* tool outputs a coarse-grained mapping with equilibrium bond lengths, angles and standard MARTINI equilibrium constants. However, the standard bond and angle constants do not always produce accurate results with respect to a molecule's distribution function[573] or its self-aggregation behaviour.

We therefore extend the baseline coarse-graining procedure by further fine-tune the bonded interactions (and also equilibrium bond length and angles) by means of all-atom simulations of a single molecule of interest solvated in water. The molecule is charge-equilibrated and GAFF forcefield parameters are assigned, both using the Antechamber python parser interface *acpype*[569]. Atomic charges are assigned using the AM1-BBC model.[574] The output Gromacs files are then used to solvate the target molecule in TIP3P water.[575] The system is energy minimized and equilibrated using short NVT and NPT runs at T=300K. The NPT production run is carried out for 5ns at an integration timestep of 2fs. Dumping to a trajectory file is performed every 5ps, resulting in 1000 frames to process for the fine-tuning routine. This methodology is similar to the procedure for CGG discussed in the previous chapter. However, transitioning to the GAFF forcefield in Gromacs provides both a higher accuracy of the baseline all-atom simulations for surfactant molecules and significant speed-up for the single molecule AA-MD. PyCGTool[503] takes the coarse-grained mapping and bond connections from *cg_param.py* and the atomistic trajectory from the Gromacs production run as inputs. An Iterative Boltzmann Inversion (IBI) is then performed in PyCGTool as outlined in Ref.[503] and in chapter 6. PyCGTool maps atomistic trajectories to the respective centre of mass coordinates of the coarse-grained beads and assigns equilibrium bond lengths, angles and force constants based on the bond and angle distributions. The output of the IBI is a set of fine-tuned bond and angle distributions for the coarse-grained molecule. Finally, the updated bonded interactions and coarse-grained mapping are merged and converted to a LAMMPS data file using the open-source tool *intermol*.[570] A Moltemplate file is generated from the LAMMPS data file using the ltemplify.py extension from Moltemplate. Furthermore, a coordinate file (.xyz) which is required for the system assembly tool packmol[369] is generated in LAMMPS. After a successful parametrization run, the new coarse-grained molecule will be added to the molecule database.

For a given composition which can consist of a (theoretically) unlimited number of different unique molecule types and flexible number of molecules per such type, all relevant templates are queried from the database and passed to a custom Python routine (*lamify.py*) to assign a unique bead type in LAMMPS and obtain the MARTINI 2 forcefield parameters and global MD simulation settings. Since the implementation of this tool, Moltemplate has also added a standard MARTINI forcefield database by default. However, the present code can easily account for new or custom bead types such as in the case of the previously discussed cellulose CG beads. Packmol

is launched to generate coordinates for a randomly packed lubricant film. This is then used in Moltemplate to assemble the lubricant film LAMMPS input file. This file is subsequently merged with two substrate data files to generate the semiperiodic contact. If preliminary squeeze-out is selected, this contact will be transferred to a vacuum environment. The size of the system box is automatically scaled based on the contact thickness to always provide at least 8 nm of separation above the contact. In this work, the preliminary squeeze-out is always be used. It is recommended to only shortcut this step if one already knows the contact composition for a given normal load. Upon completion of the squeeze-out step, the contact composition is updated based on the number of remaining molecules. This updated composition is obtained from a sub-region of the contact with a width of half of the substrate in the y direction to exclude edge effects. Finally, the semiperiodic system with updated composition is equilibrated, compressed and NEMD simulations are launched at the selected normal load and sliding velocity.

It is worth noting that the tool is solely suitable for contacts containing water and small molecules. Macromolecules are currently not supported by either the CG parametrization routine nor the preliminary squeeze-out step. Another noteworthy limitation of the routine is that rigid bond constraints within lubricant molecules other than water are not supported as they will not be detected automatically for use with the SHAKE algorithm. This is expected to be rare for small molecules in *MARTINI 2* but cannot be fully ruled out and should be checked manually in the PyCGTool output of newly parametrized molecules.

8.3.2 Numerical details

As in the preceding work, the *MARTINI* forcefield with the polarizable water model was used in this section. A detailed description of this model is therefore omitted here. The computationally most expensive step of the presented workflow by far are the preliminary squeeze-out simulations which need to be carried out for each new combination of contact composition and contact pressure. Two options were tested to potentially accelerate this step: The baseline squeeze-out with an explicit water bath as described in previous chapters was benchmarked against a contact in vacuum. The original motivation behind the squeeze-out in an explicit water bath was the low pressure-viscosity coefficient of water which leads to water being squeezed out from contacts when being placed in vacuum. However, we found that this configuration is also prone to freezing when transitioning from hair contacts to more crystalline substrates like cellulose. As a result, it was decided to only use the squeeze-out in vacuum for systems with surfactants. For pure water cases, both explicit bath and vacuum simulations were conducted, leading to similar equilibrium contact compositions in the present range of normal loads.

All numerical parameters are in accordance with the previous chapters, including long-

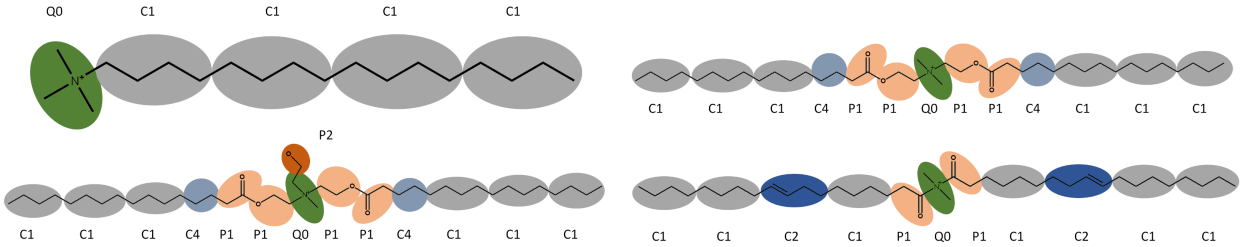


Figure 8.6: Cationic quat surfactant architectures considered for NEMD sliding simulations with corresponding coarse-graining parametrizations.

Table 8.3: Overview of system parameters for automated cotton-on-cotton friction screening with cationic surfactants relevant in fabric softeners.

Parameter	Symbol	Values
Surfactant type	X	CTAB; DEEDMAC; DPEHEMS; DOE
Initial number of CG water molecules	$N_{w,0}$	3000
Contact pressure	σ	1 MPa; 10 MPa; 30 MPa; 50 MPa
Sliding velocity	v_s	0.1 ms^{-1}
Sliding angle	φ	45°

Table 8.4: Overview of simulation test cases with different initial cationic surfactant content N_0.

Test case	N_0 =	CTAB	DEEDMAC	DPEHEMS	DOE
I		0	0	0	0
II		100	100	100	100
III		400	200	200	200
IV		700	350	350	350
V		1000	500	500	500

range electrostatics, cutoffs, thermostat and barostat settings. The polarizable water model[306] is used again with SHAKE for constraining water bonds. NEMD simulations were run for at least 50 ns with statistics obtained after 20 ns of run-in. A sliding angle of 45 degrees relative to the primary orientation of cellulose chains was applied.

8.4 Case study: model & fabric softener surfactants in cotton cellulose contacts

8.4.1 Overview

Linear and hairpin quaternary ammonium surfactants (quats) were subjected to frictional screening using NEMD simulations. Four different cationic surfactant architectures are considered in this chapter:

1. Cetrimonium bromide (CTAB), a baseline linear model quat,
2. Diethyl ester dimethyl ammonium chloride (DEEDMAC), a methyldiethanolamine-based ester quat,
3. Dipalmitoylethyl hydroxyethylmonium methosulfate (DPEHEMS),[a] a triethanolamine-based ester quat,

a DPEHEMS: this abbreviation was chosen based on the full compound name and may differ from how this molecule is called in the industry.

4. Dioleoyl dimethylammonium chloride (DOE), a methyldiethanolamine-based ester quat with unsaturated alkyl chains.

The corresponding chemical structures are shown in Fig. 8.6. CTAB represents a simple, well-validated model surfactant, while the latter three architectures have been used in fabric softeners[549,550] and typically adopt a hairpin conformation in solution. The investigated simulation parameters for cotton-on-cotton model contacts are summarized in Table 8.3 and Table 8.4. The chosen range of normal loads of $\sigma = 1$-50 MPa is a trade-off between the requirement of desirably high signal-to-noise ratios from shear stress signals and realism. Normal loads in colloidal probe AFM studies typically lead to contact pressures in the range of hundres of kPa rather than MPa[541] which are infeasible with the present models due to low signal-to-noise ratios. For pure water cases, preliminary simulations also indicated a piece-wise linear frictional response with respect to the contact pressure, which is why additional simulations were performed in the range of 45-60 MPa.

Apart from CTAB, none of the molecules have been parametrized in MARTINI in the literature to the best of the author's knowledge. The new parametrizations are obtained automatically from the new workflow routine and are provided in section A.6 in the appendix. Adsorption isotherms of CTAB on hydrophobic and hydrophilic cellulose surfaces from neutron reflectivity experiments[548] suggest adsorption densities of $\Gamma = 0.66$-3.91 nm^{-2} for bulk surfactant concentrations of $c = 0.1$-5 mM. Monolayer adsorption was observed on hydrophobic cellulose, while cooperative adsorption in the form of bilayers was observed on hydrophilic cellulose.[548] For the square cellulose model substrates with a base area of 131.7 nm^2, the adsorption densities from the experimental reference correspond to approximately 174-1030 molecules per contact. Thus, we choose to investigate systems with the following four initial numbers of CTAB surfactants in the contact: $N_0 = 100$, 400, 700, 1000. For hairpin surfactant, no quantitative adsorption isotherms were available in the literature. Therefore, we assume adsorption mass densities similar to CTAB but considered a smaller concentration range of $N_0 = 100$, 200, 350, 500 to account for the lower expected packing density and approximately double molecular weight of hairpin surfactants. The initial surfactant concentrations for each test case (I-V) are summarized in Table 8.4.

It is also worth noting that previous adsorption experiments of DEEDMAC and other similar hairpin surfactants reported larger aggregates such as vesicles depositing on cotton.[283] The size of these aggregates (up to several µm) is currently inaccessible in MARTINI with explicit water. However, it has also been established that these vesicles break up upon drying to form supported bilayers which may be responsible for lubrication.[282,285,547] External normal loads might also further support to vesicle breakdown, especially during wet fabric manipulations. More insights from either experiments or adsorption simulations are needed to clarify this hypothesis which is beyond the scope of this work. The initial amount of water $N_{w,0}$ was fixed at 3000 polarizable

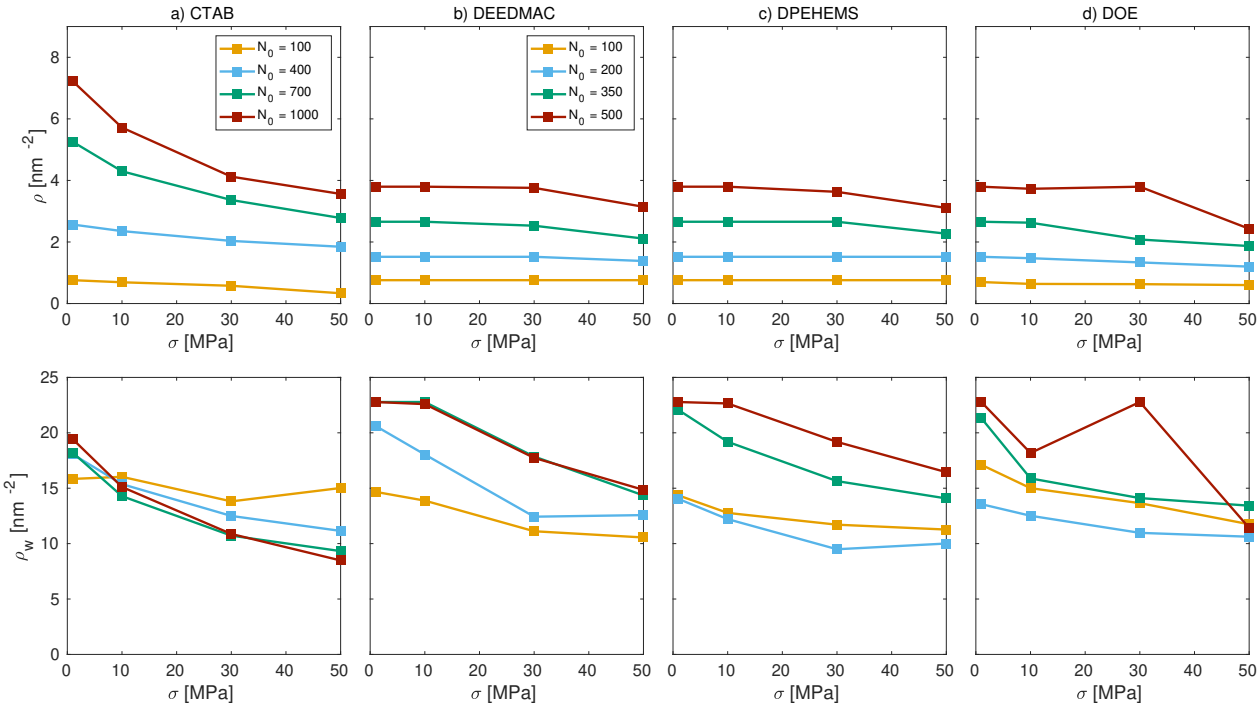


Figure 8.7: Equilibrium molecule density per unit area of surfactants (top) and water (bottom) after squeeze-out as a function of the contact pressure for (a) CTAB, (b) DEEDMAC, (c) DPEHEMS, and (d) DOE.

water molecules throughout all simulations. This mimics more viscous, surfactant-rich films as the number of surfactants N_0 in the contact is increased.

8.4.2 Squeeze-out & NEMD

Before investigating wet contacts with surfactants, the performance of the rough cellulose model was briefly tested in dry contact sliding simulations. Here, previous atomistic NEMD simulations of friction between atomically smooth cellulose crystal sheets due to Wue et al.[551] are available for qualitative comparison. The shear stress was found to be approximately linear with respect to σ. As in prior chapters, we therefore fit this data to the extended Amontons-Coulomb law, see Eq. 2.1. For dry contacts, a COF of $\mu = 0.05$ is found, which is in excellent agreement with the AA-MD average COF ($\mu = 0.06$).[551] Due to the incommensurate contact setup, we did not observe any noticeable wear of roughness features in dry contacts. Therefore, friction forces mostly arise from contacting asperities in the same crystal plane as in the reference AA-MD. It is worth noting that the range of contact pressures σ in Ref.[551] may be different from ours, as no estimate of σ could be obtained from Ref.[551]. Moreover, the applied normal force in our simulation will be distributed across the contacting asperities. This is why no comparison of the Derjaguin offset ($\tau_0 = 1.7$ MPa) with the AA-MD was attempted. For the pure water case, a slight reduction in the COF ($\mu = 0.04$) and considerable decrease in the Derjaguin offset ($\tau_0 = 0.9$ MPa) are observed compared to the dry case.

For wet and surfactant simulations, a preliminary squeeze-out step was performed as part of the automation workflow, starting from the prescribed initial number of

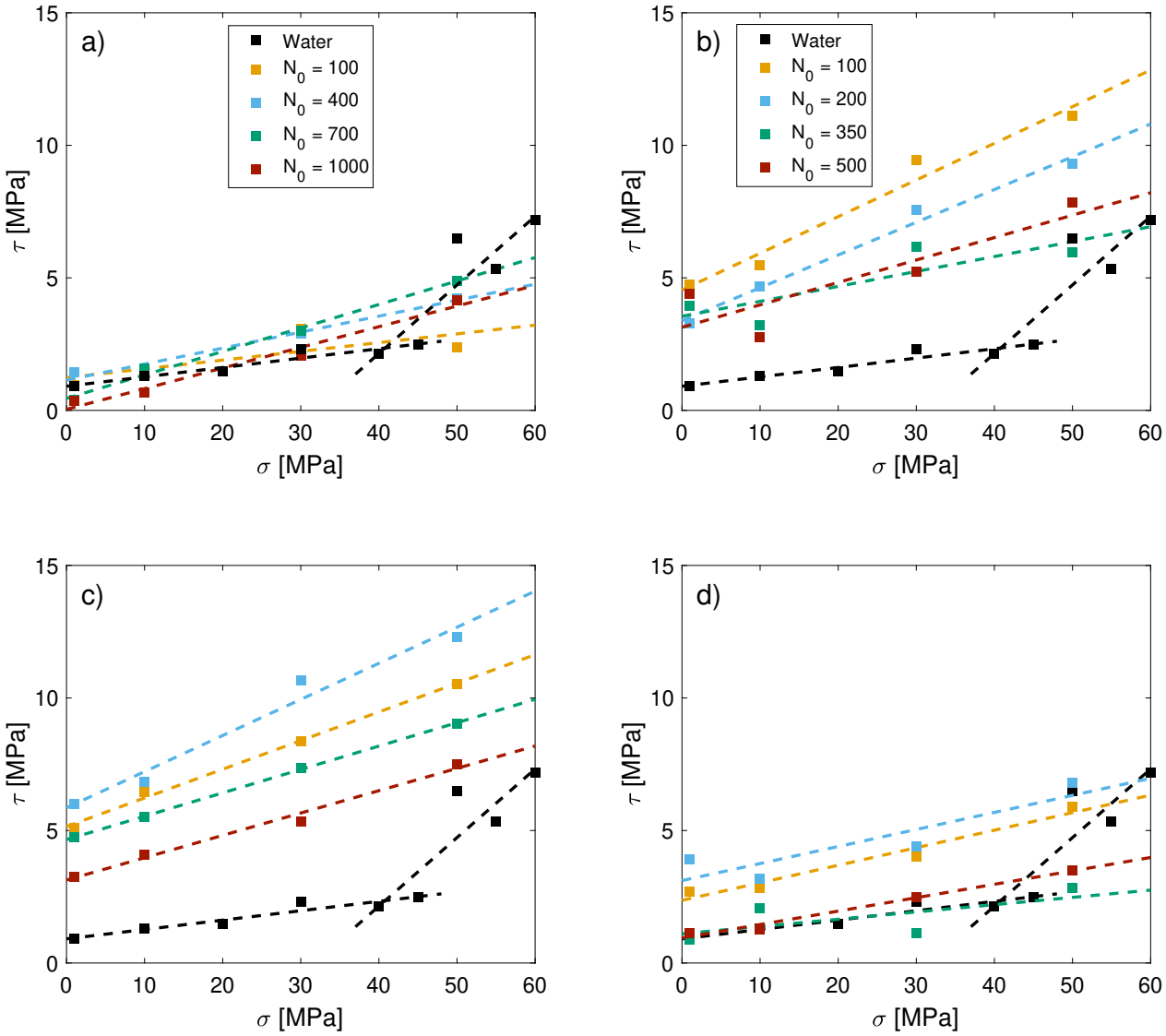


Figure 8.8: Shear stress profiles as a function of the contact pressure at various initial compositions N_0 for (a) CTAB, (b) DEEDMAC, (c) DPEHEMS, and (d) DOE at $v_s = 0.1$ ms^{-1}.

surfactants N_0 and CG water molecules $N_{w,0} = 3000$. Fig. 8.7 shows the equilibrium composition of contacts after squeeze-out at various normal loads and initial compositions. The water and surfactant content decreases with increasing normal load. CTAB is more prone to being squeezed out than hairpin surfactants. In fact, DEEDMAC, DPEHEMS and DOE are fully retained for most configurations below $\sigma = 50$ MPa. This could be due to various reasons such as a stronger self-aggregation behaviour, a different water solubility, or stronger hydrophobic interactions with the substrates. Specifically, hairpin surfactants might produce more rigid aggregates; we will return to analyse this later in the context of the NEMD results. A stronger electrostatic adsorption of hairpin surfactants on the surfaces is not expected to contribute to this behaviour since all cationic surfactant headgroups in this study are monovalent. Moreover, the overall number of cationic headgroups is generally lower in hairpin surfactants.

Fig. 8.8 shows the shear stress τ in cotton-on-cotton contacts as a function of the

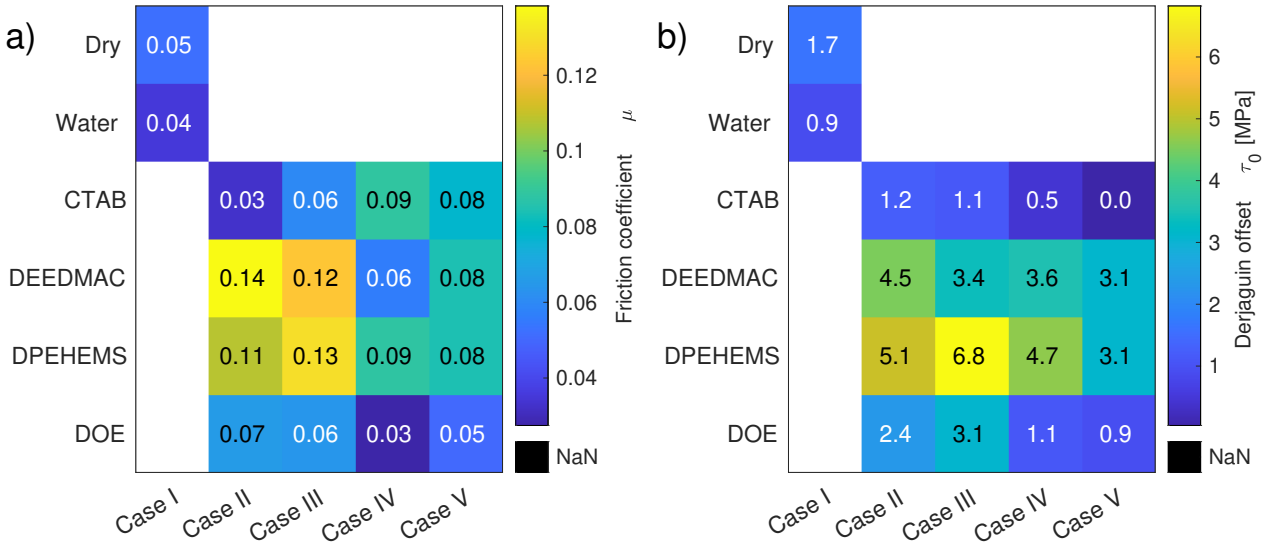


Figure 8.9: (a) friction coefficients μ and (b) Derjaguin offsets τ_0 from fits of the extended Amontons-Coulomb law to the cotton-on-cotton contact shear stress data. Only the low-friction regime data is shown for pure water cases.

contact pressure σ. The extended Amontons-Coulomb friction law is fitted to individual shear stress profiles. The coefficient of friction μ (COF) is obtained as the slope of these fits, while the Derjaguin offset τ_0 is defined as the zero intercept. Figure 8.9 summarizes the fitting results across all surfactant types and compositions. A piecewise linear frictional response is observed for contacts with pure water with respect to the shear stress. At relatively low loads, asperities are separated by a water film which leads to moderate increases in shear stress with normal load, μ_I=0.04. Above approximately 45 MPa, the shear stress sharply increases, signaling that asperities are in contact between the opposing substrates. Similar load-dependent profiles have also been reported on conditioned hair, where a load-dependent depletion of cationic surfactants led to a two-stage frictional behaviour.[16] In the second friction regime in this work, which is probably above the range of physiologically relevant loads, the fitted COF, μ_{II}=0.26, is even above the level observed in dry asperity-contacting systems. This is likely due to the remaining residual water between asperities leading to increased dissipative resistance. The COF with water in the non-contacting linear regime (I) is lower than what has been observed in previous colloidal probe AFM friction measurements between a cellulose sphere and nanocrystalline cellulose ($\mu = 0.41$).[542] The colloidal probe in these experiments was significantly rougher than our model surfaces (RMS = 32 nm) and also contained cellulose II rather than cellulose I. The latter is predominant in natural fibres.[542] A monotonic decrease of the COF observed by Stiernstedt et al.[542] with lower overall contact surface roughness suggests that even lower friction could be expected in experiments when also considering nanocrystalline celluloes I_β for the colloidal probe.

For contacts containing cationic quaternary ammonium surfactants, the shear stress is sensitive to the surfactant architecture and contact composition. CTAB at $N_0 = 100$

and DOE $N_0 = 350$ yield friction reductions by means of the COF ($\Delta\mu$ = -25%). The COF with DPEHEMS is similar to that with pure water while the shear stress with DEEDMAC is increased compared to the baseline at low concentrations. Systems with varying initial CTAB concentrations show a comparable lubrication behaviour to pure water with low Derjaguin offsets and similar COF values. Friction reductions from fitting the data to the extended Amontons-Coulomb law are found for low to intermediate CTAB concentrations. However, it should be noted that both the fluctuations across different contact pressures and the temporal fluctuation in the shear stress profiles and are high. The standard deviation of these friction signals can serve as an indicator for the prevalence of stick-slip and will be investigated at the end of this section. For hairpin surfactants, the absolute friction forces and COF values vary strongly between the different types, with DOE providing the lowest COF across all initial concentrations. A non-monotonic behaviour of the friction coefficient is observed with increasing initial concentrations. A minimum COF is observed at $N_0 = 350$ for all three surfactant types. As highlighted in the previous chapters, it is important to not only use the COF as a measure for friction in soft contacts but rather consider the absolute shear stress under inclusion of the Derjaguin offset. A trend of decreasing τ_0 is observed with increasing concentrations for most surfactant An variation in the Derjaguin offset τ_0 with N_0 is most prominent for systems with DPEHEMS. An elevated Derjaguin offset is commonly observed when depositing cationic compounds on hydrophilic substrates due to the increase in adhesive forces between exposed surfactant alkane tails, see Ref.[17,70] and chapter 5 of this work. Interestingly, despite similar architectures and overall increases in shear stress, changes in the total shear stress in DPEHEMS systems at different N_0 are caused by varying τ_0 at relatively constant COFs, while DEEDMAC displays strong changes the COF while maintaining a relatively constant τ_0.

The various system properties and NEMD trajectories are now further analyzed for identifying characteristic mechanisms to explain the distinct frictional response with (a) different surfactant types and (b) variation in the surfactant concentration. First, the effect of the system composition after squeeze-out is analyzed as previous chapters indicated a strong sensitivity to the contact thickness and composition. No clear correlation between the shear stress and the lubricant film thickness or lubricant mass after squeeze-out is evident from the data. The more pronounced CTAB depletion at higher initial concentrations compared to hairpin surfactant cases could possibly explain the inverse trend in the COF compared to hairpin surfactants which are more resistant to squeeze-out. Water squeeze-out is also comparable across all four surfactant cases which suggests that changes in the water composition do not account for the observed differences in friction.

Mass density profiles of the lubricants at various N_0 are shown in Fig. 8.10. At low surfactant concentrations, we observe a strong layering in the surface-normal direction z all surfactant types and water. This is consistent with previous adsorption experi-

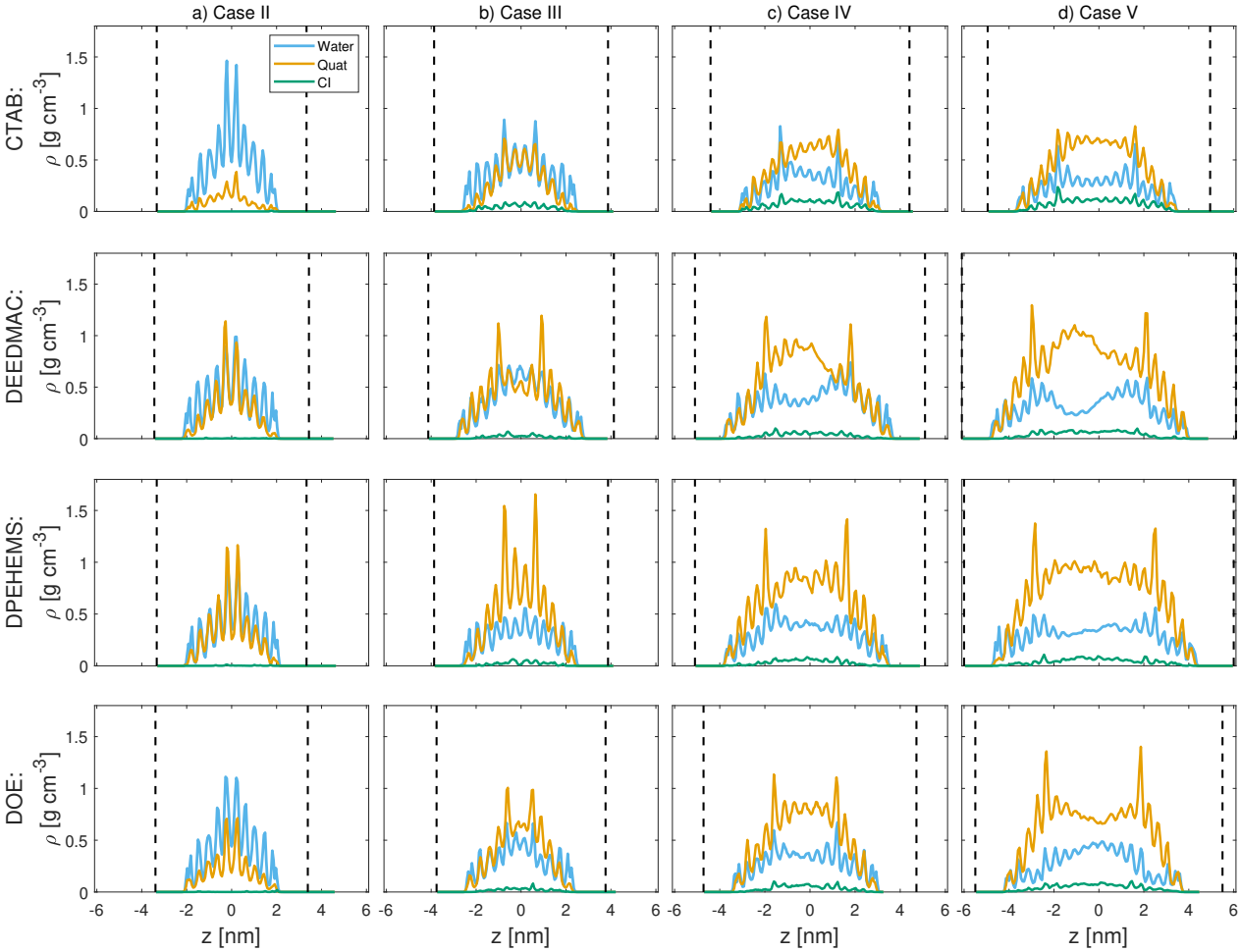


Figure 8.10: Mass density profiles at different N_0 for cotton-on-cotton contacts with four different surfactant types at $\sigma = 10$ MPa and $v_s = 0.1$ ms^{-1}. Cellulose mass density profiles are strongly layered and are therefore not shown to improve readability.

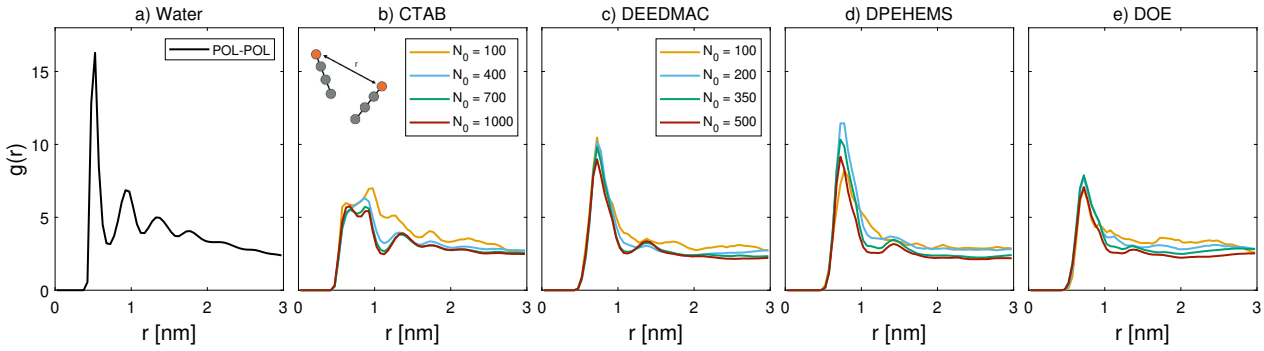


Figure 8.11: Radial distribution functions at various initial surfactant concentrations in cotton-on-cotton contacts at $\sigma = 10$ MPa and $v_s = 0.1$ ms^{-1}.

ments of water on cotton fibres revealing an ice-like ordering on those surfaces.[576] At higher N_0, a more amorphous lubricant film develops at the centre of the contact, but molecules remain layered near the crystalline substrates. However, no clear differences are evident in the mass density profiles of systems with different surfactant types which could explain the different frictional response. The radial distribution functions (RDF) for water and between the quaternary ammonium headgroups are

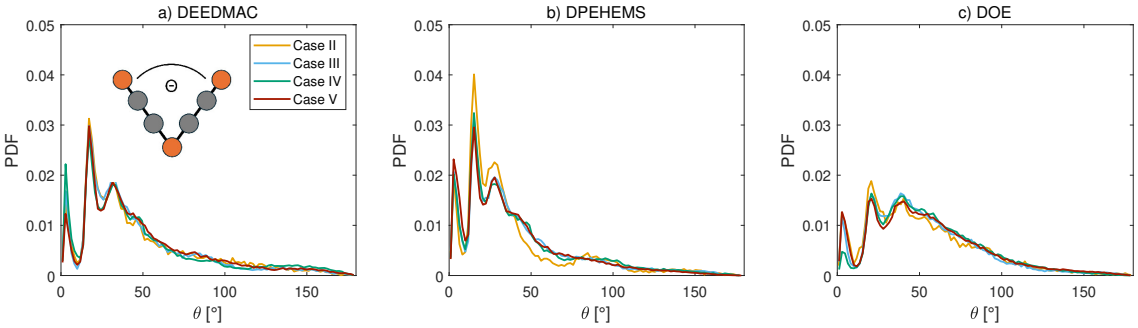


Figure 8.12: Distribution of the molecule opening angle in hairpin surfactants during sliding, i.e., (a) DEEDMAC, (b) DPEHEMS and (c) DOE at different initial concentrations N_0 (cases II-V).

shown in Fig. 8.11. For pure water, the RDF is shown between the central beads of polarizable water molecules. The RDF of water suggests short-range ordering which is stronger than for polarizable water in bulk.[306] This ordering in the RDF is expected to be a symptom of confinement between the predominantly crystalline substrates. DEEDMAC and DPEHEMS show the highest tendency for headgroup aggregation at short distances which coincides with the highest observed COF among all systems with surfactants. The primary peak in the RDF for all hairpin surfactants is found at $r \approx 0.7$-0.8 nm. Snapshots for each configuration during sliding at all N_0 and a contact pressure of $\sigma = 10$ MPa are shown in Fig. 8.13-8.16. A top view of confined surfactants is also shown to illustrate the formation of aggregates which is indeed observed for all four surfactant types. Hydrophobic interactions between alkane tails dominate the aggregation which is in line with the observed increases in the Derjaguin offset. CTAB tends to form wormlike micellar aggregates at high concentrations. Moreover, the higher short-range RDF peaks for DEEDMAC and DPEHEMS signal a tendency for surfactants to form aggregates with more closely-packed cationic headgroups. Since all configurations display strong aggregation, a (partial) transition from spherical or disordered aggregates to monolayers or bilayers is suggested here. It is hypothesized that higher friction from misaligned bilayers as opposed to micellar aggregates. Bilayers which are not oriented in the direction of sliding present a higher energy barrier to overcome through (local) alignment at rough interfaces.

Next, to further investigate this hypothesis, we will investigate the conformation, orientation and ordering properties of cationic surfactants. DEEDMAC, DPEHEMS and DOE typically reside in a hairpin conformation which can be quantified by the opening angle between the two hydrophobic tails of these molecules. Figure 8.12 shows the distribution of the opening angle for the three hairpin surfactants at the considered concentrations. All three surfactant types predominantly adopt a hairpin conformation with peaks in the opening angles at $\Theta < 50°$. No strong differences with respect to the surfactant concentration are evident. However, DPEHEMS and DEEDMAC adopt a more narrow distribution of smaller angles compared to DOE. The order of the magnitude of the primary peak in the PDFs is: DPEHEMS > DEEDMAC > DOE. This is consistent with the short-range packing observed in the RDF

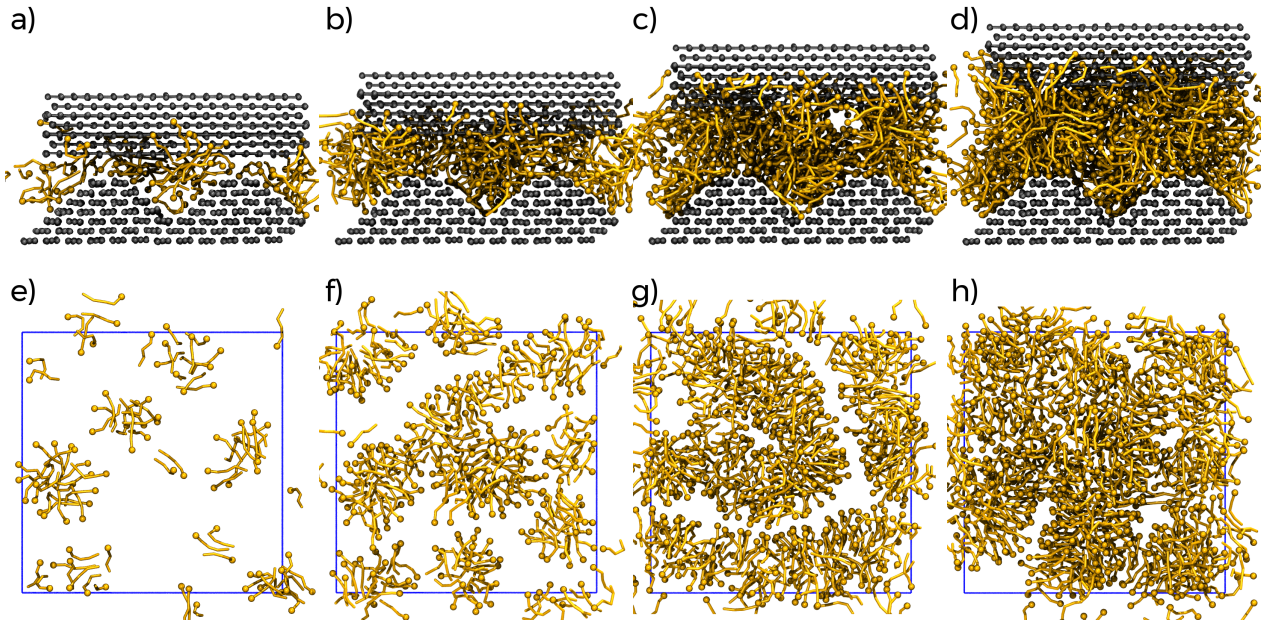


Figure 8.13: Snapshots of full contacts (top) and top views of lubricant films (bottom) in cotton-on-cotton contacts with CTAB at various $N_0 = 100$ (a,e), 400 (b,f), 700 (c,g), and 1000 (d,h) at $\sigma = 10$ MPa. Surfactants are shown in orange. Rendered using VMD.[349]

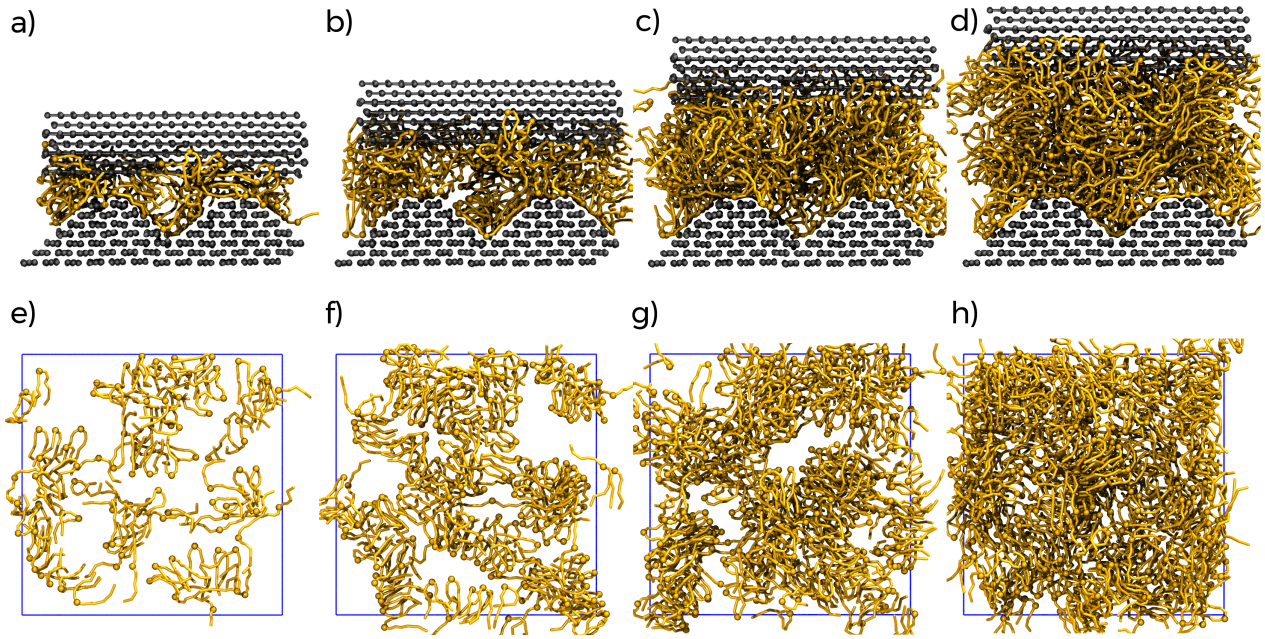


Figure 8.14: Snapshots of full contacts (top) and top views of lubricant films (bottom) in cotton-on-cotton contacts with DEEDMAC at various $N_0 = 100$ (a,e), 200 (b,f), 350 (c,g), and 500 (d,h) at $\sigma = 10$ MPa. Surfactants are shown in orange. Rendered using VMD.[349]

profiles. This in turn might facilitate overall surfactant packing which could directly influence the shape of aggregates and therefore friction. The wider opening angles in DOE are expected to be a result of the unsaturated hydrocarbon tails which is reflected in a more narrow angle between CG beads (120°) at the unsaturated CG bead.

As shown in Fig. 8.13-8.16, the overall aggregation of of surfactants remains disordered, even at increasing film thickness. This rules out the formation of characteristic slip

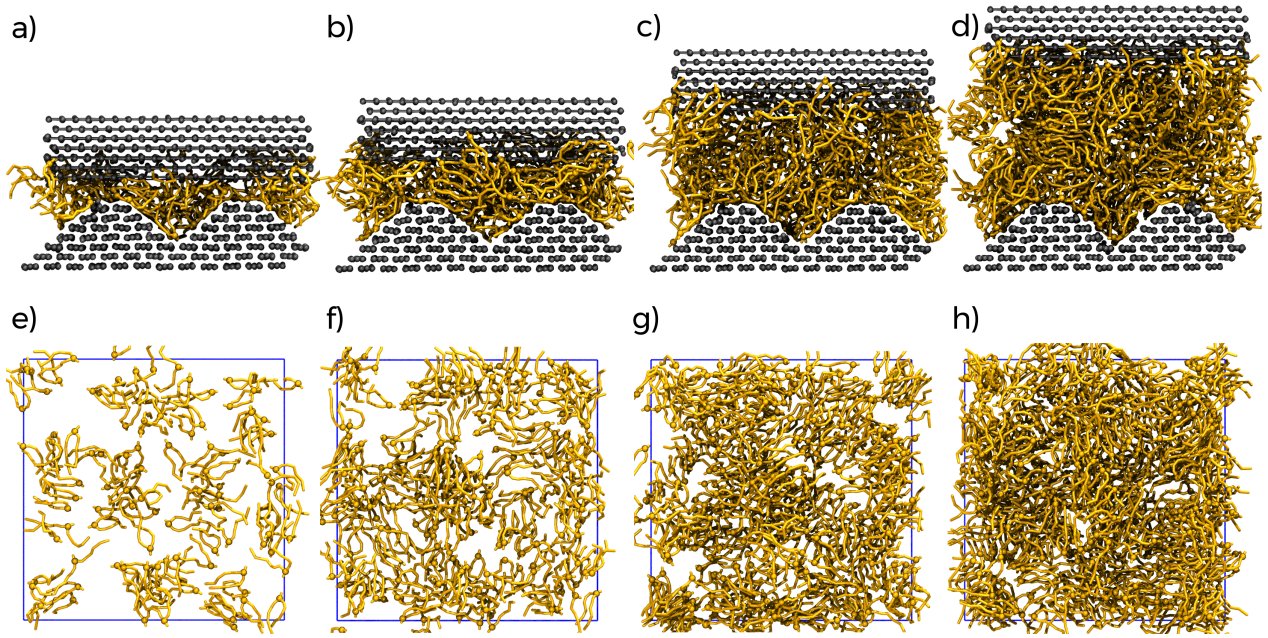


Figure 8.15: Snapshots of full contacts (top) and top views of lubricant films (bottom) in cotton-on-cotton contacts with DPEHEMS at various $N_0 = 100$ (a,e), 200 (b,f) 350 (c,g), and 500 (d,h) at $\sigma = 10$ MPa. Surfactants are shown in orange. Rendered using VMD.[349]

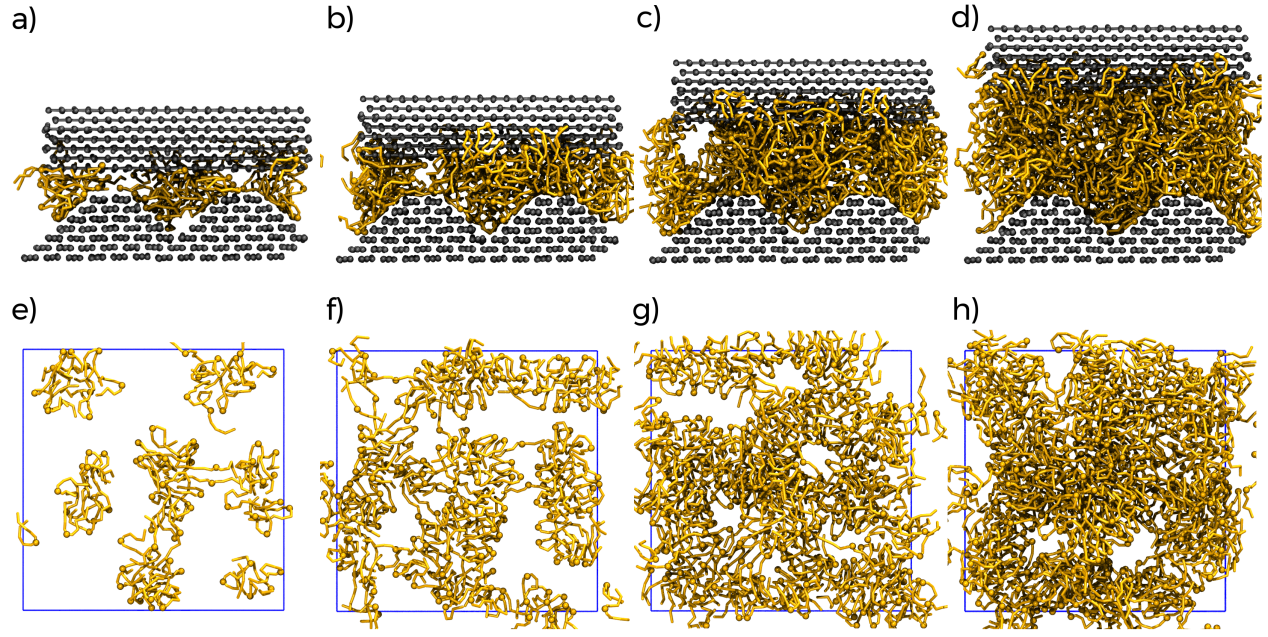


Figure 8.16: Snapshots of full contacts (top) and top views of lubricant films (bottom) in cotton-on-cotton contacts with DOE at various $N_0 = 100$ (a,e), 200 (b,f), 350 (c,g), and 500 (d,h) at $\sigma = 10$ MPa. Surfactants are shown in orange. Rendered using VMD.[349]

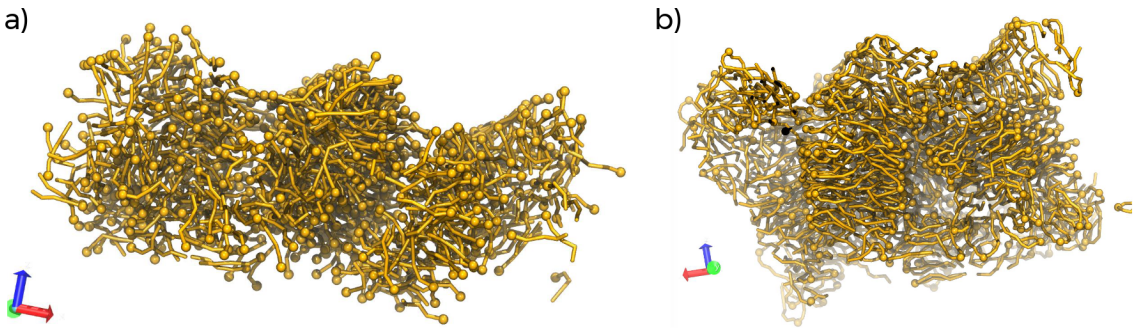


Figure 8.17: Snapshots of (a) CTAB at N_0=1000 (case V) and (b) DEEDMAC at N_0=500 (case V) in sliding cotton-on-cotton contacts at $\sigma = 10$ MPa. Water, counterions and cotton surfaces are not shown. Rendered using VMD.[349] Depth cueing has been applied in the orthogonal views to highlight specific ordered regions.

planes in the direction of sliding as evidence for the lower observed friction coefficient. The corresponding RDF profiles in Fig. 8.11 suggest that short-range ordering is weaker in contacts with DOE than in the other hairpin surfactant cases. Therefore, friction reductions with DOE might be a result of the more rigid diformyl(dimethyl)-azanium headgroup of DOE compared to the methyldiethanolamine and triethanolamine groups on DEEDMAC and DPEHEMS, promoting a more disordered packing. This conformational change is captured during coarse-graining to MARTINI via two short, rigid bonds between the central Q_0 bead and adjacent 2-hydroxyethol P_1 polar beads. Additionally, the unsaturated 1-butene group in the DOE chains, represented by apolar C_2 bead, could also affect packing and interactions with the substrate and water.

By visual inspection of the three-dimensional system trajectories, local ordering of surfactants between substrate asperities was observed. Figure 8.17 depicts two snapshots for CTAB and DEEDMAC respectively. While all systems show some surfactant disorder, CTAB had a tendency to form cylindrical micelles, while DEEDMAC, DPEHEMS and to some extent DOE aggregate in local fragmented bilayers. This tendency to form bilayers is indeed consistent with the behaviour of such surfactants in bulk solution, where they form vesicles consisting of one or multiple bilayered membranes.[283,285,488] When these vesicles break down during drying, they might still reside in a bilayer conformation[282,285,547] similar to what is observed locally in our simulations. To test whether there is a preferential alignment of lubricant molecules, the orientation of surfactants was probed. The orientation of surfactants relative to the surface-normal axis z was checked and is shown in Fig. A.6.27 in the appendix. The probability distributions indicate a primary peak at 90° for all four surfactant types. At low concentrations, this most likely corresponds to surfactant molecules which are confined between cellulose asperities in a flat conformation. Remarkably, the 90-degree peak remains dominant even at high concentrations where the asperities are fully separated. This alignment might be a result of the specific shape of the roughness features which confine surfactant aggregates in pockets between asperities. On flat surfaces, the highest contribution to the orientation PDFs would be expected at 0 and 180 degrees,

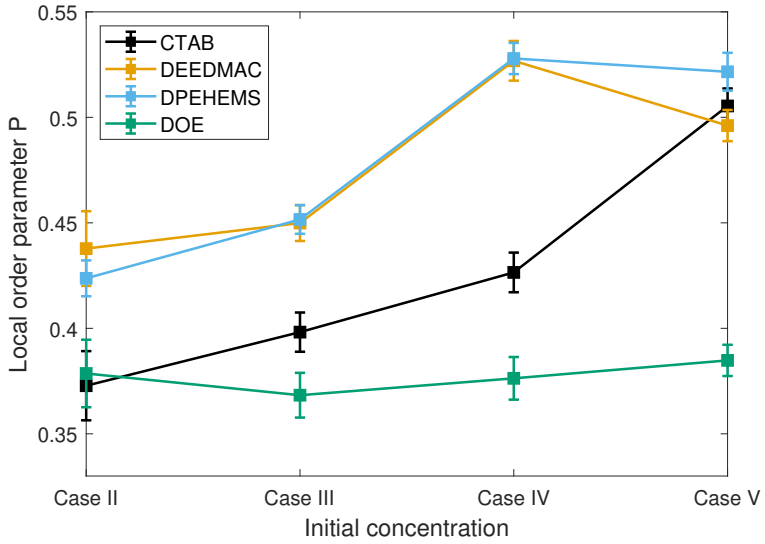


Figure 8.18: Local order parameter for surfactants at different initial concentrations. Error bars indicate the standard deviation around the mean.

as observed in chapter 5. However, no strong differences between the different initial concentrations or surfactant types are evident, so this cannot explain the observed differences in the frictional response.

To identify the prevalence of locally ordered aggregates in the contact, a local version of the order parameter as originally defined in Refs.[577,578] was applied to the NEMD trajectories:

$$\langle P \rangle = \left\langle \frac{1}{N_{\mathrm{k,loc}}} \sum_{i=1}^{N_{\mathrm{loc}}} (\vec{v}_k \cdot \vec{v}_i)^2 \right\rangle, \tag{8.1}$$

where $\vec{v}$ is the vector of the principal component of a single surfactant molecule. The average ordering between $N_{k,loc}$ nearest neighbors of each surfactant molecule is calculated and ensemble-averaged across all molecules in the system. Furthermore, $\langle P \rangle$ is averaged in time. This local version of the ordering parameter is expected to be suitable for multiple aggregates and systems with changes in the local levels of (dis)order. For a uniformly distributed orientation of surfactants $\langle P \rangle$ converges to 1/3 while systems with parallely-aligned molecules yield a value of 1. It is worth noting that even surfactants in 2D (cylindrical) or 3D (spherical) micellar conformation can render a uniform distribution of orientations along at least one axis, thus are expected to lead to lower $\langle P \rangle$.

Figure 8.18 shows the evolution of the local ordering parameter considering six nearest neighbors. This value was found to be suitable for both low and high surfactant concentration to restrict the calculation to relatively short separation distances between neighboring surfactants. Overall, DEEDMAC and DPEHEMS show a higher local ordering across different surfactant concentrations. This is consistent with the higher short-range ordering of surfactant headgroups as found for the RDF profiles in Fig. 8.11. On the other hand, $\langle P \rangle$ increases as a function of the initial concentration for both hairpin surfactants and CTAB. This behaviour is expected as surfactants might be

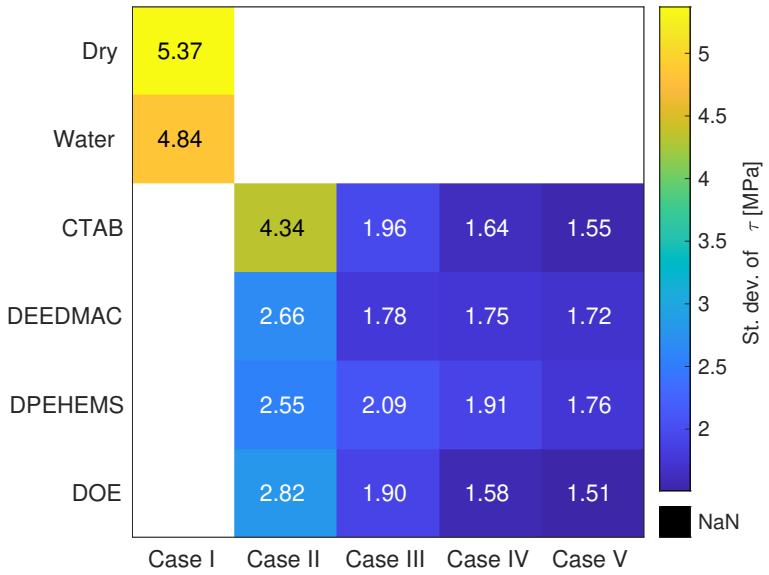


Figure 8.19: Stick-slip tendency in contacts by means of the standard deviation of the friction signals around the mean.

more prone to aggregating at higher concentrations even under confinement. While this might account for overall higher COF for DEEDMAC and DPEHEMS, this cannot explain the non-monotonic changes in friction as a function of the initial concentration per single surfactant type. Interestingly, DOE displays a low degree of ordering. Since snapshots of DOE in Fig. 8.16 also indicate surfactant aggregation, this suggests that molecules within these aggregates are more uniformly orientated which might be beneficial for friction in rough contacts.

In summary, we report that local ordering of entire surfactants may be a suitable handle for differentiating the overall frictional response between distinct molecules. A higher local ordering of DEEDMAC and DPEHEMS correlated with higher absolute shear stresses which is attributed to the formation of misaligned bilayer fragments which resist sliding. Adhesive contributions to the shear stress by means of the Derjaguin offset are correlated to the peak surfactant headgroup ordering observed in the RDF. It may be worth investigating if these observations are also found on more ideal, flat cellulose surfaces as well as on fully amorphous, rough cellulose substrates in future studies.

Finally, the effectiveness of surfactants to suppress stick-slip behaviour is investigated. This is important because softness is not only associated with the mean kinetic COF but also with the oscillatory behaviour which is easily picked up by the human skin.[23,371,415] Figure 8.19 shows the standard deviation from shear stress signals around the mean for all considered surfactant types. Generally, the standard deviation only weakly increases with the normal load, thus only the average across all normal loads is shown. Large signal fluctuations are observed for both dry and wet cases. Pure water is easily squeezed-out leading to contacting asperities with only residual water remaining in

the pockets. Therefore, water is not efficient at suppressing stick-slip which is consistent with previous experiments on other biological substrates such as hair.[184] For systems with surfactants, an increase in surfactant concentration monotonically reduces stick-slip across all surfactant types. The separation of asperities rather than the organization of surfactants tends to be the driving factor for stick-slip suppression. This is consistent with the decrease in surface-normal lubricant layering with increasing concentrations observed in the mass density profiles in Fig. 8.10.

8.5 Conclusions

In this chapter, a coarse-grained MARTINI substrate model for the surface of bleached and scoured cotton cellulose was developed and validated in nanodroplet wetting simulations with polar and non-polar solvents. Secondly, an automation workflow was presented for the virtual friction screening of soft interfaces with small lubricant molecules. This new tool leveraged a set of open-source coarse-graining, atomistic MD tools and the essential steps for soft surface NEMD introduced in the previous chapters. The new tool was then applied to investigate the lubrication performance of several quaternary ammonium surfactants relevant in fabric softener formulations in nanoscale cotton-on-cotton contacts. NEMD simulations were sensitive to the surfactant architecture, with linear (CTAB) and unsaturated alkyl chain hairpin surfactants (DOE) providing the lowest overall friction. This is likely due to a more spherical local packing which promotes lubrication in rough contacts. Furthermore, all cationic surfactants were effective at reducing stick-slip with increasing concentrations due to the formation of a more disordered lubricant film.

The work in this chapter also underlines that the coefficient of friction should not be the only metric to evaluate the shear resistance in textile and more generally soft biomimetic contacts. Rather, the Derjaguin offset which is a measure of adhesion arising from the extended Amontons-Coulomb law should be taken into account as well. Adhesion was particularly strong in contacts with ester-based hairpin surfactants (DPEHEMS) relevant in fabric softeners. This might be attributed to the tendency of such surfactant types to aggregate in bilayers or even vesicles at larger scales. While vesicle deposition is critical for deposition for fabric softeners, their bilayer aggregation behaviour may not be beneficial for lubrication under nanoscale confinement on rough surfaces. The local ordering of DPEHEMS and DEEDMAC was attributed to an overall higher shear stress due to the misalignment of aggregates with the surfaces during sliding. The surfactant headgroup packing was also related to increasing adhesive contributions.

A key finding of this work is that friction coefficients with cationic surfactants tend to be higher than in pure water contacts. This is in contrast to the idea that fabric softeners generally aim at improving tactile perception, thus lower friction in both

cotton-on-cotton and skin-on-cotton contacts. However, the suppression of stick-slip oscillations with higher surfactant concentrations observed here might in fact be equally important, as such oscillatory behaviour is easily picked up by the receptors in skin and might lead to a stronger perception of roughness. On the other hand, there is currently a lack of publicly-available (nanoscale) friction experiments with quaternary ammonium surfactants relevant in fabric softeners. Colloidal probe and sharp-tip AFM are regarded as suitable tools to further probe the nanoscale lubrication mechanisms and thin films considered in this work. These tools coupled with simulations would also be suitable to study the break-down mechanisms of larger deposited structures such as vesicles under load.

As a general recommendation from this chapter, it is suggested to increase the sliding velocity by a factor of 5-10 compared to the present value ($v_s = 0.1$ ms^{-1}). This is because velocity profiles in the surface-normal direction are currently inaccessible due to slow convergence of temporal averages as thermal fluctuations dominate at the present v_s. Velocity profiles can give valuable insights into the formation of slip planes as demonstrated in the previous chapters. The shear stress might also weakly depend on the sliding speed as shown in colloidal probe AFM friction experiments on cellulose.[540] It would therefore also be interesting to simulate a wider range of different sliding velocities. It may also be useful to study friction on cellulose using a flat version of the substrate model. While this does not necessarily reflect the roughness observed in real cotton, it will allow for a somewhat more systematic separation between roughness and surface chemistry effects. Additionally, amorphous cellulose models and rotational effects of nanofibrils along the crystalline axis may also be of interest. The outer shell of cotton nanofibrils has been found to be more disordered in humid environments[534] which is only partially captured in the new model (see Fig. 8.4) as a constant fibril connectivity is enforced.

In the future, the presented workflow could be leveraged to look at more sophisticated compositions such as oppositely charged surfactants[550] or even systems with more than two non-aqueous components. The use of macromolecules would also be beneficial but will require further extensions to the squeeze-out, molecule preparation and equilibration steps. The automation tool developed in this chapter is also transferable to studying hair contacts as well as heterogeneous contacts between any available substrate models (cellulose and hair). Substrate models of the stratum corneum of skin (work in progress) and other textiles such as polyester will also be compatible with this tool. The coarse-grained parametrization routine presented as part of the workflows in this work will also be beneficial to assessing other consumer care and cosmeceutical formulations and other coarse-graining approaches such as dissipative particle dynamics (DPD).

9 Conclusions & outlook

Parts of section 9.2 of this chapter are in preparation for submission as a review article to Advances in Colloid and Interface Science.

9.1 Conclusions

This work introduced a new coarse-grained molecular simulation framework for studying friction between biomimetic hair surfaces and more generally soft interfaces in the presence of molecules relevant for personal care products. Following a review of the state-of-the art research in hair tribology in chapter 2, a new surface model of the F-layer of human hair at various degrees of chemical damage was developed using the coarse-grained *MARTINI 2* forcefield in chapter 3. This model was validated against existing and new structural and wetting experimental data. Combining the experimental data with the structural and wetting insights from simulations, we established baseline model surfaces with a lipid monolayer coverage representative of 'virgin' and 'medium bleached' hair surfaces.

The new F-layer model was subsequently applied to studying hair friction in dry and wet conditions using non-equilibrium molecular dynamics (NEMD) simulations at physiologically relevant contact pressures and sliding velocities. NEMD simulations at various degrees of hair damage were compared to new biomimetic chemical colloidal probe atomic force microscopy (CCP-AFM) experiments [a] and hair friction measurements from the literature. In chapter 5, the deposition of ionic surfactants on virgin and bleached model hair surfaces was investigated. Hair surfaces with adsorbed surfactants were then probed for changes in their frictional and wetting properties. While cationic surfactants are highly relevant as deposition agents in hair conditioning products, more complex formulations are used in shampoos fulfilling various purposes such as cleansing and conditioning. Oppositely-charged cationic polyelectrolyte-anionic surfactant complexes which are commonly found in such products were therefore investigated next in chapters 6 and 7. A new parametrization for cationic guar gum (CGG), a biocompatible polyelectrolyte, was derived for the *MARTINI 2* forcefield. Highly charged CGG and anionic surfactants (SDS) were sequentially deposited at hair surfaces and then used in NEMD simulations of hair contacts. In a second step, CGG properties such as the charge density, adsorption density and chain length were systematically tested for their effect on deposition and hair friction.

a Courtesy of Dr. Yuri Roiter (P&G)

Finally, the learnings and workflows established for the nanotribological studies on model hair surfaces were applied to study the friction on cotton cellulose in the presence of surfactants relevant in fabric softeners. As part of this investigation, a new tool for automated nanoscale friction screening on soft surfaces was implemented.

The key findings of this work and answers to the objective questions expressed in the introduction, chapter, 1 are summarized below:

1. Coarse-grained MD was demonstrated to be a suitable tool for investigating the nanoscale interfacial properties of human hair. The new F-layer model introduced in this work is capable of reproducing changes in the frictional and wetting response of hair upon chemical damage, comparable to observations from experiments.
2. NEMD simulations and new CCP-AFM experiments of wet hair friction uncovered counterion trapping as a new potential mechanism for increased friction in chemically damaged human hair. This shows that surface chemistry can also explain experimental observations of increased friction with higher damage, rather than solely changes in the local surface roughness. This is in line with the experimental observations reviewed in chapter 2 where higher frictional increases due to damage were observed in nanoscale compared to macroscopic experiments (Fig. 2.12).
3. Preliminary squeeze-out simulations are essential to establishing reliable contact compositions in soft surface contacts. For highly viscous lubricants with low amounts of water, the explicit water bath could possibly be removed for computational efficiency. For macromolecules, care should be taken when partial squeeze-out is observed.
4. A multistage adsorption behaviour was found for cationic surfactant adsorption consistent with previous experiments despite a much higher surfactant concentration in bulk. On bleached model hair surfaces, cationic surfactants could also successfully restore low friction due to mono-/bilayer adsorption and hydrophobicity. Excess surfactants residing in a bilayer were found to be sheared during sliding which would be expected to lead to depletion from the contact in non-periodic systems.
5. A new coarse-grained *MARTINI 2* parametrization of cationic guar gum (CGG) was developed based on all-atom simulations and previous works on the coarse-grained parametrization of polysaccharide.[490,497]
6. The sequential deposition of oppositely and strongly charged PE-surfactant complexes containing CGG and SDS on hair yields synergistic effects leading to ultra-low friction at low and moderate loads on both virgin and bleached hair, even at low degrees of polyelectrolyte coverage.
7. Friction on biomimetic hair surfaces is strongly dependent on the architecture of the adsorbed PE. Intermediate and high PE charge densities led to an improved

hair lubricity in the presence of anionic surfactants than low-charge-density PE's which could be easily squeezed out and did not entrap enough surfactants. At increased PE adsorption densities, further friction reductions were observed and friction was independent of the degree of hair damage due to a fully developed lubricant layer. For chains with a more realistic length and a degree of substitution of 30%, surfactant entrapment was too weak which outweighed the formation of loops and tails on the surface.

8. The presented workflows are also suitable for virtual screening of nanoscale soft biomimetic contacts in general. This was demonstrated for cotton cellulose contacts with cationic fabric softener surfactants. Surfactants with shorter hydrocarbon chains were found to be more effective at lubricating rough, bleached cellulose contacts under nanoscale confinement.

9. A new tool for automated CG-NEMD frictional screening of soft biomimetic contacts was established which can also be used to obtain new CG parametrizations for small molecules in *MARTINI 2* by embedding and extending a range of open-source software. This tool will be beneficial for high-throughput screening of existing and new molecules and formulation compositions in hair, cotton and skin contacts.

9.2 Perspectives for hair and soft surface (nano)-tribology

In addition to the above findings, the newly developed computational workflows and soft surface nano-tribological tools developed in this work offer new opportunities for screening new formulations for personal care and cosmeceutical products. This work predominantly focused on hair tribology in sliding contacts. However, adhesive properties of hair are equally relevant for a good detangling performance and avoiding hair clumping. The presented F-layer model and preliminary squeeze-out routines are also expected to be directly applicable to studying hair-on-hair adhesion by virtual force-distance curves. Work is currently underway to evaluate the feasibility of such simulations by comparison to biomimetic CCP-AFM experiments.

The most urgent challenge in the hair and personal care industry is probably the requirement for more sustainable and biocompatible ingredients and for a more responsible and eco-friendly product lifecycle. Recently, Luengo et al.[10] provided a comprehensive review on the matter of green chemistry in hair care products. The authors stressed the importance of replacing controversial components such as petroleum-based, phosphates, silicones and even cationic components by sustainable alternatives without compromising the formulation performance.[10] Numerous works already studied the deposition mechanisms of biocompatible ingredients, e.g., see Refs.[114,123,579] Some studies have already focused on hair tribology in this area to some extent: The friction response of bio-sourced polysaccharides such as guar gum and cellulose derivatives on hair has been subject to research for more than two

decades now.[36,291,297,482] Additionally, biosurfactants are also regarded as a promising surrogate and have therefore been focus in formulation research.[580–582] Specifically, glycolipids such as mannosylerythritol lipids (MEL)[580,581] acidic sophorolipid (ASL) and alkyl polyglucoside (APG)[582] have shown promising lubricating properties on hair in macroscopic friction experiments. However, a large fraction of today's hair care products typically contain some of the problematic components mentioned above. Cationic surfactants and silicones are in fact essential to the conditioning performance of many products. The search for novel components that are responsibly sourced and biocompatible should include tribological hair screening to ensure a reliable product performance. The tools developed in this work pave way for screening much wider ranges of green, biocompatible surfactant and polymer architectures on biomimetic hair and soft interfaces at the early stage of product development. A follow-up project will look at the specific role of biosurfactants such as glycolipids on hair friction.

Due to the multiscale nature of hair and the need for new chemistries as well as for high-throughput friction screening, it is conceivable that tribological investigations from the nanoscale to the macroscale will remain important. Nanoscale experiments and simulations will further prove their value in the search for novel and yet unclear lubrication mechanisms. Recently, Guryanov et al. highlighted the potential of nanoarchitectonics of hair.[583] The deposition of lubricants and conditioner molecules by nanomaterials is a promising alternative to the equally complex dilution-deposition mechanism. The deposition of compounds from structures such as vesicles, lipisomes or liquid crystals is indeed already heavily used in cosmeceutical,[584] homecare applications[585] and even to some extent in hair care.[586] However, the implications of colloidal delivery structures on hair friction are yet to be explored.

The majority of experimental studies in hair tribology have focused on either combing, AFM or hair-on-hair friction. In chapter 2, the available literature on hair-skin friction was reviewed, which is important for quantifying and understanding the mechanisms associated to the tactile perception of hair. Most quantitative studies in this area have been focusing on either *in vivo* or artificial skin investigations on the macroscale. Sensory panel tests are likely still required at a later stage of the formulation design process for subjective evaluations of the tactile perception.[5] However, they cannot be used in the early development stage for identifying specific lubrication mechanisms. Nanoscale experiments as well as molecular models of hair-skin contacts have not been explored in the literature to the best of the authors' knowledge. This might be due to the multiscale structure, highly non-linear elasticity and high deformability of human skin which is difficult to model at the small scale. Some coarse-grained molecular models of the stratum corneum (SC) of the epidermis in human skin have been developed recently,[587–592] which provide a suitable basis for molecular hair-skin tribology studies. An early version of a nanoscale SC model has been tested for NEMD simulations as part of this project and will be discussed in future work. This model will

also be integrated into the automation tool established in chapter, 8 thus enabling heterogeneous contacts between hair or cotton and skin.

Molecular models are expected to play an even more important role in hair surface science and care product development. This work already demonstrated the capability of capturing nanoscale hair friction under both boundary lubrication, while other studies have also considered hydrodynamic lubrication.[36] One fundamental pathway for improving the speed of hair modeling is the use of multiscale frameworks. Such approaches have only been employed in hair modeling in a few instances[244,299] which also did not focus on tribology. One conceivable solution to capturing larger structures of polymer-surfactant complexes on hair would be to couple all-atom or coarse-grained MD to self-consistent field theory (SCFT) calculations which have been used extensively in hair research, e.g. Ref.[128–130,247]. Equilibrium SCFT density profiles could then be used to generate an initial conformation of compounds on hair or in the bulk. Another example of successful coupling between the scales is the combination of atomistic, coarse-grained and finite element method simulations in multi-scale modeling studies on the adhesion of gecko feet.[593–599] The underlying surface chemistry of gecko feet is indeed loosely comparable to that of human hair, so future multi-scale approaches on hair tribology might draw inspiration from these studies. The use of machine learning for rapid force field tuning[598] in surface sciences is a further promising perspective to reducing the computational workload of multi-scale models. Hair multiscale approaches considering mesoscale particle or continuum models could bridge the gap between the nanoscale friction mechanisms and contributions from macroscopic surface roughness features on hair such as cuticle scales and striations. These models might also allow for studying hair products with respect to their cleansing performance of excess fats and detrius. Full hair filament interaction models[234,235] could also be extended to incorporate fibre-fibre friction and adhesion forces obtained from smaller-scale models. Overall, multiscale models are expected to significantly reduce simulation times if computational load can be reduced on the smallest (nanoscale) part of the chain and shifted to the generally faster-performing (although typically more inaccurate) larger scale continuum models. An acceleration would in fact be highly beneficial for further driving the emergence of high-throughput and virtual screening approaches[241,242] for the development of hair care formulations.[243]

9.3 Practical challenges

There are also some practical questions that arise from this work which could be subject to future investigations. In chapter 4, the suitability of the polarizable *MARTINI* water model for capturing bulk viscosity was briefly evaluated to render robust results below a bulk pressure of around 100 MPa. However, it might also be interesting to evaluate both this water model and alternatives such as the non-polarizable water

model and the *MARTINI 3* version[331]. This could also include testing the isothermal compressibility which can be easily compared to experiments and atomistic models. As mentioned in previous chapters, the introduction of the *MARTINI 3* forcefield[331] has also seen a range of new models for polyelectrolytes and coacervation.[494,526] Since this work is still based on the previous version, *MARTINI 2*, it will be interesting to reach compatibility between parts of this work and these new models. At the time of writing this work, there is no polarizable water model available for *MARTINI 3* to the best of the author's knowledge. This is seen to be critical to capturing some of the interfacial properties in the presence of a large number of charges. A short-term solution might be to port some of the new *MARTINI 3* parametrizations back to *MARTINI 2.2*.

One challenge of molecular simulations is determination of accurate formulation concentrations for different levels of surface charges and more importantly as a function of the normal load. It is conceivable that the contact thickness and composition will vary depending on the external load. Preliminary squeeze-out simulations[354] were originally introduced to establish a more realistic contact composition for systems containing organic friction modifiers confined between two solid substrates.[354] In this work, the technique was found to be crucial hair contacts with water, with ionic surfactants and for systems of hair surfaces with pre-adsorbed larger polyelectrolytes and anionic surfactants. However, the finite system size limitation and the requirement for a relatively large surrounding water bath make this technique challenging for cases in which aggregates are freely distributed in solution or are subjected to partial squeeze-out. An alternative approach to capturing the realistic contact composition for such systems includes the use of grand-canonical molecular dynamics (GCMD).[600–605] A drawback of GCMD has been its poor computational efficiency[20] and parallelizability which limits the approach to relatively small systems, thus excluding macromolecules such as polymers. However, small and intermediate sized systems might still be suitable to test for enabling a squeeze-out approach in hair and other soft tribological contacts. Kim et al.[606] recently presented a new implementation of a hybrid GCMD framework in LAMMPS which drastically improves the computational efficiency in parallel computing environments. It will be interesting to test this new framework for preliminary squeeze-out. Exploring the use of implicit solvent models might be another option which could increase computational efficiency for parts of the simulations discussed in this work. This will interesting for adsorption of molecules, where hydrodynamic contributions to interfacial forces are not necessary. Explicit water models are expected to be remain a requirement for accurate squeeze-out and NEMD simulations.

Bibliography

1 A. Berg *et al.*, The beauty market in 2023: A special State of Fashion report, *https://www.mckinsey.com/industries/retail/our-insights/the-beauty-market-in-2023-a-special-state-of-fashion-report (accessed 10 January 2024)*, 2023.

2 M. I. Carretero, Clay minerals and their beneficial effects upon human health. A review, *Applied Clay Science*, 2002, **21**, 155–163.

3 P. Vossen, Olive oil: history, production, and characteristics of the world's classic oils, *HortScience*, 2007, **42**, 1093–1100.

4 M. F. R. G. Dias, Hair Cosmetics: An Overview, *International Journal of Trichology*, 2015, **7**, 2–15.

5 G. S. Luengo *et al.*, Surface science of cosmetic substrates, cleansing actives and formulations, *Advances in Colloid and Interface Science*, 2021, **290**, 102383.

6 R. M. Trüeb, Shampoos: Ingredients, efficacy and adverse effects, *Journal of the German Society of Dermatology*, 2007, **5**, 356–365.

7 Z. D. Draelos, Essentials of hair care often neglected: Hair cleansing, *International journal of trichology*, 2010, **2**, 24–29.

8 A. C. Kogawa *et al.*, Synthetic detergents: 100 years of history, *Saudi pharmaceutical journal*, 2017, **25**, 934–938.

9 J. Cumming *et al.*, The fate of polymeric quaternary ammonium salts from cosmetics in wastewater treatment plants, *Water, Air, & Soil Pollution*, 2011, **216**, 441–450.

10 G. S. Luengo *et al.*, Physico-chemical challenges on the self-assembly of natural and bio-based ingredients on hair surfaces: towards sustainable haircare formulations, *Green Chem.*, 2023, 7863–7882.

11 S. New, G. Daniels and C. L. Gummer, Measuring the frequency of consumer hair combing and magnitude of combing forces on individual hairs in a tress and the implications for product evaluation and claims substantiation, *International Journal of Cosmetic Science*, 2018, **40**, 461–466.

12 D. Dowson, *History of tribology. 2nd edition*, John Wiley & Sons, Ltd, London, 1979.

13 D. Dowson, Bio-tribology, *Faraday discussions*, 2012, **156**, 9–30.

14 F. Di Puccio and L. Mattei, Biotribology of artificial hip joints, *World journal of orthopedics*, 2015, **6**, 77.

15 G. Limbert *et al.*, Biotribology of the ageing skin—Why we should care, *Biotribology*, 2019, **17**, 75–90.

16 N. Nikogeorgos *et al.*, Nanotribological characterization of human head hair by friction force microscopy in dry atmosphere and aqueous environment, *Biointerphases*, 2010, **5**, 60.

17 C. LaTorre and B. Bhushan, Nanotribological characterization of human hair and skin using atomic force microscopy, *Ultramicroscopy*, 2005, **105**, 155–175.

18 L. Fernández-Peña *et al.*, Study of the Dilution-Induced Deposition of Concentrated Mixtures of Polyelectrolytes and Surfactants, *Polymers*, 2022, **14**, 1335.

19 L. Fernández-Peña *et al.*, Dilution-Induced Deposition of Concentrated Binary Mixtures of Cationic Polysaccharides and Surfactants, *Polymers*, 2023, **15**, 3011.

20 J. P. Ewen, D. M. Heyes and D. Dini, Advances in nonequilibrium molecular dynamics simulations of lubricants and additives, *Friction*, 2018, **6**, 349–386.

21 M. G. Saunders and G. A. Voth, Coarse-Graining Methods for Computational Biology, *Ann. Rev. Biophys.*, 2013, **42**, 73–93.

22 D. Dowson, A tribological day, *Proceedings of the Institution of Mechanical Engineers, Part J*, 2009, **223**, 261–273.

23 A. Galliano *et al.*, Tribology of an assembly of hairs: Influence of multiscale surface chemistry and structure on sensorial tactile properties, *Skin Research and Technology*, 2021, **27**, 607–617.

24 B. J. Briscoe and A. Winkler, A statistical analysis of the frictional forces generated between monofilaments during intermittent sliding, *Journal of Physics D: Applied Physics*, 1985, **18**, 2143–2167.

25 J. Swift, Fine details on the surface of human hair, *International journal of cosmetic science*, 1991, **13**, 143–159.

26 M. J. Adams, B. J. Briscoe and T. K. Wee, The differential friction effect of keratin fibres, *Journal of Physics D: Applied Physics*, 1990, **23**, 406–414.

27 B. Bhushan, G. Wei and P. Haddad, Friction and wear studies of human hair and skin, *Wear*, 2005, **259**, 1012–1021.

28 H. Mizuno, G. S. Luengo and M. W. Rutland, New Insight on the Friction of Natural Fibers. Effect of Sliding Angle and Anisotropic Surface Topography, *Langmuir*, 2013, **29**, 5857–5862.

29 S. Breakspear, J. R. Smith and G. S. Luengo, Effect of the covalently linked fatty acid 18-MEA on the nanotribology of hair's outermost surface, *Journal of Structural Biology*, 2005, **149**, 235–242.

30 G. Wei, B. Bhushan and P. M. Torgerson, Nanomechanical characterization of human hair using nanoindentation and SEM, *Ultramicroscopy*, 2005, **105**, 248–266.

31 B. Bhushan, Nanoscale characterization of human hair and hair conditioners, *Progress in Materials Science*, 2008, **53**, 585–710.

32 X. Zeng *et al.*, An in vivo methodology for studying the interfacial interactions between skin and hair with respect to tactile friction and sensory properties, *Measurement*, 2021, **179**, 109499.

33 Y. K. Kamath and H.-D. Weigmann, Measurement of combing force, *Journal of the Society of Cosmetic Chemists*, 1984, **37**, 111–124.

34 G. Roscioli, S. Taheri-Mousavi and C. C. Tasan, How hair deforms steel, *Science.*, 2020, **369**, 689–694.

35 B. Kasemo, Biological surface science, *Surface Science*, 2000, **500**, 656–677.

36 B. J. Coscia *et al.*, Shearing friction behaviour of synthetic polymers compared to a functionalized polysaccharide on biomimetic surfaces: models for the prediction of performance of eco-designed formulations, *Physical Chemistry Chemical Physics*, 2023, **25**, 1768–1780.

37 G. S. Luengo, A. Galliano and C. Dubief, in *Aqueous Lubrication in Cosmetics*, ed. N. Spencer, World Scientific Publishing Ltd, London, UK, 2014, ch. Chapter 4, pp. 103–144.

38 G. S. Luengo, H. Mizuno and M. W. Rutland, in *Hair-Hair Contact Dynamics and Interactions Studied with Atomic Force Microscopy*, ed. P. Humbert *et al.*, Springer International Publishing, 2017, pp. 835–845.

39 S. Tokunaga, H. Tanamachi and K. Ishikawa, Degradation of hair surface: Importance of 18-MEA and epicuticle, *Cosmetics*, 2019, **6**, 31.

40 C. F. Cruz *et al.*, Human hair and the impact of cosmetic procedures: A review on cleansing and shape-modulating cosmetics, *Cosmetics*, 2016, **3**, 1–22.

41 J. A. Swift and J. R. Smith, Microscopical investigations on the epicuticle of mammalian keratin fibres, *Journal of Microscopy*, 2001, **204**, 203–211.

42 C. LaTorre and B. Bhushan, Nanotribological effects of hair care products and environment on human hair using atomic force microscopy, *Journal of Vacuum Science & Technology A: Vacuum, Surfaces, and Films*, 2005, **23**, 1034–1045.

43 R. A. Lodge and B. Bhushan, Wetting properties of human hair by means of dynamic contact angle measurement, *Journal of Applied Polymer Science*, 2006, **102**, 5255–5265.

44 L. J. Wolfram, Human hair: A unique physicochemical composite, *Journal of the American Academy of Dermatology*, 2003, **48**, S106–S114.

45 I. P. Seshadri and B. Bhushan, In situ tensile deformation characterization of human hair with atomic force microscopy, *Acta Materialia*, 2008, **56**, 774–781.

46 R. Dawber, Hair: Its structure and response to cosmetic preparations, *Clinics in Dermatology*, 1996, **14**, 105–112.

47 B. Buffoli *et al.*, The human hair: from anatomy to physiology, *International Journal of Dermatology*, 2013, **53**, 331–341.

48 M. Birbeck and E. Mercer, The electron microscopy of the human hair follicle. I. Introduction and the hair cortex., *The Journal of biophysical and biochemical cytology*, 1957, **3**, 203–214.

49 W. T. Astbury and H. J. Woods, X-Ray studies of the structure of hair, wool, and related fibres. II.- the molecular structure and elastic properties of hair keratin, *Philosophical Transactions of the Royal Society of London. Series A, Containing Papers of a Mathematical or Physical Character*, 1933, **232**, 333–394.

50 C. Popescu and H. Höcker, Hairâ€"the most sophisticated biological composite material, *Chemical Society Reviews*, 2007, **36**, 1282–1291.

51 S. P. Gurden *et al.*, Quantitative analysis and classification of AFM images of human hair, *Journal of Microscopy*, 2004, **215**, 13–23.

52 M. G. Dobb *et al.*, 12—Morphology of the Cuticle Layer in Wool Fibres and Other Animal Hairs, *Journal of the Textile Institute Transactions*, 1961, **52**, T153–T170.

53 J. A. Swift, Human hair cuticle: Biologically conspired to the owner's advantage, *Journal of the Society of Cosmetic Chemists*, 1999, **50**, 23–47.

54 J. Leeder and J. Bradbury, The discontinuous nature of epicuticle on the surface of keratin fibers, *Textile Research Journal*, 1971, **41**, 563–568.

55 J. R. Smith and J. A. Swift, Lamellar subcomponents of the cuticular cell membrane complex of mammalian keratin fibres show friction and hardness contrast by AFM, *Journal of Microscopy*, 2002, **206**, 182–193.

56 S. Breakspear *et al.*, Cuticle â€" Designed by nature for the sake of the hair, *International Journal of Cosmetic Science*, 2022, **44**, 343–362.

57 G. E. Rogers, Known and Unknown Features of Hair Cuticle Structure: A Brief Review, *Cosmetics*, 2019, **6**, 32.

58 L. N. Jones and D. E. Rivett, The Role of 18-Methyleicosanoic Acid in the Structure and Formation of Mammalian Hair Fibres, *Micron*, 1997, **28**, 469–485.

59 J. D. Leeder and J. A. Rippon, Changes Induced in the Properties of Wool by Specific Epicuticle Modification, *Journal of the Society of Dyers and Colourists*, 1985, **101**, 11–16.

60 P. Wertz, Integral lipids of hair and stratum corneum., *Exs*, 1997, **78**, 227–237.

61 D. J. Evans and M. Lanczki, Cleavage of Integral Surface Lipids of Wool by Aminolysis, *Textile Research Journal*, 1997, **67**, 435–444.

62 D. J. Evans *et al.*, 7th International Wool Textile Research Conference, 1985, pp. 135–142.

63 Y. K. Kamath, C. J. Dansizer and H.-D. Weigmann, Surface Wettability of Human Hair. II. Effect of Temperature on the Deposition of Polymers and Surfactants, *Journal of Applied Polymer Science*, 1985, **30**, 925–936.

64 R. Molina *et al.*, Chemical modifications on human hair studied by means of contact angle determination, *Journal of Colloid and Interface Science*, 2001, **237**, 40–46.

65 D. W. Cheong, F. C. Lim and L. Zhang, Insights into the structure of covalently bound fatty acid monolayers on a simplified model of the hair epicuticle from molecular dynamics simulations, *Langmuir*, 2012, **28**, 13008–13017.

66 J. M. Maxwell and M. G. Huson, Scanning probe microscopy examination of the surface properties of keratin fibres, *Micron*, 2005, **36**, 127–136.

67 M. Huson *et al.*, New insights into the nature of the wool fibre surface, *Journal of structural biology*, 2008, **163**, 127–136.

68 N. Baghdadli and G. S. Luengo, Journal of Physics: Conference Series, 2008, p. 52034.

69 Y. K. Kamath, C. J. Dansizer and H.-D. Weigmann, Wetting Behavior of Human Hair Fibers, *Journal of Applied Polymer Science*, 1978, **22**, 2295–2306.

70 R. L. McMullen and S. P. Kelty, Investigation of human hair fibers using lateral force microscopy, *Scanning*, 2001, **23**, 337–345.

71 N. Nishikawa *et al.*, Structural change of keratin protein in human hair by permanent waving treatment1This work was presented at the 44th Annual Meeting of the Society of Polymer Science, Japan; 1996, Nagoya, Japan.1, *Polymer*, 1998, **39**, 3835–3840.

72 F.-J. Wortmann *et al.*, Investigations of cosmetically treated human hair by differential scanning calorimetry in water, *Journal of cosmetic science*, 2002, **53**, 219–228.

73 A. C. Brown and J. A. Swift, Hair breakage: the scanning electron microscope as a diagnostic tool, *Journal of the Society of Cosmetic Chemists*, 1975, **26**, 289–297.

74 M. Okamoto *et al.*, ToF-SIMS characterization of the lipid layer on the hair surface. II : Effect of the 18-MEA lipid layer on surface hydrophobicity, *Surface and Interface Analysis*, 2011, **43**, 298–301.

75 J. R. Smith and J. A. Swift, Maple syrup urine disease hair reveals the importance of 18-methyleicosanoic acid in cuticular delamination, *Micron*, 2005, **36**, 261–266.

76 M. A. A. Ghani *et al.*, Matting of hair: A multifactorial enigma, *Dermatology*, 2000, **201**, 101–104.

77 S. Shiel, Hair health and management of common hair disorders, *Journal of Cosmetic Dermatology*, 2007, **6**, 12–17.

78 F. J. Wortmann, G. Wortmann and E. Schulze Zur Wiesche, Spatial probing of the properties of the human hair surface using wilhelmy force profiles, *Langmuir*, 2010, **26**, 7365–7369.

79 V. Dupres *et al.*, Wetting and electrical properties of the human hair surface: Delipidation observed at the nanoscale, *Journal of Colloid and Interface Science*, 2007, **306**, 34–40.

80 N. Wang *et al.*, Effect of Surface Treatments on the Nanomechanical Properties of Human Hair, *ACS Biomaterials Science & Engineering*, 2018, **4**, 3063–3071.

81 C. Robbins, Hair breakage during combing. I. Pathways of breakage, *International Journal of Cosmetic Science*, 2007, **29**, 485–486.

82 K. Takada *et al.*, Influence of Oxidative and/or Reductive Treatment on Human Hair (I): Analysis of Hair-Damage after Oxidative and/or Reductive Treatment, *Journal of Oleo Science*, 2003, **52**, 541–548.

83 J. A. Swift, The mechanics of fracture of human hair, *International Journal of Cosmetic Science*, 1999, **21**, 227–239.

84 M. Richena and C. A. Rezende, Structure of photo-damaged white and naturally pigmented human hair, *Journal of Photochemistry and Photobiology B: Biology*, 2020, **202**, 111673.

85 X. Qu *et al.*, Pollution damage and protection of Asian hair, *Cosmetics*, 2018, **5**, 17.

86 R. L. Mcmullen, T. Gillece and T. Schiess, Physicochemical Properties of Textured Hair, *J. Cosmet. Sci*, 2021, **72**, 711–731.

87 I. P. Seshadri and B. Bhushan, Effect of ethnicity and treatments on in situ tensile response and morphological changes of human hair characterized by atomic force microscopy, *Acta Materialia*, 2008, **56**, 3585–3597.

88 G. Daniels, A. Fraser and G. E. Westgate, How different is human hair? A critical appraisal of the reported differences in global hair fibre characteristics and properties towards defining a more relevant framework for hair type classification, *International Journal of Cosmetic Science*, 2023, **45**, 50–61.

89 A. Elzubair *et al.*, Tribological and mechanical properties of brazilian hair, *Biotribology*, 2017, **12**, 33–42.

90 Y. Liu *et al.*, Capturing coacervate formation and protein partition by molecular dynamics simulation, *Chemical Science*, 2022, **14**, 1168–1175.

91 M. K. Gaines *et al.*, Reimagining Hair Science: A New Approach to Classify Curly Hair Phenotypes via New Quantitative Geometric and Structural Mechanical Parameters, *Accounts of Chemical Research*, 2023, **56**, 1330–1339.

92 M. Korte *et al.*, Distribution and localization of hydrophobic and ionic chemical groups at the surface of bleached human hair fibers, *Langmuir*, 2014, **30**, 12124–12129.

93 Y. Masukawa *et al.*, Damage to Human Hair Caused by Repeated Bleaching Combined with Daily Weathering during Daily Life Activities, *Exogenous Dermatology*, 2004, **3**, 273–281.

94 M. Okamoto *et al.*, Investigation of the damage on the outermost hair surface using ToF-SIMS and XPS, *Surface and Interface Analysis*, 2012, **44**, 736–739.

95 T. Takahashi *et al.*, Age-dependent changes in damage processes of hair cuticle, *Journal of Cosmetic Dermatology*, 2015, **14**, 2–8.

96 L. Coderch *et al.*, The Role of Lipids in the Process of Hair Ageing, *Cosmetics*, 2022, **9**, 124.

97 M. B. C. Maymone, S. E. Pollock and N. Vashi, Hair Aging in Different Races and Ethnicities, *Journal of Clinical and Aesthetic Dermatology*, 2021, **14**, 38–44.

98 L. D. Bloch *et al.*, Chemical and physical treatments damage Caucasian and Afro-ethnic hair fibre: analytical and image assays, *Journal of the European Academy of Dermatology and Venereology*, 2019, **33**, 2158–2167.

99 F. M. Maddar *et al.*, Nanoscale Surface Charge Visualization of Human Hair, *Analytical Chemistry*, 2019, **91**, 4632–4639.

100 T. Gao *et al.*, Study of hair surface energy and conditioning, *Journal of Cosmetic Science*, 2011, **62**, 127–137.

101 P. A. Cornwell, A review of shampoo surfactant technology: consumer benefits, raw materials and recent developments, *International Journal of Cosmetic Science*, 2018, **40**, 16–30.

102 C. J. Thompson *et al.*, Shampoo Science: A Review of the Physiochemical Processes behind the Function of a Shampoo, *Macromolecular Chemistry and Physics*, 2023, 2200420.

103 C. A. Dreiss, Wormlike micelles: Where do we stand? Recent developments, linear rheology and scattering techniques, *Soft Matter*, 2007, **3**, 956–970.

104 B. Bhushan, Frontiers in nanotribology: Magnetic storage, bio/nanotechnology, cosmetics, and bioinspiration, *Journal of Colloid and Interface Science*, 2020, **577**, 127–162.

105 C. La Torre *et al.*, Nanotribological effects of silicone type, silicone deposition level, and surfactant type on human hair using atomic force microscopy., *Journal of Cosmetic Science*, 2006, **57**, 37–56.

106 T. Iwata and K. Aramaki, Effect of the behenyl trimethyl ammonium counterion on the lamellar gel property, *IFSCC Magazine*, 2013, **16**, 249–254.

107 A. Davies and S. Amin, Microstructure design of CTAC:FA and BTAC:FA lamellar gels for optimized rheological performance utilizing automated formulation platform, *International Journal of Cosmetic Science*, 2020, **42**, 259–269.

108 A. Harvey, C. Carr and A. Pereira, Time-of-flight secondary ion mass spectrometry (ToF-SIMS) analysis of the application of a cationic conditioner to “clean” hair, *Journal of Cosmetic Science*, 2004, **55**, 265—279.

109 G. Ran *et al.*, The adsorption behavior of cationic surfactant onto human hair fibers, *Colloids and Surfaces B: Biointerfaces*, 2009, **68**, 106–110.

110 K. Sindelka *et al.*, Interactions of cationic surfactant-fatty alcohol monolayers with natural human hair surface: Insights from dissipative particle dynamics, *Journal of Molecular Liquids*, 2023, **375**, 121385.

111 L. Fernández-Peña and E. Guzmán, Physicochemical Aspects of the Performance of Hair-Conditioning Formulations, *Cosmetics*, 2020, **7**, 26.

112 P. Hössel *et al.*, Conditioning polymers in today’s shampoo formulations - Efficacy, mechanism and test methods, *International Journal of Cosmetic Science*, 2000, **22**, 1–10.

113 M. Miyake, Recent progress of the characterization of oppositely charged polymer/-surfactant complex in dilution deposition system, *Advances in Colloid and Interface Science*, 2017, **239**, 146–157.

114 L. Fernández-Peña *et al.*, Dilution-Induced Deposition of Concentrated Binary Mixtures of Cationic Polysaccharides and Surfactants, *Polymers*, 2023, **15**, 3011.

115 A. V. Svensson *et al.*, Surface Deposition and Phase Behavior of Oppositely Charged Polyion-Surfactant Ion Complexes. 2. A Means to Deliver Silicone Oil to Hydrophilic Surfaces, *ACS Applied Materials and Interfaces*, 2010, **2**, 143–156.

116 M. Clauzel *et al.*, Surface deposition and phase behavior of oppositely charged polyion-surfactant ion complexes. Delivery of silicone oil emulsions to hydrophobic and hydrophilic surfaces, *ACS Applied Materials and Interfaces*, 2011, **3**, 2451–2462.

117 E. D. Goddard, Polymer/surfactant interaction—Its relevance to detergent systems, *Journal of the American Oil Chemists’ Society*, 1994, **71**, 1–16.

118 T. Nylander, Y. Samoshina and B. Lindman, *Formation of polyelectrolyte-surfactant complexes on surfaces*, 2006.

119 L. Fernández-Peña *et al.*, Impact of the bulk aggregation on the adsorption of oppositely charged polyelectrolyte-surfactant mixtures onto solid surfaces, *Advances in Colloid and Interface Science*, 2020, **282**, 102203.

120 C. D. Bain *et al.*, Complexes of surfactants with oppositely charged polymers at surfaces and in bulk, *Advances in Colloid and Interface Science*, 2010, **155**, 32–49.

121 S. Llamas *et al.*, Adsorption of polyelectrolytes and polyelectrolytes-surfactant mixtures at surfaces: A physico-chemical approach to a cosmetic challenge, *Advances in Colloid and Interface Science*, 2015, **222**, 461–487.

122 A. V. Svensson *et al.*, Surface deposition and phase behavior of oppositely charged polyion/surfactant ion complexes. 1. Cationic guar versus cationic hydroxyethylcellulose in mixtures with anionic surfactants, *ACS Applied Materials and Interfaces*, 2009, **1**, 2431–2442.

123 L. Fernández-Peña *et al.*, Effect of molecular structure of eco-friendly glycolipid biosurfactants on the adsorption of hair-care conditioning polymers, *Colloids and Surfaces B: Biointerfaces*, 2020, **185**, 110578.

124 A. Puente-Santamaría *et al.*, Dilution-controlled deposition of mixtures of a synthetic polycation and a natural origin polyelectrolyte with anionic surfactants on negatively charged surfaces, *Colloids and Surfaces A: Physicochemical and Engineering Aspects*, 2024, 133137.

125 I. J. Gresham *et al.*, Comparing polymer-surfactant complexes to polyelectrolytes, *Journal of Colloid and Interface Science*, 2024, **655**, 262–272.

126 B. Yu *et al.*, Complex coacervation of statistical polyelectrolytes: role of monomer sequences and formation of inhomogeneous coacervates, *Molecular Systems Design & Engineering*, 2021, **6**, 790–804.

127 M. Ghasemi *et al.*, A Molecular Thermodynamic Model of Coacervation in Solutions of Polycations and Oppositely Charged Micelles, *Langmuir*, 2023, **39**, 10335–10351.

128 S. Banerjee *et al.*, Modeling of Polyelectrolyte Adsorption from Micellar Solutions onto Biomimetic Substrates, *Journal of Physical Chemistry B*, 2017, **121**, 8638–8651.

129 F. A. M. Leermakers *et al.*, Turning autophobic wetting on biomimetic surfaces into complete wetting by wetting additives, *Soft Matter*, 2020, **16**, 4823–4839.

130 E. Guzmán *et al.*, Self-consistent mean field calculations of polyelectrolyte-surfactant mixtures in solution and upon adsorption onto negatively charged surfaces, *Polymers*, 2020, **12**, 624.

131 J. B. Speakman and E. Stott, A contribution to the theory of milling - Part 1, *Journal of the Textile Institute Transactions*, 1931, **32**, T339.

132 J. B. Speakman and J. R. Greenwood, The oiling of wool, *Journal of the Textile Institute Proceedings*, 1935, **26**, P271–P288.

133 A. J. P. Martin, Observations on the Theory of Felting, *Journal of the Society of Dyers and Colourists*, 1944, **60**, 325–328.

134 E. H. Mercer, Frictional Properties of Wool Fibres, *Nature*, 1945, **155**, 573–574.

135 H. M. S. Thomson and J. B. Speakman, Frictional Properties of Wool, *Nature*, 1946, **157**, 804.

136 N. Gralén and B. Olofsson, Measurement of Friction Between Single Fibers, *Textile Research Journal*, 1947, **17**, 488–496.

137 E. H. Mercer and K. R. Makinson, The frictional properties of wool and other textile fibres, *Journal of the Textile Institute Transactions*, 1947, **38**, T227–T240.

138 K. R. Makinson, On the cause of the frictional difference of the wool fibre, *Transactions of the Faraday Society*, 1948, **44**, 279–282.

139 D. Frishman, A. L. Smith and M. Harris, Measurement of the Frictional Properties of Wool Fibers, *Textile Research Journal*, 1948, **18**, 475–480.

140 J. Lindberg and N. Gralén, Measurement of Friction Between Single Fibers: II. Frictional Properties of Wool Fibers Measured by the Fiber-Twist Method, *Textile Research Journal*, 1948, **18**, 287–301.

141 J. Lindberg, Measurement of Friction Between Single Fibers III. Influence of Different Treatments on the Frictional Properties of Wool Fibers, *Textile Research Journal*, 1948, **18**, 470–474.

142 J. Lindberg and N. Gralén, Measurement of Friction Between Single Fibers: IV. Influence of Various Oxidizing and Reducing Agents on the Frictional Properties of Wool Fibers, *Textile Research Journal*, 1949, **19**, 183–201.

143 L. N. Jones, Hair Structure Anatomy and Comparative Anatomy, *Clinics in Dermatology*, 2001, **19**, 95–103.

144 F. P. Bowden and L. Leben, Nature of sliding and the analysis of friction, *Proceedings of the Royal Society of London, Series A*, 1939, **169**, 371–391.

145 E. Mercer and A. Rees, Structure of the cuticle of wool, *Nature*, 1946, **157**, 589–590.

146 B. Derjaguin, Molekulartheorie der äußeren Reibung, *Zeitschrift für Physik*, 1934, **88**, 661–675.

147 J. P. Gao *et al.*, Frictional forces and Amontons' law: From the molecular to the macroscopic scale, *J. Phys. Chem. B*, 2004, **108**, 3410–3425.

148 P. Grosberg, The Differential Friction of Wool, *Journal of the Textile Institute Transactions*, 1955, **46**, T233–T246.

149 G. F. Flanagan, Felting and Ratchet Action of Wool Fibers, *Textile Research Journal*, 1966, **36**, 55–65.

150 H. L. Röder, Measurements of the influence of finishing agents on the friction of fibres, *Journal of the Textile Institute Transactions*, 1953, **44**, T247–T265.

151 A. M. Schwartz and D. C. Knowles, Frictional effects in human hair, *J. Soc. Cosmet. Chem.*, 1963, **14**, 455–463.

152 A. Dussaud and L. Fieschi-Corso, Influence of functionalized silicones on hair fiber–fiber interactions and on the relationship with the macroscopic behavior of hair assembly, *International Journal of Cosmetic Science*, 2010, **32**, 160–160.

153 N. R. Chevalier, Hair-on-hair static friction coefficient can be determined by tying a knot, *Colloids and Surfaces B: Biointerfaces*, 2017, **159**, 924–928.

154 W. Newman, G. L. Cohen and C. Hayes, A quantitative characterization of combing force, *Journal of the Society of Cosmetic Chemists*, 1973, **24**, 773–782.

155 C. R. Robbins and R. J. Crawford, A method to evaluate hair body, *Journal of the Society of Cosmetic Chemists*, 1984, **35**, 369–377.

156 K. A. Vaynberg and M. Nall, The Aqualon SLT: A novel device for measuring hair stiffness and lubricity, *International Journal of Cosmetic Science*, 2010, **32**, 156–156.

157 W. C. Waggoner and G. Scott, Instrumental method for the determination of hair raspiness, *J Soc Cosmet Chem*, 1966, **17**, 171–179.

158 Y. Miyamae, Y. Yamakawa and Y. Ozaki, Evaluation of Physical Properties of Human Hair by Diffuse Reflectance Near-Infrared Spectroscopy, *Appl. Spectrosc.*, 2007, **61**, 212–217.

159 G. V. Scott and C. R. Robbins, Effects of surfactant solutions on hair fiber friction, *Journal of the Society of Cosmetic Chemists*, 1980, **31**, 179–200.

160 M. Adams *et al.*, *Supramolecular and colloidal structures in biomaterials and biosubstrates*, World Scientific, 2000, pp. 277–294.

161 T. Miyamoto *et al.*, Tribological Properties between Taut Hair Fibers in Wet Conditions: A New Shampoo Formulation for Eliminating Stick-Slip Friction, *Journal of Surfactants and Detergents*, 2021, **24**, 501–510.

162 T. Miyamoto *et al.*, Aqueous lubrication with the molecularly confined films of silicone-based amphiphilic block copolymer aggregates, *Langmuir*, 2019, **35**, 15784–15794.

163 F. J. Wortmann and A. Schwan-Jonczyk, Investigating hair properties relevant for hair 'handle'. Part I: hair diameter, bending and frictional properties, *International Journal of Cosmetic Science*, 2006, **28**, 61–68.

164 N. Fair and B. S. Gupta, Effects of chlorine on friction and morphology of human hair, *Journal of the Society of Cosmetic Chemists*, 1982, **35**, 229–242.

165 J. Bico *et al.*, Elastocapillary coalescence in wet hair, *Nature*, 2004, **432**, 690–690.

166 J. Jachowicz, Hair damage and attempts to its repair, *Journal of the Society of Cosmetic Chemists*, 1987, **38**, 263–286.

167 O. J. Morel and R. M. Christie, Current trends in the chemistry of permanent hair dyeing, *Chemical Reviews*, 2011, **111**, 2537–2561.

168 M. L. Garcia and J. Diaz, Combability Measurements on Human Hair, *Journal of the Society of Cosmetic Chemists*, 1976, **29**, 379–398.

169 C. R. Robbins and C. Reich, Prediction of hair assembly characteristics from single-fiber properties. Part II. The relationship of fiber curvature, friction,stiffness,and diameter to combing behavior, *Journal of the Society of Cosmetic Chemists*, 1986, **37**, 141–158.

170 Y. Lim, C. Park and J. Kim, Hair conditioning effect of amino silicone softeners in varied treatment conditions, *Fibers and Polymers*, 2010, **11**, 507–515.

171 H. Tanamachi *et al.*, Deposition of 18-MEA onto alkaline-color-treated weathered hair to form a persistent hydrophobicity., *Journal of Cosmetic Science*, 2009, **60**, 31–44.

172 Y. Nagahara *et al.*, Structure and Performance of Cationic Assembly Dispersed in Amphoteric Surfactants Solution as a Shampoo for Hair Damaged by Coloring, *Journal of Oleo Science*, 2007, **56**, 289–295.

173 J. Jachowicz, M. Berthiaume and M. Garcia, The effect of the amphiprotic nature of human hair keratin on the adsorption of high charge density cationic polyelectrolytes, *Colloid and Polymer Science*, 1985, **263**, 847–858.

174 M. Nomura *et al.*, Translating the human hair surface state into sound, *IFSCC Mag*, 2017, **20**, 3–7.

175 R. L. McMullen *et al.*, Evaluation of the surface properties of hair with acoustic emission analysis, *International Journal of Cosmetic Science*, 2021, **43**, 88–101.

176 A. M. Benhur, J. Diaz and S. Amin, Impact of polyelectrolyte-surfactant interactions on the rheology and wet lubrication performance of conditioning shampoo, *International Journal of Cosmetic Science*, 2021, **43**, 246–253.

177 H. Tanamachi, Temperature as a moisture cue in haptics on hair, *International Journal of Cosmetic Science*, 2011, **33**, 25–36.

178 L. D. Bloch *et al.*, Chemical and physical damage affect the perceptions of hair attributes: A quantitative sensory assessment by a trained panel, *Journal of Sensory Studies*, 2021, **36**, e12621.

179 Y. Akiyama, Y. Matsue and S. Nishijima, 2010 World Automation Congress, 2010, pp. 1–6.

180 T. Kawasoe, M. Kakizawa and H. Shimizu, Tribology in the Hair Surface and Tactile Perception, *Tribol. Online*, 2008, **3**, 127–130.

181 W. Tang *et al.*, Ageing effects on the diameter, nanomechanical properties and tactile perception of human hair, *International Journal of Cosmetic Science*, 2016, **38**, 155–163.

182 Y. Aita and Y. Nonomura, Friction and surface temperature of wet hair containing water, oil, or oil-in-water emulsion, *Journal of Oleo Science*, 2016, **65**, 493–498.

183 C. Thieulin, R. Vargiolu and H. Zahouani, Effects of cosmetic treatments on the morphology, biotribology and sensorial properties of a single human hair fiber, *Wear*, 2019, **426-427**, 186–194.

184 M. Sano, H. Mayama and Y. Nonomura, Friction dynamics of human hair treated with water or cationic surfactant aqueous solution, *Journal of Surfactants and Detergents*, 2023, **26**, 185–193.

185 L. Skedung *et al.*, Feeling small: Exploring the tactile perception limits, *Scientific Reports*, 2013, **3**, 2617.

186 L. Skedung *et al.*, Feeling Smooth: Psychotribological Probing of Molecular Composition, *Tribology Letters*, 2018, **66**, 1–10.

187 A. Klöcker *et al.*, Physical factors influencing pleasant touch during tactile exploration, *PLoS ONE*, 2013, **8**, 1–8.

188 H. Tanamachi *et al.*, 18-MEA and hair appearance, *Journal of Cosmetic Science*, 2010, **61**, 147–160.

189 S. Comaish and E. Bottoms, The skin and friction: deviations from Amonton's laws, and the effects of hydration and lubrication, *British Journal of Dermatology*, 1971, **84**, 37–43.

190 T. Okuyama *et al.*, Development of tactile sensor for measuring hair touch feeling, *Microsystem technologies*, 2011, **17**, 1153–1160.

191 C. LaTorre and B. Bhushan, Investigation of scale effects and directionality dependence on friction and adhesion of human hair using AFM and macroscale friction test apparatus, *Ultramicroscopy*, 2006, **106**, 720–734.

192 W. Tang *et al.*, Characterization of tactile perception and optimal exploration movement, *Tribology Letters*, 2015, **58**, 1–14.

193 G. Binnig, C. F. Quate and C. Gerber, Atomic force microscope, *Physical review letters*, 1986, **56**, 930.

194 S. D. O'Connor, K. L. Komisarek and J. D. Baldeschwieler, Atomic force microscopy of human hair cuticles: A microscopic study of environmental effects on hair morphology, *Journal of Investigative Dermatology*, 1995, **105**, 96–99.

195 J. Smith, Use of atomic force microscopy for high-resolution non-invasive structural studies of human hair, *Journal of the Society of Cosmetic Chemists*, 1997, **48**, 199–208.

196 J. Smith, A quantitative method for analysing AFM images of the outer surfaces of human hair, *Journal of microscopy*, 1998, **191**, 223–228.

197 J. A. Swift and J. R. Smith, Atomic force microscopy of human hair, *Scanning*, 2000, **22**, 310–318.

198 J. Blach *et al.*, Surface characterization of human hair by atomic force microscopy in the imaging and F-d modes, *International journal of cosmetic science*, 2001, **23**, 165–174.

199 N. Chen and B. Bhushan, Morphological, nanomechanical and cellular structural characterization of human hair and conditioner distribution using torsional resonance mode with an atomic force microscope, *Journal of Microscopy*, 2005, **220**, 96–112.

200 V. Dupres *et al.*, Atomic force microscopy imaging of hair: Correlations between surface potential and wetting at the nanometer scale, *Journal of Colloid and Interface Science*, 2004, **269**, 329–335.

201 B. Singh and S. Umapathy, Effect of SDS on human hair: Study on the molecular structure and morphology, *Journal of Biophotonics*, 2011, **4**, 315–323.

202 R. Humphry, N. Wang and C. Durkan, Site-specific variations in surface structure and Young's modulus of human hair surfaces at the nanometer scale as induced through bleach treatment, *Journal of the Mechanical Behavior of Biomedical Materials*, 2022, **126**, 105001.

203 R. A. Lodge and B. Bhushan, Surface potential measurement of human hair using Kelvin probe microscopy, *J. Vac. Sci. Technol. A*, 2007, **25**, 893–902.

204 J. M. Neumeister and W. A. Ducker, Lateral, normal, and longitudinal spring constants of atomic force microscopy cantilevers, *Review of scientific instruments*, 1994, **65**, 2527–2531.

205 R. L. McMullen, J. Jachowicz and S. P. Kelty, Correlation of AFM/LFM with combing forces of human hair, *IFSCC Magazine*, 2000, **3**, 39–45.

206 A. Schirmeisen, U. D. Schwarz and H. Hölscher, in *Friction Force Microscopy*, ed. B. Bhushan, Springer Netherlands, Dordrecht, 2012, pp. 884–892.

207 G. Wei and B. Bhushan, Nanotribological and nanomechanical characterization of human hair using a nanoscratch technique, *Ultramicroscopy*, 2006, **106**, 742–754.

208 J. R. Smith *et al.*, AFM friction and adhesion mapping of the substructures of human hair cuticles, *Applied Surface Science*, 2013, **285**, 638–644.

209 S. Lee *et al.*, Adsorption and Lubricating Properties of Poly(l-lysine)-graft-poly(ethylene glycol) on Human-Hair Surfaces, *ACS Applied Materials and Interfaces*, 2009, **1**, 1938–1945.

210 E. Max *et al.*, A novel AFM based method for force measurements between individual hair strands, *Ultramicroscopy*, 2010, **110**, 320–324.

211 H. Mizuno, G. S. Luengo and M. W. Rutland, Interactions between crossed hair fibers at the nanoscale, *Langmuir*, 2010, **26**, 18909–18915.

212 C. Wood *et al.*, From conditioning shampoo to nanomechanics and haptics of human hair, *Journal of Cosmetic Science*, 2011, **62**, 259–264.

213 H. Mizuno *et al.*, Friction measurement between polyester fibres using the fibre probe SPM, *Australian journal of chemistry*, 2006, **59**, 390–393.

214 J. Bowen *et al.*, Friction and wear of human hair fibres, *Surface Topography: Metrology and Properties*, 2016, **4**, 024008.

215 W. A. Ducker, T. J. Senden and R. M. Pashley, Direct measurement of colloidal forces using an atomic force microscope, *Nature*, 1991, **353**, 239–241.

216 M. Sadaie *et al.*, Studies of human hair by friction force microscopy with the hair-model-probe, *Colloids and Surfaces B: Biointerfaces*, 2006, **51**, 120–129.

217 J. Israelachvili *et al.*, Recent advances in the surface forces apparatus (SFA) technique, *Reports on Progress in Physics*, 2010, **73**, 036601.

218 T. R. Cristiani *et al.*, Automated Measurement of Spatially Resolved Hair-Hair Single Fiber Adhesion, *Langmuir*, 2019, **35**, 15614–15627.

219 R. A. Lodge and B. Bhushan, Surface characterization of human hair using tapping mode atomic force microscopy and measurement of conditioner thickness distribution, *Journal of Vacuum Science & Technology A*, 2006, **24**, 1258–1269.

220 L. Labarre *et al.*, Hair surface interactions against different chemical functional groups as a function of environment and hair condition, *International Journal of Cosmetic Science*, 2023, **45**, 224–235.

221 H.-U. Krotil, T. Stifter and O. Marti, Concurrent measurement of adhesive and elastic surface properties with a new modulation technique for scanning force microscopy, *Review of Scientific Instruments*, 2000, **71**, 2765–2771.

222 Y. K. Kamath and H.-D. Weigmann, Measurement of interfiber adhesion, *Journal of Cosmetic Science*, 2000, **51**, 351–366.

223 S. J. Eder, A. Vernes and G. Betz, On the Derjaguin Offset in Boundary-Lubricated Nanotribological Systems, *Langmuir*, 2013, **29**, 13760–13772.

224 J. P. Ewen *et al.*, Nonequilibrium molecular dynamics simulations of stearic acid adsorbed on iron surfaces with nanoscale roughness, *Tribology International*, 2017, **107**, 264–273.

225 Y. K. Kamath, C. J. Dansizer and H. Weigmann, Surface wettability of human hair. I. Effect of Deposition of Polymers and Surfactants, *Journal of Applied Polymer Science*, 1984, **29**, 1011–1026.

226 Y. K. Kamath, C. J. Dansizer and H.-D. Weigmann, Surface wettability of human hair. III. Role of surfactants in the surface deposition of cationic polymers, *Journal of Applied Polymer Science*, 1985, **30**, 937–953.

227 E. Schulze Zur Wiesche *et al.*, Prevention of hair surface aging, *Journal of Cosmetic Science*, 2011, **62**, 237–249.

228 L. Wilhelmy, Ueber die Abhängigkeit der Capillaritätskonstanten des Alkohols von Substanz und Gestalt des benetzten festen Körpers, *Annalen der Physik*, 1863, **195**, 177–217.

229 B. J. Briscoe and D. C. Evans, The shear properties of Langmuir-Blodgett layers, *Proceedings of the Royal Society of London, Series A*, 1982, **380**, 389–407.

230 E. Oshimura, H. Abe and R. Oota, Hair and amino acids: The interactions and the effects, *Journal of Cosmetic Science*, 2007, **58**, 347–357.

231 C. Barba *et al.*, Restoring Important Hair Properties with Wool Keratin Proteins and Peptides, *Fibers and Polymers*, 2010, **11**, 1055–1061.

232 D. K. Owens and R. C. Wendt, Estimation of the Surface Free Energy of Polymers, *Journal of Applied Polymer Science*, 1969, **13**, 1741–1747.

233 M. Lee and H. Ockendon, A continuum model for entangled fibres, *European Journal of Applied Mathematics*, 2005, **16**, 145–160.

234 T. B. Plumb-Reyes, N. Charles and L. Mahadevan, Combing a double helix, *Soft Matter*, 2022, **18**, 2767–2775.

235 J. Hughes *et al.*, 2021 IEEE 4th International Conference on Soft Robotics (RoboSoft), 2021, pp. 487–494.

236 K. Ward *et al.*, A survey on hair modeling: Styling, simulation, and rendering, *IEEE transactions on visualization and computer graphics*, 2007, **13**, 213–234.

237 F. Bertails *et al.*, SIGGRAPH '08, New York, NY, USA, 2008, pp. 1–154.

238 G. Daviet, F. Bertails-Descoubes and L. Boissieux, Proceedings of the 2011 SIGGRAPH Asia Conference, New York, NY, USA, 2011.

239 P. S. Nerenberg and T. Head-Gordon, *New developments in force fields for biomolecular simulations*, 2018.

240 H. I. Ingólfsson *et al.*, *The power of coarse graining in biomolecular simulations*, 2014.

241 J. Bajorath, Integration of virtual and high-throughput screening, *Nature Reviews Drug Discovery*, 2002, **1**, 882–894.

242 T. Bereau, Computational compound screening of biomolecules and soft materials by molecular simulations, *Modelling and Simulation in Materials Science and Engineering*, 2021, **29**, 023001.

243 J. L. McDonagh *et al.*, What can digitisation do for formulated product innovation and development?, *Polymer International*, 2021, **70**, 248–255.

244 R. L. Akkermans and P. B. Warren, Multiscale modelling of human hair, *Philos. Trans. R. Soc. A*, 2004, **362**, 1783–1793.

245 E. Antunes *et al.*, The effects of solvent composition on the affinity of a peptide towards hair keratin: Experimental and molecular dynamics data, *RSC Advances*, 2015, **5**, 12365–12371.

246 O. Evers, J. Scheutjens and G. Fleer, Statistical thermodynamics of block copolymer adsorption. 1. Formulation of the model and results for the adsorbed layer structure, *Macromolecules*, 1990, **23**, 5221–5233.

247 S. Banerjee *et al.*, Surfactant-polymer interactions: Molecular architecture does matter, *Soft Matter*, 2015, **11**, 2504–2511.

248 A. Naderi *et al.*, Trapped non-equilibrium states in aqueous solutions of oppositely charged polyelectrolytes and surfactants: Effects of mixing protocol and salt concentration, *Colloids and Surfaces A: Physicochemical and Engineering Aspects*, 2005, **253**, 83–93.

249 B. C. Beard and J. Hare, Surface interaction of quaternary amines with hair, *Journal of Surfactants and Detergents*, 2002, **5**, 145–150.

250 I. Efremenko, R. Zach and Y. Zeiri, Adsorption of explosive molecules on human hair surfaces, *J. Phys. Chem. C*, 2007, **111**, 11903–11911.

251 R. L. McMullen and S. P. Kelty, Molecular dynamic simulations of eicosanoic acid and 18-methyleicosanoic acid langmuir monolayers, *Journal of Physical Chemistry B*, 2007, **111**, 10849–10852.

252 L. D. Schuler, X. Daura and W. F. V. Gunsteren, An improved GROMOS96 force field for aliphatic hydrocarbons in the condensed phase, *Journal of Computational Chemistry*, 2001, **22**, 1205–1218.

253 U. Natarajan and C. Robbins, The thickness of 18-MEA on an ultra-high-sulfur protein surface by molecular modeling, *Journal of cosmetic science*, 2010, **61**, 467–477.

254 A. P. Negri, H. J. Cornell and D. E. Rivett, A Model for the Surface of Keratin Fibers, *Text. Res. J.*, 1993, **63**, 109–115.

255 R. S. Singh *et al.*, Molecular modeling and structural characterization of a high glycine-tyrosine hair keratin associated protein, *Physical Chemistry Chemical Physics*, 2017, **19**, 8575–8583.

256 R. J. Ward *et al.*, Surface Analysis of Wool by X-Ray Photoelectron Spectroscopy and Static Secondary Ion Mass Spectrometry, *Textile Research Journal*, 1993, **63**, 362–368.

257 W. L. Jorgensen, D. S. Maxwell and J. Tirado-Rives, Development and Testing of the OPLS All-Atom Force Field on Conformational Energetics and Properties of Organic Liquids, *Journal of the American Chemical Society*, 1996, **118**, 11225–11236.

258 G. A. Kaminski *et al.*, Evaluation and Reparametrization of the OPLS-AA Force Field for Proteins via Comparison with Accurate Quantum Chemical Calculations on Peptidesâ€ , *Journal of Physical Chemistry B*, 2001, **105**, 6474–6487.

259 J. A. Swift and A. W. Holmes, Degradation of human hair by papain part III: Some electron microscope observations, *Text. Res. J.*, 1965, **35**, 1014–1019.

260 R. Ward *et al.*, Surface Analysis of Wool by X-Ray Photoelectron Spectroscopy and Static Secondary Ion Mass Spectrometry, *Textile Research Journal*, 1993, **63**, 362–368.

261 H. Zahn, H. Messinger and H. Hocker, Covalently Linked Fatty Acids at the Surface of Wool: Part of the Cuticle Cell Envelope, *Textile Research Journal*, 1994, **64**, 554–555.

262 J. M. Sanders *et al.*, Exploring the Effects of Wetting and Free Fatty Acid Deposition on an Atomistic Hair Fiber Surface Model Incorporating Keratin-Associated Protein 5-1, *Langmuir*, 2023, **39**, 5263–5274.

263 C. Lu *et al.*, OPLS4: Improving Force Field Accuracy on Challenging Regimes of Chemical Space, *Journal of Chemical Theory and Computation*, 2021, **17**, 4291–4300.

264 S. J. Marrink *et al.*, The MARTINI force field: Coarse grained model for biomolecular simulations, *Journal of Physical Chemistry B*, 2007, **111**, 7812–7824.

265 S. J. Marrink and D. P. Tieleman, Perspective on the Martini Model, *Chemical Society Reviews*, 2013, **42**, 6801–6822.

266 T. I. Morozova *et al.*, Adsorption and Desorption of Polymers on Bioinspired Chemically Structured Substrates, *ACS Applied Materials & Interfaces*, 2021, **13**, 30086–30097.

267 I. Adroher-Benítez *et al.*, Effect of polymer architecture on the adsorption and coating stability on heterogeneous biomimetic surfaces, *Macromolecules*, 2023, **56**, 10285–10295.

268 S. Amin *et al.*, Revealing New Structural Insights from Surfactant Micelles through DLS, Microrheology and Raman Spectroscopy, *Materials*, 2015, **8**, 3754–3766.

269 A. Ishihara *et al.*, Analysis of water distribution in delipidated human hair by small-angle neutron scattering (SANS), *International Journal of Cosmetic Science*, 2021, **43**, 653–661.

270 H. You and L. Yu, Atomic force microscopy as a tool for study of human hair, *Scanning*, 1997, **19**, 431–437.

271 L. Kreplak *et al.*, Investigation of human hair cuticle structure by microdiffraction: direct observation of cell membrane complex swelling, *Biochimica et Biophysica Acta (BBA)-Protein Structure and Molecular Enzymology*, 2001, **1547**, 268–274.

272 S. Thibaut *et al.*, Chronological ageing of human hair keratin fibres, *International Journal of Cosmetic Science*, 2010, **32**, 422–434.

273 T. Takahashi *et al.*, Age-dependent changes in damage processes of hair cuticle, *Journal of Cosmetic Dermatology*, 2015, **14**, 2–8.

274 R. M. Trüeb, H. D. Rezende and M. F. R. G. Dias, A comment on the science of hair aging, *International journal of trichology*, 2018, **10**, 245.

275 J. Bowen, H. L. Rossetto and K. Kendall, Adhesion between silica surfaces due to hydrogen bonding, *Surface Topography: Metrology and Properties*, 2016, **4**, 034001.

276 C. Durkan and N. Wang, Nanometre-scale investigations by atomic force microscopy into the effect of different treatments on the surface structure of hair, *International Journal of Cosmetic Science*, 2014, **36**, 598–605.

277 E. Liamas *et al.*, Friction between soft contacts at nanoscale on uncoated and protein-coated surfaces, *Nanoscale*, 2021, **13**, 2350.

278 Y. Jiang *et al.*, Comparative study of instrumental measurement and sensory evaluation methods for the repairing effect of mildly damaged hair bundles, *Skin Research and Technology*, 2023, **29**, e13394.

279 J. P. Ewen *et al.*, A Comparison of Classical Force-Fields for Molecular Dynamics Simulations of Lubricants, *Materials 2016, Vol. 9, Page 651*, 2016, **9**, 651.

280 M. Doig, C. P. Warrens and P. J. Camp, Structure and Friction of Stearic Acid and Oleic Acid Films Adsorbed on Iron Oxide Surfaces in Squalane, *Langmuir*, 2013, **30**, 186–195.

281 H. Spikes, Stress-augmented thermal activation: Tribology feels the force, *Friction 2017 6:1*, 2018, **6**, 1–31.

282 E. Reimhult, F. Höök and B. Kasemo, Intact vesicle adsorption and supported biomembrane formation from vesicles in solution: influence of surface chemistry, vesicle size, temperature, and osmotic pressure, *Langmuir*, 2003, **19**, 1681–1691.

283 A. Kumar *et al.*, Intact deposition of cationic vesicles on anionic cellulose fibers: Role of vesicle size, polydispersity, and substrate roughness studied via streaming potential measurements, *Journal of colloid and interface science*, 2016, **473**, 152–161.

284 R. Sorkin *et al.*, Mechanical stability and lubrication by phosphatidylcholine boundary layers in the vesicular and in the extended lamellar phases, *Langmuir*, 2014, **30**, 5005–5014.

285 T. Igarashi *et al.*, Elucidation of softening mechanism in rinse cycle fabric softeners. Part 1: Effect of hydrogen bonding, *Journal of surfactants and detergents*, 2016, **19**, 183–192.

286 A. Pfau *et al.*, The interaction of cationic polymers with human hair, *Macromolecular Symposia*, 1998, **126**, 241–252.

287 S. Jahn, J. Seror and J. Klein, Lubrication of articular cartilage, *Annual review of biomedical engineering*, 2016, **18**, 235–258.

288 E. Guzmán *et al.*, Effect of a natural amphoteric surfactant in the bulk and adsorption behavior of polyelectrolyte-surfactant mixtures, *Colloids and Surfaces A*, 2020, **585**, 124178.

289 M. Kobayashi and A. Takahara, Tribological properties of hydrophilic polymer brushes under wet conditions, *The Chemical Record*, 2010, **10**, 208–216.

290 S. K. Son *et al.*, Effect of the Coacervate Systems in Shampoo Formulation on Hair Damage, *Journal of the Society of Cosmetic Scientists of Korea*, 2018, **44**, 141–149.

291 W. Wu *et al.*, Quantitative methods for evaluating optical and frictional properties of cationic polymers, *Journal of Cosmetic Science*, 2001, **52**, 51–65.

292 S. Lee and N. D. Spencer, Sweet, Hairy, Soft, and Slippery, *Science.*, 2008, **319**, 575–577.

293 R. C. Bernardi, M. C. Melo and K. Schulten, Enhanced sampling techniques in molecular dynamics simulations of biological systems, *Biochimica et Biophysica Acta (BBA)-General Subjects*, 2015, **1850**, 872–877.

294 Y. I. Yang *et al.*, Enhanced sampling in molecular dynamics, *The Journal of chemical physics*, 2019, **151**, 070902.

295 S. Ozkan, C. Alonso and R. L. McMullen, Rheological fingerprinting as an effective tool to guide development of personal care formulations, *International Journal of Cosmetic Science*, 2020, **42**, 536–547.

296 O. Ajayi, A. Davies and S. Amin, Impact of Processing Conditions on Rheology, Tribology and Wet Lubrication Performance of a Novel Amino Lipid Hair Conditioner, *Cosmetics*, 2021, **8**, 77.

297 R. L. McMullen *et al.*, Investigation of the interactions of cationic guar with human hair by electrokinetic analysis, *International Journal of Cosmetic Science*, 2021, **43**, 375–390.

298 C. E. Sing, *Development of the modern theory of polymeric complex coacervation*, 2017.

299 E. Weiand *et al.*, Coarse-grained molecular models of the surface of hair, *Soft Matter*, 2022, **18**, 1779–1792.

300 S. Banerjee *et al.*, Surfactant-polymer interactions: Molecular architecture does matter, *Soft Matter*, 2015, **11**, 2504–2511.

301 K. Sindelka and M. Lisal, Interplay between surfactant self-assembly and adsorption at hydrophobic surfaces: insights from dissipative particle dynamics, *Molecular Physics*, 2021, **119**, e1857863.

302 R. Alessandri, F. Grünewald and S. J. Marrink, The Martini Model in Materials Science, *Adv. Mater.*, 2021, **33**, 2008635.

303 Y. Atsmon-Raz and D. P. Tieleman, Parameterization of Palmitoylated Cysteine, Farnesylated Cysteine, Geranylgeranylated Cysteine, and Myristoylated Glycine for the Martini Force Field, *Journal of Physical Chemistry B*, 2017, **121**, 11132–11143.

304 S. Wang and R. G. Larson, Coarse-grained molecular dynamics simulation of tethered lipid assemblies, *Soft Matter*, 2013, **9**, 480–486.

305 M. Vögele, C. Holm and J. Smiatek, Coarse-grained simulations of polyelectrolyte complexes: MARTINI models for poly(styrene sulfonate) and poly(diallyldimethylammonium), *The Journal of Chemical Physics*, 2015, **143**, 243151.

306 S. O. Yesylevskyy *et al.*, Polarizable water model for the coarse-grained MARTINI force field, *PLoS Computational Biology*, 2010, **6**, 1–17.

307 D. Wu and X. Yang, Coarse-grained molecular simulation of self-assembly for nonionic surfactants on graphene nanostructures, *Journal of Physical Chemistry B*, 2012, **116**, 12048–12056.

308 E. J. Wallace and M. S. Sansom, Carbon nanotube/detergent interactions via coarse-grained molecular dynamics, *Nano Letters*, 2007, **7**, 1923–1928.

309 E. J. Wallace and M. S. Sansom, Blocking of carbon nanotube based nanoinjectors by lipids: A simulation study, *Nano Letters*, 2008, **8**, 2751–2756.

310 D. Sergi, G. Scocchi and A. Ortona, Coarse-graining MARTINI model for molecular-dynamics simulations of the wetting properties of graphitic surfaces with nonionic, long-chain, and T-shaped surfactants, *Journal of Chemical Physics*, 2012, **137**, 094904.

311 F. Grunewald *et al.*, Transferable MARTINI Model of Poly(ethylene Oxide), *Journal of Physical Chemistry B*, 2018, **122**, 7436–7449.

312 C. Xing and R. Faller, Coarse-grained simulations of supported and unsupported lipid monolayers, *Soft Matter*, 2009, **5**, 4526–4530.

313 A. Lamberg and T. Taniguchi, Coarse-Grained Computational Studies of Supported Bilayers: Current Problems and Their Root Causes, *Journal of Physical Chemistry B*, 2014, **118**, 10643–10652.

314 A. Ramazani, T. Mandal and R. G. Larson, Modeling the Hydrophobicity of Nanoparticles and Their Interaction with Lipids and Proteins, *Langmuir*, 2016, **32**, 13084–13094.

315 J. Chen *et al.*, Quantifying Gauche Defects and Phase Evolution in Self-Assembled Monolayers through Sessile Drops, *ACS Omega*, 2017, **2**, 2072–2084.

316 J. F. Liljeblad *et al.*, Self-assembly of long chain fatty acids: Effect of a methyl branch, *Phys. Chem. Chem. Phys.*, 2014, **16**, 17869–17882.

317 A. V. Titov, P. Král and R. Pearson, Sandwiched graphene-membrane superstructures, *ACS Nano*, 2010, **4**, 229–234.

318 C. Gobbo *et al.*, MARTINI model for physisorption of organic molecules on graphite, *J. Phys. Chem. C*, 2013, **117**, 15623–15631.

319 L. Coderch *et al.*, Exogenous and endogenous lipids of human hair, *Skin Research and Technology*, 2017, **23**, 479–485.

320 Y. Masukawa *et al.*, Damage to human hair caused by repeated bleaching combined with daily weathering during daily life activities, *Exog. Dermatology*, 2004, **3**, 273–281.

321 B. D. Cassie and S. Baxter, Wettability of porous surfaces, *Trans. Faraday Soc.*, 1944, **40**, 546–551.

322 J. Michalowsky *et al.*, A refined polarizable water model for the coarse-grained MARTINI force field with long-range electrostatic interactions, *Journal of Chemical Physics*, 2017, **146**, 054501.

323 Z. Wu, Q. Cui and A. Yethiraj, A new coarse-grained force field for membrane-peptide simulations, *Journal of Chemical Theory and Computation*, 2011, **7**, 3793–3802.

324 V. Miguel, M. A. Perillo and M. A. Villarreal, Improved prediction of bilayer and monolayer properties using a refined BMW-MARTINI force field, *Biochimica et Biophysica Acta - Biomembranes*, 2016, **1858**, 2903–2910.

325 S. Wu *et al.*, Influence of Surface Roughness on Cetyltrimethylammonium Bromide Adsorption from Aqueous Solution, *Langmuir*, 2011, **27**, 6091–6098.

326 F. Goujon *et al.*, How Does the Surface Tension Depend on the Surface Area with Coarse-Grained Models?, *J. Chem. Theory Comput.*, 2018, **14**, 2644–2651.

327 N. B. Vargaftik, B. N. Volkov and L. D. Voljak, International Tables of the Surface Tension of Water, *Journal of Physical and Chemical Reference Data*, 1983, **12**, 817–820.

328 D. M. Mitrinović *et al.*, Noncapillary-Wave Structure at the Water-Alkane Interface, *Physical Review Letters*, 2000, **85**, 582.

329 M. Ndao *et al.*, Coarse-Graining the Liquid–Liquid Interfaces with the MARTINI Force Field: How Is the Interfacial Tension Reproduced?, *Journal of Chemical Theory and Computation*, 2015, **11**, 3818–3828.

330 H. J. Berendsen, D. van der Spoel and R. van Drunen, GROMACS: A message-passing parallel molecular dynamics implementation, *Computer Physics Communications*, 1995, **91**, 43–56.

331 P. C. T. Souza *et al.*, Martini 3: a general purpose force field for coarse-grained molecular dynamics, *Nature Methods*, 2021, **18**, 382–388.

332 A. P. Thompson *et al.*, LAMMPS - a flexible simulation tool for particle-based materials modeling at the atomic, meso, and continuum scales, *Computer Physics Communications*, 2022, **271**, 108171.

333 L. Verlet, Computer "Experiments" on Classical Fluids. I. Thermodynamical Properties of Lennard-Jones Molecules, *Physical Review*, 1967, **159**, 98.

334 J. P. Ryckaert, G. Ciccotti and H. J. C. Berendsen, Numerical integration of the cartesian equations of motion of a system with constraints: molecular dynamics of n-alkanes, *Journal of Computational Physics*, 1977, **23**, 327–341.

335 I. C. Yeh and M. L. Berkowitz, Ewald summation for systems with slab geometry, *Journal of Chemical Physics*, 1999, **111**, 3155–3162.

336 R. W. Hockney and J. W. Eastwood, *Computer Simulation Using Particles*, CRC Press, New York, 1989.

337 A. I. Jewett *et al.*, Moltemplate: A Tool for Coarse-Grained Modeling of Complex Biological Matter and Soft Condensed Matter Physics, *J. Mol. Biol.*, 2021, **433**, 166841.

338 A. J. Grosvenor *et al.*, The physical and chemical disruption of human hair after bleaching - studies by transmission electron microscopy and redox proteomics, *Int. J. Cosmet. Sci.*, 2018, **40**, 536–548.

339 Y. Z. Hessefort, B. T. Holland and R. W. Cloud, True porosity measurement of hair: A new way to study hair damage mechanisms, *J. Cosmet. Sci.*, 2008, **59**, 303–315.

340 S. Nosé, A molecular dynamics method for simulations in the canonical ensemble, *Molecular Physics*, 1984, **52**, 255–268.

341 W. G. Hoover, Canonical Dynamics: Equilibrium Phase-Space Distributions, *Physical Review A*, 1985, **31**, 1695–1697.

342 W. Shinoda, M. Shiga and M. Mikami, Rapid estimation of elastic constants by molecular dynamics simulation under constant stress, *Phys. Rev. B*, 2004, **69**, 134103.

343 M. J. de Ruijter, T. D. Blake and J. De Coninck, Dynamic wetting studied by molecular modeling simulations of droplet spreading, *Langmuir*, 1999, **15**, 7836–7847.

344 T. Werder *et al.*, On the water-carbon interaction for use in molecular dynamics simulations of graphite and carbon nanotubes, *Journal of Physical Chemistry B*, 2003, **107**, 1345–1352.

345 H. G. Ozcelik, E. Satiroglu and M. Barisik, Size dependent influence of contact line pinning on wetting of nano-textured/patterned silica surfaces, *Nanoscale*, 2020, **12**, 21376–21391.

346 H. J. C. Berendsen, J. R. Grigera and T. P. Straatsma, The missing term in effective pair potentials, *Journal of Physical Chemistry*, 1987, **91**, 6269–6271.

347 G. Scocchi *et al.*, Wetting and contact-line effects for spherical and cylindrical droplets on graphene layers: A comparative molecular-dynamics investigation, *Phys. Rev. E*, 2011, **84**, 061602.

348 T. R. Underwood and H. C. Greenwell, The Water-Alkane Interface at Various NaCl Salt Concentrations: A Molecular Dynamics Study of the Readily Available Force Fields, *Scientific Reports 2017 8:1*, 2018, **8**, 1–11.

349 W. Humphrey, A. Dalke and K. Schulten, VMD: Visual molecular dynamics, *Journal of Molecular Graphics and Modelling*, 1996, **14**, 33–38.

350 ASTM D7490-13, *Standard Test Method for Measurement of the Surface Tension of Solid Coatings, Substrates and Pigments using Contact Angle Measurements*, 2013.

351 N. M. Dingle and M. T. Harris, A robust algorithm for the simultaneous parameter estimation of interfacial tension and contact angle from sessile drop profiles, *J. Colloid Interf. Sci.*, 2005, **286**, 670–680.

352 M. Hoorfar and A. W. Neumann, Recent progress in Axisymmetric Drop Shape Analysis (ADSA), *Adv. Colloid Interf.*, 2006, **121**, 25–49.

353 A. F. Stalder *et al.*, Low-bond axisymmetric drop shape analysis for surface tension and contact angle measurements of sessile drops, *Colloids Surf. A*, 2010, **364**, 72–81.

354 J. P. Ewen *et al.*, Nonequilibrium molecular dynamics simulations of organic friction modifiers adsorbed on iron oxide surfaces, *Langmuir*, 2016, **32**, 4450–4463.

355 M. Biesalski and J. Rühe, Swelling of a polyelectrolyte brush in humid air, *Langmuir*, 2000, **16**, 1943–1950.

356 Y.-L. Chen and J. N. Israelachvili, Effects of Ambient Conditions on Adsorbed Surfactant and Polymer Monolayers, *J. Phys. Chem*, 1992, **96**, 7752–7760.

357 M. Chu, M. Miller and P. Dutta, Interfacial Density Profiles of Polar and Nonpolar Liquids at Hydrophobic Surfaces, *Langmuir*, 2020, **36**, 906–910.

358 P. Letellier, A. Mayaffre and M. Turmine, Drop size effect on contact angle explained by nonextensive thermodynamics. Young's equation revisited, *J. Colloid Interface Sci.*, 2007, **314**, 604–614.

359 C. Lam *et al.*, The effect of liquid properties to contact angle hysteresis, *Colloids Surf. A*, 2001, **189**, 265–278.

360 J. N. Israelachvili and M. L. Gee, Contact Angles on Chemically Heterogeneous, *Langmuir*, 1989, **5**, 288–289.

361 J. Wang, D. Bratko and A. Luzar, Probing surface tension additivity on chemically heterogeneous surfaces by a molecular approach, *Proc. Natl. Acad. Sci. U.S.A*, 2011, **108**, 6374–6379.

362 E. Weiand *et al.*, Nanoscale friction of biomimetic hair surfaces, *Nanoscale*, 2023, **15**, 7086–7104.

363 C. Klein *et al.*, Tunable transition from hydration to monomer-supported lubrication in zwitterionic monolayers revealed by molecular dynamics simulation, *Soft Matter*, 2015, **11**, 3340–3346.

364 A. Chatterjee, D. K. Dubey and S. K. Sinha, Effect of Loading on the Adhesion and Frictional Characteristics of Top Layer Articular Cartilage Nanoscale Contact: A Molecular Dynamics Study, *Langmuir*, 2021, **37**, 46–62.

365 W. K. Den Otter and S. A. Shkulipa, Intermonolayer Friction and Surface Shear Viscosity of Lipid Bilayer Membranes, *Biophysical Journal*, 2007, **93**, 423–433.

366 A. Zgorski, R. W. Pastor and E. Lyman, Surface Shear Viscosity and Interleaflet Friction from Nonequilibrium Simulations of Lipid Bilayers, *J. Chem. Theory Comput.*, 2019, **15**, 6471–6481.

367 Z. Liu, X. Shi and H. Wu, Coarse-grained molecular dynamics study of wettability influence on protein translocation through solid nanopores, *Nanotechnology*, 2019, **30**, 165701.

368 A. I. Jewett *et al.*, Moltemplate: A Tool for Coarse-Grained Modeling of Complex Biological Matter and Soft Condensed Matter Physics, *Journal of Molecular Biology*, 2021, **433**, 166841.

369 L. Martinez *et al.*, PACKMOL: A Package for Building Initial Configurations for Molecular Dynamics Simulations, *Journal of Computational Chemistry*, 2009, **30**, 2157–2164.

370 M. Parrinello and A. Rahman, Polymorphic transitions in single crystals: A new molecular dynamics method, *Journal of Applied Physics*, 1998, **52**, 7182.

371 S. Derler and G. M. Rotaru, Stickâ€“slip phenomena in the friction of human skin, *Wear*, 2013, **301**, 324–329.

372 D. Toton *et al.*, Temperature control in molecular dynamic simulations of non-equilibrium processes, *J. Phys. Condens. Mat.*, 2010, **22**, 074205.

373 R. Khare, J. de Pablo and A. Yethiraj, Molecular simulation and continuum mechanics study of simple fluids in non-isothermal planar Couette flows, *J. Chem. Phys.*, 1997, **107**, 2589.

374 T. Schneider and E. Stoll, Molecular-dynamics study of a three-dimensional one-component model for distortive phase-transitions, *Physical Review B*, 1978, **17**, 1302–1322.

375 N. Selway, V. Chan and J. R. Stokes, Influence of fluid viscosity and wetting on multiscale viscoelastic lubrication in soft tribological contacts, *Soft Matter*, 2017, **13**, 1702–1715.

376 F. Liu *et al.*, Coarse-grained molecular dynamics study on the rheological behaviors of surfactant aqueous solution, *Journal of Molecular Liquids*, 2018, **265**, 572–577.

377 S. D. Peroukidis *et al.*, Quantitative Prediction of the Structure and Viscosity of Aqueous Micellar Solutions of Ionic Surfactants: A Combined Approach Based on Coarse-Grained MARTINI Simulations Followed by Reverse-Mapped All-Atom Molecular Dynamics Simulations, *Journal of Chemical Theory and Computation*, 2020, **16**, 3363–3372.

378 H. Alasiri, Determining Critical Micelle Concentrations of Surfactants Based on Viscosity Calculations from Coarse-Grained Molecular Dynamics Simulations, *Energy & Fuels*, 2019, **33**, 2408–2412.

379 M. S. Green, Markoff Random Processes and the Statistical Mechanics of Time-Dependent Phenomena. II. Irreversible Processes in Fluids, *The Journal of Chemical Physics*, 2004, **22**, 398.

380 R. Kubo, Statistical-Mechanical Theory of Irreversible Processes. I. General Theory and Simple Applications to Magnetic and Conduction Problems, *http://dx.doi.org/10.1143/JPSJ.12.570*, 2013, **12**, 570–586.

381 K. R. Harris and L. A. Woolf, Temperature and Volume Dependence of the Viscosity of Water and Heavy Water at Low Temperatures, *Journal of Chemical and Engineering Data*, 2004, **49**, 1064–1069.

382 M. A. González and J. L. Abascal, The shear viscosity of rigid water models, *The Journal of Chemical Physics*, 2010, **132**, 096101.

383 M. W. Mahoney and W. L. Jorgensen, Diffusion constant of the TIP5P model of liquid water, *The Journal of Chemical Physics*, 2000, **114**, 363.

384 E. Liamas *et al.*, Probing the frictional properties of soft materials at the nanoscale, *Nanoscale*, 2020, **12**, 2292–2308.

385 C. P. Green *et al.*, Normal and torsional spring constants of atomic force microscope cantilevers, *Rev. Sci. Instrum.*, 2004, **75**, 1988–1996.

386 S. Karamdoust *et al.*, Preparation of antibacterial surfaces by hyperthermal hydrogen induced cross-linking of polymer thin films, *J. Mater. Chem.*, 2012, **22**, 4881–4889.

387 P. Pacher *et al.*, Characterizing Chemically Reactive Thin Layers: Surface Reaction of [2-[4-(Chlorosulfonyl)phenyl]ethyl]trichlorosilane with Ammonia, *J. Phys. Chem. C*, 2007, **111**, 12407–12413.

388 Y. Tran and P. Auroy, Complexation and distribution of counterions in a grafted polyelectrolyte layer, *Eur. Phys. J. E*, 2001, **5**, 65–79.

389 B. M. Fry *et al.*, Adsorption of Organic Friction Modifier Additives, *Langmuir*, 2020, **36**, 1147–1155.

390 K. Bierbaum *et al.*, A Near Edge X-ray Absorption Fine Structure Spectroscopy and X-ray Photoelectron Spectroscopy Study of the Film Properties of Self-Assembled Monolayers of Organosilanes on Oxidized Si(100), *Langmuir*, 1995, **11**, 512–518.

391 P. Fontaine, M. Goldmann and F. Rondelez, Influence of Headgroup Cross-Linking on Chain Packing in Langmuir Monolayers of n-Alkyltrialkoxysilanes, *Langmuir*, 1999, **15**, 1348–1352.

392 J.-G. Ma, B. J. Boyd and C. J. Drummond, Positional isomers of linear sodium dodecyl benzene sulfonate: Solubility, self-assembly, and air/water interfacial activity, *Langmuir*, 2006, **22**, 8646–8654.

393 J. Israelachvili, Solvation forces and liquid structure, as probed by direct force measurements, *Acc. Chem. Res.*, 1987, **20**, 415–421.

394 K. L. Johnson, K. Kendall and A. D. Roberts, Surface energy and the contact of elastic solids, *Proc. R. Soc. London, Ser. A*, 1971, **324**, 301–313.

395 A. Perriot and E. Barthel, Elastic contact to a coated half-space: Effective elastic modulus and real penetration, *Journal of Materials Research*, 2004, **19**, 600–608.

396 S. Inaba, S. Fujino and K. Morinaga, Young's Modulus and Compositional Parameters of Oxide Glasses, *J. Am. Ceram. Soc.*, 1999, **82**, 3501–3507.

397 G. W. Tormoen, J. Drelich and E. R. Beach, Analysis of atomic force microscope pull-off forces for gold surfaces portraying nanoscale roughness and specific chemical functionality, *Journal of Adhesion Science and Technology*, 2004, **18**, 1–17.

398 S. Biggs, R. Cain and N. W. Page, Lateral force microscopy study of the friction between silica surfaces, *Journal of Colloid and Interface Science*, 2000, **232**, 133–140.

399 V. V. Tsukruk *et al.*, Organic Molecular Films under Shear Forces: Fluid and Solid Langmuir Monolayers, *Langmuir*, 1996, **12**, 4840–4849.

400 E. D. Reedy, Thin-coating contact mechanics with adhesion, *J. Mater. Res.*, 2006, **21**, 2660–2668.

401 S. Campen *et al.*, On the increase in boundary friction with sliding speed, *Tribology Letters*, 2012, **48**, 237–248.

402 M. H. Müser, Nature of Mechanical Instabilities and Their Effect on Kinetic Friction, *Physical Review Letters*, 2002, **89**, 224301.

403 A. M. Smith *et al.*, Quantized friction across ionic liquid thin films, *Phys. Chem. Chem. Phys.*, 2013, **15**, 15317–15320.

404 H. Eyring, Viscosity, plasticity, and diffusion as examples of absolute reaction rates, *J Chem Phys*, 1936, **4**, 283–291.

405 C. Drummond, J. Israelachvili and P. Richetti, Friction between two weakly adhering boundary lubricated surfaces in water, *Physical Review E*, 2003, **67**, 066110.

406 G. He and M. O. Robbins, Simulations of the kinetic friction due to adsorbed surface layers, *Tribology Letters 2001 10:1*, 2001, **10**, 7–14.

407 M. R. Farrow *et al.*, Molecular simulations of kinetic-friction modification in nanoscale fluid layers, *Tribology Letters*, 2011, **42**, 325–337.

408 R. M. Overney *et al.*, Anisotropy in Friction and Molecular Stick-Slip Motion, *Phys. Rev. Lett.*, 1994, **72**, 3546.

409 A. Jabbarzadeh, Friction anisotropy and asymmetry in self assembled monolayers, *Tribol. Int.*, 2016, **102**, 600–607.

410 J. M. D. Lane *et al.*, Water in nanoconfinement between hydrophilic self-assembled monolayers, *Langmuir*, 2008, **24**, 5209–5212.

411 C. D. Lorenz *et al.*, Nanotribology of water confined between hydrophilic alkylsilane self-assembled monolayers, *Model. Simul. Mater. Sci. Eng.*, 2010, **18**, 034005.

412 A. Striolo *et al.*, Water adsorption in carbon-slit nanopores, *Langmuir*, 2003, **19**, 8583–8591.

413 C. Sendner *et al.*, Interfacial water at hydrophobic and hydrophilic surfaces: Slip, viscosity, and diffusion, *Langmuir*, 2009, **25**, 10768–10781.

414 N. Dhopatkar, A. P. Defante and A. Dhinojwala, Ice-like water supports hydration forces and eases sliding friction, *Science Advances*, 2016, **2**, e1600763.

415 W. Chen *et al.*, Stick-Slip Control in Nanoscale Boundary Lubrication by Surface Wettability, *Phys. Rev. Lett.*, 2015, **114**, 095502.

416 R. Szoszkiewicz and E. Riedo, Nucleation time of nanoscale water bridges, *Phys. Rev. Lett.*, 2005, **95**, 135502.

417 H. K. Christenson, J. N. lsraelachvili and R. M. Pashley, Properties of Capillary Fluids at the Microscopic Level, *SPE Res. Eng.*, 1987, **2**, 155–165.

418 C. Cafolla and K. Voïtchovsky, Impact of water on the lubricating properties of hexadecane at the nanoscale, *Nanoscale*, 2020, **12**, 14504–14513.

419 A. A. Feiler *et al.*, Effect of capillary condensation on friction force and adhesion, *Langmuir*, 2007, **23**, 517–522.

420 K. B. Jinesh and J. W. M. Frenken, Experimental evidence for ice formation at room temperature, *Physical Review Letters*, 2008, **101**, 036101.

421 S. Hanot, S. Lyonnard and S. Mossa, Sub-diffusion and population dynamics of water confined in soft environments, *Nanoscale*, 2016, **8**, 3314–3325.

422 K. Krynicki, C. D. Green and D. W. Sawyer, Pressure and temperature dependence of self-diffusion in water, *Faraday Discuss. Chem. Soc.*, 1978, **66**, 199–208.

423 F. Y. Hansen *et al.*, Diffusion of water and selected atoms in DMPC lipid bilayer membranes, *J. Chem. Phys.*, 2012, **137**, 204910.

424 R. Zangi and A. E. Mark, Bilayer ice and alternate liquid phases of confined water, *J. Chem. Phys.*, 2003, **119**, 1694–1700.

425 S. Han *et al.*, Phase transitions in confined water nanofilms, *Nat. Phys.*, 2010, **6**, 685–689.

426 U. Raviv, P. Laurat and J. Klein, Fluidity of water confined to subnanometre films, *Nature*, 2001, **413**, 51–54.

427 K. Koga, H. Tanaka and X. C. Zeng, First-order transition in confined water between high-density liquid and low-density amorphous phases, *Nature*, 2000, **408**, 564–567.

428 N. Giovambattista, P. J. Rossky and P. G. Debenedetti, Effect of pressure on the phase behavior and structure of water confined between nanoscale hydrophobic and hydrophilic plates, *Phys. Rev. E*, 2006, **73**, 041604.

429 R. R. Netz, Electrofriction and Dynamic Stern Layers at Planar Charged Surfaces, *Phys. Rev. Lett.*, 2003, **91**, 138101.

430 G. Kagata, J. P. Gong and Y. Osada, Friction of Gels. 7. Observation of Static Friction between Like-Charged Gels, *The Journal of Physical Chemistry B*, 2003, **107**, 10221–10225.

431 E. Weiand *et al.*, Effects of surfactant adsorption on the wettability and friction of biomimetic surfaces, *Phys. Chem. Chem. Phys.*, 2023, 21916–21934.

432 Z. Liu *et al.*, Comprehensive review on surfactant adsorption on mineral surfaces in chemical enhanced oil recovery, *Advances in Colloid and Interface Science*, 2021, **294**, 102467.

433 C. McFadden, C. Soto and N. D. Spencer, Adsorption and surface chemistry in tribology, *Tribology International*, 1997, **30**, 881–888.

434 D. Bajpai and V. K. Tyagi, Laundry Detergents: An Overview, *Journal of Oleo Science*, 2007, **56**, 327–340.

435 A. Striolo, Studying surfactants adsorption on heterogeneous substrates, *Current Opinion in Chemical Engineering*, 2019, **23**, 115–122.

436 K. Kizawa *et al.*, Dissimilar effect of perming and bleaching treatments on cuticles: Advanced hair damage model based on elution and oxidation of S100A3 protein, *Journal of Cosmetic Science*, 2005, **56**, 219–226.

437 K. Ohbu *et al.*, Binding characteristics of ionic surfactants with human hair, *Colloid and Polymer Science*, 1986, **264**, 798–802.

438 F. Pan *et al.*, Surface active complexes formed between keratin polypeptides and ionic surfactants, *Journal of Colloid and Interface Science*, 2016, **484**, 125–134.

439 G. V. Scott, C. R. Robbins and J. D. Barnhurst, Sorption of Quaternary Ammonium Surfactants by Human Hair, *Journal of the Society of Cosmetic Chemists*, 1969, **20**, 135–152.

440 B. C. Beard and J. Hare, Surface Interactions of Quaternary Amines with Hair, *Journal of Surfactants and Detergents*, 2002, **5**, 145–159.

441 V. André *et al.*, The role of polymer-surfactant interactions in the adsorption process of hair-conditioning polymers, *Macromolecular Symposia*, 1999, **145**, 169–179.

442 S. T. Regismond *et al.*, Fluorescence Microscopy Observation of the Adsorption onto Hair of a Fluorescently Labeled Cationic Cellulose Ether, *Langmuir*, 1999, **15**, 3007–3010.

443 M. Rincón-Fontán *et al.*, Adsorption of natural surface active compounds obtained from corn on human hair, *RSC Advances*, 2016, **6**, 63064–63070.

444 E. Guzmán *et al.*, Self-consistent mean field calculations of polyelectrolyte-surfactant mixtures in solution and upon adsorption onto negatively charged surfaces, *Polymers*, 2020, **12**, 624.

445 J. Klebes *et al.*, The Role of Chemical Heterogeneity in Surfactant Adsorption at Solid-Liquid Interfaces, *Journal of Chemical Theory and Computation*, 2020, **16**, 7135–7147.

446 S. D. Anogiannakis, P. C. Petris and D. N. Theodorou, Promising Route for the Development of a Computational Framework for Self-Assembly and Phase Behavior Prediction of Ionic Surfactants Using MARTINI, *Journal of Physical Chemistry B*, 2020, **124**, 556–567.

447 S. Illa-Tuset, D. C. Malaspina and J. Faraudo, Coarse-grained molecular dynamics simulation of the interface behaviour and self-assembly of CTAB cationic surfactants, *Physical Chemistry Chemical Physics*, 2018, **20**, 26422–26430.

448 S. Liu, D. Wu and X. Yang, Coarse-grained molecular simulation of self-assembly nanostructures of CTAB on nanoscale graphene, *Molecular Simulation*, 2016, **42**, 31–38.

449 S. Wang and R. G. Larson, Coarse-grained molecular dynamics simulation of self-assembly and surface adsorption of ionic surfactants using an implicit water model, *Langmuir*, 2015, **31**, 1262–1271.

450 S. Jalili and M. Akhavan, A coarse-grained molecular dynamics simulation of a sodium dodecyl sulfate micelle in aqueous solution, *Colloids and Surfaces A: Physicochemical and Engineering Aspects*, 2009, **352**, 99–102.

451 Y. Ruiz-Morales and A. Romero-Martínez, Coarse-Grain Molecular Dynamics Simulations to Investigate the Bulk Viscosity and Critical Micelle Concentration of the Ionic Surfactant Sodium Dodecyl Sulfate (SDS) in Aqueous Solution, *Journal of Physical Chemistry B*, 2018, **122**, 3931–3943.

452 G. J. Martyna, D. J. Tobias and M. L. Klein, Constant pressure molecular dynamics algorithms, *The Journal of Chemical Physics*, 1994, **101**, 4177–4189.

453 P. Lianos and R. Zana, Surfactant-alcohol mixed-micelle formation: Cetyltrimethylammonium bromide-1-butanol system, *Chemical Physics Letters*, 1980, **72**, 171–175.

454 C. Ma *et al.*, Determination of the first and second CMCs of surfactants by adsorptive voltammetry, *Colloids and Surfaces A: Physicochemical and Engineering Aspects*, 1998, **143**, 89–94.

455 J. Rassing, P. J. Sams and E. Wyn-Jones, Kinetics of micellization from ultrasonic relaxation studies, *Journal of the Chemical Society, Faraday Transactions 2*, 1974, **70**, 1247–1258.

456 A. Patist *et al.*, Kinetics of micellization: Its significance to technological processes, *Colloids and Surfaces A: Physicochemical and Engineering Aspects*, 2001, **176**, 3–16.

457 D. Glikman and B. Braunschweig, Nanoscale Effects on the Surfactant Adsorption and Interface Charging in Hexadecane/Water Emulsions, *ACS Nano*, 2021, **15**, 20136–20147.

458 B. N. Persson, On the fractal dimension of rough surfaces, *Tribology Letters*, 2014, **54**, 99–106.

459 D. Avnir, D. Farin and P. Pfeifer, Molecular fractal surfaces, *Nature*, 1984, **308**, 261–263.

460 C. Yang, U. Tartaglino and B. N. Persson, Influence of surface roughness on superhydrophobicity, *Physical Review Letters*, 2006, **97**, 116103.

461 V. V. Ginzburg *et al.*, Modeling the adsorption of rheology modifiers onto latex particles using coarse-grained molecular dynamics (CG-MD) and self-consistent field theory (SCFT), *Macromolecules*, 2015, **48**, 8045–8054.

462 B. Bera *et al.*, Counteracting Interfacial Energetics for Wetting of Hydrophobic Surfaces in the Presence of Surfactants, *Langmuir*, 2018, **34**, 12344–12349.

463 K. Fontell, Liquid Crystallinity in Lipid-Water Systems, *Molecular Crystals and Liquid Crystals*, 1981, **63**, 59–82.

464 N. K. Raman, M. T. Anderson and C. J. Brinker, Template-Based Approaches to the Preparation of Amorphous, Nanoporous Silicas, *Chemistry of Materials*, 1996, **63**, 59–82.

465 M. Tornblom, U. Henriksson and M. Ginley, A Field Dependent 2H Nuclear Magnetic Relaxation Study of the Aggregation Behavior in Micellar Solutions of CTAB and SDS, *The Journal of Physical Chemistry*, 1994, **98**, 7041–7051.

466 J. J. Harris, G. A. Pantelopulos and J. E. Straub, Finite-Size Effects and Optimal System Sizes in Simulations of Surfactant Micelle Self-Assembly, *Journal of Physical Chemistry B*, 2021, **125**, 5068–5077.

467 J. F. Kraft *et al.*, Modeling the Self-Assembly and Stability of DHPC Micelles Using Atomic Resolution and Coarse Grained MD Simulations, *Journal of Chemical Theory and Computation*, 2012, **8**, 1556–1569.

468 E. Tyrode, M. W. Rutland and C. D. Bain, Adsorption of CTAB on hydrophilic silica studied by linear and nonlinear optical spectroscopy, *Journal of the American Chemical Society*, 2008, **130**, 17434–17445.

469 G. Tsagkaropoulou *et al.*, Self-assembly and adsorption of cetyltrimethylammonium bromide and didodecyldimethylammonium bromide surfactants at the mica-water interface, *Soft Matter*, 2019, **15**, 8402–8411.

470 R. D. C. C. Wagner and I. Joekes, Hair protein removal by sodium dodecyl sulfate, *Colloids and Surfaces B: Biointerfaces*, 2005, **41**, 7–14.

471 C. Yang and H. Sun, Surface-bulk partition of surfactants predicted by molecular dynamics simulations, *Journal of Physical Chemistry B*, 2014, **118**, 10695–10703.

472 L. Lajtar, J. Narkiewicz-Michalek and W. Rudzinski, A New Theoretical Approach to Adsorption of Ionic Surfactants at Water/Oxide Interfaces: Studies of the Mechanism of Cationic Surfactant Adsorption, *Langmuir*, 1994, **10**, 3754–3764.

473 B. Li and E. Ruckenstein, Adsorption of Ionic Surfactants on Charged Solid Surfaces from Aqueous Solutions, *Langmuir*, 1996, **12**, 5052–5063.

474 R. Atkin *et al.*, The influence of chain length and electrolyte on the adsorption kinetics of cationic surfactants at the silica-aqueous solution interface, *Journal of Colloid and Interface Science*, 2003, **266**, 236–244.

475 J. A. Faucher, E. D. Goddard and R. B. Hannan, Sorption and Desorption of a Cationic Polymer by Human Hair: Effects of Salt Solutions, *Textile Research Journal*, 1977, **47**, 616–620.

476 M. Suttipong *et al.*, Salt-specific effects in aqueous dispersions of carbon nanotubes, *Soft Matter*, 2013, **9**, 3712–3719.

477 N. R. Tummala, B. P. Grady and A. Striolo, Lateral confinement effects on the structural properties of surfactant aggregates: SDS on graphene, *Phys. Chem. Chem. Phys.*, 2010, **12**, 13137–13143.

478 J. Jachowicz, S. Maxey and C. Williams, Sorption/desorption of ions by dynamic electrokinetic and permeability analysis of fiber plugs, *Langmuir*, 1993, **9**, 3085–3092.

479 A. D. Berman, S. D. Cameron and J. N. Israelachvili, Mobility of surfactants in and between adsorbed monolayers, *Journal of Physical Chemistry B*, 1997, **101**, 5692–5697.

480 G. Silbert, N. Kampf and J. Klein, Normal and shear forces between charged solid surfaces immersed in cationic surfactant solution: The role of the alkyl chain length, *Langmuir*, 2014, **30**, 5097–5104.

481 A. Z. Summers *et al.*, Influence of Surface Morphology on the Shear-Induced Wear of Alkylsilane Monolayers: Molecular Dynamics Study, *Langmuir*, 2016, **32**, 2348–2359.

482 E. Weiand *et al.*, Boundary lubrication performance of polyelectrolyte-surfactant complexes on biomimetic surfaces, *Langmuir (accepted manuscript)*, 2024, –.

483 J. V. Gruber *et al.*, Examining cationic polysaccharide deposition on keratin surfaces through biopolymer fluorescent labeling, *Journal of Cosmetic Science*, 2001, **52**, 119–129.

484 M. Gradzielski and I. Hoffmann, Polyelectrolyte-surfactant complexes (PESCs) composed of oppositely charged components, *Current Opinion in Colloid and Interface Science*, 2018, **35**, 124–141.

485 L. Qian *et al.*, Dynamic Friction by Polymer/Surfactant Mixtures Adsorbed on Surfaces, *Journal of Physical Chemistry B*, 2004, **108**, 18608–18614.

486 W. H. Briscoe, Aqueous boundary lubrication: Molecular mechanisms, design strategy, and terra incognita, *Current Opinion in Colloid and Interface Science*, 2017, **27**, 1–8.

487 D. Mudgil, S. Barak and B. S. Khatkar, Guar gum: Processing, properties and food applications - A Review, *Journal of Food Science and Technology*, 2014, **51**, 409–418.

488 E. K. Oikonomou *et al.*, Design of eco-friendly fabric softeners: Structure, rheology and interaction with cellulose nanocrystals, *Journal of Colloid and Interface Science*, 2018, **525**, 206–215.

489 M. Gradzielski, Polyelectrolyte-Surfactant Complexes As a Formulation Tool for Drug Delivery, *Langmuir*, 2022, **38**, 13330–13343.

490 A. T. Shivgan *et al.*, Extending the Martini Coarse-Grained Force Field to N-Glycans, *Journal of Chemical Information and Modeling*, 2020, **60**, 3864–3883.

491 Z. Yuan *et al.*, A Study of the Surface Adhesion and Rheology Properties of Cationic Conditioning Polymers, *Industrial and Engineering Chemistry Research*, 2019, **58**, 9390–9396.

492 H. Xu and S. Matysiak, Effect of pH on chitosan hydrogel polymer network structure, *Chemical Communications*, 2017, **53**, 7373–7376.

493 S. Gotla, C. Tong and S. Matysiak, Load-Bearing Nanostructures in Composites of Chitosan with Anionic Surfactants: Implications for Programmable Mechanomaterials, *ACS Applied Nano Materials*, 2022, **2022**, 6473.

494 M. Tsanai *et al.*, Coacervate formation studied by explicit solvent coarse-grain molecular dynamics with the Martini model, *Chemical Science*, 2021, **12**, 8521–8530.

495 C. A. López *et al.*, Martini coarse-grained force field: Extension to carbohydrates, *Journal of Chemical Theory and Computation*, 2009, **5**, 3195–3210.

496 P. S. Schmalhorst *et al.*, Overcoming the Limitations of the MARTINI Force Field in Simulations of Polysaccharides, *Journal of Chemical Theory and Computation*, 2017, **13**, 5039–5053.

497 H. Liang *et al.*, Understanding the Structure and Rheology of Galactomannan Solutions with Coarse-Grained Modeling, *Macromolecules*, 2022, **56**, 177–187.

498 W. Damm *et al.*, OPLS all-atom force field for carbohydrates, *Journal of Computational Chemistry*, 1997, **18**, 1955–1970.

499 D. Kony *et al.*, An improved OPLS-AA force field for carbohydrates, *Journal of Computational Chemistry*, 2002, **23**, 1416–1429.

500 W. L. Jorgensen and J. Tirado-Rives, Potential energy functions for atomic-level simulations of water and organic and biomolecular systems, *Proceedings of the National Academy of Sciences*, 2005, **102**, 6665–6670.

501 L. S. Dodda *et al.*, 1.14*CM1A-LBCC: Localized Bond-Charge Corrected CM1A Charges for Condensed-Phase Simulations, *The Journal of Physical Chemistry B*, 2017, **121**, 3864–3870.

502 L. S. Dodda *et al.*, LigParGen web server: an automatic OPLS-AA parameter generator for organic ligands, *Nucleic Acids Research*, 2017, **45**, W331–W336.

503 J. A. Graham, J. W. Essex and S. Khalid, PyCGTOOL: Automated Generation of Coarse-Grained Molecular Dynamics Models from Atomistic Trajectories, *J. Chem. Inf. Model.*, 2017, **57**, 650–656.

504 H. C. Thielemann *et al.*, From GROMACS to LAMMPS: GRO2LAM, *Journal of Molecular Modeling*, 2019, **25**, 147.

505 Y. Cheng and R. K. Prud'homme, Enzymatic degradation of guar and substituted guar galactomannans, *Biomacromolecules*, 2000, **1**, 782–788.

506 O. Anthony, C. M. Marques and P. Richetti, Bulk and Surface Behavior of Cationic Guars in Solutions of Oppositely Charged Surfactants, *Langmuir*, 1998, **14**, 6086–6095.

507 E. Guzmán *et al.*, Adsorption of conditioning polymers on solid substrates with different charge density, *ACS Applied Materials and Interfaces*, 2011, **3**, 3181–3188.

508 P. Hössel *et al.*, Conditioning polymers in today's shampoo formulations - Efficacy, mechanism and test methods, *International Journal of Cosmetic Science*, 2000, **22**, 1–10.

509 I. Varga and R. A. Campbell, General physical description of the behavior of oppositely charged polyelectrolyte/surfactant mixtures at the air/water interface, *Langmuir*, 2017, **33**, 5915–5924.

510 A. Dedinaite, P. M. Claesson and M. Bergström, Polyelectrolyte-surfactant layers: adsorption of preformed aggregates versus adsorption of surfactant to preadsorbed polyelectrolyte, *Langmuir*, 2000, **16**, 5257–5266.

511 Y. Samoshina, T. Nylander and B. Lindman, Cationic Amphiphilic Polyelectrolytes and Oppositely Charged Surfactants at the Silica-Aqueous Interface, *Langmuir*, 2005, **21**, 4490–4502.

512 E. Terada *et al.*, Adsorption of cationic cellulose derivative/anionic surfactant complexes onto solid surfaces. II. Hydrophobized silica surfaces, *Langmuir*, 2004, **20**, 6692–6701.

513 E. Terada *et al.*, Adsorption of cationic cellulose derivatives/anionic surfactant complexes onto solid surfaces. I. Silica surfaces, *Langmuir*, 2004, **20**, 1753–1762.

514 Y. Z. Hessefort, B. T. Holland and R. W. Cloud, True porosity measurement of hair: A new way to study hair damage mechanisms, *Journal of Cosmetic Science*, 2008, **59**, 303–315.

515 P. H. Elworthy and K. J. Mysels, The surface tension of sodium dodecylsulfate solutions and the phase separation model of micelle formation, *Journal of Colloid and Interface Science*, 1966, **21**, 331–347.

516 V. Shubin, Adsorption of Cationic Polymer onto Negatively Charged Surfaces in the Presence of Anionic Surfactant, *Langmuir*, 1994, **10**, 1093–1100.

517 O. J. Rojas *et al.*, Coadsorption and Surface Forces for Selective Surfaces in Contact with Aqueous Mixtures of Oppositely Charged Surfactants and Low Charge Density Polyelectrolytes, *Langmuir*, 2004, **20**, 3221–3230.

518 M. A. Plunkett *et al.*, Comparison of the adsorption of different charge density polyelectrolytes: A quartz crystal microbalance and X-ray photoelectron spectroscopy study, *Langmuir*, 2003, **19**, 4673–4681.

519 Y. Roiter and S. Minko, Adsorption of polyelectrolyte versus surface charge: In situ single-molecule atomic force microscopy experiments on similarly, oppositely, and heterogeneously charged surfaces, *Journal of Physical Chemistry B*, 2007, **111**, 8597–8604.

520 L. Dai *et al.*, Identifying the Mechanisms of Polymer Friction through Molecular Dynamics Simulation, *Langmuir*, 2011, **27**, 14861–14867.

521 J. Mees *et al.*, Molecular Mechanisms of Self-mated Hydrogel Friction, *Tribology Letters*, 2023, **71**, 74.

522 A. Dedinaite and P. M. Claesson, Synergies in lubrication, *Physical Chemistry Chemical Physics*, 2017, **19**, 23677–23689.

523 A. Dedinaite *et al.*, Lubrication by organized soft matter, *Soft Matter*, 2010, **6**, 1520–1526.

524 S. T. Hyde, Microstructure of Bicontinuous Surfactant Aggregates, *The Journal of Physical Chemistry*, 1989, **93**, 1458–1464.

525 R. Kumar, Y. K. Lee and Y. S. Jho, Martini coarse-grained model of hyaluronic acid for the structural change of its gel in the presence of monovalent and divalent salts, *International Journal of Molecular Sciences*, 2020, **21**, 4602.

526 Y. Liu *et al.*, Capturing coacervate formation and protein partition by molecular dynamics simulation, *Chemical Science*, 2023, **14**, 1168–1175.

527 X. Wan *et al.*, Determination of the degree of substitution of cationic guar gum by headspace-based gas chromatography during its synthesis, *Journal of Agricultural and Food Chemistry*, 2017, **65**, 7012–7016.

528 T.-A. Le and T.-P. Huynh, Current advances in the Chemical functionalization and Potential applications of Guar gum and its derivatives, *European Polymer Journal*, 2023, 111852.

529 F. L. Figueira *et al.*, Coupled matrix kinetic Monte Carlo simulations applied for advanced understanding of polymer grafting kinetics, *Reaction Chemistry & Engineering*, 2021, **6**, 640–661.

530 C. Fernandes *et al.*, On Hair Care Physicochemistry: From Structure and Degradation to Novel Biobased Conditioning Agents, *Polymers*, 2023, **15**, 608.

531 S. Chen *et al.*, Tactile perception of fabrics with an artificial finger compared to human sensing, *Textile Research Journal*, 2015, **85**, 2177–2187.

532 M. Easson *et al.*, Structure/function analysis of nonwoven cotton topsheet fabrics: multi-fiber blending effects on fluid handling and fabric handle mechanics, *Materials*, 2018, **11**, 2077.

533 T. Topalovic *et al.*, XPS and contact angle study of cotton surface oxidation by catalytic bleaching, *Colloids and Surfaces A: Physicochemical and Engineering Aspects*, 2007, **296**, 76–85.

534 M. Martínez-Sanz *et al.*, Structure of cellulose microfibrils in mature cotton fibres, *Carbohydrate polymers*, 2017, **175**, 450–463.

535 Y.-L. Hsieh and B. Yu, Liquid wetting, transport, and retention properties of fibrous assemblies: Part I: Water wetting properties of woven fabrics and their constituent single fibers, *Textile Research Journal*, 1992, **62**, 677–685.

536 Y.-L. Hsieh, J. Thompson and A. Miller, Water wetting and retention of cotton assemblies as affected by alkaline and bleaching treatments, *Textile research journal*, 1996, **66**, 456–464.

537 D. C. Malaspina and J. Faraudo, Molecular insight into the wetting behavior and amphiphilic character of cellulose nanocrystals, *Advances in Colloid and Interface Science*, 2019, **267**, 15–25.

538 T. C. Pesacreta, L. C. Carlson and B. A. Triplett, Atomic force microscopy of cotton fiber cell wall surfaces in air and water: quantitative and qualitative aspects, *Planta*, 1997, **202**, 435–442.

539 E. Amelina *et al.*, Effect of cationic polyelectrolyte and surfactant on cohesion and friction in contacts between cellulose fibers, *Colloids and Surfaces A: Physicochemical and Engineering Aspects*, 2000, **167**, 215–227.

540 S. Zauscher and D. J. Klingenberg, Friction between cellulose surfaces measured with colloidal probe microscopy, *Colloids and Surfaces A: Physicochemical and Engineering Aspects*, 2001, **178**, 213–229.

541 J. Stiernstedt *et al.*, Friction between cellulose surfaces and effect of xyloglucan adsorption, *Biomacromolecules*, 2006, **7**, 2147–2153.

542 J. Stiernstedt *et al.*, Friction and forces between cellulose model surfaces: A comparison, *Journal of colloid and interface science*, 2006, **303**, 117–123.

543 Z. Zhang *et al.*, Morphological and quantitative frictional measurements of cotton fibres using friction force microscopy, *Journal of Materials Chemistry*, 2010, **20**, 8531–8538.

544 F. Hosseinali and J. A. Thomasson, Variability of fiber friction among cotton varieties: Influence of salient fiber physical metrics, *Tribology International*, 2018, **127**, 433–445.

545 F. Hosseinali and J. A. Thomasson, Multiscale frictional properties of cotton fibers: A review, *Fibers*, 2018, **6**, 49.

546 F. Hosseinali and J. A. Thomasson, Probing of Nanoscale Friction and Mechanical Characteristics of Cotton Fiber's Surface, *Fibers*, 2019, **7**, 64.

547 E. K. Oikonomou *et al.*, Silicone incorporation into an esterquat based fabric softener in presence of guar polymers, *Colloids and Surfaces A: Physicochemical and Engineering Aspects*, 2021, **615**, 126175.

548 J. Penfold *et al.*, Surfactant adsorption onto cellulose surfaces, *Langmuir*, 2007, **23**, 8357–8364.

549 D. S. Murphy, Fabric softener technology: A review, *Journal of Surfactants and Detergents*, 2015, **18**, 199–204.

550 T. Igarashi and K. Nakamura, Improvement of the Water Absorbency of Softener-treated Fabric: Addition of a New Hydrophilic Surface, *Journal of Oleo Science*, 2021, **70**, 509–519.

551 X. Wu, R. J. Moon and A. Martini, Atomistic simulation of frictional sliding between cellulose Iβ nanocrystals, *Tribology Letters*, 2013, **52**, 395–405.

552 A. Paajanen *et al.*, Atomistic molecular dynamics simulations on the interaction of TEMPO-oxidized cellulose nanofibrils in water, *Cellulose*, 2016, **23**, 3449–3462.

553 C. Zhang *et al.*, Hydrogen bonds dominated frictional stick-slip of cellulose nanocrystals, *Carbohydrate Polymers*, 2021, **258**, 117682.

554 V. Modi and A. J. Karttunen, Molecular Dynamics Simulations on the Elastic Properties of Polypropylene Bionanocomposite Reinforced with Cellulose Nanofibrils, *Nanomaterials*, 2022, **12**, 3379.

555 G. Bellesia *et al.*, Coarse-grained model for the interconversion between native and liquid ammonia-treated crystalline cellulose, *The Journal of Physical Chemistry B*, 2012, **116**, 8031–8037.

556 C. A. López *et al.*, MARTINI coarse-grained model for crystalline cellulose microfibers, *The Journal of Physical Chemistry B*, 2015, **119**, 465–473.

557 R. A. Moreira, S. A. Weber and A. B. Poma, Martini 3 Model of cellulose microfibrils: on the route to capture large conformational changes of polysaccharides, *Molecules*, 2022, **27**, 976.

558 R. J. Maurer, A. F. Sax and V. Ribitsch, Molecular simulation of surface reorganization and wetting in crystalline cellulose I and II, *Cellulose*, 2013, **20**, 25–42.

559 L. N. Trentin *et al.*, Nanoscale wetting of crystalline cellulose, *Biomacromolecules*, 2021, **22**, 4251–4261.

560 C. T. Brett, Cellulose microfibrils in plants: Biosynthesis, deposition, and integration into the cell wall, *Int. Rev. Cytol.*, 2000, **199**, 161–199.

561 R. M. Brown Jr, Cellulose structure and biosynthesis: what is in store for the 21st century?, *Journal of Polymer Science Part A: Polymer Chemistry*, 2004, **42**, 487–495.

562 B. T. Nixon *et al.*, Comparative structural and computational analysis supports eighteen cellulose synthases in the plant cellulose synthesis complex, *Scientific reports*, 2016, **6**, 28696.

563 D. P. Oehme *et al.*, Unique aspects of the structure and dynamics of elementary I β cellulose microfibrils revealed by computational simulations, *Plant physiology*, 2015, **168**, 3–17.

564 V. G. Vandavasi *et al.*, A structural study of CESA1 catalytic domain of Arabidopsis cellulose synthesis complex: evidence for CESA trimers, *Plant physiology*, 2016, **170**, 123–135.

565 N. Abidi, in *Chemical Properties of Cotton Fiber and Chemical Modification*, ed. D. D. Fang, Springer International Publishing, Cham, 2018, pp. 95–115.

566 A. Tarbuk *et al.*, Adsorption of plant extracts on cationized cotton, *Zbornik radova Tehnološkog fakulteta u Leskovcu*, 2009, 257–264.

567 D. Van Der Spoel *et al.*, GROMACS: fast, flexible, and free, *Journal of computational chemistry*, 2005, **26**, 1701–1718.

568 T. D. Potter, E. L. Barrett and M. A. Miller, Automated coarse-grained mapping algorithm for the Martini force field and benchmarks for membrane–water partitioning, *Journal of Chemical Theory and Computation*, 2021, **17**, 5777–5791.

569 A. W. Sousa da Silva and W. F. Vranken, ACPYPE-Antechamber python parser interface, *BMC research notes*, 2012, **5**, 1–8.

570 M. R. Shirts *et al.*, Lessons learned from comparing molecular dynamics engines on the SAMPL5 dataset, *Journal of computer-aided molecular design*, 2016, 1–15.

571 G. Landrum *et al.*, *rdkit/rdkit: Release_2023.09.5*, 2024, https://doi.org/10.5281/zenodo.10633624.

572 J. Wang *et al.*, Development and testing of a general amber force field, *Journal of computational chemistry*, 2004, **25**, 1157–1174.

573 T. Bereau and K. Kremer, Automated parametrization of the coarse-grained Martini force field for small organic molecules, *Journal of chemical theory and computation*, 2015, **11**, 2783–2791.

574 A. Jakalian, D. B. Jack and C. I. Bayly, Fast, efficient generation of high-quality atomic charges. AM1-BCC model: II. Parameterization and validation, *Journal of computational chemistry*, 2002, **23**, 1623–1641.

575 W. L. Jorgensen *et al.*, Comparison of simple potential functions for simulating liquid water, *The Journal of chemical physics*, 1983, **79**, 926–935.

576 K. Kohata *et al.*, FUNDAMENTAL STUDIES ON THE INTERACTION BETWEEN MOISTURE AND TEXTILES PART I. MOISTURE SORPTION AND DESORPTION ISOTHERMS OF CELLULOSIC FIBERS, *Sen'i Gakkaishi*, 1986, **42**, T136–T154.

577 J. A. Wallace and J. K. Shen, Probing the strand orientation and registry alignment in the propagation of amyloid fibrils, *Biochemistry*, 2010, **49**, 5290–5298.

578 B. H. Morrow, P. H. Koenig and J. K. Shen, Atomistic simulations of pH-dependent self-assembly of micelle and bilayer from fatty acids, *The Journal of Chemical Physics*, 2012, **137**, 194902.

579 M. Hernández-Rivas *et al.*, Deposition of synthetic and bio-based polycations onto negatively charged solid surfaces: Effect of the polymer cationicity, ionic strength, and the addition of an anionic surfactant, *Colloids and Interfaces*, 2020, **4**, 33.

580 T. Morita *et al.*, Glycolipid Biosurfactants, Mannosylerythritol Lipids, Repair the Damaged Hair, *Journal of Oleo Science*, 2010, **59**, 267–272.

581 D. Kitamoto *et al.*, Glycolipid Biosurfactants, Mannosylerythritol Lipids: Distinctive Interfacial Properties and Applications in Cosmetic and Personal Care Products, *Journal of Oleo Science*, 2021, **71**, ess21358.

582 K. Yorke and S. Amin, High performance conditioning shampoo with hyaluronic acid and sustainable surfactants, *Cosmetics*, 2021, **8**, –.

583 I. Guryanov, E. Naumenko and R. Fakhrullin, Hair surface engineering: Combining nanoarchitectonics with hair topical and beauty formulations, *Applied Surface Science Advances*, 2022, **7**, 100188.

584 I. P. Kaur *et al.*, Vesicular systems in ocular drug delivery: an overview, *International journal of pharmaceutics*, 2004, **269**, 1–14.

585 T. Ogura *et al.*, Small angle X-ray scattering and electron spin resonance spectroscopy study on fragrance infused cationic vesicles modeling scent-releasing fabric softeners, *Journal of oleo science*, 2018, **67**, 177–186.

586 M. Brown *et al.*, Liquid crystal colloidal structures for increased silicone deposition efficiency on colour-treated hair, *International journal of cosmetic science*, 2010, **32**, 193–203.

587 T. C. Moore *et al.*, A coarse-grained model of stratum corneum lipids: free fatty acids and ceramide NS, *The Journal of Physical Chemistry B*, 2016, **120**, 9944–9958.

588 T. C. Moore *et al.*, Molecular dynamics simulations of stratum corneum lipid mixtures: A multiscale perspective, *Biochemical and Biophysical Research Communications*, 2018, **498**, 313–318.

589 Y. Badhe, R. Gupta and B. Rai, Development and application of coarse-grained MARTINI model of skin lipid ceramide [AP], *Journal of Molecular Modeling*, 2020, **26**, 182.

590 Y. Badhe *et al.*, Investigating the nanostructure of a CER [NP]/CER [AP]-based stratum corneum lipid matrix model: a combined neutron diffraction & molecular dynamics simulations approach, *Biochimica et Biophysica Acta (BBA)-Biomembranes*, 2022, **1864**, 184007.

591 P. Shamaprasad *et al.*, Using molecular simulation to understand the skin barrier, *Progress in lipid research*, 2022, 101184.

592 P. Shamaprasad *et al.*, Multiscale simulation of ternary stratum corneum lipid mixtures: effects of cholesterol composition, *Langmuir*, 2022, **38**, 7496–7511.

593 K. S. Endoh, T. Kawakatsu and F. Müller-Plathe, Coarse-Grained Molecular Simulation Model for Gecko Feet Keratin, *Journal of Physical Chemistry B*, 2018, **122**, 2203–2212.

594 M. Khani *et al.*, Water uptake by gecko β-keratin and the influence of relative humidity on its mechanical and volumetric properties, *Journal of the Royal Society Interface*, 2022, **19**, 20220372.

595 T. Materzok *et al.*, How Does Gecko Keratin Stick to Hydrophilic and Hydrophobic Surfaces in the Presence and Absence of Water? An Atomistic Molecular Dynamics Investigation, *ACS Nano*, 2022, **16**, 19261–19270.

596 T. Materzok *et al.*, Gecko Adhesion on Flat and Rough Surfaces: Simulations with a Multi-Scale Molecular Model, *Small*, 2022, **18**, 2201674.

597 T. Materzok, S. Gorb and F. Müller-Plathe, Gecko adhesion: a molecular-simulation perspective on the effect of humidity, *Soft Matter*, 2022, **18**, 1247–1263.

598 T. Materzok *et al.*, Understanding Humidity-Enhanced Adhesion of Geckos: Deep Neural Network-Assisted Multi-Scale Molecular Modeling, *Small*, 2023, **19**, 2206085.

599 H. Eslami, T. Materzok and F. Müller-Plathe, Molecular Structure and Dynamics in Wet Gecko β-Keratin, *ACS Biomaterials Science and Engineering*, 2023, **9**, 257–268.

600 M. Lupkowski and F. van Swol, Ultrathin films under shear, *The Journal of Chemical Physics*, 1991, **95**, 1995–1998.

601 J. Gao, W. D. Luedtke and U. Landman, Structure and solvation forces in confined films: Linear and branched alkanes, *The Journal of Chemical Physics*, 1997, **106**, 4309–4318.

602 I. G. Elliott, T. L. Kuhl and R. Faller, A Molecular Dynamics Technique to Extract Forces in Soft Matter Systems Under Compression With Constant Solvent Chemical Potential, *Journal of Chemical Theory and Computation*, 2012, **8**, 1072–1077.

603 F. Goujon, P. Malfreyt and D. J. Tildesley, Dissipative Particle Dynamics Simulations in the Grand Canonical Ensemble: Applications to Polymer Brushes, *ChemPhysChem*, 2004, **5**, 457–464.

604 Y. Leng *et al.*, A comparative study by the grand canonical Monte Carlo and molecular dynamics simulations on the squeezing behavior of nanometers confined liquid films, *The Journal of Chemical Physics*, 2013, **139**, 074704.

605 O. J. Melling *et al.*, Enhanced Grand Canonical Sampling of Occluded Water Sites Using Nonequilibrium Candidate Monte Carlo, *Journal of Chemical Theory and Computation*, 2023, **19**, 1050–1062.

606 J. Kim, L. Belloni and B. Rotenberg, Grand-canonical molecular dynamics simulations powered by a hybrid 4D nonequilibrium MD/MC method: Implementation in LAMMPS and applications to electrolyte solutions, *The Journal of Chemical Physics*, 2023, **159**, 144802.

Appendix

A.1 Supplementary information for chapter 3

a) F-layer model force field parameters

Molar mass values in parenthesis are only valid for lipid terminal beads (C_1, C_2). Here, length units are given in Angstrom for consistency with LAMMPS *real* units. By convention, bond and angle constants are not multiplied by 1/2 in LAMMPS. Force field parameters are obtained from the original MARTINI model[264] for monolayer bead interactions and from the polarisable water model paper[306] for water-water, water-monolayer and charged bead interactions.

Bead Types

Bead type	Charge q/e [-]	Molar mass M [kg/kmol]
C_1	-	72.0 (90.0)
C_2	-	72.0 (90.0)
C_5	-	72.0
P_5	-	72.0
Q_a	-1.0	72.0
Q_d	$+1.0$	72.0
N_a	-	72.0
W	-	24.0
WM	-0.46	24.0
WP	$+0.46$	24.0

Non-Bonded Interactions $E_{\mathrm{LJ}} = 4\varepsilon\left[\left(\frac{\sigma}{r}\right)^{12} - \left(\frac{\sigma}{r}\right)^{6}\right] + S_{\mathrm{LJ}}(r)$

Bead A	Bead B	Type[264,306]	ε [kcal/mol]	σ [Å]	Bead A	Bead B	Type[264,306]	ε [kcal/mol]	σ [Å]
C_1	C_1	IV	0.8365	4.7	C_5	P_5	V	0.7409	4.7
C_1	C_2	IV	0.8365	4.7	C_5	Q_a	IV	0.8365	4.7
C_1	C_5	V	0.7409	4.7	C_5	Q_d	IV	0.8365	4.7
C_1	P_5	VIII	0.4780	4.7	C_5	W	V	0.7034	4.7
C_1	Q_a	VII	0.5497	4.7	P_5	P_5	O	1.3384	4.7
C_1	Q_d	VII	0.5497	4.7	P_5	Q_a	O	1.3384	4.7
C_1	W	VIII	0.4538	4.7	P_5	Q_d	O	1.3384	4.7
C_2	C_2	IV	0.8365	4.7	P_5	W	O	1.2707	4.7
C_2	C_5	V	0.7409	4.7	Q_a	Q_a	IV	0.8365	4.7
C_2	P_5	VII	0.5497	4.7	Q_a	Q_d	III	0.9556	4.7
C_2	Q_a	VII	0.5497	4.7	Q_a	W	I	1.1942	4.7
C_2	Q_d	VII	0.5497	4.7	Q_d	Q_d	IV	0.8365	4.7
C_2	W	VII	0.5222	4.7	Q_d	W	I	1.1942	4.7
C_5	C_5	IV	0.8365	4.7	W	W	-	0.9554	4.7
WP	*	-	0	-	WM	*	-	0	-
C_1 (ghost)	*	-	0	-					

Bonds		$E_\mathrm{b} = K_\mathrm{b}\,(r - r_0)$	
Bead A	Bead B	K_b [kcal/mol/Å^2]	r_0 [Å]
C$_*$, P$_*$, Q$_*$	C$_*$, P$_*$, Q$_*$	1.4938	4.7
W	WM, WP	$K_b \to \infty$ (SHAKE)	1.2

Angles			$E_\theta = K_\theta\,[\cos(\theta) - \cos(\theta_0)]^2$	
Bead A	Bead B	Bead C	K_θ [kcal/mol]	θ_0 [°]
C$_*$, P$_*$, Q$_*$	C$_*$, P$_*$, Q$_*$	C$_*$, P$_*$, Q$_*$	2.9876	180
WM	W	WP	0.5019	0

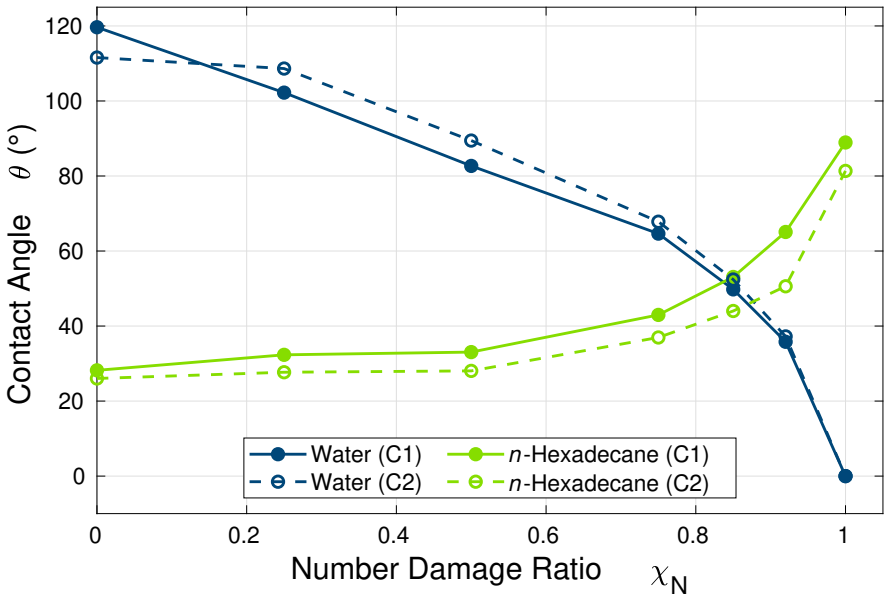


Figure A.1.1: Water droplet contact angles on hair surfaces of various degrees of damage and C_1 and C_2 monolayer terminal beads with the original polarisable water model.[306] Contact angles are shown against the number damage ratio χ_N instead of the surface damage ratio χ_S to provide alignment of data points in the x position of the graph for better readability. Uncertainty bars are also omitted for improved readibility.

b) F-layer terminal bead comparison

As expected, the surface became progressively less hydrophobic when transitioning from a C_1 (alkyl) to a C_2 (thioester) terminal bead. The trends found in this evaluation are comparable with the observations of water droplet wetting on an FCC surface.[314] The fully-functionalised system with the C_2 terminal bead was found to yield the best agreement with experimental data for water on virgin hair than the C_2 terminal bead.[227] For the slightly damaged surfaces, the systems with the C_2 terminal bead become more hydrophobic than the corresponding surfaces with a C_1 bead, despite the stronger LJ interactions between these beads and the water beads. This is because the stronger LJ interactions cause more agglomeration of the chains and thus less of the hydrophilic sulfonate surface is exposed. Moreover, C_2 bead leads to underestimation of the contact angle for non-polar fluids, such as n-hexadecane, on hair (see main text). Therefore, the C_1 terminal bead is selected for the final model version.

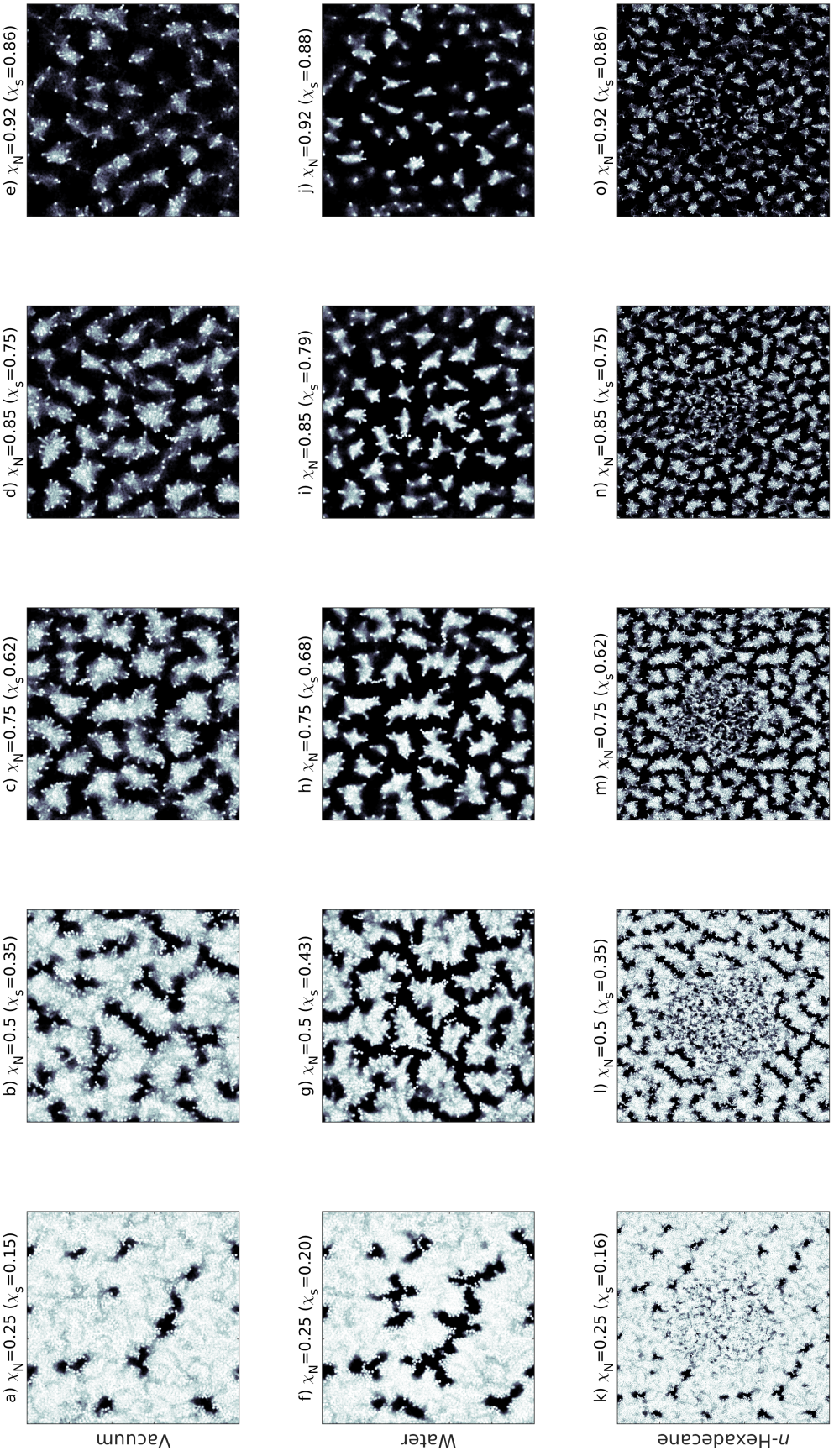


Figure A.1.2: Projected lipid coverage on hair model surfaces in vacuum and with water and n-hexadecane as wetting fluids for different degrees of random damage χ_N. White regions correspond to coverage by at least one monolayer bead during all sampled timesteps while black regions indicate projected densities equal to zero. Projected surface coverage is given by χ_S. The time-averaged data have been sampled from 40 equidistant timesteps (10 for n-hexadecane) within the last 2 ns of each simulation. The shown coverage maps represent one periodic box of side lengths $\mathcal{L}_{x,water} = 35.7$ ($\mathcal{L}_{x,hex} = 71.5$) nm and $\mathcal{L}_{y,water} = 30.9$ nm ($\mathcal{L}_{y,hex} = 61.9$ nm).

d) Contact angle fits for water (AA-MD)

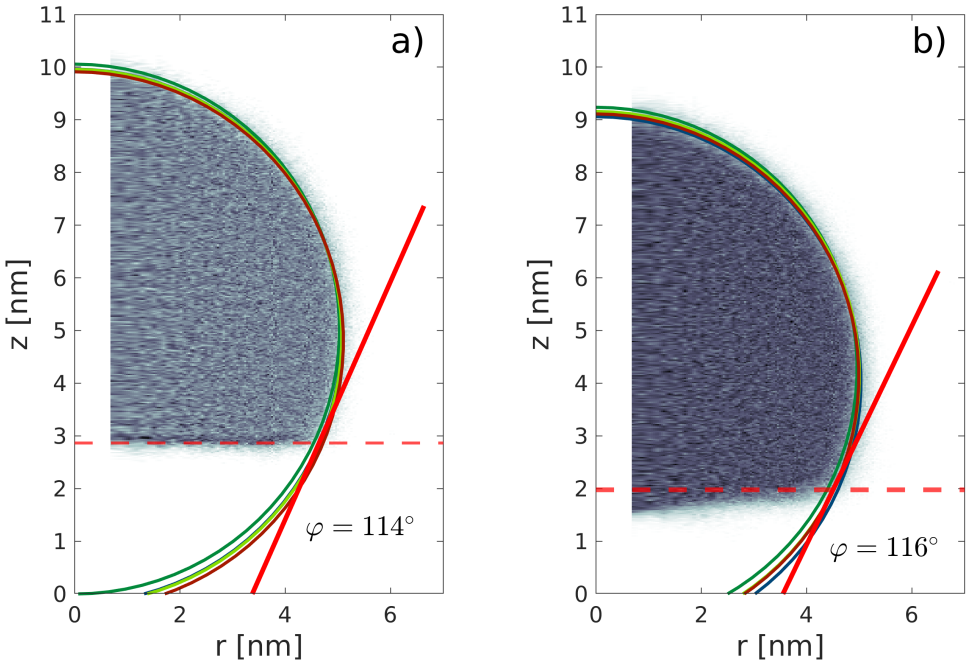


Figure A.1.3: Circular surface fits of a water droplets on monolayers with a grafting distance of (a) $d_{\mathrm{graft}} = 0.49$ nm and (b) $d_{\mathrm{graft}} = 0.65$ nm from the AA-MD simulations. Four temporal bin fits for the droplet surface (solid circles) are shown. Averaged contact angles (solely from the shown four temporal bins) are indicated by bold red lines. The surface-normal position for the contact angle measurement is shown (dashed red line). Individual surface density fits in the radial direction are omitted for the sake of clarity.

Wetting data

Table A.1.1: Fully-functionalised monolayer structure and wetting data for all-atomistic (AA), coarse-grained (CG) MD cases and comparison to reference AA-MD data[65] for 18-MEA.

Property	Unit	d_{graft} [nm]	Cheong et al.[65] 18-MEA	AA-MD 18-MEA	CG-MD EA	CG-MD Cys-18-MEA
Monolayer thickness	[nm]	0.49	2.64	2.59	2.78	2.63
		0.65	2.01	2.03	2.19	1.53
Monolayer tilt angle	[°]	0.49	5.0	7.7	6.0	1.7
		0.65	50	45	33	45
Water penetration depth	[nm]	0.49	n/a	0.29	n/a	0.20
		0.65	n/a	1.29	n/a	0.85
Contact angle (water)	[°]	0.49	n/a	114	n/a	116
		0.65	n/a	116	n/a	120

e) Contact angle experimental comparison

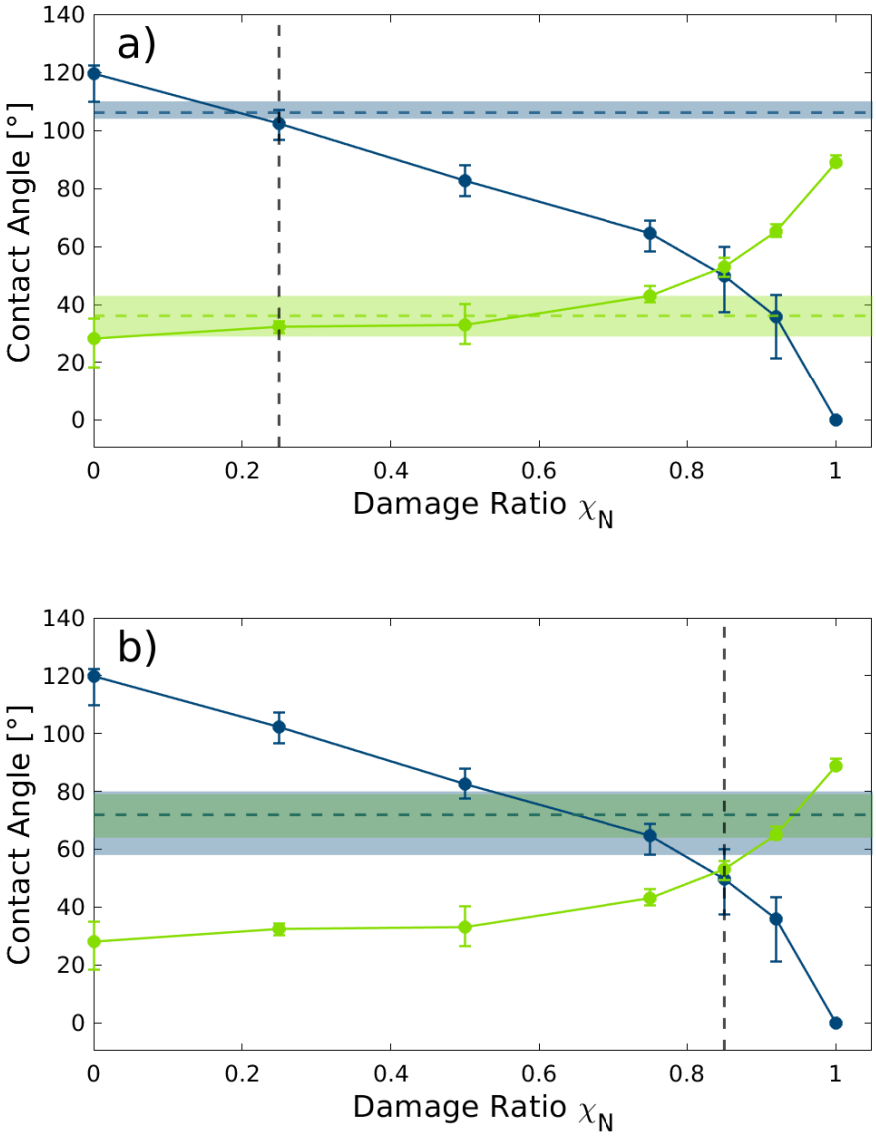


Figure A.1.4: Water (blue) and n-hexadecane (green) droplet contact angles as a function of number damage ratio χ_N compared to dynamic contact angle measurements for a) virgin hair and b) medium bleached hair. For the simulations, the points are mean values and the vertical bars show the minimum and maximum values observed across the temporal binning of the different position and seed trials. Coloured solid lines are guides for the eye. Average experimental values are shown by horizontal dashed lines and the coloured regions represent the uncertainty limits. Good agreement between simulations and experiments is found when $\chi_N = 0.25$ for virgin hair and $\chi_N = 0.85$ for medium bleached hair, as indicated by vertical dashed lines in a) and b), respectively.

A.2 Supplementary information for chapter 4

a) Polarizable MARTINI water model viscosity

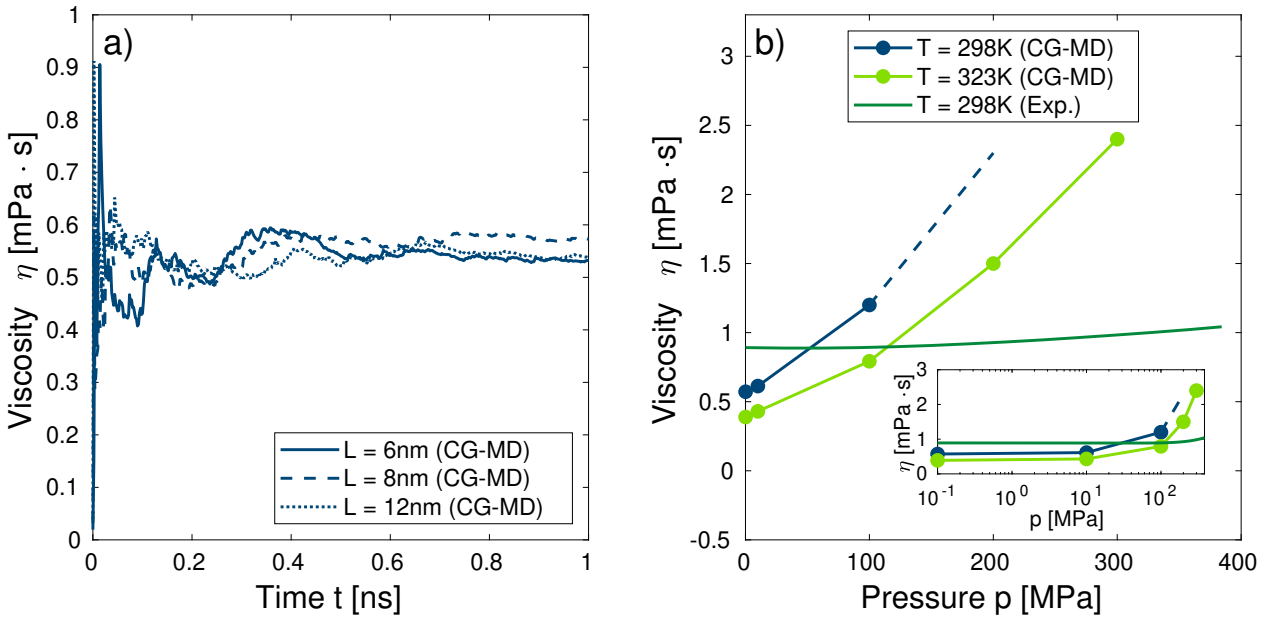


Figure A.2.5: Dynamic viscosity of bulk system of polarizable MARTINI water beads[306] a) at $p = 1$ atm and $T = 300$ K and three different simulation box sizes ($\mathcal{L} = 6, 8, 12$ nm) and b) at different pressures with constant box size ($\mathcal{L} = 8$ nm). The Green-Kubo formalism[379,380] has been applied to obtain the bulk viscosities. Experimental reference data at $T = 298$ K[381] are shown for comparison.

b) Dry interdigitation volume and SATA energy barrier

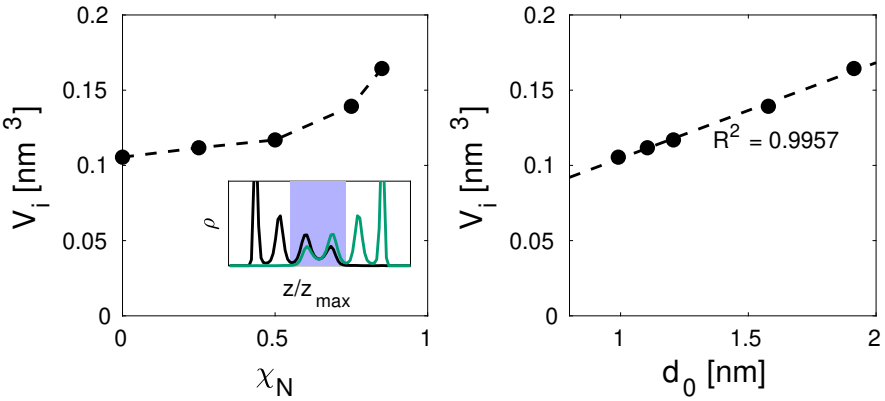


Figure A.2.6: Average volume per CG bead in the region of interdigitation as a function of a) damage and b) barrier distance d_0. An example of the region of interdigitation is highlighted in the inset in a). A linear fit (dashed line in b) confirms that interdigitation directly correlates with the theoretical predictions of a physical barrier to sliding.

c) Dry lipid tilt angles

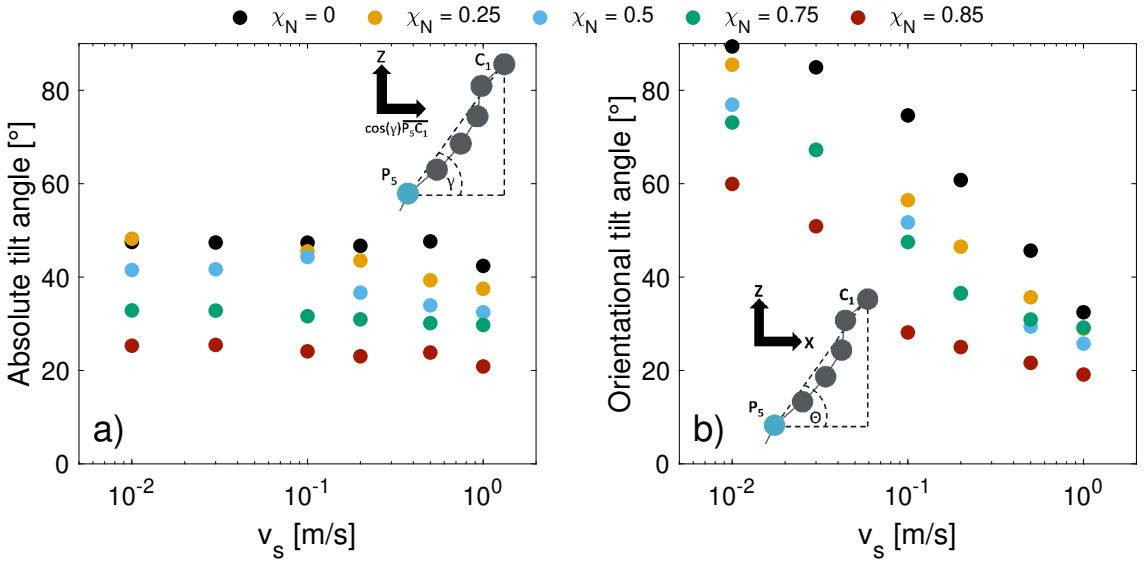


Figure A.2.7: Absolute lipid tilt angles and orientational tilt angles relative to the direction of sliding for dry contacts as a function of sliding speed and surface damage.

d) Water droplet structures

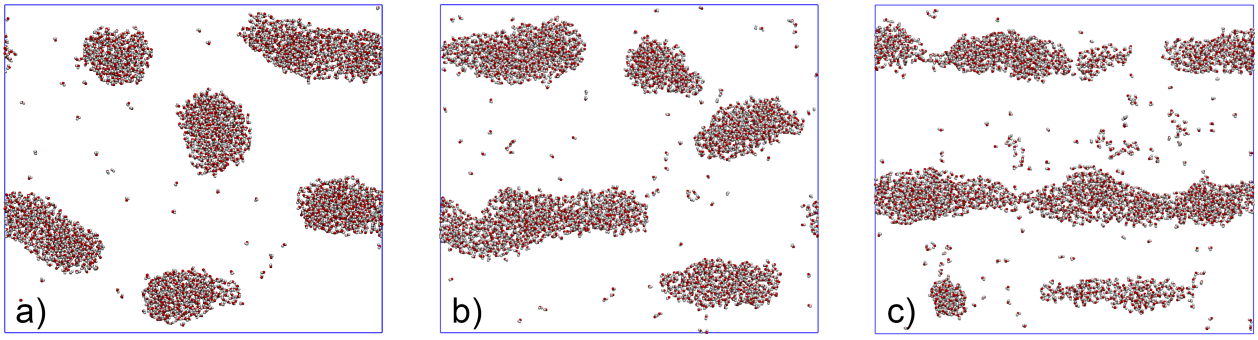


Figure A.2.8: Top view snapshots of water structures confined between fully-functionalised hair surfaces ($\chi_N = 0$) at sliding speeds of a) $v_s = 0.01$ m s^{-1}, b) $v_s = 0.1$ m s^{-1}, and c) $v_s = 1$ m s^{-1}.

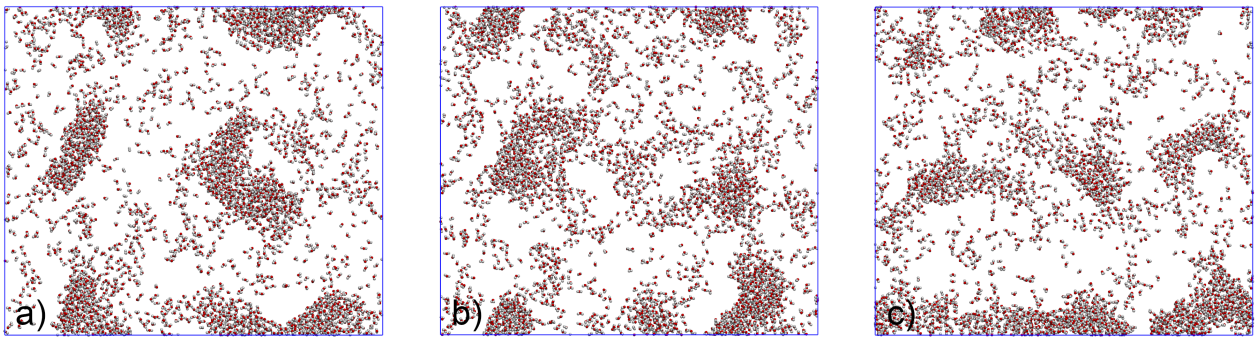


Figure A.2.9: Top view snapshots of water structures confined between hair surfaces representative of virgin hair ($\chi_N = 0.25$) at sliding speeds of a) $v_s = 0.01$ m s^{-1}, b) $v_s = 0.1$ m s^{-1}, and c) $v_s = 1$ m s^{-1}.

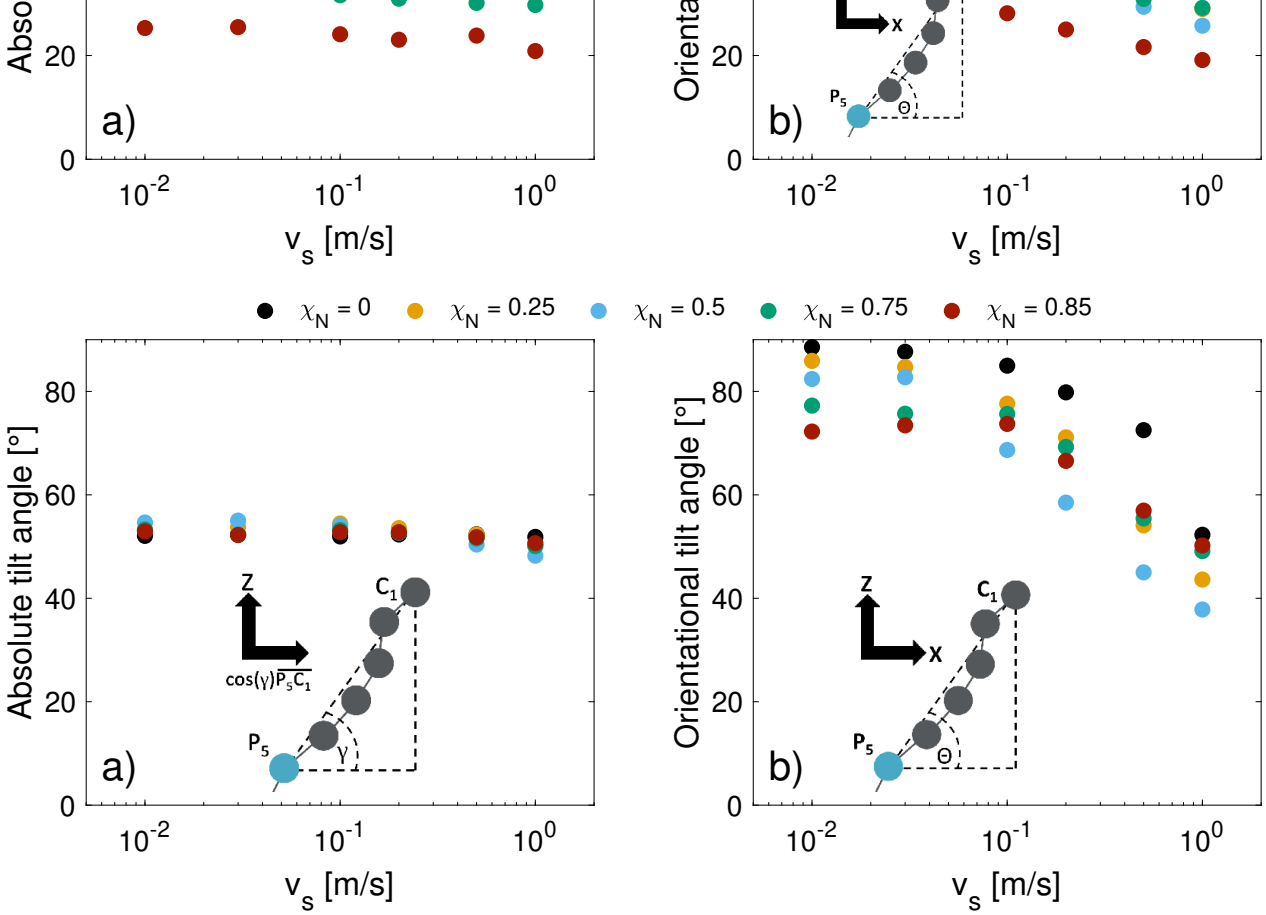


Figure A.2.10: Absolute lipid tilt angles and orientational tilt angles relative to the direction of sliding for wet contacts as a function of sliding speed and surface damage.

f) Wet contact SATA fitting parameters

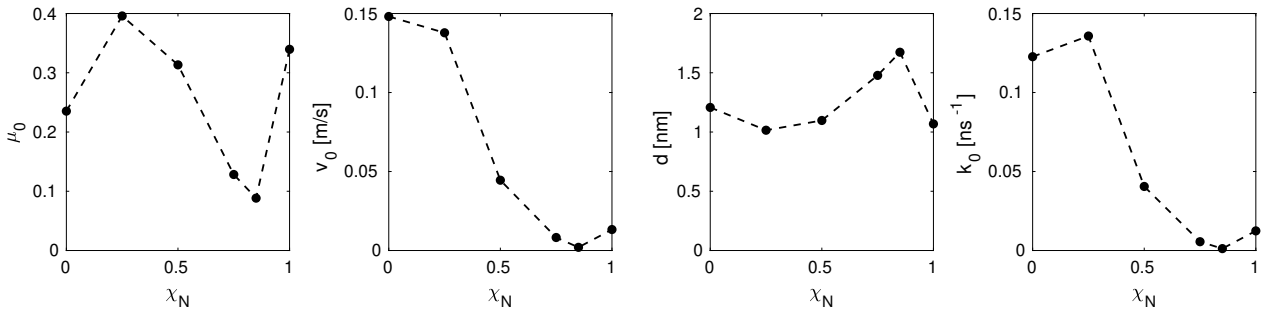


Figure A.2.11: Wet friction fitting parameters according to Ref.[280] a) Reference CoF μ_0, b) reference velocity v_0 and corresponding c) energy barrier distance d and d) hopping rate constant k_0.

g) Water interfacial area

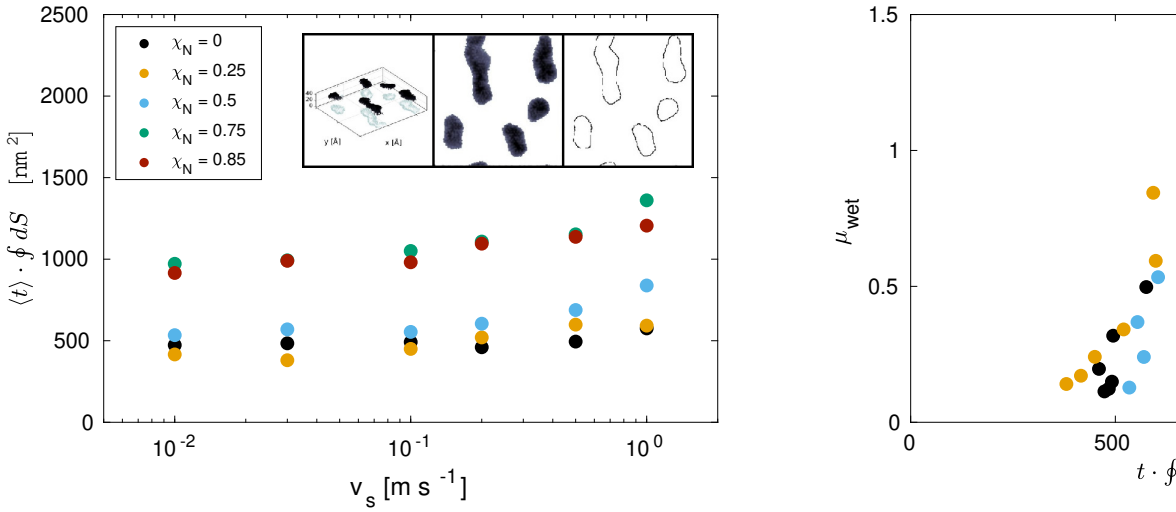


Figure A.2.12: Water-lipid interfacial area, approximated as the perimeter of each water droplet penetrating the contact down to the thioester bond of the 18-MEA/cysteic acid residues multiplied by the thickness of such structures. The inset shows the extraction of the perimeter by 1) identifying penetrating droplets, 2) obtaining the surface coverage and 3) applying an edge-finding algorithm.

h) Counterion structure and diffusion

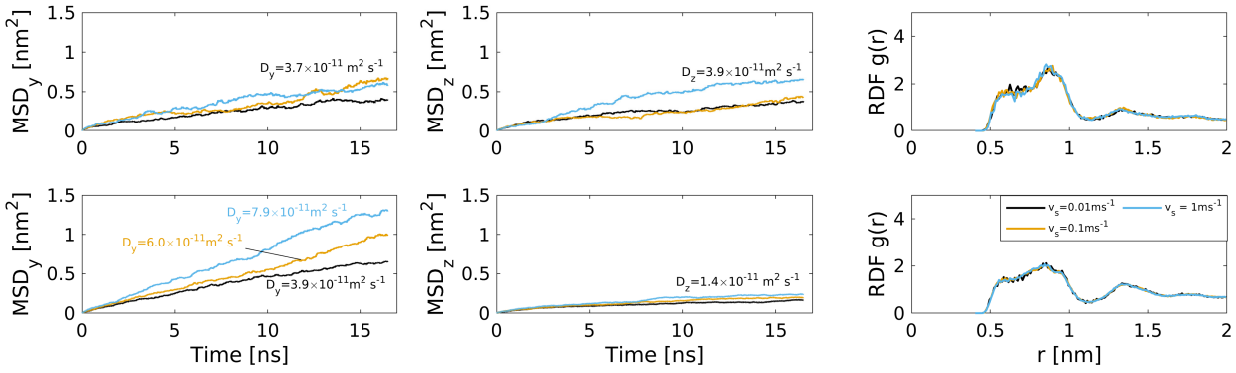


Figure A.2.13: Counterion mobility by means of MSD_y and MSD_z and RDF as a function of the sliding velocity. Virgin hair, i.e. $\chi_\mathrm{N} = 0.25$ (top) and medium bleached, i.e. $\chi_\mathrm{N} = 0.85$ (bottom) NEMD model surface configurations are considered.

i) Biomimetic friction forces as a function of CCP load

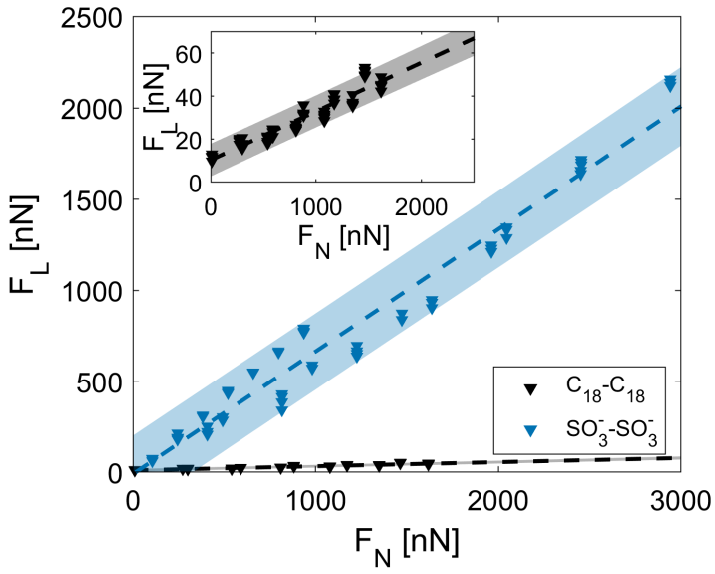


Figure A.2.14: CCP AFM friction forces as a function of normal force for biomimetic surfaces in water. Linear fits to the raw data are shown as dashed lines. Corresponding prediction intervals on the experimental data with 95% confidence are shown as shaded areas.

j) CG-MD normal load study: water content

Table A.2.2: Number of water molecules ($4 \cdot N_{\mathrm{w,CG}}$) per surface area $N_w A^{-1}$ for different normal loads and levels of hair damage. Units are in nm^{-2}.

$\chi =$	0	0.25	0.85	1
$p = 5$ MPa	17.7	25.8	62.4	86.1
$p = 10$ MPa	17.0	25.5	65.0	96.1
$p = 20$ MPa	14.7	21.3	53.5	78.7
$p = 35$ MPa	7.5	17.2	39.3	65.9
$p = 50$ MPa	7.2	18.7	41.2	66.3

A.3 Supplementary information for chapter 5

a) Squeeze-out simulation contact composition

Table A.3.3: CG water surface densities in the contact at the end of the squeeze-out simulations with pre-adsorbed CTAB as a function of normal pressure σ, hair damage and CTAB adsorption density Γ. Corresponding values for pure water hair contacts are reported in Ref.[362]

	a) Virgin hair		b) Med. bleached hair	
σ [MPa]	ρ_w ($\Gamma = 1.1$ μMm^{-2}) [nm^{-2}]	ρ_w ($\Gamma = 2.0$ μMm^{-2}) [nm^{-2}]	ρ_w ($\Gamma = 2.3$ μMm^{-2}) [nm^{-2}]	ρ_w ($\Gamma = 4.0$ μMm^{-2}) [nm^{-2}]
10	2.65	3.73	8.06	5.42
20	5.95	4.40	8.07	5.85
35	4.99	3.74	6.38	4.13
50	5.38	3.71	5.56	4.47

b) Combined lipid mass density profiles during NEMD simulations

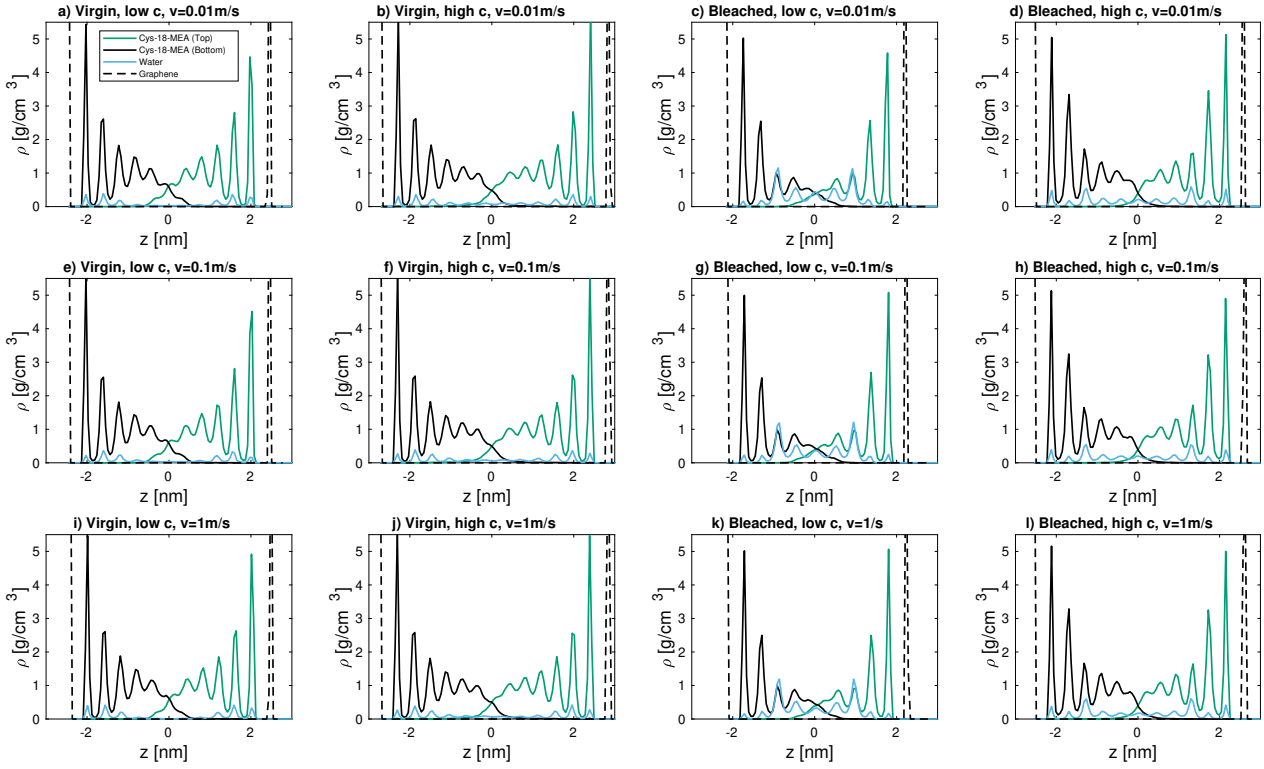


Figure A.3.15: Mass density profiles for water and for lipids - comprised of both Cys-18-MEA and cationic surfactants (CTAB), i.e., $\rho = \rho_{\mathrm{MEA}} + \rho_{\mathrm{CTAB}}$ during sliding simulations for various v_s, degrees of hair damage χ and CTAB coverage Γ.

c) CTAB mobility during sliding

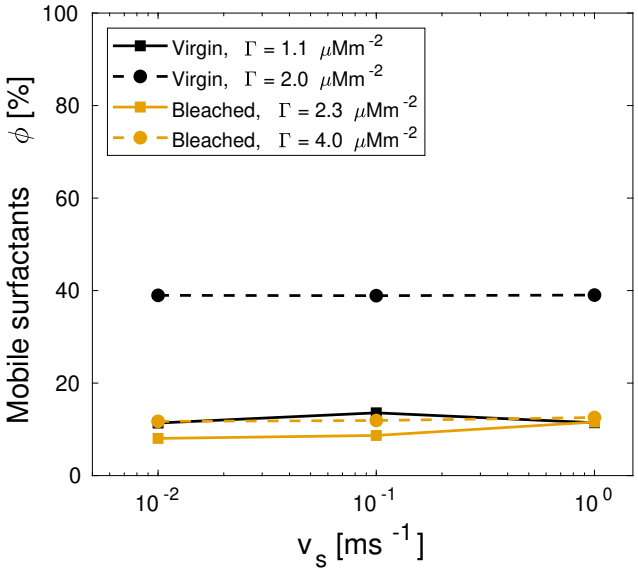


Figure A.3.16: Mobility fraction[481] of cationic sites on CTAB for virgin and medium bleached hair surfaces at various degrees of surfactant coverage during sliding. CTAB molecules are considered to be desorbed if their cationic head group (Q_0) is located outside of a threshold ($d_a = 1.2$ nm) from the graphene sheet of each surface. The distance d_a is chosen to coincides with the first minimum after the primary adsorption peaks in the charge density profiles.

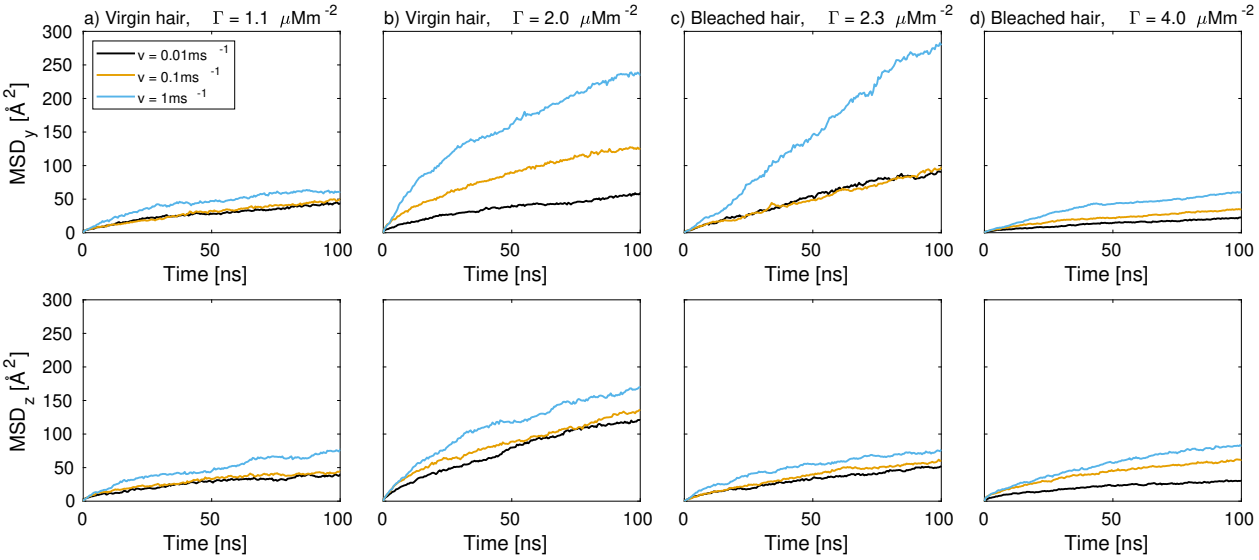


Figure A.3.17: Mean-square-displacement in the y direction (MSD_y) and z direction (MSD_z) of cationic sites on CTAB for virgin and medium bleached hair surfaces at various degrees of surfactant coverage during sliding.

d) Surface charge separation

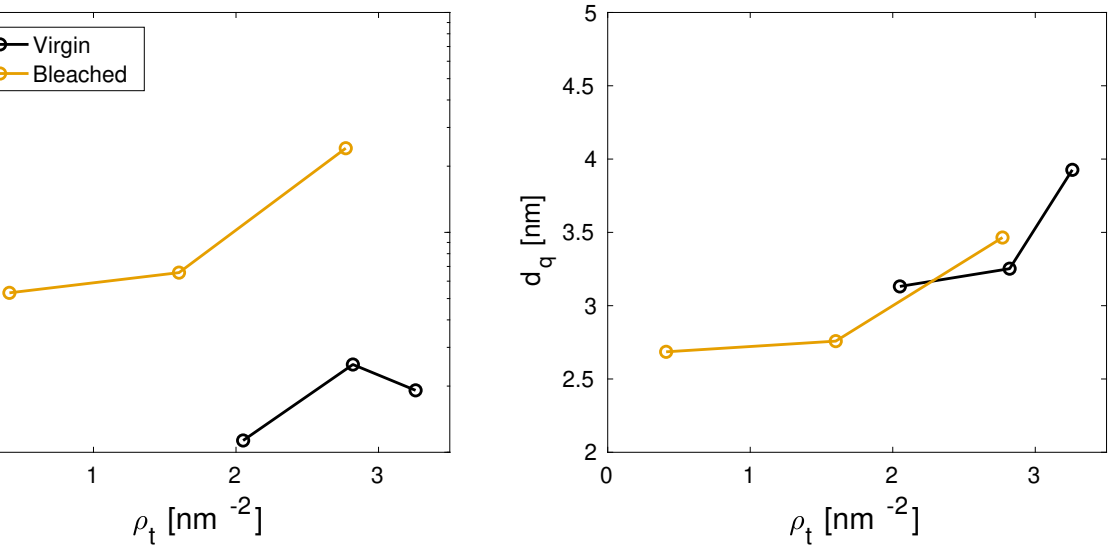


Figure A.3.18: Distance between the charged cysteic acid groups on the two opposing surfaces for virgin (black) and bleached (orange) model hair surfaces.

e) CTAB nematic order

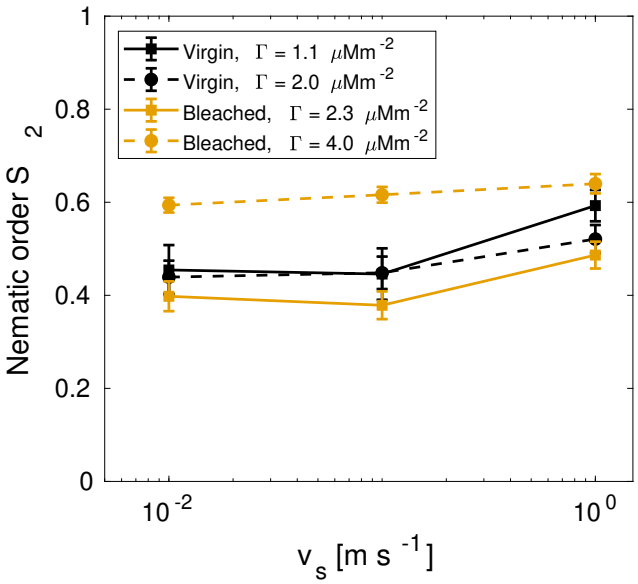


Figure A.3.19: Nematic order[481] of cationic sites on CTAB for virgin and medium bleached hair surfaces at various degrees of surfactant coverage during sliding.

A.4 Supplementary information for chapter 6

a) CGG MARTINI force field parameters

Table A.4.4: MARTINI 2 bead type definitions for CGG.

Bead Types				
Building block	Bead name	MARTINI type	Charge, q [e]	Molar mass, M [kg/kmol]
Chloride counterion	Q_a	Q_a	-1.0	72.0
Quaternary amine	Q_0	Q_0	$+1.0$	72.0
Hydroxypropyl	P_1	P_1	-	72.0
Galactose-I	GL_1	P_1	-	72.0
Galactose-II	GL_2	SP_2	-	54.0
Galactose-III	GL_3	P_4	-	72.0
Mannose-I	M_1, M_4	P_1	-	72.0
Mannose-II	M_2, M_5	SP_2	-	54.0
Mannose-III	M_3, M_6	P_4	-	72.0

There are four main types of interaction sites in MARTINI 2, which are differentiated: polar (P), nonpolar (N), apolar (C), and charged (Q).[264] The special class of ring-type particles (S) have a reduced interaction strengths. Each particle type has a number of subtypes, which allows for a more accurate representation of the chemical nature of the underlying atomic structure.[264] Within a main type, subtypes are either distinguished by a letter denoting the hydrogen-bonding capabilities, (d) donor, (a) acceptor, (da) both, or (0) none, or by a number indicating the degree of polarity (from 1, low polarity, to 5, high polarity).[264] The MARTINI 2 mapping we used for CGG was adapted from that proposed by Shivgan et al.,[490] which was modified from the original mapping due to López et al.[495]. Bond and angle interaction parameters for CGG are derived from iterative Boltzmann inversionn (IBI) from atomistic simulations using PyCGTOOL[503], as described in the main text.

Table A.4.5: Pol-MARTINI 2 non-bonded Lennard-Jones parameters for CGG.

LJ interactions

Bead A	Bead B	Interaction strength	ε [kcal/mol]	σ [Å]
Q_0	Q_0	IV	0.8361	4.7
	P_1	II	1.0750	4.7
	GL_1	II	1.0750	4.7
	GL_2	I	1.1945	4.7
	GL_3	O	1.3378	4.7
	M_1 / M_4	II	1.0750	4.7
	M_2 / M_5	I	1.1945	4.7
	M_3 / M_6	O	1.3378	4.7
P_1	P_1	II	1.0750	4.7
	GL_1	II	1.0750	4.7
	GL_2	II	1.0750	4.7
	GL_3	II	1.0750	4.7
	M_1 / M_4	II	1.0750	4.7
	M_2 / M_5	II	1.0750	4.7
	M_3 / M_6	II	1.0750	4.7
GL_1	GL_1	II	1.0750	4.7
	GL_2	II	1.0750	4.7
	GL_3	II	1.0750	4.7
	M_1 / M_4	II	1.0750	4.7
	M_2 / M_5	II	1.0750	4.7
	M_3 / M_6	II	1.0750	4.7
GL_2	GL_2	S-II	0.8063	4.3
	GL_3	II	1.0750	4.7
	M_1 / M_4	II	1.0750	4.7
	M_2 / M_5	S-II	0.8063	4.3
	M_3 / M_6	II	1.0750	4.7
GL_3	GL_3	I	1.1945	4.7
	M_1 / M_4	II	1.0750	4.7
	M_2 / M_5	II	1.0750	4.7
	M_3 / M_6	I	1.1945	4.7
M_1 / M_4	M_1 / M_4	II	1.0750	4.7
	M_2 / M_5	II	1.0750	4.7
	M_3 / M_6	II	1.0750	4.7
M_2 / M_5	M_2 / M_5	S-II	0.8063	4.3
	M_3 / M_6	II	1.0750	4.7
M_3 / M_6	M_3 / M_6	I	1.1945	4.7

Table A.4.6: CGG MARTINI 2 bond parameters.

Bonds		$E_\mathrm{b} = K_\mathrm{b}\left(r - r_0\right)^2$	
Bead A	Bead B	K_b [kcal/mol/Å^2]	r_0 [Å]
Q_0	P_1	75	3.42
P_1	GL_1	27	3.90
GL_1	GL_2	12	2.41
GL_2	GL_3	15	2.41
GL_2	M_4	16	5.20
M_4	M_5	88	2.22
M_5	M_6	69	2.09
M_5	M_2	64	5.66
M_1	M_2	79	2.41
M_2	M_3	27	2.30
M_2	M_5'	50	4.54

Table A.4.7: CGG MARTINI 2 angle parameters.

Angles			$E_\theta = K_\theta\left[\cos\left(\theta\right) - \cos\left(\theta_0\right)\right]^2$	
Bead A	Bead B	Bead C	K_θ [kcal/mol]	θ_0 [°]
Q_0	P_1	GL_1	22	108
P_1	GL_1	GL_2	558	162
GL_1	GL_2	GL_3	63	141
GL_1	GL_2	M_4	46	75
GL_3	GL_2	M_4	79	67
GL_2	M_4	M_5	87	122
M_4	M_5	M_6	832	161
M_4	M_5	M_2	90	99
M_6	M_5	M_2	156	96
M_5	M_2	M_1	243	74
M_5	M_2	M_3	379	58
M_1	M_2	M_3	128	126
M_4	M_5	M_6	832	161
M_1	M_2	M_5'	194	89
M_3	M_2	M_5'	175	123
M_5	M_2	M_5'	15	154
M_2	M_5'	M_2'	30	162

b) Guar gum parametrization validation

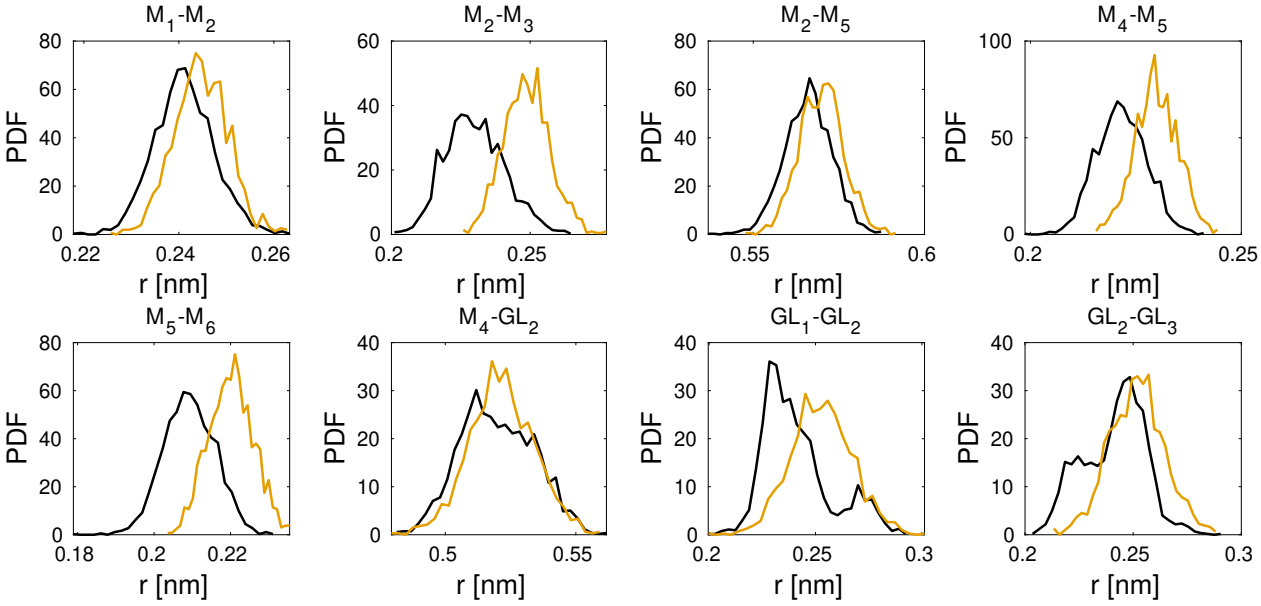


Figure A.4.20: Guar gum bond distributions from atomistic and coarse-grained simulations.

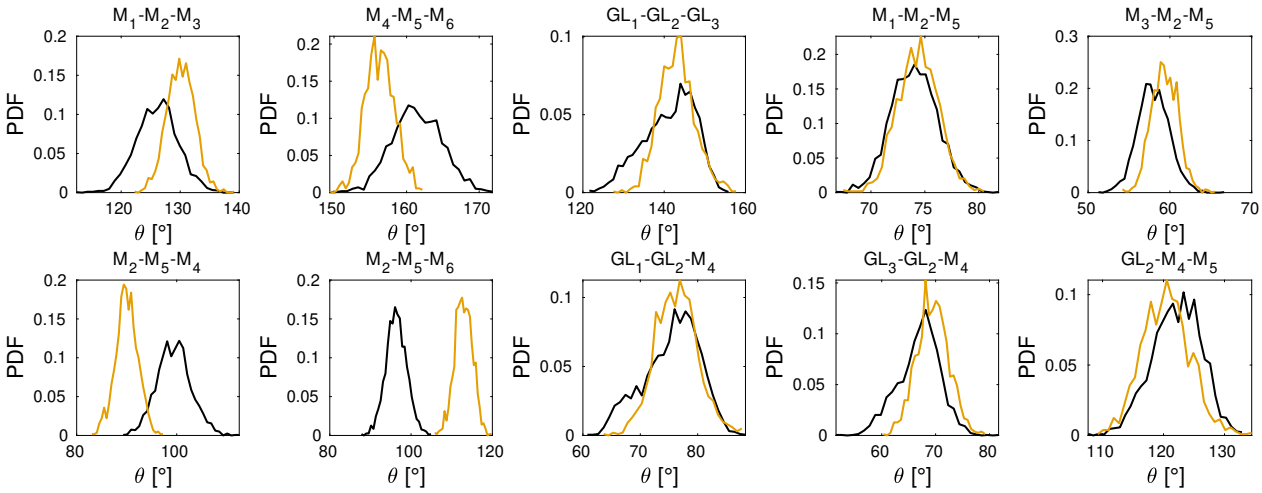


Figure A.4.21: Guar gum angle distributions from atomistic and coarse-grained simulations.

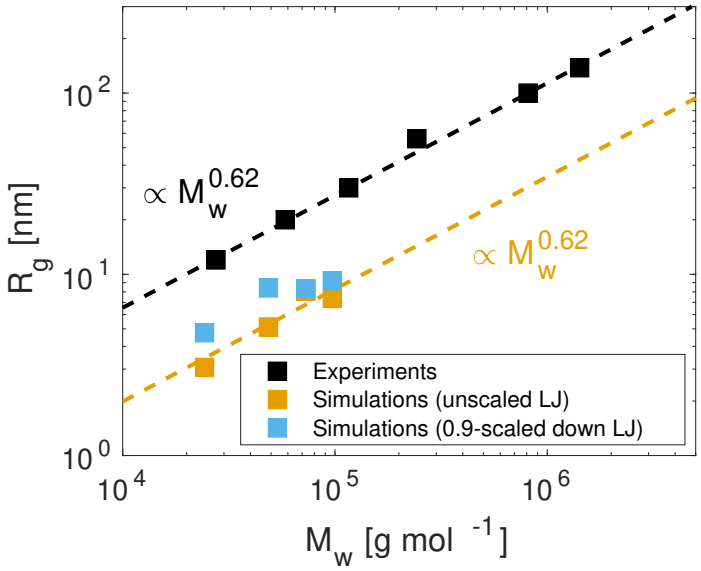


Figure A.4.22: Guar gum radius of gyration as a function of molecular weight from CG-MD simulations and from experiments due to Ref.[497]

c) CGG-SDS squeeze-out

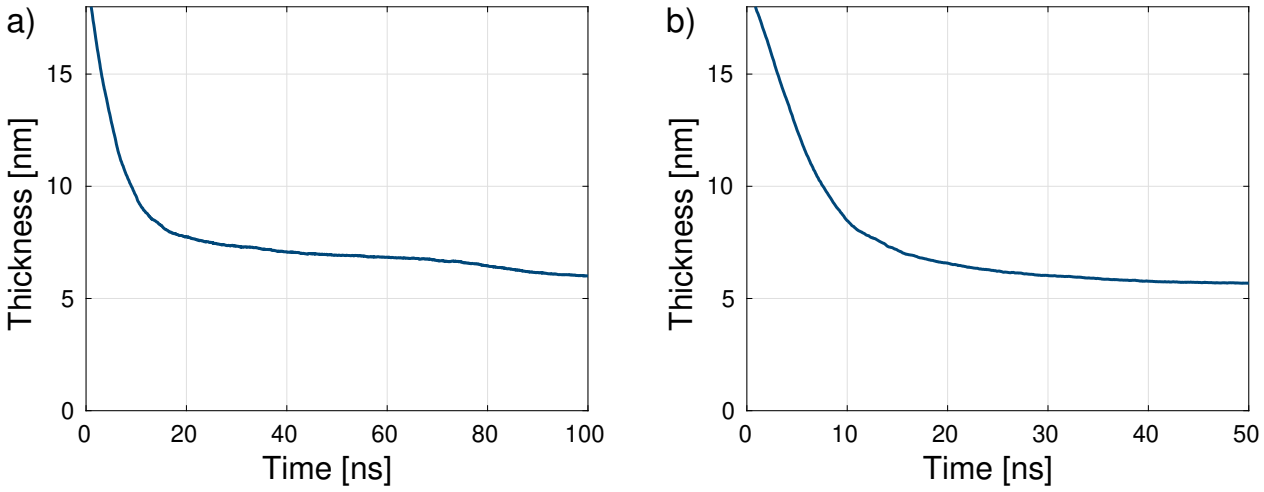


Figure A.4.23: Temporal evolution of the contact thickness during squeeze-out at $\sigma = 10$ MPa with CGG and SDS on a) virgin and b) medium bleached hair model hair surfaces.

d) Normal-load variation: charge density profiles

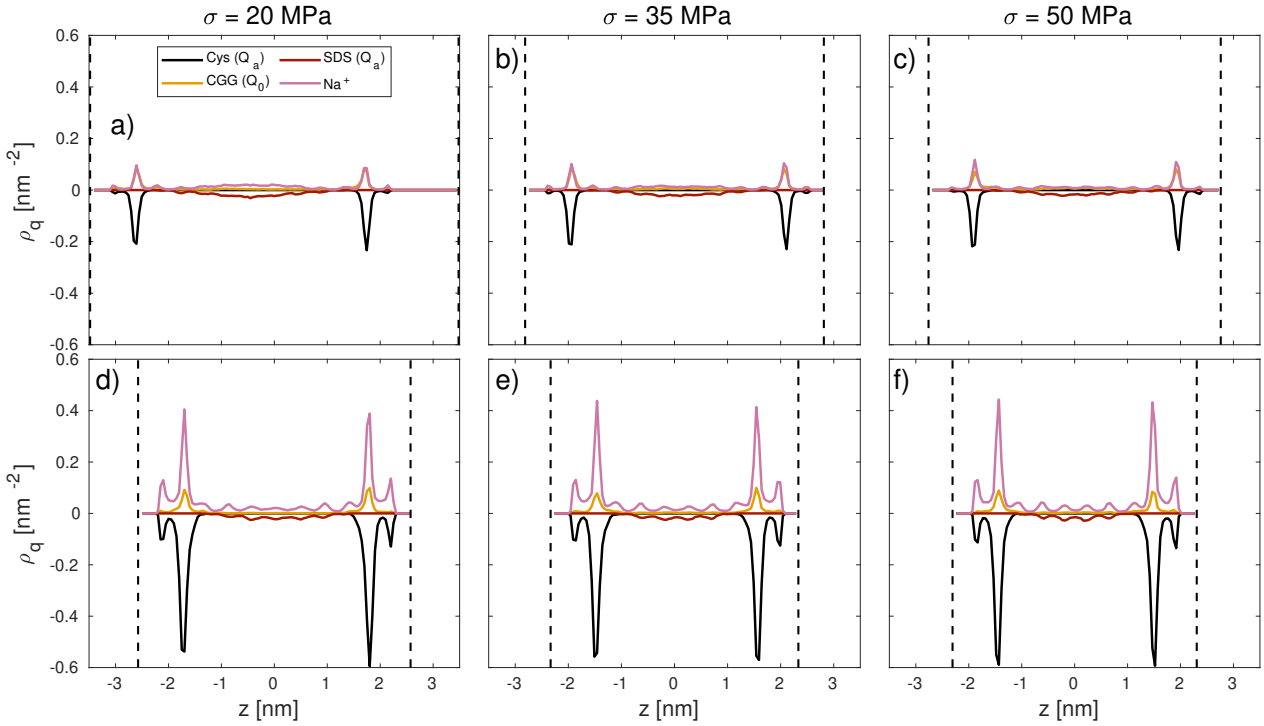


Figure A.4.24: Through-film charge density profiles from NEMD of different normal stresses $\sigma = 20{-}50$ MPa on virgin (a-c) and medium bleached hair (d-f) at $v_s = 0.1$ m s^{-1}.

A.5 Supplementary information for chapter 7

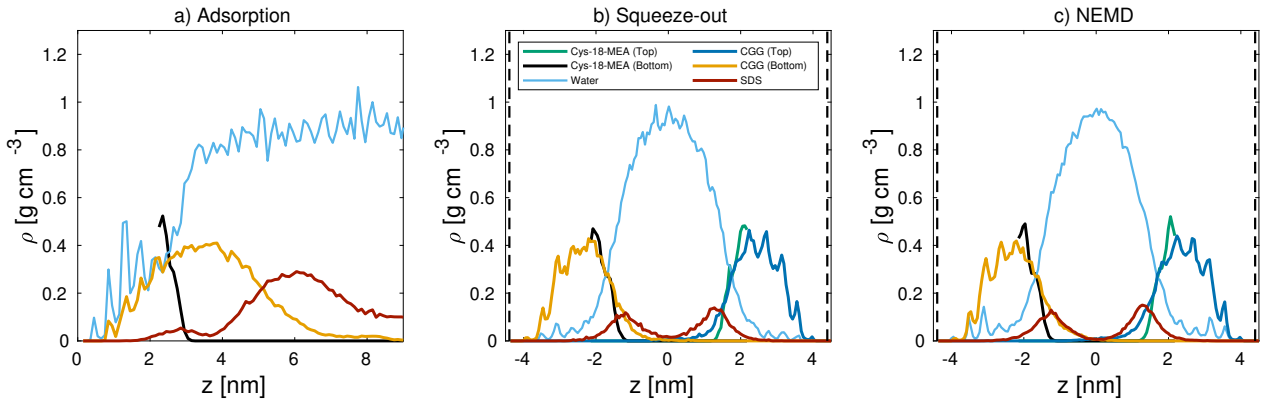


Figure A.5.25: Mass density profiles of the 18-MEA, guar, SDS and water at the end of the a) single-surface adsorption stage, b) squeeze-out stage, and c) NEMD stage on virgin hair. The 18-MEA density profiles are only partially shown for clarity. The dehydration and compression of the guar layer occurs during squeeze-out (from a) to b)). No strong change in the guar hydration and layer thickness is observed during NEMD simulations.

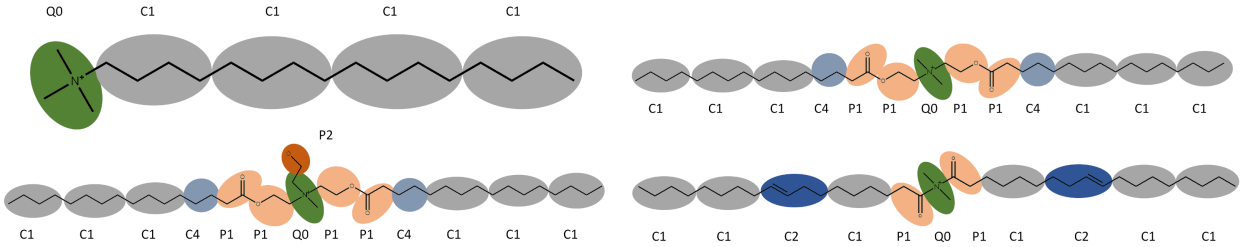


Figure A.6.26: Cationic quat surfactant architectures considered with corresponding coarse-graining parametrizations.

A.6 Supplementary information for chapter 8

a) Quaternary ammonium surfactant MARTINI parametrizations

i) DEEDMAC

Table A.6.8: MARTINI 2 bead types definitions for DEEDMAC.

Bead Types				
Building block	Bead name	MARTINI type	Charge, q [e]	Molar mass, M [kg/kmol]
Quaternary amine	Q_0	Q_0	+1.0	54.0
2-hydroxyethyl	$P_{1,1}$	P_1	-	54.0
2-hydroxyethyl	$P_{1,2}$	P_1	-	54.0
Acetaldehyde	$P_{1,3}$	P_1	-	54.0
Acetaldehyde	$P_{1,4}$	P_1	-	54.0
Ethane	$C_{4,1}$	C_4	-	36.0
Ethane	$C_{4,2}$	C_4	-	36.0
Butane	$C_{1,1}$	C_1	-	72.0
Butane	$C_{1,2}$	C_1	-	72.0
Butane	$C_{1,3}$	C_1	-	72.0
Butane	$C_{1,4}$	C_1	-	72.0
Butane	$C_{1,5}$	C_1	-	72.0
Butane	$C_{1,6}$	C_1	-	72.0

Table A.6.9: CGG MARTINI 2 bond parameters for DEEDMAC.

Bonds		$E_b = K_b (r - r_0)^2$	
Bead A	Bead B	K_b [kcal/mol/Å^2]	r_0 [Å]
Q_0	$P_{1,1}$	14.5	2.79
Q_0	$P_{1,2}$	8.3	2.74
$P_{1,1}$	$P_{1,3}$	13.5	2.75
$P_{1,2}$	$P_{1,4}$	12.8	2.71
$P_{1,3}$	$C_{4,1}$	8.9	2.80
$P_{1,4}$	$C_{4,2}$	8.0	2.73
$C_{4,1}$	$C_{1,1}$	4.8	3.51
$C_{4,2}$	$C_{1,2}$	7.0	3.56
$C_{1,1}$	$C_{1,3}$	3.5	4.50
$C_{1,2}$	$C_{1,4}$	2.2	4.46
$C_{1,3}$	$C_{1,5}$	2.2	4.49
$C_{1,4}$	$C_{1,6}$	2.8	4.54

Table A.6.10: CGG MARTINI 2 angle parameters for DEEDMAC.

Angles			$E_\theta = K_\theta \left[\cos\left(\theta\right) - \cos\left(\theta_0\right)\right]^2$	
Bead A	Bead B	Bead C	K_θ [kcal/mol]	θ_0 [°]
$P_{1,1}$	Q_0	$P_{1,2}$	8.2	82
Q_0	$P_{1,1}$	$P_{1,3}$	15.1	141
Q_0	$P_{1,3}$	$P_{1,4}$	11.7	138
$P_{1,1}$	$P_{1,3}$	$C_{4,1}$	5.0	132
$P_{1,2}$	$P_{1,4}$	$C_{4,2}$	5.4	134
$P_{1,3}$	$C_{4,1}$	$C_{1,1}$	5.1	141
$P_{1,4}$	$C_{4,2}$	$C_{1,2}$	6.1	141
$C_{4,1}$	$C_{1,1}$	$C_{1,3}$	8.5	143
$C_{4,2}$	$C_{1,2}$	$C_{1,4}$	8.0	140
$C_{1,1}$	$C_{1,3}$	$C_{1,5}$	5.1	140
$C_{1,2}$	$C_{1,4}$	$C_{1,6}$	4.6	139

ii) DPEHEMS

Table A.6.11: MARTINI 2 bead types definitions for DPEHEMS.

Bead Types				
Building block	Bead name	MARTINI type	Charge, q [e]	Molar mass, M [kg/kmol]
1-hydroxyethyl	P_2	P_2	-	36.0
Quaternary amine	Q_0	Q_0	$+1.0$	54.0
2-hydroxyethyl	$P_{1,1}$	P_1	-	54.0
2-hydroxyethyl	$P_{1,2}$	P_1	-	54.0
Acetaldehyde	$P_{1,3}$	P_1	-	54.0
Acetaldehyde	$P_{1,4}$	P_1	-	54.0
Ethane	$C_{4,1}$	C_4	-	36.0
Ethane	$C_{4,2}$	C_4	-	36.0
Butane	$C_{1,1}$	C_1	-	72.0
Butane	$C_{1,2}$	C_1	-	72.0
Butane	$C_{1,3}$	C_1	-	72.0
Butane	$C_{1,4}$	C_1	-	72.0
Butane	$C_{1,5}$	C_1	-	72.0
Butane	$C_{1,6}$	C_1	-	72.0

Table A.6.12: CGG MARTINI 2 bond parameters for DPEHEMS.

Bonds		$E_\mathrm{b} = K_\mathrm{b} \left(r - r_0\right)^2$	
Bead A	Bead B	K_b [kcal/mol/Å^2]	r_0 [Å]
P_2	Q_0	20.4	2.50
Q_0	$P_{1,1}$	20.0	2.93
Q_0	$P_{1,2}$	20.3	2.86
$P_{1,1}$	$P_{1,3}$	12.5	2.72
$P_{1,2}$	$P_{1,4}$	15.4	2.77
$P_{1,3}$	$C_{4,1}$	12.5	2.86
$P_{1,4}$	$C_{4,2}$	7.9	2.76
$C_{4,1}$	$C_{1,1}$	8.6	3.57
$C_{4,2}$	$C_{1,2}$	11.9	3.60
$C_{1,1}$	$C_{1,3}$	2.4	4.45
$C_{1,2}$	$C_{1,4}$	2.8	4.58
$C_{1,3}$	$C_{1,5}$	2.1	4.43
$C_{1,4}$	$C_{1,6}$	3.0	4.49

Table A.6.13: CGG MARTINI 2 angle parameters for DPEHEMS.

Angles			$E_\theta = K_\theta \left[\cos\left(\theta\right) - \cos\left(\theta_0\right)\right]^2$	
Bead A	Bead B	Bead C	K_θ [kcal/mol]	θ_0 [°]
P_2	Q_0	$P_{1,1}$	7.2	91
P_2	Q_0	$P_{1,2}$	44.1	155
$P_{1,1}$	Q_0	$P_{1,2}$	42.8	71
Q_0	$P_{1,1}$	$P_{1,3}$	16.4	146
Q_0	$P_{1,3}$	$P_{1,4}$	16.3	146
$P_{1,1}$	$P_{1,3}$	$C_{4,1}$	6.3	134
$P_{1,2}$	$P_{1,4}$	$C_{4,2}$	5.0	131
$P_{1,3}$	$C_{4,1}$	$C_{1,1}$	5.3	141
$P_{1,4}$	$C_{4,2}$	$C_{1,2}$	11.5	150
$C_{4,1}$	$C_{1,1}$	$C_{1,3}$	5.5	135
$C_{4,2}$	$C_{1,2}$	$C_{1,4}$	7.3	140
$C_{1,1}$	$C_{1,3}$	$C_{1,5}$	3.1	132
$C_{1,2}$	$C_{1,4}$	$C_{1,6}$	6.9	139

iii) DOE

Table A.6.14: MARTINI 2 bead types definitions for DOE.

Bead Types				
Building block	Bead name	MARTINI type	Charge, q [e]	Molar mass, M [kg/kmol]
Quaternary amine	Q_0	Q_0	$+1.0$	54.0
Acetaldehyde	$P_{1,1}$	P_1	-	54.0
Acetaldehyde	$P_{1,2}$	P_1	-	54.0
Butane	$C_{1,1}$	C_1	-	72.0
Butane	$C_{1,2}$	C_1	-	72.0
1-butene	$C_{2,1}$	C_2	-	72.0
1-butene	$C_{2,2}$	C_2	-	72.0
Butane	$C_{1,3}$	C_1	-	72.0
Butane	$C_{1,4}$	C_1	-	72.0
Butane	$C_{1,5}$	C_1	-	72.0
Butane	$C_{1,6}$	C_1	-	72.0

Table A.6.15: CGG MARTINI 2 bond parameters for DOE.

Bonds		$E_\mathrm{b} = K_\mathrm{b}\left(r - r_0\right)^2$	
Bead A	Bead B	K_b [kcal/mol/Å^2]	r_0 [Å]
Q_0	$P_{1,1}$	- (SHAKE)	2.38
Q_0	$P_{1,2}$	- (SHAKE)	2.38
$P_{1,1}$	$C_{1,1}$	3.5	3.52
$P_{1,2}$	$C_{1,2}$	4.7	3.58
$C_{1,1}$	$C_{2,1}$	2.6	4.38
$C_{1,2}$	$C_{2,2}$	1.7	4.28
$C_{2,1}$	$C_{1,3}$	3.2	4.24
$C_{2,2}$	$C_{1,4}$	2.5	4.21
$C_{1,3}$	$C_{1,5}$	2.8	4.57
$C_{1,4}$	$C_{1,6}$	3.2	4.67

Table A.6.16: CGG MARTINI 2 angle parameters for DOE.

Angles			$E_\theta = K_\theta \left[\cos\left(\theta\right) - \cos\left(\theta_0\right)\right]^2$	
Bead A	Bead B	Bead C	K_θ [kcal/mol]	θ_0 [°]
$P_{1,1}$	Q_0	$P_{1,2}$	80.7	83
Q_0	$P_{1,1}$	$C_{1,1}$	15.9	138
Q_0	$P_{1,2}$	$P_{1,2}$	11.5	143
$P_{1,1}$	$C_{1,1}$	$C_{2,1}$	5.3	131
$P_{1,2}$	$C_{1,2}$	$C_{2,2}$	4.6	134
$C_{1,1}$	$C_{2,1}$	$C_{1,3}$	1.8	120
$C_{1,2}$	$C_{2,2}$	$C_{1,4}$	1.9	119
$C_{2,1}$	$C_{1,3}$	$C_{1,5}$	3.7	134
$C_{2,2}$	$C_{1,4}$	$C_{1,6}$	3.3	125

b) Surfactant orientation relative to mean surface-normal direction

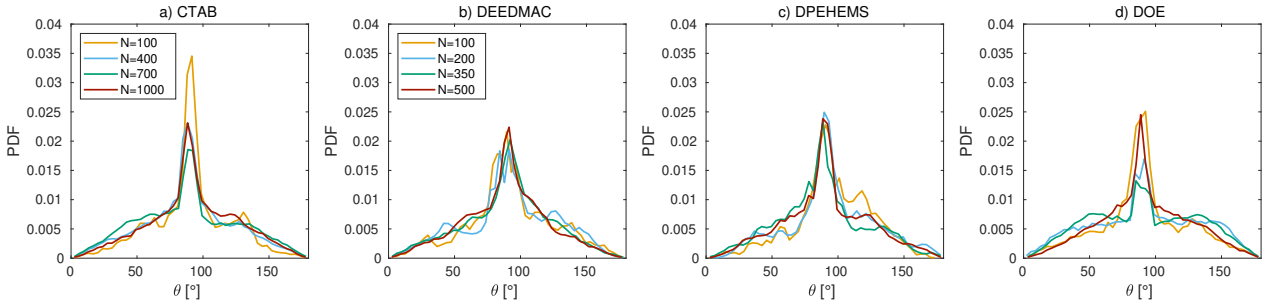


Figure A.6.27: Distribution of surfactant orientations relative to the surface-normal direction z for (a) CTAB, (b) DEEDMAC, (c) DPEHEMS and (d) DOE at various initial concentrations N_0.

A.7 Third-party permissions

Reprinted from external sources (not involved as a co-author) which require special permissions:

1. Chapter 2, Fig. 2.1b) reprints Fig. 1 from Ref.[41].
2. Chapter 2, Fig. 2.3 reprints Fig. 7 from Ref.[92].
3. Chapter 2, Fig. 2.4 reprints Fig. 5 from Ref.[99].
4. Chapter 2, Fig. 2.8 reprints Fig. 8 from Ref.[17].
5. Chapter 2, Fig. 2.9 reprints Fig. 8 from Ref.[210].

The corresponding licenses to re-use are attached below. All remaining reprints are licensed under open access (CC-BY-NC or CC-BY) licenses.

JOHN WILEY AND SONS LICENSE
TERMS AND CONDITIONS

Mar 04, 2024

This Agreement between Mr. Erik Weiand ("You") and John Wiley and Sons ("John Wiley and Sons") consists of your license details and the terms and conditions provided by John Wiley and Sons and Copyright Clearance Center.

License Number	5741850444873
License date	Mar 04, 2024
Licensed Content Publisher	John Wiley and Sons
Licensed Content Publication	Journal of Microscopy
Licensed Content Title	Microscopical investigations on the epicuticle of mammalian keratin fibres
Licensed Content Author	J. R. Smith, J. A. Swift
Licensed Content Date	Dec 21, 2001
Licensed Content Volume	204
Licensed Content Issue	3
Licensed Content Pages	9

Type of use	Dissertation/Thesis
Requestor type	University/Academic
Format	Electronic
Portion	Figure/table
Number of figures/ tables	1
Will you be translating?	No
Title of new work	Coarse-grained molecular simulations of interfaces between fluid formulations and soft biomimetic surfaces
Institution name	Imperial College London
Expected presentation date	May 2024
Portions	Fig. 1
Requestor Location	Mr. Erik Weiand South Kensington Campus London, SW7 2AZ United Kingdom Attn: Imperial College London
Publisher Tax ID	EU826007151
Total	0.00 GBP

Terms and Conditions

TERMS AND CONDITIONS

This copyrighted material is owned by or exclusively licensed to John Wiley & Sons, Inc. or one of its group companies (each a"Wiley Company") or handled on behalf of a society with which a Wiley Company has exclusive publishing rights in relation to a particular work (collectively "WILEY"). By clicking "accept" in connection with completing this licensing transaction, you agree that the following terms and conditions apply to this transaction (along with the billing and payment terms and conditions established by the Copyright Clearance Center Inc., ("CCC's Billing and Payment terms and conditions"), at the time that you opened your RightsLink account (these are available at any time at http://myaccount.copyright.com).

Terms and Conditions

- The materials you have requested permission to reproduce or reuse (the "Wiley Materials") are protected by copyright.

- You are hereby granted a personal, non-exclusive, non-sub licensable (on a stand-alone basis), non-transferable, worldwide, limited license to reproduce the Wiley Materials for the purpose specified in the licensing process. This license, **and any CONTENT (PDF or image file) purchased as part of your order,** is for a one-time use only and limited to any maximum distribution number specified in the license. The first instance of republication or reuse granted by this license must be completed within two years of the date of the grant of this license (although copies prepared before the end date may be distributed thereafter). The Wiley Materials shall not be used in any other manner or for any other purpose, beyond what is granted in the license. Permission is granted subject to an appropriate acknowledgement given to the author, title of the material/book/ journal and the publisher. You shall also duplicate the copyright notice that appears in the Wiley publication in your use of the Wiley Material. Permission is also granted on the understanding that nowhere in the text is a previously published source acknowledged for all or part of this Wiley Material. Any third party content is expressly excluded from this permission.

- With respect to the Wiley Materials, all rights are reserved. Except as expressly granted by the terms of the license, no part of the Wiley Materials may be copied, modified, adapted (except for minor reformatting required by the new Publication), translated, reproduced, transferred or distributed, in any form or by any means, and no derivative works may be made based on the Wiley Materials without the prior permission of the respective copyright owner.**For STM Signatory Publishers clearing permission under the terms of the STM Permissions Guidelines only, the terms of the license are extended to include subsequent editions and for editions in other**

languages, provided such editions are for the work as a whole in situ and does not involve the separate exploitation of the permitted figures or extracts, You may not alter, remove or suppress in any manner any copyright, trademark or other notices displayed by the Wiley Materials. You may not license, rent, sell, loan, lease, pledge, offer as security, transfer or assign the Wiley Materials on a stand-alone basis, or any of the rights granted to you hereunder to any other person.

- The Wiley Materials and all of the intellectual property rights therein shall at all times remain the exclusive property of John Wiley & Sons Inc, the Wiley Companies, or their respective licensors, and your interest therein is only that of having possession of and the right to reproduce the Wiley Materials pursuant to Section 2 herein during the continuance of this Agreement. You agree that you own no right, title or interest in or to the Wiley Materials or any of the intellectual property rights therein. You shall have no rights hereunder other than the license as provided for above in Section 2. No right, license or interest to any trademark, trade name, service mark or other branding ("Marks") of WILEY or its licensors is granted hereunder, and you agree that you shall not assert any such right, license or interest with respect thereto

- NEITHER WILEY NOR ITS LICENSORS MAKES ANY WARRANTY OR REPRESENTATION OF ANY KIND TO YOU OR ANY THIRD PARTY, EXPRESS, IMPLIED OR STATUTORY, WITH RESPECT TO THE MATERIALS OR THE ACCURACY OF ANY INFORMATION CONTAINED IN THE MATERIALS, INCLUDING, WITHOUT LIMITATION, ANY IMPLIED WARRANTY OF MERCHANTABILITY, ACCURACY, SATISFACTORY QUALITY, FITNESS FOR A PARTICULAR PURPOSE, USABILITY, INTEGRATION OR NON-INFRINGEMENT AND ALL SUCH WARRANTIES ARE HEREBY EXCLUDED BY WILEY AND ITS LICENSORS AND WAIVED BY YOU.

- WILEY shall have the right to terminate this Agreement immediately upon breach of this Agreement by you.

- You shall indemnify, defend and hold harmless WILEY, its Licensors and their respective directors, officers, agents and employees, from and against any actual or threatened claims, demands, causes of action or proceedings arising from any breach of this Agreement by you.

- IN NO EVENT SHALL WILEY OR ITS LICENSORS BE LIABLE TO YOU OR ANY OTHER PARTY OR ANY OTHER PERSON OR ENTITY FOR ANY SPECIAL, CONSEQUENTIAL, INCIDENTAL, INDIRECT, EXEMPLARY OR PUNITIVE DAMAGES, HOWEVER CAUSED, ARISING OUT OF OR IN CONNECTION WITH THE DOWNLOADING, PROVISIONING, VIEWING OR USE OF THE MATERIALS REGARDLESS OF THE FORM OF ACTION, WHETHER FOR BREACH OF CONTRACT, BREACH OF

WARRANTY, TORT, NEGLIGENCE, INFRINGEMENT OR OTHERWISE (INCLUDING, WITHOUT LIMITATION, DAMAGES BASED ON LOSS OF PROFITS, DATA, FILES, USE, BUSINESS OPPORTUNITY OR CLAIMS OF THIRD PARTIES), AND WHETHER OR NOT THE PARTY HAS BEEN ADVISED OF THE POSSIBILITY OF SUCH DAMAGES. THIS LIMITATION SHALL APPLY NOTWITHSTANDING ANY FAILURE OF ESSENTIAL PURPOSE OF ANY LIMITED REMEDY PROVIDED HEREIN.

- Should any provision of this Agreement be held by a court of competent jurisdiction to be illegal, invalid, or unenforceable, that provision shall be deemed amended to achieve as nearly as possible the same economic effect as the original provision, and the legality, validity and enforceability of the remaining provisions of this Agreement shall not be affected or impaired thereby.

- The failure of either party to enforce any term or condition of this Agreement shall not constitute a waiver of either party's right to enforce each and every term and condition of this Agreement. No breach under this agreement shall be deemed waived or excused by either party unless such waiver or consent is in writing signed by the party granting such waiver or consent. The waiver by or consent of a party to a breach of any provision of this Agreement shall not operate or be construed as a waiver of or consent to any other or subsequent breach by such other party.

- This Agreement may not be assigned (including by operation of law or otherwise) by you without WILEY's prior written consent.

- Any fee required for this permission shall be non-refundable after thirty (30) days from receipt by the CCC.

- These terms and conditions together with CCC's Billing and Payment terms and conditions (which are incorporated herein) form the entire agreement between you and WILEY concerning this licensing transaction and (in the absence of fraud) supersedes all prior agreements and representations of the parties, oral or written. This Agreement may not be amended except in writing signed by both parties. This Agreement shall be binding upon and inure to the benefit of the parties' successors, legal representatives, and authorized assigns.

- In the event of any conflict between your obligations established by these terms and conditions and those established by CCC's Billing and Payment terms and conditions, these terms and conditions shall prevail.

- WILEY expressly reserves all rights not specifically granted in the combination of (i) the license details provided by you and accepted in the course of this licensing transaction, (ii) these terms and conditions and (iii) CCC's Billing and Payment terms and conditions.

- This Agreement will be void if the Type of Use, Format, Circulation, or Requestor Type was misrepresented during the licensing process.

- This Agreement shall be governed by and construed in accordance with the laws of the State of New York, USA, without regards to such state's conflict of law rules. Any legal action, suit or proceeding arising out of or relating to these Terms and Conditions or the breach thereof shall be instituted in a court of competent jurisdiction in New York County in the State of New York in the United States of America and each party hereby consents and submits to the personal jurisdiction of such court, waives any objection to venue in such court and consents to service of process by registered or certified mail, return receipt requested, at the last known address of such party.

WILEY OPEN ACCESS TERMS AND CONDITIONS

Wiley Publishes Open Access Articles in fully Open Access Journals and in Subscription journals offering Online Open. Although most of the fully Open Access journals publish open access articles under the terms of the Creative Commons Attribution (CC BY) License only, the subscription journals and a few of the Open Access Journals offer a choice of Creative Commons Licenses. The license type is clearly identified on the article.

The Creative Commons Attribution License

The Creative Commons Attribution License (CC-BY) allows users to copy, distribute and transmit an article, adapt the article and make commercial use of the article. The CC-BY license permits commercial and non-

Creative Commons Attribution Non-Commercial License

The Creative Commons Attribution Non-Commercial (CC-BY-NC)License permits use, distribution and reproduction in any medium, provided the original work is properly cited and is not used for commercial purposes.(see below)

Creative Commons Attribution-Non-Commercial-NoDerivs License

The Creative Commons Attribution Non-Commercial-NoDerivs License (CC-BY-NC-ND) permits use, distribution and reproduction in any medium, provided the original work is properly cited, is not used for commercial purposes and no modifications or adaptations are made. (see below)

Use by commercial "for-profit" organizations

Use of Wiley Open Access articles for commercial, promotional, or marketing purposes requires further explicit permission from Wiley and will be subject to a fee.

Further details can be found on Wiley Online Library http://olabout.wiley.com/WileyCDA/Section/id-410895.html

Other Terms and Conditions:

v1.10 Last updated September 2015

Questions? customercare@copyright.com.

RightsLink

EW

Distribution and Localization of Hydrophobic and Ionic Chemical Groups at the Surface of Bleached Human Hair Fibers

Author: Michael Korte, Sabri Akari, Harald Kühn, et al
Publication: Langmuir
Publisher: American Chemical Society
Date: Oct 1, 2014

Copyright © 2014, American Chemical Society

PERMISSION/LICENSE IS GRANTED FOR YOUR ORDER AT NO CHARGE

This type of permission/license, instead of the standard Terms and Conditions, is sent to you because no fee is being charged for your order. Please note the following:

- Permission is granted for your request in both print and electronic formats, and translations.
- If figures and/or tables were requested, they may be adapted or used in part.
- Please print this page for your records and send a copy of it to your publisher/graduate school.
- Appropriate credit for the requested material should be given as follows: "Reprinted (adapted) with permission from {COMPLETE REFERENCE CITATION}. Copyright {YEAR} American Chemical Society." Insert appropriate information in place of the capitalized words.
- One-time permission is granted only for the use specified in your RightsLink request. No additional uses are granted (such as derivative works or other editions). For any uses, please submit a new request.

If credit is given to another source for the material you requested from RightsLink, permission must be obtained from that source.

BACK CLOSE WINDOW

© 2024 Copyright - All Rights Reserved | Copyright Clearance Center, Inc. | Privacy statement | Data Security and Privacy | For California Residents | Terms and ConditionsComments? We would like to hear from you. E-mail us at customercare@copyright.com

RightsLink

EW

Nanoscale Surface Charge Visualization of Human Hair

Author: Faduma M. Maddar, David Perry, Rhiannon Brooks, et al
Publication: Analytical Chemistry
Publisher: American Chemical Society
Date: Apr 1, 2019

Copyright © 2019, American Chemical Society

PERMISSION/LICENSE IS GRANTED FOR YOUR ORDER AT NO CHARGE

This type of permission/license, instead of the standard Terms and Conditions, is sent to you because no fee is being charged for your order. Please note the following:

- Permission is granted for your request in both print and electronic formats, and translations.
- If figures and/or tables were requested, they may be adapted or used in part.
- Please print this page for your records and send a copy of it to your publisher/graduate school.
- Appropriate credit for the requested material should be given as follows: "Reprinted (adapted) with permission from {COMPLETE REFERENCE CITATION}. Copyright {YEAR} American Chemical Society." Insert appropriate information in place of the capitalized words.
- One-time permission is granted only for the use specified in your RightsLink request. No additional uses are granted (such as derivative works or other editions). For any uses, please submit a new request.

If credit is given to another source for the material you requested from RightsLink, permission must be obtained from that source.

BACK CLOSE WINDOW

© 2024 Copyright - All Rights Reserved | Copyright Clearance Center, Inc. | Privacy statement | Data Security and Privacy | For California Residents | Terms and ConditionsComments? We would like to hear from you. E-mail us at customercare@copyright.com

ELSEVIER LICENSE
TERMS AND CONDITIONS

Mar 04, 2024

This Agreement between Mr. Erik Weiand ("You") and Elsevier ("Elsevier") consists of your license details and the terms and conditions provided by Elsevier and Copyright Clearance Center.

License Number	5741850855722
License date	Mar 04, 2024
Licensed Content Publisher	Elsevier
Licensed Content Publication	Ultramicroscopy
Licensed Content Title	Nanotribological characterization of human hair and skin using atomic force microscopy
Licensed Content Author	Carmen LaTorre,Bharat Bhushan
Licensed Content Date	Nov 1, 2005
Licensed Content Volume	105
Licensed Content Issue	1-4
Licensed Content Pages	21
Start Page	155

End Page	175
Type of Use	reuse in a thesis/dissertation
Portion	figures/tables/illustrations
Number of figures/ tables/illustrations	1
Format	electronic
Are you the author of this Elsevier article?	No
Will you be translating?	No
Title of new work	Coarse-grained molecular simulations of interfaces between fluid formulations and soft biomimetic surfaces
Institution name	Imperial College London
Expected presentation date	May 2024
Portions	Fig. 8
Requestor Location	Mr. Erik Weiand South Kensington Campus London, SW7 2AZ United Kingdom Attn: Imperial College London
Publisher Tax ID	GB 494 6272 12
Total	0.00 GBP

Terms and Conditions

INTRODUCTION

1. The publisher for this copyrighted material is Elsevier. By clicking "accept" in connection with completing this licensing transaction, you agree that the following terms and conditions apply to this transaction (along with the Billing and Payment terms and conditions established by Copyright Clearance Center, Inc. ("CCC"), at the time that you opened your RightsLink account and that are available at any time at https://myaccount.copyright.com).

GENERAL TERMS

2. Elsevier hereby grants you permission to reproduce the aforementioned material subject to the terms and conditions indicated.

3. Acknowledgement: If any part of the material to be used (for example, figures) has appeared in our publication with credit or acknowledgement to another source, permission must also be sought from that source. If such permission is not obtained then that material may not be included in your publication/copies. Suitable acknowledgement to the source must be made, either as a footnote or in a reference list at the end of your publication, as follows:

"Reprinted from Publication title, Vol /edition number, Author(s), Title of article / title of chapter, Pages No., Copyright (Year), with permission from Elsevier [OR APPLICABLE SOCIETY COPYRIGHT OWNER]." Also Lancet special credit - "Reprinted from The Lancet, Vol. number, Author(s), Title of article, Pages No., Copyright (Year), with permission from Elsevier."

4. Reproduction of this material is confined to the purpose and/or media for which permission is hereby given. The material may not be reproduced or used in any other way, including use in combination with an artificial intelligence tool (including to train an algorithm, test, process, analyse, generate output and/or develop any form of artificial intelligence tool), or to create any derivative work and/or service (including resulting from the use of artificial intelligence tools).

5. Altering/Modifying Material: Not Permitted. However figures and illustrations may be altered/adapted minimally to serve your work. Any other abbreviations, additions, deletions and/or any other alterations shall be made only with prior written authorization of Elsevier Ltd. (Please contact Elsevier's permissions helpdesk here). No modifications can be made to any Lancet figures/tables and they must be reproduced in full.

6. If the permission fee for the requested use of our material is waived in this instance, please be advised that your future requests for Elsevier materials may attract a fee.

7. Reservation of Rights: Publisher reserves all rights not specifically granted in the combination of (i) the license details provided by you and accepted in the course of this licensing transaction, (ii) these terms and conditions and (iii) CCC's Billing and Payment terms and conditions.

8. License Contingent Upon Payment: While you may exercise the rights licensed immediately upon issuance of the license at the end of the licensing process for the transaction, provided that you have disclosed complete and accurate details of your proposed use, no license is finally effective unless and until full payment is received from you (either by publisher or by CCC) as provided in CCC's Billing and Payment terms and conditions. If full payment is not received on a timely basis, then any license preliminarily granted shall be deemed automatically revoked and shall be void as if never granted. Further, in the event that you breach any of these terms and conditions or any of CCC's Billing and Payment terms and conditions, the license is automatically revoked and shall be void as if never granted. Use of materials as described in a revoked license, as well as any use of the materials beyond the scope of an unrevoked license, may constitute copyright infringement and publisher reserves the right to take any and all action to protect its copyright in the materials.

9. Warranties: Publisher makes no representations or warranties with respect to the licensed material.

10. Indemnity: You hereby indemnify and agree to hold harmless publisher and CCC, and their respective officers, directors, employees and agents, from and against any and all claims arising out of your use of the licensed material other than as specifically authorized pursuant to this license.

11. No Transfer of License: This license is personal to you and may not be sublicensed, assigned, or transferred by you to any other person without publisher's written permission.

12. No Amendment Except in Writing: This license may not be amended except in a writing signed by both parties (or, in the case of publisher, by CCC on publisher's behalf).

13. Objection to Contrary Terms: Publisher hereby objects to any terms contained in any purchase order, acknowledgment, check endorsement or other writing prepared by you, which terms are inconsistent with these terms and conditions or CCC's Billing and Payment terms and conditions. These terms and conditions, together with CCC's Billing and Payment terms and conditions (which are incorporated herein), comprise the entire agreement between you and publisher (and CCC) concerning this licensing transaction. In the event of any conflict between your obligations established by these terms and conditions and those established by CCC's Billing and Payment terms and conditions, these terms and conditions shall control.

14. Revocation: Elsevier or Copyright Clearance Center may deny the permissions described in this License at their sole discretion, for any reason or no reason, with a full refund payable to you. Notice of such denial will be made using the contact information provided by you. Failure to receive such notice will not alter or invalidate the denial. In no event will Elsevier or Copyright Clearance Center be responsible or liable for any costs, expenses or damage incurred by you as a result of a denial of your permission request, other than a refund of the amount(s) paid by you to Elsevier and/or Copyright Clearance Center for denied permissions.

LIMITED LICENSE

The following terms and conditions apply only to specific license types:

15. **Translation**: This permission is granted for non-exclusive world **English** rights only unless your license was granted for translation rights. If you licensed translation rights you may only translate this content into the languages you requested. A professional translator must perform all translations and reproduce the content word for word preserving the integrity of the article.

16. **Posting licensed content on any Website**: The following terms and conditions apply as follows: Licensing material from an Elsevier journal: All content posted to the web site must maintain the copyright information line on the bottom of each image; A hyper-text must be included to the Homepage of the journal from which you are licensing at http://www.sciencedirect.com/science/journal/xxxxx or the Elsevier homepage for books at http://www.elsevier.com; Central Storage: This license does not include permission for a scanned version of the material to be stored in a central repository such as that provided by Heron/XanEdu.

Licensing material from an Elsevier book: A hyper-text link must be included to the Elsevier homepage at http://www.elsevier.com . All content posted to the web site must maintain the copyright information line on the bottom of each image.

Posting licensed content on Electronic reserve: In addition to the above the following clauses are applicable: The web site must be password-protected and made available only to bona fide students registered on a relevant course. This permission is granted for 1 year only. You may obtain a new license for future website posting.

17. **For journal authors:** the following clauses are applicable in addition to the above:

Preprints:

A preprint is an author's own write-up of research results and analysis, it has not been peer-reviewed, nor has it had any other value

added to it by a publisher (such as formatting, copyright, technical enhancement etc.).

Authors can share their preprints anywhere at any time. Preprints should not be added to or enhanced in any way in order to appear more like, or to substitute for, the final versions of articles however authors can update their preprints on arXiv or RePEc with their Accepted Author Manuscript (see below).

If accepted for publication, we encourage authors to link from the preprint to their formal publication via its DOI. Millions of researchers have access to the formal publications on ScienceDirect, and so links will help users to find, access, cite and use the best available version. Please note that Cell Press, The Lancet and some society-owned have different preprint policies. Information on these policies is available on the journal homepage.

Accepted Author Manuscripts: An accepted author manuscript is the manuscript of an article that has been accepted for publication and which typically includes author-incorporated changes suggested during submission, peer review and editor-author communications.

Authors can share their accepted author manuscript:

- immediately
  - via their non-commercial person homepage or blog
  - by updating a preprint in arXiv or RePEc with the accepted manuscript
  - via their research institute or institutional repository for internal institutional uses or as part of an invitation-only research collaboration work-group
  - directly by providing copies to their students or to research collaborators for their personal use
  - for private scholarly sharing as part of an invitation-only work group on commercial sites with which Elsevier has an agreement
- After the embargo period
  - via non-commercial hosting platforms such as their institutional repository
  - via commercial sites with which Elsevier has an agreement

In all cases accepted manuscripts should:

- link to the formal publication via its DOI
- bear a CC-BY-NC-ND license - this is easy to do
- if aggregated with other manuscripts, for example in a repository or other site, be shared in alignment with our hosting policy not be added to or enhanced in any way to appear more like, or to substitute for, the published journal article.

Published journal article (JPA): A published journal article (PJA) is the definitive final record of published research that appears or will appear in the journal and embodies all value-adding publishing activities including peer review co-ordination, copy-editing,

formatting, (if relevant) pagination and online enrichment.

Policies for sharing publishing journal articles differ for subscription and gold open access articles:

Subscription Articles: If you are an author, please share a link to your article rather than the full-text. Millions of researchers have access to the formal publications on ScienceDirect, and so links will help your users to find, access, cite, and use the best available version.

Theses and dissertations which contain embedded PJAs as part of the formal submission can be posted publicly by the awarding institution with DOI links back to the formal publications on ScienceDirect.

If you are affiliated with a library that subscribes to ScienceDirect you have additional private sharing rights for others' research accessed under that agreement. This includes use for classroom teaching and internal training at the institution (including use in course packs and courseware programs), and inclusion of the article for grant funding purposes.

Gold Open Access Articles: May be shared according to the author-selected end-user license and should contain a CrossMark logo, the end user license, and a DOI link to the formal publication on ScienceDirect.

Please refer to Elsevier's posting policy for further information.

18. **For book authors** the following clauses are applicable in addition to the above: Authors are permitted to place a brief summary of their work online only. You are not allowed to download and post the published electronic version of your chapter, nor may you scan the printed edition to create an electronic version. **Posting to a repository:** Authors are permitted to post a summary of their chapter only in their institution's repository.

19. **Thesis/Dissertation**: If your license is for use in a thesis/ dissertation your thesis may be submitted to your institution in either print or electronic form. Should your thesis be published commercially, please reapply for permission. These requirements include permission for the Library and Archives of Canada to supply single copies, on demand, of the complete thesis and include permission for Proquest/UMI to supply single copies, on demand, of the complete thesis. Should your thesis be published commercially, please reapply for permission. Theses and dissertations which contain embedded PJAs as part of the formal submission can be posted publicly by the awarding institution with DOI links back to the formal publications on ScienceDirect.

Elsevier Open Access Terms and Conditions

You can publish open access with Elsevier in hundreds of open access

journals or in nearly 2000 established subscription journals that support open access publishing. Permitted third party re-use of these open access articles is defined by the author's choice of Creative Commons user license. See our open access license policy for more information.

Terms & Conditions applicable to all Open Access articles published with Elsevier:

Any reuse of the article must not represent the author as endorsing the adaptation of the article nor should the article be modified in such a way as to damage the author's honour or reputation. If any changes have been made, such changes must be clearly indicated.

The author(s) must be appropriately credited and we ask that you include the end user license and a DOI link to the formal publication on ScienceDirect.

If any part of the material to be used (for example, figures) has appeared in our publication with credit or acknowledgement to another source it is the responsibility of the user to ensure their reuse complies with the terms and conditions determined by the rights holder.

Additional Terms & Conditions applicable to each Creative Commons user license:

CC BY: The CC-BY license allows users to copy, to create extracts, abstracts and new works from the Article, to alter and revise the Article and to make commercial use of the Article (including reuse and/or resale of the Article by commercial entities), provided the user gives appropriate credit (with a link to the formal publication through the relevant DOI), provides a link to the license, indicates if changes were made and the licensor is not represented as endorsing the use made of the work. The full details of the license are available at http://creativecommons.org/licenses/by/4.0.

CC BY NC SA: The CC BY-NC-SA license allows users to copy, to create extracts, abstracts and new works from the Article, to alter and revise the Article, provided this is not done for commercial purposes, and that the user gives appropriate credit (with a link to the formal publication through the relevant DOI), provides a link to the license, indicates if changes were made and the licensor is not represented as endorsing the use made of the work. Further, any new works must be made available on the same conditions. The full details of the license are available at http://creativecommons.org/licenses/by-nc-sa/4.0.

CC BY NC ND: The CC BY-NC-ND license allows users to copy and distribute the Article, provided this is not done for commercial purposes and further does not permit distribution of the Article if it is changed or edited in any way, and provided the user gives appropriate credit (with a link to the formal publication through the relevant DOI), provides a link to the license, and that the licensor is not represented as endorsing the use made of the work. The full details of the license

are available at http://creativecommons.org/licenses/by-nc-nd/4.0. Any commercial reuse of Open Access articles published with a CC BY NC SA or CC BY NC ND license requires permission from Elsevier and will be subject to a fee.

Commercial reuse includes:

- Associating advertising with the full text of the Article
- Charging fees for document delivery or access
- Article aggregation
- Systematic distribution via e-mail lists or share buttons

Posting or linking by commercial companies for use by customers of those companies.

20. **Other Conditions**:

v1.10

Questions? customercare@copyright.com.

ELSEVIER LICENSE
TERMS AND CONDITIONS

Mar 04, 2024

This Agreement between Mr. Erik Weiand ("You") and Elsevier ("Elsevier") consists of your license details and the terms and conditions provided by Elsevier and Copyright Clearance Center.

License Number	5741851009358
License date	Mar 04, 2024
Licensed Content Publisher	Elsevier
Licensed Content Publication	Ultramicroscopy
Licensed Content Title	A novel AFM based method for force measurements between individual hair strands
Licensed Content Author	Eva Max,Wolfgang Häfner,Frank Wilco Bartels,Albert Sugiharto,Claudia Wood,Andreas Fery
Licensed Content Date	Mar 1, 2010
Licensed Content Volume	110
Licensed Content Issue	4
Licensed Content Pages	5

Start Page	320
End Page	324
Type of Use	reuse in a thesis/dissertation
Portion	figures/tables/illustrations
Number of figures/ tables/illustrations	1
Format	electronic
Are you the author of this Elsevier article?	No
Will you be translating?	No
Title of new work	Coarse-grained molecular simulations of interfaces between fluid formulations and soft biomimetic surfaces
Institution name	Imperial College London
Expected presentation date	May 2024
Portions	Fig. 8
Requestor Location	Mr. Erik Weiand South Kensington Campus London, SW7 2AZ United Kingdom Attn: Imperial College London
Publisher Tax ID	GB 494 6272 12

Total 0.00 GBP

Terms and Conditions

INTRODUCTION

1. The publisher for this copyrighted material is Elsevier. By clicking "accept" in connection with completing this licensing transaction, you agree that the following terms and conditions apply to this transaction (along with the Billing and Payment terms and conditions established by Copyright Clearance Center, Inc. ("CCC"), at the time that you opened your RightsLink account and that are available at any time at https://myaccount.copyright.com).

GENERAL TERMS

2. Elsevier hereby grants you permission to reproduce the aforementioned material subject to the terms and conditions indicated.

3. Acknowledgement: If any part of the material to be used (for example, figures) has appeared in our publication with credit or acknowledgement to another source, permission must also be sought from that source. If such permission is not obtained then that material may not be included in your publication/copies. Suitable acknowledgement to the source must be made, either as a footnote or in a reference list at the end of your publication, as follows:

"Reprinted from Publication title, Vol /edition number, Author(s), Title of article / title of chapter, Pages No., Copyright (Year), with permission from Elsevier [OR APPLICABLE SOCIETY COPYRIGHT OWNER]." Also Lancet special credit - "Reprinted from The Lancet, Vol. number, Author(s), Title of article, Pages No., Copyright (Year), with permission from Elsevier."

4. Reproduction of this material is confined to the purpose and/or media for which permission is hereby given. The material may not be reproduced or used in any other way, including use in combination with an artificial intelligence tool (including to train an algorithm, test, process, analyse, generate output and/or develop any form of artificial intelligence tool), or to create any derivative work and/or service (including resulting from the use of artificial intelligence tools).

5. Altering/Modifying Material: Not Permitted. However figures and illustrations may be altered/adapted minimally to serve your work. Any other abbreviations, additions, deletions and/or any other alterations shall be made only with prior written authorization of Elsevier Ltd. (Please contact Elsevier's permissions helpdesk here). No modifications can be made to any Lancet figures/tables and they must be reproduced in full.

6. If the permission fee for the requested use of our material is waived in this instance, please be advised that your future requests for Elsevier materials may attract a fee.

7. Reservation of Rights: Publisher reserves all rights not specifically granted in the combination of (i) the license details provided by you and accepted in the course of this licensing transaction, (ii) these terms and conditions and (iii) CCC's Billing and Payment terms and conditions.

8. License Contingent Upon Payment: While you may exercise the rights licensed immediately upon issuance of the license at the end of the licensing process for the transaction, provided that you have disclosed complete and accurate details of your proposed use, no license is finally effective unless and until full payment is received from you (either by publisher or by CCC) as provided in CCC's Billing and Payment terms and conditions. If full payment is not received on a timely basis, then any license preliminarily granted shall be deemed automatically revoked and shall be void as if never granted. Further, in the event that you breach any of these terms and conditions or any of CCC's Billing and Payment terms and conditions, the license is automatically revoked and shall be void as if never granted. Use of materials as described in a revoked license, as well as any use of the materials beyond the scope of an unrevoked license, may constitute copyright infringement and publisher reserves the right to take any and all action to protect its copyright in the materials.

9. Warranties: Publisher makes no representations or warranties with respect to the licensed material.

10. Indemnity: You hereby indemnify and agree to hold harmless publisher and CCC, and their respective officers, directors, employees and agents, from and against any and all claims arising out of your use of the licensed material other than as specifically authorized pursuant to this license.

11. No Transfer of License: This license is personal to you and may not be sublicensed, assigned, or transferred by you to any other person without publisher's written permission.

12. No Amendment Except in Writing: This license may not be amended except in a writing signed by both parties (or, in the case of publisher, by CCC on publisher's behalf).

13. Objection to Contrary Terms: Publisher hereby objects to any terms contained in any purchase order, acknowledgment, check endorsement or other writing prepared by you, which terms are inconsistent with these terms and conditions or CCC's Billing and Payment terms and conditions. These terms and conditions, together with CCC's Billing and Payment terms and conditions (which are incorporated herein), comprise the entire agreement between you and publisher (and CCC) concerning this licensing transaction. In the event of any conflict between your obligations established by these

terms and conditions and those established by CCC's Billing and Payment terms and conditions, these terms and conditions shall control.

14. Revocation: Elsevier or Copyright Clearance Center may deny the permissions described in this License at their sole discretion, for any reason or no reason, with a full refund payable to you. Notice of such denial will be made using the contact information provided by you. Failure to receive such notice will not alter or invalidate the denial. In no event will Elsevier or Copyright Clearance Center be responsible or liable for any costs, expenses or damage incurred by you as a result of a denial of your permission request, other than a refund of the amount(s) paid by you to Elsevier and/or Copyright Clearance Center for denied permissions.

LIMITED LICENSE

The following terms and conditions apply only to specific license types:

15. **Translation**: This permission is granted for non-exclusive world **English** rights only unless your license was granted for translation rights. If you licensed translation rights you may only translate this content into the languages you requested. A professional translator must perform all translations and reproduce the content word for word preserving the integrity of the article.

16. **Posting licensed content on any Website**: The following terms and conditions apply as follows: Licensing material from an Elsevier journal: All content posted to the web site must maintain the copyright information line on the bottom of each image; A hyper-text must be included to the Homepage of the journal from which you are licensing at http://www.sciencedirect.com/science/journal/xxxxx or the Elsevier homepage for books at http://www.elsevier.com; Central Storage: This license does not include permission for a scanned version of the material to be stored in a central repository such as that provided by Heron/XanEdu.

Licensing material from an Elsevier book: A hyper-text link must be included to the Elsevier homepage at http://www.elsevier.com . All content posted to the web site must maintain the copyright information line on the bottom of each image.

Posting licensed content on Electronic reserve: In addition to the above the following clauses are applicable: The web site must be password-protected and made available only to bona fide students registered on a relevant course. This permission is granted for 1 year only. You may obtain a new license for future website posting.

17. **For journal authors:** the following clauses are applicable in addition to the above:

Preprints:

A preprint is an author's own write-up of research results and analysis, it has not been peer-reviewed, nor has it had any other value added to it by a publisher (such as formatting, copyright, technical enhancement etc.).

Authors can share their preprints anywhere at any time. Preprints should not be added to or enhanced in any way in order to appear more like, or to substitute for, the final versions of articles however authors can update their preprints on arXiv or RePEc with their Accepted Author Manuscript (see below).

If accepted for publication, we encourage authors to link from the preprint to their formal publication via its DOI. Millions of researchers have access to the formal publications on ScienceDirect, and so links will help users to find, access, cite and use the best available version. Please note that Cell Press, The Lancet and some society-owned have different preprint policies. Information on these policies is available on the journal homepage.

Accepted Author Manuscripts: An accepted author manuscript is the manuscript of an article that has been accepted for publication and which typically includes author-incorporated changes suggested during submission, peer review and editor-author communications.

Authors can share their accepted author manuscript:

- immediately
    - via their non-commercial person homepage or blog
    - by updating a preprint in arXiv or RePEc with the accepted manuscript
    - via their research institute or institutional repository for internal institutional uses or as part of an invitation-only research collaboration work-group
    - directly by providing copies to their students or to research collaborators for their personal use
    - for private scholarly sharing as part of an invitation-only work group on commercial sites with which Elsevier has an agreement
- After the embargo period
    - via non-commercial hosting platforms such as their institutional repository
    - via commercial sites with which Elsevier has an agreement

In all cases accepted manuscripts should:

- link to the formal publication via its DOI
- bear a CC-BY-NC-ND license - this is easy to do
- if aggregated with other manuscripts, for example in a repository or other site, be shared in alignment with our hosting policy not be added to or enhanced in any way to appear more like, or to substitute for, the published journal article.

Published journal article (JPA): A published journal article (PJA) is

the definitive final record of published research that appears or will appear in the journal and embodies all value-adding publishing activities including peer review co-ordination, copy-editing, formatting, (if relevant) pagination and online enrichment.

Policies for sharing publishing journal articles differ for subscription and gold open access articles:

Subscription Articles: If you are an author, please share a link to your article rather than the full-text. Millions of researchers have access to the formal publications on ScienceDirect, and so links will help your users to find, access, cite, and use the best available version.

Theses and dissertations which contain embedded PJAs as part of the formal submission can be posted publicly by the awarding institution with DOI links back to the formal publications on ScienceDirect.

If you are affiliated with a library that subscribes to ScienceDirect you have additional private sharing rights for others' research accessed under that agreement. This includes use for classroom teaching and internal training at the institution (including use in course packs and courseware programs), and inclusion of the article for grant funding purposes.

Gold Open Access Articles: May be shared according to the author-selected end-user license and should contain a CrossMark logo, the end user license, and a DOI link to the formal publication on ScienceDirect.

Please refer to Elsevier's posting policy for further information.

18. **For book authors** the following clauses are applicable in addition to the above: Authors are permitted to place a brief summary of their work online only. You are not allowed to download and post the published electronic version of your chapter, nor may you scan the printed edition to create an electronic version. **Posting to a repository:** Authors are permitted to post a summary of their chapter only in their institution's repository.

19. **Thesis/Dissertation**: If your license is for use in a thesis/ dissertation your thesis may be submitted to your institution in either print or electronic form. Should your thesis be published commercially, please reapply for permission. These requirements include permission for the Library and Archives of Canada to supply single copies, on demand, of the complete thesis and include permission for Proquest/UMI to supply single copies, on demand, of the complete thesis. Should your thesis be published commercially, please reapply for permission. Theses and dissertations which contain embedded PJAs as part of the formal submission can be posted publicly by the awarding institution with DOI links back to the formal publications on ScienceDirect.

Elsevier Open Access Terms and Conditions

You can publish open access with Elsevier in hundreds of open access journals or in nearly 2000 established subscription journals that support open access publishing. Permitted third party re-use of these open access articles is defined by the author's choice of Creative Commons user license. See our open access license policy for more information.

Terms & Conditions applicable to all Open Access articles published with Elsevier:

Any reuse of the article must not represent the author as endorsing the adaptation of the article nor should the article be modified in such a way as to damage the author's honour or reputation. If any changes have been made, such changes must be clearly indicated.

The author(s) must be appropriately credited and we ask that you include the end user license and a DOI link to the formal publication on ScienceDirect.

If any part of the material to be used (for example, figures) has appeared in our publication with credit or acknowledgement to another source it is the responsibility of the user to ensure their reuse complies with the terms and conditions determined by the rights holder.

Additional Terms & Conditions applicable to each Creative Commons user license:

CC BY: The CC-BY license allows users to copy, to create extracts, abstracts and new works from the Article, to alter and revise the Article and to make commercial use of the Article (including reuse and/or resale of the Article by commercial entities), provided the user gives appropriate credit (with a link to the formal publication through the relevant DOI), provides a link to the license, indicates if changes were made and the licensor is not represented as endorsing the use made of the work. The full details of the license are available at http://creativecommons.org/licenses/by/4.0.

CC BY NC SA: The CC BY-NC-SA license allows users to copy, to create extracts, abstracts and new works from the Article, to alter and revise the Article, provided this is not done for commercial purposes, and that the user gives appropriate credit (with a link to the formal publication through the relevant DOI), provides a link to the license, indicates if changes were made and the licensor is not represented as endorsing the use made of the work. Further, any new works must be made available on the same conditions. The full details of the license are available at http://creativecommons.org/licenses/by-nc-sa/4.0.

CC BY NC ND: The CC BY-NC-ND license allows users to copy and distribute the Article, provided this is not done for commercial purposes and further does not permit distribution of the Article if it is

changed or edited in any way, and provided the user gives appropriate credit (with a link to the formal publication through the relevant DOI), provides a link to the license, and that the licensor is not represented as endorsing the use made of the work. The full details of the license are available at http://creativecommons.org/licenses/by-nc-nd/4.0. Any commercial reuse of Open Access articles published with a CC BY NC SA or CC BY NC ND license requires permission from Elsevier and will be subject to a fee.

Commercial reuse includes:

- Associating advertising with the full text of the Article
- Charging fees for document delivery or access
- Article aggregation
- Systematic distribution via e-mail lists or share buttons

Posting or linking by commercial companies for use by customers of those companies.

20. **Other Conditions**:

v1.10

Questions? customercare@copyright.com.